DOE CONF – 911125
NIPER–558/1

PREPRINTS
VOLUME 1: Technical Papers

THIRD INTERNATIONAL
RESERVOIR CHARACTERIZATION
TECHNICAL CONFERENCE

November 3 – 5, 1991
Tulsa, Oklahoma

Co-Sponsors

IIT Research Institute • National Institute for Petroleum and Energy Research
and
U.S. Department of Energy

TABLE OF CONTENTS

3RC-94 *Integrated Outcrop and Subsurface Reservoir Characterization: Carbonate Sequence Stratigraphy and Reservoir Behavior of the Giant Aneth Oil Field, SE Utah*, F.M. Wright and L.J. Weber, Mobil Exploration and Producing U.S. Inc., Midland, Texas

3RC-53 *Comparison of Geostatistical Estimation Methods for the Kern River Field*, Joseph P. Vogt, Texaco, Inc., Houston, Texas

Technical Session 3 – Modeling/Description of Interwell Region
Co-Chairmen: Steve Begg, BP Exploration, Anchorage, Alaska;
Mohan Kelkar, University of Tulsa, Tulsa, Oklahoma

3RC-29 *An Application of the "PETRA" Geological Simulator to the Frontier Formation, Wyoming*, P. Armitage and R.J. Norris, Winfrith Technology Centre, Dorchester, United Kingdom

3RC-87 *Assessing Distributions of Reservoir Properties Using Horizontal Well Data*, G. Perez and M. Kelkar , University of Tulsa, Tulsa, Oklahoma

3RC-17 *Variograms and Reservoir Continuity,* Li-Ping Yuan, Rudy Strobl, and Dave Cuthiell, Alberta Geological Survey, Edmonton, Alberta, Canada

3RC-36 *Artificial Intelligence Developments in Geostatistical Reservoir Characterization*, Roussos Dimitrakopoulos, McGill University, Montreal, Quebec, Canada

3RC-41 *Modeling Heterogeneous and Fractured Reservoirs with Inverse Methods Based on Iterated Function Systems*, Jane C.S. Long, Christine Doughty, Kevin Hestir, and Stephen Martel, Lawrence Berkeley Laboratory, Berkeley, California

3RC-72 *Hierarchical Scaling of Constitutive Relationships Controlling Multiphase Flow in Fractured Geologic Materials*, Carl A. Mendoza and Edward A. Sudicky, University of Waterloo, Waterloo, Ontario, Canada

3RC-01 *Geostatistical Modeling Incorporating Well Log and Seismic Data*, U.G. Araktingi, T.T. Tran, T.A. Hewett, and W.M. Bashore, Chevron Oil Field Research Company, La Habra, California

Technical Session 4 – Optimization of Reservoir Management
Co-Chairmen: Mike Fowler, Exxon Co., USA, Midland, Texas;
Susan Jackson, National Institute for Petroleum and Energy Research, Bartlesville, Oklahoma

3RC-86 *Assessment of Uncertainty in the Production Characteristics of a Sand Stone Reservoir,* Henning Omre and Hakon Tjelmeland, Norwegian Computing Center, Oslo; Yuanchang Oi, IBM/EPAC, Stavanger; and Leif Hinderaker, Norwegian Oil Directorate, Stavanger, Norway

3RC-39 *Screening Enhanced Oil Recovery Methods With Fuzzy Logic*, W. J. Parkinson, K.H. Duerre, J.J. Osowski, Los Alamos National Laboratory; G.F. Luger, University of New Mexico; and R.E. Bretz, New Mexico Institute of Mining and Technology

3RC-43 *Effect of Pore Pressure Drawdown on In Situ Stress and Permeability of Naturally Fractured Reservoirs*, Lawrence W. Teufel, Sandia National Laboratories, Albuquerque, New Mexico

3RC-54 *After the Fire Is Out: A Post In Situ Combustion Audit and Steamflood Operating Strategy for a Heavy Oil Reservoir, San Joaquin Valley, CA*, Paul G. Soustek, James M. Eagan, Mark A. Nozaki, and Mary L. Barrett, Mobil Exploration & Producing U.S. Inc., Bakersfield, California

3RC-28 *The Depletion of the Rannoch-Etive Sand Unit in Brent Sands Reservoirs in the North Sea*, J. M. D. Thomas and R. Bibby, Winfrith Technology Centre, Dorchester, United Kingdom

3RC-81 *Reservoir Description and Modelling of the Pen Field, Graham County, Kansas*, Rod Phares, Gary Gould, D.W. Green, T. Walton, and G.P. Willhite, University of Kansas, Lawrence, Kansas

3RC-74 *Applying a Geological Model to the Formulation of Production Decline Type Curves to the Austin Chalk*, S.W. Poston and H.Y. Chen, Texas A&M University, College Station, Texas

SESSION 1

Heterogeneities/Anisotropies

Co-Chairmen

William Almon, Texaco E&P

Rodney R. Boade, Phillips Petroleum Company

A STOCHASTIC MODEL FOR COMPARING PROBE PERMEAMETER AND CORE PLUG MEASUREMENTS

Jerry L. Jensen
Patrick W. M. Corbett

Department of Petroleum Engineering
Heriot-Watt University
Edinburgh, Scotland EH14 4AS

I. INTRODUCTION

The past few years has seen a growing awareness of the influence of small-scale (i.e., mm to dm size) heterogeneities upon reservoir behaviour. At this scale, lamination and bedform are the prevalent geologic elements of the reservoir. While there are often significant visual similarities (e.g., geometry and contrast) between the many laminae and bedforms which make up the reservoir, the corresponding permeability contrasts are only recently being established by detailed mapping (e.g., van Veen, 1975; Corbett and Jensen, 1992). As shown by Kortekaas (1985), Ringrose et al. (1991), Kelkar and Gupta (1991), and others, the impact of these permeability heterogeneities can be to significantly impair the recovery of oil for a variety of recovery processes.

For a given reservoir and recovery process, the impact of small-scale variations can only be assessed once their presence is recognised and their correlation and variability quantified. In the past, both core flooding and core plug data have been used for these purposes. Each technique has its own particular advantages and shortcomings. Core floods can provide flow-based information on how the formation heterogeneity affects a process, but they are expensive and must be undertaken on cores which represent well (i.e., at the appropriate scale, magnitude, and structure) the variability in the reservoir. In contrast, core plugs are less expensive and can be used to more extensively sample the reservoir. Consequently, core plugs have become the industry standard method for conveying small-scale variability.

Plug data, however, require a flow model in order to translate the observed variability into an impact on performance. Furthermore, because of the cost and mechanics of taking core plugs, selection depths may be biased towards the thicker, more permeable strata, giving a false impression of the

permeability variation and its structure. For these and other reasons, permeability data from core plugs have been found in some cases (e.g., van Veen, 1975; Weber, 1986; Martin and Evans, 1988) to poorly capture small-scale variability.

An alternative to core plug permeability measurements is to use the probe (or mini) permeameter. Although not new in concept (e.g., Dykstra and Parsons, 1950), the probe permeameter has only recently seen widespread use to assess small-scale permeability variation. It has the advantages of being a relatively inexpensive, non-destructive measurement which can be made almost anywhere on the rock surface. A number of studies (e.g., Weber et. al., 1972; Goggin et. al., 1988a; Dreyer et. al., 1990; Corbett and Jensen, 1992) have used the probe permeameter to successfully explore small-scale variability on outcrop surfaces as well as subsurface cores. Similar to core plug permeabilities, probe data must be interpreted with a flow model in order to translate variability into effect on process performance. Probe measurements are often made under less favourable conditions than core plugs. Factors such as residual fluids, poor seal integrity, and non-Darcy effects can degrade the measurement. Hence, probe measurements are not necessarily a substitute for core plug data.

So when can probe data augment or replace core plug measurements? When does the ability to measure frequently--if less accurately--give better, more reliable variability assessments? In this study, we propose a measurement model which attempts to address these questions.

The model we propose and subsequently describe is a computer model which uses the Monte Carlo method. It enables us to assess and compare different sampling methods and strategies. The model also provides a way of assessing the sensitivities of sampling strategies to changes in formation features. After describing the measurement model, we investigate three applications: correlations of permeability with wireline density data; permeability variation; and medium-scale permeability prediction. The results

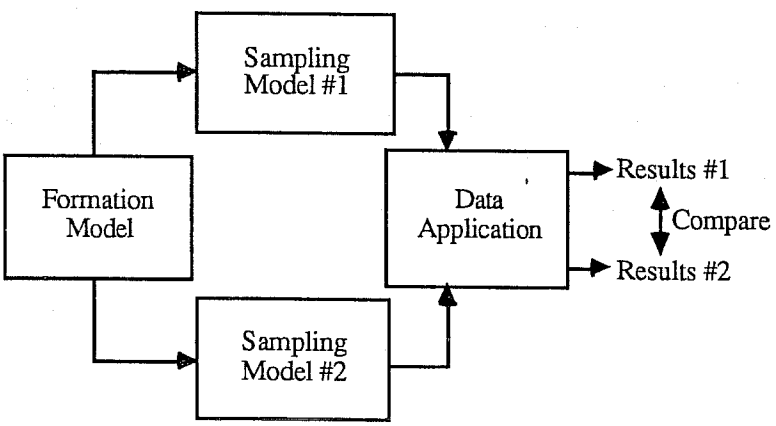

Fig. 1. The three measurement model components being used to compare two different sampling strategies.

are compared to observations using field data. We find that the model, despite having some simplified features, gives results which agree with measurements from a North Sea field.

II. MEASUREMENT MODEL DESCRIPTION

The model consists of three components: the formation model, the sampling model, and the data application (Fig. 1). Together, the three components emulate any process which collects formation data and applies them to make some decision or estimate concerning the formation. We first describe each component in general terms, then we discuss their interrelationships and how they are used together. A specific example will be presented in Section III.

The formation model (Fig. 2) consists of a series of discrete rock "elements" which collectively represent an interval of the formation. The properties (thickness, lithology, porosity, permeability, etc.) are assigned either in a deterministic or a probabilistic manner to each element. Depending on the sophistication of the rock property assignments, any element property may be influenced by the properties of neighboring elements. In this study, each element has constant properties and we assume that a vertical section is being emulated. More elaborate formation models could, for example, incorporate variation within each element to reflect local lateral variation in cores. For the homogeneous elements used here, the element size physically represents a compromise between the true scale of permeability variation (mm's) and the resolution (cm's) of the measurements modeled.

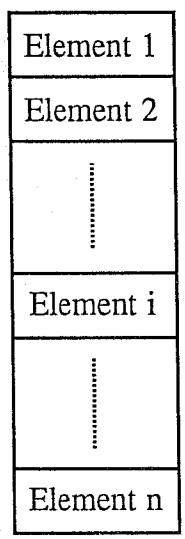

Fig. 2. The basic discretised formation model.

The sampling model captures how the properties of the rock elements are measured. The sampling model encompasses three features of any measurement: the measurement locations, the volume of investigation, and the measurement precision. Measurement locations depend on the measurement being modeled. For example, core plug samples might be taken at discrete points 30cm apart. Additional features involving location can be included, such as skipping a measurement if the element lithology at the chosen location is a shale. The investigation volume concerns the number of rock elements whose properties are being measured at a given location and how that measurement weights the contribution of each element. A 3cm diameter horizontal core plug, for example, reflects the properties of only one element if the elements are 5cm thick. The measurement precision depends upon any further disturbing influences which might be included such as statistical errors, variations in the environment (e.g., mudcake), sample treatment, or operator error.

The third component, the data application, uses the measurements obtained from the sampling model. It emulates the way the data will be analysed and used. For this model, we require a quantitative application involving a well defined procedure. For example, computing the average of permeability measurements can be easily modeled. Zonations could be more difficult to systematise.

Together, the formation and sampling models represent the data acquisition process. They represent both the vagaries and physics of the formation and the data acquisition process. The sampling and formation models produce a series of measurements, precise or otherwise, which reflect properties of the formation and which are used in the application. The application model is necessary because only after the application is considered can an assessment be made of the impact of measurement errors and imprecision on the ultimate outcome. To fully compare the performance of two measurement techniques (Fig. 1), the measurements from both methods need to be used in the intended application and the results compared.

By using the measurement model with the Monte Carlo method, the merits of measurements and procedures can be explored. The Monte Carlo method generates hundreds of "formations" using the formation model, makes "measurements" of the formations, and uses the measurements in the data application. The results can then be examined for sensitivities and behaviour which reflect the appropriateness of a particular measurement procedure and data application. Clearly, the more realistic are the formation, sampling, and data application models, the better the results will reflect the observed measurement behaviour. We have found, however, that even simple models can give useful results.

III. EXAMPLE APPLICATION

The procedure to be modeled is the correlation of the wireline bulk densities, ρ_b, with permeability measurements. The aim of the procedure is

to develop a reliable predictor of permeability for use in uncored wells. In the modelling, we will use both core plug and probe measurements and see which method gives a better result. We assume that a relationship between porosity (ϕ) and permeability (k) exists at the formation element scale and that core plug measurements are "correct". The differences in vertical investigation between the wireline, core plug, and probe measurements are addressed. We assess the quality of the resulting k--ρ_b relationships using the coefficients of correlation and the slopes of the regression lines. The role of sample spacing is also investigated.

A. The Formation Model

Figure 3 shows the formation model geometry, which represent a vertical section through a hypothetical clastic reservoir 12m thick with 3cm elements. The section thickness was chosen to give a large number of elements while still being computationally tractable. The reservoir is flanked by shoulder beds of shale each over 50cm thick, so that measurements towards the top and bottom of the section may be influenced by these shoulder beds.

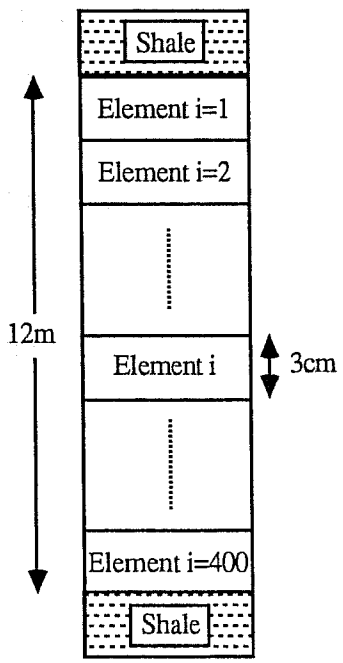

Fig. 3. The formation model. Each element can be either sand or shale except for the shoulder elements, which are shale.

For element i, $1 \le i \le 400$, the formation model assigns lithology (l_i), porosity (ϕ_i), permeability (k_i), and density (ρ_i) values by the following steps.

1. The lithology of either sandstone ($l_i = 1$) or shale ($l_i = 0$) is randomly assigned, assuming the average amount of shale is V (%) for the reservoir and no correlation exists between the lithologies of neighboring elements.
2. ϕ_i is assigned according to l_i and l_{i-1}. If $l_i = 0$ (shale), no porosity is defined. If $l_i = 1$ (sand) and $l_{i-1} = 0$, ϕ_i is assigned a random value from a normally distributed population with mean porosity $\bar{\phi}$ and standard deviation σ_ϕ [abbreviated as $\phi_i \sim N(\bar{\phi}, \sigma_\phi^2)$]. If $l_{i-1} = l_i = 1$, then

$$\phi_i = \bar{\phi} + r_\phi(\phi_{i-1} - \bar{\phi}) + t_i\sigma_\phi\sqrt{1 - r^2}, \qquad (1)$$

where r_ϕ is the correlation coefficient of porosity between adjacent sandstone elements and $t_i \sim N(0, 1)$. Eq. (1) is a first order Markov model (Haan, 1977, p. 294) which uses a nearest-neighbour approach to introduce interelement correlation.
3. The permeability of each sandstone element is given by $k_i = \exp(a\phi_i + b + \varepsilon_i)$ md, where $\varepsilon_i \sim N(0, \sigma_\varepsilon^2)$, while the permeability of each shale element is set at $k_i = 0$. The exponential relationship is used so that the sandstone permeability distribution is log normal, i.e., $\ln(k_i) \sim N(a\bar{\phi} + b, a^2\sigma_\phi^2 + \sigma_\varepsilon^2)$. ε_i is a "noise" element which causes the ϕ--log(k) correlation to be imperfect. It accounts, for example, for any textural and diagenetic influences which the porosity does not reflect, but which do affect the permeability. The values of a and b are selected to give a realistic variation in permeability values:

$$a = \frac{\sqrt{\ln(C_v^2 + 1) - \sigma_\varepsilon^2}}{\sigma_\phi} \qquad (2)$$

and

$$b = \ln(250) - \bar{\phi}\, a, \qquad (3)$$

where C_v is the coefficient of variation, a common measure of permeability heterogeneity (Lake and Jensen, 1991), and the constant 250 chosen to set the median (i.e., 50th percentile) permeability at 250 md. Eq. (2) was derived from the fact that

$$C_v = \sqrt{\exp\left(a^2\sigma_\phi^2 + \sigma_\varepsilon^2\right) - 1}$$

because the k_i are log-normally distributed.

4. Element densities are either $\rho_i = 2.45$ g/cc for $l_i = 0$ or $\rho_i = 2.68(1 - \phi_i) + \phi_i$ g/cc for $l_i = 1$, assuming a grain density of 2.68 g/cc and a pore fluid density of 1.0 g/cc.

The shale shoulder beds also have permeability 0 and a density of 2.45 g/cc, giving $\rho_i = 2.45$ g/cc and $k_i = 0$ for $i<1$ and $i>400$. Thus, each element has a permeability and a density assigned to it for the sampling models to operate on.

B. The Measurement Models

Three sampling models are considered because three measurements are involved. The wireline density log sampling model (Fig. 4) is described first. Typically, wireline density data, $(\rho_b)_i$, are recorded every 15cm of tool travel and the vertical investigation is about 30cm. So that, at the measurement depth, the tool is responding to the formation densities within approximately ±15cm from that depth. We modeled this volumetric averaging as an arithmetic average of the element densities within ±5 units of the measure point:

$$(\rho_b)_i = \frac{1}{11}\sum_{j=i-5}^{j=i+5} \rho_j.$$

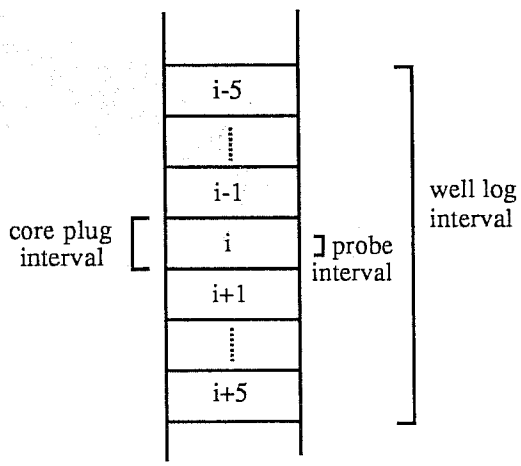

Fig. 4. The sampling relationships of the three measurements modeled.

We did not include noise on the density log data since corruption would not affect the core plug--probe comparison; it would simply degrade both correlations.

The core plug sampling model was straightforward, given that the elements are sufficiently large and sized so that a plug never has to come from more than one element. The measurement location of the plug, however, involves an appreciation that plugs are often not taken in shalier lithologies. Thus, while plug sampling points have a nominal spacing of 30cm (10 elements), that spacing may vary if a plug point lands on a shale. In this model of measurement location, if the 30cm plug point fell on a shale element, the program searched for the nearest sandstone element and, provided that it was within 6cm, the permeability of that sandstone element was assigned to the plug. The measure point which was ascribed to the plug was not changed, however. If the program could find no sandstone element within 6cm of the plug point, the plug was assigned a 0 md permeability. Hence, the core plug permeability at location i, $(k_p)_i = k_j$ where $i-2 \leq j \leq i+2$. This model of core plug permeability measurement is somewhat idealised but, since we are using core plugs as the "standard", we only need to be careful about how we characterise the probe permeameter measurements in comparison with core plug measurements.

The probe sampling model consisted of a measurement taken every element, i.e., every 3cm. The probe measurement at location i, $(k_m)_i$, included a multiplicative noise component δ_i: $(k_m)_i = k_i \cdot \exp(\delta_i)$, where $\delta_i \sim N(0, 0.35)$. This model is based on Fig. 5, a comparison of core plug and probe permeameter measurements for Rannoch Formation samples. For each plug, four probe measurements were made on each end, giving eight probe data per plug value.

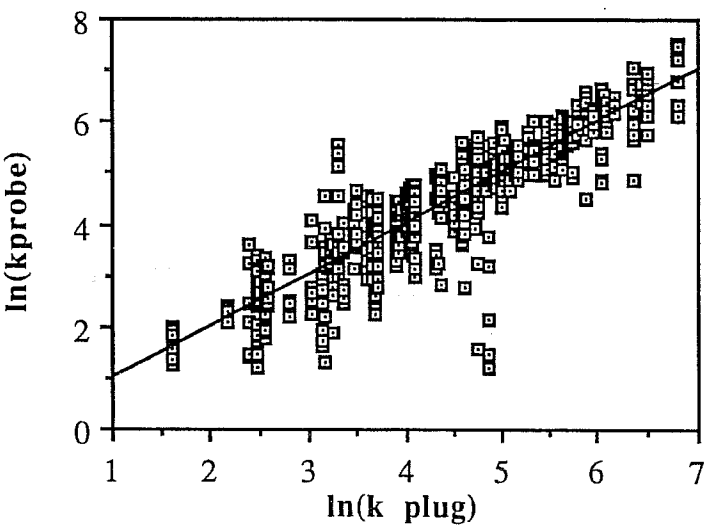

Fig. 5. Core plug--probe permeability relationship. Each plug has eight probe measurements.

The "noise" factor, δ, includes surface preparation, invasion, surface roughness, and sample heterogeneity effects as they existed for the samples measured. Since this model comes from a laboratory one-to-one comparison of core plug and probe measurements, it accounts for all differences observed between core plug and probe permeabilities taken on the same rock sample, including the differences in resolution. It does not, however, compensate for differences in measurement when different samples are used. For example, core plug permeability measurements are usually made on cleaned rock, whereas probe measurements are often made on uncleaned samples (e.g., Corbett and Jensen, 1992). A separate factor may need to be included if this were the case. Another element which can significantly change δ is the pore structure of the rock. Figure 8 of Goggin et al. (1988), obtained using their probe permeameter on a number of sandstone plugs, gives a surprisingly similar model to the one for the probe we have used (Jensen, 1990). Goggin (1991), however, shows a much larger variability with probe measurements and carbonate plugs.

The final part of the probe sampling model includes a running average (arithmetic average) taken of every p^{th} probe measurement ($p = 1, 2, 5$, or 10) to form a permeability "log" with approximately the same measurement resolution as that of the wireline density log (Fig. 4). The permeability log measure point was taken to be the centre of the 11-element span of the running average:

$$(k_{log})_i = \frac{p}{10+p} [(k_m)_{i-5} + (k_m)_{i-5+p} + \ldots + (k_m)_{i+5}].$$

C. The Data Application

The data application, correlation of density log data with permeability measurements, conceptually results in the production of two plots for each formation generated: ρ_b versus $\log(k_p)$ and ρ_b versus $\log(k_{log})$. Each plot has 40 points on it, corresponding to the 40 depths (i.e., every 30 cm) at which core plug, permeability log, and density log data were calculated. Because the Monte Carlo process generates many realisations of the formation, we chose to analyse two statistics from each plot rather than try to study individually the many correlations generated. The statistics chosen were the coefficient of correlation, r, and the slope of the least-square regression line, m. The coefficients of correlation obtained from the ρ_b versus $\log(k_p)$ and ρ_b versus $\log(k_{log})$ correlations are termed r_p and r_{log}, respectively. Similarly, the slopes of the regression lines (i.e., log(k) on ρ_b) are m_p and m_{log}.

D. Model Results

Table I gives the results for the case of V = 10% shale and $r_\phi = 0.95$. All results for the simulations, m_p, m_{log}, r_p, r_{log}, and $r_{log} \div r_p$ are listed in terms of their median (50%) values (rather than arithmetic averages) for the 500 iterations performed per case. The slope inter-quartile ranges (i.e., the differences between the 75% and 25% points) are listed in brackets to indicate the variability of the results over all the simulations. Expressing the results in quartiles (i.e., the 25, 50, and 75% points) has two advantages over the arithmetic average and standard deviation. Firstly, median values are invariant under monotonic transformations so that the median values of other statistics (e.g., the coefficient of determination, R^2) are simply related to the median values of the statistics listed. Secondly, for robustness since we did not analyse the results from each realisation. That is, one or two wild results could substantially influence the average or standard deviation, whereas the quartiles would not budge. See, for example, Lewis and Orav (1989, Ch. 6) for a discussion of robust estimators.

The values of r_p in Table I are realistic for ρ_b--log(k_p) correlations. The ρ_b--log(k_{log}) relation shows a stronger linear element (as measured by r) than the ρ_b--log(k_p) correlation. The coefficients of correlation have a weak sensitivity to C_v. The median $r_{log} \div r_p$ increases with C_v. This behaviour reflects the fact that, as C_v increases, the relative influence of the measurement corruption, δ, diminishes. Increasing σ_ε degrades the strength of both relationships; r_p is more sensitive to σ_ε than r_{log} and, hence, the ratio $r_{log} \div r_p$ usually increases as σ_ε increases.

Table I. Measurement Model Regression and Correlation Performance for the Bulk Density--Permeability Application. Variabilities are in parenthesis.

C_v	σ_ε	$-a \div 1.68$	m_p	m_{log}	r_p	r_{log}	$r_{log} \div r_p$
0.50	0.10	-5.50	-6.36 (0.95)	-6.01 (0.84)	-0.84	-0.87	1.04
	0.25	-4.77	-5.42 (1.22)	-5.27 (0.97)	-0.73	-0.82	1.12
	0.40	-2.99	-3.46 (1.62)	-3.31 (0.96)	-0.45	-0.64	1.40
1.00	0.10	-9.84	-11.1 (1.44)	-10.4 (0.94)	-0.85	-0.93	1.10
	0.25	-9.45	-10.8 (1.93)	-9.99 (1.05)	-0.82	-0.92	1.12
	0.40	-8.69	-9.96 (2.07)	-9.26 (1.13)	-0.76	-0.90	1.18
1.50	0.10	-12.9	-14.7 (2.05)	-13.5 (1.30)	-0.85	-0.93	1.09
	0.25	-12.6	-14.4 (2.22)	-13.2 (1.20)	-0.84	-0.93	1.11
	0.40	-12.0	-13.9 (2.57)	-12.7 (1.54)	-0.80	-0.92	1.15

The value -a÷1.68, also listed on Table I, represents the slope one might expect for the ρ_b--log(k) plots because this is the slope of the ρ_b--log(k) relation for the sandstone elements. Neither the core plug nor the permeability log plots consistently give this slope, although the probe data come closest. If the measurement model for the core plugs had not had the shale avoidance scheme, m_p would be significantly altered from the listed values. Both m_p and m_{log} are about equally affected by C_v. The variability of m_p is always greater than the variability of m_{log}. σ_ε does not appear to exert a substantial effect upon either m_p or m_{log} for the two higher C_v cases.

The porosity--log permeability relationship for the sandstone elements is linear in this model. The ρ_b--log(k) correlations, however, may not necessarily reflect that relationship because of several corrupting factors: the noise ε; the density log response is a combination of the porosity of several elements; and shales, which have a different density-permeability relationship, are also present. Two other factors for the permeability "log" which may impair correlation are the noise δ on the probe measurements and the nonlinear behaviour of the logarithmic function. Hence, r may not be 1 for either correlation.

Figure 6 is a plot of the median of r_{log}÷r_p versus p for the case V = 0.1, C_v = 0.75 and σ_ε = 0.25. The median ratio declines rapidly when fewer samples are used to produce the permeability log. The steepness of the decline suggests that, for this application, closely spaced samples quickly lose their utility as the spacing increases.

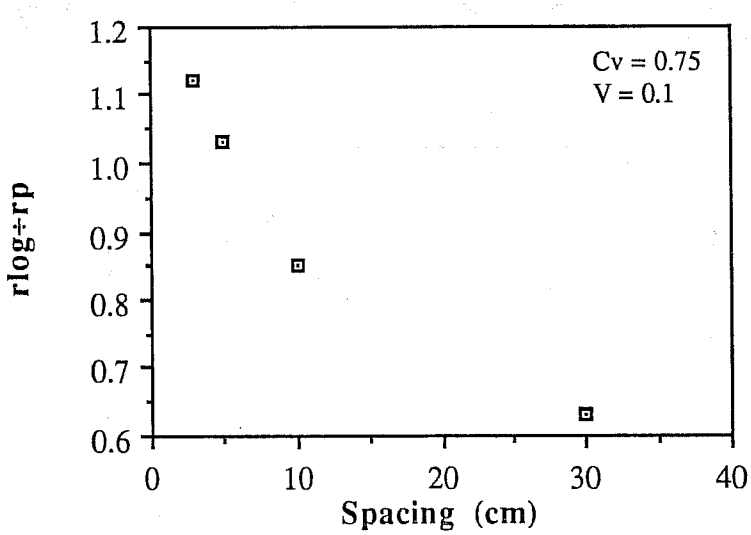

Fig. 6. Degradation of the median probe-based correlation as sample spacing increases.

Thus, the model results suggest that probe data, suitably averaged, may perform as well or better than core plug data for correlations with wireline density measurements. Since no measurement errors were included in the core plug permeability measurement model, we can expect the model results to be on the conservative side. The two measurement methods, as modeled, do not produce exactly the same product. k_{log} represents the permeability of the total formation, shale as well as sand. k_p, on the other hand, pertains only to the sand if the shale avoidance scheme always finds sand within two elements of the intended sampling depth. Depending on the needs of the user, probe measurements show promise for providing a more reliable predictor of formation permeability for uncored wells.

E. Comparsion of Model Results and Field Measurements

The preceding results were compared to those obtained from measurements taken on Rannoch Formation core taken from the Statfjord Field. The Rannoch is a very laminated micaceous, fine-grained sandstone whose permeability variation is predominantly controlled by the amount of mica. The laminae thicknesses are highly variable, ranging from a few mm to a few cm. The study of Corbett and Jensen (1992), however, suggests that some formation parameters can be estimated without sampling every laminae. Thus, it seems likely that the measurement model, having 3cm element thickness, can still give results which are useful for comparison with Rannoch data.

The permeabilities of two four-meter intervals of Rannoch slabbed core were measured at 1cm spacing along four lines with the Statoil probe permeameter. Core plug porosity and permeability data were also available on 30cm spacing. See Corbett and Jensen (1992) for further details of the sampling program.

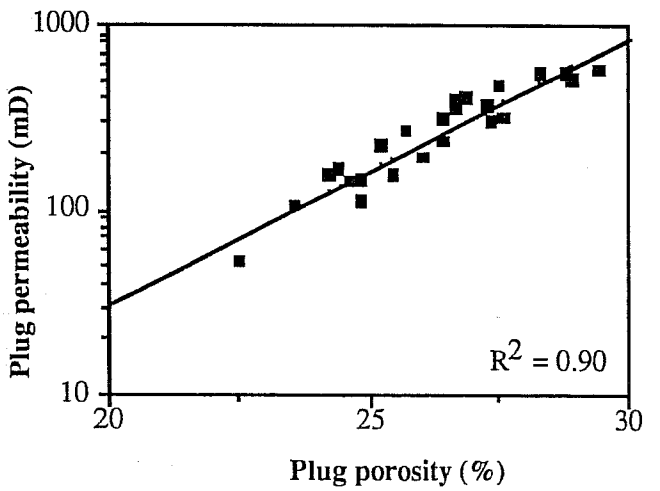

Fig. 7. Rannoch Formation core plug porosity--permeability correlation.

At the core plug scale, the porosity-permeability relation was very strong (Fig. 7). After depth adjustment, the density-core plug permeability association was also good (Fig. 8 left). The probe data were averaged similar to the previously described model prior to correlating with the wireline density. At each core plug depth, 30 probe measurements (i.e., 15 1cm measurements above and below the plug depth) were averaged to obtain a "permeability log". Figure 8 (right) shows the resulting correlation with the bulk density. The cloud of data about the least-squares regression line is clearly reduced and the influence of the high density point (ρ_b = 2.36g/cc) is diminished for the latter plot. The slope of the line is also slightly reduced, indicating that the probe-based predictor would give smaller predictions. This reflects the fact that, in these intervals, the core plugs missed some of the low permeability regions (Corbett and Jensen, 1992). The variability of the correlation strengths with sample spacing was also examined for both permeability measurements.

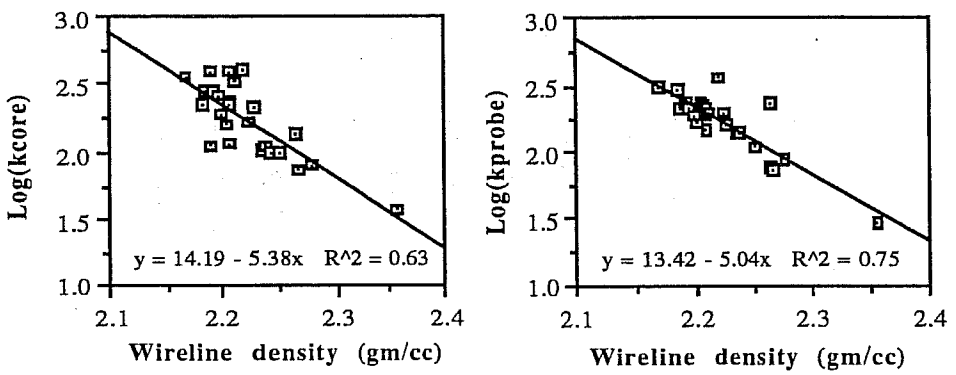

Fig. 8. Density--permeability relations for the idealised plug and averaged probe data.

Figure 9 shows the degradation of R^2 with sample density. The median decline is surprisingly low as the probe spacing increases. The variability of probe-based results, however, increases substantially.

Figure 10 shows the median ratio $r_{log} \div r_{plug}$ versus spacing for the model and field data. The parameter values chosen for the model (i.e., C_V, $\bar{\phi}$, etc.) closely duplicated the actual formation and probe figures. The value of $r_\phi = 0.95$ was based on correlograms of core plug porosity giving a first-lag (30cm) correlation of about 0.6, so that at 3cm, the correlation is $(0.6)^{0.1} = 0.95$. The shale percentage, V = 0, was chosen because no permeability measurement was less than 2mD. While the short spacing results are close, the longer spacing model results are more pessimistic than the field performance. This discrepancy could be caused by a too simplistic porosity correlation model, an insufficiently discretised formation model, or assuming perfect plug measurements. The match at the extremes could have been improved by increasing r_ϕ to 0.96 or 0.97, but we had no justification for the change. In all, the similarity of results is very encouraging and suggests that the model is capturing the important features of this data application.

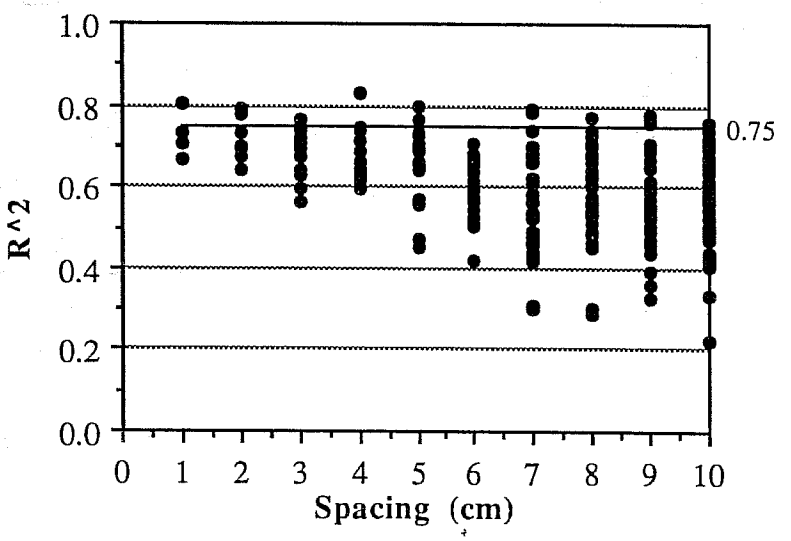

Fig. 9. Decline in correlation and increase in variability for Rannoch data with increasing sample spacing.

IV. FURTHER MEASUREMENT MODEL APPLICATIONS

We now consider two other applications of the model: prediction of average permeability and quantitative estimates of permeability variability. Again, we investigate the precision and relative variability of estimates derived from probe and core plug measurements.

A. Predicting Average Permeability

During the scaling-up process of reservoir properties, small-scale permeability measurements are used to predict the aggregate permeability of portions of the reservoir. The arithmetic or harmonic averages are often used to combine small-scale measurements to reflect bed-parallel or bed-transverse flow, respectively. The behaviour of both core plug and probe data for both averages were examined using the model previously described. We did not examine the merits of either average to represent the bulk permeability in this study.

The formation model consisted of a sand-only (V = 0) formation with uncorrelated, 3cm thick elements of 250 md median permeability. The core plug sampling model, as in the previous application, was an uncorrupted permeability measurement, $(k_p)_i$, every 10 elements (30cm). The probe measurement model differed from the previous application in that no permeability "log" was produced; only the probe data $(k_m)_i$ were used.

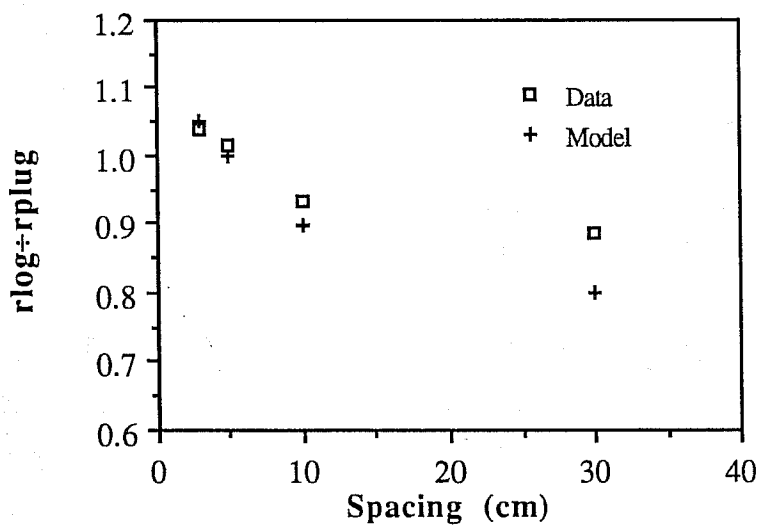

Fig. 10. Comparison of model and Rannoch Formation results for four sample spacings.

The true harmonic and arithmetic means of the formation, $(k_t)_h$ and $(k_t)_a$, are given by

$$(k_t)_h = \exp(\mu - \tfrac{1}{2}\sigma^2) \tag{4a}$$

and $$(k_t)_a = \exp(\mu + \tfrac{1}{2}\sigma^2) \tag{4b}$$

where $\ln(k) \sim N(\mu, \sigma^2)$, as previously described in Step 3 of the formation model. $\sqrt{(k_t)_a(k_t)_h}$ is also the median permeability of the formation (250 md) as determined by Eq. (3). From Eqs. (2) and (4) it follows that

$$(k_t)_h = \exp\left\{ \mu - \tfrac{1}{2}\left[\ln(1+ C_v^2)\right]^2 \right\} \tag{5a}$$

and $$(k_t)_a = \exp\left\{ \mu + \tfrac{1}{2}\left[\ln(1+ C_v^2)\right]^2 \right\}. \tag{5b}$$

The data applications were the harmonic and arithmetic averages of the core plug ($(k_p)_h$ and $(k_p)_a$) and probe data ($(k_m)_h$ and $(k_m)_a$):

$$(k_x)_h = \left\{ \frac{1}{n} \sum_{i=1}^{n} [(k_x)_i]^{-1} \right\}^{-1} \tag{6a}$$

and $$(k_x)_a = \left\{ \frac{1}{n} \sum_{i=1}^{n} (k_x)_i \right\}, \tag{6b}$$

where x=p or m and the summations are over n = 400 data for the probe or n = 40 data for the core plug measurements.

Table II. Model results for harmonic and arithmetic permeability averages.

C_v	$(k_t)_h$	$(\bar{k}_p)_h$	$(\bar{k}_m)_h$	$(k_t)_a$	$(\bar{k}_p)_a$	$(\bar{k}_m)_a$
0.50	224	225 (±18)	197 (±7)	280	280 (±21)	316 (±12)
1.00	177	181 (±28)	157 (±10)	354	353 (±59)	401 (±26)
1.50	139	147 (±32)	124 (±11)	451	451 (±103)	513 (±46)

The model is examining the competing effects of a few precise samples (ideal core plug data) and many less precise samples (probe data). Table II, which shows the averages for 500 iterations along with the standard deviations in parenthesis, indicates two distinct differences in behaviour for estimates based on the two sampling methods. First, the increased number of measurements reduces the variability of the estimates for all cases. The probe averages have about one-half to one-third the plug variabilities. Only for the two higher C_v cases, however, does the plug variability exceed 15% of the true average value. Second, the probe averages are biased compared to the plug averages at all heterogeneity levels. The probe harmonic averages are about 12% low and the arithmetic averages are about 12% too large. This level of bias is still probably acceptable for most reservoir description purposes.

Figure 11 shows model results for $(k_m)_h$ variability (in md) as the sample distance increases. For these results, n = 130 elements were used to permit comparison with Rannoch Formation data from one of the four-meter intervals. The satisfactory match suggests that the model is emulating the sampling behaviour well.

Consequently, the model results suggest that, to estimate the aggregate permeability of a region using the harmonic average, the corrupted probe measurements can give consistently better results than the few, idealised plug measurements. However, when the arithmetic average is to be used, more careful selection may be required, depending upon the formation heterogeneity. Considering the errors of actual plug measurements, the previous constraints on probe utility could probably be relaxed somewhat.

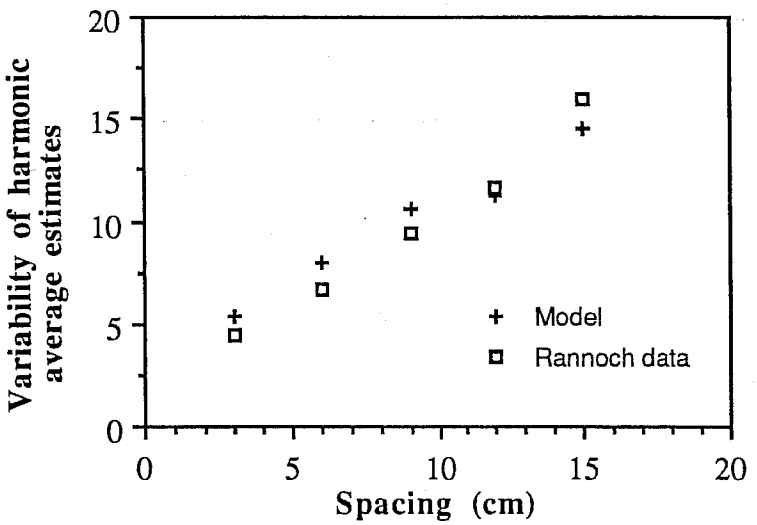

Fig. 11. Comparison of model and Rannoch Formation harmonic average performance.

B. Estimation of Permeability Variation

Formation heterogeneity can be assessed in a variety of ways. For this study, we chose C_v as the measure to be estimated:

$$(C_v^x)_{est} = \frac{\sqrt{\left\{\frac{1}{n-1}\sum_{i=1}^{n}\left[(k_x)_i - (k_x)_a\right]^2\right\}}}{(k_x)_a}, \qquad (7)$$

where x = p or m. Eq. 7 is the standard deviation divided by the arithmetic average. The model was used to give average values and standard deviations of $(C_v)_{est}$ for various C_v for the two measurement methods.

The model results (Fig. 12) indicated that the variability of $(C_v^m)_{est}$ was similar to that of $(C_v^p)_{est}$ for all heterogeneity levels. The model results, however, show that the estimated values differed significantly for the two sampling methods. The variability of the probe measurement (δ) appears as a formation with a heterogeneity of about $C_v = 0.6$ which, when combined with the intrinsic formation variation for $C_v = 0.5$, produces a formation with an apparent $C_v = 0.8$. This result agrees with theory that uncorrelated variations add according to the variances:

$$\sigma^2_{measurement} + \sigma^2_{formation} = \sigma^2_{total}$$

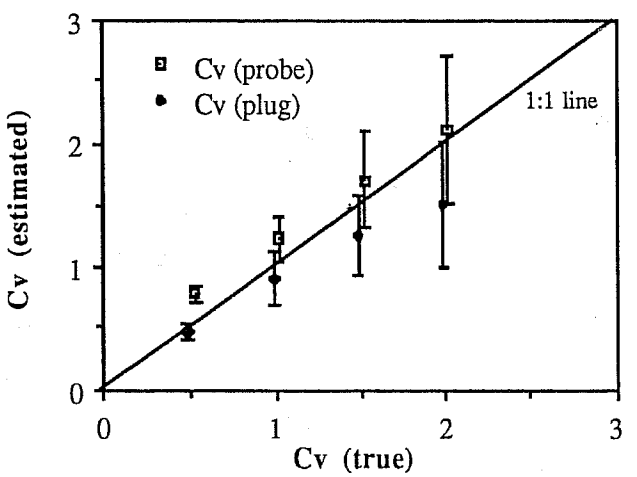

Fig. 12. Comparison of averaged heterogeneity estimates based on probe and idealised plug measurements.

where $\sigma = \ln(1 + C_v^2)$. The effect, however, diminishes rapidly for formations with $C_v > 1$, since $\sigma^2_{measurement} < \frac{1}{2}\sigma^2_{formation}$. At these higher C_v levels, the insufficient sampling of the plugs becomes evident.

Hence, statistical heterogeneity assessments on relatively homogeneous sediments may not benefit by taking many, less precise measurements instead of a few precise measurements. The advantages gained using one method instead of another will depend on the errors associated with each measurement along with the intrinsic formation variability to be quantified. For very heterogeneous ($C_v > 1$) materials, the probe measurement is preferred because of the low cost and non-destructive benefits; for homogeneous materials ($C_v < 0.5$) plugs, being more accurate and because few samples are required, are to be preferred; and for heterogeneous materials ($0.5 < C_v < 1.0$) both measurements have their merits. Spacing of the required number of samples (e.g., see Corbett and Jensen, 1991) will determine which method is to be preferred. For example, in an aeolian sandstone described by Weber (1987), the crossbed sets are clearly laminated and heterogeneous ($C_v \sim 1.5$). Hence, probe assessment of heterogeneity in this case is appropriate and may be usefully used with correlations (e.g., Kelkar and Gupta, 1991) to predict the recovery performance of this facies.

V. FURTHER COMMENTS

The general approach of measurement modelling used here builds on the concepts of Jensen (1990). The model components, however, have been improved and the results tested against field data. The model shows that having many more data does not always bring advantages.

More sophisticated models for plugs (e.g., noise and systematic errors), formation (e.g., greater variety and correlation of lithologies and lateral permeability variations) and probe (e.g., residual fluids and core damage) can be developed. These can be used to investigate systematic differences between plug and probe performance. Differences between plugs and probe measurement are to be expected in all comparative studies. This model highlights differences that are due solely to the statistics of sampling and provides a means of quantifying them. Hence, comparisons of measurements with this knowledge will shed light on the reservoir significance of differences.

The harmonic average was investigated here because of its relevance to bed-series flow and, hence, vertical permeability estimation. Our experience shows that low permeability laminae that are present in many reservoirs are below the resolution of many probes (i.e., < 5mm) when horizontal measurements are taken on slabbed surfaces. This model can be used to explore how the distribution of these laminae affects both vertical plugs and horizontal probe measurements, leading to a better understanding of the

meaning and performance of the harmonic average as an estimator of vertical permeability.

VI. CONCLUSIONS

We have proposed a measurement model which permits examination of sampling schemes and comparison of measurement methods. We used the measurement model for three different formation evaluation purposes and found that it gave results in agreement with field measurements. The model results showed that more data than the usual one-foot (30cm) sampling schemes may achieve significantly improved formation permeability estimates. The benefits, however, depend on the measurement type and the data application.

The model, when used to compare probe permeameter and idealised core plug measurements for correlations with the wireline bulk density log, showed that:

1. Averaged probe measurements can give stronger correlations than core plugs.
2. The probe--bulk density relationship degrades as fewer probe measurements are made.
3. The degradation behaviour of the model is slightly pessimistic compared to field data

Estimation of the harmonic and arithmetic average permeability generally benefitted from the more frequent probe measurements. Probe-based estimates showed lower variability but more bias than estimates from idealised plug data. Heterogeneity estimates (C_v) are positively biased at low heterogeneity levels ($C_v \leq 0.5$) but give equal or better performance at higher levels ($C_v \geq 1$). The model gives clear guidance on the appropriateness of plug and probe measurements and their respective sampling schemes.

ACKNOWLEDGEMENTS

The authors would like to thank Greg Geehan, Andy Hurst, and Christian Halvorsen for their help in the acquisition of the Rannoch Formation data. Statoil and BP are also thanked for technical support and their partners for allowing use of these data.

REFERENCES

1. Corbett, P. W. M., and Jensen, J. L.: "How Many Permeability Measurements Do You Need?" presented at The Third EAPG Annual Conference, Florence (1991), May 26-30, 11p.
2. Corbett, P. W. M., and Jensen, J. L.: "Variation of Reservoir Statistics According to Sample Spacing and Measurement Type for Some Intervals in the Lower Brent Group," *The Log Analyst* (1992) **33**, in press.
3. Dreyer, T., Scheie, Å., and Walderhaug, O.: "Minipermeameter-Based Study of Permeability Trends in Channel Sand Bodies," *AAPG Bulletin* (April 1990) **74**, No. 4, 359-374.
4. Dykstra, H., and Parsons, R. L.: "The Prediction of Oil Recovery by Water Flood," *API Secondary Recovery of Oil in the United States,* API, Washington, DC (1950) 160-174.
5. Goggin D. J.: "Minipermeametry: Is It Worth the Effort?," *Proc.*, Petroleum Science and Technology Institute Minipermeametry in Reservoir Studies Conference, Edinburgh (1991), June 27, 21p.
6. Goggin, D. J., Chandler, M. A., Kocurek, G., and Lake, L. W.: "Patterns of Permeability in Eolian Deposits: Page Sandstone (Jurassic), Northeastern Arizona," *SPEFE* (June 1988a) 297-306.
7. Goggin, D. J., Thrasher, R. L., and Lake, L. W.: "A Theoretical and Experimental Analysis of Minipermeameter Response Including Gas Slippage and High Velocity Flow Effects," *In Situ* (1988b) **12**, No. 1&2, 79-116.
8. Haan, C. T.: *Statistical Methods in Hydrology*, Iowa State Univ. Press, Ames (1977), 378p.
9. Jensen, J. L.: "A Model for Small-Scale Permeability Measurement With Applications to Reservoir Characterization," paper SPE/DOE 20265 presented at the 1990 Enhanced Oil Recovery Symposium, Tulsa, Apr. 22-25, 10p.
10. Kelkar, M. G., and Gupta, S. P.: "A Numerical Study of Viscous Instabilities: Effect of Controlling Parameters and Scaling Considerations," *SPERE* (Feb. 1991) 121-128.
11. Kortekaas, T. F. M.: "Water/Oil Displacement Characteristics in Crossbedded Reservoir Zones," *SPEJ* (Dec. 1985) 917-926.
12. Lake, L. W., and Jensen, J. L.: "A Review of Heterogeneity Measures Used in Reservoir Characterization," *In Situ* (1991) **15**, No. 4, in press.
13. Lewis, P. A. W., and Orav, E. J.: *Simulation Methodology for Statisticians, Operations Analysts, and Engineers*, **1**, Wadsworth and Brooks/Cole Inc., Belmont, Ca. (1989), 416p.
14. Martin, J. H., and Evans, P. F.: "Reservoir Modeling of Marginal Aeolian/Sabkha Sequences, Southern North Sea (UK Sector)," paper SPE 18155 presented at the 1988 Annual Technical Conference and Exhibition of the SPE, Houston, Oct. 2-5.
15. Ringrose, P. S., Sorbie, K. S., Feghi, F., Pickup, G. E., and Jensen, J. L.: "Relevant Reservoir Characterisation: Recovery Process,

Geometry and Scale," *Proc.*, Sixth European IOR Symposium, Stavanger (1991), May 21-23, 15-25.
16. van Veen, F. R.: "Geology of the Leman Gas-Field," *Petroleum and the Continental Shelf of North-West Europe*, A. W. Woodland (ed.), Applied Science Pubs. Ltd., Essex (1975) **1**, 223-231.
17. Weber, K. J., Eijpe, R., Leijnse, D., and Moens, C.: "Permeability Distribution in a Holocene Distributary Channel-Fill Near Leerdam (The Netherlands)," *Geologie En Mijnbouw* (1972) **51**, No. 1, 53-62.
18. Weber, K. J.: "How Heterogeneity Affects Oil Recovery," *Reservoir Characterization,* L. W. Lake and H. B. Carroll, Jr. (eds.), Academic Press, Orlando (1986), 487-544.
19. Weber, K. J.: "Computation of Initial Well Productivities in Aeolian Sandstone on the Basis of a Geological Model, Leman Gas Field, U. K.," *Reservoir Sedimentology*, R. W. Tillman and K. J. Weber (eds.), Society of Economic Paleontologists and Mineralogists, Tulsa (1987) **40**, 333-354.

PERMEABILITY HETEROGENEITIES OF CLASTIC DIAGENESIS

By Thomas L. Dunn and Ronald C. Surdam

Department of Geology & Geophysics
University of Wyoming
Laramie, Wyoming 82071

ABSTRACT

Within clastic sediments post-depositional processes (e.g., infiltration, compaction and chemical diagenesis) produce and alter permeability heterogeneity and anisotropy on a range of scales from microscopic fabrics, through bedding and laminations, up to basin wide features. Diagenetic alterations have been shown to be complexly but systematically related to the burial and thermal histories of the sediments. Cementation patterns alter the dimensions of depositionally-related macroscopic features. The recently recognized need for dimensional data on reservoir heterogeneity related to depositional systems has renewed emphasis on outcrop studies. Because the burial histories and diagenetic alterations of subsurface reservoirs and their outcropping depositional analogs may be significantly different, it is important to understand what changes in clastic reservoir heterogeneity can be attributed solely to post-depositional processes.

Sandstone reservoirs from deltaic, eolian and fluvial settings were examined to ascertain the impact post-depositional processes have on heterogeneity. Within these environments, permeability distributions change systematically with diagenesis. Intervals marked by extensive cementation and alteration are characterized by positively skewed log permeability distributions. Intervals characterized by small amounts of cementation or those which have undergone extensive intergranular cement dissolution show negatively skewed log permeability distributions.

Within the fluvial sandstones, variations of 0.10 to 0.15 in the Dykstra-Parsons coefficient of permeability heterogeneity can be attributed to diagenetic events related to meteoric invasion and uplift. Similar variations can be ascribed to the presence of infiltrated materials. Compactional processes are observed to decrease heterogeneity where their effects can be isolated.

RESERVOIR HETEROGENEITIES, VALLEY-FILL SANDSTONE RESERVOIRS, SOUTHWEST STOCKHOLM FIELD, KANSAS

Roderick W. Tillman
Consulting Sedimentologist/Stratigrapher
Tulsa, Oklahoma

Edward D. Pittman
Consulting Petrologist
Tulsa, Oklahoma

ABSTRACT

Valley-fill heterogenous reservoirs in the Morrowan (Pennsylvanian) age Stateline Trend along the Kansas-Colorado border produce from the Stockholm Sandstone. Analysis of Southwest Stockholm field valley-fill reservoirs has verified that they are internally complex, contain geographically and vertically limited reservoirs and can only be effectively drained if the internal reservoir architecture of the reservoirs is understood. Development of detailed geologic models for river, tidal and other shoreline-filled valley-fill reservoirs in the Morrow are expected to enhance results of reservoir simulation, secondary recovery and possible tertiary production. Only by including the location and degree of impermeability of barriers to flow at the margins of and within the valley-fill reservoirs can historical simulation modeling and secondary processes yield satisfactory economic results.

The valleys in which the reservoirs occur were cut by rivers during drops in sea level and remained as conduits (narrow open valleys trending perpendicular to the regional shoreline). At a later time, as sea level rose, the valleys were filled from the landward side by rivers or from the seaward side by shoreline processes or alternately by both processes.

Detailed geologic analysis of cores from the field combined with cross sections and isopach and structure maps yield details of reservoir heterogeneity. Reservoir production properties vary greatly between the two major producing facies, river and tidal (estuarine) valley-fill sandstones in Southwest Stockholm field, Kansas. Within the

approximately 150-ft thick valley-fill vertical sequence, just one of the three sandstones produces. Topographic highs on the valley bottom, covering an area as large as 1/2 section, reduce the depositional thickness of the reservoir sandstones. Impermeable limestones and shales commonly form lateral barriers to flow at valley margins and locally within the valleys. Erosion of portions of potentially productive sandstones within the valleys was found to be important in isolating reservoirs (flow units).

Tidally deposited (estuarine) sands are finer grained and are more clay prone than the river sandstones and as a result have poorer reservoir properties. River deposits have average porosities of 16% (range from 11 to 20%) and average permeabilities of 700 md (range from 129-1890 md). Tidal channel sandstones have average porosities of 14% (range from 11 to 17%) and permeabilities of 80 md (range 50 to 111 md). Where tidal sandstones interfinger with river sandstones, vertical permeability is diminished and flow units are fragmented.

Valley-fill deposits in Southwest Stockholm field differ from deltaic deposits geologically, geometrically and in the distribution of heterogeneities. Overbank and fine-grained levee deposits are absent at the margins of valley-fill deposits.

Secondary, post burial events affected the production characteristics of the reservoirs. The post depositional events, which affected the reservoirs, were significantly different in some of the seven geological facies. Where millimeter thick shale lenses were deposited within tidally deposited sands, pressure solution of quartz in contact with the clay has reduced porosity. Up to half of the porosity in Southwest Stockholm field may be leached (secondary) porosity.

Reservoir characteristics are relatively similar within units interpreted to be the same geologic facies and significantly different among different geologic facies. Although other types of sandstones were vertically or laterally "connected" to the better reservoir facies, perforated intervals were commonly limited to valley-filling river sandstones in Southwest Stockholm field. Understanding the differences in heterogeneity between river and shoreline fills of valleys, such as those studied herein, allows proper economic evaluation and more efficient reservoir management of these unique types of reservoirs.

I. INTRODUCTION

One of the most important relatively small sandstone reservoirs being explored for and developed today are valley-fill sandstone reservoirs. Because of their relatively small size (1/2 x 4 miles), poorly understood origins and difficult to predict occurrences, valley-fill reservoirs have not always been an important type of drilling prospect. However, in the last few years it has become a very important type of prospect and some valley-fill reservoirs are undergoing secondary production. Because of the absence of adequate geologic reservoir descriptions, valley-fill reservoirs have, in the past, commonly not been differentiated from deltaic and river channel sandstones. Because there are significant differences in the distribution of reservoir seals and internal heterogeneities in valley-fill reservoirs, compared to deltaic and river channel reservoirs, different patterns of production will occur within individual fields and pools from these distinctly different geologic environments.

A sequence of depositional events is involved in forming valley-fill reservoirs. The initial step in forming most, if not all, valley-fill reservoirs requires a sea level drop (Suter and Berryhill, 1985; Hine and Snyder, 1985). When sea level drops, the shoreline moves seaward and rivers draining the area cut down into underlying sediments at a rate and to a depth controlled by the drop in sea level. The rivers initially cut down to form an open valley, mostly devoid of sediment (Fig. 1). In the initial phases of valley formation the river sediment is moved seaward bypassing the valley. As long as sea level is relatively low, little sediment will be

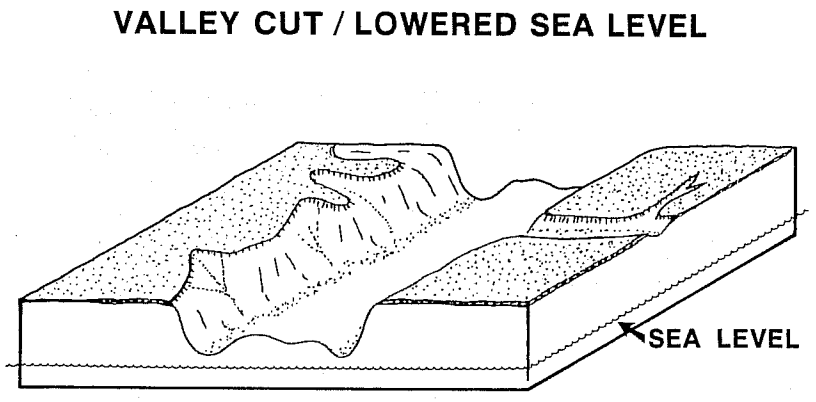

Fig. 1 - Valley cut into sediment during sea level drop. At this time the valley is an open conduit in which no sediment is accumulating. (from Farmer, 1981)

deposited in the valley conduit, however, with rise in sea level several processes may cause deposition of sediment in coastal areas in the previously cut valley.

Rising sea level causes the rivers flowing in the valley to aggrade (begin to deposit sediment) a short distance upstream from the ocean and the formerly open channel will begin to fill with sand. Aggradation occurs when a stream is supplied with more sediment load than it can transport. During periods of river high water, overbank flooding may deposit clayey deposits in adjacent swamps, marshes and in in the previously cut valley (Fig. 2). Because the valleys open into the ocean, marine shoreline processes may fill the seaward ends of the valleys. When the sea floods a valley it is designated as an estuary. Because the mouths of the valleys are commonly several miles wide, normal shoreline processes may partially fill the mouth of the estuary. Where an embayed shoreline is present, in a direction away from the ocean, shoreline wave and current processes give way to tidal sandstone depositional processes in lagoons and in the most landward portions, to river deposition. A vertical sequence of intertonguing discrete fluvial, tidal and shoreline sandstones may be preserved within the valley or estuary with rise in sea level. The complete vertical sequence of potential reservoir facies may not be preserved because erosion by currents in the river may remove portions of the sand deposited in the valley. Another important process in the shoreline area of the valley is the destructive erosional process resulting from the landward movement of the sea (transgression). The landward movement of the sea commonly

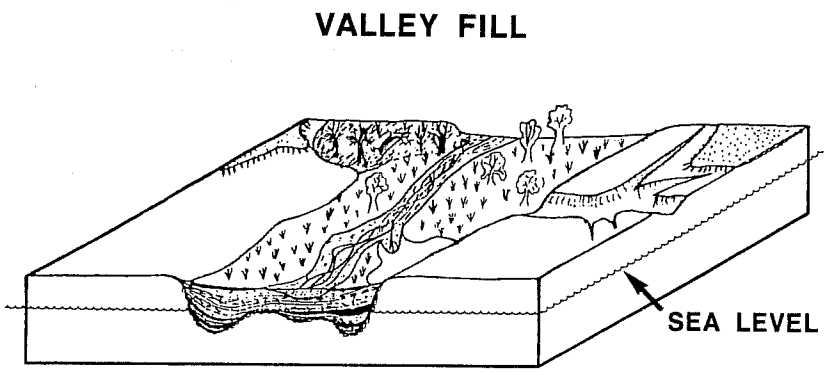

Fig. 2 - Valley fill during period of sea level rise. Valley is filled with river (potential sandstone reservoir) and swamp and marsh deposits (non-reservoir). Fill may be a mixture of marine (below sea level) and non-marine river deposits. (from Farmer, 1981)

forms a ravinement surfaces which removes most or all of the beach and barrier island sands along the shoreline. The ravinement process (Stamp, 1921; Vail, et al., 1977) "scoops down into" and erodes the underlying beds. The destruction of potential reservoirs by the ravinement process is associated with the breaking of fairweather waves, and especially storm waves and currents on the shore during periods of rising sea level. As the sea moves slowly over the land, much of the sand at the shoreline is carried seaward and the previously deposited potential shoreline reservoir sandstones may be destroyed. This ravinement process is believed to erode only to a finite depth (possibly less than 30') and all sediment below this depth (including significant thicknesses of valley-fill sands) will be preserved. Near the most seaward location of the shoreline formed during the maximum sea level drop some valley-fills may be relatively straight, whereas many landward areas may be characterized by meandering valley-fill patterns as observed in Southwest Stockholm field (Fig. 3).

Because valley-fill reservoir sandstones occur in deeply cut incisions in the shoreline areas on the edges of continents, the preservation potential of the sandstones during periods of rising sea level is significantly greater than many other shallow marine and shoreline sandstones. Barrier island and beach sandstone reservoirs commonly are removed by the erosional ravinement process, which occurs during rising sea level, whereas the valley-fill, which extends below the ravinement surface, is preserved.

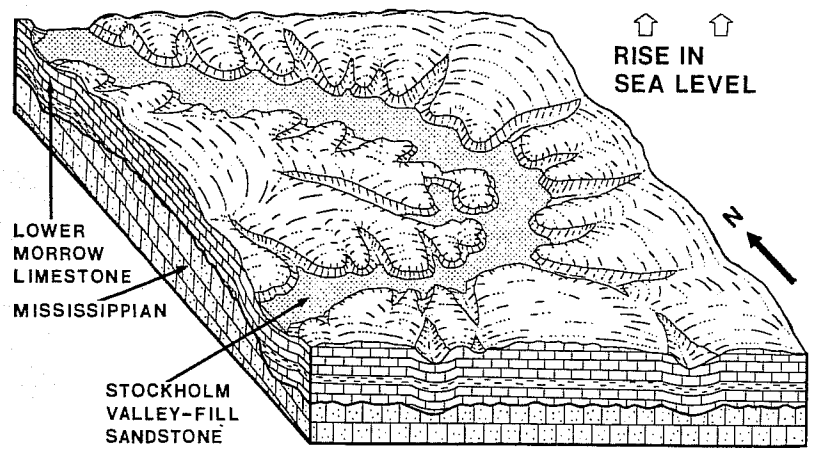

Fig. 3 - Valley-fill sandstone reservoir in Southwest Stockholm field. Valley may be filled entirely with sandstone or partially with limestone and/or shale as observed in Southwest Stockholm field, Kansas. (from Shumard, 1991)

The sandstones, which form the valley-fill reservoirs in Southwest Stockholm field, are geologically characterized as estuaries (flooded river mouths), marine shoreline sandstones and river channel sandstones. The geometry and reservoir characteristics of each of these types of sandstones is different. Where these three types of sandstone locally interfinger, complex barriers to flow may occur among them. Prior

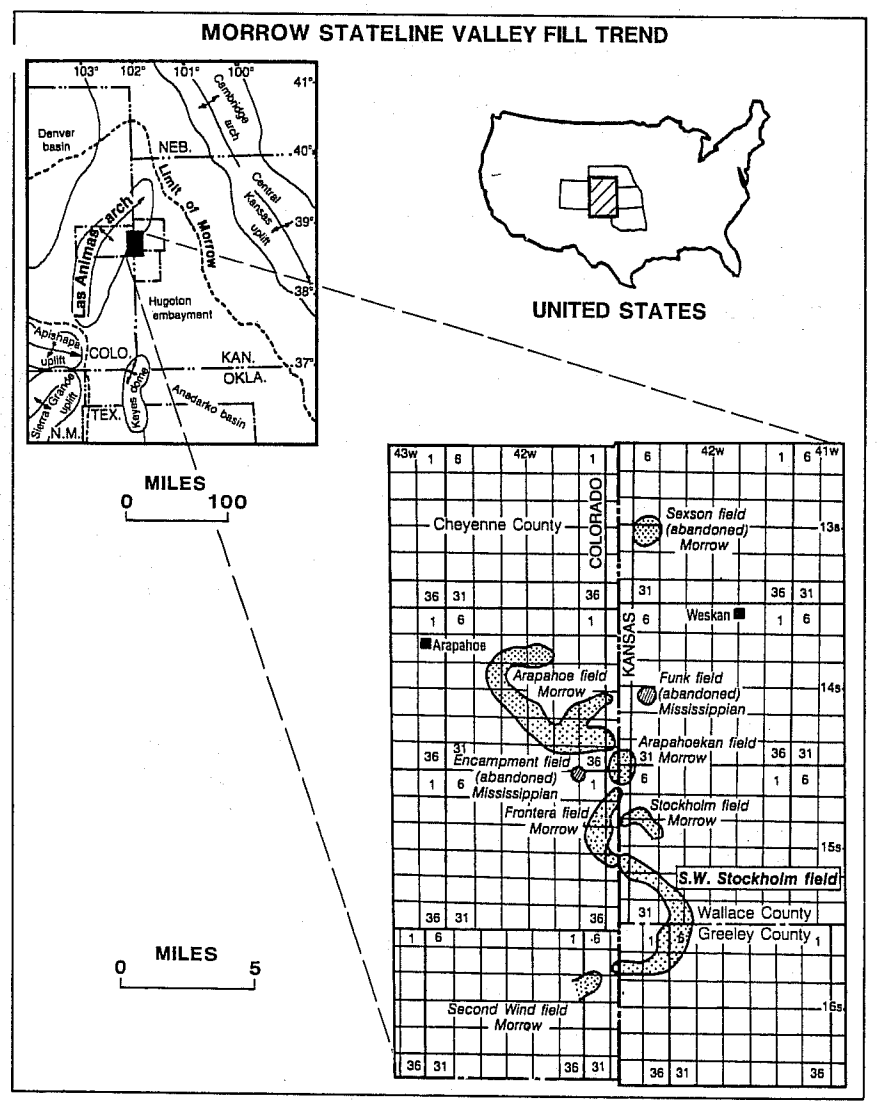

Fig. 4 - Location of 20 mile long "Stateline Trend" Morrow Sandstone fields, which produce from valley-fill sandstone reservoirs. Southwest Stockholm field, Kansas, is located in Greeley and Wallace counties, Kansas. (Shumard and Avis, 1990).

to this study, the significance of the barriers to flow between these different types of sandstone has not been determined, nor has quantitative documentation been obtained to determine flow units.

II. SOUTHWEST STOCKHOLM FIELD

A very active play involving exploration and development of valley-fill reservoirs has been underway for the last few years in the Morrow Sandstone in "Stateline Trend" of southeastern Colorado and westernmost Kansas (Sonnenberg, 1985; Sonnenberg et al., 1990; Weimer, et al., 1988; Krystinik, 1989a, b; Krystinik et al., 1990; Blakeney, et al., 1990). One of the more productive valley-fill fields in the trend is Southwest Stockholm field (Fig. 4), which was discovered in 1979 and was the subject of our study. The field has 87 wells and has produced over 5.5 million barrels of oil from the estimated 42 million barrels in place. The field has been interpreted by Shumard (1989) and Brown et al. (1990) and confirmed by the authors to consist of valley-fill fluvial and estuarine (tidal) sandstones. The composite valley-fills in the field range up to 150' in thickness in the Stockholm valley. The major producing reservoir in the field is the Stockholm Sandstone, which is commonly from 15-30' thick. Core porosity averages 17% (range 10-22%) whereas permeability averages 400 md (range 50-4600 md) (Shumard, 1989; Brown, et al., 1990). The field covers approximately 2000 acres and ranges from 1/4 to 1/2 mile wide and is six miles long. The "Stateline Trend", which includes Southwest Stockholm field, also includes within it's snakelike geometry at least three other fields including Second Wind, Frontera and Arapahoe (Fig. 4). Oil in place along the "Stateline Trend" is estimated by Brown, et al. (1990) to be approximately 170 million barrels. These other valley-fill fields have similar but probably slightly different production characteristics than Southwest Stockholm field.

Along the "Stateline Trend", which extends in a north-south direction on both sides of the border of Kansas and Colorado, are Morrowan Age valley-fill reservoirs, which occur in sinuous valleys that were cut into marine limestones, shales and sandstones during periods when sea level was relatively low. When sea level rose, reservoir sandstones and non-reservoir shales and limestones were deposited within the valleys. Some of the sandstones now are reservoirs, others have relatively poor producing characteristics and form impediments to fluid flow. A type log developed by Shumard and

Avis (1990) for the field shows the vertical sequence of lithologies and the characteristics typical of the formations (Fig. 5).

TYPE LOG

Texas Oil and Gas 4 Evans E, NW NE SE 11-16s-43w

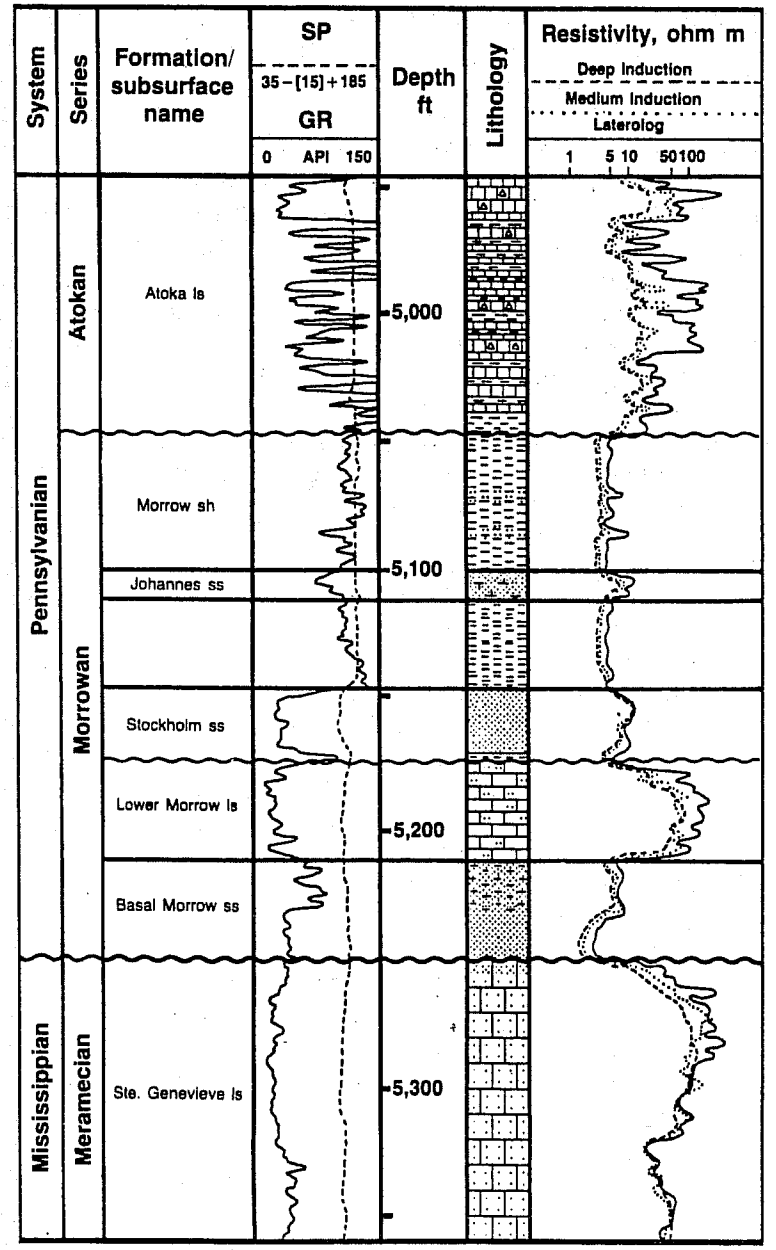

In 1990, several geologic models were proposed for valley-fill deposition in areas such as Southwest Stockholm field. The model proposed by Wheeler, et al. (1990; Fig. 6) for Morrow valley-fill deposits appears to be appppropriate for at least portions of Southwest Stockholm field.

SCHEMATIC, MORROW VALLEY FILL DEPOSITS

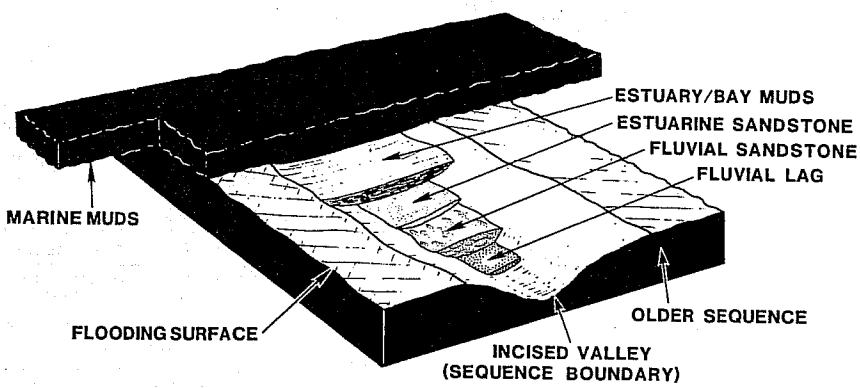

Fig. 6 - Schematic of valley-fill deposits formed in portions of Southwest Stockholm field, Kansas. Incised valley cut into older sequence of rocks is filled initially by coarse river deposits (fluvial lag). Finer grained productive reservoir river (fluvial) sandstones fill medial portions of valley prior to relative sea level rise into valley. As sea level rises, estuary- and bay-deposited sandstones are locally deposited above and seaward of river sands. As sea level rises still further, the estuary becomes muddier and estuarine mud blankets and seals the reservoir sandstones. With further rise in relative sea level, marine muds blanket valleys and intervalley areas. (Modified from Wheeler, et al., 1990).

Fig. 5 - Type log for Southwest Stockholm field. Geographic location shown on Figure 9 (Well No. 124). Note that three potentially productive sandstones are present in Morrow interval. At Southwest Stockholm field, Basal Morrow Sandstone is non-productive as is the Lower Morrow Limestone. The Basal Morrow Sandstone is limited in distribution by valley walls. The Stockholm and Johannes valley-fill sandstones are both productive in Southwest Stockholm field. The base of the Morrow is a regional unconformity, which in most areas forms the bottom of the valley that is filled with numerous lithologies including sandstone, limestone and shale. Significant relief on the unconformity at the base of the Stockholm Sandstone is limited for the most part to the width of the valley(s).

TEXAS OIL AND GAS, EVANS 2E
MORROW SANDSTONE, SHALE AND LIMESTONE p. 1 of 2
SW STOCKHOLM FIELD, NW SE Sec. 11 T16S R43W, Greeley Co., KS

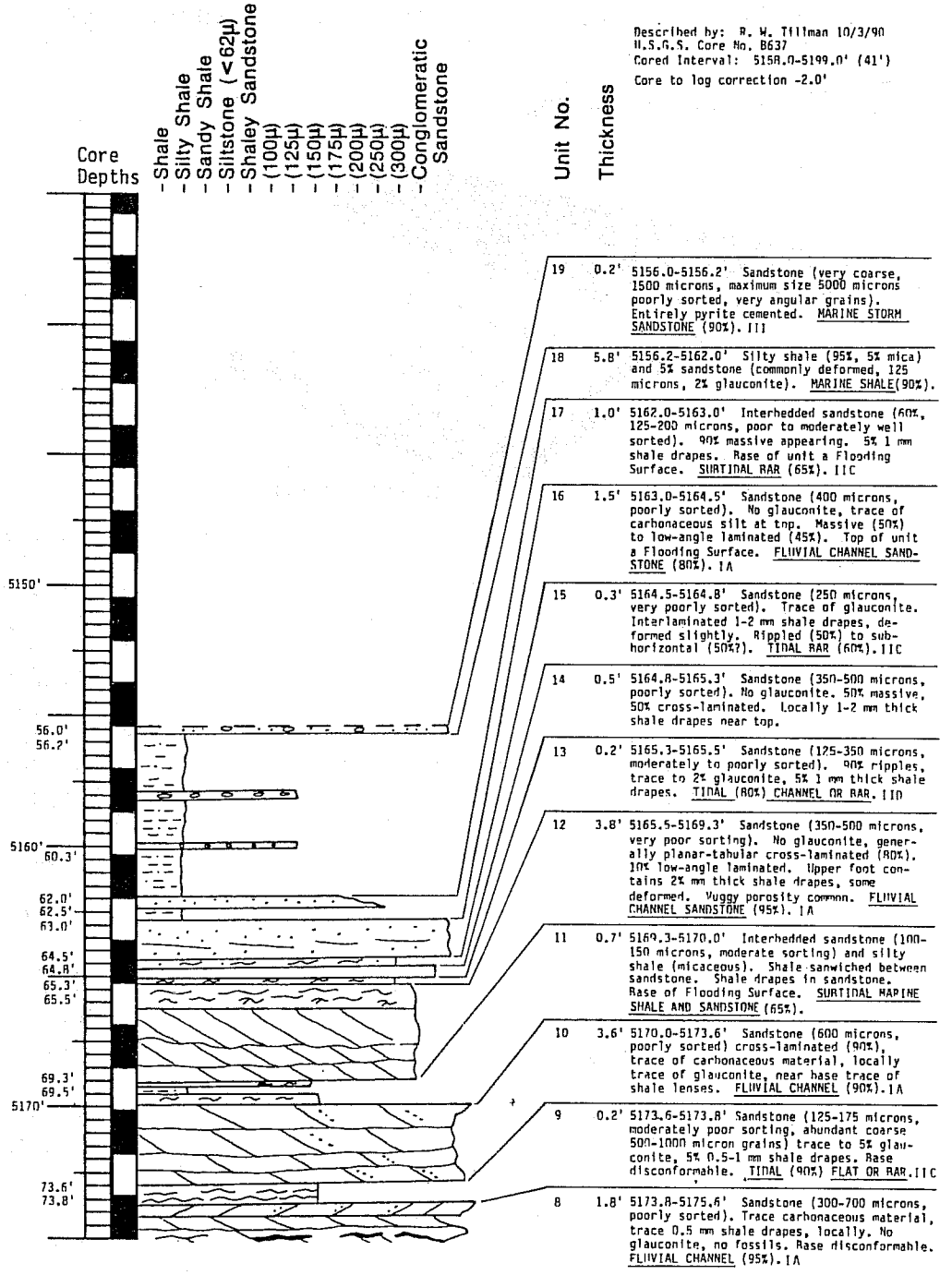

Fig. 7A - Geologic core description, Morrow Sandstone, Southwest Stockholm field portion of "Stateline Trend". For

A. Macroheterogeneities

In order to determine the distribution of reservoir boundaries and the distribution of macroheterogeneities associated with the valley-fill reservoir at Southwest Stockholm field, all the available cores within the field were described and geologically interpreted (Figs. 7A, 7B, 8A, 8B). The log suite for the cored wells were qualitatively calibrated to the core interpretation; log shape, gamma ray and resitivity readings were used to extend the geologic facies observed in core to nearby non-cored wells. Two cross sections were constructed, which included the cored wells. Portions of these cross sections are included as figures.

The Morrowan geologic section at Southwest Stockholm field is complex, as may be observed in the type log (Fig. 5). Three Morrowan sandstone units within the valley-fill are potential reservoirs. The Stockholm Sandstone is the major producing unit in Southwest Stockholm field. A second producing sandstone is the "Johannes Sandstone", which produces locally. The Basal Morrow Sandstone is non-productive within the borders of the field (Fig. 9).

The base of the valley from which Southwest Stockholm field produces is marked by a major unconformity at the top of the Mississippian limestones (Fig. 5). A significant thickness of Mississippian limestones was probably removed during the period of valley cutting prior to deposition of the Basal Morrow Sandstone. The Basal Morrow Sandstone is limited in distribution within the valley and may have been removed from portions of the northeast area of the field by a second period of erosion. Following erosion(?) of the Basal Morrow Sandstone a siginificant rise in sea level occurred and a "blanket" of marine lime sediment was deposited within the valley and in areas outside the valley. A third sea level drop occurred (top of Lower Morrow Limestone, Fig. 5) and much of the limestone was eroded within the area of the valley, forming a valley within a valley.

In this valley within a valley the highly productive Stockholm Sandstone was deposited. The Stockholm Sandstone

geographic location refer to Well 131 on Figure 9 base map. Reservoir is composed primarily of coarse-grained fluvial (river) deposited sandstones (Units 6, 8, 10, 12). Interbedded on 1-5' scale are thin (0.2-0.7' thick) finer grained and more clayey tidally deposited sandstones. These finer grained units impede vertical flow in the reservoir at and near this well.

TEXAS OIL AND GAS, EVANS 2E
MORROW SANDSTONE, SHALE AND LIMESTONE
SW STOCKHOLM FIELD, NW SE Sec. 11 T16S R43W, Greeley Co., KS

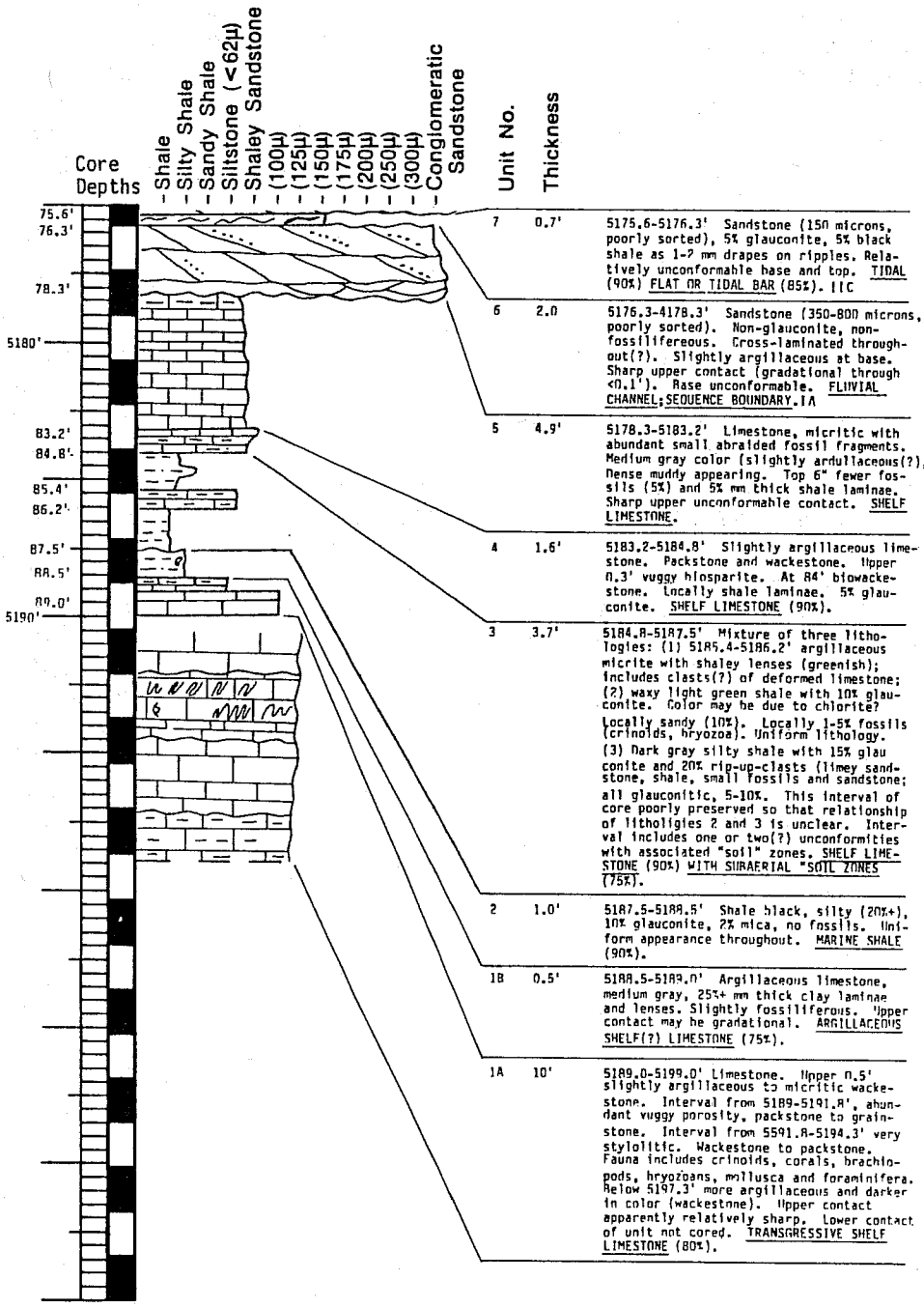

Unit No.	Thickness	
7	0.7'	5175.6-5176.3' Sandstone (150 microns, poorly sorted), 5% glauconite, 5% black shale as 1-2 mm drapes on ripples. Relatively unconformable base and top. TIDAL (90%) FLAT OR TIDAL BAR (85%). IIC
6	2.0	5176.3-4178.3' Sandstone (350-800 microns, poorly sorted). Non-glauconite, non-fossiliferous. Cross-laminated throughout(?). Slightly argillaceous at base. Sharp upper contact (gradational through <0.1'). Base unconformable. FLUVIAL CHANNEL;SEQUENCE BOUNDARY.IA
5	4.9'	5178.3-5183.2' Limestone, micritic with abundant small abraided fossil fragments. Medium gray color (slightly ardullaceous(?), dense muddy appearing. Top 6" fewer fossils (5%) and 5% mm thick shale laminae. Sharp upper unconformable contact. SHELF LIMESTONE.
4	1.6'	5183.2-5184.8' Slightly argillaceous limestone. Packstone and wackestone. Upper 0.3' vuggy biosparite. At 84' biowackestone. Locally shale laminae. 5% glauconite. SHELF LIMESTONE (90%).
3	3.7'	5184.8-5187.5' Mixture of three lithologies: (1) 5185.4-5186.2' argillaceous micrite with shaley lenses (greenish); includes clasts(?) of deformed limestone; (2) waxy light green shale with 10% glauconite. Color may be due to chlorite? Locally sandy (10%). Locally 1-5% fossils (crinoids, bryozoa). Uniform lithology. (3) Dark gray silty shale with 15% glauconite and 20% rip-up-clasts (limey sandstone, shale, small fossils and sandstone; all glauconitic, 5-10%. This interval of core poorly preserved so that relationship of litholigies 2 and 3 is unclear. Interval includes one or two(?) unconformities with associated "soil" zones. SHELF LIMESTONE (90%) WITH SUBAERIAL "SOIL ZONES (75%).
2	1.0'	5187.5-5188.5' Shale black, silty (20%+), 10% glauconite, 2% mica, no fossils. Uniform appearance throughout. MARINE SHALE (90%).
1B	0.5'	5188.5-5189.0' Argillaceous limestone, medium gray, 25%+ mm thick clay laminae and lenses. Slightly fossiliferous. Upper contact may be gradational. ARGILLACEOUS SHELF(?) LIMESTONE (75%).
1A	10'	5189.0-5199.0' Limestone. Upper 0.5' slightly argillaceous to micritic wackestone. Interval from 5189-5191.8', abundant vuggy porosity, packstone to grainstone. Interval from 5591.8-5194.3' very stylolitic. Wackestone to packstone. Fauna includes crinoids, corals, brachiopods, bryozoans, mollusca and foraminifera. Below 5197.3' more argillaceous and darker in color (wackestone). Upper contact apparently relatively sharp. Lower contact of unit not cored. TRANSGRESSIVE SHELF LIMESTONE (80%).

[Fig. 7B - Part 2 of 2]

is variable vertically and horizontally. The most accurate analysis of the heterogeneities within the reservoirs were determined by detailed geologic (sedimentologic) description and interpretation on a unit-by-unit basis of the four cores available from the field. Geologic maps were constructed and the production characteristics of each of the units were determined and compared with other similar and dissimilar geologic units. Heterogeneities recognized in core descriptions were compared to log parameters in the same and adjacent wells and cross sections, and geologic and production maps were completed. As may be observed in the type log (Fig. 5) and subsequently described cross sections, the major reservoir boundary seals for the Stockholm sandstones are dense non-porous cabonates below and locally lateral to the sandstone and an overlying marine shale. Within the reservoir a significant number of macroheterogeneites are recognized which either inhibit or prevent fluid flow.

1. Discussion of TXO Evans 2E Core

The cored interval in the TXO Evans 2E well (well number 131, Fig. 9) includes, below the reservoir, approximately 21' of non-reservoir Lower Morrow Limestone and, above the reservoir, 7' of non-permeable marine shales. Details of these units are described in Figure 7.

The Stockholm Sandstone in Figure 7 consists of porous and permeable medium- to coarse-grained (0.3-0.7 mm mean diameter) river-deposited standstone with thin interbeds of thin, presumably laterally persistent, tidally deposited, slightly shaley and glauconitic sandstones with relatively poorer reservoir characteritics.

In this core the internal features of the river-deposited (fluvial) sandstones are primarily steeply inclined cross laminations (Units 6, 8, 10 and 12). The bases of the river deposits are sharp and the tops are either eroded (Units 6, 8 and 10) or reworked (Unit 12). The interbedded tidal- to marine-deposited units (7, 9, and 11) are much finer grained, (0.1-0.15 mm mean diameter) and contain lenses and beds of clay including trace amounts of the greenish mineral glauconite, which is believed to form primarily on shallow marine shelfs from chemical alteration of fecal pellets. As discussed in more detail under microheterogeneities, the thin shale laminae, in addition to being partial barriers to flow within the sandstone, cause significant secondary pore-filling immediately adjacent to the laminae. Where any combination of impediments to flow occurs (tidally deposited fine-grained sands, shales layers or relatively abundant clayey laminae) in this well, the Stockholm Sandstone has poor vertical flow

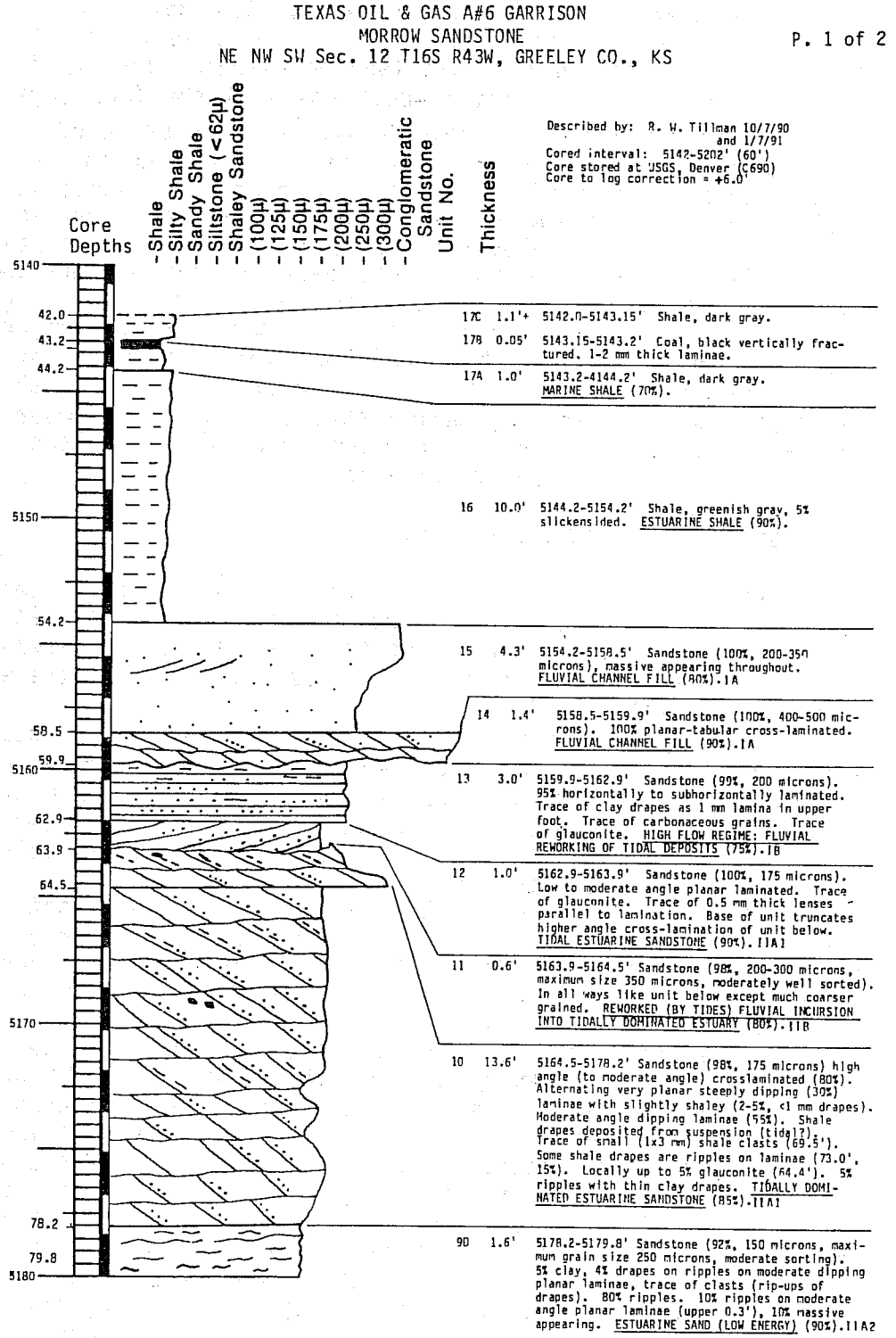

Fig. 8B - Geologic core description and interpretations, Morrow Sandstone, "Stateline Trend", Southwest Stockholm field. For

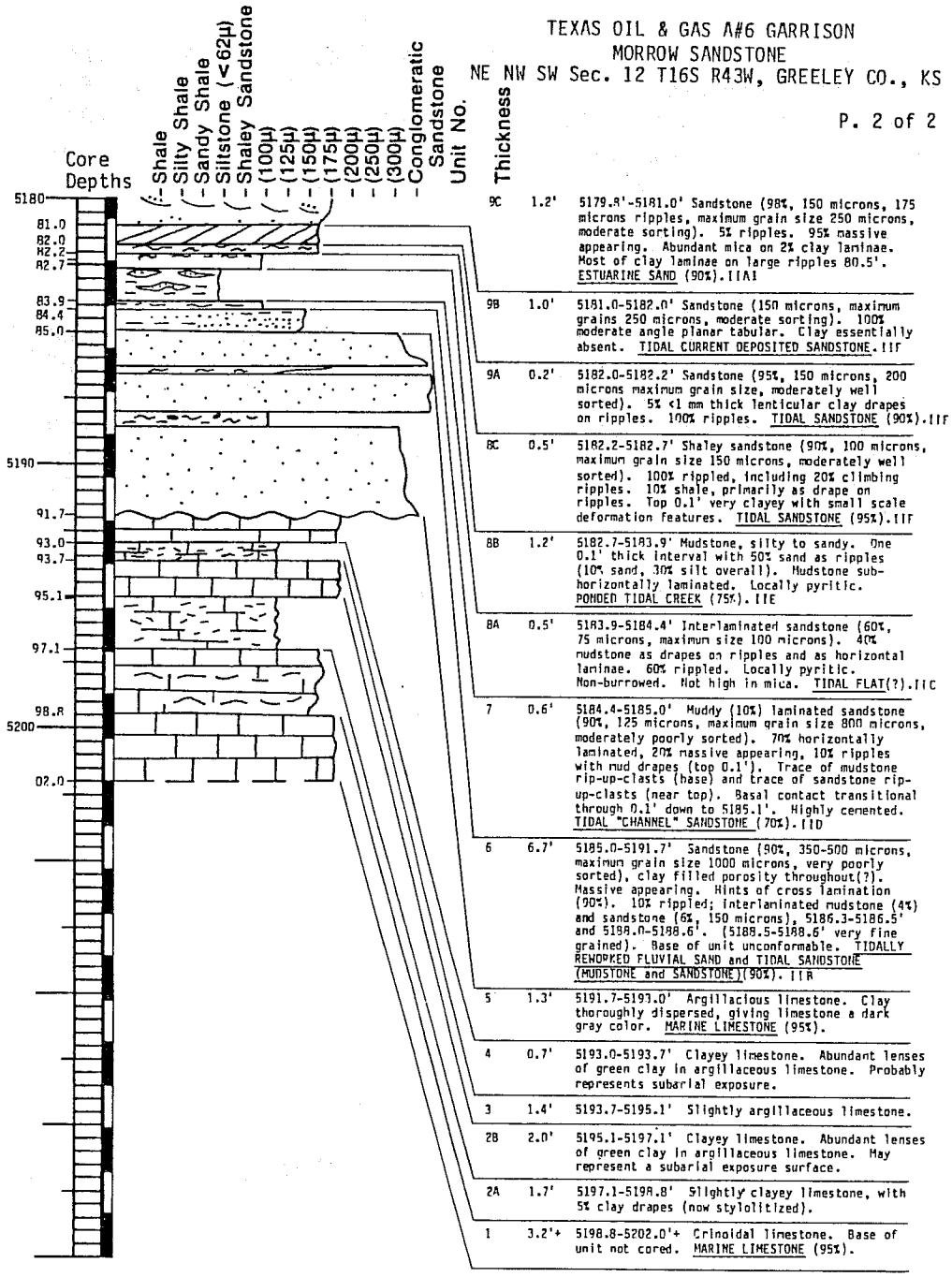

[Fig. 8A - Part 1 of 2]

geographic location refer to Well 128 on Figure 9 base map. Reservoir is composed primarily of tidally deposited sandstones (Units 7-12). Perforated interval 5160-5170' (log depth), 5154-5164' (core depth). This well is included in cross section in Figure 11. River-deposited Units are 13-15.

characteristics since the river deposited reservoir sandstones are separated every 2 to 4 feet vertically by thin (0.2-1.0' thick) tidal sandstones and shales. These thin barriers to flow are only barely perceptible on the log of the Evan 2E (Fig. 10) but are identifiable in the core.

2. Discussion of TXO Garrison A6 Core

The core through the Stockholm Sandstone in TXO A6 Garrison is quite different from that encountered in the TXO Evans 2E. In the A6 Garrison, a 30' complex sequence of tidally deposited estuarine and possibly shallow marine sandstones are overlain by 8-10 feet of river-deposited sandstone. Nonproductive Lower Morrow limestones occur below the reservoir and 10' of greenish gray estuarine shale is

TABLE I

SANDSTONE FACIES STOCKHOLM SANDSTONE
SOUTHWEST STOCKHOLM FIELD

I. River (Fluvial) Sandstones

- A. Channel Fill
- B. Reworked Tidal Sands

II. Tidally Deposited Sandstones

- A. Estuary Channels
  - 1) Sandstone Fill
  - 2) Low Energy Fill
- B. Fluvial Channel Sands Reworked by Tides
- C. Tidal Bar or Tidal Flat
- D. Tidal Channels
- E. Ponded Tidal Creek Fill
- F. Tidal Sandstone

III. Marine Shelf Sandstones

immediately above the reservoir (Fig. 8). These estuarine shales are overlain sharply by dark-gray marine shales. These shales mark a significant "flooding surface".

Only the river sandstone is perforated in this well and it yielded an initial flow of 326 BOPD (compared to an inital flow of only 115 BOPD in the highly interbedded tidal and riverine TXO Evans 2E well). As shown in a portion of cross section Y-Y' (Fig. 11) this well is in a relatively thin portion of the river-deposited sands. As was the case in the TXO Evans 2E, the tidally deposited sandstones are generally much finer grained (0.1-0.18 mm mean size) than the river sandstones. Table I lists the various sandstone facies that occur in the Stockholm Sandstone. Virtually all of the facies listed in Table I occur in the cored interval in the TXO A6 Garrison. As will be discussed in a subsequent section, sparse porosity and permeability data available for this well (Table II) indicates that the permeabilites and K/Ø ratios are significantly different for river and tidally deposited sandstones.

TABLE II

RESERVOIR PARAMETERS FOR INDIVIDUAL SAMPLES,
S.W. STOCKHOLM FIELD, STOCKHOLM SANDSTONE*

WELL	GEOLOGIC CORE UNIT	SAMPLE DEPTH (ft)	K (md)	Ø (%)	K/Ø	R35 m
TXO Garrison A-6						
	15	5155	1400	19.5	71.8	29.3
	14	5159.5	140	12.4	11.3	11.2
Mean, River Sandstones			725	16.0	45.3	12.7
	10	5169	111	15.5	7.2	8.1
	9C	5181	80	15.3	5.2	6.7
Mean, Tidal Sandstones			95.5	15.4	6.2	7.4
TXO White AB-1						
	8	5174	1890	20.6	92.2	33.5
	8	5185	432	16.0	27.0	17.4
	8	5187	316	17.9	17.7	13.2
Mean, River Sandstones			879	18.2	45.6	25.8
TXO Bergquist 2 River						
	7B	5115.5	129	11.7	11.0	11.2
	7A	5113	50	12.3	4.1	6.2
	4	5121.5	84	14.1	6.0	7.4
	4	5122.5	83	17.8	4.7	6.0
	2	5125	77	11.5	6.7	8.4
Mean, Tidal Sandstones			73.5	13.9	5.4	7.0

* Raw data from Core Laboratory Inc. Report File 203-87028

3. Discussion of TXO Bergquist No. 2 Core

Twenty-eight feet of Well No. 60 (Fig. 9, TXO Bergquist No. 2) was cored and a geologic description and interpretation of the core was made. The core penetrated the upper two-thirds of the Stockholm Sandstone. Tidally deposited sandstones predominate in the lower 9' of the core. In the upper portion of the sandstone, fluvial (river) sandstones alternate with tidally deposited and/or reworked estuarine sandstones. Limited porosity and permeability data (Table III) suggest that in this well, as well as in others where porosity and permeability data were available, the river sandstones have better productive characteristics (Ø = 14%, K = 74 md). The lower values of permeability in the tidal sandstones are in part due to the presence of thin clay drapes and laminae within the sandstone. The whole Stockholm Sandstone was perforated in this well so the contribution to hydrocarbon production of tidal vs river deposited sandstone is not immediately determinable.

4. Southwest Stockholm Maps

Two isopach maps were among those constructed for the Southwest Stockholm field area using input supplied by the principal investigator to a Scientific Computer Application (SCA) mapping program. The maps are (1) Stockholm Sandstone, Net Sand Isopach, (2) Lower Morrow Limestone, Isopach Map. These maps are similar to, but less interpretive than, those by Shumard and Avis, 1990, and Shumard (in press, AAPG).

A top of Morrow structure map (Fig. 4, Shumard and Avis, 1990) indicates that a crescent-shaped structural low extends from Sec. 11, T16S, R43W to Sec. 29, T15S, R42W (Fig. 9). As

TABLE III

RESERVOIR PARAMETERS FOR GEOLOGIC FACIES
SOUTHWEST STOCKHOLM FIELD

	K (md)	Ø (%)	K/Ø	R35 m
River Sandstones				
Mean	703	16.3	39.8	19.0
Range	129-1890	11.7-20.6	11.0-92.2	11.2-33.5
Tidal Sandstones				
Mean	80.8	14.4	5.6	7.1
Range	50-111	11.5-17.8	4.1-7.2	6.0-8.4

can be observed when compared with the Stockholm Sandstone Net Sand Isopach Map (Fig. 12), this crescent shaped area is the area of thickest Stockholm Sandstone reservoir sands.

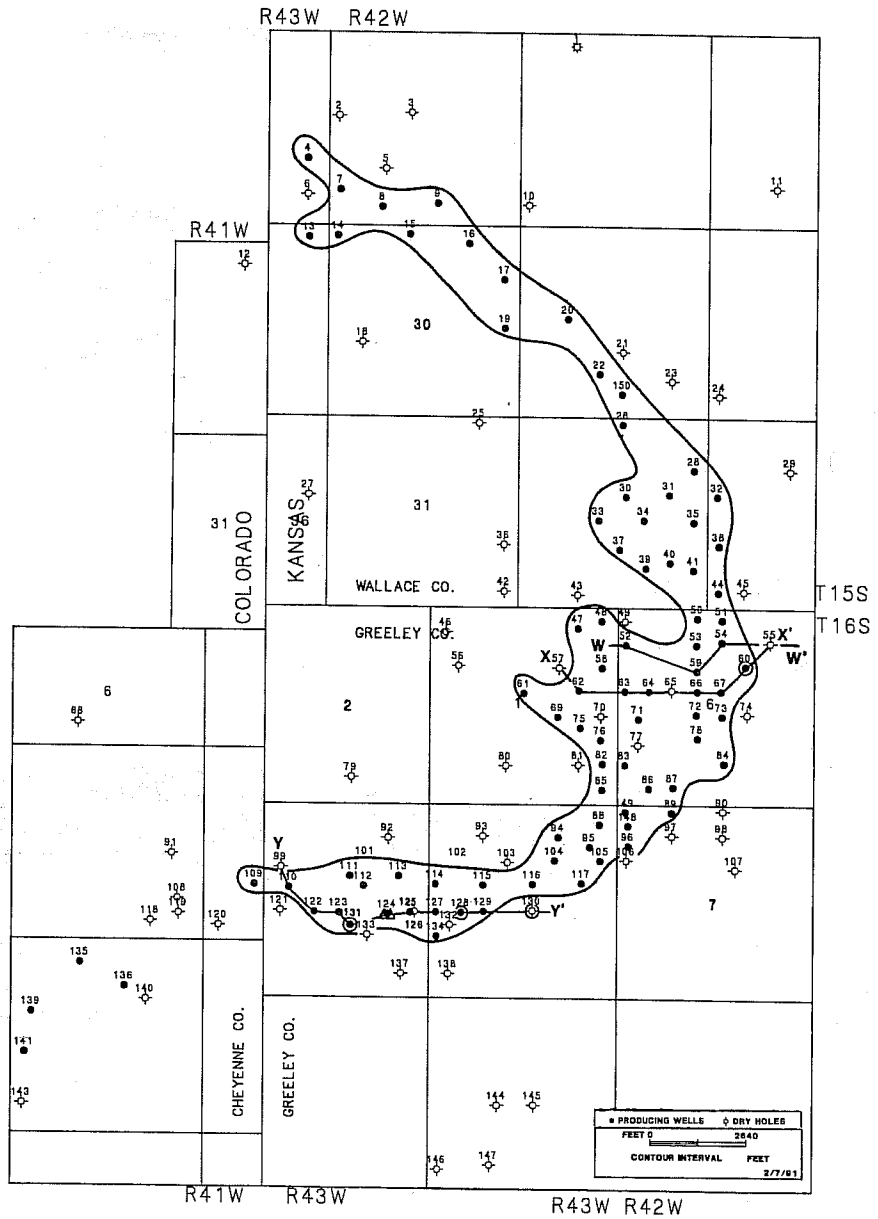

Fig. 9 - Base map, outlining borders of Southwest Stockholm field, Kansas. Location of stratigraphic cross sections X-X', Y-Y' and W-W' is indicated. Cored wells described in this study are indicated by circles. Type log well (Fig. 5) is indicated by a triangle. A list of all numbered wells on this map is available from the senior author.

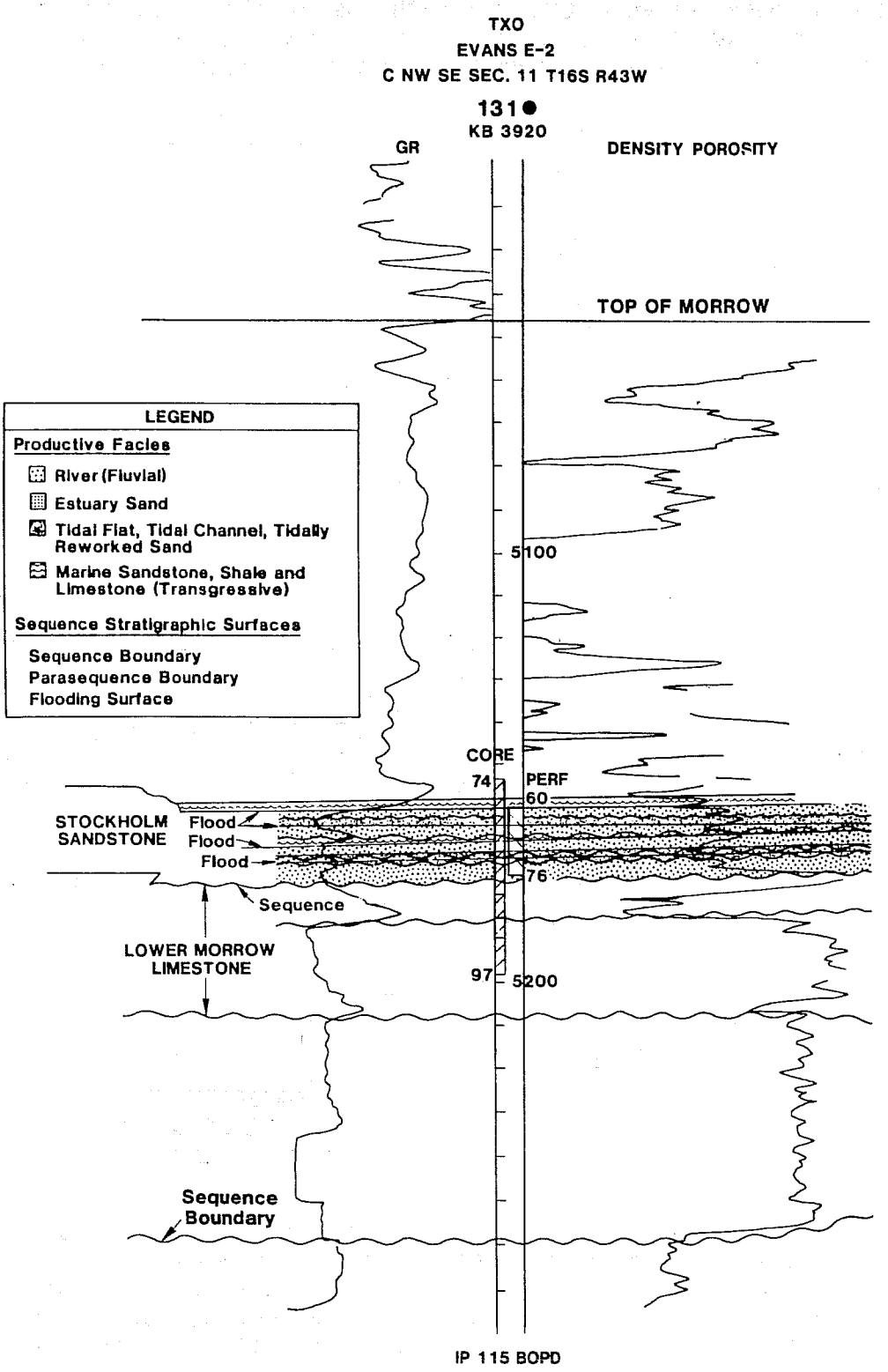
TXO
EVANS E-2
C NW SE SEC. 11 T16S R43W
131●
KB 3920
GR
DENSITY POROSITY
TOP OF MORROW
LEGEND
Productive Facies
River (Fluvial)
Estuary Sand
Tidal Flat, Tidal Channel, Tidally Reworked Sand
Marine Sandstone, Shale and Limestone (Transgressive)
Sequence Stratigraphic Surfaces
Sequence Boundary
Parasequence Boundary
Flooding Surface
5100
CORE
74
PERF
60
STOCKHOLM SANDSTONE
Flood
Flood
Flood
76
Sequence
LOWER MORROW LIMESTONE
97
5200
Sequence Boundary
IP 115 BOPD

The Stockholm Sandstone is a lenticular sandstone in Southwest Stockholm field (Fig. 12). The thickness patterns are somewhat irregular and reflect the affects of both the bottom topography on the floor of the valley immediately prior to deposition of the sandstone and to the macroheterogeneities and microheterogeneities within the sandstone. As would be expected, the sandstone thickens away from the edges of the valley.

The thicker net sand intervals (30') tend to be near the center of the valley where the valley is relatively wide. It is only in the area just south of the boundary between T15S and T16S that the maximum thickness is skewed to one side of the channel (Fig. 12). At this location, an area approximately 1/2 x 1 mile in dimension contains no net Stockholm sand.

The Lower Morrow Limestone Isopach Map (Fig. 13) indicates that the absence of sand in the westernmost part of Sec. 11 (Fig. 12) was due to the presence of a 40-60' thick "plateau" of remnant (non-eroded) limestone (Fig. 13). Because the valley was by river erosion into more or less uniformly resistant rocks during lowstand of the sea, a roughly equal cross section area for the valley was probably maintained all along the length of the field during maximum stream flow. In order to maintain a roughly equivalent cross section, the channel within the valley eroded deeper in the narrower areas. A shallow and narrow channel was also cut west of the "limestone plateau" (Figs. 13 and 14). Reactivation of basement faulting in Sec. 11, T16S, R43W prior to filling of the valley (Brown et at., 1990; Fig. 2) may have been responsible for what appears to be anomalous narrowing of the sand trend in the south part of the field near the Colorado-Kansas border.

The "Johannes Sandstone" (Fig. 5) is a thin discontinuous sandstone, which is separated from the underlying Stockholm Sandstone by estuarine and marine shales. No cores were available from the "Johannes Sandstone" so the environment of deposition was not determined. Isopach mapping of the gross sand thickness of the "Johannes" sandstones suggests that a portion of the "limestone plateau" in the west half of

Fig. 10 - Gamma Ray Density Log showing interpreted heterogeneities affecting fluid flow. Erosional unconformities occur at base of Basal Morrow Sandstone and at base of Stockholm Sandstone. Thin fine-grained, more clayey tidally deposited marine(?) sands are interbedded with river sands in the Stockholm Sandstone in this well and form impedements to vertical flow at this location.

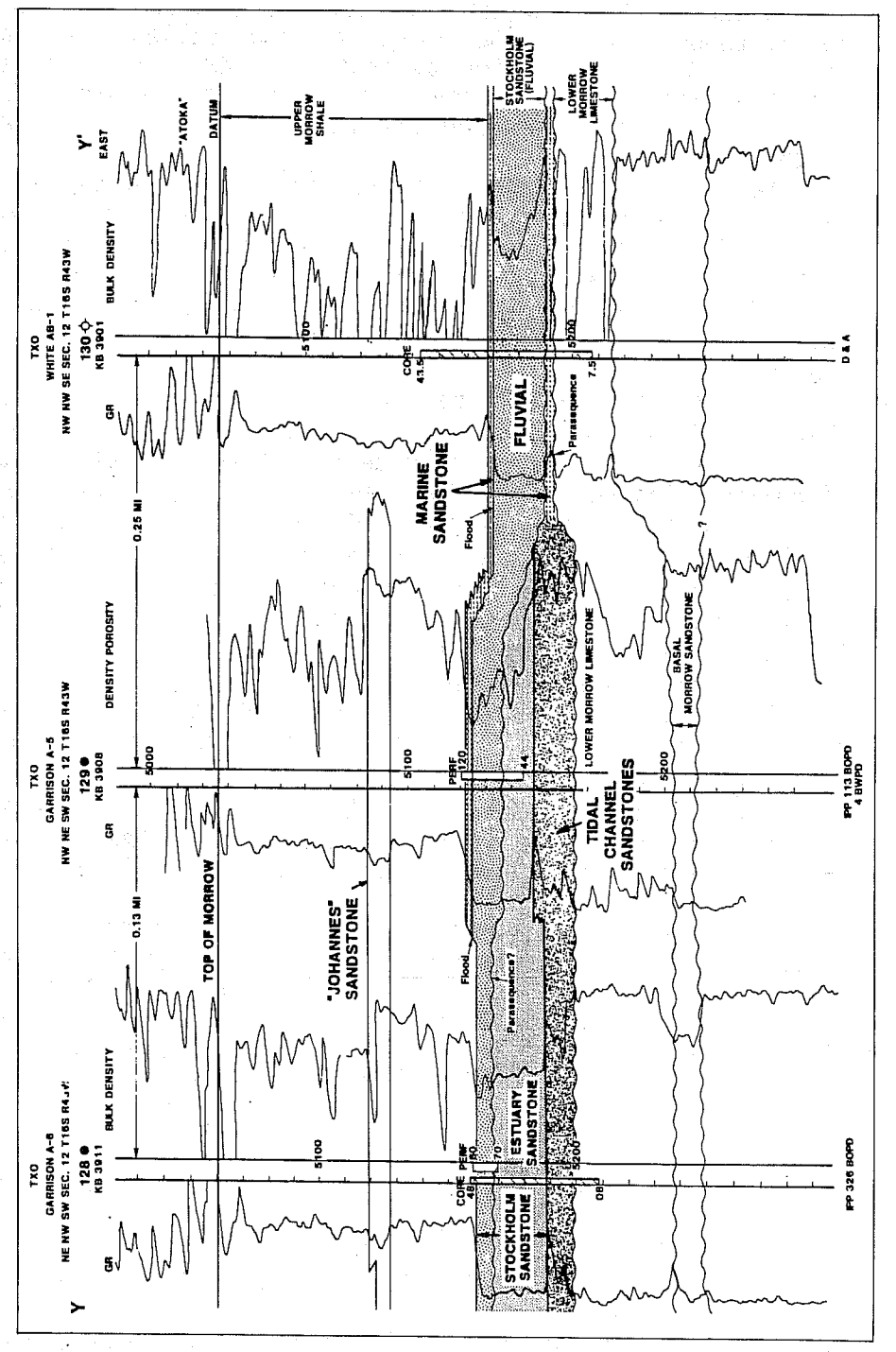
Y
TXO
GARRISON A-8
NE NW SW SEC. 12 T16S R43W
128 ●
KB 3911
GR
BULK DENSITY
0.13 MI
TOP OF MORROW
"JOHANNES" SANDSTONE
CORE 48
PERF 80
STOCKHOLM SANDSTONE
ESTUARY SANDSTONE
Parasequence?
Flood
5100
5200
TXO
GARRISON A-5
NW NE SW SEC. 12 T16S R43W
129 ●
KB 3908
GR
DENSITY POROSITY
0.25 MI
5000
5100
PERF 120
144
LOWER MORROW LIMESTONE
MARINE SANDSTONE
FLUVIAL
Flood
Parasequence
TIDAL CHANNEL SANDSTONES
BASAL MORROW SANDSTONE
5200
IPP 113 BOPD
4 BWPD
TXO
WHITE AB-1
NW NW SE SEC. 12 T16S R43W
130 ◇
KB 3901
GR
BULK DENSITY
Y'
EAST
"ATOKA"
DATUM
UPPER MORROW SHALE
5100
CORE 43.5
STOCKHOLM SANDSTONE (FLUVIAL)
LOWER MORROW LIMESTONE
5200
7.5
Parasequence
D & A
IPP 326 BOPD

Sec. 11, T16S, R43W was still a deterent to sand deposition as late as "Johannes time" because no "Johannes Sandstone" occurs in an area of approximately 1/8 section. Rather than being a more or less continuous reservoir over portions of the field, as suggested by Shumard and Avis (1990), our work indicates that the "Johannes" is subdivided into at least four geographically separated pods or lenses, which were probably depositionally separate. Only a small portion of the "Johannes Sandstone" calculates as productive (Shumard and Avis, 1990).

The non-productive Lower Morrow Limestone was deposited between the Basal Morrow Sandstone and the Stockholm Sandstone (Fig. 5). The Lower Morrow Limestone isopach map (Fig. 13) shows areas of thinning within the valley compared to a thickness of 60 to 80' outside the valley. Thinning of the limestone within the valley resulted from (1) deposition over relatively thick areas of Lower Morrow Sandstone, and (2) erosion of the upper portions of the Lower Morrow Limestone within the valley prior to deposition of the Stockholm Sandstone. In some area of the field (S 1/2 Sec. 6, T16S, R42W) the limestone was completely removed. The thickest valley limestones (87') occur in the area of the "limestone plateau", an area of little or no erosion of the limestone (Fig. 14). In the south-central portion of the field, where the underlying Basal Morrow Sandstone is thickest, the Lower Morrow Limestone thickness was controlled primarily by the relief on the pre-limestone depositional surfaces within the valley (i.e., between wells 129 and 130, Fig. 11). Where the valley was already filled by 50' or more of

Fig. 11 - This figure along with Figure 15 are portions of stratigraphic cross section Y-Y' (not included in paper). Location of the cross section is indicated on Figure 9. Note lenticularity of sandstone facies identified in three cored wells (128, 130, 131). Erosional unconformities occur at base of Basal Morrow Sandstone and at base of Stockholm Sandstone. Perforated intervals are primarily in river-deposited sand intervals. Estuarine sands (cross bedded, clayey, fine grained) form much of the sandstone in Well 130. High clay content, etc. of tidal flat sandstones cause this facies to be marginal to non-reservoir. Sharp lateral change between marine and tidal flat sandstones occurs between wells 129 and 130. Note also that river apparently cut down through previously deposited estuarine sandstones between wells 129 and 130 and that river sandstones were deposited in the cut down. The reason for non-productivity of well No. 130 is not known as it contains reservoir quality sandstone.

Basal Morrow Sandstone, less of the thickness of the valley remained to be filled by limestone. The Basal Morrow Sand-

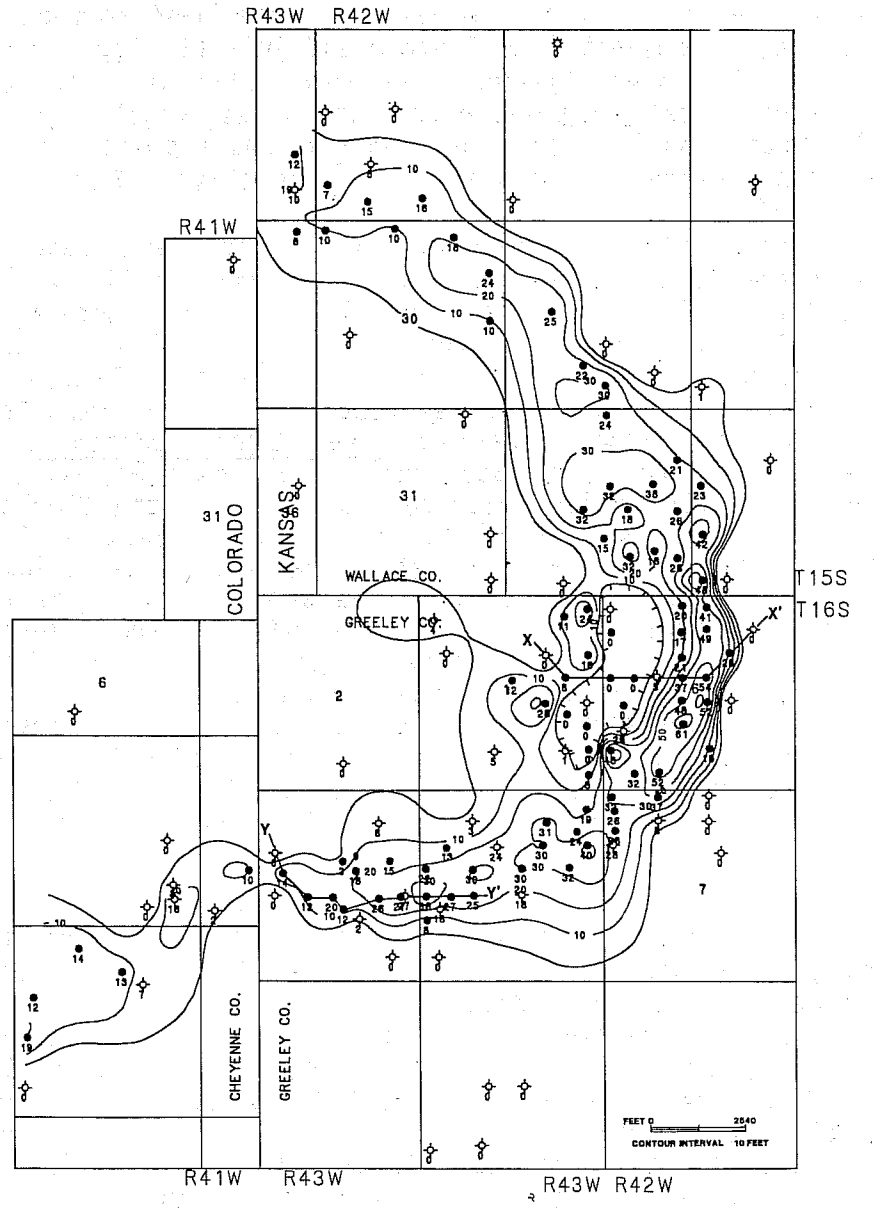

Fig. 12 - Stockholm Sandstone, Net Sand Isopach Map, Southwest Stockholm field, Kansas. Note lenticularity and sharp boundary of sand body, which is constrained laterally by edges of eroded valleys. Note also that maximum sand thickness (60') occurs in a narrow portion of channel adjacent to the hachered area where no sand was deposited due to relief (40-60') of underlying Lower Morrow Limestone (Sec. 6, T16S, R42W, Kansas). Thicknesses are posted for individual wells.

stone is generally limited to the valley and thins abruptly at the edge of the valley (Fig. 15).

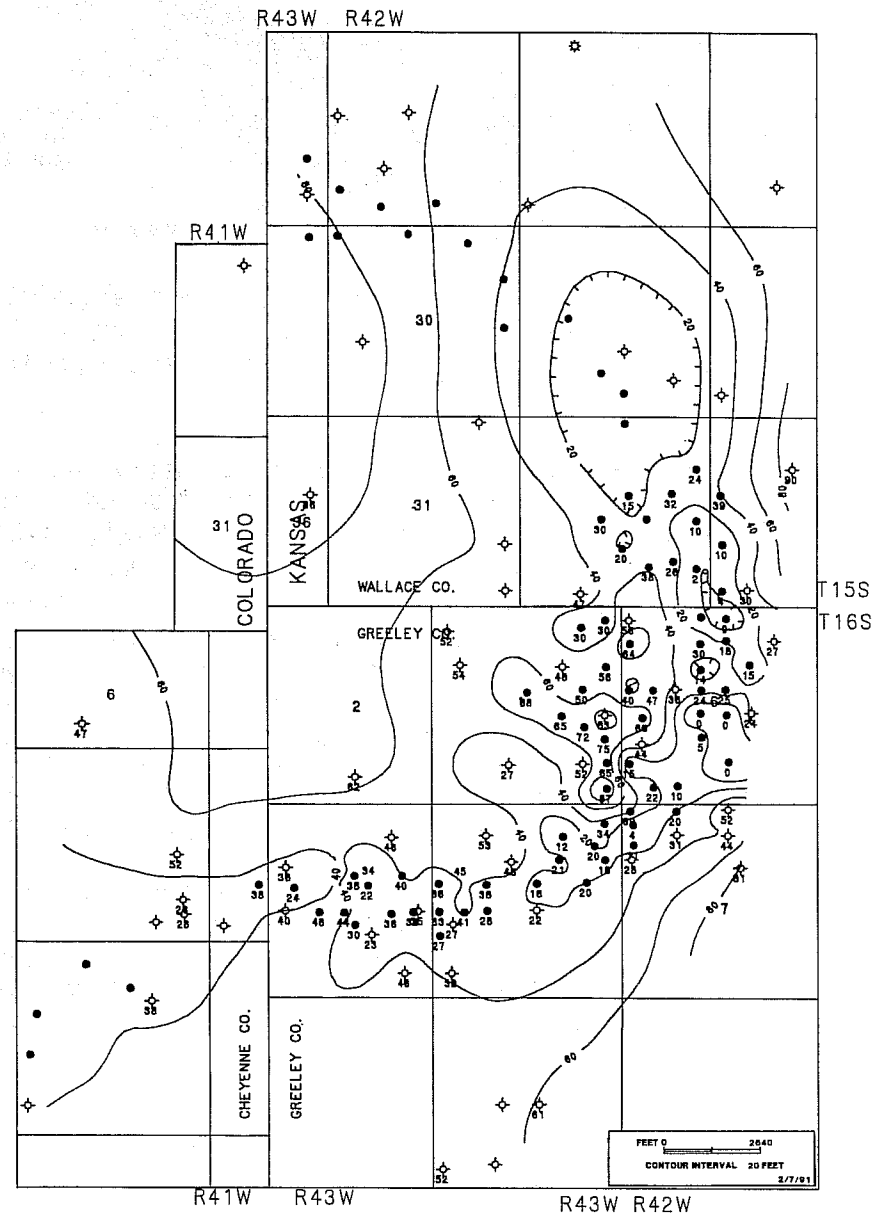

Fig. 13 - Lower Morrow Limestone Isopach Map, Southwest Stockholm field, Kansas. Refer to Fig. 11 for stratigraphic location. Thinning of limestone is limited primarily to the width of the valley. The limestone deposited during a period of relatively high sea level and was partially eroded during a subsequent drop in sea level. Thicknesses are posted for individual wells.

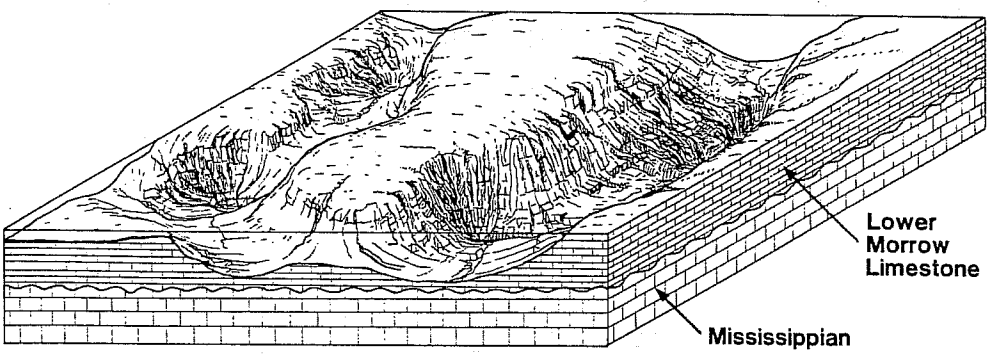

Fig. 14 - Relief in area of Southwest Stockholm field valley following erosion of Lower Morrow Limestone. Upon this irregular surface the Stockholm Sandstone was deposited.

In order to understand the reservoir geometry of the field, a series of cross sections were constructed. The locations of three of these cross sections (W-W', X-X', Y-Y') are shown in Figure 9. A summary version of W-W' (Fig. 16) was published by Brown et al. (1990) along with a seismic section paralleling the stratigraphic log section. This cross section shows the relief on the surface of the Lower Morrow Limestone which was filled by the Stockholm Sandstone and at least locally by shale that preceded Stockholm Sandstone deposition. The thickening of the valley is very obvious in the seismic section in Figure 16. This section also contains one of the described and interpreted cores (TXO Bergquist No. 2).

In the 80 miles along the Colorado-Kansas border, where Lower Morrow Sandstones produce from valley-fills, at least seven unconformities occur on which valley-fills have been mapped (Fig. 17). Each of these unconformities separates valley-fills from underlying marine and estuarine shales and/or carbonates.

Fig. 15 - A portion of the western end of stratigraphic cross section Y-Y' (not included in paper). Erosional unconformities occur at base of Basal Morrow Sandstone and at base of Stockholm Sandstone. The Basal Morrow Sandstone pinches out abruptly against the northwest side of valley between wells 110 and 122. Following deposition of the Basal Morrow Sandstone, minor erosion (cut down) occured at the top of the sandstone at location of well 122 prior to deposition of the Lower Morrow Limestone.

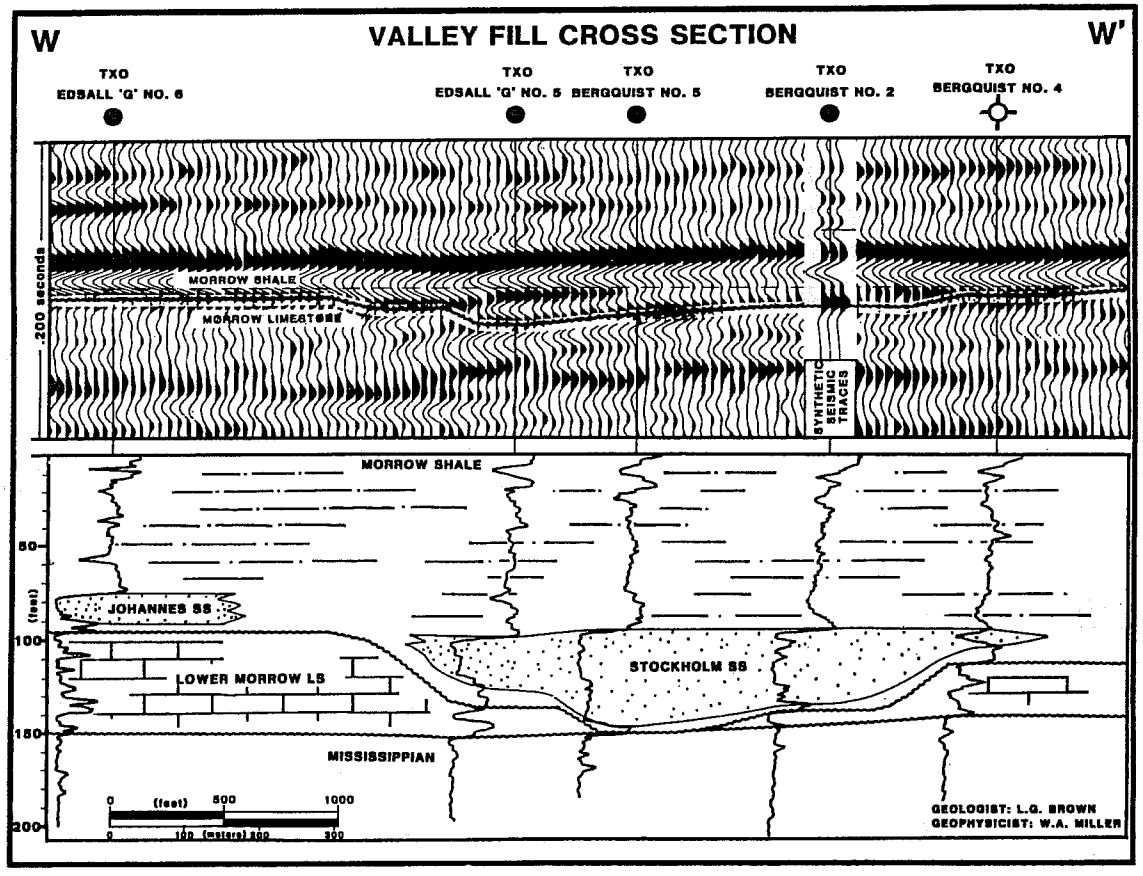

Fig. 16 - Stratigraphic and seismic cross sections through two Morrow Sandstone valley-fill reservoirs at Southwest Stockholm field, Kansas. One of cores described in this study is the

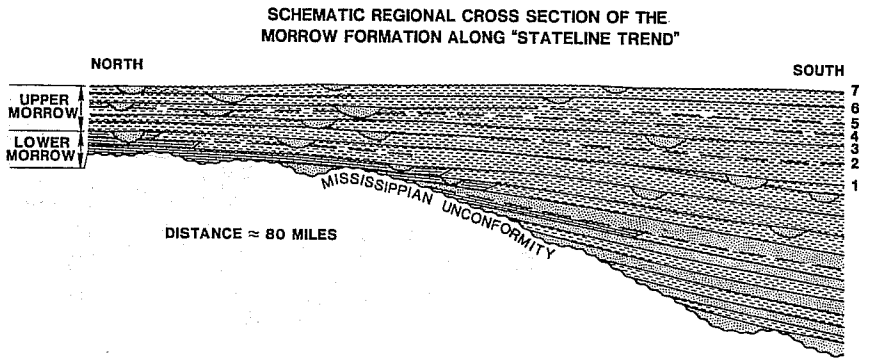

Fig. 17 - Schematic regional cross section of the Morrow Formation along the "Stateline Trend" of the Kansas-Colorado border. A subaerial unconformity is interpreted to separate each of the valley-fills from the underlying marine shales and/or carbonates. The unconformities observed in the Southwest Stockholm field and to the north are numbered from the base to top, 1 through 7.

5. Discussion of Stratigraphic Cross Section X-X'

Stratigraphic cross section X-X' was constructed across the northern part of the field using gamma-ray-density logs. A portion of the cross section is shown in Figure 18. Due to confinement of the valley walls, the Stockholm Sandstone is essentially absent northwest of Well No. 64 and to the east of Well No. 60 (Fig. 12). As described above, the Stockholm Sandstone in this part of the field consists primarily of tidal estuarine sandstones in the lower portion and interbedded river and tidally deposited sandstones in the upper portion of the reservoir. Table 3, which is based on a relatively limited number of data points (12), suggests that significantly higher production rates should be expected from river sandstones, which average 16% porosity and 700 md permeability. In contrast, tidally deposited sands average 14% porosity and only 80 md permeability. Cross section X-X' indicates that there is significant relief on the erosion surface at the top of Lower Morrow Limestone (Figs. 11 and

TXO Bergquist No. 2. Note that the Stockholm Sandstone fills an erosional "channel". Flow in the "channel" was out of the diagram. The Johannes Sandstone is also limited areally by the valley walls but is more lenticular and is present in discontinuous lenses.

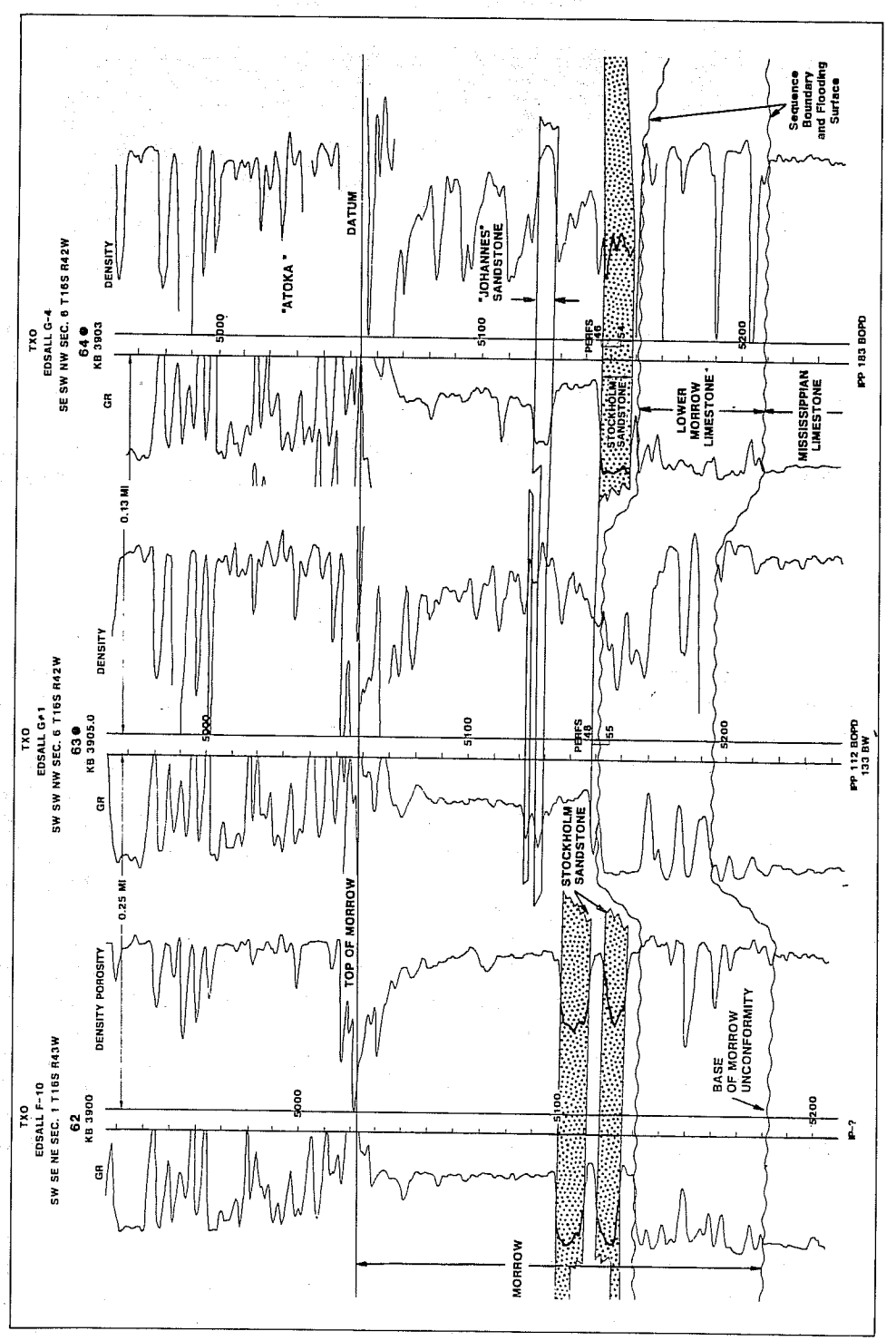
TXO
EDSALL F-10
SW SE NE SEC. 1 T16S R43W
62
KB 3900
GR
DENSITY POROSITY
0.25 MI
TXO
EDSALL G+1
SW SW NW SEC. 6 T16S R42W
63
KB 3905.0
GR
DENSITY
0.13 MI
TXO
EDSALL G-4
SE SW NW SEC. 6 T16S R42W
64
KB 3903
GR
DENSITY
5000
5100
5200
TOP OF MORROW
DATUM
"ATOKA"
"JOHANNES" SANDSTONE
STOCKHOLM SANDSTONE
PERFS 46
PERFS 48
55
54
LOWER MORROW LIMESTONE
MISSISSIPPIAN LIMESTONE
BASE OF MORROW UNCONFORMITY
Sequence Boundary and Flooding Surface
IP-7
IPP 112 BOPD
133 BW
IPP 183 BOPD
MORROW

18). In the center of the valley the distance from the pre-Stockholm erosional surface to the top of the Stockholm Sandstone is 55' (Well No. 67, Fig. 9). Within 0.2 mile laterally this interval thins to 30' (Well No. 60) and within 0.4 mile from the "valley center" it thins to 15' (Well No. 55). A similar sequence of thinning occurs along the northwest valley margin. Where river sands are absent the wells appear to be non-economic and D&A. River sands appear to be absent in wells No. 55 and 65, and both are D&A. In the thicker portion of the Stockholm Valley fill, shale was deposited and was preserved above the basal erosion surface and below the Stockholm Sandstone (i.e., Well No. 64, Fig. 18). These shales are presumably marine, non-productive and form a basal and possibly locally a lateral hydrocarbon seal.

The erosional surface separating the Mississippian limestones from the Lower Morrow Limestone has a similar profile to the erosional topography, which controlled the depositional thickness of the Stockholm Sandstone in the central part of the valley; however, near the edges of the valley (Wells 61, 62, 55) there is little relationship between the surfaces. Note also that the Basal Morrow Sandstone (Fig. 5) is apparently absent along the transect of this cross section. The "Johannes Sandstone" is lenticular and non-productive in the wells in cross section X-X'. The "Johannes Sandstone" probably is lenticular over much of the field area and probably consists of several different sand bodies with differing origins.

Fig. 18 - Cross section Southwest Stockholm field, Kansas. Includes three wells from near the west end of a longer (not included) east-west stratigraphic cross section X-X', which extends across the valley. Location of cross section is indicated on Figure 9. A number of significant observations concerning the cross section: (1) Significant erosion has recurred on unconformities at the base and the top of the Lower Morrow Sandstone; (2) The Stockholm Sandstone abruptly pinches out at the edge of the valley in the area between wells 63 and 64; (3) The thickness of the valley-fill deposited following deposition of the Lower Morrow Limestone varies from 55' in well No. 57 (Fig. 9) to less than five feet in well No. 63. This valley, in which the Stockholm Sandstone is deposited, is partially filled with reservoir quality sandstone and partially filled with non-reservoir sandstones and shales. The "Johannes" Sandstones are lenticular, non-continuous and individual lenses do not always appear to be correlatable with adjacent Johannes lenses.

6. Discussion of Stratigraphic Cross Section Y-Y'

Stratigraphic cross section Y-Y' extends across the valley in the southern portion of the field (Fig. 9). Figures 11 and 15 include portions of cross section Y-Y'. Three cored wells are included in this cross section. Cored intervals in Wells No. 128 and 131 have previously been discussed. Well No. 130, the TXO White AB-1, was cored completely through the Stockholm Sandstone (Fig. 11). At this well location all but two, less than 1' thick sandstones at the top and base of the Stockholm Sandstone, are interpreted to be river deposits. This well was plugged and abandoned, however, as shown in Table II, even though porosity and permeability (18%, 879 md) are excellent the reason for the absence of production is not known.

The Basal Morrow Sandstone occurs over the whole extent of cross section Y-Y'. This sandstone calculates on logs as non-productive and DST's of this unit are rare. The Basal Morrow Sandstone pinches out against the valley wall between wells 110 and 122 (Fig. 15). The non-productive Lower Morrow Limestone fill thickness is generally inversely proportional to the thickness of the underly Basal Morrow Sandstone.

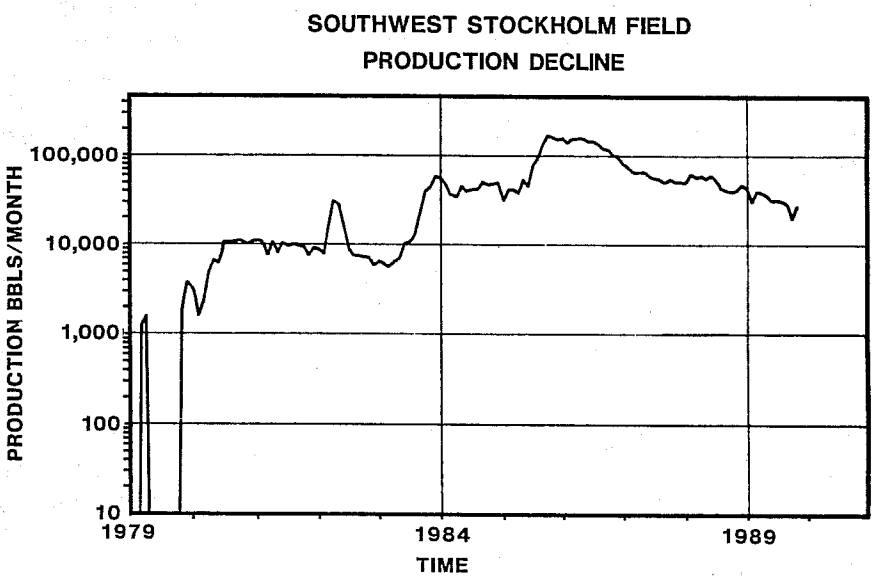

Fig. 19 - Production decline over period 1979-1990. Field has produced 5.5 million barrels of oil (primary production). Ultimate primary production is estimated to be approximately 7.5 million barrels, using 42 million barrels in place and a 17% recovery factor. It has been estimated by Brown, et al. (1990) that 15% of the remaining oil in place can be produced using enhanced production techniques from the 66 producing wells in the field.

The Stockholm Sandstone in cross section Y-Y' is relatively well understood because of the availability of three cored wells included in the section. As discussed earlier, the three cores contain quite different percentages of river, tidal (estuary) and marine transgressive sandstones. Well No. 130 (Fig. 11) is 98% river deposited sandstone, Well No. 129 (Fig. 11) is approximately one-third river sandstones and two-thirds tidal sandstones with less than 5% transgressive marine sandstones at the top of the reservoir. Well No. 131 (Fig. 10) contains highly interbedded thicker (2-4' thick) river sandstones interbedded with very thin (0.5-1.0' thick) tidal- (estuarine and marine) deposited sand stones. This high degree of depositional variability is believed to be typical within the Stockholm Sandstone. River sandstones have the best reservoir characteristics in this part of the field, as they also did to the north.

River sandstone forms the major portion of the perforated interval in Well No. 129 (Fig. 11) and all of the perforated intervals in Well No. 128 (Fig. 11). Well No. 130 (Fig. 11) contains thick river sands but is unexplicably non-productive. An apparently younger, "non-connected" portion of the Stockholm Sandstone, occurs in well No. 110 (Fig. 15).

One of the most characteristic aspects of the valley-fill is illustrated in the section (Fig. 11) extending through wells 128, 129 and 130 where the river sands thicken from 9' to 20' at the expense of the underlying estuarine and other tidally deposited sandstones. In this area, the surface at the base of the river sands is interpreted to have been eroded into the tidal sandstones. Similar erosional affects will be shown in map view in a subsequent section of this study.

The "Johannes Sandstone" in cross section Y-Y' is a 10' thick nonproductive sandstone present in all the wells east of and including No. 124 (Fig. 9). It is absent in wells to the west.

B. Production

Southwest Stockholm field has produced 5.5 million barrels of oil from the Stockholm Sandstone during primary production. Brown et al. (1990) estimated that the field has 42 million barrels in place and using a 17% recovery factor 7.5 million barrels will ultimately be produced. From mid 1980 to 1990 the field produced in excess of 10,000 barrels per month from 66 wells (Fig. 19).

C. Microheterogeneities; Petrology of Stockholm Sandstone

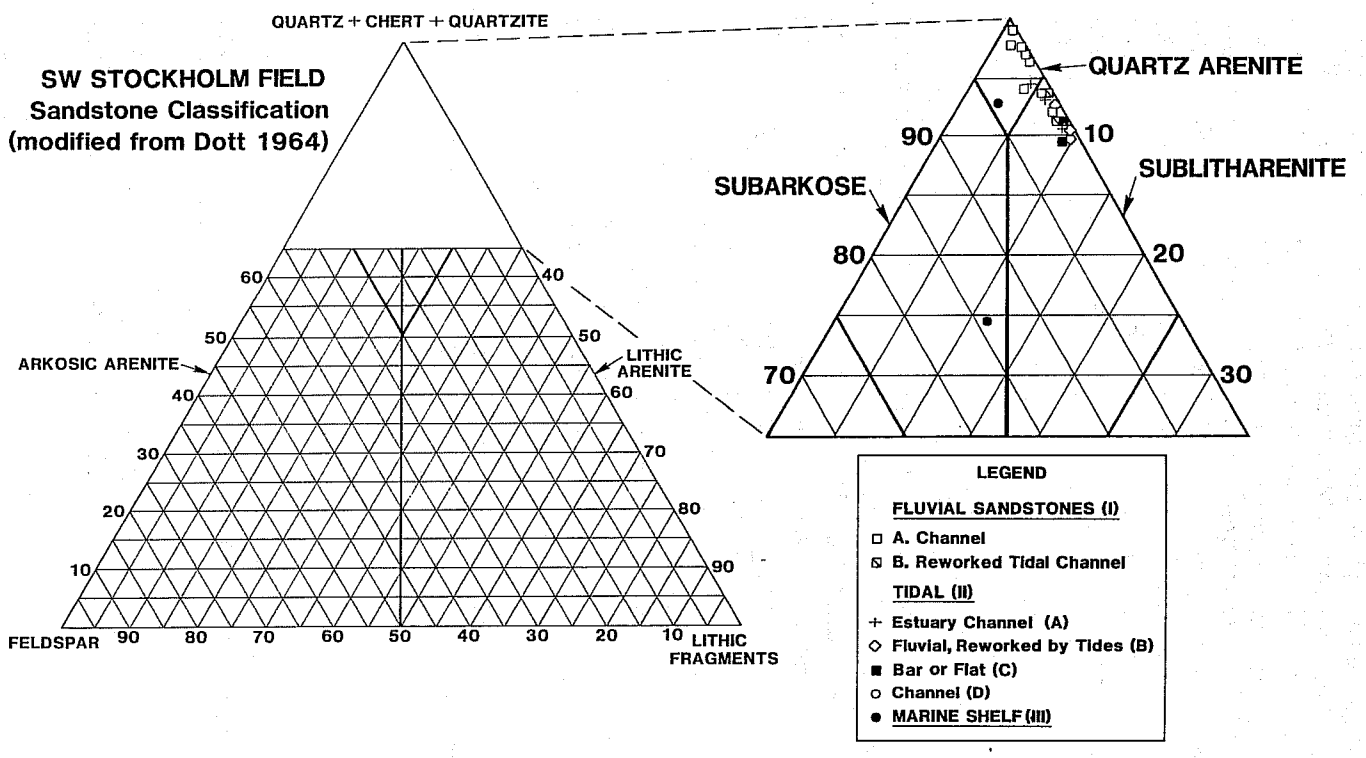

Fig. 20 - Composition of Stockholm Sandstone facies, Southwest Stockholm field, based on point-count data. Most of the samples are quartz arenites or quartz rich sub-litharenites in a modified Dott (1964) classification. The- finer grained Stockholm Marine Shelf Sandstone Facies is more feldspathic than the other facies.

1. Composition and Texture

The Stockholm Sandstone is quartz-rich as shown on the ternary diagram of Figure 20. The composition of the grains in the rock was determined from microscopic thin section analysis. The mean composition of sand grains for 24 point-counted samples was 93% quartz (Q93), 1% feldspar (F1) and 6% lithic (L6) fragments. No significant composition difference exists among the various facies except for the Stockholm Marine Shelf Sandstone Facies III, which (based on two samples) is more feldspar-rich with a mean of Q83.4,F9.6,L7.0. Tables B1 to B7 contain the composition of the various facies based on modal point-count thin section analysis. Detrital grains (and the range in volume percent) noted in thin section include monocrystalline quartz (25.5-68.2%), polycrystalline quartz (2.5-44.3%), plagioclase (0-10%), shale lithic fragments (0.5-7.3%), glauconite (<1%), collophane (<1%), muscovite (<1%) and trace amounts of heavy minerals including tourmaline and zircon. The percentage of polycrystalline quartz increases with increasing grain size. Significant authigenic (secondarily formed in place) minerals include ankerite, siderite, quartz, and kaolinite. Pyrite occurs as a pervasive cement in a few thin streaks. In a few samples, trace amounts of grains growing into the pores include feldspar overgrowths and elongate barite crystals in primary and secondary pores.

There are significant differences in grain size among the various facies. The fluvial facies is coarse-grained and typically either poorly sorted or bimodal. The Stockholm Marine Shelf Sandstone Facies III is very fine-grained with argillaceous laminae.

Sandstones in Southwest Stockholm field are unusual because there is no correlation of grain size with composition, porosity, or permeability (Figs. 21 and 22). Grain size was measured using a binocular microscope to make a visual comparison of sand grains in the core with grain size images printed on a comparator constructed on a sheet of transparent plastic (Figures 21 and 22).

2. Secondary Processes

Similar pore-filling or pore-creating processes occur in all sandstone facies in the field, however, the importance of certain processes varies among facies. The major porosity destruction processes were compaction, quartz cementation, carbonate cementation, and kaolinite cementation. Carbonate minerals also replaced feldspar, shale lithic fragments, and the margins of quartz grains. Dissolution of carbonate

cement to create secondary porosity was, at least locally, an important development of the reservoir at Southwest Stockholm field. Figure 23 is a general diagram showing the relative sequence of major diagenetic (secondary) events and the evidence to support the sequence for Morrowan sandstones.

Compaction in sandstones is important in reducing porosity and permeability. Intergranular volume (IGV) provides a measure of the amount of compaction that has taken place in a sandstone (Houseknecht, 1987). Figure 24 is a plot, devised by Houseknecht (1987), of intergranular volume versus intergranular cement. Samples that plot above the dashed line are dominated by cementation processes, whereas samples that plot below the dashed line are dominated by compaction processes. Intergranular volume (sometimes called minus cement porosity or precement porosity) is the sum of the intergranular cement plus intergranular porosity. It is important to exclude cement that replaces grains and intragranular and moldic porosity in determining intergranular volume. The smaller the intergranular volume the greater the amount of compaction that has occurred. Note that the Stockholm Tidal Channel Facies IID and Stockholm Marine Shelf Sandstone Facies III are distinct from the other samples. The former is strongly

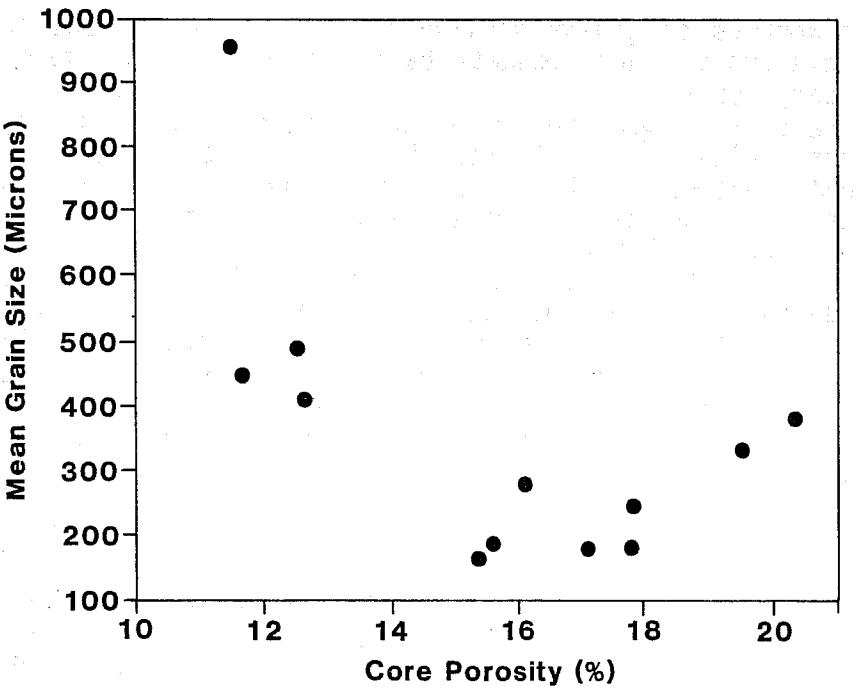

Fig. 21 - Core porosity versus mean grain size, Stockholm Sandstone. Grain size was measured using a comparator under a binocular microscope.

dominated by compaction, whereas the latter is strongly dominated by cementation. The other samples overlap the dashed boundary line, but there are more samples in the compaction field than in the cementation field.

The major effects of secondary processes affecting the Stockholm Tidal Channel IID and Stockholm Marine Shelf Sandstone Facies III differ significantly from the other geologic facies. The Stockholm Tidal Channel Facies IID is characterized by extensive compaction as shown by the low IGV (13.5%). If it is assumed that the initial porosity was 40%, the pore volume lost by compaction was 26.5%. The Stockholm Marine Shelf Sandstone Facies III is characterized by pervasive carbonate cement (26.3%). This cement formed relatively early as shown by the moderately high IGV (26.8%). If one assumes that the initial intergranular porosity was 40% then only 13.7% pore volume of Facies III was lost by compaction. The only other facies that has a distinctive diagenesis is Stockholm Tidal Bar Facies IIC, which is fine-grained with low porosity primarily due to quartz cement and fairly extensive compaction (IGV=17.6%). This compaction includes physical compaction as well as chemical compaction (pressure

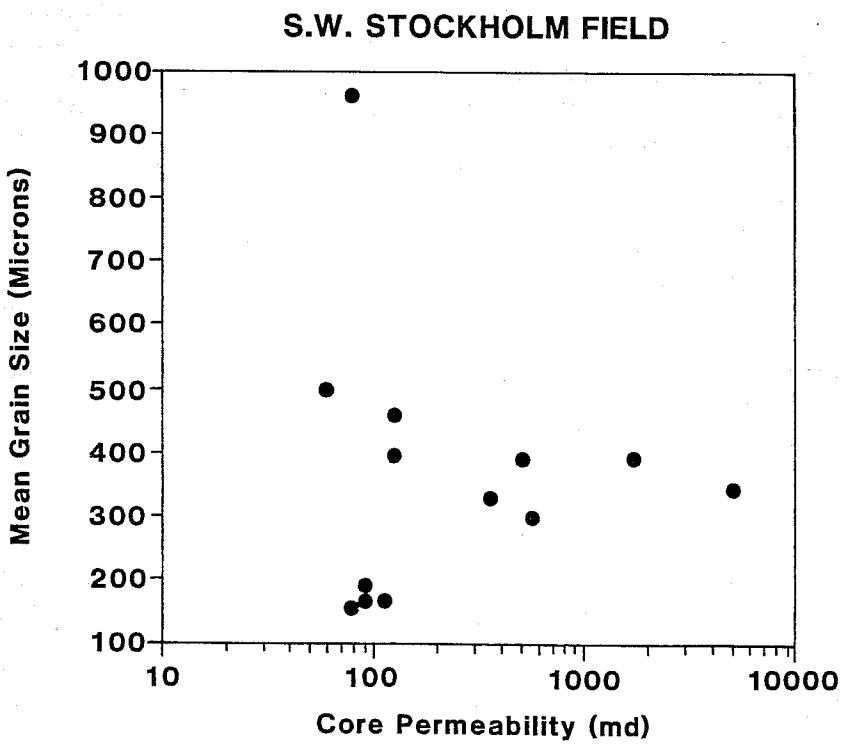

Fig. 22 - Core permeability versus mean grain size, Stockholm Sandstone. Grain size measured as described in Fig. 21.

Diagenetic sequence of events for Morrow Sandstone.

EVENT	RELATIVE SEQUENCE* TIME →	COMMENTS
COMPACTION		Replacement Kaolinite deformed in coarse-grained ss; glauconite not deformed in some fine-grained ss.
QUARTZ OVERGROWTHS		Underlies ankerite cement.
ANKERITE CEMENT AND REPLACEMENT		Partially replaced feld. ,sh. lithic fragments and margins of quartz grains.
SIDERITE CEMENT		Replaced ankerite cement.
KAOLINITE	REPLACEMENT; VOID-FILL	Replaced feldspar and formed as void-fill in primary and secondary pores.
DISSOLUTION CARB. FELD. AND SH. FRAG.		Some moldic pores from unknown min.; some secondary intergranular pores from dissol. of carb. cement.

*Feldspar overgrowths and barite are too sparse to fit into diagenetic sequence.

Fig. 23 - Diagenetic sequence of events for the Stockholm Sandstone, Southwest Stockholm field. One of most important events in some facies after burial of sediments is dissolution of carbonate cement giving significant "secondary porosity". All events listed on figure, other than dissolution, tend to decrease porosity in Morrow valley-fill sandstones.

solution). Pressure solution of quartz grains has occurred along argillaceous (shaley) laminae that make up 2.6% of the sandstone. The other facies of the Stockholm Sandstone have mean intergranular volumes that range from 20.2 to 24.1% and mean total cement that ranges from 11.2 to 16.6%.

Figure 25 shows the evolution of porosity as influenced by the major diagenetic events. This is not strictly a time or depth dependent diagram because diagenetic events commonly overlap through time as the rocks subside deeper into the earth. This diagram shows that based on the thin sections studied, the present porosity is about the same for the Stockholm Tidal Channel Facies IID and the Stockholm Fluvial Facies IA, but the diagenetic history is different. The Stockholm Tidal Channel Facies IID underwent extensive porosity loss due to compaction, whereas the Stockholm Fluvial Facies IA was less affected by compaction, but developed more

separates fields where compaction (below the line) and cementation (above the line) are the dominant porosity destruction processes. The Stockholm Tidal Channel Sandstone, Facies 11D, is more strongly affected by compaction than the other samples. The Stockholm Marine Shelf Sandstone Facies III was pervasively cemented by a relatively early carbonate cement and therefore has no porosity and is distinctly different than the other samples.

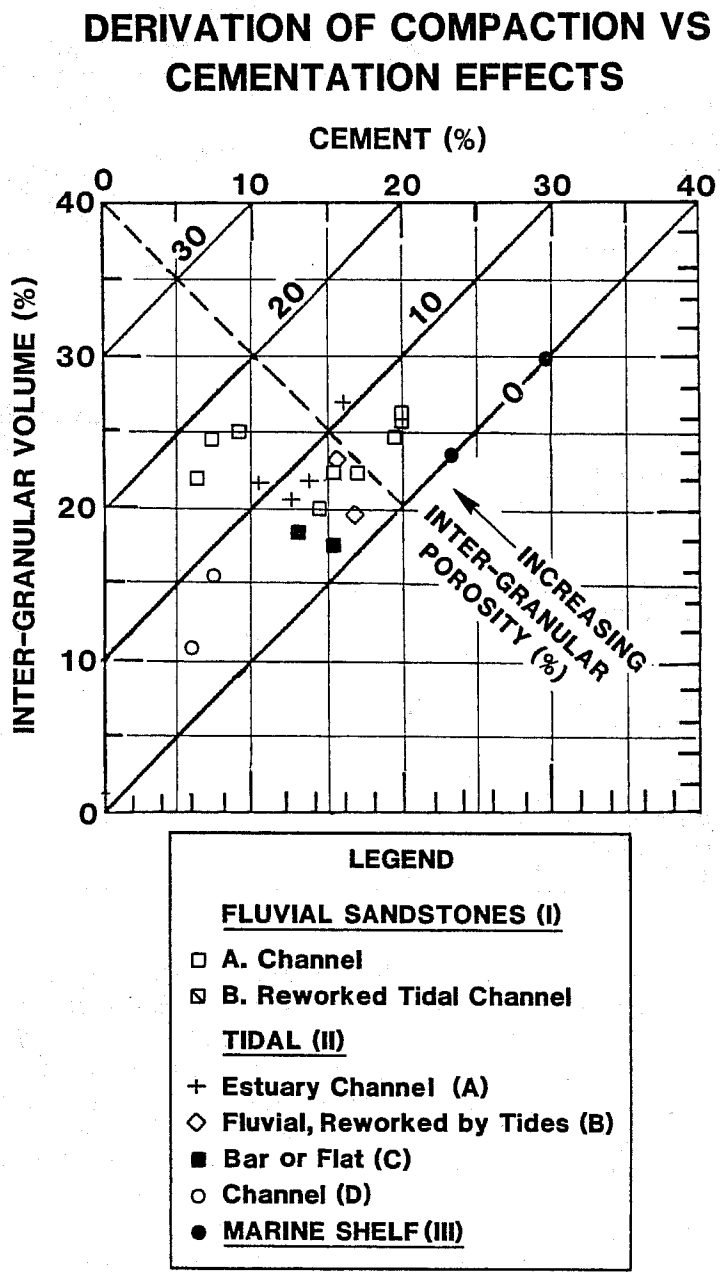

Fig. 24 - Derivation of compaction versus cementation effects, Stockholm Sandstone. This diagram is based on the assumption that the initial intergranular porosity was 40%. Intergranular porosity is destroyed by a combination of compaction and cementation. Intergranular volume is the sum of intergranular cement and intergranular porosity. A low intergranular volume indicates a strong compaction effect. Intergranular porosity can be read from the solid diagonal lines. The 45° dashed line

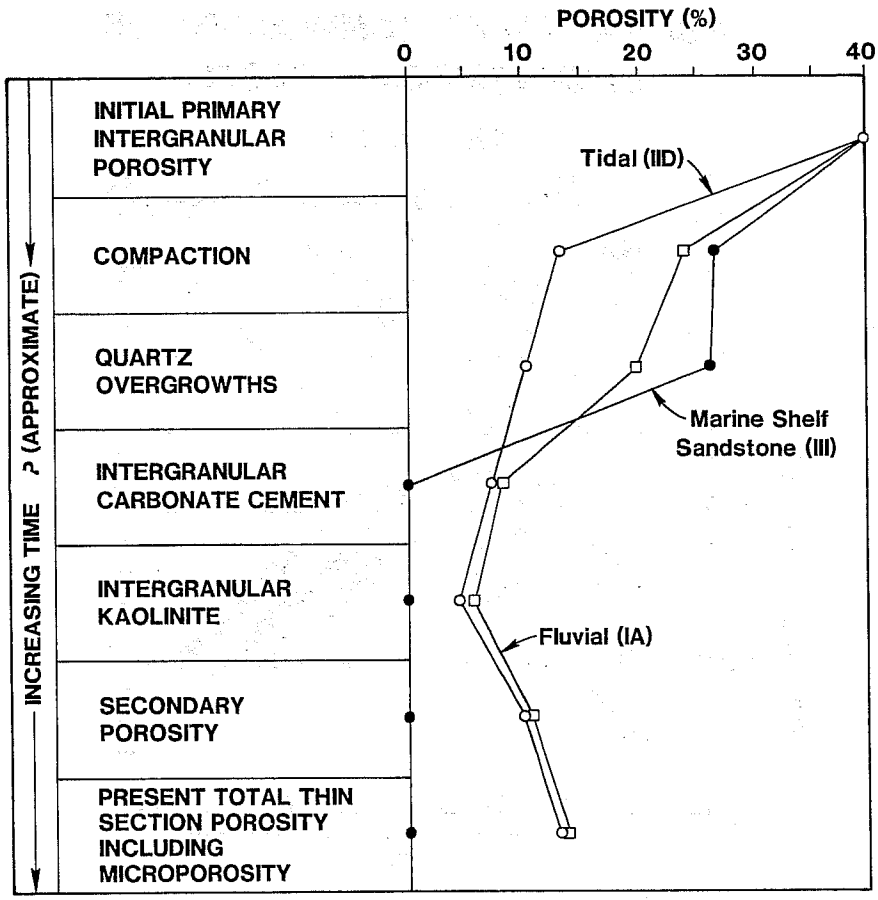

Fig. 25 - Diagram expressing the effect of the major diagenetic events on porosity for selected facies in SW Stockholm field. Interpreted sequence of porosity degradations resulting from secondary processes in three Morrow reservoir sandstone facies, fluvial (river), tidal and marine shelf. Note that due to different rock properties of each geologic facies, the method and amount of porosity decrease vary among the facies. Note especially the increase in porosity for fluvial and tidal sandstones due to formation of secondary porosity. Because diagenetic events commonly overlap through time with increasing depth of burial, this is not a time or depth diagram. For this diagram, however, except for compaction, depth and time generally increase downward. Comparison of the history of the Stockholm Tidal Facies IID (based on only two samples) and Stockholm Fluvial Facies IA indicates that compaction is more important in the Tidal Facies IID and that quartz overgrowths and carbonate cement are more important in the Fluvial Facies IA. However, the two facies, despite the differences in their history, have about the same total thin section porosity. The Stockholm

quartz and carbonate cement. In contrast, Stockholm Marine Shelf Sandstone Facies III underwent only slight compaction before pervasive carbonate cement formed to totally destroy macroporosity. This facies was not affected by the later dissolution event, perhaps because the pores were completely occluded making it difficult to get fluids into the sandstone to create secondary porosity.

3. Porosity and Permeability

a. General Comments. There is good evidence that the Stockholm sandstones were partially cemented early in their history by carbonate minerals, which were subsequently dissolved to create secondary intergranular porosity. Evidence for this comes from (1) preservation of significant carbonate cement with a distinctive dissolution texture in the TXO White 1-AB (Fig. 26C), (2) porous sandstone containing quartz grains with irregular outlines and embayments caused by partial replacement of the margins of quartz grains by carbonate that has been dissolved (Fig. 26D), and (3) the presence of partially replaced quartz overgrowths in porous rock, which suggests that carbonate once was present overlying the quartz and was removed by dissolution (Fig. 27A-B).

These conclusions were reached knowing that the contact between carbonate cement and quartz grains in a thin section can appear to be embayed (irregular) because of an overlapping grain relationship in thin sections. The difference in hardness between quartz and carbonate minerals and the fact that carbonates have three good cleavages and quartz has no cleavage leads to partial plucking of carbonate and may give the appearance of an irregular (replacive-appearing) contact between the two minerals, which is misleading. To evaluate this effect, a portion of the thin section was photodocumented (Fig. 27C) and then the carbonate was dissolved with HCl acid and the same area was rephotographed (Fig. 27D). Comparison of these photographs shows that the carbonate does replace the margins of quartz grains. Therefore, it appears that a partial replacement of quartz grain margins is the most likely explanation for embayed grains in the porous sandstone that now contain only slight amounts of carbonate cement. A conservative estimate is that about half of the intergranular pores are of secondary origin.

Marine Shelf Sandstone, Facies III, developed pervasive carbonate cement that destroyed porosity. The later dissolution event did not dissolve the carbonate, probably because the low permeability did not permit entry of the leaching solutions.

Porosity in the Stockholm Sandstone is a mixture of intergranular macroporosity, intragranular/moldic macroposority, and microporosity. The microporosity occurs among authigenic kaolinite crystals, within partially dissolved shale lithic fragments, and within sparse glauconite pellets. Because of its very small pore size the microporosity does not contribute producable fluids. Intergranular porosity in Southwest Stockholm field is of primary and secondary origin. The intragranular/moldic macroposority was formed by the partial or complete dissolution of feldspars (Fig. 26A) and lithic grains. Preserved clay infiltration rims outline framework grains of unknown mineralogy, which have been dissolved to create moldic porosity (Fig. 26B).

Reservoir parameters for the general categories of river (fluvial) and tidal sandstones is given in Table II. Mean porosities and permeabilities are River 16.3%, 703 md; Tidal 14.4%, 80.8 md.

b. Stockholm Sandstone Fluvial Facies IA. Subfacies of the tidal and fluvial facies may be recognized in core. The best part of the reservoir in Southwest Stockholm Field is Fluvial Facies IA of the Stockholm Sandstone. This sandstone has mean core porosity and permeability of 17.3% and 835 md respectively. The relatively coarse grain size partly accounts for the high permeability. Mean point-count data for 10 samples of this facies indicates 8.6% intergranular porosity and 2.2% intragranular/moldic porosity for a total macroporosity of 10.8% (Appendix Table B1).

Fig. 26 - Photomicrographs, various facies, Stockholm Sandstone. A. Feldspar (F) was partially replaced by carbonate (C). Later, the carbonate was dissolved to create intragranular porosity (blue). Note the remnants of feldspar (arrow) caught in the partially dissolved carbonate, TXO Garrison A-6, 5185.5 feet (core), plane polarized light. B. Infiltration clay (IC) coated sand grains of unknown origin, which were subsequently dissolved to create moldic porosity (MP), TXO Evans E-2, 5164.2 feet (core), plane polarized light. C. Carbonate cement has been partly dissolved giving the cement a "swiss-cheese" appearance, TXO Evans E-2, 5177.3 feet (core), plane polarized light. D. Quartz grains typically have embayed (arrows) grain outlines in porous sandstones. This is one line of textural evidence suggesting a secondary origin for some of the intergranular porosity, TXO Garrison A-6, 5160.7 feet (core), plane polarized light.

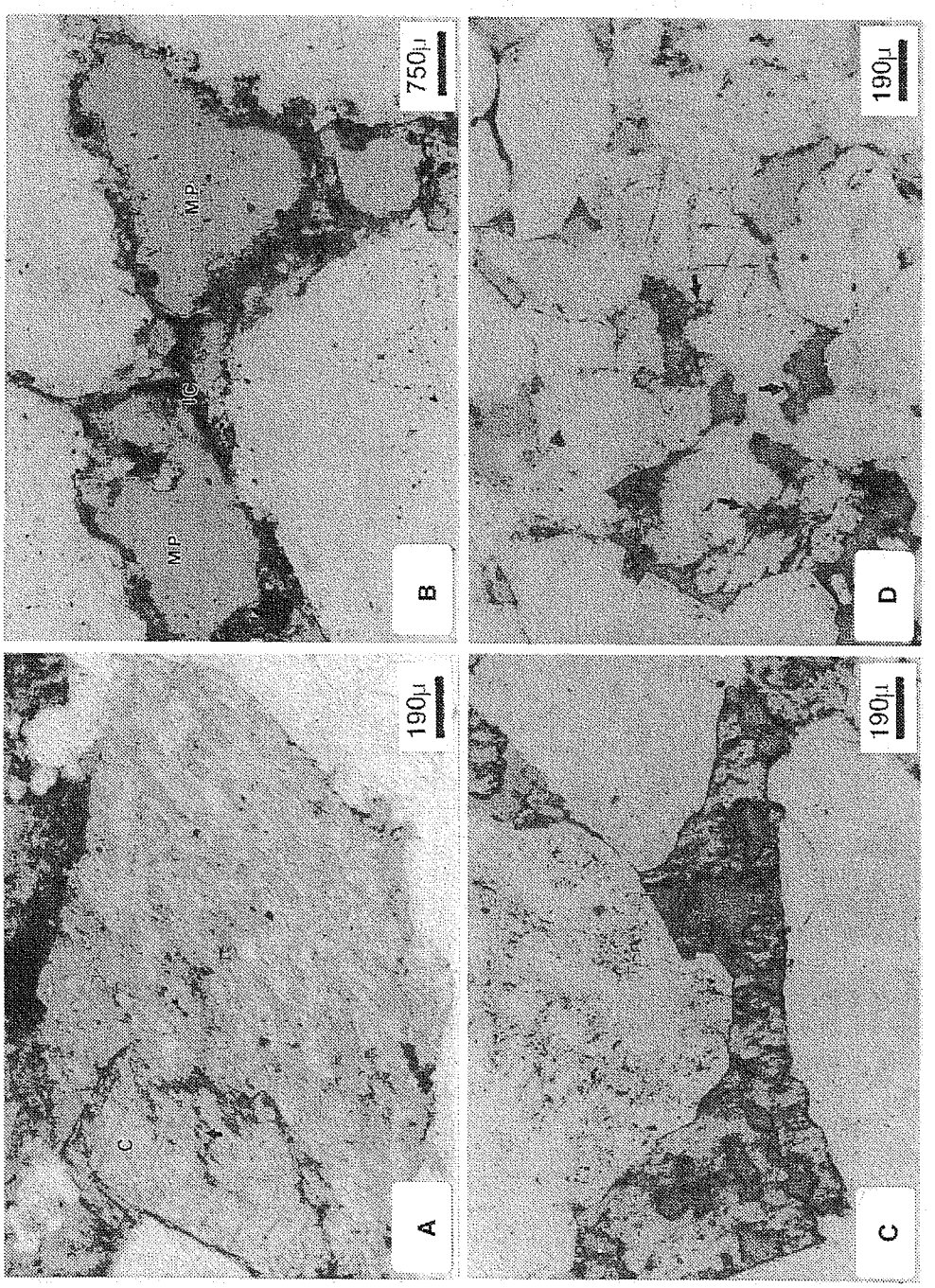
A
C
190µ
B
MP
MP
IIG
750µ
C
190µ
D
190µ

c. Stockholm Sandstone, Tidal Facies (Reworked by Fluvial Processes) IB. Only two samples were point-counted from this facies and they are quite different (Table B2). This reflects the heterogeneity of the facies and generalizations are meaningless without a larger data set.

d. Stockholm Sandstone, Tidal Estuary Channel Facies IIA. The reservoir characteristics of this facies are similar to the characteristics of the Stockholm Fluvial Facies IA, although it is finer (medium-grained). The macroporosity totals 10.9% and consists of 9.4% intergranular and 1.5% intragranular/moldic (Appendix Table B3). Permeabilities typically are about 95 md.

e. Stockholm Sandstone, Fluvial (Reworked by Tides) Facies IIB. This facies is relatively coarse (medium-grained), but the total porosity (5.5%) is relatively low based on point-counts of two samples. Most of the macroporosity is intergranular (4.8%) rather than intragranular/moldic (0.7%). This facies has low porosity, primarily because of an abundance of kaolinite (10.4%; Appendix Table B4).

Fig. 27 - Scanning electron micrographs and photomicrographs, Stockholm Sandstone. A. Scanning electron micrograph showing a quartz overgrowth with smooth appearing prism faces and with one end of the quartz crystal modified by replacement contact with carbonate cement that was subsequently removed by dissolution, TXO Evans 2-E, 5177.8 feet (core). B. Scanning electron micrograph showing quartz overgrowths that were modified by contact with an overlying carbonate cement, which partially replaced the faces of the crystal. The planar faces and face contacts are recognizable despite the rough and pitted replacement texture. This line of evidence strongly suggests that some of the intergranular porosity is secondary in origin, TXO Evans 2-E, 5164.2 feet (core). C. and D. show the same part of a thin section before and after applying HCl acid to the thin section. Note the embayed margins (arrows) of quartz grains in C. This can be an apparent embayment related to thin sectioning of irregular grains and the difference in hardness and cleavage between quartz and carbonate. Note that after dissolving the carbonate, the embayments are still there. This indicates that the carbonate has replaced the quartz and that the embayed grains in porous sandstone can be used as evidence of secondary intergranular porosity for the pore adjacent to the embayed grain, TXO Evans 2-E, 5190.4 feet. Photographs were taken in crossed polarized light.

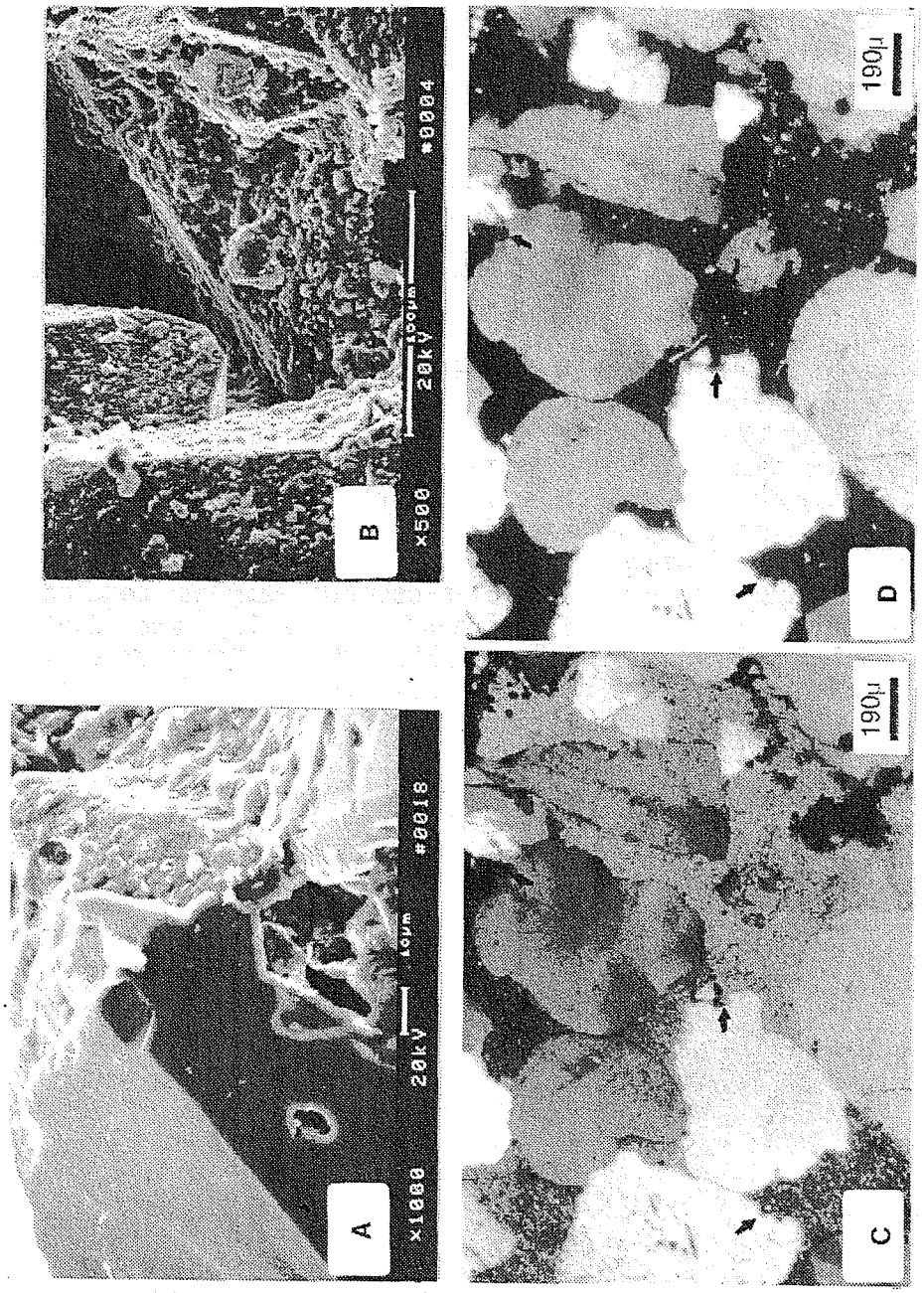
A
×1000
20kV
10μm
#0018
B
×500
20kV
100μm
#0004
C
190μ
D
190μ

f. Stockholm Sandstone, Tidal Bar Facies IIC. This facies is finer grained and better sorted than the fluvial facies that constitutes the better part of the reservoir. The Stockholm Tidal Bar Facies IIC has argillaceous laminae, considerable compaction, and a total porosity of only 4.6%, which consists of 3.6% intergranular porosity and 1.1% intragranular/moldic porosity (Appendix Table B5).

g. Stockholm Sandstone, Tidal Channel Facies IID. Based on limited core analyses, the Stockholm Tidal Channel Facies IID has a mean porosity and permeability of approximately 12.0% and 90 md, respectively. This facies has lost porosity largely because of compaction. Chemical compaction (pressure solution) is pronounced where illitic clay occurs along quartz-to-quartz grain contacts. A common observation of petrologists (e.g., Thomson, 1959) is that illitic clay films along grain contacts serve as a catalyst to promote pressure solution. The tight fit of some grains along their contacts has reduced the porosity and permeability compared to the Stockholm Fluvial Facies IA, which is similar compositionally and texturally except that illitic clay and pressure solution are less common.

The macroporosity in two point-counted samples totaled 10.2% and included 6.6% intergranular porosity and 3.6% intragranular/moldic porosity (Table B6). Microporosity occurs among kaolinite crystals (3.5%, within shale lithic fragments (5.6%), and within glauconite pellets (<1%).

h. Stockholm Sandstone, Marine Shelf Sandstone Facies III. Sandstones in this facies are very fine-grained with extensive carbonate cement (26.3%) and no macropores visible in the thin section (Appendix Table B7). This facies is non-reservoir.

4. Microscopic Heterogeneity

The reservoir sandstone facies in Southwest Stockholm field have considerable microheterogeneity and microporosity, but it is difficult to document because of the lack of publicly available porosity and permeability data. Ideally, thin sections for a study such as this would be cut from the plugs used for core analysis. Then, when point-counts are made of these thin sections it is possible to determine the amount of microporosity by subtracting thin section macroporosity from core porosity. Five thin section samples were reasonably close to the position of the core perm plugs so these five samples were given more emphasis in our reference set, Table I.

Microheterogeneities are recognizable in thin section and under the scanning electron microscope (SEM) in the form of non-producing micropores associated with kaolinite clay and partly dissolved shale grains. Because commercial core analysis includes microporosity in total porosity values, an attempt was made to evaluate the distribution of micropores in the Stockholm reservoir sandstones. This was done by plotting total thin section macroporosity versus the ratio of macroporosity to the rock volume with micropores (Fig. 28). The rock volume with microporosity was derived by summing the percentages of kaolinite, shale lithic grains, and glauconite. This was done because there was no way to directly determine microporosity for the samples. What Figure 28 suggests is that samples with low porosity are dominated by microporous rock (low ratio on y axis), whereas higher porosity sandstone has a higher ratio (y axis) suggesting that micropores are less abundant relative to macropores in good reservoir sandstone.

5. Reservoir Characteristics

Table II lists useful parameters for evaluating reservoir quality on a sample by sample basis. The k/Ø ratio and R35 have been used by Hartmann and Coalson (1990) to evaluate reservoirs. A high k/Ø ratio is indicative of a good reservoir. R_{35} is the pore aperture (throat) size on a mercury injection capillary pressure curve where the mercury saturates 35% of the pore space. Hartmann and Coalson (1990) believe that R_{35} is useful in evaluating reservoirs. Large R_{35} values are indicative of good reservoirs. It is possible to estimate R_{35} using Winland's empirical equation, which was published by Kolodzie (1980). Winland's equation, which was developed using 322 samples of sandstones and carbonates for which porosity, permeability and mercury injection data were available is: $\text{Log } R_{35} = 0.732 + 0.588 \text{ Log } K - 0.864 \text{ Log } Ø$. Figure 29 is a porosity-permeability plot with the solution to the Winland equation expressed graphically in the form of lines of equal pore aperture size. Note that the largest pore apertures are at the top of the diagram. Based on the limited core analysis data available from the Stockholm Sandstone, the fluvial sandstones generally have larger pore apertures than the tidal sandstones, although both are excellent reservoirs.

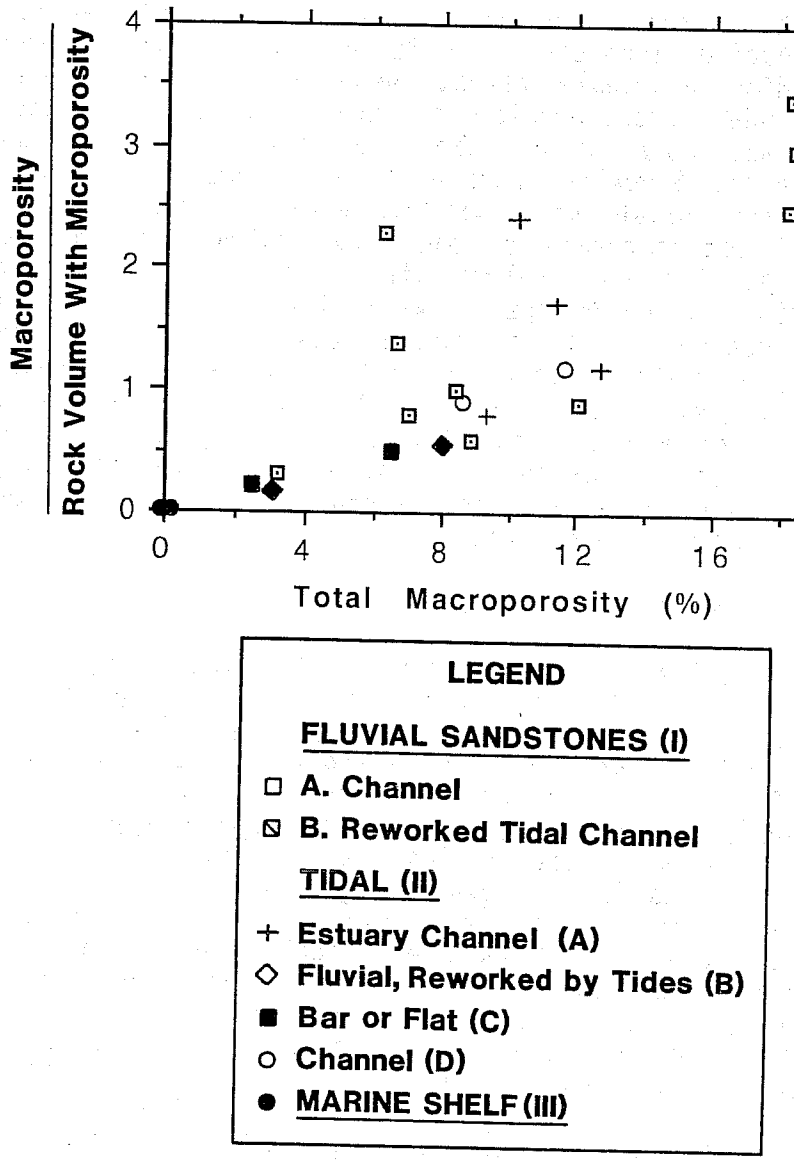

Fig. 28 - Scatter plot of total macroporosity in thin section versus the ratio of total macroporosity to the rock volume with microporosity. This approach was used because it was not possible to obtain a quantitative estimate of microporosity. This diagram suggests that sandstones with low total macroporosity have a low macro/micro ratio indicating that microporous rock (and micropores) make up a large part of the porosity. Rocks with high macroporosity tend to have a higher macro/micro ratio, implying that microporous rock is less abundant. Microporosity may be about the same for all samples of Stockholm Sandstone.

III. CONCLUSIONS

Southwest Stockholm field, which produces from Morrowan Stockholm and "Johannes" sandstones, is part of the Kansas-Colorado "Stateline Trend". In addition to the two producing sandstone reservoirs, the valley also was partially filled by a Basal Morrow Sandstone, which is non-productive in Southwest Stockholm field, and a Lower Morrow Limestone, which occurs between the Basal and Stockholm sandstones is also non-productive and forms a barrier to fluid flow between the two sandstones. Impermeable shales deposited within and outside

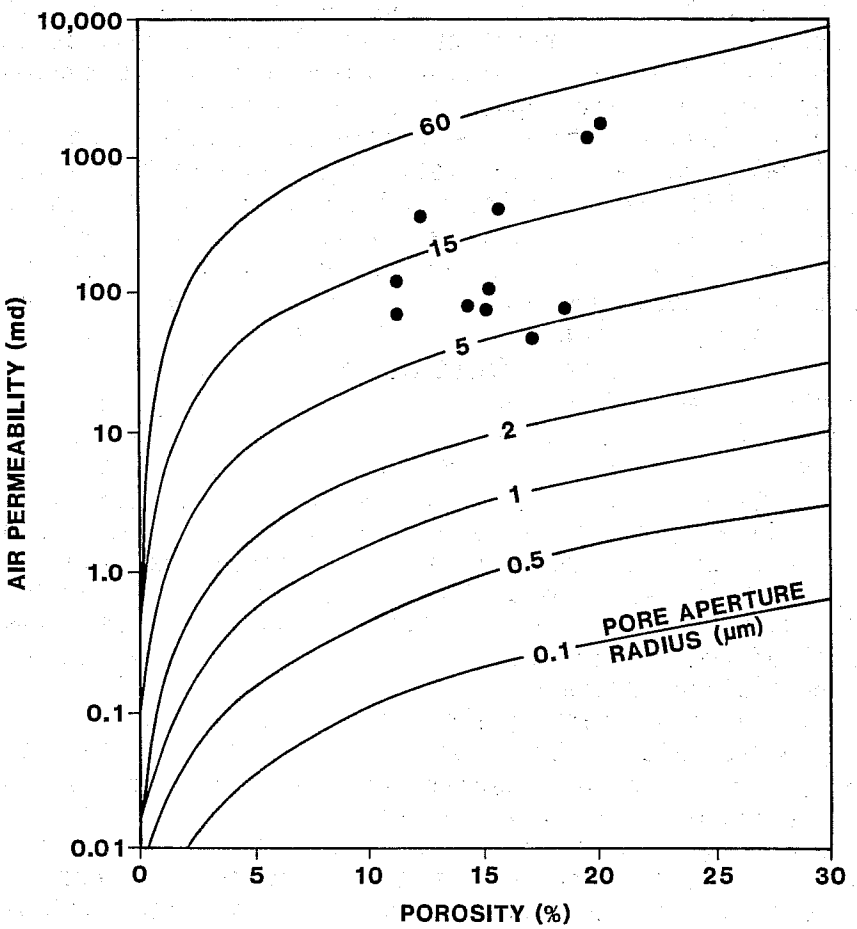

Fig. 29 - Plot of K vs Ø graphical solution to Winland's equation (from Hartmann and Coalson, 1990) showing Stockholm Sandstone samples from Southwest Stockholm Field. The Morrow Sandstones that produce from Southwest Stockholm field are primarily river valley-fill sandstones.

of the valley separate the two producing sands (Stockholm and "Johannes"). Several of the valley-fill sandstone reservoirs abruptly terminate against the lateral margins of the valleys; some reservoirs change facies within the valley. Sediments spilling over the edges of the valleys during late stage flooding are generally sand-poor and non-productive.

Within the Stockholm Sandstone the reservoirs are primarily river-deposited, however, tidal and estuarine sandstones deposited in the valley during minor sea level rises also form a significant portion of the Stockholm Sandstone. These tidal and estuarine sands are finer grained and more clay-prone than the fluvial sandstones and as a result have poorer reservoir properties. In some wells only the river-deposited portions of the sandstones are perforated. Where the finer-grained tidal sands interfinger with fluvial sands, as occurs in the TXO Evans No. 2, vertical permeability is diminished and reservoir storage capacity may be decreased.

The valleys in which the Stockholm Sandstone was deposited locally contain relatively high topographic features, which prohibit the deposition of or diminish the thickness of reservoir sandstones. Adjacent to these topographic features, the valleys are cut much deeper and the thickest portion of the Stockholm Sandstone reservoir occurs. Commonly, these topographic highs within the valley form where the underlying Lower Morrow Limestone was not removed or was only slightly eroded. These topographic features may inhibit sand deposits over an area as large as 1/4 to 1/2 sections.

River-deposited sandstones have average porosities of approximately 16% and average permeabilities of approximately 700 md. Tidally deposited sands, as a group, have decidedly inferior production characteristics; porosities average 14% and permeabilities 80 md. The coarser grained nature of the river deposits reflect their higher depositional energies and removal of most clay and very fine-grained material during the depositional process.

Thin section, scanning electron microscope and X-ray analysis yielded information on size, origin and distributions of pores in the reservoir sandstones. A series of secondary events affected the rocks after they were deposited and although today the porosity of several of the producing facies is similar, the events that affected the rocks were different in different geologic rock facies. The variability of these events contributes to variability in the rate of production of hydrocarbons from different facies. Tidal Channel Facies IID sandstones underwent extensive porosity loss due to compaction and resulting interpenetration of grains, whereas the Fluvial Facies IA sandstones had initial porosity filled with quartz and calcite cement, followed by only minor losses due to compaction. In Facies IID, as well

as other tidally deposited facies where millimeter or thicker lenses of shale were deposited by tidal currents as part of the sandstone, pressure solution of quartz grains adjacent to the shales has reduced porosity; this process is minor in the fluvial sandstones.

Many of the processes forming microheterogeneities in sandstone reservoirs decrease the porosity, however, there is strong thin-section evidence that secondarily-derived (leached) porosity may form up to half of the present day intergranular (macro) porosity in the Stockholm Sandstone in Southwest Stockholm field.

Microporosity (porosity too small to yield its hydrocarbons) occurs in those portions of the reservoir rocks that include secondary kaolinite and shale lenses. This porosity is included in that read by subsurface logs but yields no producible hydrocarbons. An estimate of the percent of microporosity is useful as an aid in more precisely interpreting log porosity.

ACKNOWLEDGMENTS

This study was carried out under SBIR/DOE contract DE-FG05-90ER80976. Dorothy Swindler aided in subsurface data gathering, data analysis and data entry. Computer mapping was performed by Richard Banks of Scientific Computer Applications Inc., Tulsa, Oklahoma. Cores were provided by the U.S. Geologic Survey core repository, Denver, Colorado.

REFERENCES

Blakeney, B. A., L. F. Krystinik, A. A. Downey, 1990, Reservoir Heterogeneity in Morrow Valley Fills, Stateline Trend: Implications for Reservoir Management and Field Expansion, Morrow Sandstones of S.E. Colorado and Adjacent Areas, S. A. Sonnenberg, L. T. Shannon, K. Rader, W. F. von Drehle, G. W. Martin (eds.), Rocky Mountain Association of Geologists, p. 131-142.

Brown, L. G., W. A. Miller, E. M. Handley-Goff and S. L. Veal, 1990, Stockholm Southwest Field, S. A. Sonnenberg, L. T. Shannon, K. Rader, W. F. von Drehle, G. W. Martin (eds), Morrow Sandstones of SE Colorado and Adjacent Areas, Rocky Mountain Association of Geologists, p. 117-130.

Dott, R. H., Jr., 1964, Wacke, graywacke and matrix - what approach to immature sandstone classification: Jour. Sedimentary Petrology, v. 34, p. 625-632.

Farmer, C. L., 1981, Tectonics and Sedimentation, Newcastle Formation (Lower Cretaceous) southwestern flank of Black Hills uplift, Wyoming and South Dakota: unpublished M. Sc. Thesis, Colorado School of Mines, 195 pages.

Hartmann, D. J. and E. B. Coalson, 1990, Evaluation of the Morrow Sandstone in Sorrento Field, Cheyenne County, Colorado: in S. A. Sonnenberg and others (eds.), Morrow Sandstones of Southeast Colorado and Adjacent Areas: The Rocky Mountain Association of Geologists, Denver, Colorado, p. 91-100.

Hine, A. C. and S. W. Snyder, 1985, Coastal Lithosome Preservation: Evidence from the Shoreface and Inner Continental Shelf off Bogere Banks, North Carolina: Marine Geology, v. 63, p. 307-330.

Houseknecht, D. W., 1987, Assessing the relative importance of compaction processes and cementation to reduction of porosity in sandstones: AAPG Bull., v. 71, p. 633-642.

Kolodzie, S., 1980, The analysis of pore throat size and the use of the Archie equation to determine OOIP in Spindle Field, Colorato: SPE 55th Annual Fall Technical Conference, Dallas, Texas, SPE Paper 9382, 4 p.

Krystinik, L. F., 1989a, Morrow Formation Facies Geometries and Rerservoir Quality in Compound Valley Fills, Central State Line area, Colorado and Kansas (abs.): Amer. Assn. Petrol. Geol. Bull., v. 73, p. 375.

Krystinik, L. F., 1989b, Sedimentary Character of Morrow Valley Fill Complexes: A Core Study and Workshop (abs.): in Exploration for Morrow Sandstone Reservoirs SE Colorado and Adjacent Areas, RMS-SEPM and RMAG Symposium, p. 5.

Krystinik, L. F. and B. A. Blakeney, 1990, Sedimentology of the Upper Morrow Formation in Eastern Colorado and Western Kansas, S. A. Sonnenberg, L. T. Shannon, K. Rader, W. F. von Drehle, G. W. Martins (eds.), Morrow Sandstones of SE Colorado and Adjacent Areas, Rocky Mountain Association of Geologists, p. 37-50.

Shumard, C. B., 1991, Stockholm Southwest Field, U.S.A., Anadarko Basin, Kansas, Stratigraphic Traps II, Treatise of Petroleum Geology Atlas of Oil and Gas Fields, Am. Assn. Petroleum Geologists, Tulsa, Oklahoma, p. 269-304.

Shumard, C. B. and L. E. Avis, 1990, Key Morrow predictive exploration model: Southwest Stockholm field, Oil and Gas Journal, vol. 88, p. 87-94.

Shumard, C. B., 1989, Stockholm SW Field; a Morrow (Lower Pennsylvanian) Valley Fill Sandstone Reservoir, Hugoton Embayment, Greely and Wallace Co., Kansas, (abs.): in Tulsa Geologic Society Newsletter Sept. 12.

Sonnenberg, S.A., 1985, Tectonic and Sedimentation Model for Morrow Sandstone Deposition, Sorrento field Area, Denver Basin, Colorado: The Mountain Geologist, v. 22, p. 180-191.

Sonnenberg, S. A., L. T. Shannon, K. Rader, W. F. Von Drehle, G. W. Martin (eds.), 1990, Morrow Sandstones of Southeast Colorado and Adjacent Areas, Rocky Mountain Association of Geologists, 236 p.

Stamp, L. D., 1921, On Cycles of Sedimentation in The Eocene Strata of the Anglo-Franco-Belgian Basin: Geological Magazine, v. 58, p. 108-114.

Suter, J. R. and H. L. Berryhill, Jr., 1985, Late Quaternary shelf margin deltas, northwest Gulf of Mexico: Am. Assoc. Petrol. Geol. Bull., v. 69, p. 77-91.

Thomsen, A. F., 1959, Pressure solution and porosity: in H. A. Ireland (ed.), Silica in Sediments, SEPM, p. 92-110. Special Publ. 7.

Vail, P. R., R. M. Mitchum, Jr., R. G. Todd, J. M. Widmier, S. Thompson, III, J. R. Sangree, J. N. Bubb and W. G. Hatfield, 1977, Seismic stratigraphy application to hydrocarbon exploration: Am. Assoc. Petrol. Geol. Memoir 26, p. 49-205.

Weimer, R. J., S. A. Sonnenberg, L. T. Shannon, 1988, Production from Valley Fill Deposits, Morrow Sandstone, South east Colorado, New Exploration Challenges and Rewards: Rocky Mountain Assoc. Geol. Outcrop, v. 37, No. 10, Oct. 1988.

Wheeler, D. M., A. J. Scott, V. J. Coringrato, P. E. Devine, 1990, Stratigraphy and Depositional History of the Morrow Formation, Southeast Colorado and Southwest Kansas, S. A. Sonnenberg, L. T. Shannon, K. Rader, W. F. von Drehle, G. W. Martins (eds.), Morrow Sandstones of SE Colorado and Adjacent Areas, Rocky Mountain Association of Geologists, p. 9-36.

	Well	Depth	Mono. Qtz.	PolyQtz.	Feld.	Shale	Glauc.	Colloph.	Unk./Other	Clay lam.	Clay Infilt.	Carb. Cmt.	Carb. Replac.	Kaol.	Qtz. Cmt.
1	Garrison A-6	5156.3	47.2	23.4	0.3	1.2	0.3	0.0	0.3	0.0	0.0	2.4	0.0	4.6	2.2
2		5155.3	61.8	6.4	0.2	5.3	0.2	0.0	0.2	0.0	0.0	1.0	0.0	1.7	5.0
3	Evans 2-E	5177.8	25.5	44.3	0.0	0.5	1.0	0.7	0.5	0.0	0.5	16.9	1.0	0.7	2.2
4		5176.5	39.4	30.5	0.0	1.9	0.0	0.0	0.5	0.0	0.0	8.4	1.2	6.5	4.6
5		5175.2	39.8	29.7	0.2	4.2	0.0	0.0	0.2	0.0	1.6	0.7	0.0	10.5	4.0
6		5171.0	34.9	32.8	0.0	2.1	0.0	0.2	0.2	0.0	0.5	14.4	2.3	2.3	3.5
7		5168.2	30.2	37.0	0.0	2.2	0.0	0.0	0.2	0.0	3.4	2.9	0.7	6.8	4.4
8		5164.2	38.4	29.0	0.0	2.7	0.0	0.0	1.2	0.0	2.2	5.1	1.0	5.4	6.6
9		5163.1	29.0	36.8	0.0	2.3	0.0	0.0	0.5	0.0	-0.5	16.0	1.4	8.7	1.8
10	White AB-1	5173.2	49.5	20.5	1.2	3.4	0.0	0.0	1.0	0.0	0.0	0.7	0.0	2.0	3.4
11	MEAN		39.6	29.0	0.2	2.6	0.2	0.1	0.5	0.0	0.9	6.9	0.8	4.9	3.2

	Tot. Cmt.	Intergran. Por.	Intragran./Moldic Por.	Tot. Por.	Mean Grain Size	IGV	Macro/Micro	Core Por.	Perm.
1	9.2	15.7	2.7	18.4	508	24.9	3.0		
2	7.7	16.5	1.7	18.2	273	24.2	2.5	19.5	1400.0
3	20.8	6.3	0.0	6.3	1111	26.1	2.3		
4	20.7	5.1	1.9	7.0	546	24.6	0.8		
5	15.2	7.3	1.6	8.9	689	22.5	0.6		
6	22.5	5.8	0.9	6.7	675	26.0	1.4		
7	14.8	5.8	6.3	12.1	868	19.9	0.9		
8	18.1	5.3	3.1	8.4	687	22.4	1.0		
9	27.9	2.1	1.1	3.2	1005	28.6	0.3		
10	6.1	15.6	2.7	18.3	360	21.7	3.4		
11	16.5	8.6	2.2	10.8	672	24.1	1.6		

Table B1 - Point-count data for the Stockholm Fluvial Sandstone Facies IA. Depth is in feet. Mean grain size (μm) is the mean of the apparent long axes of 25 quartz grains measured optically in thin section. IGV is intergranular volume (%), which is the sum of integranular cement plus intergranular porosity. Macro/micro is the ratio of macroporosity to the rock volume with microporosity. Core porosity and permeability are expressed in percent and millidarcies, respectively. The other properties are in volume percent.

	Well	Depth	Mono. Qtz.	PolyQtz.	Feld.	Shale	Glauc.	Colloph.	Unk./Other	Clay lam.	Clay Infilt.	Carb. Cmt.	Carb. Replac.	Kaol.	Qtz. Cmt.
1	Garrison A-6	5160.7	60.4	7.0	0.3	4.6	0.3	0.3	0.5	0.0	0.0	1.2	0.0	2.9	5.6
2	Evans 2-E	5162.0	43.0	32.6	0.2	2.8	0.2	0.0	0.4	0.0	0.2	3.3	0.0	4.6	4.8
3	MEAN		51.7	19.8	0.3	3.7	0.3	0.2	0.5	0.0	0.1	2.3	0.0	3.8	5.2

	Tot. Cmt.	Intergran. Por.	Intragran./Moldic Por.	Tot. Por.	Mean Grain Size	IGV	Macro/Micro
1	9.7	15.5	1.7	17.2	243	25.2	2.2
2	12.7	2.4	0.4	2.8	713	15.1	0.4
3	11.2	9.0	1.1	10.0	478	20.2	1.3

Table B2 - Point-count data for Stockholm Tidal Sandstone (Reworked by Fluvial Processes) Facies IC. Depth is in feet. Mean grain size (m) is the mean of the apparent long axes of 25 quartz grains measured optically in thin section. IGV is intergranular volume (%), which is the sum of integranular cement plus intergranular porosity. Macro/micro is the ratio of macroporosity to the rock volume with microporosity. Core porosity and permeability are expressed in percent and millidarcies, respectively. The other properties are in volume percent.

	Well	Depth	Mono. Qtz.	PolyQtz.	Feld.	Shale	Glauc.	Colloph.	Unk./Other	Clay lam.	Clay Infilt.	Carb. Cmt.	Carb. Replac.	Kaol.	Qtz. Cmt.
1	Garrison A-6	5181.2	67.7	2.5	0.2	3.7	0.0	0.0	0.2	0.0	0.0	5.4	2.0	0.5	7.7
2		5174.2	62.1	7.9	0.5	6.7	0.5	0.2	0.5	0.0	0.0	0.2	0.0	4.8	7.4
3		5172.0	68.2	3.1	0.2	3.6	0.7	0.2	2.2	0.0	0.0	3.9	0.0	2.4	4.1
4		5169.0	62.9	3.2	0.5	3.7	0.3	0.3	0.3	0.0	0.0	3.0	0.3	6.2	6.7
5	MEAN		65.2	4.2	0.4	4.4	0.4	0.2	0.8	0.0	0.0	3.1	0.6	3.5	6.5

	Tot. Cmt.	Intergran. Por.	Intragran./Moldic Por.	Tot. Por.	Mean Grain Size	IGV	Macro/Micro	Core Por.	Perm.
1	15.6	7.7	2.5	10.2	248	21.3	2.4	15.3	80.0
2	12.4	7.9	1.4	9.3	325	20.3	0.8		
3	10.4	11.1	0.2	11.3	200	21.5	1.7		
4	16.1	10.9	1.7	12.6	314	26.8	1.2	15.5	111.0
5	13.6	9.4	1.5	10.9	272	22.5	1.5		

Table B3 - Point-count data, Stockholm Tidal Estuary Channel Sandstone Facies IIA. Depth is in feet. Mean grain size (µm) is the mean of the apparent long axes of 25 quartz grains measured optically in thin section. IGV is intergranular volume (%), which is the sum of integranular cement plus intergranular porosity. Macro/micr is the ratio of macroporosity to the rock volume with microporosity. Core porosity and permeability are expressed in percent and millidarcies, respectively. The other properties are in volume percent.

	Well	Depth	Mono. Qtz.	PolyQtz.	Feld.	Shale	Glauc.	Colloph.	Unk./Other	Clay lam.	Clay Infilt.	Carb. Cmt.	Carb. Replac.	Kaol.	Qtz. Cmt.
1	Garrison A-6	5163.6	61.5	4.8	0.3	5.1	0.3	0.3	0.5	3.6	0.0	2.4	0.3	8.9	4.3
2	Evans E-2	5173.8	48.9	19.1	0.5	7.5	0.2	0.0	0.5	3.9	0.0	0.0	0.0	11.9	5.3
3	MEAN		55.2	12.0	0.4	6.3	0.3	0.2	0.5	3.8	0.0	1.2	0.2	10.4	4.8

	Tot. Cmt.	Intergran. Por.	Intragran./Moldic Por.	Tot. Por.	Mean Grain Size	IGV	Macro/Micro
1	15.9	7.2	0.7	7.9	299	22.8	0.6
2	17.2	2.4	0.7	3.1	471	19.6	0.2
3	16.6	4.8	0.7	5.5	385	21.2	0.4

Table B4 - Point-count data, Stockholm Fluvial Sandstone (Reworked by Tidal Processes) Facies IIB. Depth is in feet. Mean grain size (m) is the mean of the apparent long axes of 25 quartz grains measured optically in thin section. IGV is intergranular volume (%), which is the sum of integranular cement plus intergranular porosity. Macro/micro is the ratio of macroporosity to the rock volume with microporosity. Core porosity and permeability are expressed in percent and millidarcies, respectively. The other properties are in volume percent.

	Well	Depth	Mono. Qtz.	PolyQtz.	Feld.	Shale	Glauc.	Colloph.	Unk./Other	Clay lam.	Clay Infilt.	Carb. Cmt.	Carb. Replac.	Kaol.	Qtz. Cmt.
1	Evans 2-E	5176.0	58.4	11.8	0.5	6.4	0.2	0.5	0.7	2.1	0.0	0.9	0.0	6.8	5.2
2		5165.5	63.5	6.6	0.2	7.6	0.2	0.0	0.9	3.1	0.0	0.5	0.0	3.6	11.1
3	MEAN		61.0	9.2	0.4	7.0	0.2	0.3	0.8	2.6	0.0	0.7	0.0	5.2	8.2

	Tot. Cmt.	Intergran. Por.	Intragran./Moldic Por.	Tot. Por.	Mean Grain Size	IGV	Macro/Micro
1	12.9	5.0	1.6	6.6	182	17.9	0.5
2	15.2	2.1	0.5	2.6	225	17.3	0.2
3	14.1	3.6	1.1	4.6	204	17.6	0.4

Table B5 - Point-count data for Stockholm Tidal Bar Sandstone Facies IIC. Depth is in feet. Mean grain size (μm) is the mean of the apparent long axes of 25 quartz grains measured optically in thin section. IGV is intergranular volume (%), which is the sum of integranular cement plus intergranular porosity. Macro/macro is the ratio of macroporosity to the rock volume with microporosity. Core porosity and permeability are expressed in percent and millidarcies, respectively. The other properties are in volume percent.

	Well	Depth	Mono. Qtz.	PolyQtz.	Feld.	Shale	Glauc.	Colloph.	Unk./Other	Clay lam.	Clay Infilt.	Carb. Cmt.	Carb. Replac.	Kaol.
1	Berquist 2	5125.6	38.4	36.2	0.4	5.4	0.2	0.0	0.2	0.0	0.0	0.5	0.0	4.0
2		5115.5	36.1	34.9	0.4	5.7	0.2	0.0	0.8	6.1	0.4	1.9	0.2	3.0
3	MEAN		37.3	35.6	0.4	5.6	0.2	0.0	0.5	3.1	0.2	2.4	0.1	3.5

	Qtz. Cmt.	Tot. Cmt.	Intergran. Por.	Intragran./Moldic Por.	Tot. Por.	Mean Grain Size	IGV	Macro/Micro	Core Por.	Perm.
1	2.7	7.4	8.3	3.4	11.7	840	15.7	1.2	11.5	77.0
2	1.5	6.6	4.9	3.8	8.7	423	11.3	0.9	11.7	129.0
3	2.1	7.0	6.6	3.6	10.2	631	13.5	1.1		

Table B6 - Point-count data for the Stockholm Tidal Channel Sandstone Facies IID. Depth is in feet. Mean grain size (μm) is the mean of the apparent long axes of 25 quartz grains measured optically in thin section. IGV is intergranular volume (%), which is the sum of integranular cement plus intergranular porosity. Macro/micro is the ratio of macroporosity to the rock volume with microporosity. Core porosity and permeability are expressed in percent and millidarcies, respectively. The other properties are in volume percent.

	Well	Depth	Mono. Qtz.	PolyQtz.	Feld.	Shale	Glauc.	Colloph.	Unk./Other	Clay lam.	Clay Infilt.	Carb. Cmt.	Carb. Replac.	Kaol.	Qtz. Cmt.
1	White AB-1	5167.0	56.2	2.6	2.8	2.1	1.6	0.2	1.2	0.5	0.0	29.7	3.2	0.0	0.0
2		5159.0	48.5	2.0	10.0	7.3	0.7	0.0	2.2	3.4	0.0	22.9	2.0	0.0	1.0
3	MEAN		52.4	2.3	6.4	4.7	1.2	0.1	1.7	2.0	0.0	26.3	2.6	0.0	0.5

	Tot. Cmt.	Intergran. Por.	Intragran./Moldic Por.	Tot. Por.	Mean Grain Size	IGV	Macro/Micro
1	32.9	0.0	0.0	0.0	106	29.7	0.0
2	25.9	0.0	0.0	0.0	78	23.9	0.0
3	29.4	0.0	0.0	0.0	92	26.8	0.0

Table B7 - Point-count data, Stockholm Marine Shelf Sandstone Facies III. Mean grain size (μm) is the mean of the apparent long axes of 25 quartz grains measured optically in thin section. IGV is intergranular volume (%), which is the sum of integranular cement plus intergranular porosity. Macro/micro is the ratio of macroporosity to the rock volume with microporosity. Core porosity and permeability are expressed in percent and millidarcies, respectively. The other properties are in volume percent.

DOMINANT CONTROL ON RESERVOIR-FLOW BEHAVIOR IN CARBONATE RESERVOIRS AS DETERMINED FROM OUTCROP STUDIES*

R. K. Senger, F. J. Lucia, C. Kerans, and M. A. Ferris

Bureau of Economic Geology
The University of Texas at Austin
Austin, Texas 78713-7508

G. E. Fogg

Department of Land, Air, and Water Resources
University of California at Davis
Davis, California 95616

I. INTRODUCTION

The investigation of carbonate-ramp deposits of the upper San Andres Formation that crop out along the Algerita Escarpment, New Mexico, is a research element of ongoing geologic and petrophysical studies conducted at the Bureau of Economic Geology's Reservoir Characterization Research Laboratory (RCRL). The primary goal of the investigation is to develop an integrated strategy involving geological, petrophysical, geostatistical, and reservoir-simulation studies that can be used to better predict flow characteristics in analogous subsurface reservoirs. Geologic investigations and detailed measurements of petrophysical parameters on continuous outcrop were used to determine not only the vertical distribution of the data but also their lateral distribution, which is typically lacking in subsurface studies.

To characterize the complex heterogeneity associated with depositional and diagenetic processes at the interwell scale, detailed permeability data were collected within the overall geologic framework from the outcrop at Lawyer Canyon, Algerita Escarpment, New Mexico (fig. 1). Geologic mapping showed a series of upward-shallowing parasequences (10 to 40 ft thick and several thousand feet long). Parasequence boundaries are typically marked by tight mudstone/wackestone beds that display variable degrees of lateral continuity ranging from several hundred feet to more than 2,500 ft and are potentially important as flow barriers (fig. 2). Within these parasequences, distinct variability of facies and petrophysical characteristics is present at scales well below those of interwell spacing typical for their subsurface counterparts (660 to 1,330 ft). Pore types and permeability-porosity relationships can also be specific to individual parasequences.

*Publication authorized by the Director, Bureau of Economic Geology, The University of Texas at Austin.

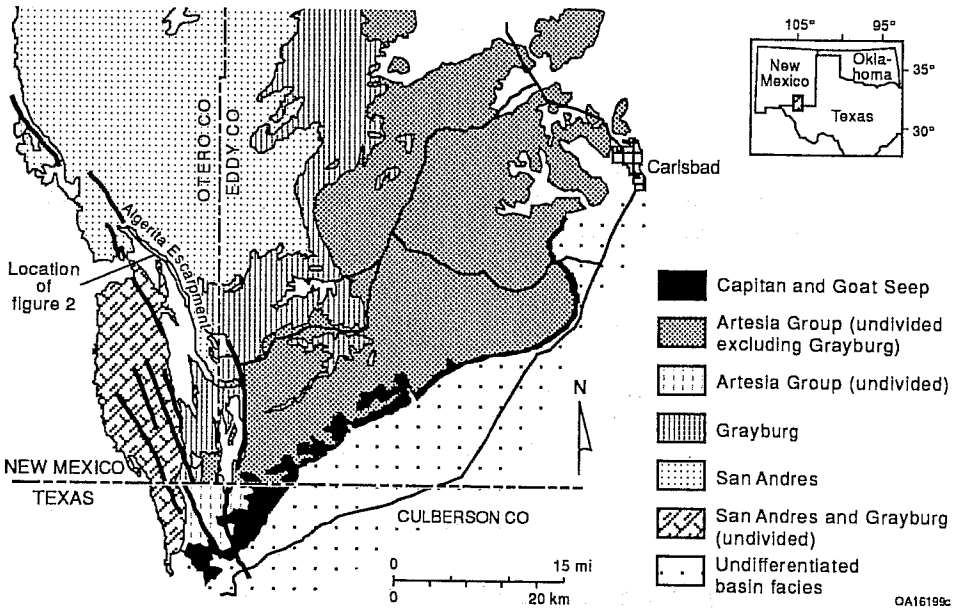

Figure 1. Geologic map of the Guadalupe Mountains compiled from Hayes (1964) and King (1948) showing the Algerita Escarpment and the Lawyer Canyon study area.

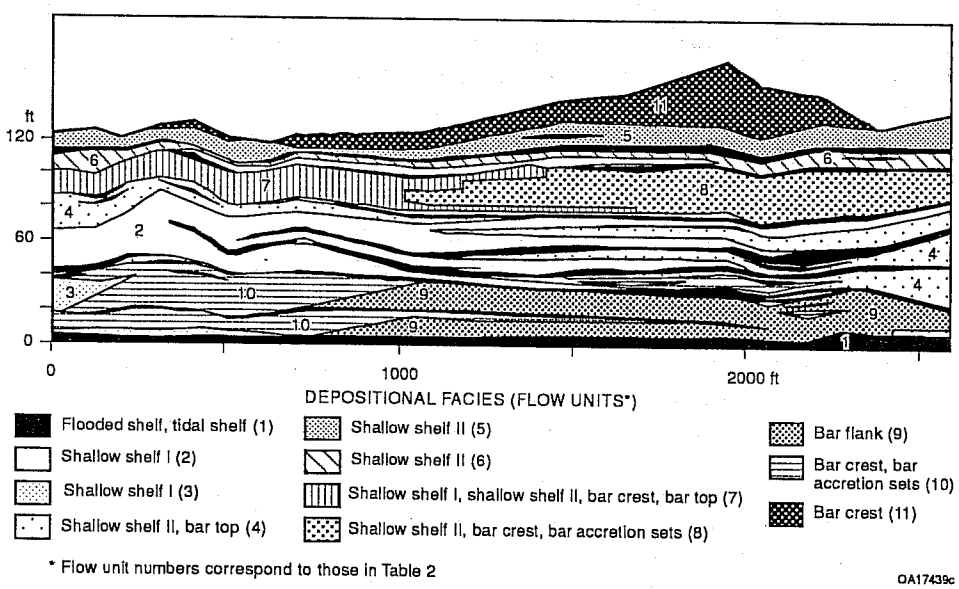

Figure 2. Distribution and geometry of depositional facies mapped in the upper San Andres parasequence window, Lawyer Canyon, Algerita Escarpment, New Mexico.

Previous studies characterizing permeability in San Andres outcrops include those of Hindrichs and others (1986) and Kittridge and others (1990). The study by Hindrichs and others was based on core plugs taken from different beds in the middle San Andres Formation. Results indicated large permeability variations within beds separated by low-permeability mudstones, with no apparent difference in permeability between horizontal and vertical cores. Kittridge and others (1990) used a mechanical field permeameter (MFP) to study spatial permeability variations at a specific site near the middle and upper San Andres Formation boundary at the Lawyer Canyon area. Geostatistical analyses of measured permeability indicated that permeability correlation lengths decreased with decreasing sample spacing and that different rock fabrics exhibited different mean permeabilities.

In this study, permeability measurements were guided by the detailed geologic mapping of continuous San Andres outcrop, which revealed a stacking pattern of parasequences and of facies and rock-fabric succession within parasequences that provide the necessary framework for petrophysical quantification of geologic models. Standard statistics were used to relate permeability to facies and rock-fabric characteristics through a petrophysical/rock-fabric approach. In addition, geostatistical analysis was applied to evaluate spatial permeability characteristics. Stochastic modeling was then used to generate a series of "realistic" permeability distributions that took into account the underlying permeability structure and the uncertainty of measurement data. Numerical waterflood simulations of selected permeability realizations were designed to characterize interwell heterogeneity and to represent heterogeneity by appropriate average properties, which can be used in reservoir-scale flow models. For the reservoir-scale flow model, a petrophysical/rock-fabric approach was used to quantify the geologic framework of the reservoir-flow model.

II. METHODOLOGY

A. Permeability Measurements

Permeability was measured with an MFP, which gauges gas-flow rates and pressure drop by pressing an injection tip against the rock surface. These data are used to calculate permeability values on the basis of a modified form of Darcy's law that incorporates effects of gas slippage at high velocity (Goggin and others, 1988). In addition, permeability and porosity were determined on the basis of conventional Hassler sleeve methods, using 1-inch-diameter core plugs taken from the outcrop. Core and MFP permeability compared reasonably well for permeabilities greater than about 1 md, which is approximately the detection limit of MFP measurements (Goggin and others, 1988).

The distribution of permeability measurements taken from the upper San Andres at Lawyer Canyon is shown in figure 3. Sampling focused on parasequence 1, composed of grainstones forming bar-crest and bar-flank facies overlying wackestones and mudstones of a flooded-shelf facies, and on parasequence 7, characterized by low-moldic and highly moldic grainstones (fig. 2). Permeability distributions were measured at scales ranging from detailed grids of 1-inch spacing to 1-ft spacing and at vertical transects that were spaced laterally between 5 and 100 ft and that contained permeability measurements at 1-ft vertical intervals.

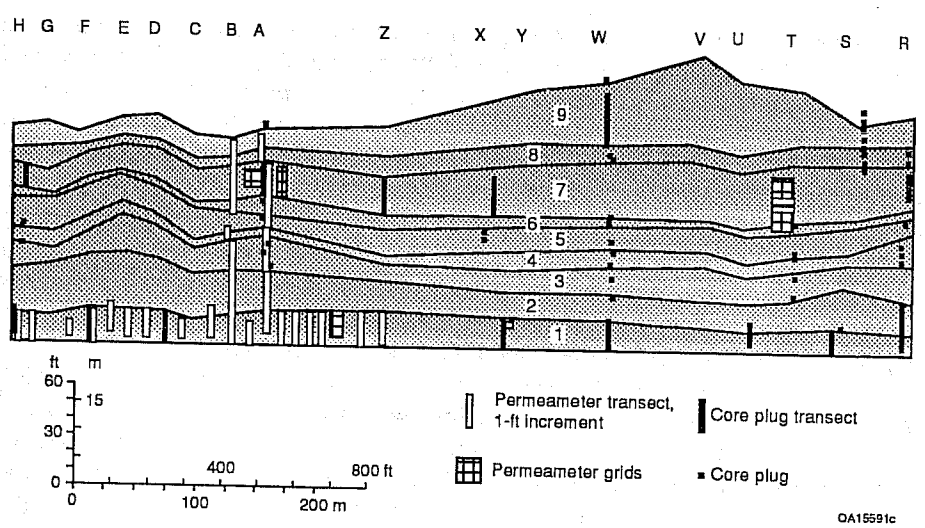

Figure 3. Location of sampling grids and transects of MFP measurements and core plugs.

The total number of MFP measurements at the Lawyer Canyon parasequence window was 1,584. Removing the outer weathering surface of the rock by chipping away an area of about 1 square inch gave the best representation of permeability (Ferris, in preparation). Preparing the sampling surface with a grinder produced permeabilities that were lower overall than those measured on chipped surfaces, owing to plugging of pore space by fines (Kittridge and others, 1990). Within each chipped area, typically several measurements were made and averaged. Depending on measurement discrepancies, as many as six different MFP readings were taken at various locations within the chipped area.

B. Geostatistics

Variography, a geostatistical technique for analyzing spatial variability of a property such as permeability, was used to help quantify the spatial permeability pattern at different scales. For further discussion of variogram analysis, refer to Journel and Huijbregts (1978) and Fogg and Lucia (1990). The variogram describes variability as a function of distance between measurements. The average variance of measurement pairs within certain distance intervals typically shows increasing variability (γ) with increasing interval range (fig. 4). Beyond a certain distance (range), γ may no longer increase. The variance that corresponds to the range is the sill, which reflects the variability where spatial correlation no longer exists; it typically corresponds to the ensemble variance of the entire data set. Small-scale heterogeneity or measurement errors can cause a variogram to originate at a high variance referred to as a nugget, representing local random variability.

Spatial permeability characteristics can often be described by the nugget, the correlation range, the sill, and the variogram model. The latter is obtained by fitting

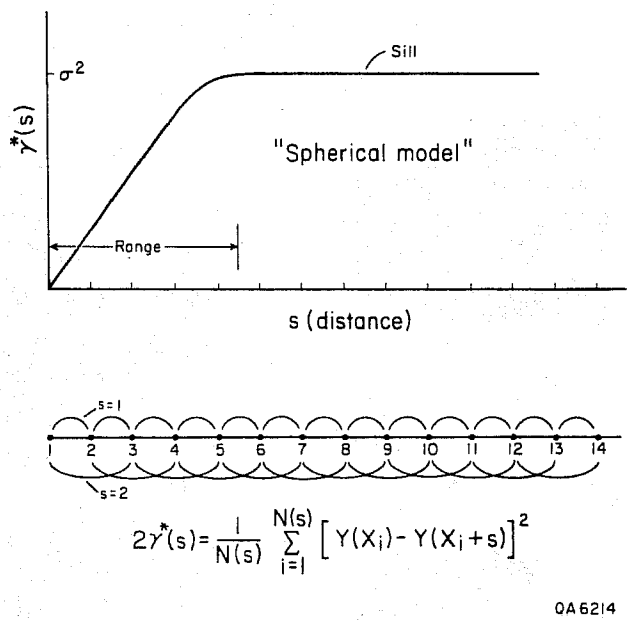

Figure 4. Schematic example of calculation of the experimental variogram.

a certain type of mathematical function to the experimental variogram. In this study the computer program GAMUK (Knudsen and Kim, 1978) was used to compute the experimental variogram. Application of the variogram to kriging or to conditional simulation usually requires an assumption of stationarity, which requires that the mean and the variogram be the same over the area of interest.

Kriging is a technique of estimating properties at points or blocks distributed over the area of interest by taking a weighted average of sample measurements surrounding a regularly spaced grid point or block. Kriging incorporates the spatial correlation structure contained in the variogram model. The kriging program is based on the program UKRIG, developed by Knudsen and Kim (1978). The permeability data were contoured with the CPS-1 contouring package (Radian Corp., 1989) and with the DI-3000 contouring package at The University of Texas Center for High Performance Computing.

Conditional simulation uses the underlying permeability structure obtained from kriging and adds the stochastic component associated with the uncertainty of the limited permeability data. Conditional simulation is performed with the program SIMPAN (Fogg, 1989). A large number of permeability realizations are screened for maximum and minimum continuity of permeable zones using the program MCSTAT (Fogg, 1989), which measures the length and thickness of domains of contiguous blocks having simulated permeability values greater than 50 md. The selection of realizations having low and high continuity of permeable zones is based on the mean horizontal continuity ($\bar{C}_h$) at the 10th and 90th percentiles, respectively. These end-member representations of "realistic" permeability distributions, conditioned on the same permeability data, are then used in waterflood simulations to evaluate

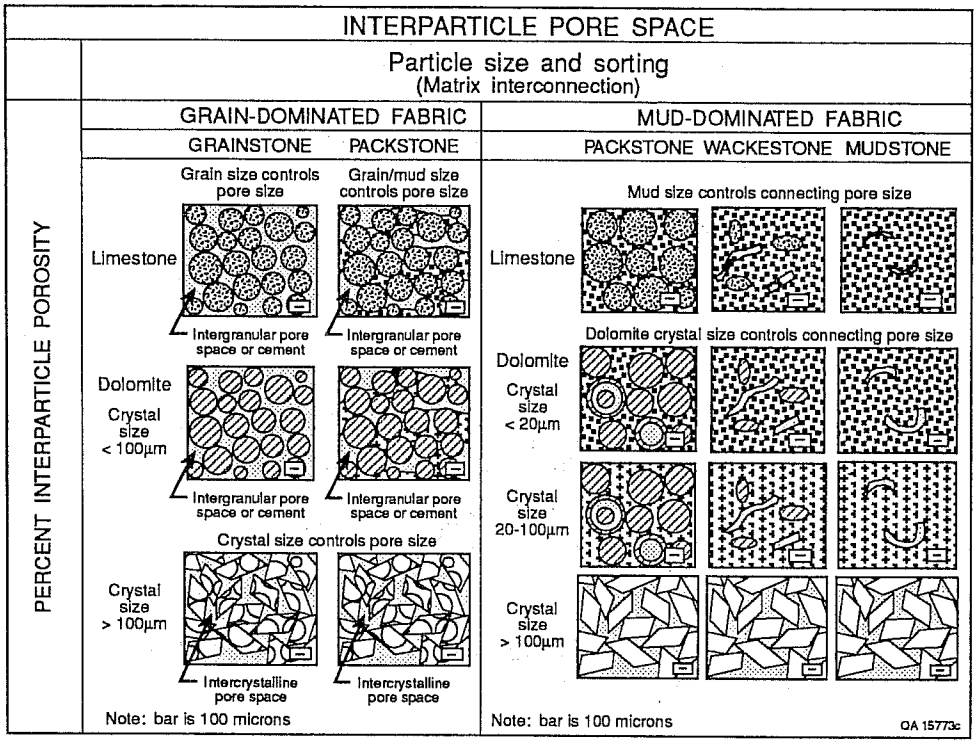

Figure 5. Classification of interparticle pore space in carbonate rocks.

reservoir-flow characteristics. For further details on stochastic reservoir simulations, refer to Fogg and others (1991). The reservoir simulator ECLIPSE (ECL Petroleum Technologies, 1990) was used in this study for two-phase waterflood simulations.

III. PERMEABILITY CHARACTERIZATION, LAWYER CANYON OUTCROP

A. Petrophysical/Rock-Fabric Approach

Petrophysical parameters such as porosity, permeability, and saturation were quantified by relating rock texture to pore-type and pore-size distribution (fig. 5). Spatial distribution of these petrophysical parameters was defined by geologic concepts of sedimentation, diagenesis, and tectonics, which provided the basis for the three-dimensional reservoir framework. Pore space in carbonate rocks can be divided into interparticle and vuggy pores on the basis of the particulate nature of carbonate rocks. Three petrophysical/rock-fabric classes for nonvuggy pore space can be distinguished on the basis of porosity, permeability, and saturation relationships (fig. 6), and vuggy pore space can be divided into separate vugs and touching vugs on the basis of the type of interconnection. The petrophysical classes for nonvuggy pores have distinct porosity-permeability relationships (fig. 7), as well as relationships between porosity and water saturation (fig. 8).

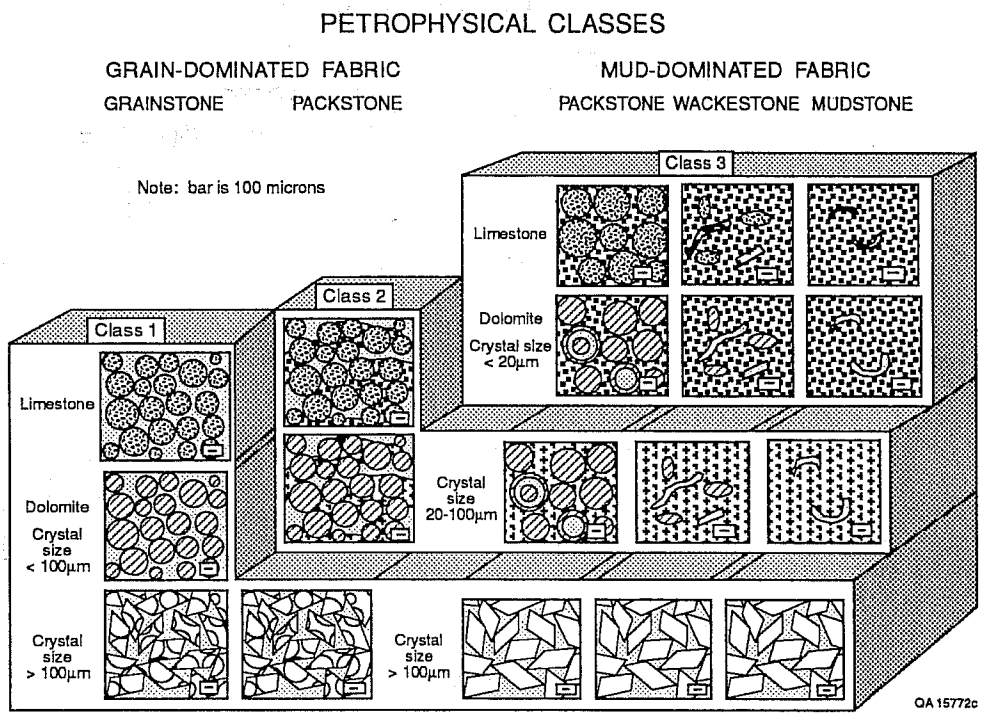

Figure 6. Petrophysical/rock-fabric classes for nonvuggy carbonates.

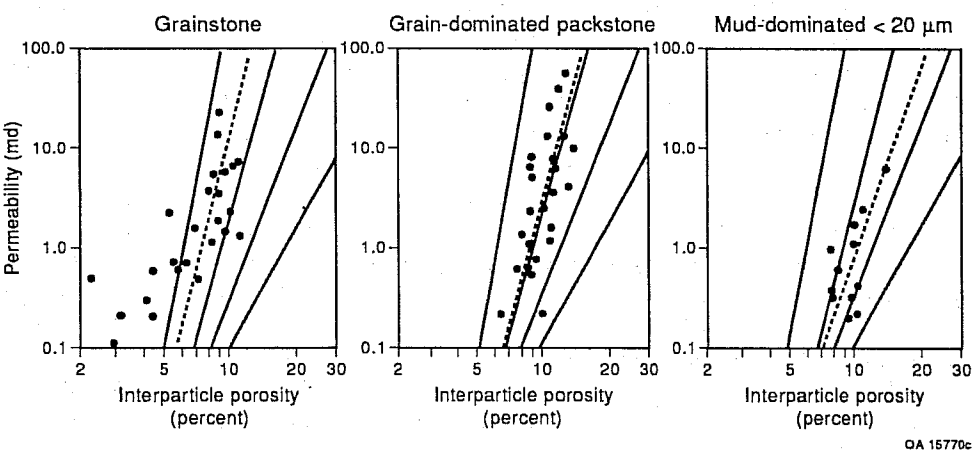

Figure 7. Porosity-permeability relationships for various rock-fabric fields in nonvuggy carbonates. Data are from core-plug measurements from the Lawyer Canyon outcrop.

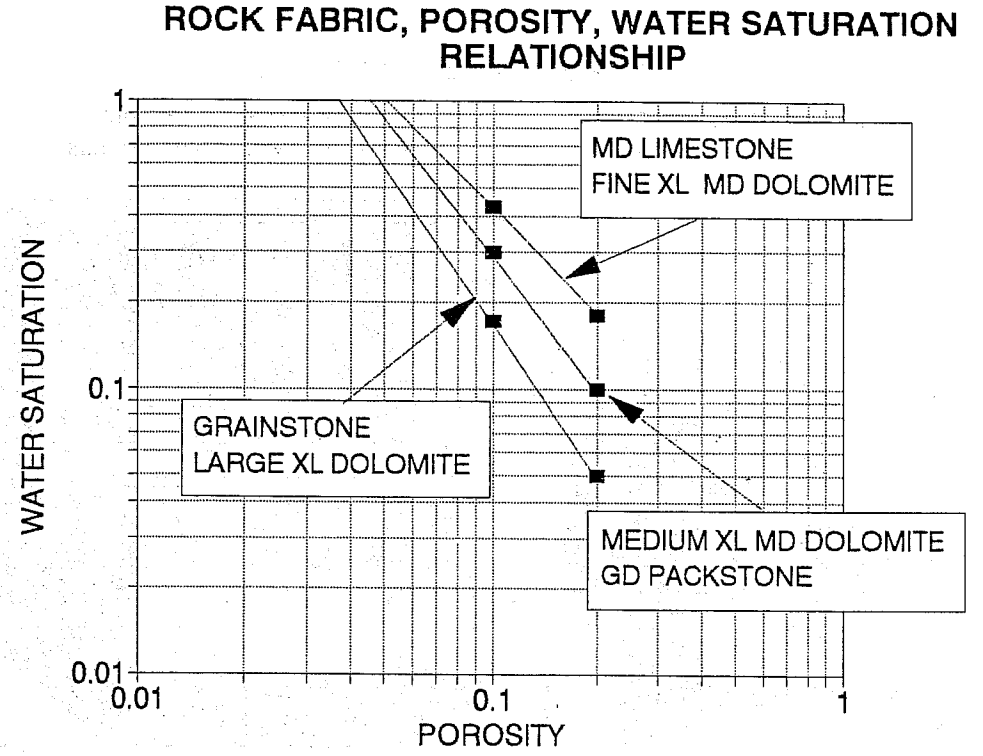

Figure 8. Rock-fabric, porosity, and water-saturation relationships from capillary-pressure curves.

In addition to the nonvuggy pore types, separate vugs were important to this study. Separate vugs, such as moldic pores, are connected only through interparticle pore space and result in a lower permeability than that which would be expected if the porosity were all interparticle; that is, they do not fall into the different porosity-permeability field for nonvuggy pore types. However, vuggy pore space is typically large enough that it can be assumed to be filled with hydrocarbons.

According to this rock-fabric classification, five productive rock-fabric units were recognized in the outcrop at the Lawyer Canyon parasequence window (fig. 9): grainstones, separate-vug grainstones, grain-dominated packstones, mud-dominated packstones and wackestones, and tight mudstones and fenestral caps. The information was derived from permeability and porosity measurements of core plugs and from a petrographic description of thin section taken from core plugs.

For the evaluation of permeability characteristics with respect to facies and fabrics, only those data were taken that follow the geologic measured sections for which spatial coordinates, facies, and fabric designations are available. The histogram of permeabilities using both core and MFP measurements (fig. 10) shows a roughly lognormal distribution. Core permeabilities are skewed toward lower permeabilities than are the MFP measurements, owing to the 1-md detection limit of the MFP data. Within relatively permeable facies (e.g., the bar-crest facies within

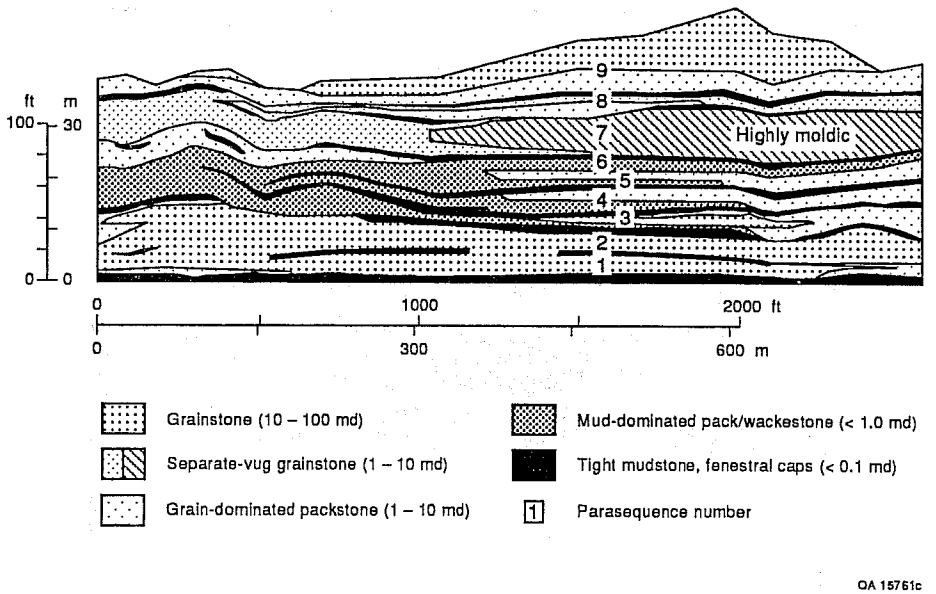

Figure 9. Rock-fabric flow units of the upper San Andres parasequence window, Lawyer Canyon, Algerita Escarpment, New Mexico.

parasequence 1), core and MFP measurements have statistically similar populations, with similar geometric means of 1.33 and 1.34 md, respectively. Statistical comparison of the two populations using a t-test indicates that the null hypothesis cannot be rejected at the 80 percent confidence level (t-statistics = –0.1318; p-value = 0.8953).

The dominant rock fabrics exhibit significant differences in mean permeability (fig. 11), with mudstone having the lowest permeability and grainstone having the highest permeability. Most of the mapped facies are also characterized by significantly different mean permeabilities (fig. 12). Generally, shelf facies exhibit significantly lower mean permeabilities than bar facies, with the bar-crest and bar-accretion-set facies having the highest mean permeability of log k = 1.1 md. The facies characteristic (fig. 12) is consistent with the rock-fabric characteristic (fig. 11) because the bar facies consist mostly of high-permeability grainstones and the shelf facies consist mostly of low-permeability, mud-dominated fabrics. Furthermore, the mapped parasequences are characterized by different facies and fabric combinations, indicating different hydraulic properties of each parasequence. Mean permeabilities in parasequences 1, 2, 7, and 9 are significantly higher than those in parasequences 3, 4, 5, 6, and 8. The latter sequences consist mostly of packstone and wackestone, whereas parasequences 1, 2, 7, and 9 consist predominantly of grainstones (fig. 9). Grainstones in parasequence 7 are characterized by moldic-pore types with high porosity but slightly lower permeability than those in the other cycles having intergranular porosity.

Within individual facies, permeability varies by as much as five orders of magnitude (fig. 12). Characterization of spatial permeability patterns within individual facies is therefore important for predicting flow behavior in these ramp-crest

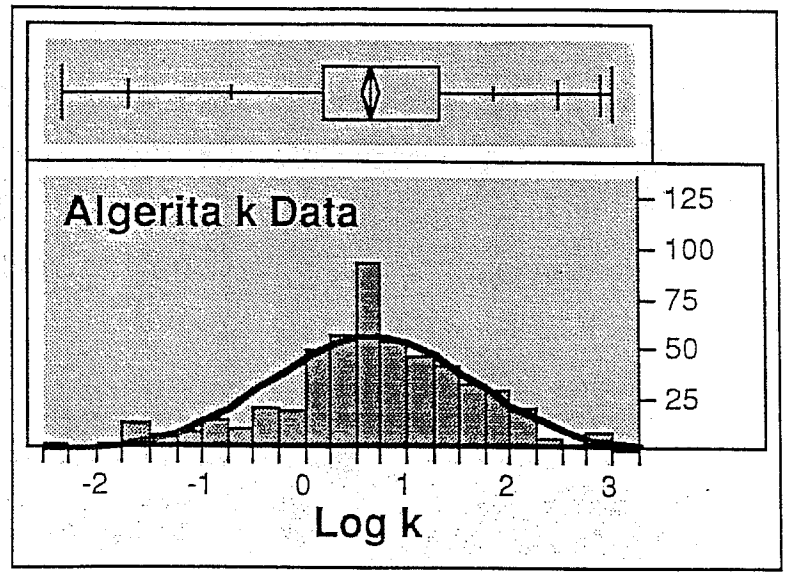

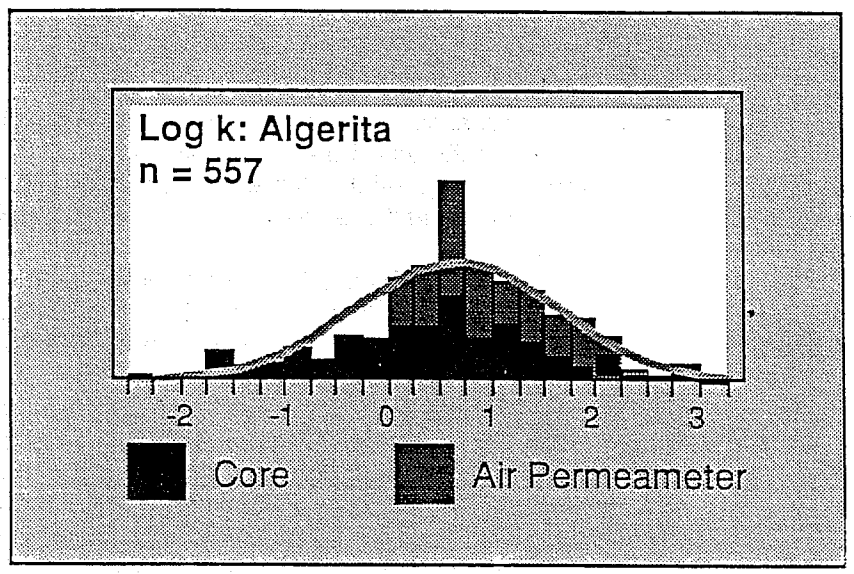

Figure 10. Histogram of permeabilities obtained along the geologically measured sections.

grainstone bar complexes. If permeability within facies is spatially uncorrelated (i.e., random), then the two-dimensional effective permeability of that facies can be estimated by taking the geometric average of the local permeabilities (Warren and Price, 1961). If permeability within facies exhibits significant spatial correlation, then effective permeability of that facies must be estimated by taking some other type of average.

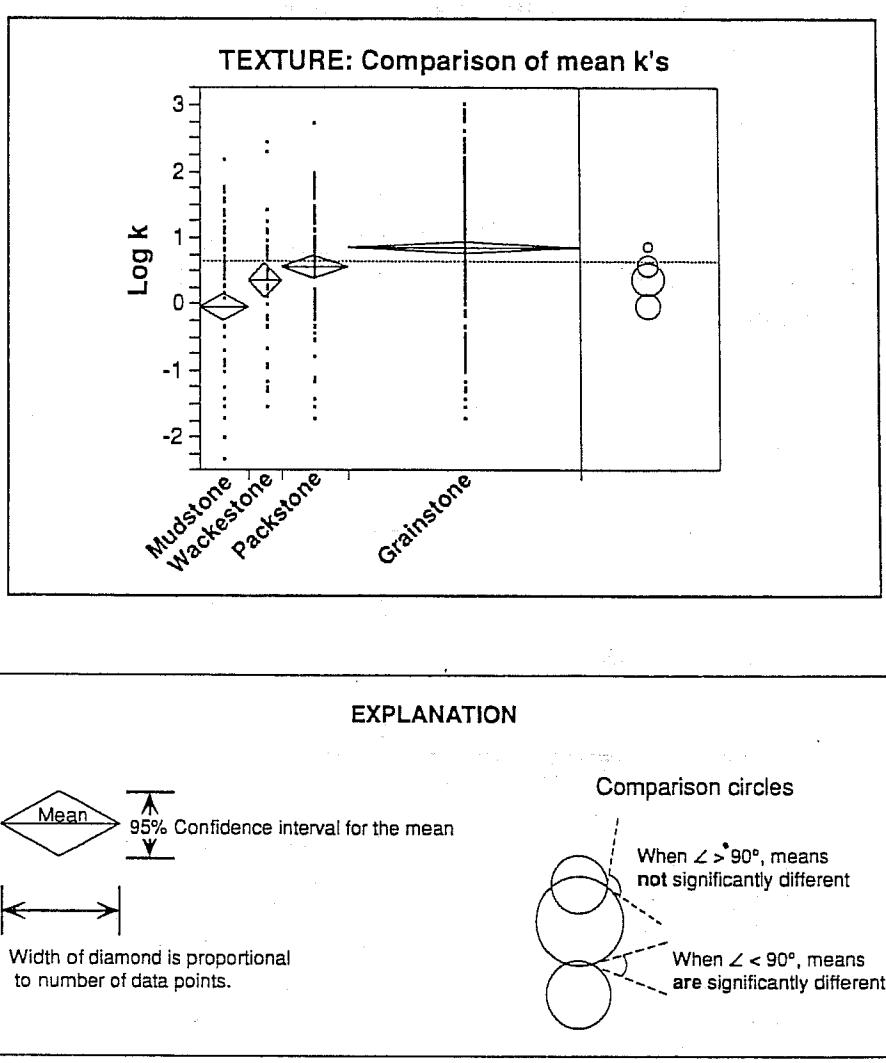

Figure 11. Statistical comparison of means of permeability for different textures. Comparison circles correspond to the 95 percent confidence intervals for the means.

B. Spatial Permeability Patterns and Variography

Spatial patterns in permeability were characterized and mapped in three steps. First, the data were contoured with an inverse-distance-squared algorithm to depict any trends or anisotropies in the data. Second, variograms were computed for different lag spacings and directions that were consistent with the data spacings and inverse-distance maps. Third, variogram models were fit to the variograms and were used to create point-kriged maps of spatial permeability patterns.

Standard contouring (inverse-distance-squared) of the detailed permeability transects spaced between 25 and 100 ft in parasequence 1 (fig. 2), using the CPS-1

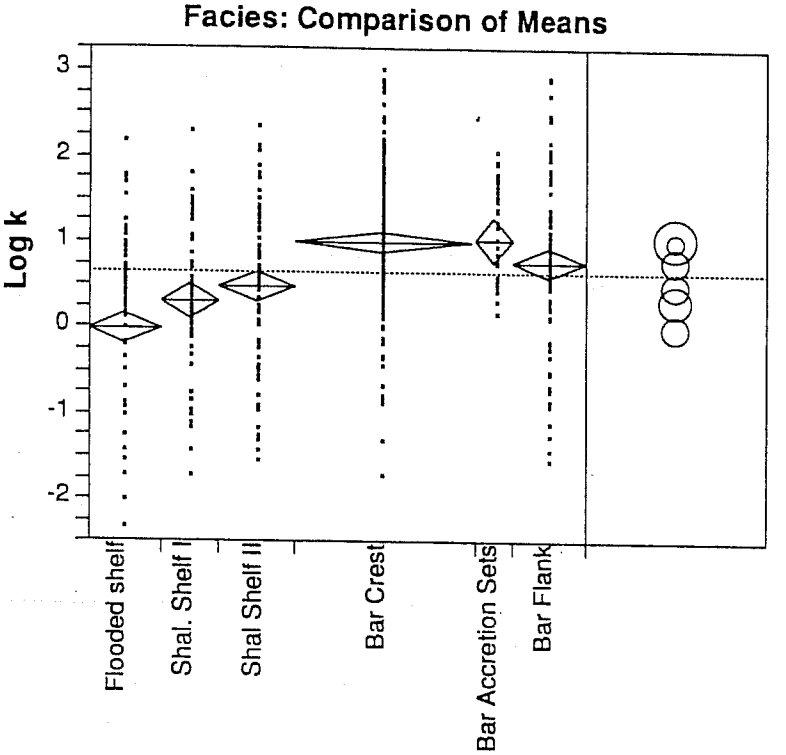

Mean Estimates

Facies	N	Mean	Std Error
Flooded shelf	82	-0.01	0.10
Shallow shelf I	48	0.25	0.13
Shallow shelf II	73	0.51	0.11
Bar crest	158	1.07	0.07
Bar top	6	0.10	0.37
Tidal flat	2	0.37	0.65
Bar accretion sets	18	1.11	0.22
Bar flank	82	0.76	0.10
Shallow shelf I (moldic)	16	0.45	0.23
Shallow shelf II (moldic)	9	0.26	0.30
Bar crest (moldic)	39	0.73	0.15
Bar accretion sets (moldic)	24	0.98	0.19

Figure 12. Statistical comparison of means of permeability for different facies. Standard error values refer to the estimated means.

contouring package, shows extreme heterogeneity (fig. 13) within the bar-crest facies, bar-flank facies, and shallow-shelf facies, which are collectively referred to as the grainstone facies of parasequence 1. Permeability is controlled by total porosity, and separate-vug porosity (intragranular microporosity) has a second-order effect.

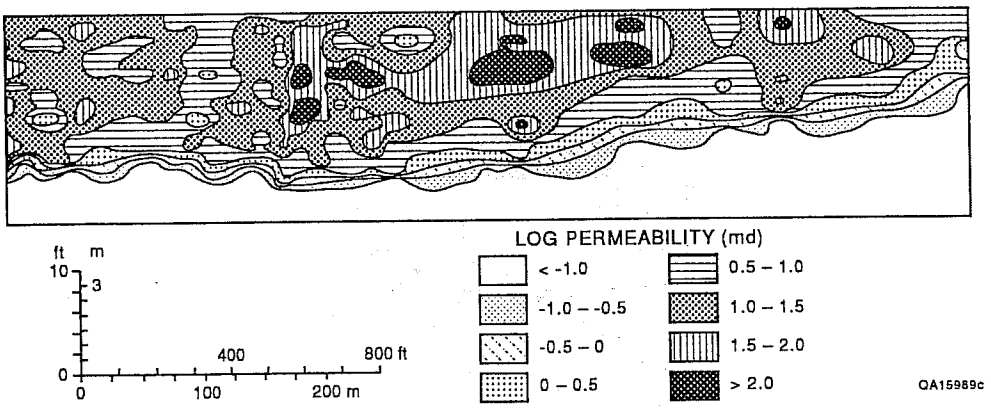

Figure 13. Permeability distribution for normalized parasequence 1 based on inverse-distance-squared contouring algorithm using CPS-1.

To evaluate heterogeneity at different scales, permeability measurements from the different measurement grids were analyzed using variography. Within the bar-crest facies of parasequence 1, permeability transects were typically spaced 25 ft apart. Between transects A and Z (fig. 3), vertical transects were spaced 5 ft apart. Horizontal and vertical variograms of the permeability data indicate a short-range correlation range of about 3 ft in the vertical direction and a possible correlation range of about 30 ft in the horizontal direction (fig. 14). In both cases, however, the spherical variogram indicates a nugget constant of $\sigma_0 = 0.2$ md^2, which is as large as the sill. This relatively large nugget indicates small-scale random variability of permeability. The small-scale random permeability variation is apparent in permeability patterns of the smaller scale grids, which were measured at regular 1-ft spacings (fig. 15) and at 1-inch spacings (not shown here). Variogram analysis of these small-scale permeability grids did not indicate a noticeable permeability correlation but showed a large variability in permeability. Measurement accuracy of the minipermeameter typically decreased toward the lower detection limit of 1 md and may have accentuated some of the observed noise in the permeability data.

Using the fitted variogram models (fig. 14), a kriged permeability map was constructed for the northern half of parasequence 1, consisting predominantly of bar-crest facies. Note that the kriged permeability map (fig. 16), based on the vertical permeability transects spaced 25 ft apart, shows a much smoother distribution than does the kriged permeability map based on the 1-ft grid (fig. 15).

C. Conditional Simulation

Even though kriging can incorporate permeability correlation structures, it tends to average permeability over larger areas, ignoring small-scale heterogeneity. On the basis of the short-range correlation of permeability data (fig. 14), a series of stochastic permeability realizations were produced for the grainstone facies in

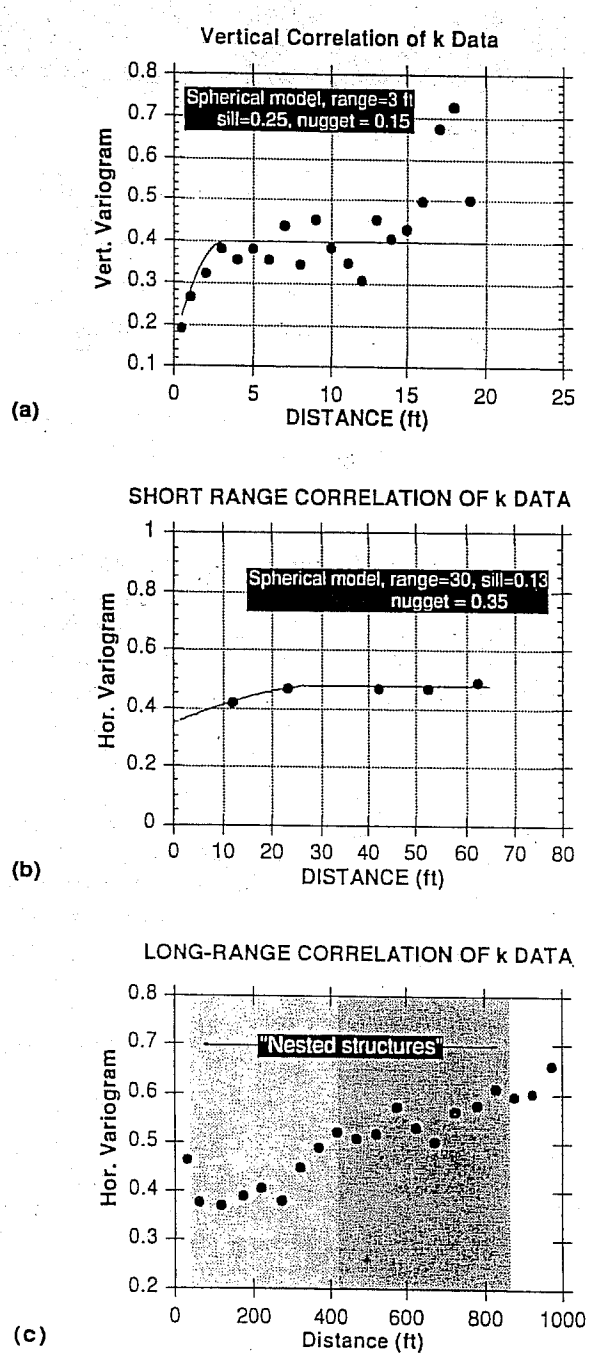

Figure 14. Sample variograms for the entire permeability transects from the grainstone facies in parasequence 1: (a) vertical variogram, (b) short-range horizontal variogram, based on the 5-ft grid, and (c) long-range horizontal variogram, based on all transects spaced about 50 ft apart.

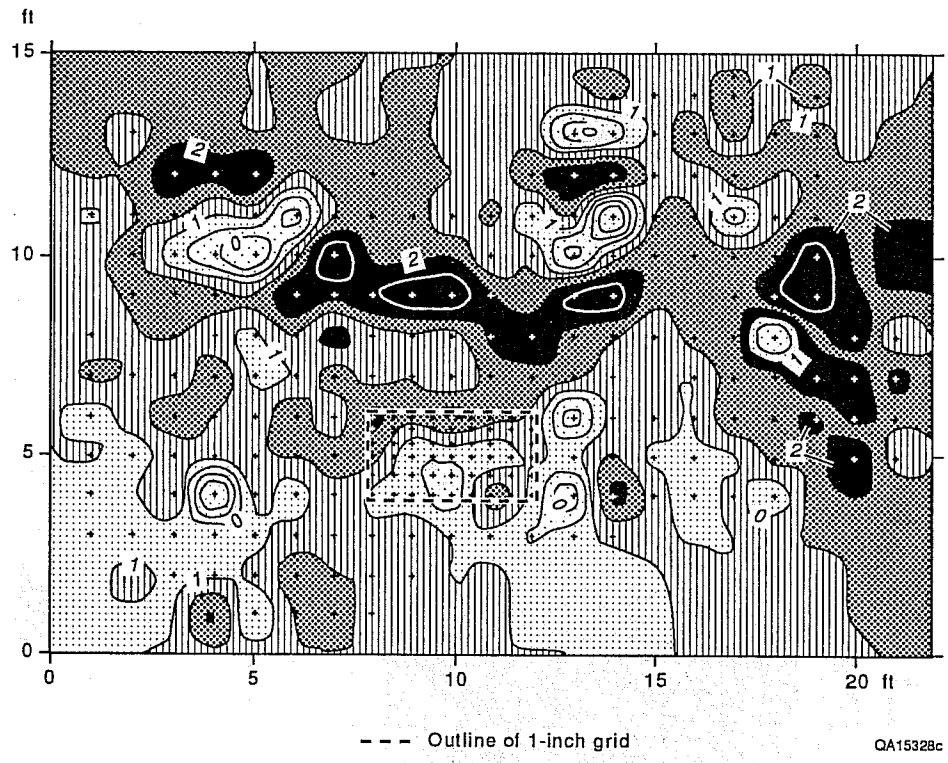

Figure 15. One-foot sampling grid in parasequence 1 with kriged permeability contours.

parasequence 1. The model extends laterally from 0 to 1,050 ft and is 17 ft thick, with block sizes of 5 ft by 1 ft. The simulations, conditioned to permeabilities measured along vertical transects spaced approximately 25 ft apart (fig. 3), incorporate the correlation structure from the variograms.

Two permeability distributions out of 200 stochastic permeability realizations were selected for flow simulations, representing maximum and minimum lateral continuity (C_h) of domains having permeability values greater than 50 md (table 1). Comparison of the two permeability realizations (figs. 17a, b) does not show a noticeable difference. The ranges of 3 ft (vertical) and 30 ft (horizontal) (figs. 14a, b) are not immediately apparent in these realizations (fig. 17); the permeability patterns appear spatially uncorrelated because of the relatively large nugget, which is of the same magnitude as the sill (fig. 14). These conditional simulated realizations, however, preserve the spatial variability exhibited in the variograms, whereas the kriged permeability map (fig. 16) averages out much of this variability.

As mentioned above, measurement uncertainty of the minipermeameter may have accentuated some of the observed noise in the permeability data, which is reflected in the relatively large nugget of the variograms (fig. 14). For comparison, unconditional permeability realizations were produced that incorporate the mean, variance, and variogram range but have a zero nugget and a sill of 0.4 md^2 and are not conditioned to the actual permeability values. All of these unconditional

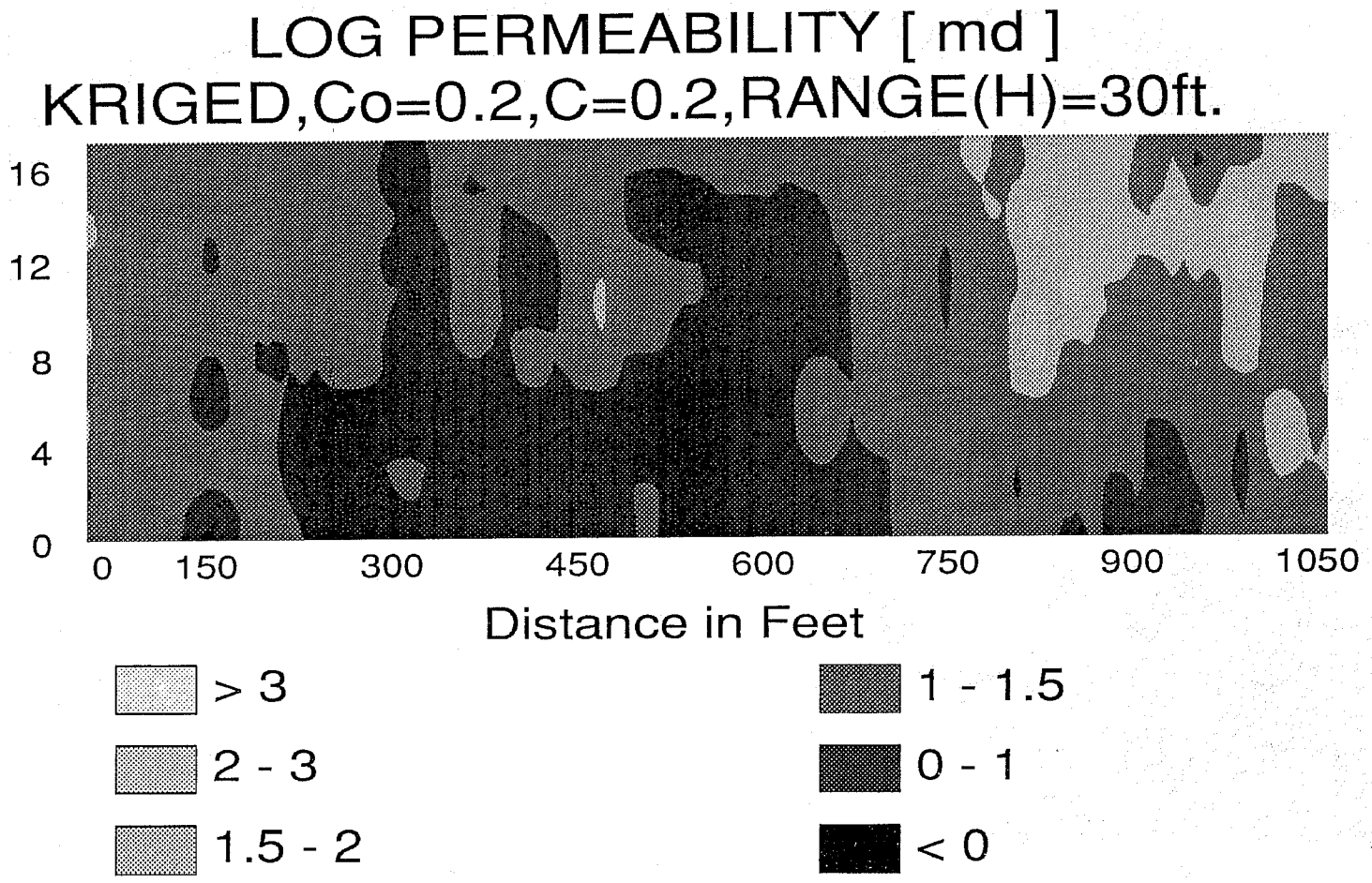

Figure 16. Kriged permeability distribution of the left part of parasequence 1, representing the bar-crest facies.

Table 1. Waterflood simulations of grainstone facies in parasequence 1.

No.	Permeability realization	Statistics: Mean log-k (md)	Variance log-k (md^2)	Nugget (md^2)	Sill (md^2)	Mean horizontal continuity ($\overline{C}_h$) (ft)
1*	7	1.219	0.42	0.2	0.2	7.53
2	7	1.219	0.42	0.2	0.2	7.53
3	11	1.219	0.45	0.2	0.2	8.82
4	45	1.219	0.38	0.0	0.4	11.95
5	kriged	1.219	0.46	0.2	0.2	N/A
6*	facies-averaged	1.219	N/A	N/A	N/A	N/A

*Single relative-permeability and capillary-pressure curves.

Fluid properties:

Oil viscosity	1.000 cP
Water viscosity	0.804 cP
Oil density	55 lb/ft^3
Water density	64 lb/ft^3

permeability realizations have mean continuity values that are higher than those of the conditional permeability realizations based on a 0.2-md^2 nugget (table 1). Unconditional realization 45 (fig. 18), which was selected on the basis of low continuity of relatively permeable zones, shows a smoother permeability pattern than that of a conditional permeability realization having a relatively high nugget (fig. 17). For comparison of waterflooding results, the different permeability realizations were corrected to the same mean permeability, which was equivalent to the data mean of log k = 1.219 md (table 1).

IV. WATERFLOOD SIMULATIONS OF PARASEQUENCE 1

A. Modeling Strategy

Waterflooding of the hypothetical two-dimensional reservoir was simulated by injecting water along the right boundary and producing along the left boundary. Injection and production were controlled by prescribed pressure conditions of 2,450 psi and 750 psi, respectively. A series of numerical simulations was performed to evaluate different effects associated with the observed heterogeneity on production characteristics (table 1). Flow simulations incorporating the observed heterogeneity were compared with those using a mean permeability to evaluate whether the observed permeability heterogeneity could be represented by a geometric-mean permeability and to determine the possible impact of short-range permeability correlation on production characteristics.

Input data for the simulator included the stochastic permeability distributions, porosities, and relative-permeability and capillary-pressure curves. Porosity-permeability relationships established on the basis of core-plug analyses for grainstones in parasequence 1 were used to calculate porosity distributions from the stochastic permeability realizations (fig. 17). The following empirical porosity-

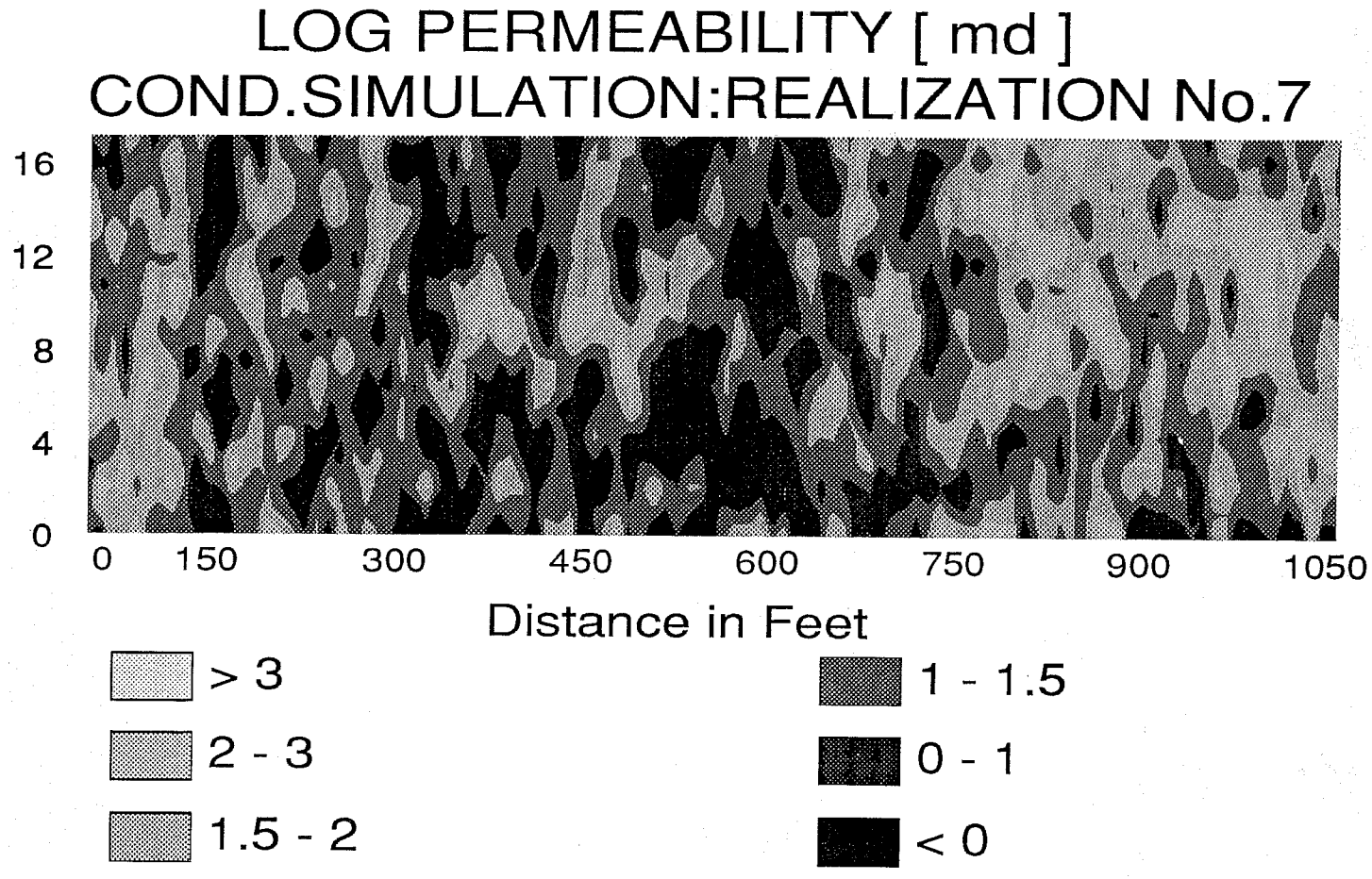

Figure 17. Conditional permeability distributions of (a) realization 7, representing lower continuity, and (b) realization 11, representing higher continuity of high-permeability zones.

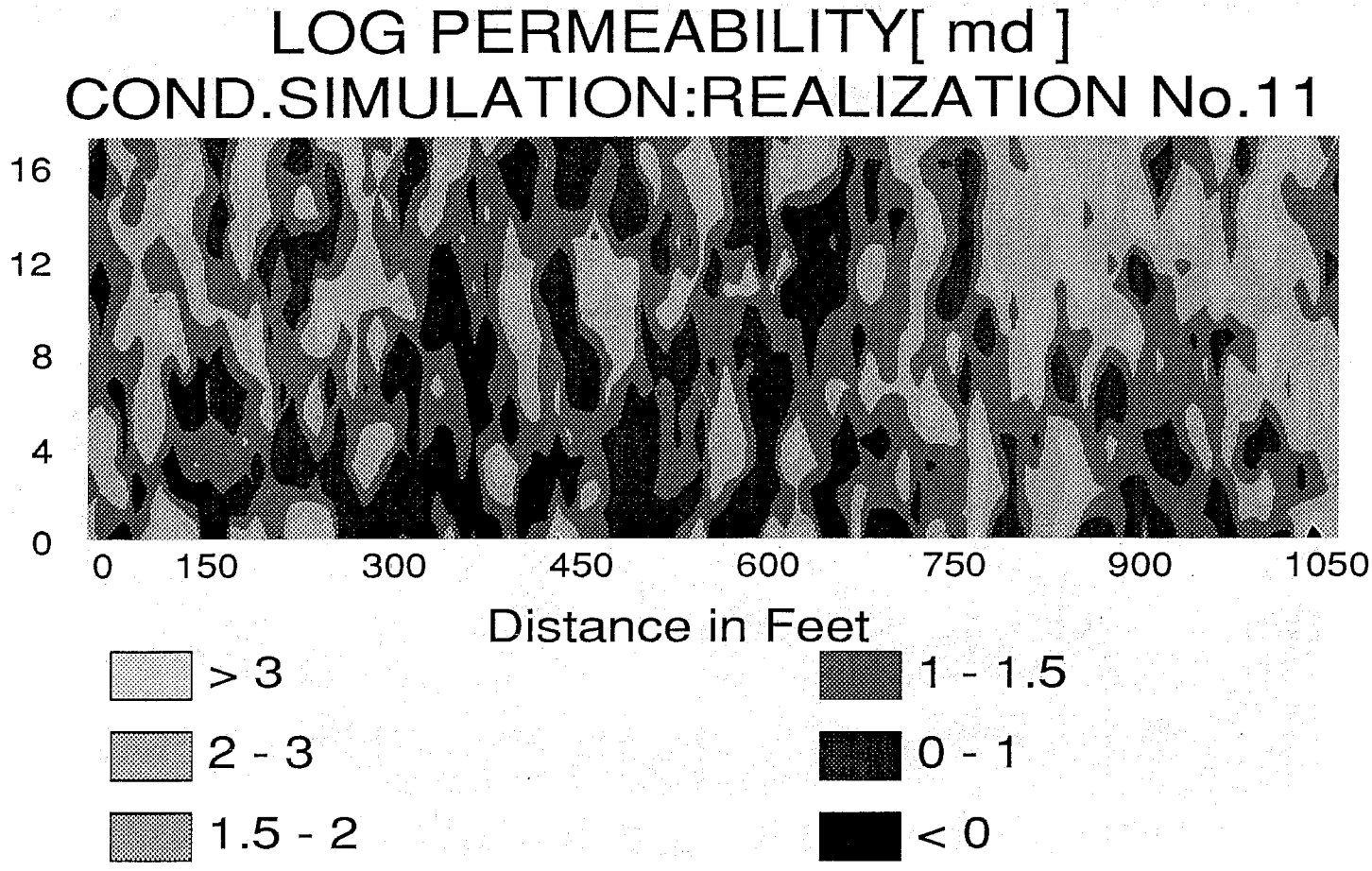
LOG PERMEABILITY[md]
COND.SIMULATION:REALIZATION No.11
16
12
8
4
0
0
150
300
450
600
750
900
1050
Distance in Feet
> 3
2 - 3
1.5 - 2
1 - 1.5
0 - 1
< 0

Figure 17b

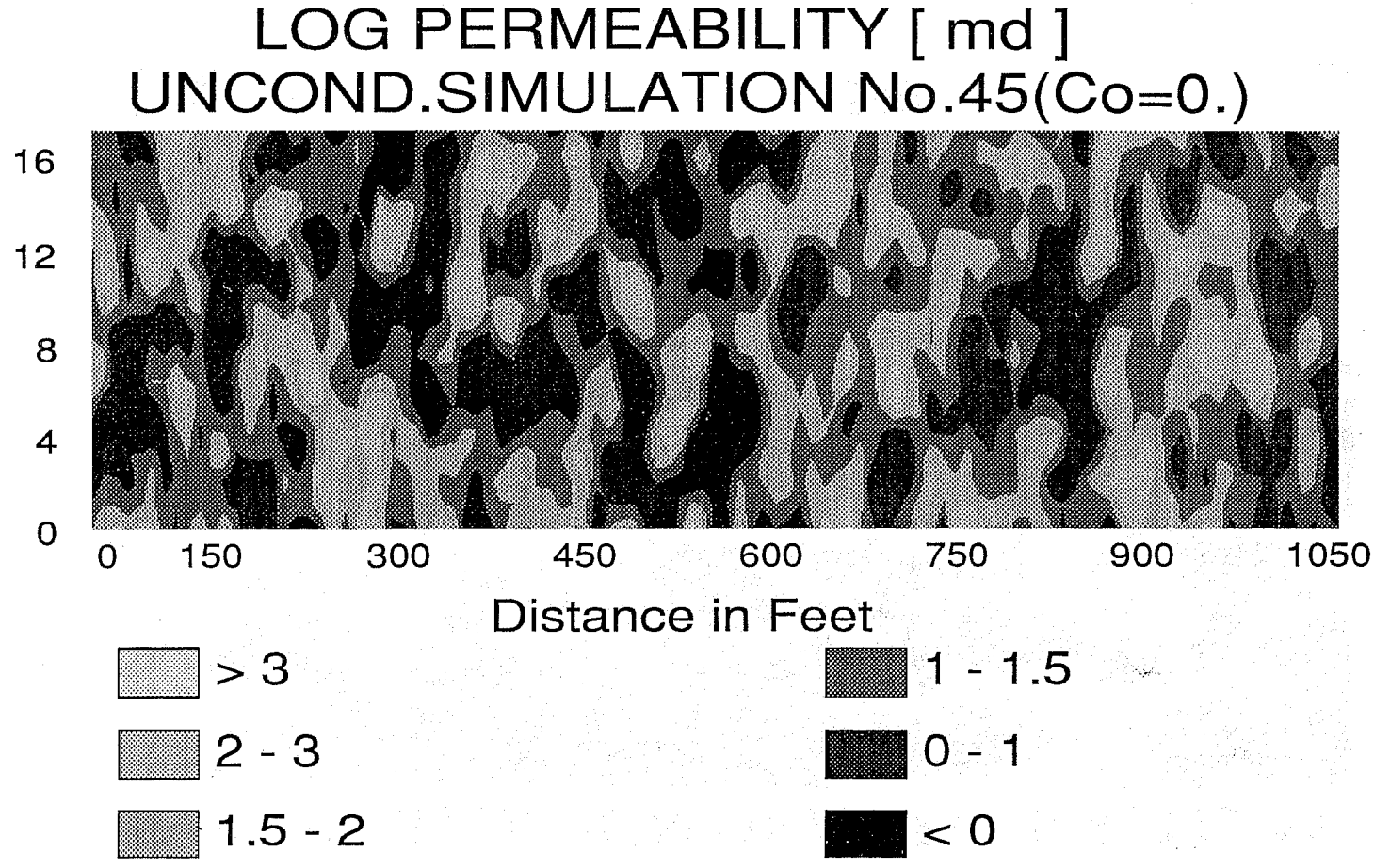

Figure 18. Unconditional permeability distribution of realization 45, representing low continuity of high-permeability zones.

permeability relation is based on a linear transform representing intergranular pore characteristics in a grainstone:

$$k = (5.01 \times 10^{-8})\,\phi^{8.33} \tag{1}$$

where k is intrinsic permeability (md) and ϕ is intergranular porosity (fraction). Similarly, an empirical relationship between water saturation, intergranular porosity, and capillary pressure, established for grainstones, was used to calculate capillary pressure as a function of water saturation and porosity of the grainstone facies in parasequence 1:

$$S_w = 68.581\, h^{-0.316}\, \phi^{-1.745} \tag{2}$$

where h represents capillary pressure as the height of the reservoir above the free-water level. Assuming that the hypothetical reservoir is 500 ft above the free-water level, initial water saturation as a function of porosity was computed using equation (2). Residual oil saturation was assumed to be uniform at 25 percent.

The relative-permeability functions for oil and water were determined from the following equation (Honarpour and others, 1982):

$$k_{rw} = k^0_{rw}\left(\frac{S_w - S_{wr}}{1 - S_{or} - S_{wr}}\right)^{N_w} \tag{3a}$$

$$k_{ro} = k^0_{ro}\left(\frac{1 - S_w - S_{wr}}{1 - S_{or} - S_{wr}}\right)^{N_o} \tag{3b}$$

where S_{or} and S_{wr} are the residual oil saturation and the residual water saturation, respectively. The exponents N_w and N_o were derived from fitting relative permeability data obtained from grainstone fabric of two Dune field cores. Both exponents were approximately 3 and were determined from the slope of the regression line representing the log of relative permeability versus the log of the normalized saturations in equations (3a) and (3b). Similarly, the relative-permeability endpoints k^0_{rw} and k^0_{ro} were derived from the intercepts of the log-log plots of the measured relative-permeability data versus saturation, which were 0.266 and 0.484, respectively, and correspond to residual oil saturation $S_{or} = 0.25$ and residual water saturation $S_{wr} = 0.1$, respectively.

Porosities derived from the different permeability realizations through the permeability-porosity transform in equation (1) typically range between 5 and 25 percent. Four relative-permeability and capillary-pressure curves representative of four porosity intervals were used: 5 to 10 percent, 10 to 15 percent, 15 to 20 percent, and 20 to 25 percent. For these porosity intervals, residual water saturations calculated from equation (2) were used to compute the relative-permeability curves according to equation (3). For simulations 1 and 4, only one relative-permeability curve and one capillary-pressure curve were used, based on the arithmetic average of porosity of realization 7. The relative-permeability and

capillary-pressure curves used in the different flow simulations are shown in figures 19 and 20, respectively.

Six numerical simulations were run (table 1), including (1) conditional permeability realization 7 (fig. 17a), representing low continuity of permeable zones and using a single relative-permeability and a single capillary-pressure curve based on the arithmetic mean of porosity; (2) conditional permeability realization 7, incorporating four porosity-dependent relative-permeability and capillary-pressure curves; (3) conditional permeability realization 11 (fig. 17b), representing high continuity of permeable zones; (4) unconditional permeability realization 45 (fig. 18), representing low continuity of permeable zones assuming zero nugget; (5) kriged permeability distribution (fig. 16), incorporating porosity-dependent relative-permeability and capillary-pressure relationships, and (6) uniform permeability distribution based on the geometric mean of measured permeability.

Computed water saturations of all simulations exhibited relatively sharp and vertical injection fronts despite the large variations in permeability, initial saturations, and capillary pressures in some simulations (table 1).

B. Simulation Results

Initial water saturation in simulation 1 (fig. 21) is uniform calculated from equation (2), using the arithmetic mean of porosity and assuming a reservoir height above the free-water level of 500 ft. Initial water saturation in simulation 2 is also calculated from equation (2), but by using variable porosity values. This results in the uneven initial saturation distribution to the left of the water-injection front (fig. 22). Water saturations in the flooded zones are dependent upon capillary pressure as well as relative and absolute permeability. In simulation 1 (fig. 21) a single capillary-pressure curve and a single relative-permeability curve (figs. 19 and 20) were used, resulting in a much smoother saturation distribution than in simulation 2 (fig. 22). Despite the relatively heterogeneous permeability distribution, the water-injection front in both simulations is relatively sharp and approximately vertical.

Production characteristics of all six simulations are shown in figures 23 through 25. Each production curve for the different permeability realizations is characterized by an initial peak, followed by a gentle decline and then a rapid decline. The rapid decline represents the relatively sharp breakthrough of the water-injection front (fig. 23). Water breakthrough is dependent on the mean continuity of permeable zones in the stochastic permeability realizations. Water breakthrough in realization 11, representing high continuity of permeable zones, occurs earlier than that in realization 7, representing low continuity of permeable zones. Although unconditional realization 45 represents low continuity of permeable zones, its mean horizontal continuity of 11.95 ft based on a zero nugget is higher than that in realization 11, which represents high continuity of permeable zones but has a nugget of 0.2 md^2 (table 1). Higher continuity of relatively permeable zones results in higher interconnection of these zones and thus produces higher effective permeability than do permeability realizations characterized by low continuity (Fogg, 1989). As a result, unconditional permeability realization 45 shows the earliest water breakthrough because of the overall higher effective permeability. Also, the production curve of unconditional realization 45 illustrates the highest

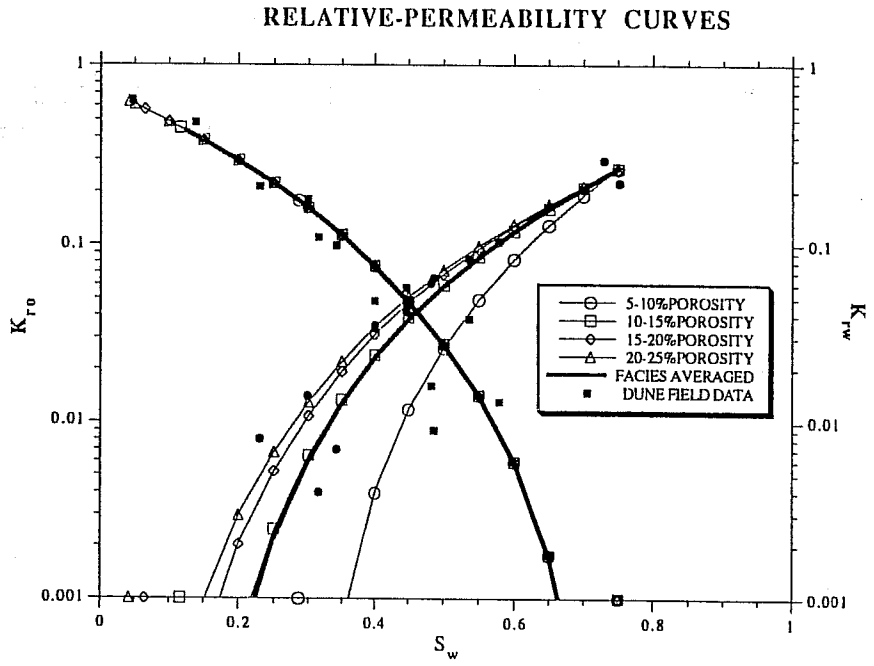

Figure 19. Relative-permeability curves used for the different waterflood simulations in parasequence 1.

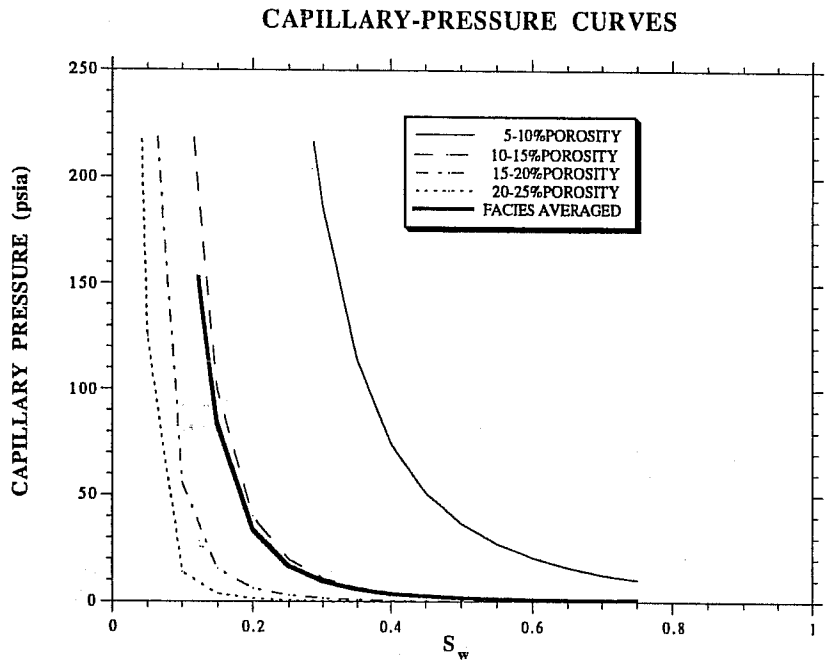

Figure 20. Capillary-pressure curves used for the different waterflood simulations in parasequence 1.

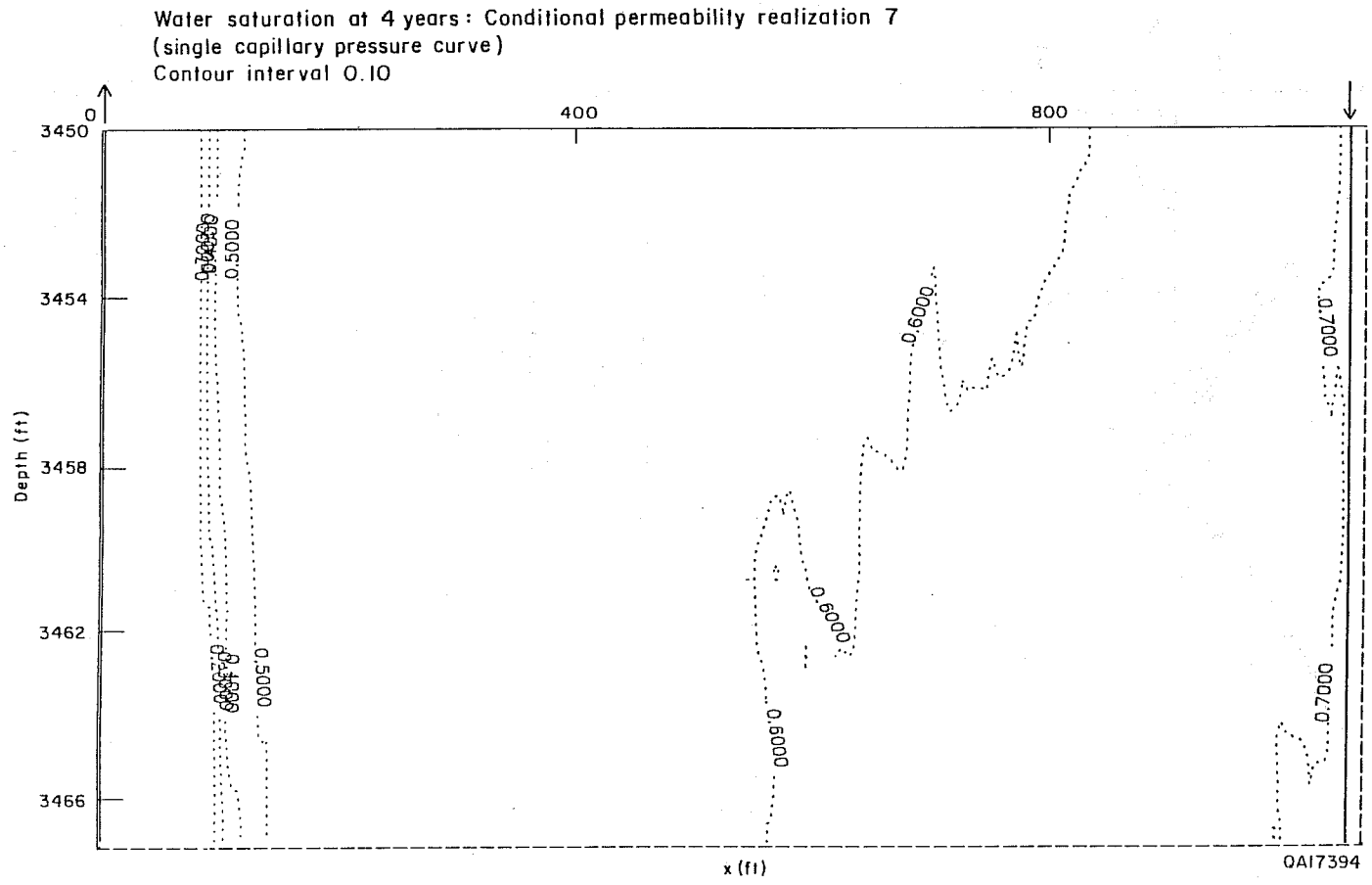

Figure 21. Computed water saturations for simulation 1 after injecting water for 4 yr, incorporating the permeability realization 7 (with uniform initial saturation and single relative-permeability and capillary-pressure curves based on arithmetic-mean porosity).

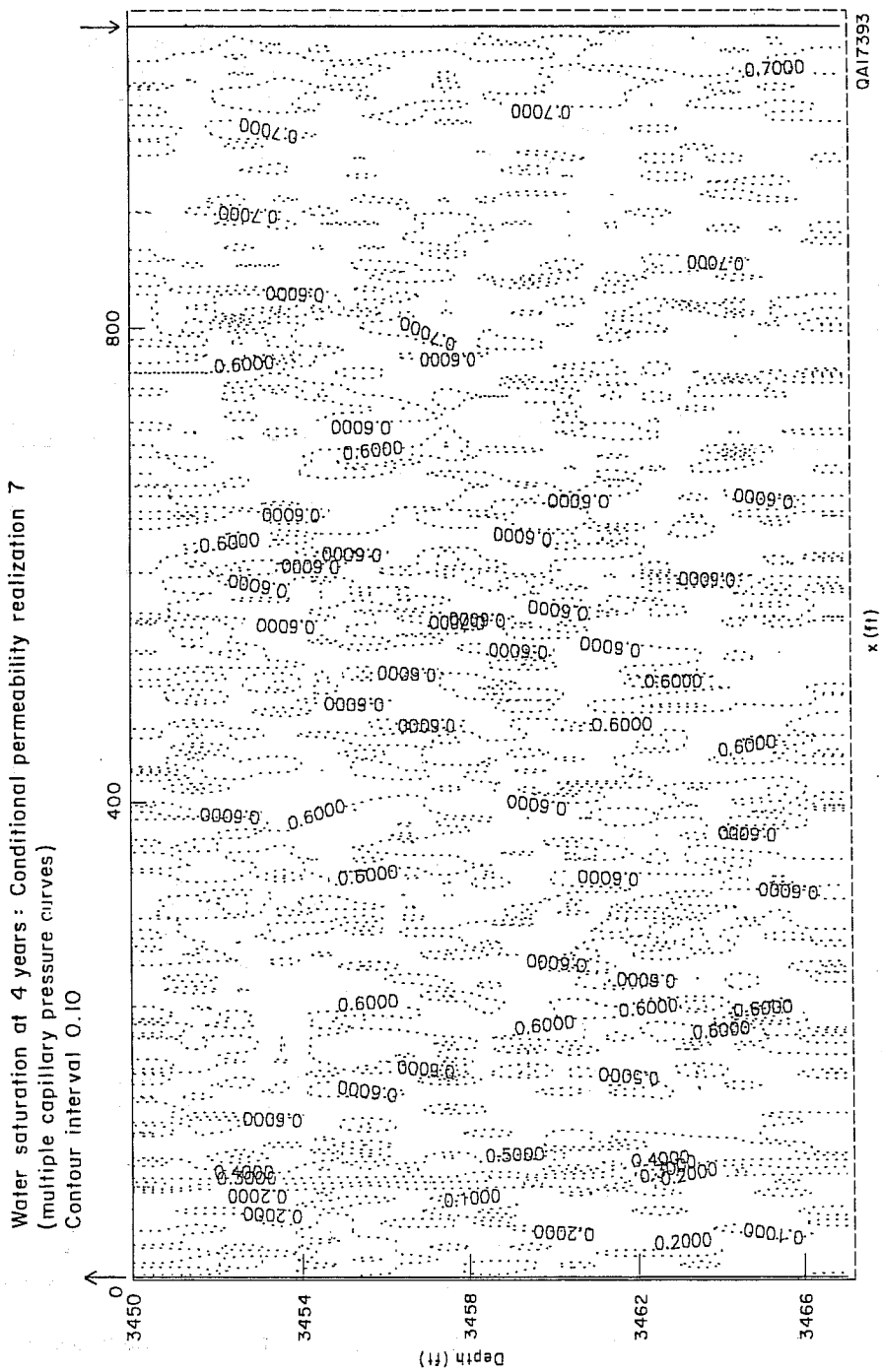

Figure 22. Computed water saturations for simulation 2 after injecting water for 4 yr, incorporating the permeability realization 7 (with relative-permeability curves and capillary-pressure curves dependent on porosity).

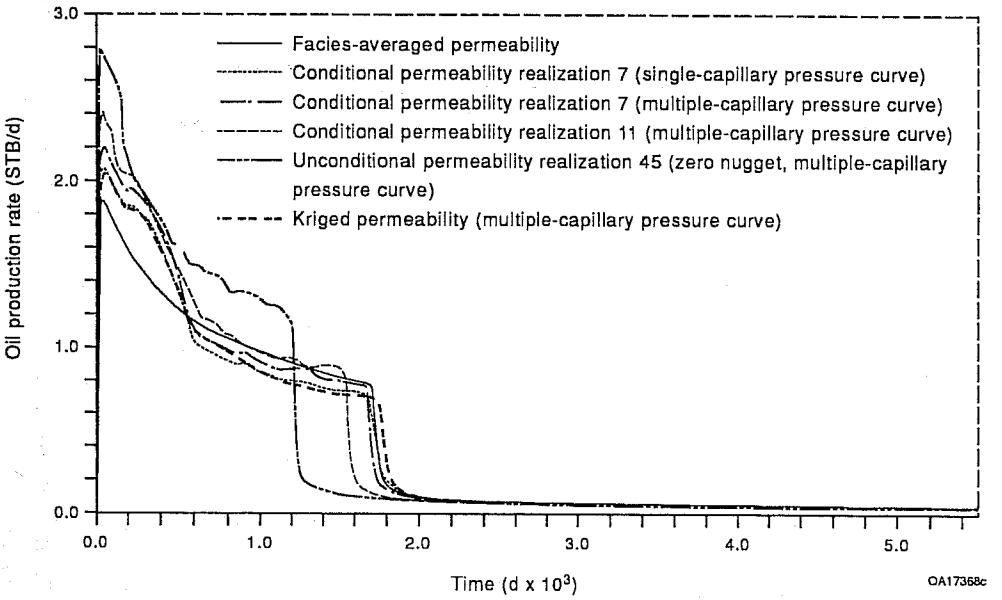

Figure 23. Oil-production rate versus time for waterflood simulations in parasequence 1.

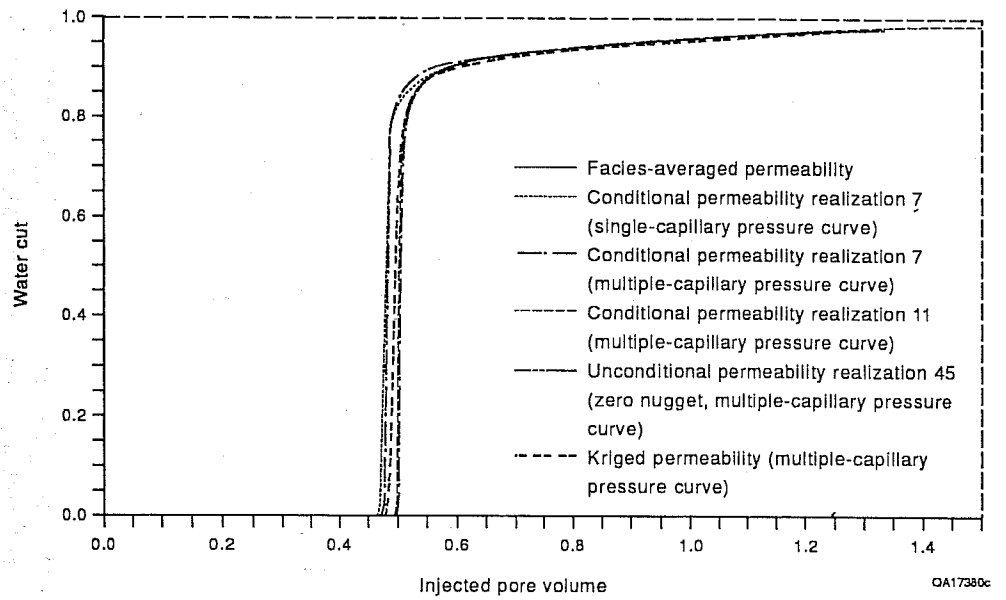

Figure 24. Water-oil ratio versus injected pore volumes for waterflood simulations in parasequence 1.

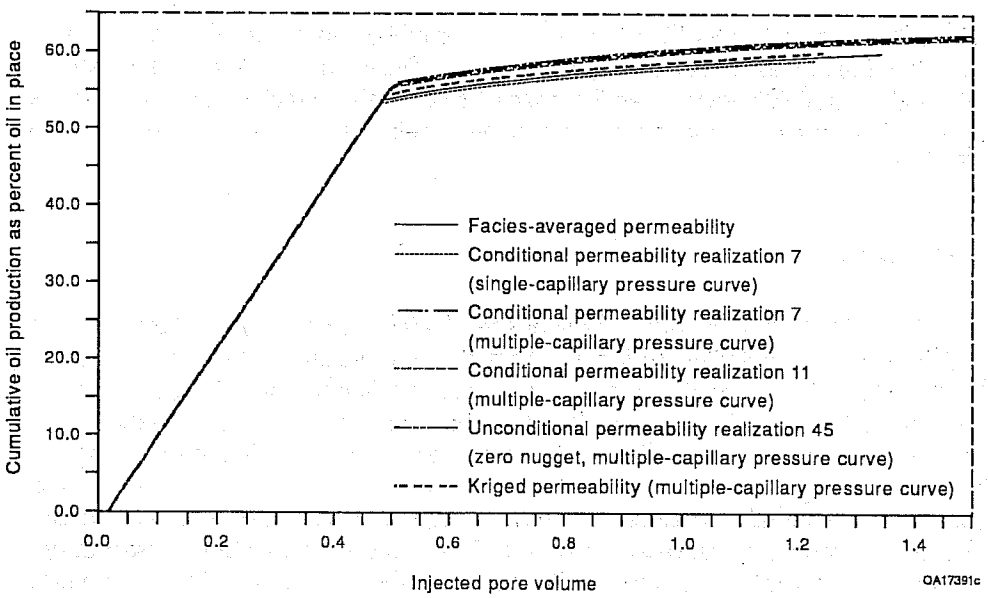

Figure 25. Cumulative oil production as percentage of original oil in place for waterflood simulations in parasequence 1.

initial production rate but a subsequently steeper decline than production curves from the conditional permeability realizations (fig. 23). As with the water breakthrough, the initial production peaks of the stochastic permeability realizations are also dependent on the mean horizontal continuity.

The kriged permeability distribution shows a production curve similar to that of the conditional permeability realizations. This suggests that the larger scale permeability variation (fig. 16) controls the overall production characteristics and that the small-scale permeability variations incorporated into the stochastic permeability realizations have little importance (figs. 17 and 18). In comparison, the facies-averaged permeability distribution, which has no spatial permeability variation, indicates a smooth, approximately exponential production decline before the water breakthrough, which occurs at approximately the same time as that in the kriged and conditional permeability realizations.

Plotting water cut against injected pore volume shows nearly identical curves for the stochastic permeability realizations, incorporating porosity-dependent capillary-pressure curves (fig. 24). Simulation 1 with permeability realization 7, incorporating a single capillary-pressure curve based on an arithmetic-mean porosity, and simulation 6 with the facies-averaged permeability distribution, incorporating a single capillary-pressure curve, show earlier water-breakthrough curves than those of the stochastic permeability realizations, incorporating porosity-dependent capillary-pressure curves (fig. 24). In comparison, the kriged permeability distribution falls between the two groups (fig. 24).

The sweep efficiency is improved using porosity-dependent capillary pressures, as indicated by the cumulative oil production as percent total oil in place (fig. 25). The waterflood simulations incorporating multiple capillary-pressure and relative-permeability curves (simulations 2 to 5) indicate higher sweep efficiency than those

with single capillary-pressure and relative-permeability curves (simulations 1 and 6). Note that the sweep efficiency in simulation 5, representing the kriged permeability distribution, is slightly lower than the stochastic permeability realizations (simulations 2 to 4), indicating that the small-scale heterogeneity causes an increase in sweep efficiency.

C. Discussion

The effect of small-scale heterogeneity and associated capillary-pressure phenomena on cumulative production characteristics is relatively small and accounts for less than a 2.5 percent increase in sweep efficiency (fig. 25). For practical purposes, the observed heterogeneity within the grainstone facies in parasequence 1 can be represented by a geometric-mean permeability distribution using an arithmetic-mean porosity for calculating uniform initial water saturation and concomitant capillary pressure according to equation (2). However, production-rate history cannot be represented by a facies-averaged permeability distribution. The kriged permeability distribution (fig. 16) yields the same production-rate pattern as the conditional permeability realizations (fig. 23), indicating that small-scale permeability variability has a negligible effect on the production rate and only the large-scale permeability patterns need to be incorporated into the flow model for history matching.

Most hydrocarbon reservoirs typically consist of several different facies or rock-fabric units. The detailed geologic framework of the entire upper San Andres outcrop at Lawyer Canyon (fig. 2) is more typical of the complexity of subsurface reservoirs in a ramp-crest depositional environment than is parasequence 1 alone. One might expect that the production characteristics of this reservoir, composed of nine parasequences separated by discontinuous, tight mudstone layers, are more dependent on the spatial relationship of the different facies and flow barriers than on the permeability pattern within individual facies if significant heterogeneity does not occur within the facies. The above flow simulations indicate that even though permeability heterogeneity within individual facies exhibits some short-range correlation, it can be represented by a geometric-mean permeability distribution that, overall, yields the same cumulative production characteristics as those incorporating the observed permeability variability. To study the effects of larger scale features associated with the spatial distribution of different rock-fabric units on reservoir-flow behavior, waterflood simulations of the entire Lawyer Canyon outcrop model (fig. 2) were performed.

V. RESERVOIR-FLOW CHARACTERIZATION, LAWYER CANYON OUTCROP

A. Conceptualization of the Outcrop Reservoir-Flow Model

The geologic model of the Lawyer Canyon parasequence window (fig. 2), in conjunction with the rock-fabric characterization of the depositional facies (fig. 9), is the basis of the conceptual reservoir-flow model. Initial saturations for the different

flow units were calculated using the porosity-saturation transforms for the three rock-fabric classes (fig. 8) and average porosities. It was assumed that the grainstones in parasequence 7, characterized by variable amounts of separate-vug porosity, have the same porosity-saturation relationship as the nonvuggy grainstones in parasequences 1, 2, 3, and 9 (fig. 9). The effect of vuggy porosity was accounted for by assigning a higher residual oil saturation to the grainstones in parasequence 7.

The constructed reservoir flow model distinguishes 11 flow units that have different average permeability, porosity, initial water saturation, and residual oil saturation (table 2). The flow model is discretized in 4,089 irregularly shaped grid blocks, representing the spatial distribution and the petrophysical properties of the different rock fabrics and depositional facies (table 2). Reservoir block sizes are 100 ft in the horizontal direction and have variable thickness in the vertical direction, ranging from less than 0.5 ft to several feet. The constructed reservoir model incorporates the general geometry and the spatial distribution of the different facies mapped in the outcrop, as shown by the distribution of initial water saturation of the discretized flow units (fig. 26).

Relative permeabilities for the different flow units are based on the shapes of relative-permeability curves derived from fitting relative-permeability data obtained from cores in the Dune field, West Texas. Similar to the relative-permeability curves in figure 19, the fitted curves were adjusted to the computed initial water saturations and to the residual oil saturations of the different flow units (table 2). Although the shape of the relative-permeability curves was obtained by fitting relative-permeability measurements from grainstone cores from the Dune field reservoir, West Texas (fig. 19), the same curve shapes were used in this study not only for the grainstone rock fabrics but also for the grain-dominated packstone and mudstone/wackestone rock fabrics. Only the relative-permeability endpoints were adjusted according to the computed initial water saturations and assumed residual oil saturations. Further investigations are in progress to characterize relative permeability within a rock-fabric/petrophysical approach.

Capillary-pressure curves were calculated on the basis of average porosities and rock-fabric classifications of the different flow units. In addition to the porosity-dependent saturation–capillary-pressure relationship for grainstones (eq. 2), the following relationships are used for the other two rock-fabric classes:

$$\text{Grain-dominated packstone} \qquad S_w = 106.524\, h^{-0.407}\, \phi^{-1.440} \tag{4}$$

$$\text{Mudstone-wackestone} \qquad S_w = 161.023\, h^{-0.505}\, \phi^{-1.2104} \tag{5}$$

where h is the height of the reservoir above the free-water level (ft) and ϕ is the porosity.

In a series of waterflood simulations, various factors affecting reservoir-flow behavior were examined (table 3) using the ECLIPSE reservoir simulator. Simulation EC-A represents the base scenario, which is used to describe waterflooding in this hypothetical reservoir. Production characteristics of simulation EC-A were compared with those from other simulations to evaluate effects of capillary pressures (simulation EC-B), model conceptualization (simulations EC-N and EC-DP), and different injection practices (simulations EC-R and EC-F).

Table 2. Properties of rock-fabric flow units for Lawyer Canyon outcrop reservoir model.

Flow units	Rock fabric	Depositional facies	Porosity (arithm. average)	Permeability (geometric average, md)	Initial water saturation	Residual oil saturation
1	Mudstone	Flooded shelf Tidal flat	0.04	0.01	0.9	0.01
2	Wackestone	Shallow shelf I	0.105	0.30	0.405	0.4
3	Grain-domin. packstone	Shallow shelf I	0.085	4.50	0.214	0.35
4	Grain-domin. packstone	Shallow shelf II Bar top	0.129	1.80	0.40	0.35
5	Grain-domin. packstone	Shallow shelf II	0.118	5.30	0.243	0.35
6	Grainstone (moldic)	Shallow shelf II	0.145	0.7	0.091	0.40
7	Grainstone (moldic)	Shallow shelf I Shallow shelf II Bar crest Bar top	0.159	2.2	0.077	0.40
8	Grainstone (highly moldic)	Shallow shelf II Bar crest Bar-accretion sets	0.23	2.5	0.041	0.40
9	Grainstone	Bar flank	0.095	9.5	0.189	0.35
10	Grainstone	Bar crest Bar-accretion sets	0.11	21.3	0.147	0.25
11	Grainstone	Bar crest	0.135	44.0	0.103	0.25

Fluid properties:

Oil viscosity	1.000 cP
Water viscosity	0.804 cP
Oil density	55 lb/ft^3
Water density	64 lb/ft^3

B. Simulation Results

Waterflooding of the hypothetical Lawyer Canyon outcrop reservoir was simulated by injecting water through a fully penetrating well along the right side of the model and by producing from a well at the left side (fig. 26) The injection and production rates were controlled by prescribed pressures of 4,350 psi and 750 psi, respectively.

The change in computed water saturation for simulation EC-A after water injection of 20 yr (fig. 27a), 40 yr (fig. 27b), and 60 yr (fig. 27c) demonstrates that the high-permeability grainstone rock-fabric units in parasequences 1, 2, and 9 are preferentially flooded. Furthermore, flooding is controlled by the relatively tight mudstone units separating most of the parasequences. The grainstone facies in parasequences 7 and 8 are characterized by somewhat lower permeabilities and

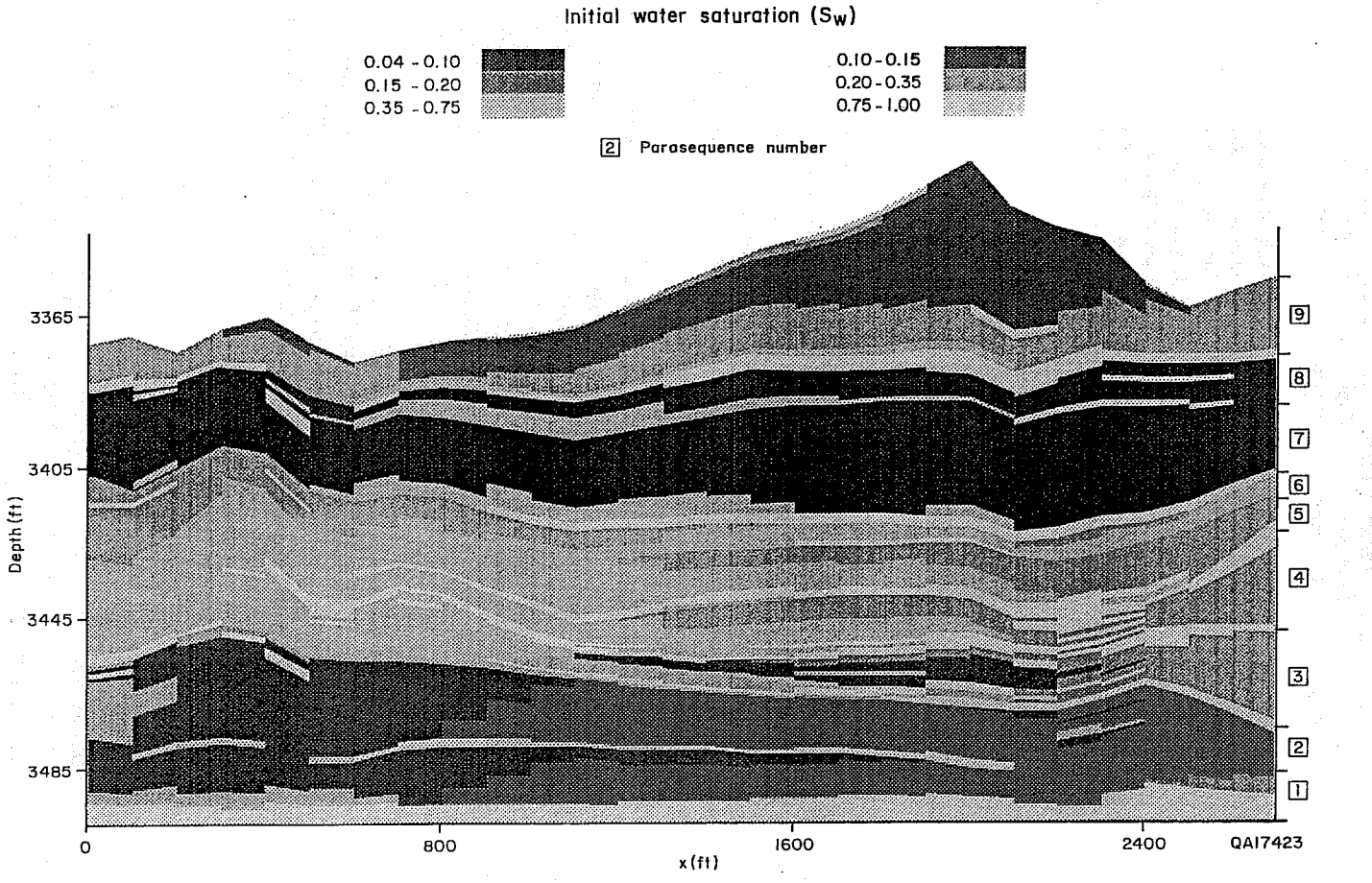

Figure 26. Initial water saturation of the flow units of the outcrop model.

Table 3. Waterflood simulations of the Lawyer Canyon outcrop model.

Sim. no.	Model scenario: Grid	Production well location	Capillary pressure	Permeability data
EC-A	Irregular	Right	Yes	Facies-averaged
EC-B	Irregular	Right	No	Facies-averaged
EC-N	Normalized	Right	Yes	Facies-averaged
EC-DP	Normalized	Right	Single	Linear interpol. between wells
EC-R	Irregular	Left	Yes	Facies-averaged
EC-F	Irregular	Middle	Yes	Facies-averaged

Fluid properties:

Oil viscosity	1.000 cP
Water viscosity	0.804 cP
Oil density	55 lb/ft^3
Water density	64 lb/ft^3

higher porosities than those in parasequences 1, 2, and 9, owing to vuggy pore structure (table 2); consequently, the water-injection front does not advance as far as that in parasequence 9 (fig. 27). However, the water-injection front in parasequences 3 through 6 appears to have advanced farther than that in parasequences 7 and 8, although the permeability of the predominantly wackestone rock fabrics in parasequences 3 through 6 is lower than that of the moldic grainstone rock fabrics in parasequence 7.

In the upper left of the model, the change in computed water saturation after 40 and 60 yr indicates cross flow of water from parasequence 9 into parasequence 7, thereby bypassing the injection front within parasequences 7 and 8. As a result, an area of unswept, mobile oil develops in the right part of the model, as shown by the computed water saturation distribution after 60 yr of waterflooding (fig. 28). Although the mudstone layers, representing the parasequence boundaries, are continuous in this area and permeability at 0.01 md is assumed to be very low, cross flow occurs (fig. 27).

The production characteristics of simulation EC-A and the other simulations (table 3) are shown in figure 29 (production rate), figure 30 (water cut), and figure 31 (cumulative production as percent oil in place). Comparison of the production characteristics of the different simulations were used to evaluate various factors affecting reservoir-flow behavior.

1. Effect of Capillary Pressure

In the first test, effects of capillary pressure were studied. Simulation EC-B does not incorporate capillary pressures (table 3). Production rates in simulation EC-B show a more stepwise decline with time, reflecting the flooding of the grainstone-dominated parasequences (fig. 29). Production rates are initially lower than those in simulation EC-A, which incorporates capillarity, but simulation EC-B maintains higher rates after 16,000 days. The stepwise decline in production rate is also reflected in the stepwise increase in water cut (fig. 30). Neglecting capillary

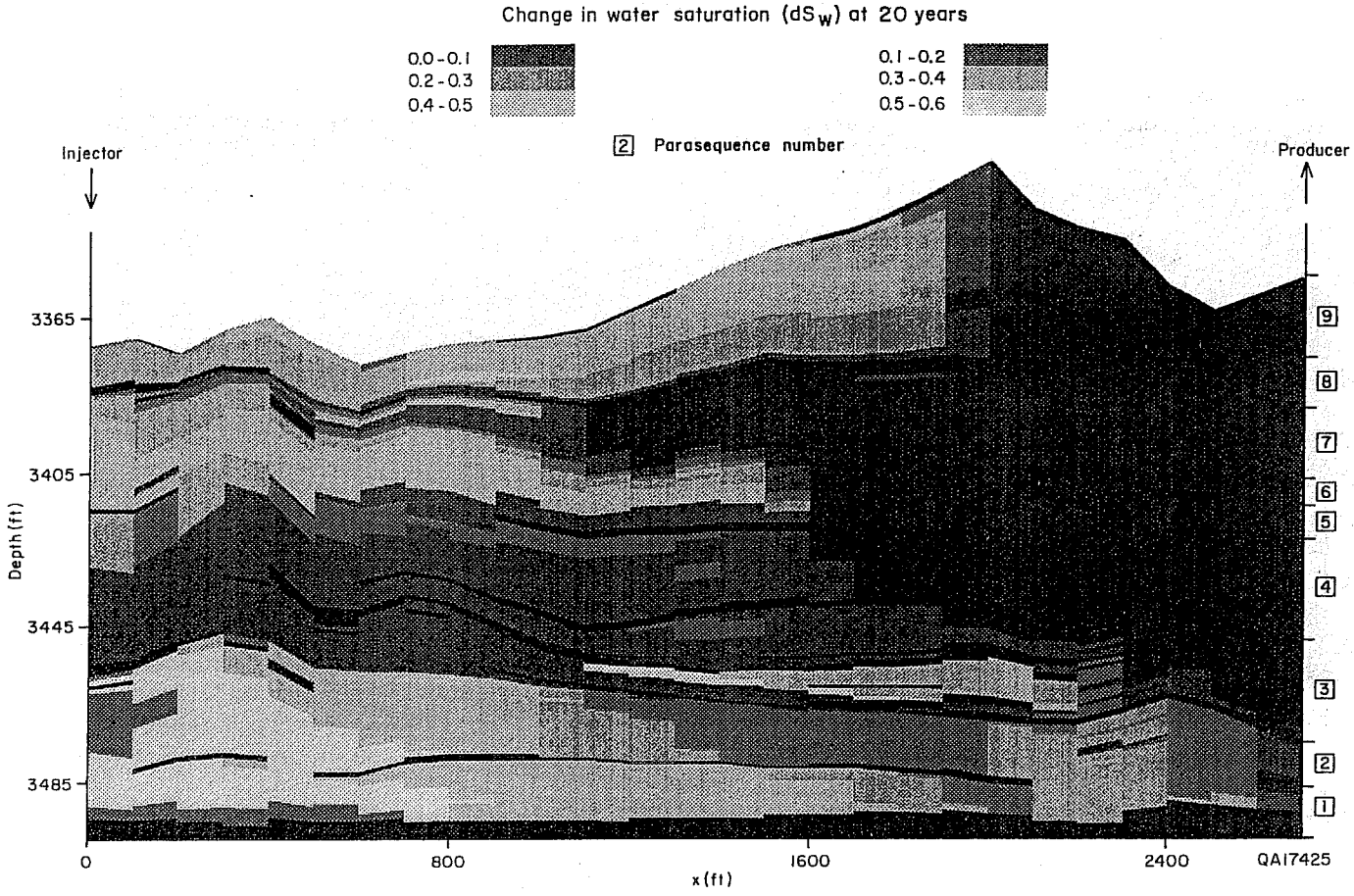

Figure 27. Computed changes in water saturation for simulation EC-A after waterflooding of (a) 20 yr, (b) 40 yr, (c) 60 yr.

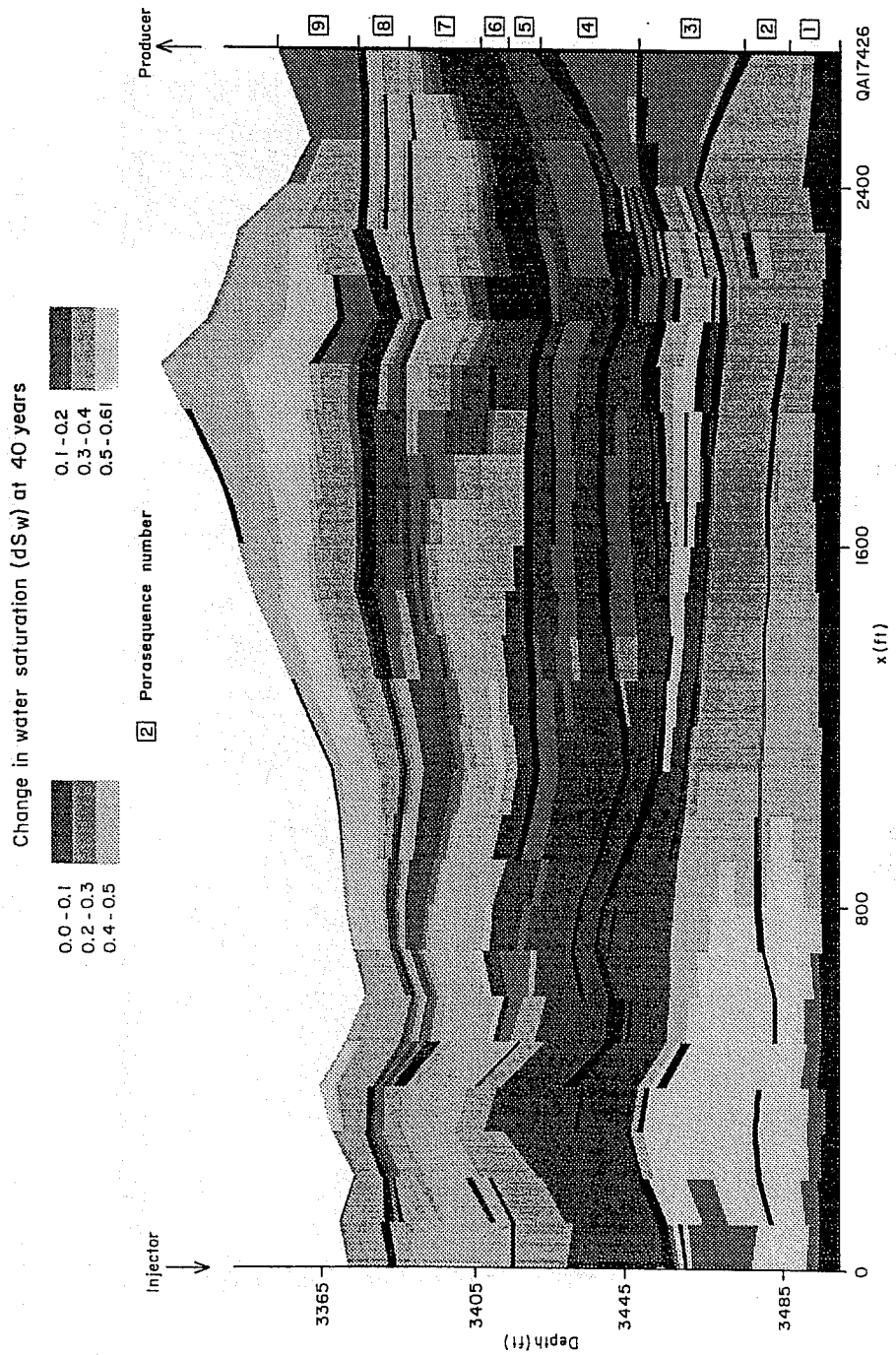
Change in water saturation (dSw) at 40 years
0.0 - 0.1
0.2 - 0.3
0.4 - 0.5
0.1 - 0.2
0.3 - 0.4
0.5 - 0.61
Parasequence number
Injector
Producer
Depth (ft)
3365
3405
3445
3485
0
800
1600
2400
x (ft)
QA17426

Figure 27b

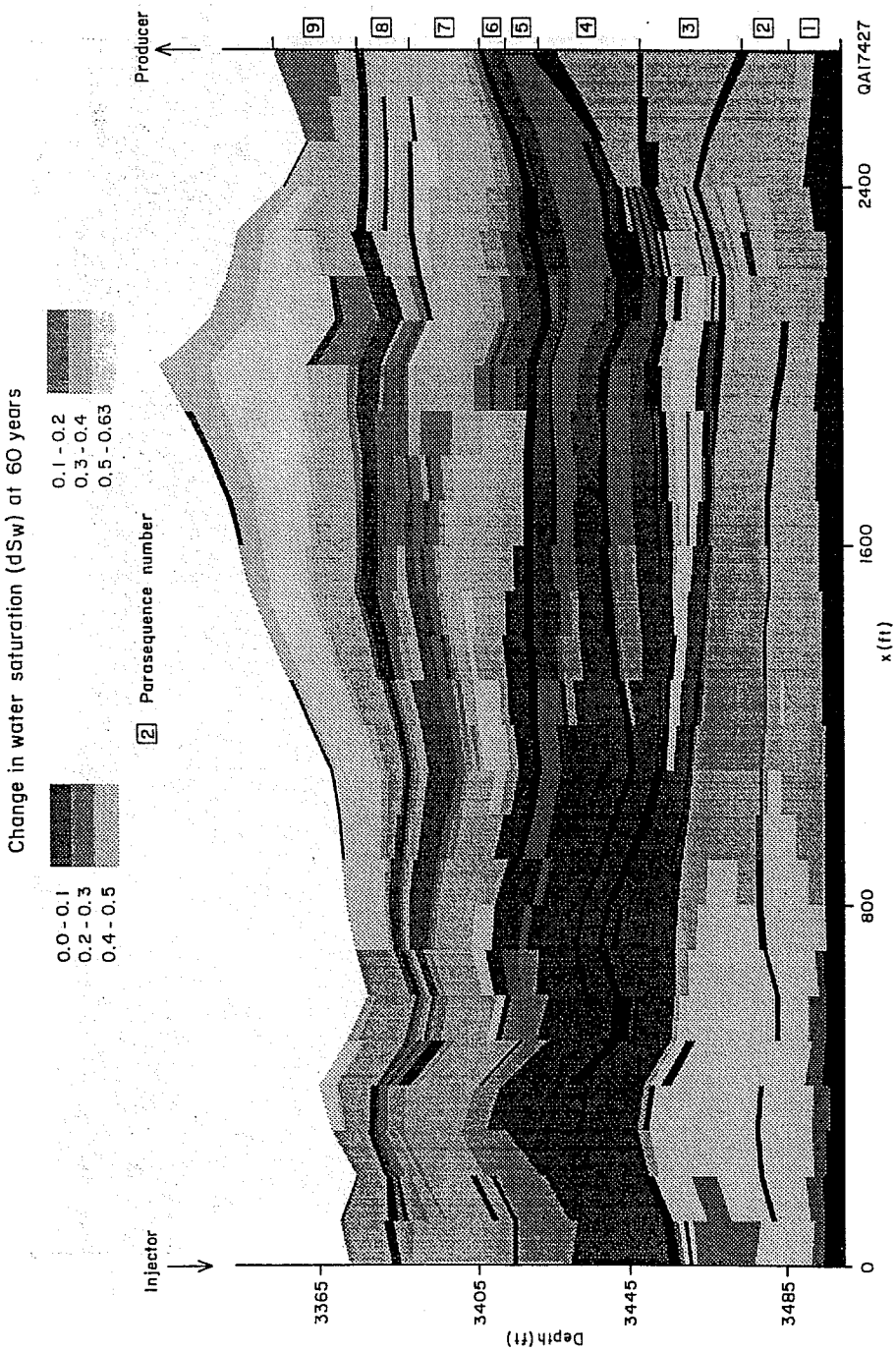
Change in water saturation (dSw) at 60 years
0.0 - 0.1
0.2 - 0.3
0.4 - 0.5
0.1 - 0.2
0.3 - 0.4
0.5 - 0.63
Injector
Producer
2 Parasequence number
9
8
7
6
5
4
3
2
1
3365
3405
3445
3485
Depth (ft)
0
800
1600
2400
x (ft)
QAI7427

Figure 27c

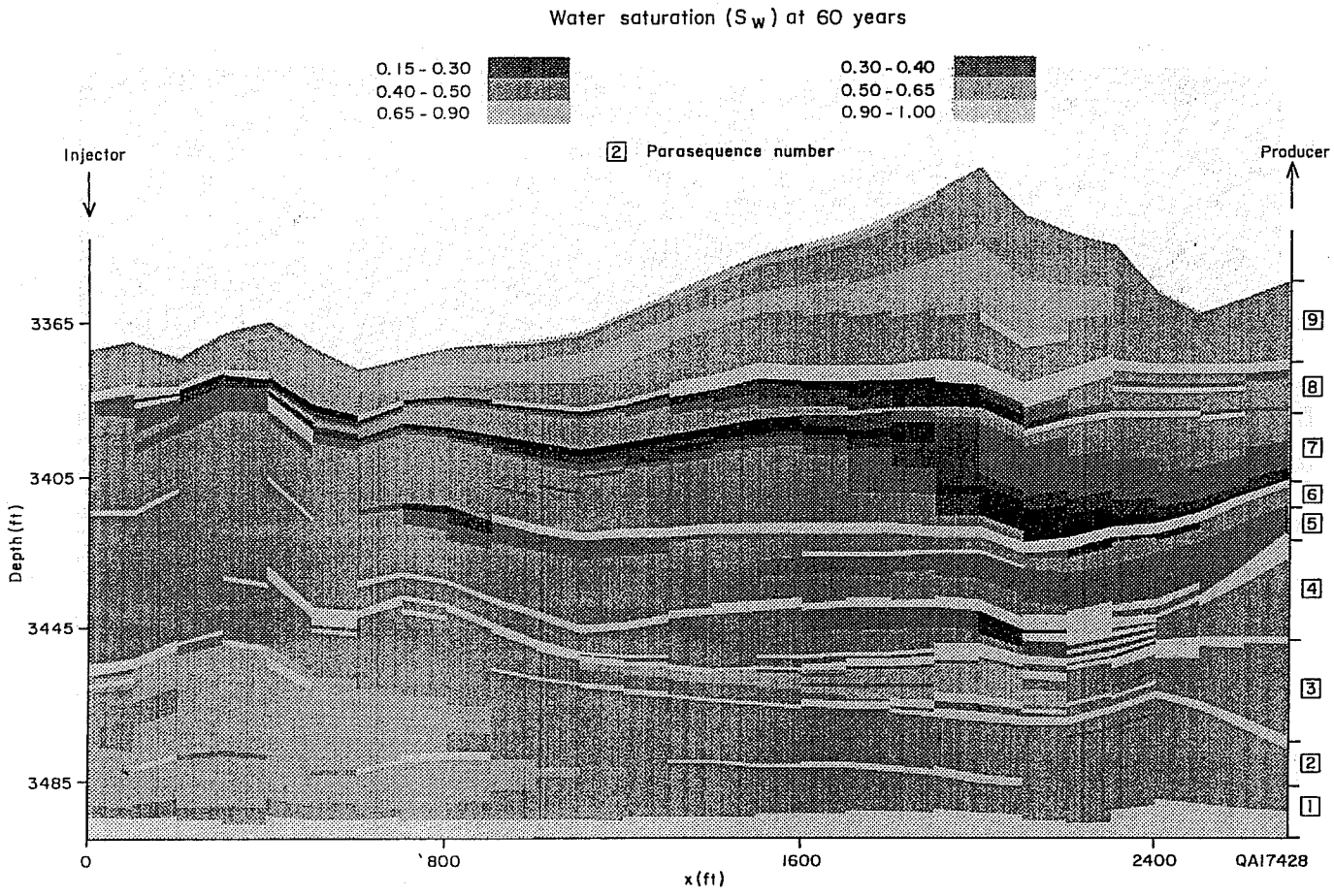

Figure 28. Computed water saturation for simulation EC-A after water injection of 60 yr.

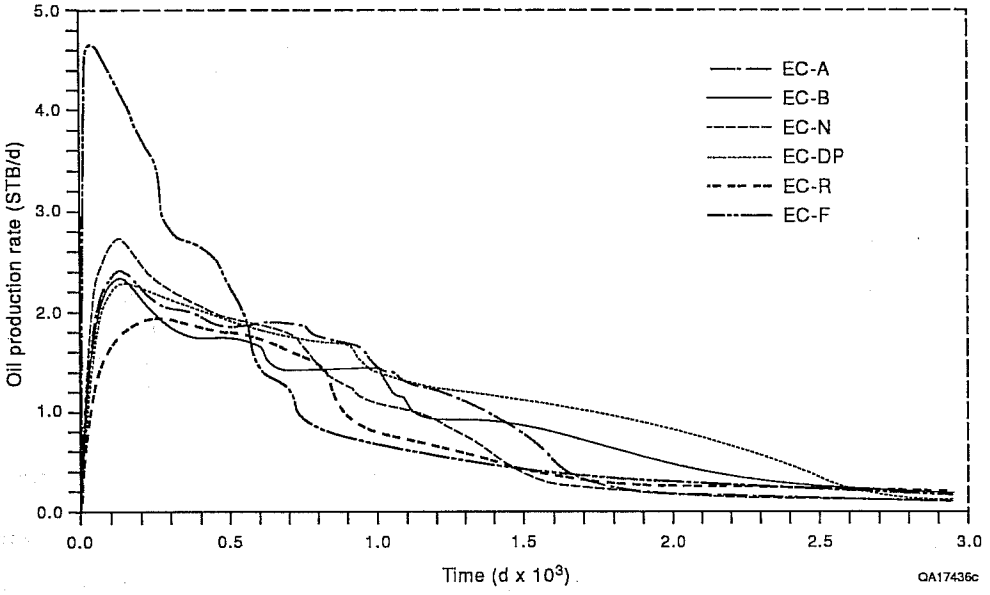

Figure 29. Oil-production rate versus time for simulations of the Lawyer Canyon outcrop model.

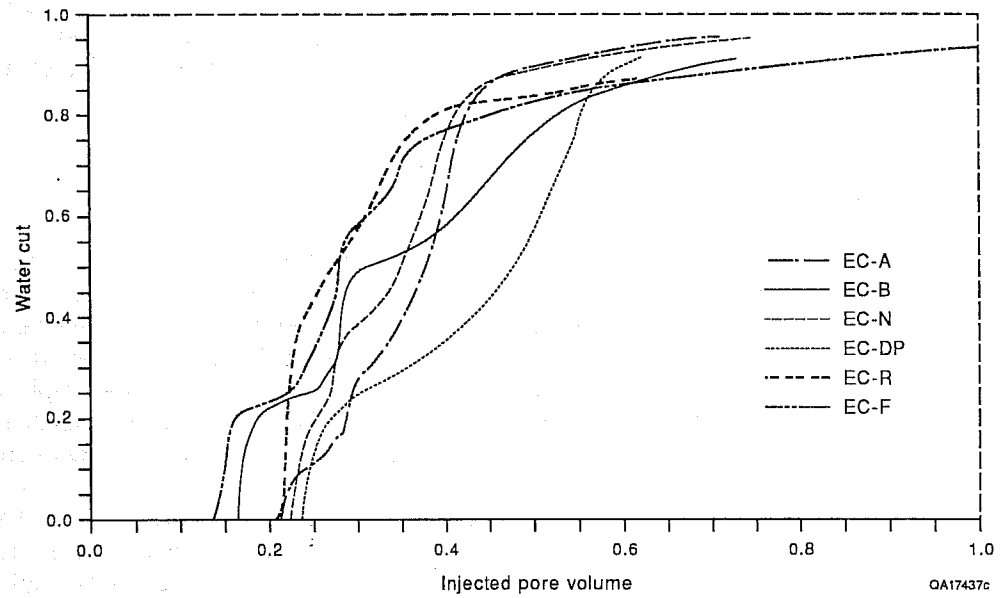

Figure 30. Water-oil ratio versus injected pore volume for simulations of the Lawyer Canyon outcrop model.

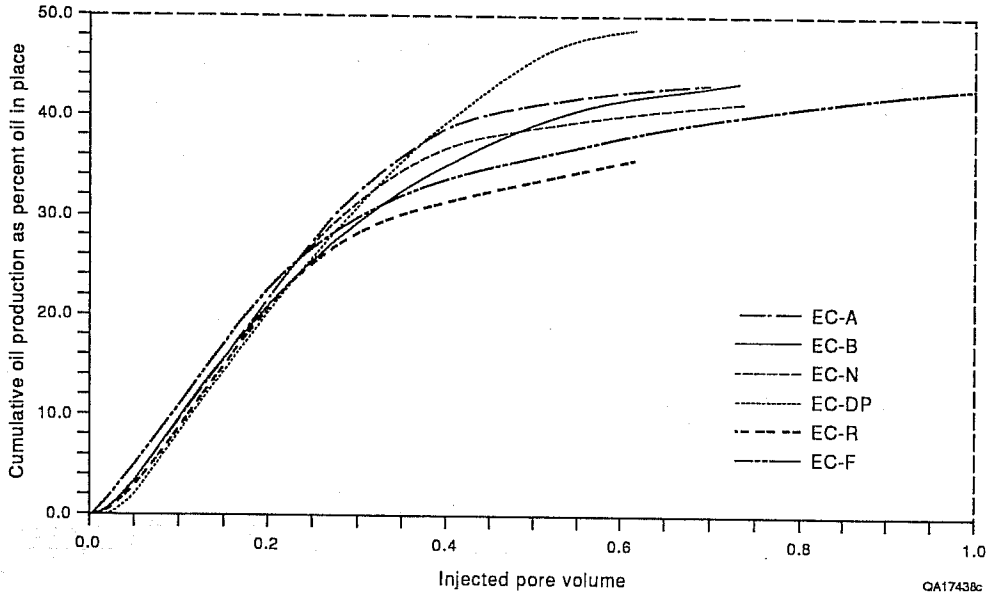

Figure 31. Cumulative oil production as percentage of original oil in place for simulations of the Lawyer Canyon outcrop model.

pressures results in a lower seep efficiency, as shown by the cumulative production curve (fig. 31). In simulation EC-A, capillary pressure improves sweep of the less permeable zones in parasequences 3 through 6, whereas in simulation EC-B, waterflooding is restricted to the more permeable grainstone facies in parasequences 1, 2, 7, and 9. Ultimate oil recovery of the two simulations, however, is the same (fig. 31).

2. Effect of Model Conceptualization

The effect of irregular formation geometry as compared with that of normalized formation geometry was evaluated in simulations EC-N and EC-DP (table 3). In simulation EC-N, the nine parasequences were normalized to a constant thickness, approximating the spatial distribution of the mapped facies (fig. 2). Production rates are initially higher than those in simulation EC-A, but they drop off more rapidly (fig. 29). The water-breakthrough curve for the normalized reservoir model (simulation EC-N) is steeper than that in simulation EC-A (fig. 30) and shows a lower recovery efficiency (fig. 31).

In simulation EC-DP, the reservoir model was constructed using the permeabilities of the individual flow units at the injection and production wells and then linearly interpolating permeability between wells using the normalized grid from simulation EC-N. This scenario represents a typical reservoir model constructed from well data, where the facies and permeability distributions of the interwell area are unknown. When using well data from only the left and right sides of the outcrop model (fig. 2), the relatively permeable grainstone facies in parasequence 9

is not incorporated into the layered model. Furthermore, only a single relative-permeability curve and a single capillary-pressure curve are used in simulation EC-DP.

Initial production rates in simulation EC-DP are similar to those in simulation EC-A but do not show the drop off after about 16,000 days (fig. 29), which is reflected in a less steep water-breakthrough curve than that in simulation EC-A (fig. 30). More importantly, sweep efficiency is overestimated in this layered model (fig. 31).

3. Effect of Injection Practice

Two additional flow scenarios were simulated to evaluate the effects of different injection schemes (table 3). In simulation EC-R, injection and production is reversed when the reservoir is flooded from the right side. Although the reservoir model and properties are the same in simulation EC-R and in EC-A, the production characteristics are noticeably different. Initial production rates in simulation EC-R are lower than those in simulation EC-A (fig. 29), but they remain slightly higher after 16,000 days. That is, at later times simulation EC-R produces at a lower water-oil ratio, which is characterized by the water-cut curve that levels out at a lower value than that of simulation EC-A (fig. 30). Sweep efficiency is significantly lower in simulation EC-R than in simulation EC-A (fig. 31), indicating that the spatial distribution of permeable grainstone facies relative to the direction of the waterflood (fig. 2) is important for the overall reservoir-flow behavior.

Comparing the change in water saturation after 40 yr of waterflooding shows a much larger area of unswept oil in the center of the model in simulation EC-R (fig. 32) than in simulation EC-A (fig. 27b). More importantly, cross flow occurs on the left side of the model toward the production well in simulation EC-R (fig. 32), from parasequence 9 all the way to parasequences 1 and 2. Although parasequences 3 through 6 are composed predominantly of less permeable wackestones on the left side of the model, which change to grain-dominated packstones on the right side, cross flow does not occur in simulation EC-A (fig. 27). On the other hand, cross flow across parasequences 3 through 6 on the left side of the model is facilitated by the fact that the tight mudstone layers are discontinuous, whereas on the right side they are continuous (fig. 2). However, the spatial distribution of the higher-permeablity grainstone facies on the left part of the model in parasequences 1 and 2 (table 2, unit 10) and in parasequence 9 (table 2, unit 11) are crucial for cross flow through parasequences 3 through 6 on the left. As indicated in simulation EC-A (fig. 28), continuous mudstone layers do not necessarily represent flow barriers, as shown by the cross flow between parasequences 9 and 7 in the upper right of the model.

In the final simulation EC-F, the production well was located in the center of the model, and an injection well was placed at either side of the model. Prescribed pressures were adjusted in order to create the same pressure gradient between the injection wells and production well as those used in the other simulations. As one would expect, initial production rates are much higher in simulation EC-F than those in the other simulations but subsequently show a much earlier and steeper decline. However, after 16,000 days, the production rate levels off at a slightly

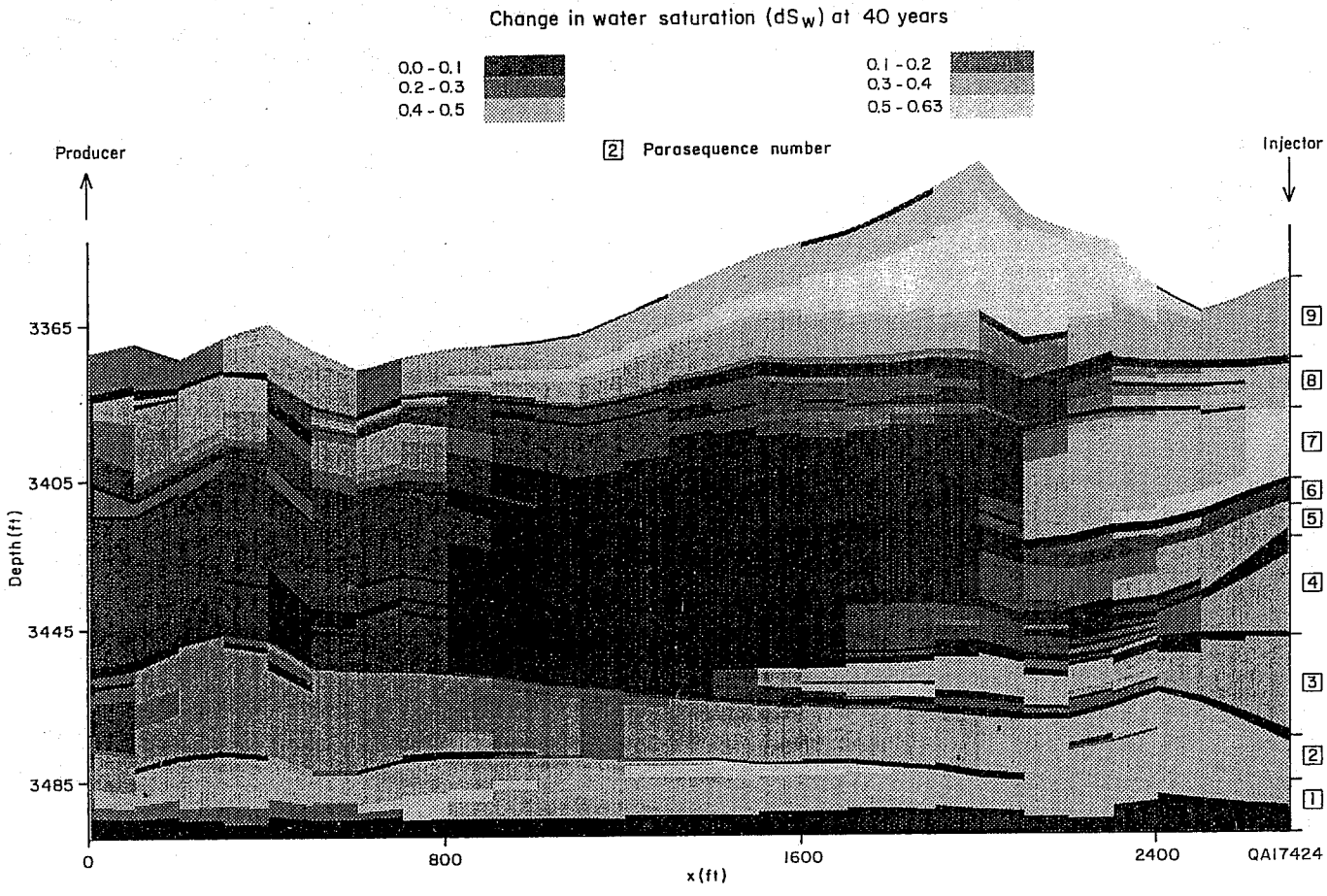

Figure 32. Computed changes in water saturation after 40 yr of waterflooding for simulation EC-R with inverse-injection pattern.

higher rate than that in simulation EC-A. Similar to the reverse-injection pattern in simulation EC-R, the water-cut curve breaks at a lower water-oil ratio than that in simulation EC-A (fig. 30). The sweep efficiency of simulation EC-F is also lower than in simulation EC-A, but slightly higher than in simulation EC-R (fig. 31).

VII. DISCUSSION

A. Implications of Outcrop Studies on Reservoir Characterization

Detailed geologic mapping of the upper San Andres Formation at the Lawyer Canyon area, Algerita Escarpment, yielded deterministic images of geologic facies architecture and corresponding porosity-permeability structure at scales ranging from a foot to tens of feet vertically and a foot to hundreds of feet laterally. The horizontal resolution of both the geologic facies mapping and the rock-property measurements allowed for detailed deterministic characterization of interwell heterogeneity. The geologic mapping within a sequence-stratigraphic framework calls for application to subsurface San Andres reservoirs in other parts of the Permian Basin, as well as to similar carbonate-ramp systems worldwide. A companion study is applying the general concepts derived from the outcrop study to the San Andres Seminole field, West Texas.

Geologic mapping revealed a series of upward-shallowing parasequences (10 to 40 ft thick and several thousand feet long). Parasequence boundaries are typically marked by tight mudstone/wackestone beds that display variable degrees of lateral continuity ranging from several hundred feet to more than 2,500 ft. Facies development within a parasequence can be highly variable. Generally, the thicker the parasequence, the more laterally variable is the resultant facies mosaic.

As documented by the flow simulations, the spatial distribution of permeable grainstone facies relative to the parasequence boundaries that show variable degrees of lateral continuity are crucial for understanding reservoir performance. Although it is difficult to extrapolate facies geometry in the interwell region in subsurface reservoirs, the outcrop study provides insight into the internal architecture of individual parasequences. Depositional processes in a ramp-crest environment produces upward-shallowing, upward-coarsening facies within a parasequence, starting with mudstone deposition associated with a rapid sea-level rise. Subsequently, carbonates are deposited as wackestone/packstone facies and finally as bar-crest and bar-flank grainstones and packstones. However, the lateral dimensions of these facies are highly variable and may not be penetrated by wells. The grainstones facies in parasequence 9 reaches a maximum thickness of 38 ft but quickly thins laterally and is completely absent at the northern and southern edges of the Lawyer Canyon parasequence window (fig. 2).

Within grainstones, permeability varies by as much as five orders of magnitude (fig. 11). Variogram analysis of spatial permeability in grainstone facies of parasequence 1 indicates short-range correlation but relatively high, locally random heterogeneity, reflected in a relatively high nugget compared with the sill (fig. 14). Similar permeability structures were obtained from the vuggy grainstone facies in parasequence 7 (fig. 9). Flow simulations indicate that the effective permeability within the grainstone facies can be represented by the geometric-mean permeability.

Note, however, that porosity-dependent capillary-pressure relationships, in combination with the small-scale heterogeneity, increase the sweep efficiency of individual facies (fig. 25). However, the effect is relatively small and will be outweighed by the sweep efficiency, which is largely controlled by injection practices and by the spatial distribution of individual facies relative to parasequence boundaries.

Reservoir-flow simulations of the entire outcrop model underscore the importance of knowing the facies architecture between wells. Although simulation EC-DP, representing the standard approach for a subsurface reservoir model by linearly interpolating properties between wells, shows initial production rates similar to those of simulation EC-A (fig. 29), the producing water-oil ratio is different. More importantly, simulation EC-DP overestimates the cumulative oil production compared with simulation A, which incorporates the detailed spatial facies distribution between wells (fig. 31).

B. Determination of Remaining Oil

The changes in computed water saturation for simulation EC-A (fig. 27) indicate an important mechanism for bypassing unswept oil through cross flow of injected water across low-permeability mudstones from parasequences 9 to 7. As a result, an area of unswept oil develops within parasequence 7 because of the slower advance of the water-injection front within parasequence 7. As shown in simulation EC-R, where the injection pattern is reversed, the cross-flow effect becomes more dominant and a greater area of unswept oil develops (fig. 32) than in simulation EC-A (fig. 27b). Comparison of production characteristics between simulation EC-A and EC-R indicates that simply changing the waterflood direction affects sweep efficiency. This implies that the spatial distribution of facies relative to the waterflood direction can significantly affect how the reservoir produces.

The simulations further document that although the parasequence boundaries, represented by mudstone/wackestone units, strongly control waterflooding, these low-permeability mudstone layers do not necessarily represent flow barriers but can allow for significant cross flow. If, and when, cross flow occurs through these mudstones depends on the spatial distribution of the high-permeability grainstone facies relative to the waterflood direction.

Oil recovery in these simulations approaches 45 percent of total oil in place (fig. 31), which is high compared with oil-recovery data of San Andres reservoirs in the Permian Basin. However, the limitations of the two-dimensionality of the outcrop reservoir model overestimate sweep efficiency (Fogg and Lucia, 1990). The two-dimensionality of the cross-sectional model forces all fluid flow into the vertical plane between the wells and thus represents only the most direct flow between the injection and production wells. In three dimensions, flow away from the injection well and toward the production well is represented by radial streamlines characterized by increasing path length away from the most direct streamline between the wells. As a result, the water-breakthrough curves (figs. 24 and 30) can be expected to be less steep in three-dimensional scenarios.

More important are the potential effects of three-dimensional heterogeneity, that is, possible circuitous flow paths perpendicular to the cross-sectional plane are not accounted for in the two-dimensional model. In addition to the effects of radial

flow paths, neglecting heterogeneity in the third dimension also tends to overestimate sweep efficiency in the cross-sectional outcrop model. On the other hand, even less distinct mechanisms for trapping unswept oil indicated in the cross-sectional model may be enhanced when considering heterogeneity in the third dimension. However, only three-dimensional simulation experiments can quantify these processes.

VII. SUMMARY

New approaches for reservoir characterization of heterogeneous carbonate-ramp deposits were presented that integrate geological, petrophysical, geostatistical, and reservoir-simulation studies of continuous outcrop of the San Andres Formation, New Mexico. Detailed geologic mapping revealed a series of upward-shallowing parasequences—10 to 40 ft thick and several thousand feet long—that form the geologic framework of the reservoir model. Parasequence boundaries, typically marked by tight mudstone/wackestone beds that display variable degrees of lateral continuity (ranging from several hundred feet to more than 2,500 ft) were shown to be important as potential flow barriers. To characterize the complex heterogeneity associated with depositional and diagenetic processes on the interwell scale, geologic and petrophysical data were collected from outcrops at the Lawyer Canyon area of the Algerita Escarpment. Detailed permeability measurements using both mini-air permeameter and core plugs were taken at different scales to characterize the spatial hierarchy of permeability patterns. Geostatistical analysis of permeability measurements indicated varying spatial correlation at different measurement scales. In all cases, however, permeability variability was characterized by substantial random heterogeneity at local scales.

Conditional simulations of permeability within individual facies showed apparent randomness owing to the large nugget effect. Waterflood simulations of conditional permeability realizations yielded results similar to those simulations using a geometric-mean permeability, indicating that the observed permeability heterogeneity within facies can be represented by a geometric mean. Mean permeabilities of most facies and rock fabrics differed significantly at the 95 percent confidence level and can be used to represent large-scale heterogeneity in reservoir-scale flow simulators.

Five basic rock-fabric units, identified in the Lawyer Canyon outcrop area, were incorporated into a geologic model describing the spatial distribution of depositional facies. Petrophysical parameters of these facies were derived on the basis of a petrophysical/rock-fabric approach using mean permeabilities, porosity, and saturation relationships characteristic of each rock fabric. Two-dimensional waterflood simulations were performed for the outcrop model to evaluate various factors affecting reservoir-flow behavior. The results indicated that the spatial distribution of high-permeability facies relative to the distribution of low-permeability parasequence boundaries, in conjunction with the waterflood direction, is crucial for predicting reservoir performance. The study also demonstrated that areas of unswept oil can result from cross flow across relatively low-permeability mudstone layers.

IX. REFERENCES

ECL Petroleum Technologies, 1990, ECLIPSE Reference Manual.

Ferris, M. A., in preparation, Permeability distribution on the upper San Andres Formation outcrop, Guadalupe Mountains, New Mexico: The University of Texas at Austin, Master's thesis.

Fogg, G. E., 1989, Stochastic analysis of aquifer interconnectedness: Wilcox Group, Trawick area, East Texas: The University of Texas at Austin, Bureau of Economic Geology Report of Investigations No. 189, 68 p.

Fogg, G. E., and Lucia, F. J., 1990, Reservoir modeling of restricted platform carbonates: Geologic/geostatistical characterization of interwell-scale reservoir heterogeneity, Dune field, Crane County, Texas: The University of Texas at Ausin, Bureau of Economic Geology Report of Investigations No. 190, 66 p.

Fogg, G. E., Lucia, F. J., and Senger, R. K., 1991, Stochastic simulation of interwell heterogeneity for improved prediction of sweep efficiency in a carbonate reservoir, *in* Lake, L. W., Carroll, H. B., Jr., and Wesson, T. C., eds., Reservoir Characterization II, San Diego, California: San Diego, California, Academic Press, p. 355–381.

Goggin, D. J., Thrasher, R. L., and Lake, L. W., 1988, A theoretical and experimental analysis of minipermeameter response including gas slippage and high velocity flow effects: In Situ, v. 12, no. 1/2, p. 79–116.

Hayes, P. T., 1964, Geology of the Guadalupe Mountains, New Mexico: U.S. Geological Survey Professional Paper 446, 69 p.

Hindrichs, S. L., Lucia, F. J., and Mathis, R. L., 1986, Permeability distribution and reservoir continuity in Permian San Andres shelf carbonates, Guadalupe Mountains, New Mexico, *in* Hydrocarbon Reservoir Studies — San Andres/ Grayburg Formations: Proceedings of the Permian Basin Research Conference, Permian Basin Section, Society of Economic Paleontologists and Mineralogists Publication No. 86-26, p. 31–36.

Honarpuour, Mehdi, Koederitz, L., and Harvey, H. A., 1982, Relative permeability of petroleum reservoirs: Boca Raton, Florida, CRC Press, 143 p.

Journel, A. G., and Huijbregts, Ch. J., 1978, Mining geostatistics: New York, Academic Press, 600 p.

King, P. B., 1948, Geology of the southern Guadalupe Mountains, Texas: U.S. Geological Survey Professional Paper 480, 183 p.

Kittridge, M. G., Lake, L. W., Lucia, F. J., and Fogg, G. E., 1990, Outcrop/subsurface comparisons of heterogeneity in the San Andres Formation: SPE Formation Evaluation, September 1990, p. 233–240.

Knudsen, H. P., and Kim, Y. C., 1978, A short course on geostatistical ore reserve estimation: University of Arizona, Department of Mining and Geological Engineering, 224 p.

Radian Corporation, 1989, CPS-1 user's guide.

Warren, J. E., and Price, H. S., 1961, Flow in heterogeneous porous media: Society of Petroleum Engineers Journal, September 1961, p. 153–169.

APPLICATION OF OUTCROP DATA FOR CHARACTERIZING RESERVOIRS AND DERIVING GRID-BLOCK SCALE VALUES FOR NUMERICAL SIMULATION

Liviu Tomutsa, Ming-Ming Chang, and Susan Jackson
National Institute for Petroleum and Energy Research

ABSTRACT

The objective of this study was to determine the effect of the spatial arrangement and density of core-plug scale permeability data in deriving grid-block scale values for numerical simulation. Various averaging techniques were applied to closely spaced outcrop permeability data[1,2] to generate input permeability models used in simulations. The effect of permeability models with varying amounts of detail, as well as viscosity ratio and grid block size, on waterflood oil recovery was determined by numerical simulation using BEST,[3] NIPER's improved version of BOAST, which has been shown to be adequate in performing waterflood simulations in heterogeneous reservoirs.

The results of this study provide a guideline for the degree of detail required for numerical simulator input permeability models for the specific type of rocks and conditions investigated. In the absence of the required detail, an indication of the magnitude and direction of errors that can be expected in oil recovery prediction is given.

Two sampled outcrop areas which differed in geological and permeability characteristics were modeled and simulated. One area, 5x10 ft, was relatively homogeneous with a permeability coefficient of variation of 0.58; while the second area, 4x21 ft, had discontinuous high permeability layers with contrasts of mean permeability approximately 1:50 between layers and a permeability coefficient of variation of 1.28.

The level of detail in the input permeability models ranged from one average permeability value to the incorporation of the maximum amount of information available. Input permeability models included: (1) profile layer models based on one vertical permeability profile; (2) kriged permeability models with 0, 1, and 2 standard deviations randomly imposed on the interpolated grid; (3) stochastic realizations using the indicator kriging method; (4) the turning bands method; and (5) a geological model containing the maximum amount of information available from outcrop descriptions and photographs and core-plug measurements, and considered the most accurate representation of the rocks.

Results of this study indicate the following: (1) to predict oil recovery accurately, greater detail in simulator input models is required when the reservoir is heterogeneous and the viscosity ratio is adverse however, indicator kriging and turning bands methods can adequately predict oil recovery with relatively sparse amounts of data; (2) failure to account for the distribution of discontinuous, high-permeability sand layers will result in a pessimistic prediction of waterflood production; and (3) the presence of small-scale permeability heterogeneity increases dispersivity of the water front, decreases the effective permeability, reduces fingering, and thereby improves sweep efficiency and increases oil recovery.

I. INTRODUCTION

Numerical reservoir simulation studies provide critical information for decisions on oil well commerciality, maximum efficient rate of production (MER), overall reservoir management, initiation of secondary recovery projects, and selection of optimum enhanced oil recovery (EOR) processes. Without a realistic geologic and engineering reservoir description, simulation results may be substantially in error.

Quantitative reservoir models are necessary for selecting grid block dimensions and assigning appropriate petrophysical values to the grid blocks in reservoir simulation. The level of detail obtainable from subsurface sampling is inherently inadequate to assign simulation parameters accurately to predict fluid flow on the interwell scale. Quantitative descriptions for simulation at scales less than well spacing can be obtained, however, by combining available subsurface reservoir data with a detailed quantitative model of rock composition and fluid flow characteristics constructed through statistical sampling and analysis of analogous outcrops.

The need for incorporating the effect of rock heterogeneities in reservoir models had been recognized as early as 1950 when Muskat derived analytical formulas for flow in a stratified reservoir.[4] Dykstra and Parsons[5] defined their well known coefficient which characterizes the reservoir heterogeneity and estimates the waterflood sweep efficiency in a layered heterogeneous reservoir.[6] The Dykstra-Parsons coefficient, however, does not include a spatial component of variability.

The advent of computers allowed Warren and Price[7] to study the effect of random spatial distributions of permeability values on single-phase fluid flow using Monte Carlo numerical simulators. They found that the effective reservoir permeability is equal to the geometric mean of the individual permeability values.

The effect of small-scale heterogeneities on core relative permeabilities was studied by Huppler[8] who found that channel-like effects can significantly alter the measurement results. Hearn[9] calculated pseudo relative permeabilities for stratified reservoirs with a negligible vertical pressure gradient. Kortekaas[10] simulated flow in crossbedded reservoirs by using pseudo relative permeabilities and found that oil trapping takes place behind the higher permeability foreset laminae.

The geostatistical approach in various kriging interpolation schemes is often used to generate maps of simulator input parameters (permeability, porosity, saturations, etc.) and uncertainities in these values; however, these maps are typically smoother than the actual distribution in the reservoir.

To reinstate the randomness existing in a reservoir, Monte Carlo simulations have been conducted by Smith et al.[11] and Delhome[12] in geostatistical work applied to hydrology. Recently, various methods to generate random fields have been proposed and used[13] to preserve the randomness and the correlation lengths existing in an actual reservoir. A good presentation of geostatistical theory and practice is given by Journel and Huijbregts[14] By creating reservoir models statistically compatible with existing data and by running numerical flow simulations on these models, a range of outputs is obtained, and an uncertainty in the simulation results based on the input data can be computed.

A systematic approach for handling heterogeneities from small to large scale was given by Lasseter et al.[15] by using pseudo functions. They found that while small-scale heterogeneities mainly cause oil trapping, the medium- and large-scale heterogeneities control lateral and vertical communication and ultimate oil recovery. The use of fractals in generating permeability distributions and predicting reservoir performance by use of simulations was described by Hewett et al.[16]. The method described is based on the scale range (R/S) analysis of porosity in a 1,100-ft-thick reservoir and lateral extrapolation of the reservoir properties by generating synthetic logs based on the observed fractal behavior.

Another method for calculating effective grid block values was presented by Begg et al.[17], where the rock type distribution and the effect of layer geometry was studied. They found that the effective permeabilities of the various rock types were controlled by the length to width ratio of the sand layers

A review of the application of various stochastic modeling techniques used to create

reservoir representations is given by Haldorsen and Damsleth[18]. Before one selects one or another stochastic modeling technique, the structure of the reservoir should be understood, s(i.e. layer cake, jig-saw or labirinth type,Weber and Van Geuns[19]), and the statistical and spatial information regarding the reservoir rock types present should be available..

In the present work values for directional correlation lengths available from analogous outcrop measurements and depositional environment characteristics, are used to generate realizations of rock properties (k ,ø) statistically and spatially compatible with the observed values by means of kriging, indicator kriging[20,21] and the turning bands methods[22,23]

A. Geological Background

A quantitative geologic model was developed for an outcrop of the upper Cretaceous Shannon Sandstone formation, a Shelf Sand Ridge deposit that produces oil in Hartzog Draw field, Heldt Draw field, Teapot Dome field, and many other smaller fields in the Powder River Basin. The model was based on detailed sedimentological descriptions, laboratory measurements of permeability and porosity in over 1,200 outcrop core plugs and statistical analysis of the spatial distribution of permeability across the 1,000-ft-long outcrop exposure of the Shannon Sandstone exposed around the Salt Creek anticline, north of Casper, Wyoming (Fig. 1). The resulting model was compared with subsurface data from Hartzog Draw field, located 40 miles away at a depth of approximately 9,300 ft. and Teapot Dome field , located 5 miles away. at a depth of 300 ft. Sedimentological features such as grain size, lithology, and sedimentary structures and petrophysical properties (k, ø) in the outcrop were used to determine the degree of depositional similarity. This work was reported elsewhere.[1,2] Major conclusions from this work were as follows:

1. Sedimentologically defined units (facies) within the Shannon Sandstone provide a good approximation of rock units with similar permeability characteristics in both the outcrop and Hartzog Draw field.
2. Stratification types and sedimentary structures can be related to permeability classes in both outcrop and subsurface and may be an appropriate unit for scaling-up to reservoir simulation grid-block size volumes.
3. Although the magnitude of permeabilities in the outcrop and Hartzog Draw field differ by two orders of magnitude, similar decreasing downward trends in permeability exist through the same sequence of facies and stratification types. Decreasing permeabilities correspond to decreasing depositional energy and indicate that the primary depositional permeability pattern has not been totally masked by diagenesis.

A brief geological description of the two areas used in the simulation studies is presented below.

Four units (indicated in Fig. 2) of differing lithology and bedding characteristics occur within the High Energy Ridge Margin (HERM) facies in the outcrop studied. Area A is located within Units 3a and 3b which consist of 1 to 2 ft thick trough cross-bedded sets, which extend laterally for approximately 20 ft. The sand contains 5 to 20% glauconite that is both disseminated and concentrated along cross-bed laminae. Clay drapes and limonite clasts also occur along bedding planes and cross-bed laminae. Units 3 a and b are similar, except for slight differences in the amount of glauconite and clay drapes present. Because of the difficulty of coring through shale drapes, limonite clasts, and lenses, their effects on the permeability distribution were not considered. Consequently, the model developed for this area did not contain the total amount of heterogeneity present in the rocks.

Area B is located within HERM Unit 3d, which is a highly stratified unit that consists of 0.25 to 0.5 ft thick trough and subhorizontal cross-beds which are glauconite-rich alternating with glauconite-poor, finer-grained horizontal to massive bedded layers. The glauconite-rich cross-beds have a mean permeability of about 500 md while the finer-grained beds have a mean permeability of about 50 md. The lateral extent of these beds ranges between 10 and 20 ft.

Analysis of the permeability data for Area A (Units 3a and 3b) indicates a relatively

sharp-peaked frequency distribution (Fig. 3a) with a mean natural logarithm permeability of 7.1 (1,215 md), a standard deviation of 0.94 and a coefficient of variation of 0.58 (table 1). Visual comparison of the histogram for Area A with that of Unit 3a and 3b for the entire outcrop (Fig. 3c) indicates that a similar frequency distribution exists for the two samples even though there are a greater number of measurements for the entire outcrop (202 measurements vs. 31 measurements) This similarity indicates that the permeability distribution in Area A is representative of the entire 1,000-ft-long outcrop.

The permeability distribution for Unit 3d in Area B is bimodal and reflects the presence of the two stratification types and lithologies. The mean permeability of the lower permeability group is around 12 md while the mean of the higher permeability group is approximately 650 md, yielding a permeability contrast of ~1:50 between the layers. The coefficient of variation is 1.28. As in Area A, histograms of the 47 permeability measurements from Area B also indicate a similar frequency distribution as that from the 215 measurements from the same unit for the entire outcrop (Fig 3b and d), although the distribution for the entire outcrop appears to be less bimodal than that for Area B.

II. AREA A PERMEABILITY MODELS

Six permeability models were generated using 31 permeability values measured from 1-in. diameter core plugs drilled from the face of the outcrop. The arithmetic average of the samples was 1,622 md, geometric mean was 1,215 md, and the standard deviation was 946 md (Table 1). The permeability models generated ranged from a single permeability value to the incorporation of the maximum amount of available information. Two grid configurations were used in Area A: a 40X1X20 grid which contained grid block sizes of 0.25 ft, close to the size of the outcrop plug samples, and coarser grid of 10X1X5 grid with grid-block sizes of 1 ft by 1 ft, constructed by assigning the arithmetic average value of 16 grid blocks (4X1X4 blocks from the 40X1X20 grid). The permeability models developed and simulated are as follows:

1. Uniform Permeability Model. A constant permeability of 1,215 md, the geometric average of permeability of the 31 core plugs, was assigned to all gridblocks. The geometric average was selected based on simulations of permeability fields generated by randomly sampling the permeability distribution of the measured permeability samples in Area A. This model is the least detailed, and serves as a base case for comparison of the other more complex representations.

2. Profile Layer Models. Three, five-layer models were constructed based on three vertical permeability profiles (Table 2). The permeabilities assigned to each layer were from actual measured values and extended across the entire area simulated. The Dykstra-Parsons coefficients of these three permeability profiles were 0.30, 0.31, and 0.51, which indicated relatively homogeneous permeability distributions.

3. Kriged Permeability Model (K0 Model). The permeability distribution for this model was based on the interpolation between the 31 measured core plugs in Area A. The interpolation method used was a kriging routine which assumed isotropic correlation lengths. This is justified by the fact that strong layering is not present, although a high-permeability area (more than 2,000 md) is located in the central part of Area A, while permeability drops to less than 1,000 md in the top and bottom part of the area (Fig 4).

4. Kriged Permeability plus one standard deviation noise (K1 Model). A random perturbation was imposed on the interpolated values of permeability to compensate for the smoothing effect due to interpolation and to preserve the random component naturally found in permeability distributions. Natural logarithm values of permeability and the standard deviation (946 md) were used to preserve the geometric mean of the population. A series of random numbers ranging from -0.5 to +0.5 were generated and then multiplied by the logarithmic standard deviation value of 6.85. This product was then added to the logarithmic value of the interpolated grid block permeability value and reconverted to a non-

logarithm permeability value. Figure 5 shows the permeability distribution generated using this procedure.

5. Kriged Permeability plus two standard deviations noise (K2 Model). This model was constructed as described above, except that two standard deviations were added to the kriged-based permeability values (Fig. 6).

6. Coarse Grid Model. Two coarse grid permeability models were constructed by assigning the arithmetic average value of 16 grid blocks (four by four blocks in vertical and horizontal directions) from the K0 and K2 kriging-based permeability models.

III. AREA B PERMEABILITY MODELS

The permeability models, constructed on 85x1x17 grids with square grid blocks 0.25ft x 0.25ft are described below:

1. Three-layer Model. Due to the layered nature of the area and the bimodal permeability distribution, the simplest model used in this area was a three-layer model. The three layers have constant permeabilities of the geometric mean of the samples located in that layer and are from bottom to top: 7, 157, and 14 md.

2. Profile Layer Model. This model is based on the permeability obtained from one vertical profile selected from a grid, which was generated for the geological model and is described below. Each layer has constant permeability values across the area simulated. This model is analogous to those typically used in the field, where information from one well is extrapolated across the interwell area (Table 3).

3. Geological Fine Grid Model. This model is the most detailed and therefore accurate permeability representation and serves as a bench mark for comparison to the other less detailed models. It incorporates geological information about the spatial distribution and lateral continuity of the layers obtained from outcrop descriptions and photographs with the 101 core-plug permeability measurements (Fig. 7).

The first step in model construction was the identification of rock types based on sedimentary features. The following four rock types were distinguished: (1) bioturbated 200 micron sandstone with 10% clay, 15% glauconite, and 90% burrowing (Unit 3c, bioturbated shelf-margin sand); (2) horizontal to massive bedded 200 micron sand with 5% clay (HERM Unit 3d); (3) trough and subhorizontal stratified 300 micron sand with up to 15% glauconite (HERM Unit 3d); and (4) bioturbated 125 micron sand with trace of clay, 2% glauconite, and 99% burrowing (Bioturbated Shelf Sandstone facies). (See Fig. 2 for position and thicknesses of units.) Comparison of permeability statistical parameters from the four rock types indicated distinct permeability classes for each rock type. The top and bottom layers are included as boundary layers and are from a different facies than the HERM facies of interest.

The rock type of each grid block was identified from photographs, outcrop descriptions and core-plug examination. The dimensions and distribution of the rock type/permeability layers measured from the outcrop were used to construct the model rather than interpolating between the data points because the layered nature of the rock was not preserved when isotropic interpolation methods were used.

Permeabilities were assigned to each grid block by randomly sampling the permeability distribution for that class. The measured permeability value was assigned to those 101 grid blocks which had been sampled. This method of assigning grid-block permeability values preserved the frequency distribution characteristics within each permeability class.

4. Geological Coarse Grid Model. A coarse-grid permeability model(21x1x4) was generated by taking the arithmetic average of 16 neighbouring bloks from the geological model.

5. Indicator Kriging Model. A dual rock indicator kriging model (Fig. 8) was generated using the software package developed at Stanford.University.[21] Correlation lengths of 10 ft laterally and 0.25 ft vertically, based on both on variogram analysis. Examination of outcrop photographs, were used to generate the spatial distribution of the two rock types. The correlation lengths calculated were one-half the average length of the bed sets measured from the outcrop exposure. The grid blocks for each rock type was assigned a permeability value drawn randomly from the statistical distribution for that rock type. The realizations were conditioned on the vertical profiles located at points 0 and 21 ft.

6. Turning Bands Model. The turning bands model used to generate unconditional realizations of permeability (Fig. 9) was the software package TUBA[23], developed at New Mexico Institute for Mining and Technology. The same lateral and vertical correlation lengths used in the indicator kriging model were applied here. The realizations that best approximated the geological model were based on the Bessel and exponential correlation functions and the log normal permeability distribution function.

IV. VISCOSITY RATIO

Two oil-to-water viscosity ratios: 2.78 corresponding to 35° API oil gravity and 24.5, corresponding to 20° API oil gravity were used to represent a range of viscosity ratios. The viscosity ratios used correspond to the viscosity values at 1,000 psi, which is close to the pressure occurring in the waterflood simulation. For comparison, cases of unit mobility ratio and a viscosity ratio of 405 which corresponds to 10° API gravity oil were simulated. A unit mobility ratio was obtained by assigning the same viscosity value to both the oil and water phases.

V. VERTICAL PERMEABILITY

Vertical permeability values were measured from cubes cut from 2-in.-diameter cylindrical cores. Permeability was measured from the 1.4-in.-square cubes in the x (parallel to the outcrop face), y (normal to the outcrop face) and z (vertical to bedding plane) directions. Mean permeability values measured in the 2-in.-diameter cores were similar to those measured in the x and y direction from the cubic samples (1,080, 1,021, and 1,099 md, respectively), while those measured in the z direction were lower (640 md) (Table 4). The vertical permeability values used in the simulations were represented by the relation $k_v = 0.00038\ k_h^2$ derived from a plot of measured vertical permeability versus horizontal permeability.

VI. RELATIVE PERMEABILITY

Relative permeability measurements from Teapot Dome field were used in the waterflood simulations. Teapot Dome is located approximately 5 miles from the outcrop studied and produces oil from the Shannon Sandstone at a depth of around 350 ft. In the absence of other relative permeability data, due to the close proximity and shallow depth of the reservoir, and the similarity in porosity and permeability distributions[19] the use of the Teapot Dome relative permeability tables is expected to be a good approximation for the outcrop simulations. In Area A, two relative permeability tables were used: (1) a table generated from the measurement of a sample with permeability-to-air of 850 md was used for rocks which have permeability-to-air above 200 md (Table 5a) and (2) a table generated from the measurement of a sample with permeability-to-air of 56.1 md was used for those rocks with air permeability less than 200 md (Table 5b). In Area B, the endpoints of the two relative permeability curves were shifted from 85% to 80% for permeabilities greater than 200 md and from 72% to 50% for permeabilities less than 200 md to account for the lower average permeabilities in Area B. The 200-md division was obtained from divisions observed in histograms of permeability for both Unit 3a and 3b rocks as well as unit 3d rocks (Figs.3a - d).

VII. INITIAL WATER SATURATIONS

Initial water saturation values were determined from the laboratory measurements of relative permeability. In Area A, initial water saturation values of 15 and 28% were assigned for rocks with air permeability greater and less than 200 md, respectively, while in Area B, initial water saturations of 20 and 50%, respectively were assigned. Slightly higher initial water saturations were assigned in Area B because of lower average permeability values.

VIII. WELL LOCATIONS AND FLOW RATES

The configuration of the simulation consisted of water injection (or source) assigned to all grid blocks at one edge of the model and production (or sink) to all grid blocks at the opposite edge. A constant flowrate of 5 bbl/d was applied to both wells. This flow rate is equivalent to a velocity of 3 ft/d which is common in the waterflood process. All the pore volume (PV) values presented in the text, figures, and tables are expressed as movable pore volumes (MPV).

IX. SIMULATION RESULTS

A. Waterflood Simulation of Area A

Three types of illustrations are used to analyze and compare results for 2.78 and 24.5 viscosity ratios: cumulative oil production of movable oil in place (MOIP), (Figs. 10a,b); water-oil ratio (Figs. 11a,b), both of which illustrate production performance; and oil saturation distributions at certain production times (referenced below), which aids in understanding the waterflooding behavior.

1. Uniform Permeability Model

In the uniform permeability model, 1,215 md, the geometric average of permeability from 30 outcrop samples, was assigned to each of the 800 grid blocks. Waterfloods were simulated using two types of oil and their corresponding viscosity ratio (v_r): 35° API, v_r = 2.78; 20° API, v_r = 24.5. The simulation results of this model will be used for comparison with the other more detailed models developed.

As expected, the oil recovery curves indicates that the higher the viscosity ratio, the poorer the sweep efficiency, and the lower oil the recovery is (Figs. 10a,b), due to the earlier water breakthrough (Figs.11a,b) The low viscosity ratio case exhibits a later breakthrough but faster increase in the water-oil ratio after breakthrough, than the more adverse viscosity ratios of 24.5 and 40.

Oil saturation distributions for the viscosity ratio of 2.78 after injection of 0.64 PV indicates a piston-like displacement with a slight water tongue at the bottom due to gravity effect. The oil saturation distribution for the viscosity ratio 24.5 after injection of 0.64 PV, appears also piston like. However, the width of the transition zone, defined as from 17% (residual oil) to 85% (initial oil saturation) is longer and the breakthrough is earlier than for the more favorable viscosity ratio case. The long transition zone can be considered equivalent to viscous fingering.

2. Vertical Profile Layer Models

Three, 5-layer models were constructed using three vertical profiles of permeability existing in the core-plug data (Table 2). These three cases showed similar overall waterflood performances and the lowest recovery among all models. (Fig. 10a). They also showed similar water-oil-ratio values (earlier than all other models Fig. 11a) although some minor differences exist. Profile model 2, which had the lowest Dykstra-Parsons coefficient (0.30), had 3 to 5% greater oil recovery and 0.1 PV later water breakthrough . Differences of 3% in oil production between profile models 2 and 3 which have similar Dykstra-Parsons coefficients (0.30 and 0.31, respectively) are due to the arrangement of layers rather than the degree of heterogeneity. The similarity of performances of the three layer models can be

attributed to the relatively homogeneous permeability distribution (coefficient of variation 0.58) in Area A. Figure 12 shows a typical oil saturation distribution for the first of the three profile layer models after 0.64 PV of water was injected. The water front movement in each layer was proportional to the permeability of that layer. The more pessimistic oil recovery prediction for the profile models is due to the continuous channels erroneously assumed in the model.

3. Kriged Permeability Model Without Random Components (K0 model)

After injection of 0.64 pore volumes (PV) of fluid with a unit viscosity ratio, the resulting transition zone is a relatively sharp, 1-ft wide front. An oil transition zone of similar shape, but about 7 ft wide (Fig. 13) occurred for the 2.78-viscosity ratio case, while for the more adverse, 24.5 viscosity ratio case, the width was greater than 10 feet (Fig.14). The elongated shape of the front is due, in part, to the high-permeability zone in the central part of Area A (Fig. 4) which resulted in the rapid movement of the injected water.

The effect of viscosity ratio on produced water-oil-ratio is that the longest breakthrough time followed by a fast increase in the water-oil-ratio occurred for the lower viscosity ratio case, whereas an earlier increase in water-oil-ratio occurs for the more adverse viscosity ratio of 24.5.

The oil recovery from the K0 model is 6% greater than that from the three profile models (Fig. 10a) and the breakthrough time occurs at 0.8 PV compared to 0.6 PV for the profile models (Fig. 11a).

4. Kriged Permeability Model With Random Components

The viscosity ratio has a similar effect on width of the oil saturation transition zone in the K2 model as the K0 model (Figs. 15-17). However, narrower transition zone widths occur in the K2 model indicating that better sweep efficiency occurs with greater amounts of small-scale heterogeneity. This relationship exists for all cases of mobility ratios simulated, however it is more pronounced for the more favorable viscosity ratio of 2.78.

Comparison of production performance among the three kriged models indicates that the highest oil recovery results from simulation of the K2 model for both viscosity ratios (Figs. 17a,b). The greatest small-scale permeability heterogeneity exhibits the most efficient recovery. Oil recovery from the K2 model is 7% MOIP higher than from the K0 model and 3% MOIP higher than the K1 model for the viscosity ratio of 2.78. A slightly lower difference of 5% MOIP between the K0 and K2 models exists for the less favorable viscosity ratio of 24.5. The accurate prediction of oil recovery lies within the range of oil recoveries resulting from the simulation of the 3 kriged models for each viscosity ratio.

The benefits of small-scale heterogeneity are also illustrated in figure 18a where, for a viscosity ratio of 2.78, the permeability model with the greatest small-scale variability (K2) has the latest breakthrough time. This effect is due to the presence of heterogeneity which diverts the flow from a straight line path and thereby increases the dispersivity of the water front. The increase in dispersivity reduces the fingering phenomena, delays the water breakthrough and thereby improves the sweep efficiency. In the case of the less favorable viscosity ratio of 24.5, delay in breakthrough time and the increase of water-oil ratio also occur from the addition of small-scale heterogeneity in the permeability models (Fig. 18b).

An increase in small-scale permeability heterogeneity appears to reduce the effective permeability and causes a larger pressure gradient at a constant flow rate. Figures 19a-c show pressure distributions resulting from waterflood simulations of the K0, K1 and K2 models respectively, using a viscosity ratio of 2.78. A pressure drop of 12 psi was obtained across the 10 ft simulated for the K0 model (Fig. 19a), while pressure drops of 15 and 18 psi were observed for the K1 (Fig. 19b) and K2 (Fig. 19c) models respectively, after injection of 0.17 PV.

5. Kriged Permeability Models - Coarse Grid

Regardless of the permeability perturbations imposed on the original kriged permeability model, the 16-block averaging coarse grid showed similar oil saturation distributions. They also showed similar waterflood performance with the kriged model (KO) (Fig. 10a) for the favorable viscosity ratio and more optimistic recovery for the unfavorable viscosity ratio

(Fig 10 b). For both viscosity ratios the coarse grid models showed a slightly earlier break through than the five good kriged model (Figs. 11a,b). This is due to the loss of local permeability heterogeneity in the model through the averaging procedure.

X. DISCUSSION

A. Viscosity ratio 2.78

In the case of the favorable viscosity ratio (2.78), a maximum difference of 11% MOIP in cumulative oil recovery prediction occurs between the uniform permeability model and the vertical profile layer model (vertical profile 2), while oil recoveries from the coarse-grid and fine-grid kriged models are essentially the same (Fig. 10a). The vertical profile model (profile 2), is 6% lower in oil recovery than the kriged model and gives a slightly pessimistic prediction of oil recovery.

The oil recovery curve for the uniform model lies within the same 7% range of predicted recoveries from the three kriged models. Since the range of oil recoveries from the various kriged models is assumed to encompass the accurate prediction of waterflood recovery, the similarity in cumulative oil recovery suggests that the uniform model, a single geometric average value, is an acceptable representation of permeability for this area which has a relatively homogeneous permeability distribution.

B. Viscosity ratio 24.5

In the case of the less favorable viscosity ratio (24.5), a maximum difference of 11% MOIP cumulative oil recovery occurs between the uniform permeability model and kriged fine-grid model (Fig. 10b). Since this is outside the 5% range previously discussed of the three kriged models, the uniform permeability model is not an adequate representation of permeability when the viscosity ratio is 24.5 as it was in the more favorable viscosity ratio case.

The range of oil recoveries among the various kriged models is 5%, which is 2% less than the 7% range found in the 2.78-viscosity ratio case. The lower range of oil recoveries indicates a decreased sensitivity to permeability variation of the water flow under an adverse mobility ratio.

Oil recoveries from the coarse grid model are 5% more than that resulting from the K0 model (Fig. 10b). The oil recovery curve from the coarse grid model falls within the range of the three kriged models which suggests that the model is an acceptable representation of permeability, as it was for the fine-grid model.

Waterflood Simulation of Area B

As in Area A, three types of illustrations are used to analyze and compare results for 2.78 and 24.5 viscosity ratios: cumulative oil production of movable oil-in-place (MOIP), (Figs. 20a,b); water-oil-ratio (Figs.21a,b), and oil saturation distributions at certain production times (Figs. 22-33).

Three-Layer Model

Simulations of the three-layer model with a viscosity ratio of 2.78 indicated piston-like displacement with a sharp front due to the single, higher permeability layer. This model exhibits the latest breakthrough and the most rapid increase in water-oil-ratio after breakthrough of all models studied (fig. 21a). The three-layer coarse grid model also showed piston-like displacement; however, an earlier breakthrough and therefore a slower buildup of production water-oil-ratio occurred in the coarse grid model case (Fig. 21a).

Comparison of simulation results of the fine-grid model with a viscosity ratio of 24.5 to that with a 2.78 viscosity ratio indicate a wider transition zone (Fig. 22) and less oil recovery - 67% MOIP for the 24.5-viscosity ratio case (Fig. 20b) versus greater than 90% MOIP for the 2.78 viscosity ratio case (Fig. 20a) after 2.5 PV water injection.

Simulation results for the 24.5 viscosity ratio, uniform coarse grid model indicate similar results as the uniform fine-grid model except for an earlier breakthrough (Fig. 21b) and 4% MOIP less oil recovery after 1 PV water injection (Fig. 20b).

Profile Layer Model

Three fingers were observed from the waterflood simulation for the 2.78 viscosity ratio after injection of 0.32 PV due to the three continuous permeable layers in the permeability model (Fig. 23). The highest permeability finger caused an early breakthrough. Distribution after the breakthrough of a water injection of and courses a significant quantity of oil to be left unswept in the lower permeability layers (Fig. 24).

Similar channeling and early breakthrough occurred in the 24.5 viscosity ratio case, however, differences in viscosity ratio resulted in a 10% decrease in oil recovery. After water injection of 1 PV, 52% MOIP was recovered for the 2.78 viscosity ratio case, whereas 42% MOIP was recovered for the 24.5 case.

Geologic Fine-Grid Model

The permeability distribution is shown in Fig. 7 and the initial oil saturation distribution used for simulation of the geological fine-grid model is presented in Fig. 25. The sequence of oil saturation distribution during waterflood of the 2.78 viscosity ratio case illustrates good sweep efficiency in spite of high permeability contrast layers because the high permeability layers are not continuous across the simulation area (Figs. 26-29). One continuous, 3-in. thick flow channel and another 8-ft.-long relatively high-permeability layer caused fingering which is reflected in the oil saturation distribution after 0.32 PV water injection (Fig. 26). The injected water flowed from these two "layers" to four other discontinuous, good permeability layers which ranged from 2 to 11 ft. in length. This cross-flow caused a late water breakthrough and a relatively uniform sweep that is apparent in the oil saturation distribution after 0.85 PV water injection (Fig. 27). After water injection of 1.75 PV, most oil located between the permeable sand layers were swept out. Residual oil was found on the top and the bottom of the model, areas which were bypassed by the water. In contrast to the 2.78 viscosity ratio case, waterflood results of the 24.5 viscosity ratio showed a very early breakthrough (Fig. 21b) and therefore poor sweep efficiency. The adverse viscosity ratio caused channeling (Fig. 28) and reduced the amount of cross-flow of injected water which resulted in early breakthrough. The residual oil saturation distribution after an injection of 0.85 PV is shown in figure 29 and illustrates the lower MOIP recovery for this unfavorable viscosity ratio case when compared to the more favorable viscosity ratio production.

Geological Coarse-Grid Model

Comparison of the residual oil saturation distributions resulting from the coarse-grid geologic model, 2.78 viscosity ratio case with that of the fine grid model indicates higher saturations on the bottom close to the producer. This difference is due to the averaging procedure which distorted the original permeability continuity. The permeability channel close to the bottom of the producer was eliminated by the neighboring low-permeability rock in the averaging process.

Other differences include an earlier breakthrough and higher water-oil ratio for the coarse-grid model (Fig. 21a,b), lower ultimate oil recovery for the viscosity ratio 2.78 (Fig 20a,b) and a higher oil recovery for the viscosity ratio 24.5 compared to the geological fine grid model.

Indicator Kriging Model

The permeability distributions shown in figure 8 is typical of the various realizations generated using the 10 ft lateral correlation length and 0.5 ft vertical correlation length. Figure 8 shows a marked similarity to the geological model (Fig. 7). This is due both to the choice of correlation lengths and to the conditioning of the realizations on the two extreme vertical profiles. The high permeability zone present in the lower part of both the geological and indicator kriging model is the main source of similar oil saturation distributions for the two models. The indicator kriging initially overestimates the oil production for the low viscosity ratio but after 2 PV injected, both models show the same cumulative oil production (Figs. 20a,b). For the high viscosity ratio case, the indicator kriging model matches the geological model for less than 0.3 PV injected but then due to

less continuity under estimates the oil recovery. Again after 2 PV injected both cumulative productions coverage toward 40% MOIP.

A significant difference between the two waterfloods is in the water-oil ratio for the high viscosity case. While after breakthrough, the geological model produces a rapid rise in WOR the indicator kriging model predicts a value which increases asymptotically toward 10 (Fig. 21b). The saturation distributions after 0.32 PV and 0.85 PV for the 2.78 viscosity ratio are shown in Figures 30-31. They show a sharper front than the geological model with a more complete sweep behind the front.

Turning Bands Model

Although the permeability distribution generated using the Bessel function correlation form (Fig. 9) is not as close to the geological model (which is to be expected as this was not a conditional simulation), both the saturation distributions (Figs. 32-33) and the cumulative oil production, (Figs.20a,b) are very close to the results from the geological model. The Bessel function model slightly underestimates the oil recovery for the viscosity ratio 2.78 and overstimates the initial oil recovery for the 24.5 viscosity ratio. For less than 0.5 PV injected this model behaves like the profile model but for values greater than 0.5 PV its predictions become very close to the geological model. The similarity of the fluid saturation distributions and recovery curves from the profile model can be traced to the presence of a higher permeability zone in both models. As in the indicator kriging model, the geometry of the higher permeability zone is directly controlled by the choice of lateral and vertical corelation lengths. Due to the higher continuity and permeability of the high permeability zone, the water breakthrough takes place earlier and the WOR has a higher value than in the case of the geological model.

DISCUSSION

Comparison of the predicted oil recovery from the simplest permeability model, the uniform permeability model to the most detailed model, the geological model at two viscosity ratios indicates widely different predictions in Area B. For the more favorable viscosity ratio of 2.78, after 1 PV injection, the ratio of oil recovery from the uniform model to the geological model is 1.3 (Fig. 20a); however, for the viscosity ratio of 24.5, the oil recovery ratio increases to 1.9 (Fig. 20b), indicating a larger discrepancy in the oil recovery prediction. These results suggest that the more adverse the mobility ratio, the more detailed information is required for constructing the permeability model.

Viscosity ratio 2.78

In the case of the favorable viscosity ratio (2.78), greater oil recoveries were predicted after 0.85 PV injection for the three-layer, fine-grid uniform model (87% MOIP) and lower oil recovery for the profile layer model (49% MOIP), when compared to the oil recovery for the geologic model (0.63% MOIP) (Fig. 20a). After injection of 1 PV, a 20% MOIP difference in oil recovery still exists between the three-layer fine-grid model and the geologic fine-grid model, while the indicator kriging model overpredicts by 12% MOIP and the turning bands underpredicts by 4% MOIP. However, after injection of 2 PV, the oil recoveries for the models converge toward 90% MOIP, with the exception of the profile layer and the coarse grid geological models which converge toward significantly lower recoveries.

The similarity in production of the geologic model to that of the uniform models after 2 PV injected is due to the crossflow between the good and poor permeability sand layers in the geologic fine-grid model. The cross-flow disperses the front of injected water and results in increased sweep efficiency and eventually, after 2.4 PV of water injection, oil production from the geologic fine-grid model equals that of the uniform model. The poorer production performance of the coarse grid geological model and the profile layer model indicate that failure to account for the random distribution of high permeability sand layers will result in a pessimistic prediction of production.

Comparison of the fine grid and coarse grid geological models indicates that after injection of 0.55 PV (breakthrough time) the coarse-grid geological model provides a pessimistic prediction of oil recovery compared to the fine-grid geological model (Fig. 20a). The discrepancy between the coarse-grid and fine-grid geological models increases to 22%

after injection of 2 PV and is due to the creation of a low-permeability area which is left unswept in the coarse-grid geological model. These results are in contrast to Area A, where the predicted oil recoveries from the coarse-grid model are similar to those for the kriged, fine-grid models and illustrates that more detailed permeability models are required as the degree of heterogeneity increases.

The profile layer model provides the most pessimistic prediction after injection of 0.32 PV or at breakthrough time (Figs. 20a,21a). After injection of 1.5 PV water, the difference in oil recovery between the profile layer model and the geologic fine-grid model increases to 25%. Unlike the fine-grid geological model, the absence of crossflow in the profile layer model results in a lower oil recovery.

Both the indicator kriging and the turning bands model generate results very close to those generated by using the geological fine grid model. This is due to the fact that both models preserve the characteristics of the statistics (mean, standard deviation) and of the spatial distribution (correlation lengths) of rock permeability. Although not shown in the present work, both stochastic models will generate different spatial distributions of permeability if other values for the means, standard deviations and correlation lengths are selected.

Viscosity ratio 24.5

In the case of the more unfavorable viscosity ratio (24.5), at 1 PV fluid injected simulation results from the indicator kriging, predicted the lowest oil recovery (22% MOIP), the geological model predicted 31% MOIP and the most optimistic model was the 3 layer with 59% MOIP. (Fig. 20b). After injection of 2 pore volumes of water (Fig. 20b) the three layer model predicted 62% MOIP recovery while the geological, indicator kriging and the turning bands models predicted recoveries in the 32-37% MOIP range. Both stochastic models and the geological model converge toward the same 40% MOIP ultimate oil recovery. While for the more favorable viscosity ratio of 2.78, after 1 PV injection, the ratio of oil recovery from the three layer model to the geological model is 1.3. For the unfavorable viscosity ratio of 24.5, the oil recovery ratio increases to 1.9, indicating a larger discrepancy in the oil recovery prediction by different models.

In both viscosity ratio cases, the fine-grid uniform model followed by coarse-grid uniform model, provides the highest oil recovery predictions. However, the order of the recovery from the fine-grid geological, coarse-grid geological and the profile layer models differs in the two viscosity ratio cases (Fig. 20a,b).

The profile layer model is traditionally considered to be the most pessimistic input model, and this is illustrated in the 2.78 viscosity ratio case. However, in the 24.5 viscosity ratio case, the profile layer model as well as the other models studied,with the exception of indicator kriging model, resulted in higher oil recovery predictions than the more accurate geological model. These results illustrate the importance of generating a more detailed model when the reservoir is composed of discontinuous sand layers of contrasting permeability and the viscosity ratio is relatively unfavorable.

The difference in recoveries can be attributed to the adverse mobility ratio (24.5) that enables water to move more easily, by a factor of 9, than oil. The movement of water between the discontinuous high permeability layers results in water channeling rather than the more efficient sweep created by crossflow. The water relative permeability value in the water channels increases with flooding time; therefore, the injected water follows the existing channel and leaves a large volume of formation rock unswept. This mechanism is illustrated by the increased channeling in the geological model, 24.5 viscosity ratio case which is even more pronounced than in the profile layer model.

SUMMARY AND CONCLUSIONS

1. The more heterogeneous the reservoir, the more detailed information is required for constructing the permeability model. Knowledge of permeability and porosity statistics and especially correlation lengths are essential in computing correct oil recovery.

Comparison of the difference between the simplest permeability model and the most detailed, accurate permeability model in the two areas studied varies widely. In Area A, a relatively homogeneous area, with a permeability coefficient of variation of 0.58 and no distinct heterogeneity, the difference between the two models is 4% MOIP for the 2.78 viscosity ratio case at 1 PV and 10% MOIP for the 24.5 viscosity ratio case at 1 PV. In this type of rock, a single permeability value was an adequate representation of the area simulated.

In Area B, however, a layered system with permeability contrasts of 1:50 between the layers,and a permeability coefficient of variation of 1.28, a 20% MOIP difference occurs for the 2.78 viscosity ratio case at 1 PV and 28% MOIP difference for the 24.5-viscosity ratio case, underscoring the importance of detailed information in models for oil recovery predictions.

2. The more adverse the viscosity ratio, the more detailed information is required for constructing the permeability model. Comparison of the predicted oil recovery from the simplest permeability model, the uniform permeability model, to the most detailed, the geological model at two viscosity ratios indicates widely different predictions in Area B.
3. Both indicator kriging and turning bands models can be used to accurately predict the oil recovery if the correct permeability statistics and correlation lengths are used. Geostatistical analysis of analogous outcrops can be a valuable source of such information.

4. The traditionally used profile layer model resulted in an highly optimistic oil recovery prediction in the case of a unfavorable viscosity ratio and a highly pesimistic prediction for a low viscosity ratio for a reservoir with discontinuous layers with contrasting permeabilities. Due to failure to account for the distribution of sand layers with high permeability contrasts.

5. Small-scale permeability heterogeneity increases dispersivity of the water front, decreases the effective permeability, reduces fingering, and thereby improves sweep efficiency and increases oil production and improves waterfloods.

ACKNOWLEDGMENTS

This work was sponsored by the U.S. Dept of Energy under cooperative agreement DE-FC2283FE60149, AGIP SpA, ARCO Oil and Gas, BP Exploration, IITRI and RIPED.

REFERENCES

1. Tomutsa, L., S. Jackson, M. Szpakiewicz, I. Palmer. Geostatistical Characterization and Comparison of Outcrop and Subsurface Facies: Shannon Shelf Sand Ridges. Presented at 56th California Regional SPE Meeting, April 2-4, 1986 SPE Paper No. 15127.

2. Jackson, S. R., L. Tomutsa, R. Tillman. Quantified Spatial Variations of Reservoir Parameters in Shelf Sandstone Ridge Deposits, First Annual Report, Feb. 1988, Contract Number B08677-1, (proprietary report).

3. Tomutsa, L. and J. Knight. Effect of Reservoirs Heterogeneities on Waterflood and EOR Chemical Performance. Depart of Energy Report No. NIPER-235, July 1987.

4 Muskat, M. The Effect of Permeability Stratification in Complete Water Drive Systems. Trans., AIME, v. 189, December 1950, pp. 349-358.

5. Dykstra, M. and R. L. Parsons. The Prediction of Oil Recovery by Waterflood. Secondary Recovery of Oil in the United States, 2nd Ed. API, 1950, pp. 160-170.

6. Willhite, G. P. Waterflooding. SPE monograph, 1986.

7. Warren, J. E. and H. S. Price. Flow in Heterogeneous Porous Media. SPEJ, v. 1, No. 3, Sept. 1961, pp. 153-169.

8. Huppler, J. D. Numerical Investigation of the Effects of Core Heterogeneities on Waterflood Relative Permeabilities. SPEJ, v. 10, No. 4, Dec. 1970, pp. 381-392.

9. Hearn, C. C. Simulation of Stratified Waterflooding by Pseudo Relative Permeability Curves. J. Pet. Tech., v. 23, July 1971, pp. 805-813.

10. Kortekaas, T. F. M. Water/Oil Displacement Characteristics in Cross Bedded Reservoir Zones. Pres. at Soc. Petrol. Eng. 58th Ann. Tech. Conf. and Exhib., San Francisco; SPEJ, v. 15, No. 6, Dec. 1985, pp. 917-926.

11. Smith, L. and F. W. Schwartz. Mass Transport 3. Role of Hydraulic Conductivity Data in Prediction. Water Resources Research, v. 17, No. 5, Oct. 1981, pp 1463-1479.

12. Delhomme, J. P. Spatial Variability and Uncertainty in Groundwater Flow Parameters A Geostatistical Approach. Water Resources Research, v. 15, No. 2, April 1979.

13. Sultan, Ahmand Junaid, John P. Heller and Allan L. Gutjahr. Generation and Testing of Random Fields and the Conditional Simulation of Reservoirs. Petroleum Society of CIM/SPE International Tech. Meeting, Calgary,1990.

14. Journel, A. G.and C. J. Huijbregts. Mining Geostatistics, Academic Press, 1978.

15 Lasseter, T. J., T. R. Waggoner and L. W. Lake. Reservoir Heterogeneities and Their Influence on Ultimate Recovery. In Reservoir Characterization. Eds., L. W. Lake and H. B. Carroll, Academic Press, 1986, pp. 545-560.

16. Hewett, T. A. Fractal Distributions of Reservoir Heterogeneity and Their Influence on Fluid Transport. Pres. at 61st Ann. Technical Conf. and Exhib of SPE in New Orleans, Oct. 1986. SPE paper 15386.

17 Begg, S. H., R. R. Carter, and P. Dranfield. Assigning Effective Values to Simulator Gridblock Parameters for Heterogeneous Reservoirs. November 1989. SPE Reservoir Engineering.

18. Haldorsen, H. H., E. Damsleth,. Stochastic Modeling, JPT, vol. 42, no. 4, April 1990 pp. 405-412.

19. Weber, K. J. and L. C. van Geuns. Framework for Constructing Clastic Reservoir Simulation Models. Pres. at 69 thSPE Annual Technical Conf and Exhibit, San Antonio, TX, 1989., SPE 19582.

20. Journel, A. G. and F. G. Alabert. New Method for Reservoir Mapping. In: JPT, vol. 42, no. 2, February 1990.

21 Gomez-Hernandez, J. J. and R. M. Srivastava. ISIM3D: An ANSI-C Three-Dimensional Multiple Indicator Conditional Simulation Program, Computers and Geosciences Vol. 16, No. 4, pp. 395-440, 199.

22. Wilson, J. L. and A. Gutjahr. Synthetic Generation of Random Permeability Fields for Heterogeneous Reservoir Simulation. Pres. at SPE Symposium on Reservoir Simulation, Houston, TX, Feb. 1989. SPE 18435.

23. Zimmerman, D. A. and J. L. Wilson. Description of and Users Manual for TUBA: A Computer Code for Generating Two-Dimensional Fields via the Turning Bands Method. Prepared by New Mexico Institute for Mining & Technology.,July 1990. Distributed by GRAM, Inc, Albuquerque, New Mexico.

TABLE 1. - Permeability statistics of measured core plugs

	Area A		Area B	
	Permeability, md	Natural log permeability	Permeability, md	Natural log permeability
Sample size	31	31	47	47
Average	1622	7.10	466	5.05
Geometric mean	1215	–	156	–
Standard deviation	945.75	0.94	595.10	1.94

[1]Standard deviation of permeability divided by the mean of permeability.

TABLE 2. - Permeabilities (md) assigned to layers in the Vertical Profile Layer models in Area A

Layer	Vertical profile 1	Vertical profile 2	Vertical profile 3
1	642	64	1,563
2	1,312	2,803	1,768
3	1,982	2,970	149
4	2,504	2,805	1,098
5	799	1,508	2,069

TABLE 3. - Permeabilities (md) assigned to layers in the profile layer model in Area B

Layer	Horizontal permeability
1	35
2	47
3	46
4	36
5	23
6	50
7	392
8	358
9	74
10	11
11	548
12	559
13	14
14	450
15	14
16	6
17	13

TABLE 4. - Summary statistics of directional permeabilities

	Two-inch cylindrical cores	Cubic samples, x direction	Cubic samples, y direction	Cubic sample, z direction (vertical)
Sample size	81	73	75	74
Average, md	1,079.51	1,020.78	1,099.12	639.52
Median, md	1,047.78	1,022.57	1,112.79	659.84
Geometric mean, md	622.78	592.53	742.52	221.22
Standard deviation, md	712.39	684.60	712.97	563.80
Minimum, md	1.92	3.44	2.73	0.78
Maximum, md	3,442.48	3,243.45	3,418.63	2,771.06

TABLE 5a. - Relative permeability for rocks with permeability greater than 200 md Area A

Fluid saturation	Relative permeability	
	Oil	Water
0	0.	0.
0.15	0.	0.
0.24	0.03	0.01
0.30	0.06	0.02
0.40	0.18	0.04
0.50	0.37	0.07
0.60	0.58	0.11
0.70	0.83	0.17
0.76	1.00	0.31
1.82	1.00	0.31
1.00	1.00	1.00

TABLE 5b. - Relative permeability for rocks with permeability less than 200 md Area A

Fluid saturation	Relative permeability	
	Oil	Water
0	0.	0.
0.28	0.	0.
0.32	0.03	0.0016
0.41	0.11	0.0045
0.57	0.40	0.0244
0.69	0.82	0.0481
0.72	1.00	0.0583
0.74	1.00	0.0649
1.00	1.00	0.0649

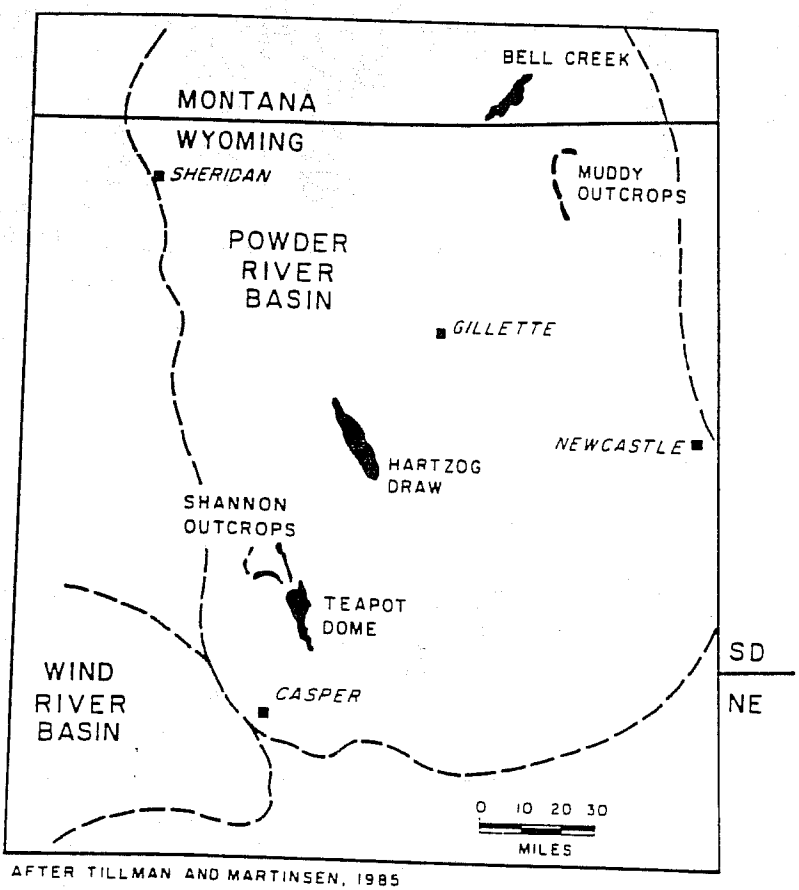

FIGURE 1. - Location of Shannon outcrops, Powder River Basin, Wyoming.

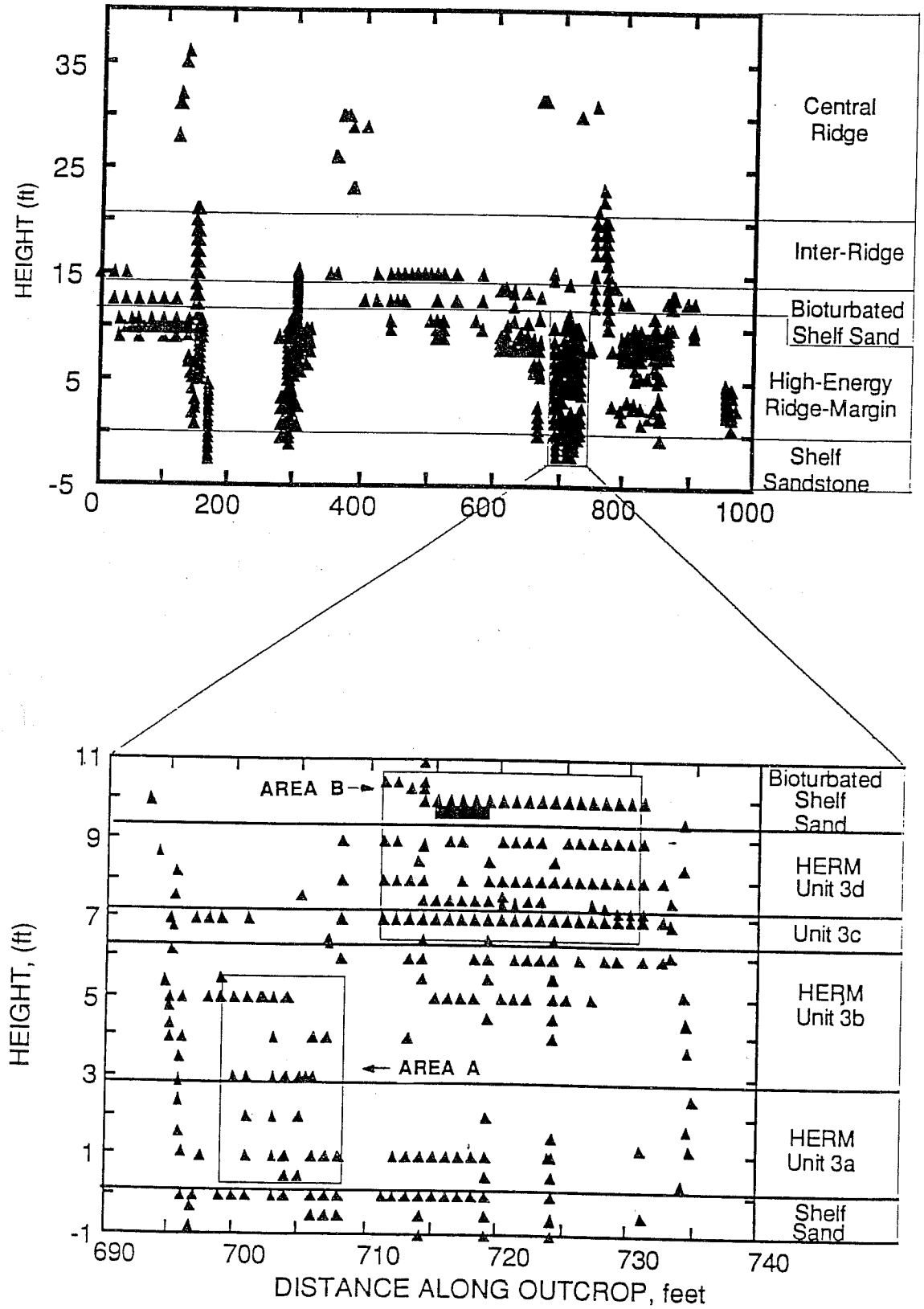

FIGURE 2. - Outcrop sample locations of 1-inch diameter core plugs.

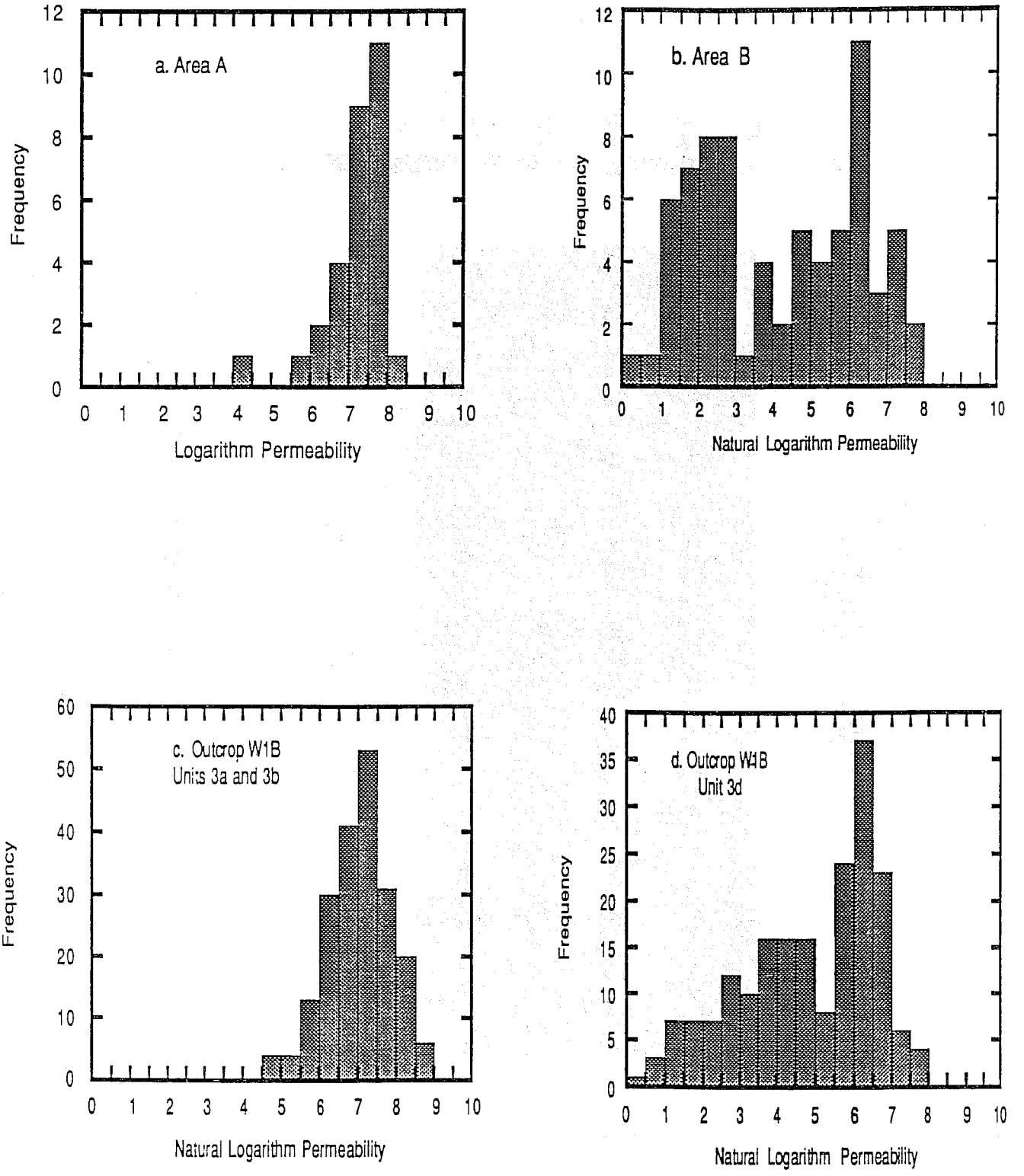

FIGURE 3. - Permeability histograms for Shannon outcrop data.

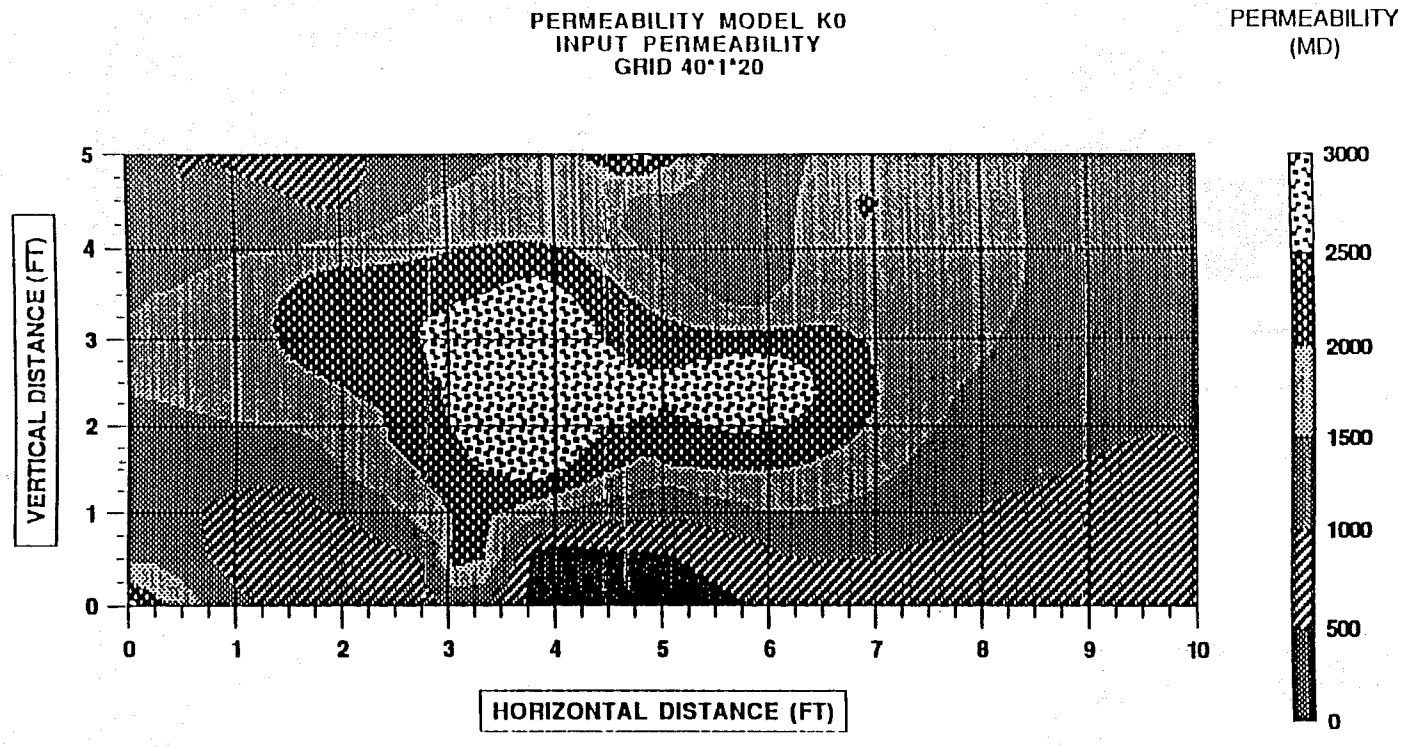

FIGURE 4 - Kriged Permeability K0 Model, grid 40x1x20, Area A.

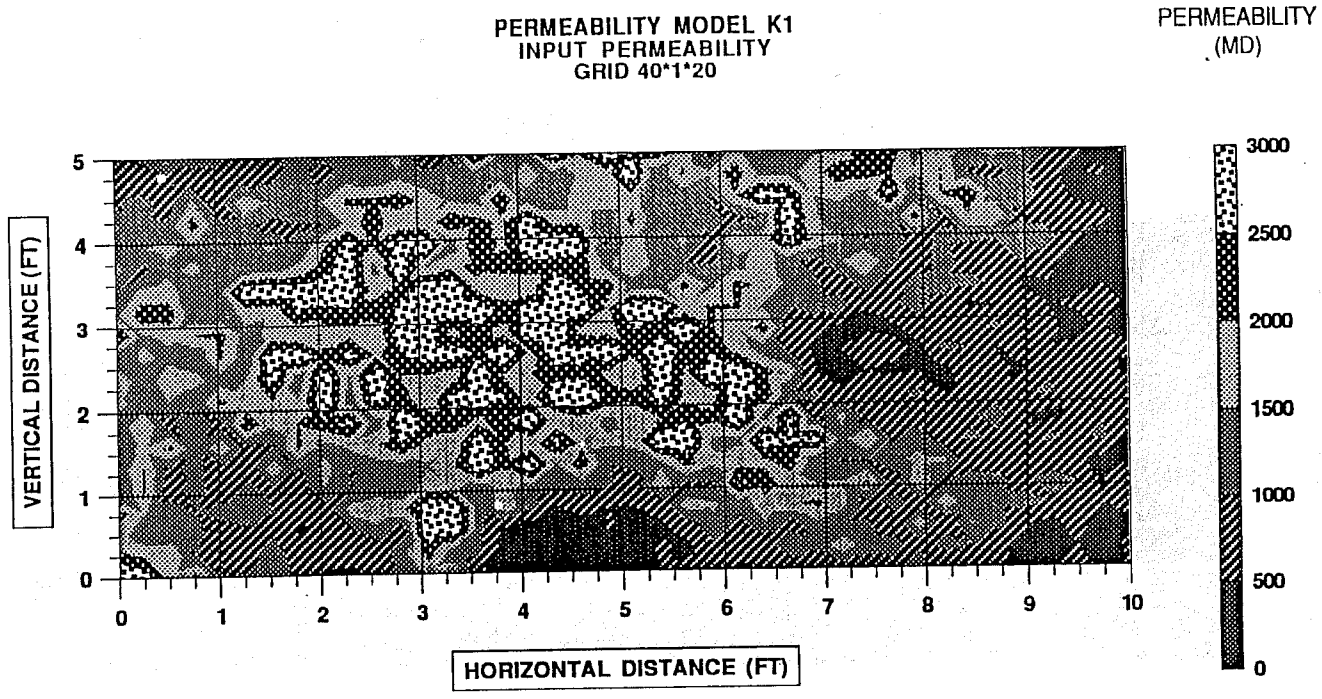

FIGURE 5 - Kriged Permeability K1 Model, grid 40x1x20, Area A.

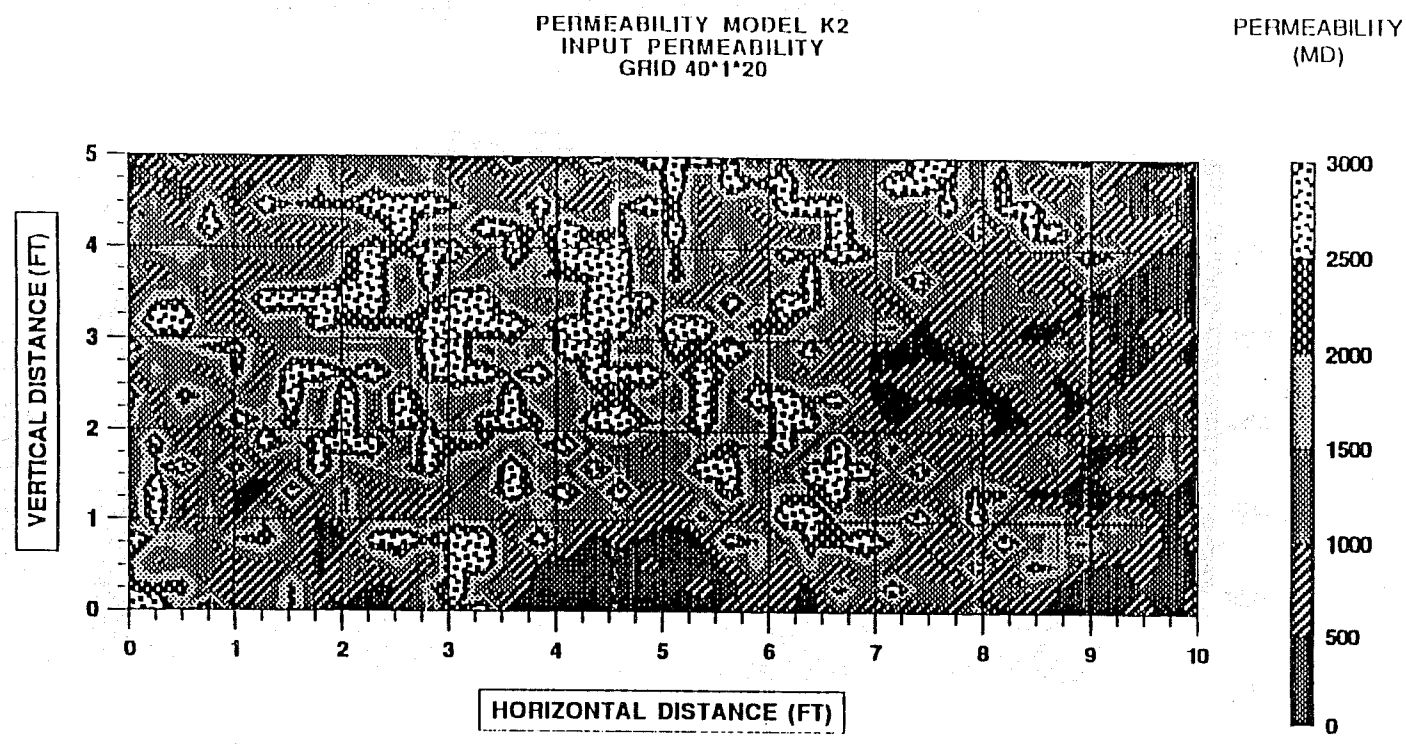

FIGURE 6 - Kriged Permeability K2 Model, grid 40x1x20, Area A.

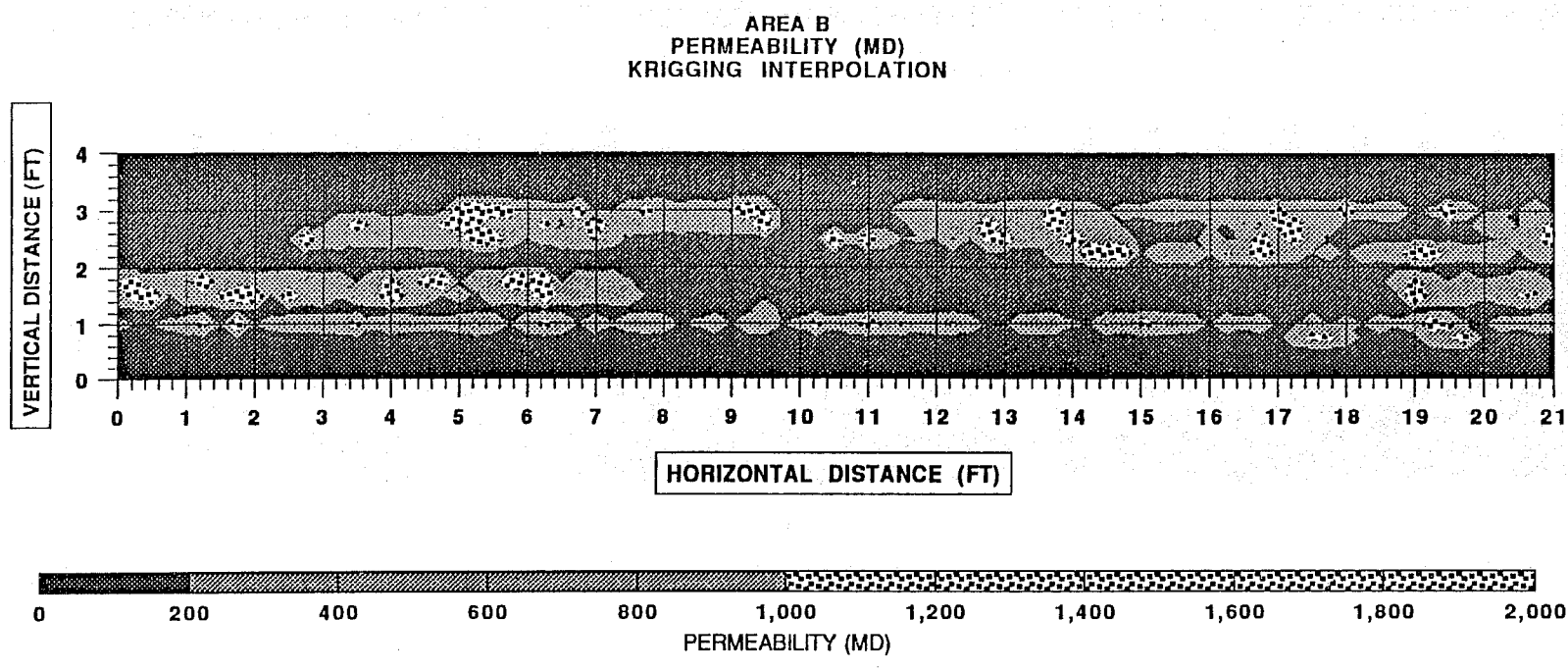

FIGURE 7. Geological Permeability Model, grid 85x1x17, Area B

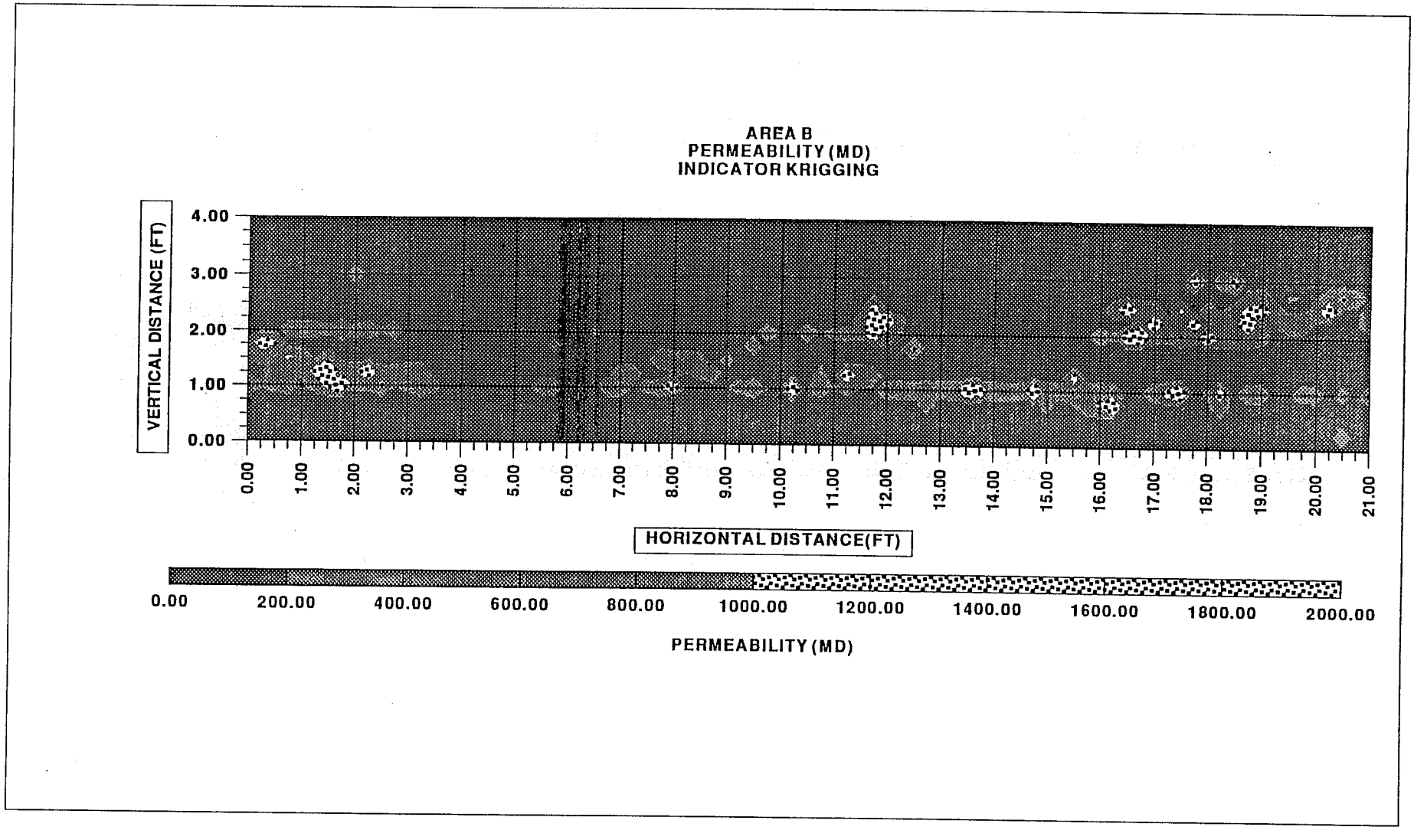

FIGURE 8. Indicator Kriging Permeability Model, Area B

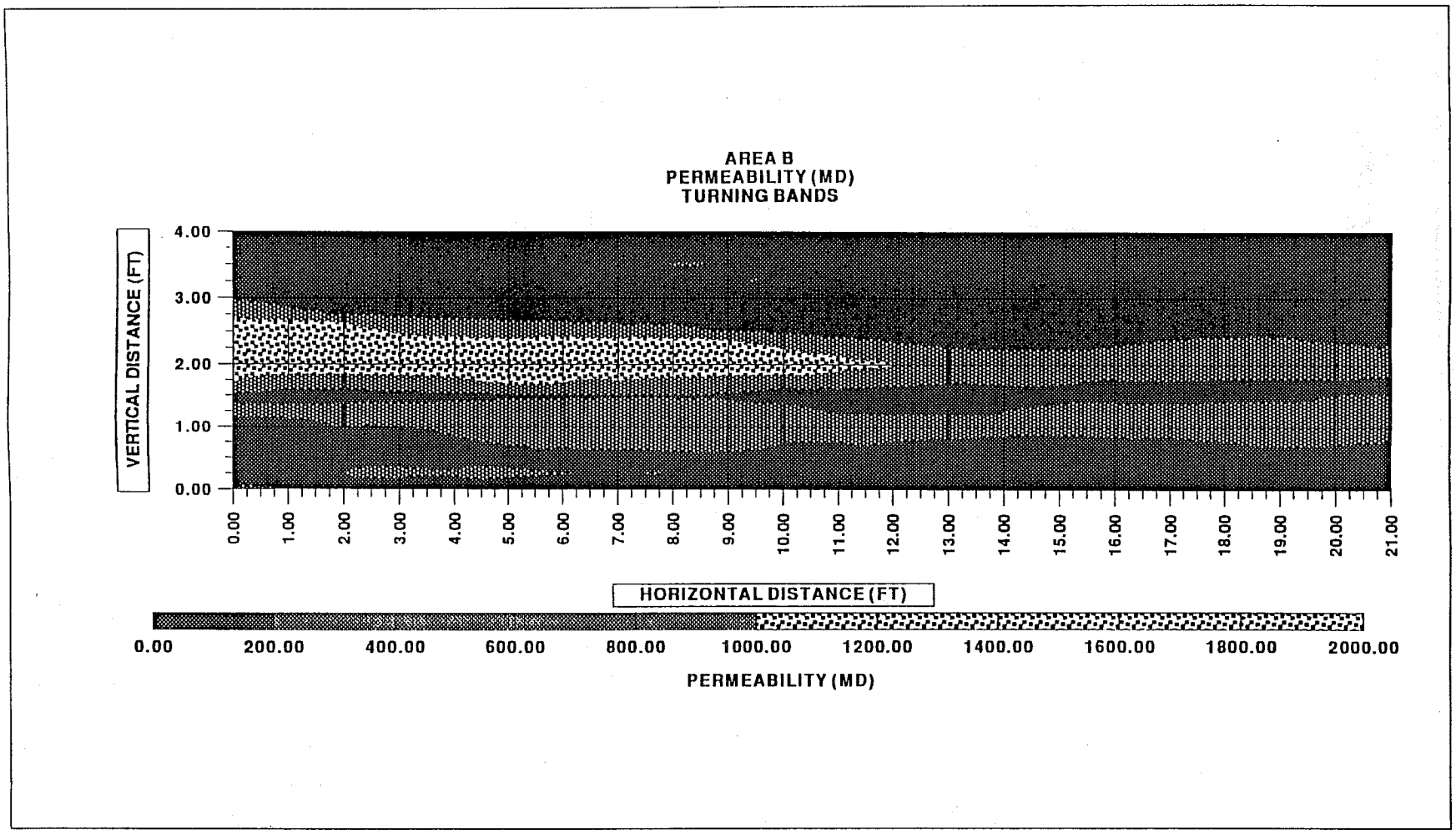

FIGURE 9. Turning Bands Permeability Model, Area B

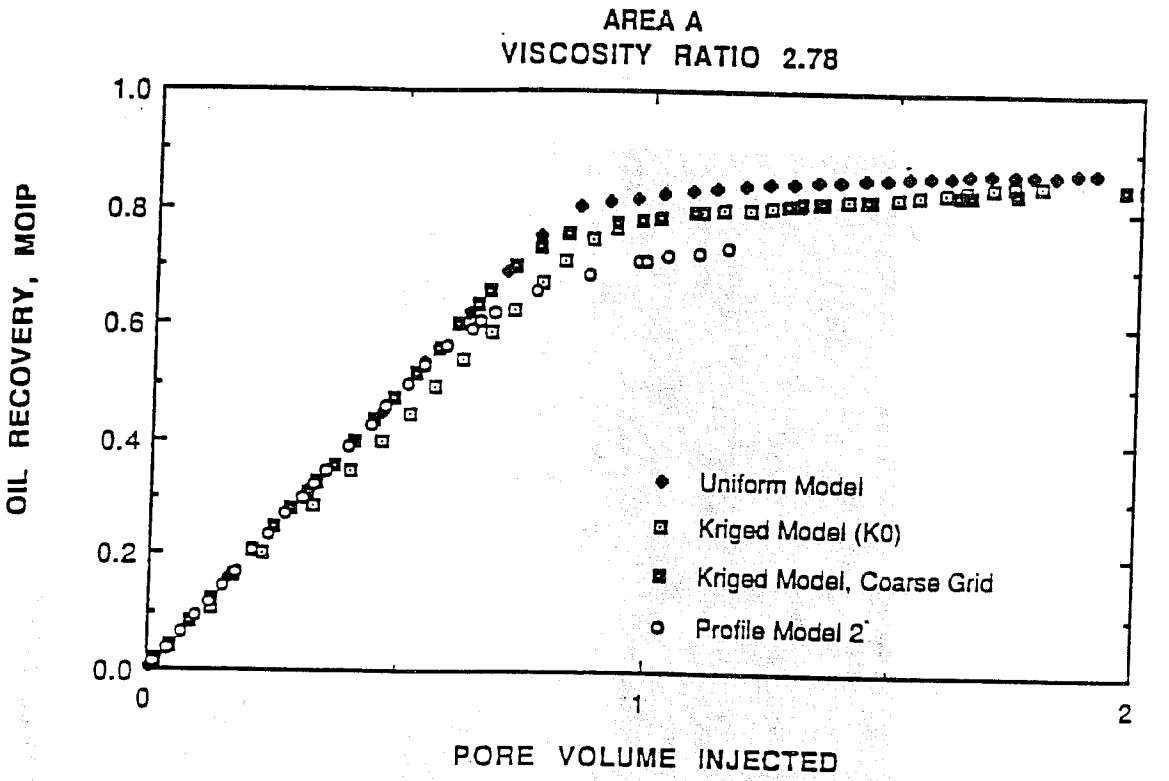

FIGURE 10a. Cumulative oil production (MOIP) for various permeability models in Area A, viscosity ratio 2.78

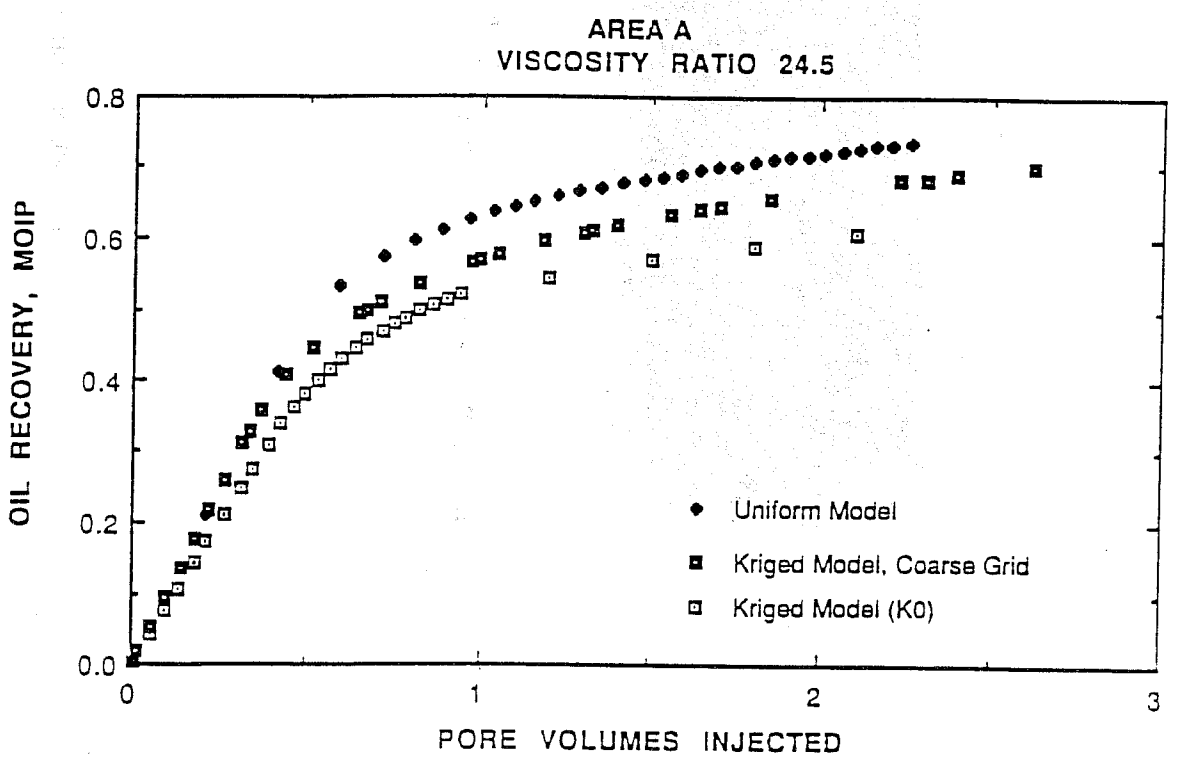

FIGURE 10b. Cumulative oil production (MOIP) for various permeability models in Area A, viscosity ratio 24.5

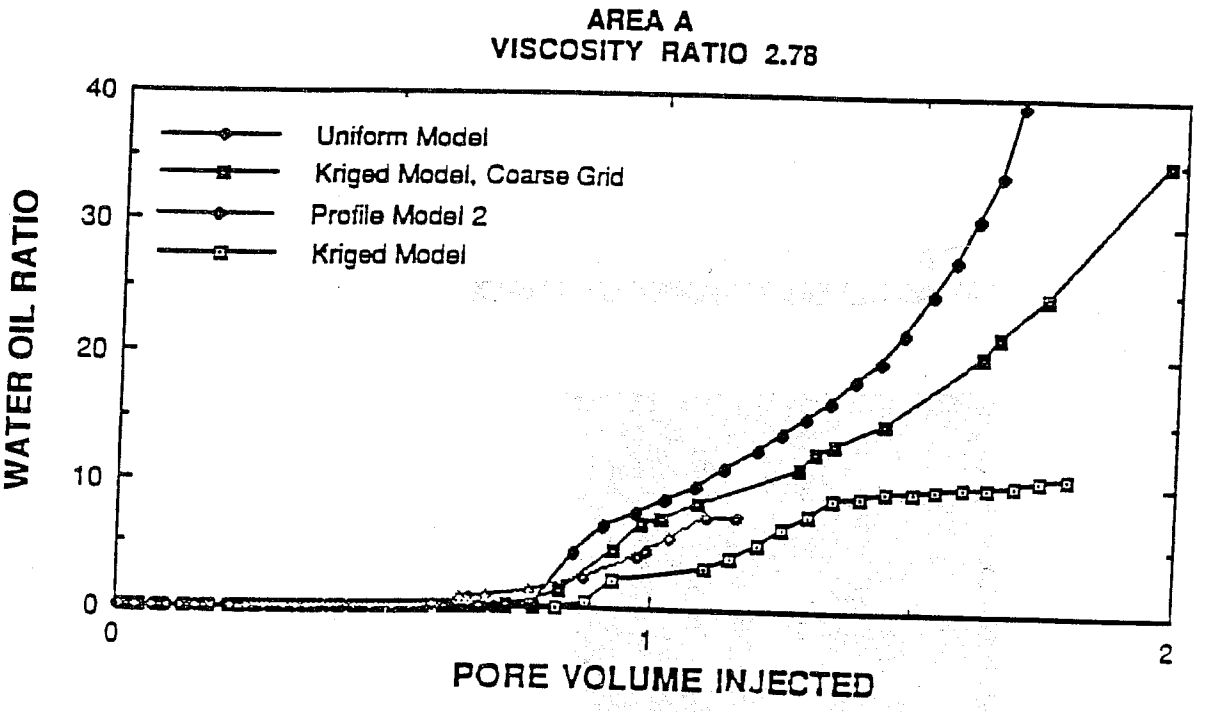

FIGURE 11a. Water-oil ratio for permeability models in Area A, viscosity ratio 2.78

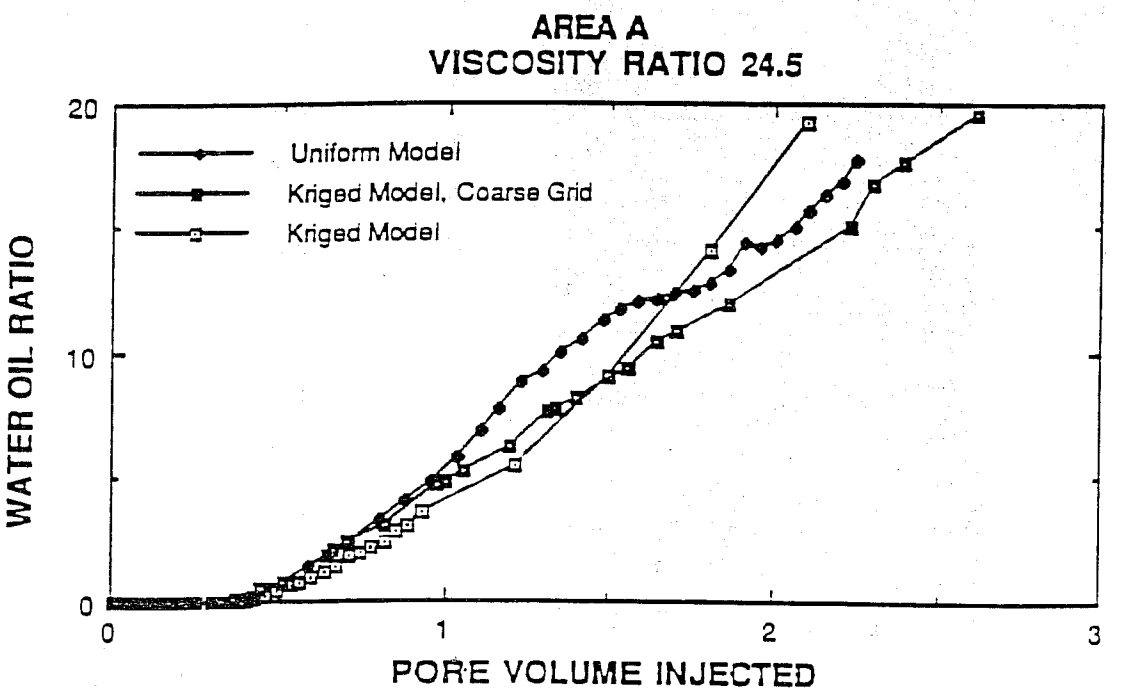

FIGURE11b. Water-oil ratio for permeability models in Area A, viscosity ratio 24.5

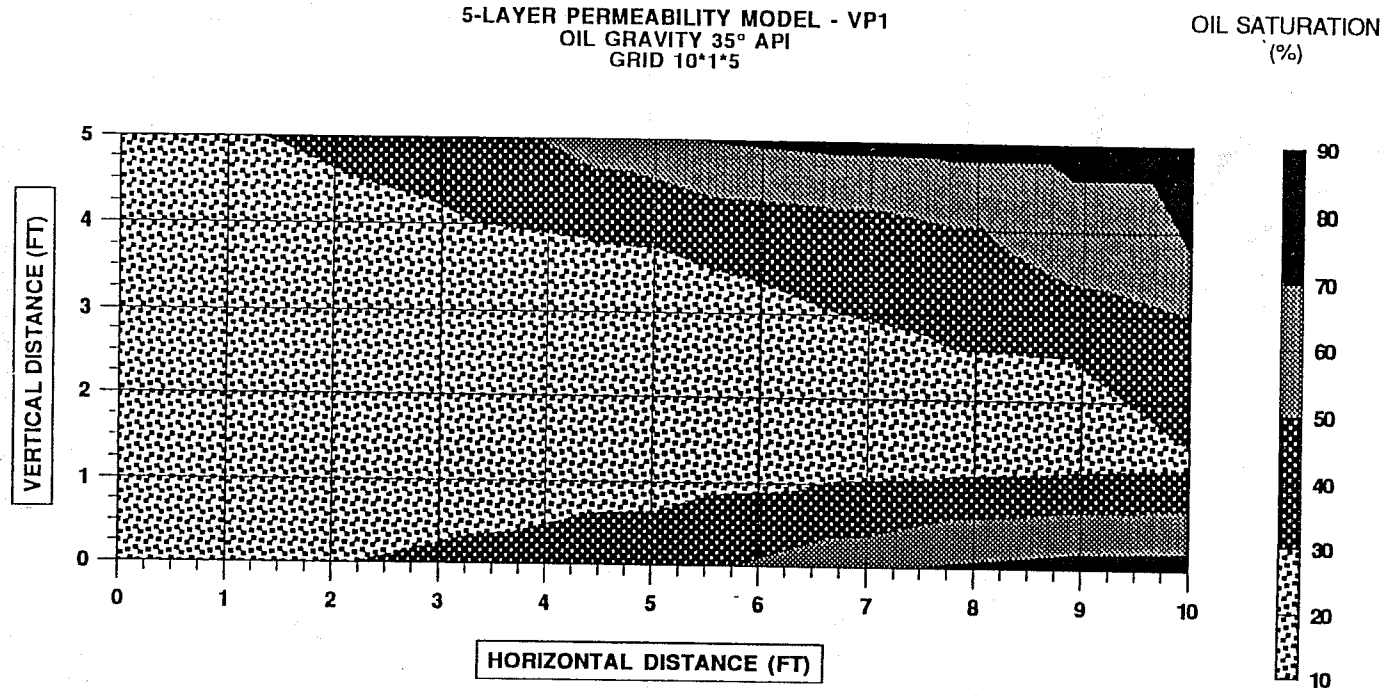

FIGURE12. Oil saturation distribution after 0.64 PV injection, Profile Layer Model, vertical profile 1 (VP1),viscosity ratio 2.78, Area A

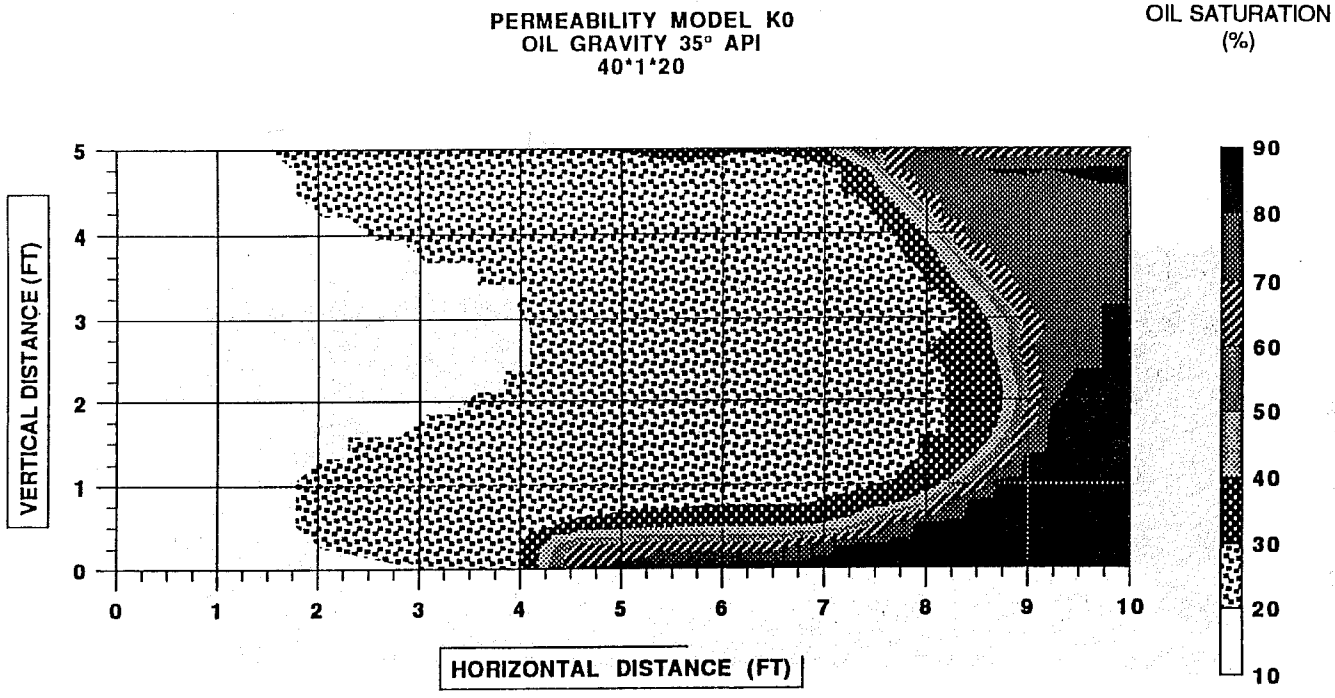

FIGURE 13. Oil saturation distribution after 0.64 PV injection, Kriged Permeability K0 Model, viscosity ratio 2.78, Area A

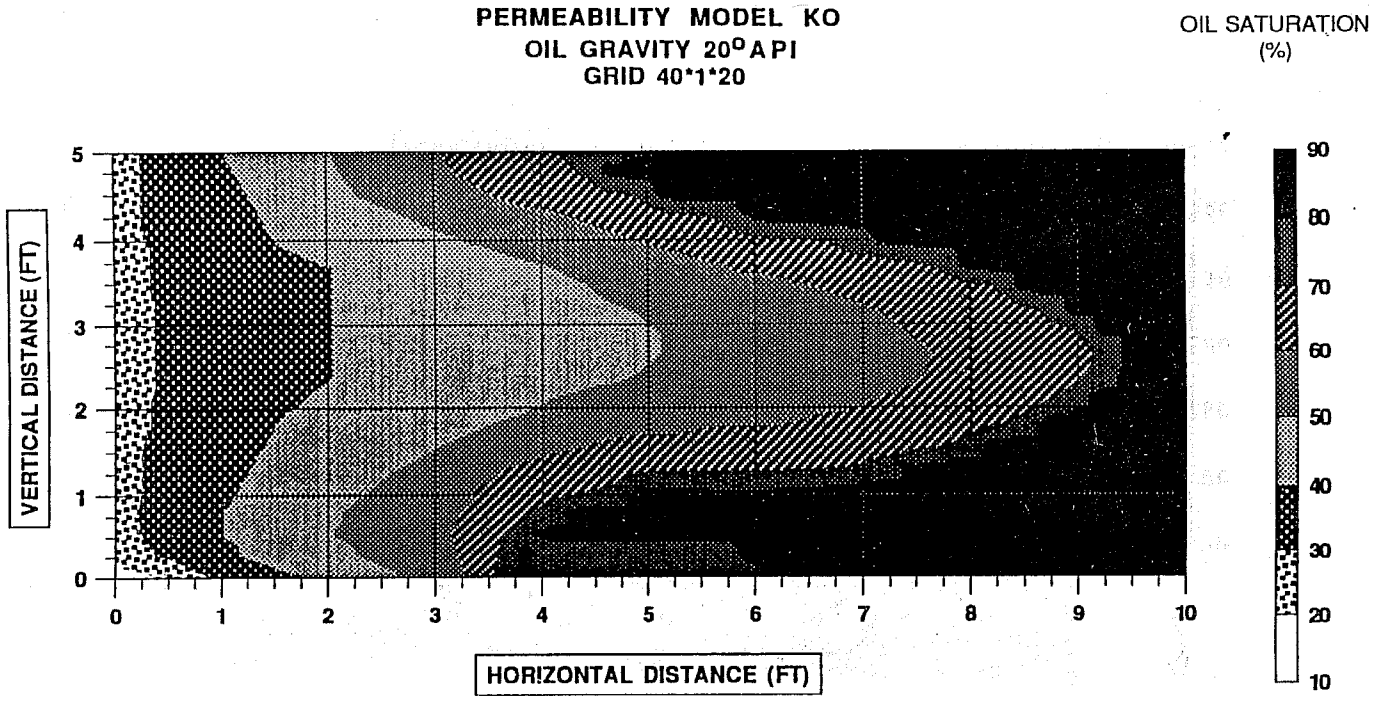

FIGURE 14. Oil saturation distribution after 0.64 PV injection, Kriged Permeability K0 Model, viscosity ratio 24.5, Area A

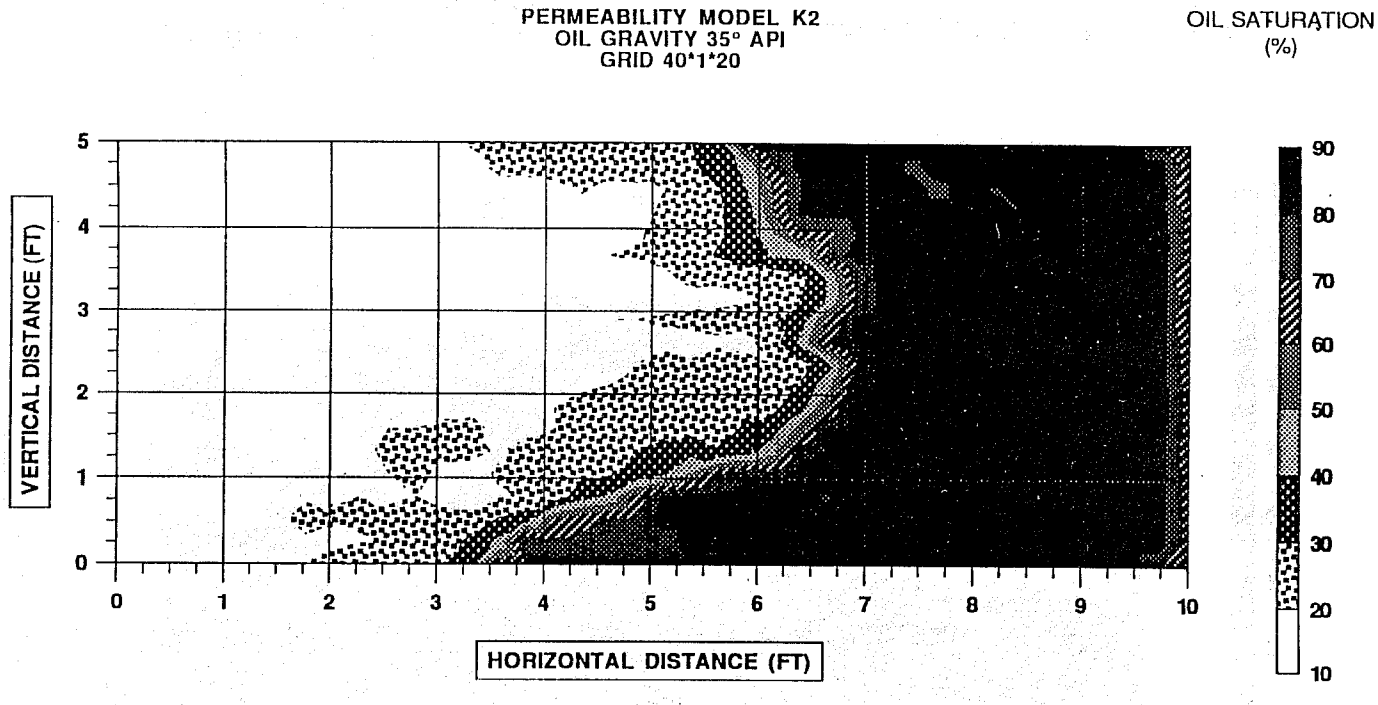

FIGURE 15. Oil saturation distribution after 0.64 PV injection, Kriged Permeability K2 Model, viscosity ratio 2.78, Area A

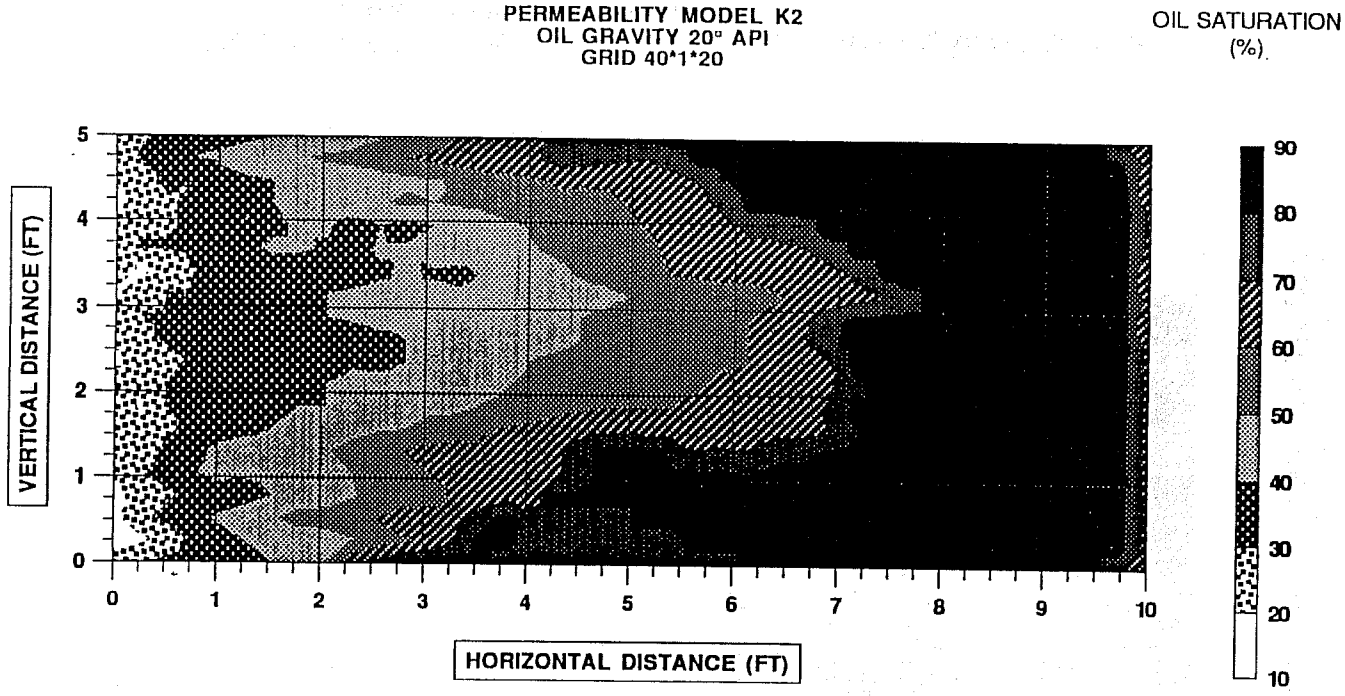

FIGURE 16. Oil saturation distribution after 0.64 PV injection, Kriged Permeability K2 Model, viscosity ratio 24.5.

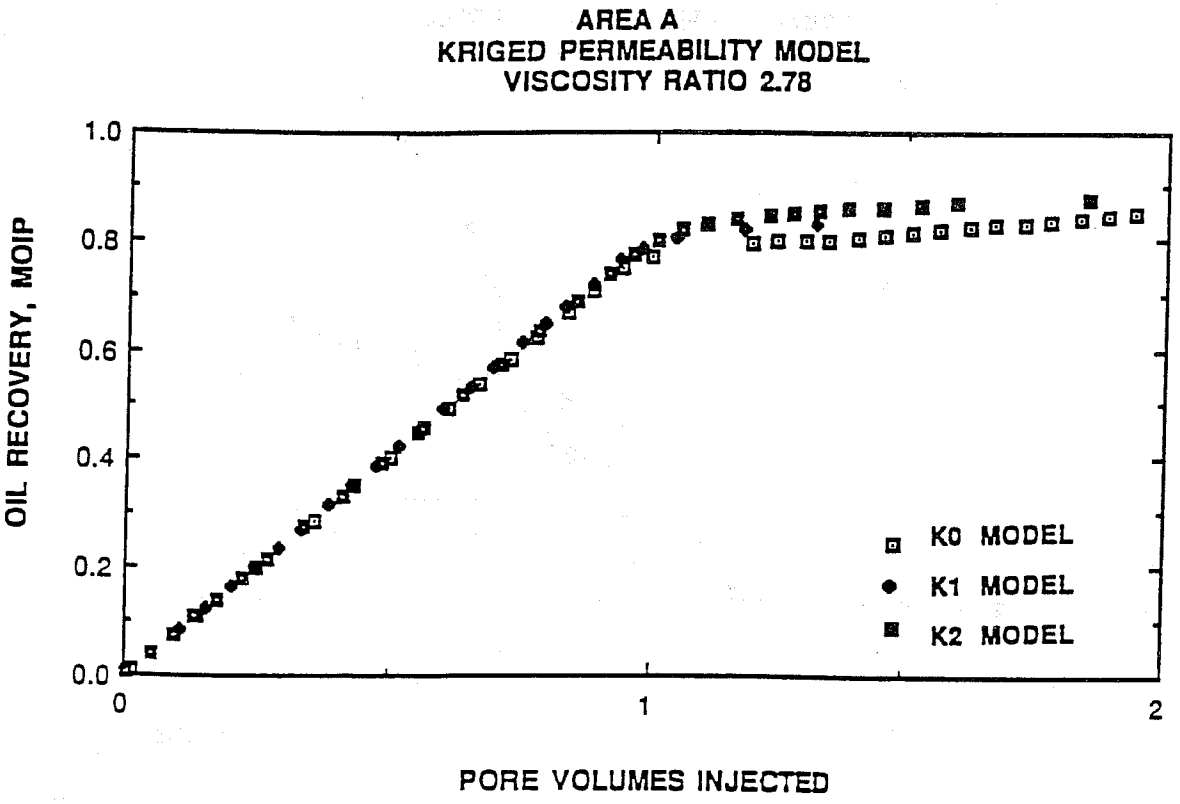

FIGURE 17a. Effect of random components on cumulative oil production (MOIP), Kriged Permeability Models, viscosity ratio 2.78, Area A

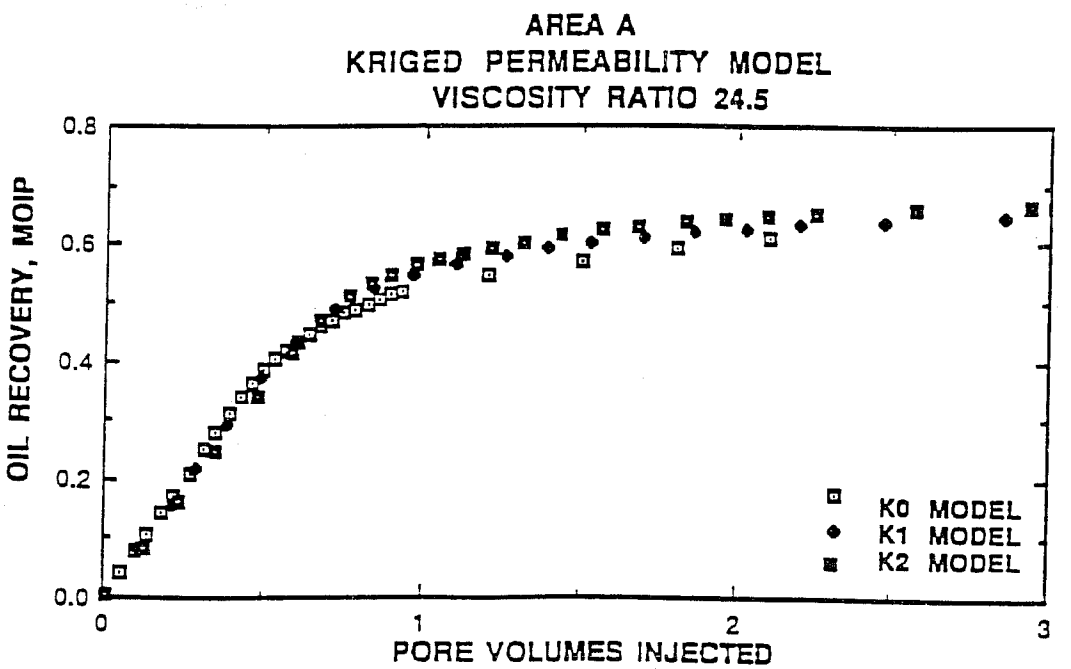

FIGURE 17b. Effect of random components on cumulative oil production (MOIP), Kriged Permeability Models, viscosity ratio 24.5, Area A

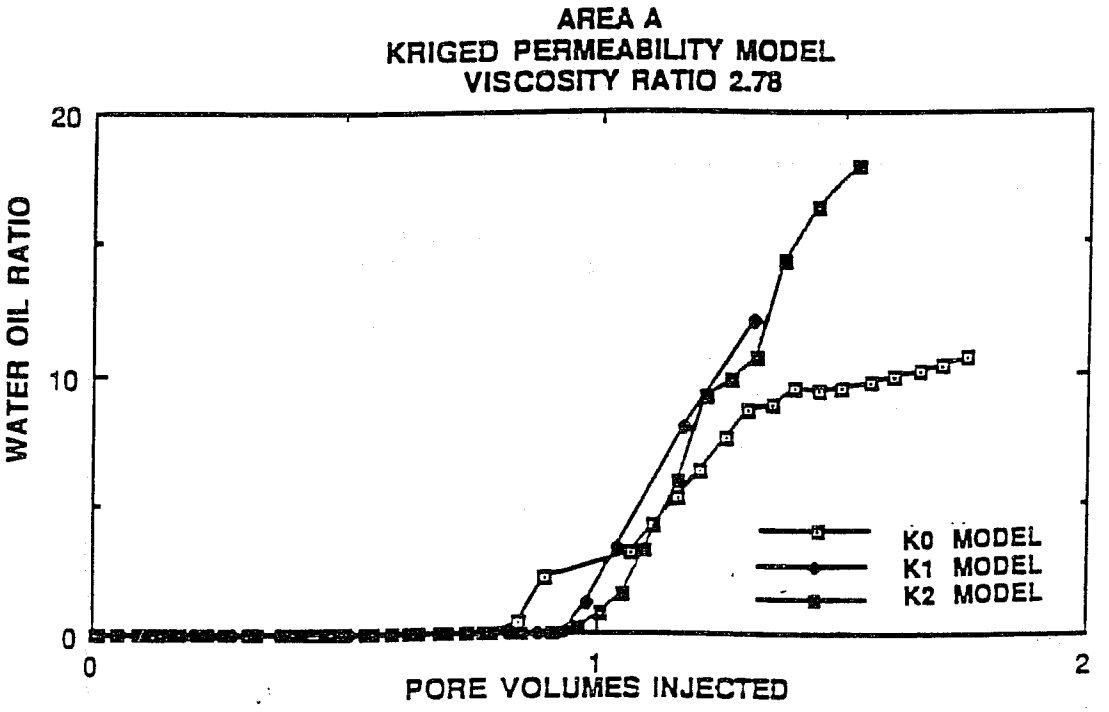

FIGURE 18a. Effect of random components on water-oil-ratio, Kriged Permeability Models, viscosity ratio 2.78, Area A

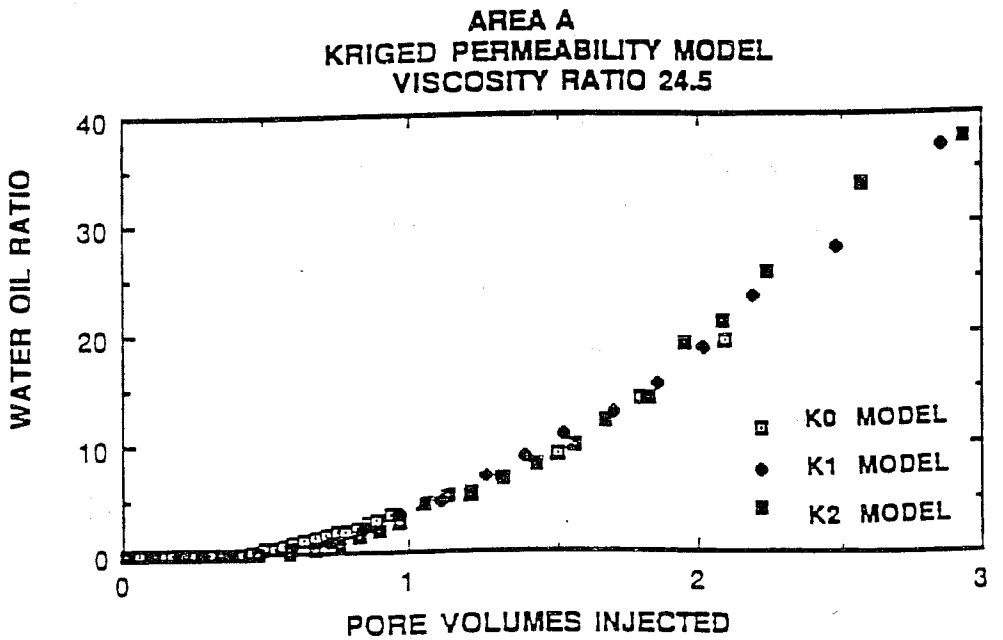

FIGURE 18b. Effect of random components on water-oil-ratio, Kriged Permeability Models, viscosity ratio 24.5, Area A

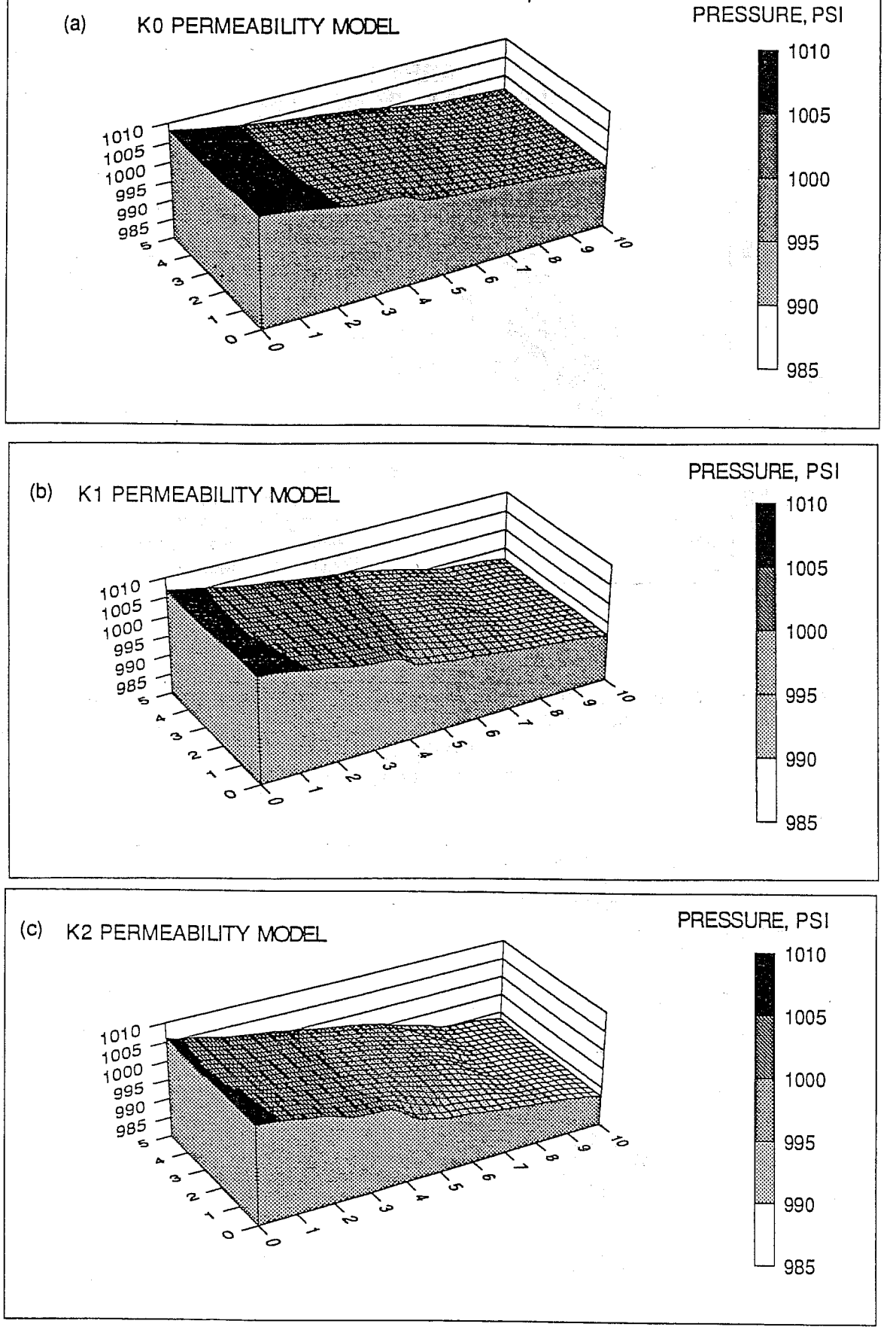

FIGURE 19. Pressure distributions resulting from waterflood simulations of (a) K0 permeability model, (b) K1 Permeability Model, and (c) K2 Permeability Model, Area A

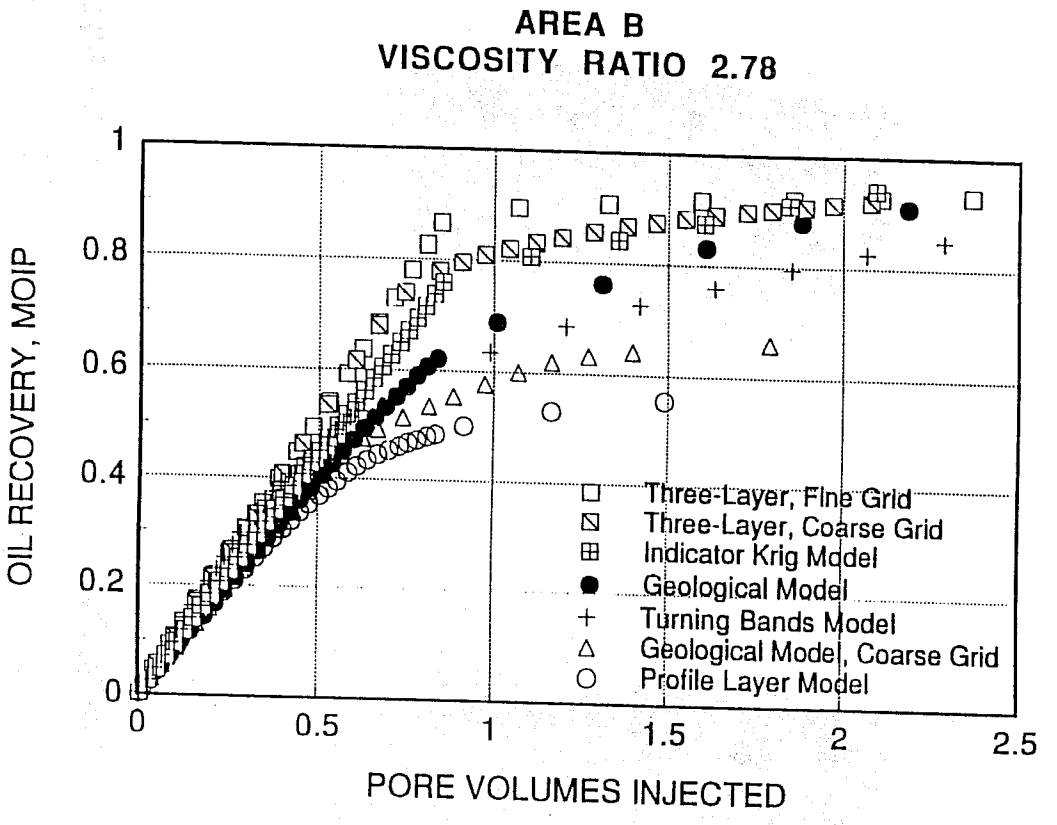

FIGURE 20a. Comparison of cumulative Oil Production (MOIP) for various permeability models, viscosity ratio 2.78, Area B

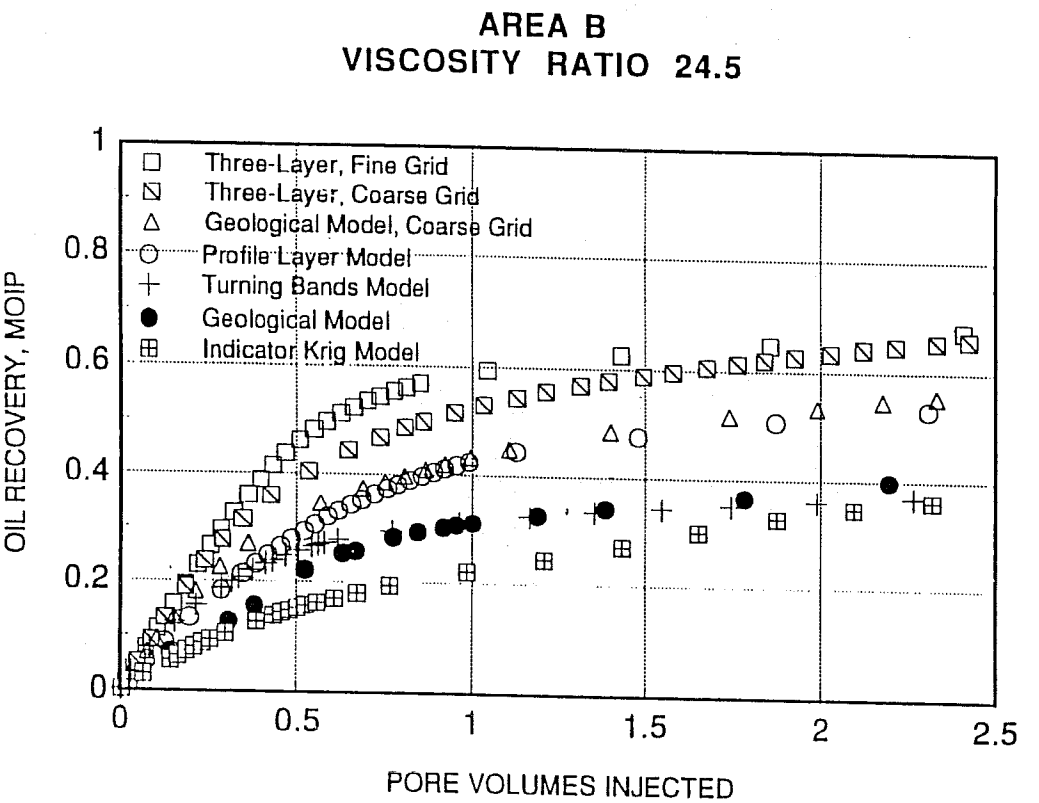

FIGURE 20b. Comparison of cumulative Oil Production (MOIP) for various permeability models, viscosity ratio 24.5, Area B

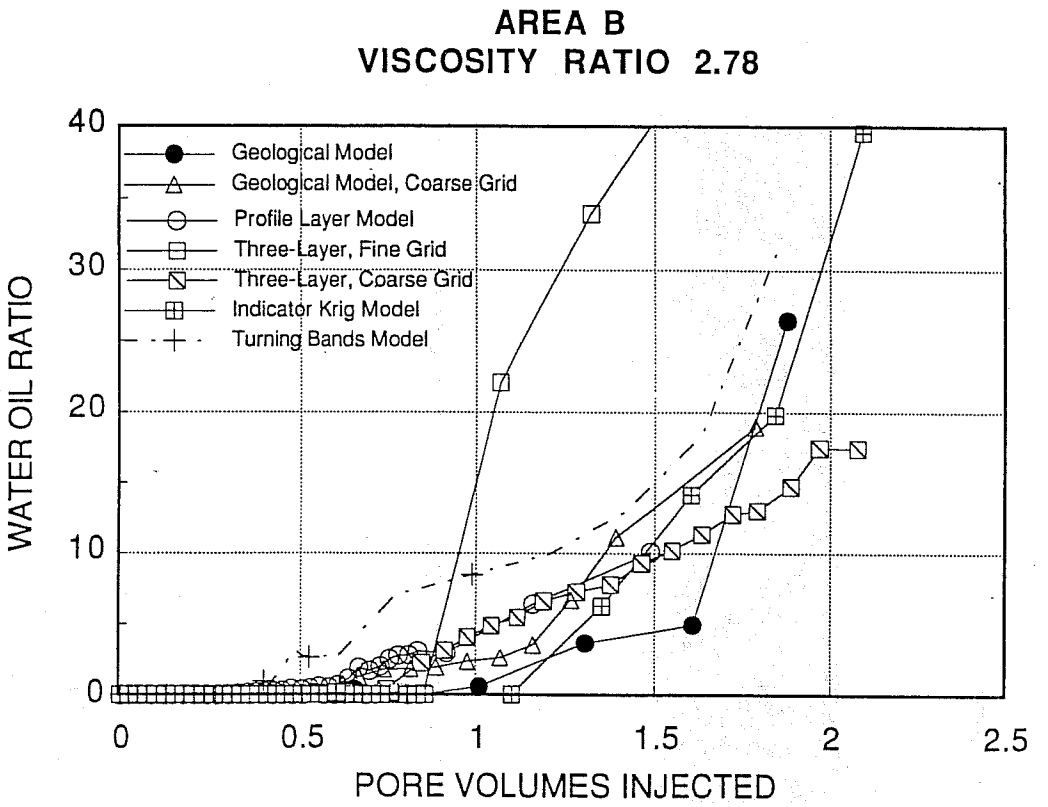

FIGURE 21a Comparison of the water-oil-ratio for the Area B Models, viscosity ratio 2.78

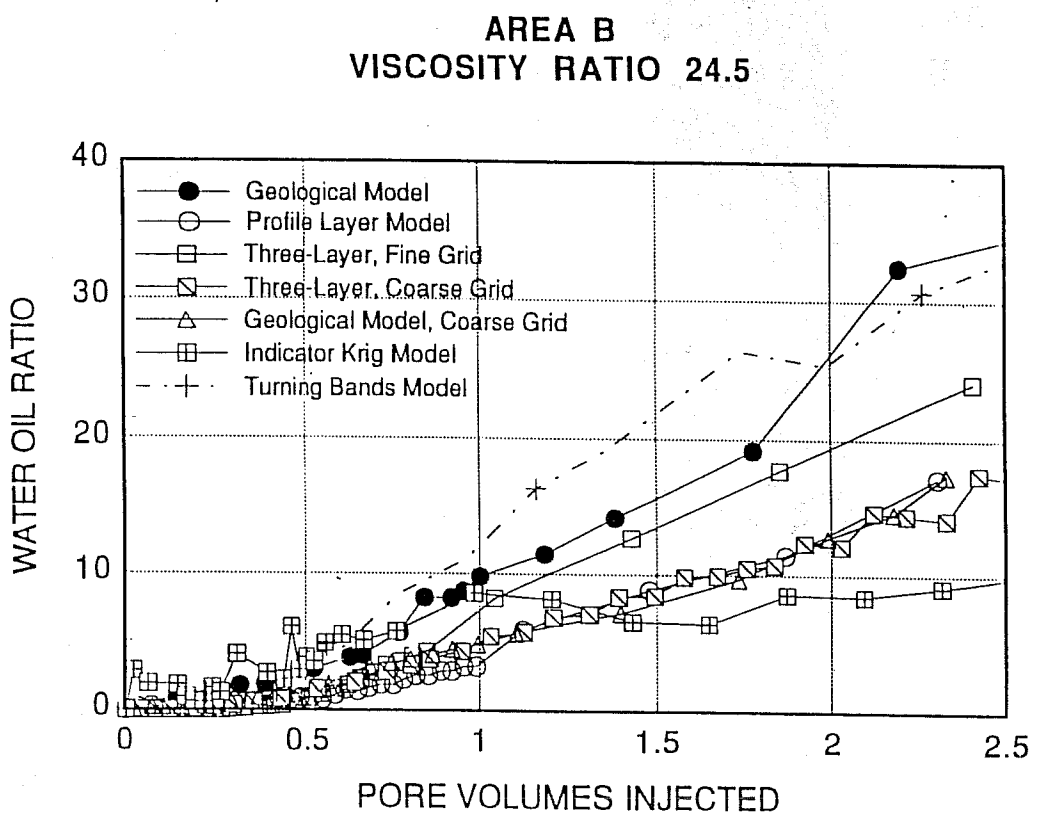

FIGURE 21b. Comparison of the water-oil-ratio for the Area B, Permeability Profile and Geological Coarse-Grid Models, viscosity ratio 24.5

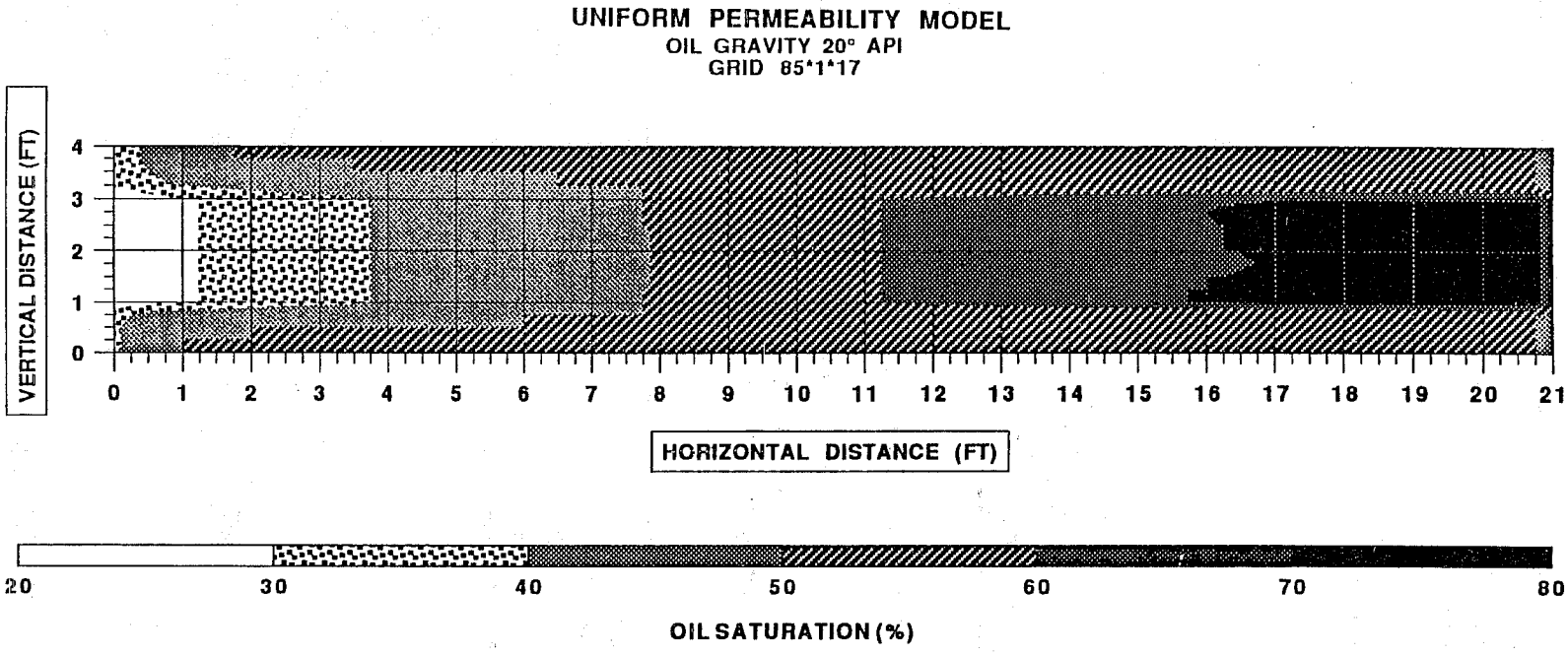

FIGURE 22 Oil saturation distribution, Uniform (three-layer) Model, viscosity ratio 24.5, Area B

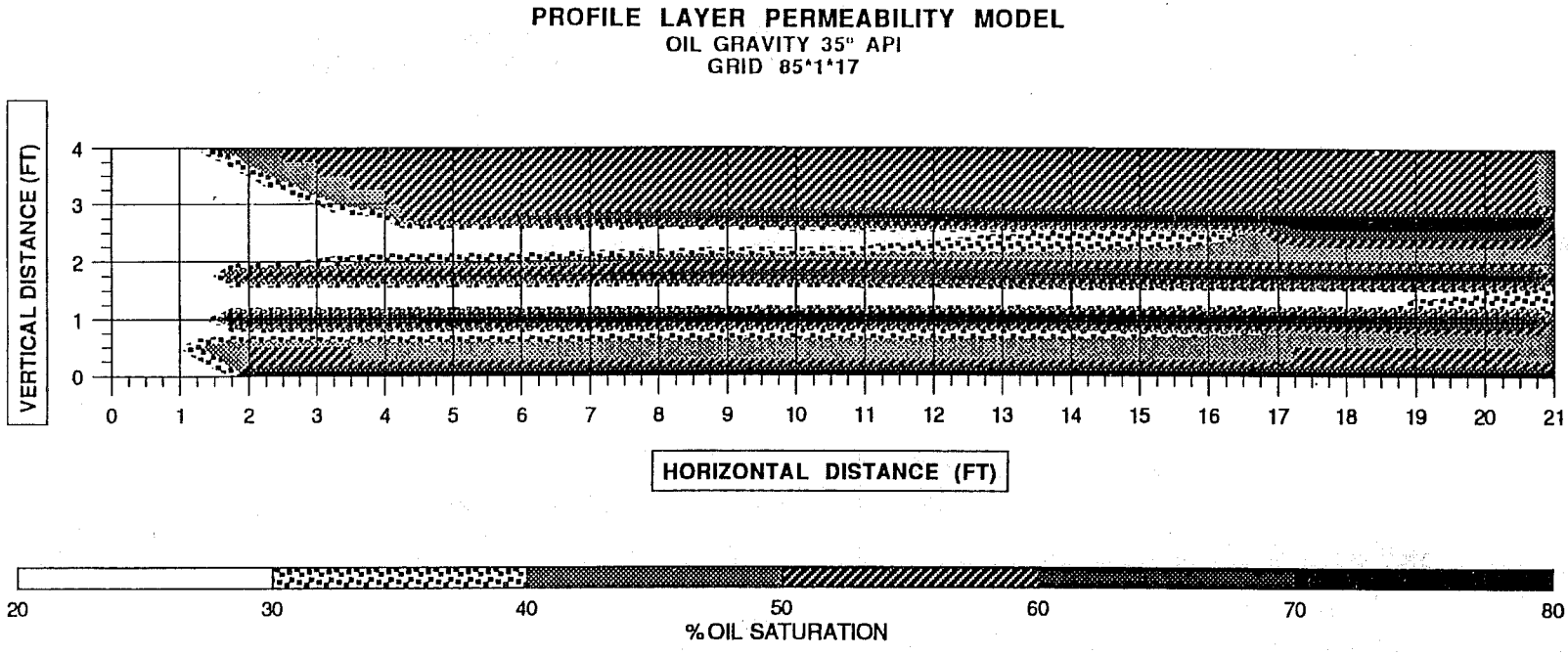

FIGURE 23. Oil saturation distribution after 0.32 PV injection, Profile Layer Model, viscosity ratio 2.78, Area B

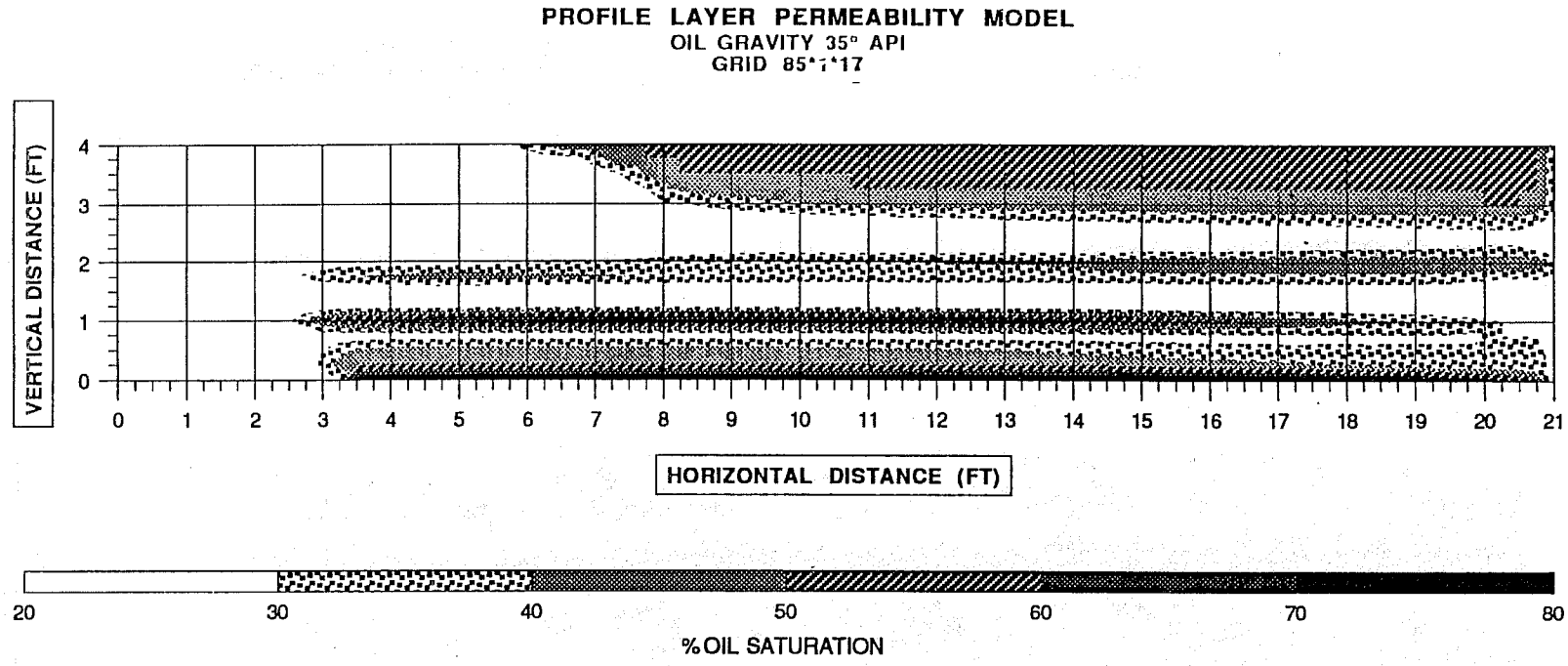

FIGURE 24. Oil saturation distribution after 0.85 PV injection, Profile Layer Model, viscosity ratio 2.78, Area B

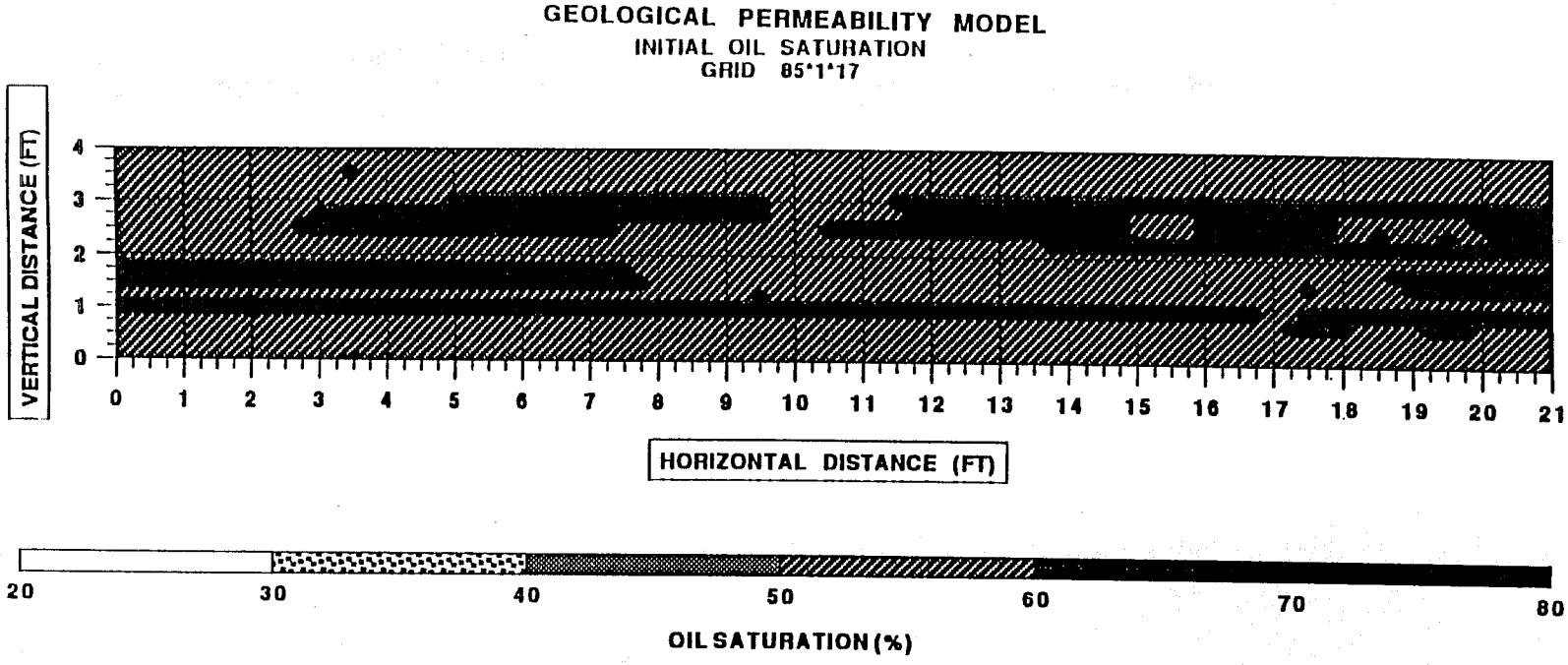

FIGURE 25. Initial oil saturation distribution, Fine-Grid Geological Model, Area B

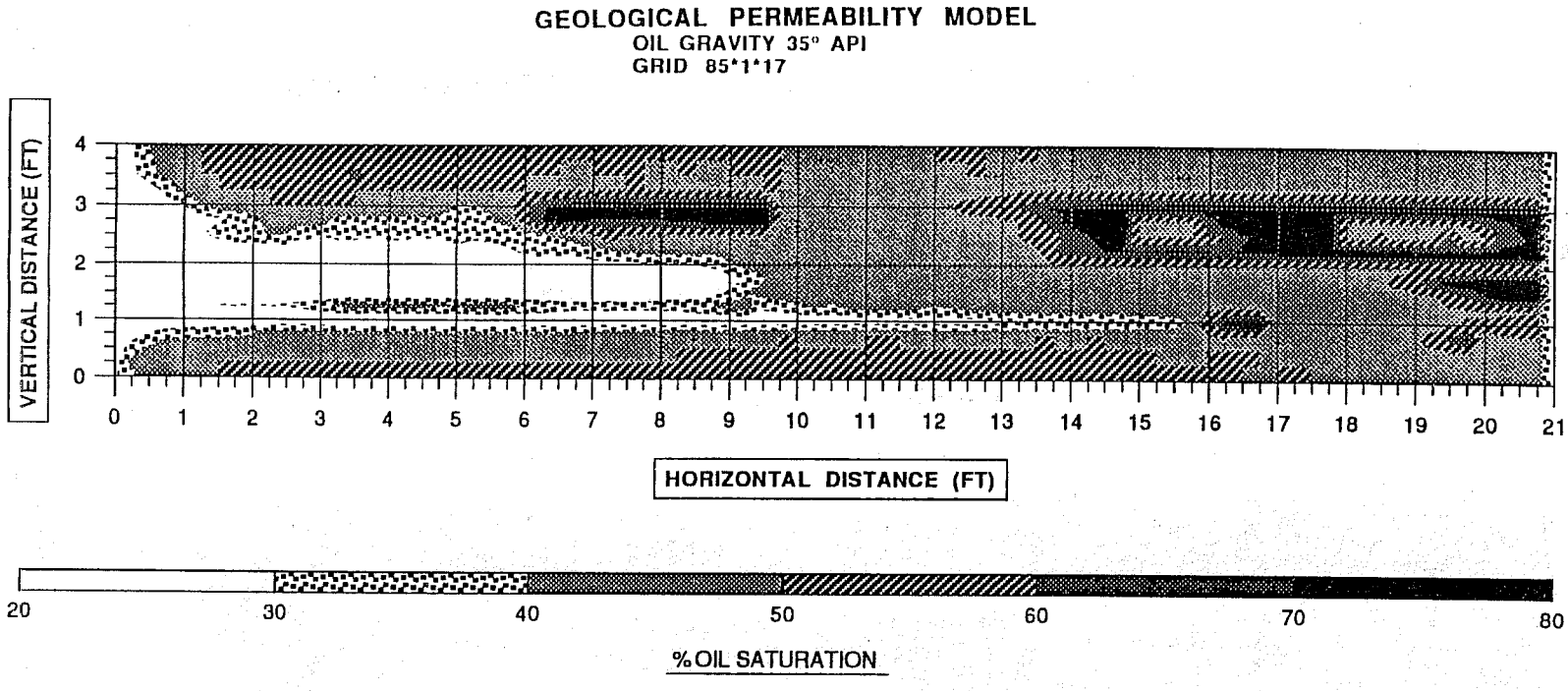

FIGURE 26. Oil saturation distribution after 0.32 PV injection, Fine-Grid Geological Model, viscosity ratio 2.78, Area B

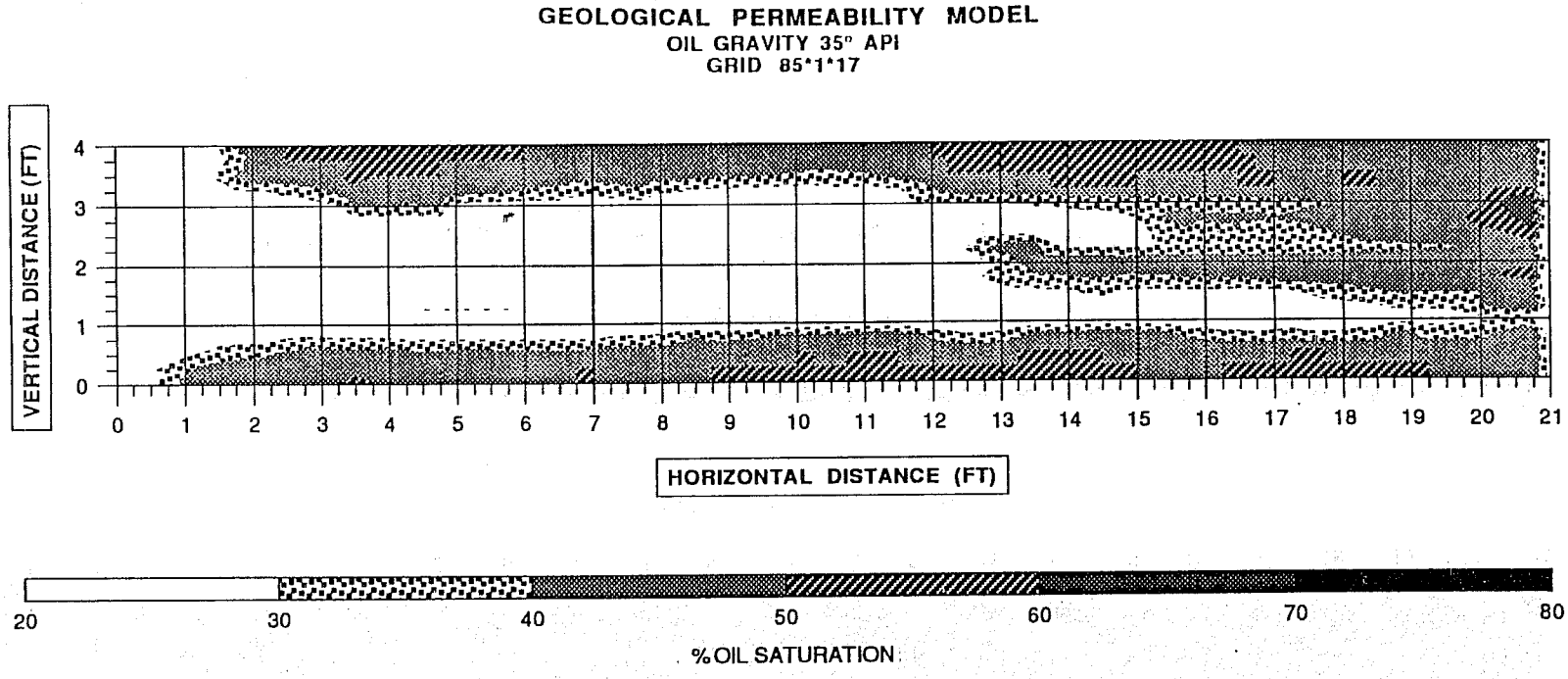

FIGURE 27. Oil saturation distribution after 0.85 PV injection, Fine-Grid Geological Model, viscosity ratio 2.78, Area B

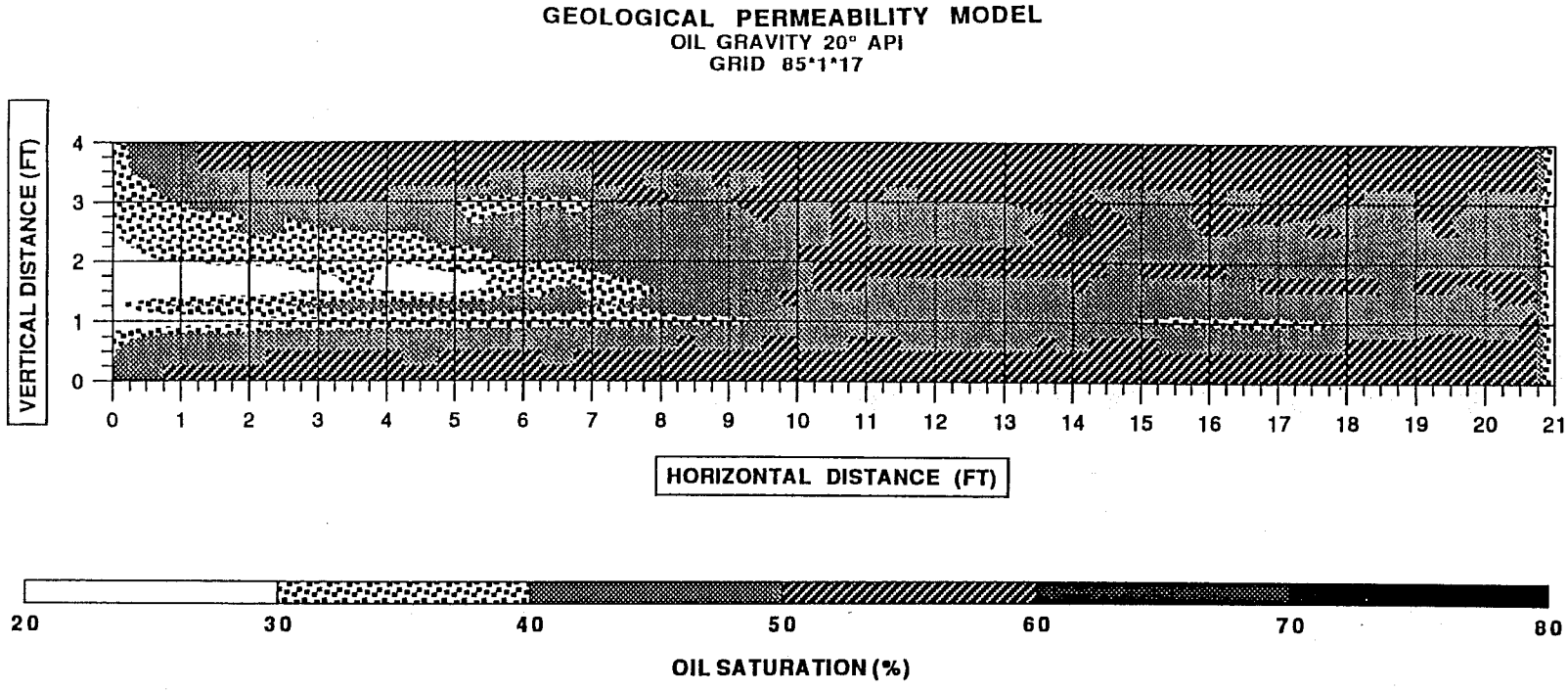

FIGURE 28. Oil saturation distribution after 0.32 PV injection, Fine-Grid Geological Model, viscosity ratio 24.5, Area B

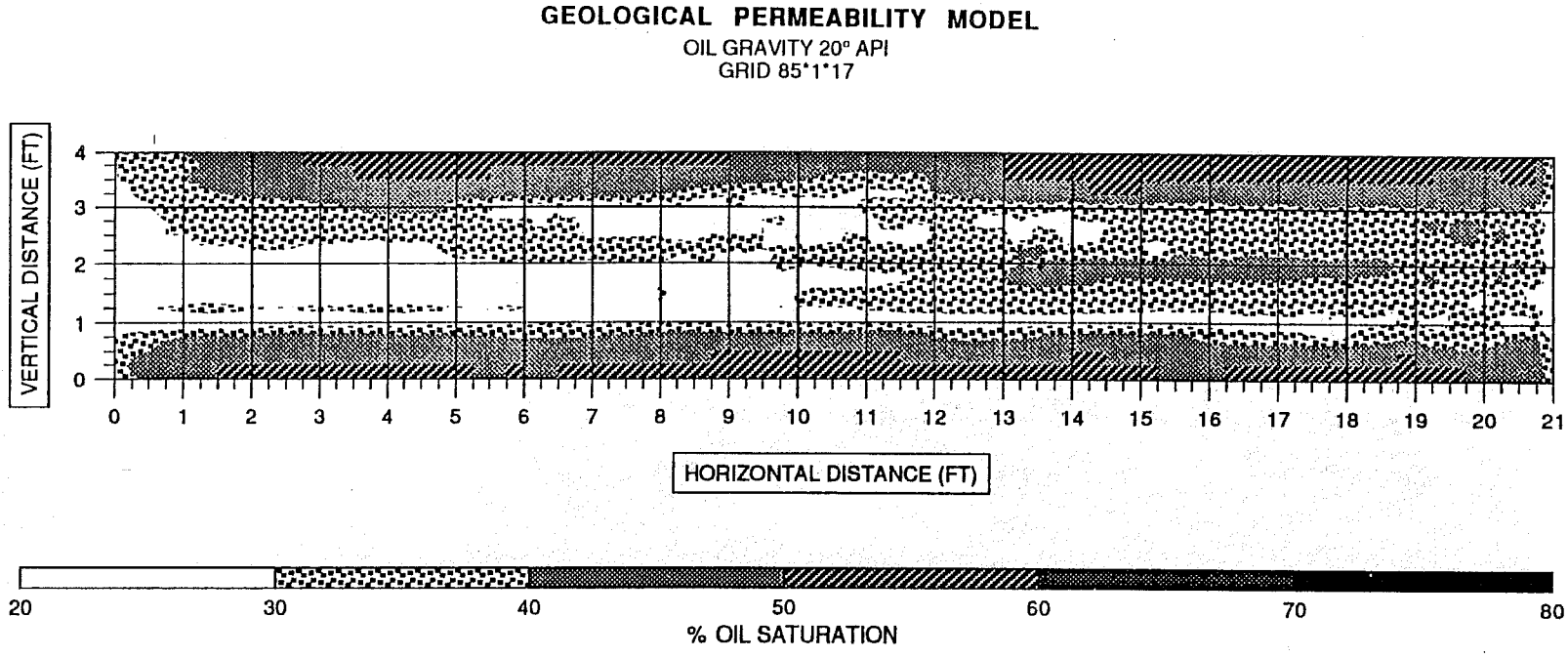

FIGURE 29. Oil saturation distribution after 0.85 PV injection, Fine-Grid Geological Model, viscosity ratio 24.5, Area B

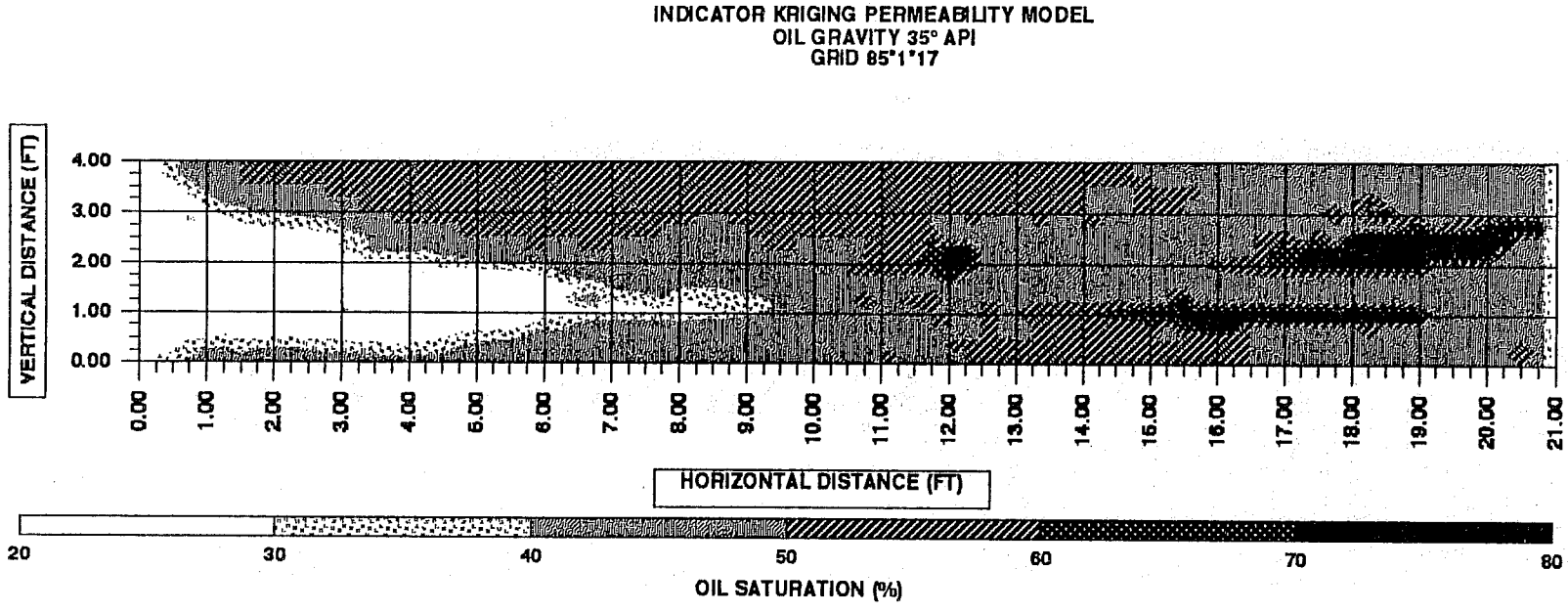

FIGURE 30. Oil saturation distribution after 0.32 PV injection, Indicator Kriging Model, viscosity ratio 2.78, Area B

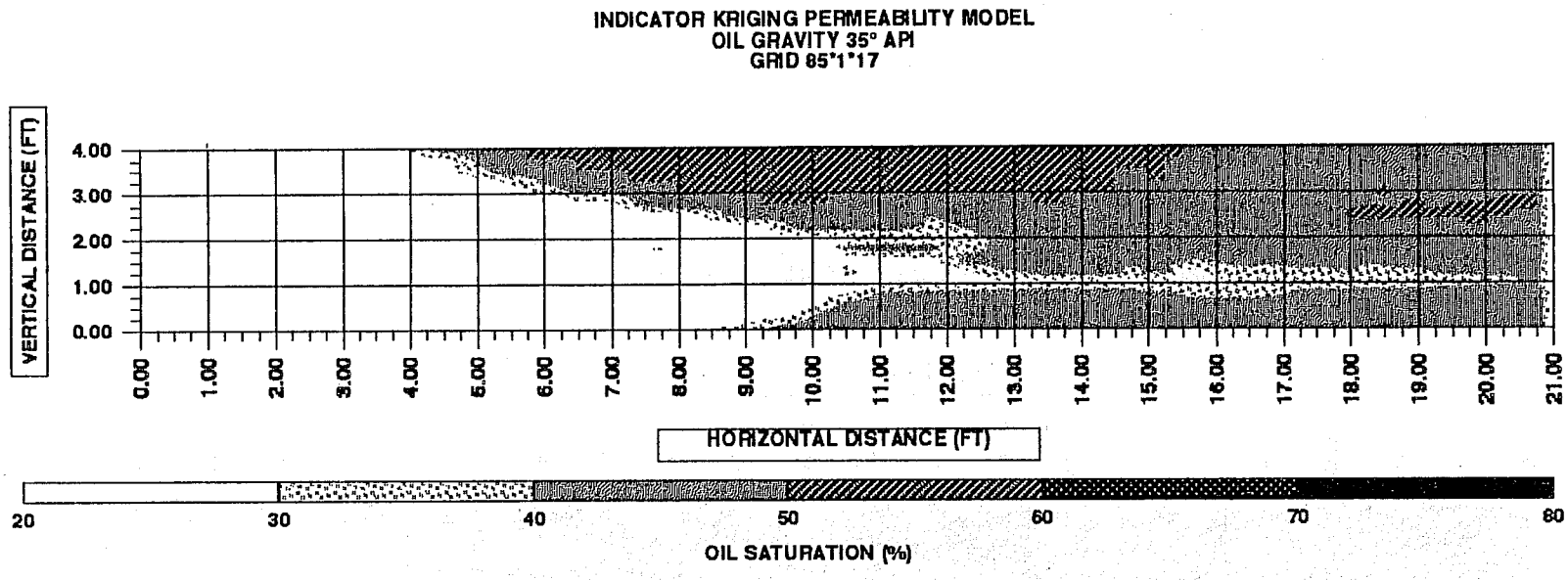

FIGURE 31. Oil saturation distribution after 0.85PV injection, Indicator Kriging Model, viscosity ratio 2.78, Area B

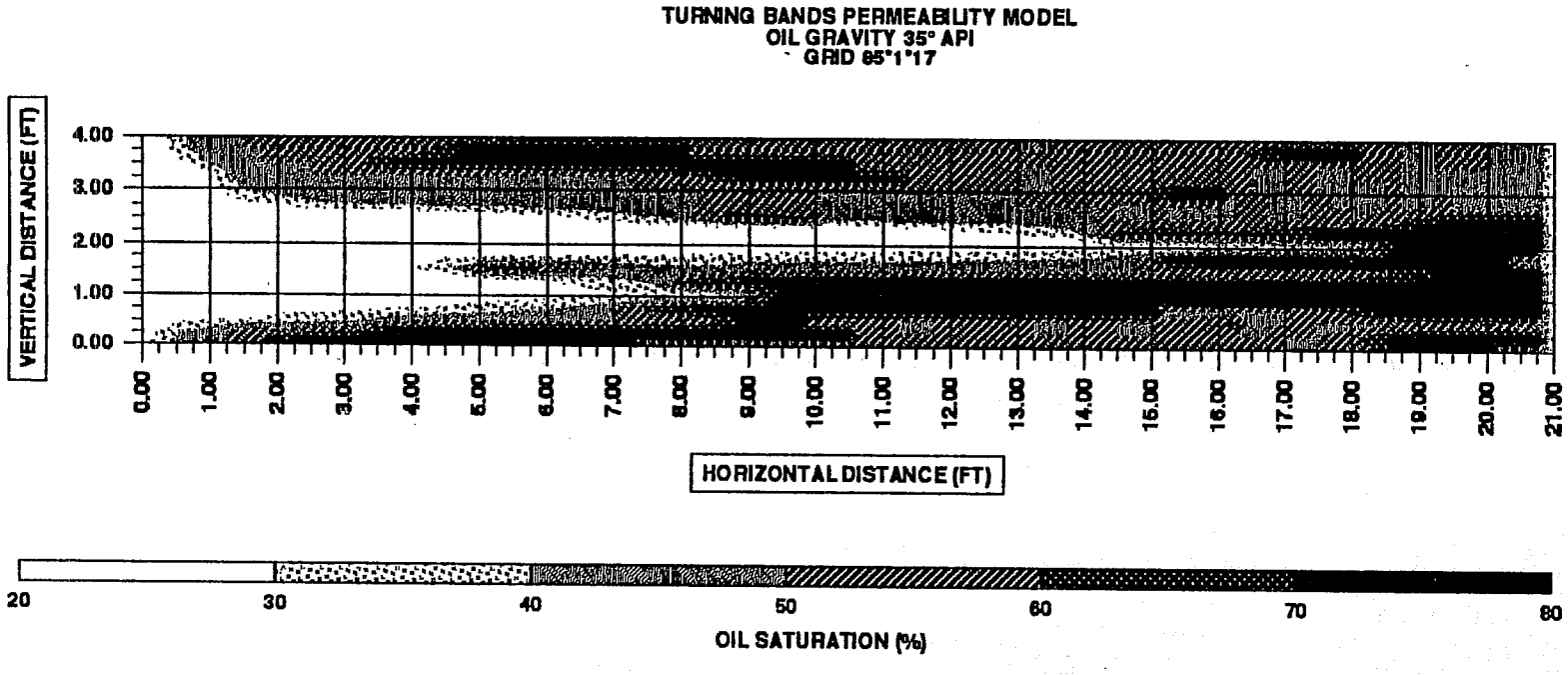

FIGURE 32. Oil saturation distribution after 0.32 PV injection, Turning Bands Model, viscosity ratio 2.78, Area B

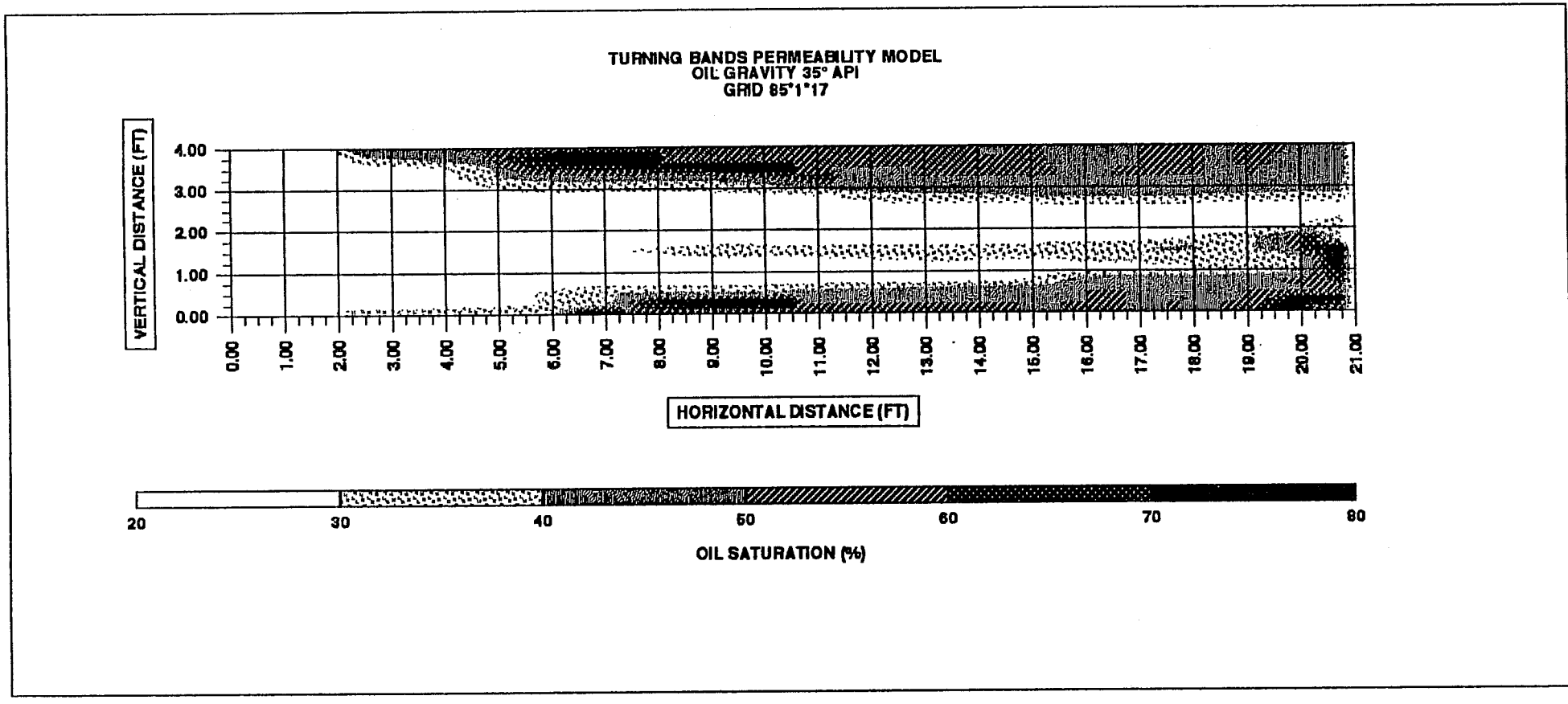

FIGURE 33 Oil saturation distribution after 0.85 PV injection, Turning Bands Model, viscosity ratio 2.78, Area B

OPTIMAL SCALES FOR REPRESENTING RESERVOIR HETEROGENEITY

R. C. Wattenbarger
Khalid Aziz
F.M. Orr

Department of Petroleum Engineering
Stanford University
Stanford, California

Abstract

The subject of this paper is the improvement of the representation of permeability heterogeneity in reservoir models. Two numerical studies are presented. The first explores the effects of changes in the scale at which permeability variations are explicitly represented—the representation scale. It shows that reservoir response may continue to change as the representation scale is decreased, and suggests that mixing due to sub-representation scale heterogeneity must be represented implicitly through effective mixing parameters, such as dispersivity. The second numerical study investigates whether this is possible. It demonstrates that the effects of small and large scale heterogeneities can be represented by a combination of explicit representation through varying gridblock permeabilities and implicit representation through effective mixing parameters.

However, at a given scale the effective mixing parameters may not be able to accurately represent the effects of mixing caused by sub-representation scale heterogeneity. If this is the case, we suggest that the robustness of the effective mixing parameters can best be improved by reducing the representation scale while holding the averaging scale of the effective mixing parameters constant. The representation scale is chosen as the maximum scale at which the effective mixing parameters are robust.

Supported by the Stanford Center for Reservoir Forecasting

I. INTRODUCTION

The goal of reservoir simulation is to provide accurate models of reservoir behavior. Often a reservoir simulator is complex enough to match the known response of a real system, but is not robust enough to predict the unknown future response. Since the future is where our interest lies, what is desired is a robust reservoir simulator that can be used with confidence in a predictive mode. Here, robustness refers to the ability of a reservoir simulator to model a wide range of flow conditions with the same degree of accuracy. Thus, a robust simulator can accurately model not just a single, history-matched scenario, but a variety of scenarios with different boundary conditions and recovery processes.

Often models are not robust because of problems associated with the modeling of permeability induced mixing.[1,2] Such mixing is traditionally modeled by the explicit representation of permeability heterogeneity through varying gridblock permeabilities and/or through the use of effective mixing parameters such as dispersivity or relative permeability. Considerable effort has been applied toward improving the explicit representation of heterogeneities[3,4,5,6] or toward the improvement of effective mixing parameters.[7,8,9,10] Although the problem of representing permeability heterogeneities is often broken into separate problems of explicit and implicit representation, this paper treats the problem as a whole. This is done by determining an adequate scale for the explicit representation of permeability.

Intuitively, the modeling of permeability heterogeneity should be more robust as the geologic representation scale (GRS) decreases. Furthermore, the amount of mixing which is not explicitly represented decreases with the GRS. Thus, the GRS represents a tradeoff between explicit and implicit heterogeneity representation. Because of the costs associated with explicit representation, it is desirable to use as coarse a GRS as possible, while retaining model accuracy and robustness. This paper investigates issues associated with choosing this maximum, or optimal, GRS.

II. PREVIOUS WORK

In a field study were the number of gridblocks is clearly constrained by computer limitations, gridblocks are often selected to delineate geo-

logic zones and oil, gas and water zones.[11] If not, Coats[12] recommends determining a suitable block size by "repeated runs using fewer blocks until resolution is lost concerning the facets of field production being estimated". Unfortunately, the block size at which response resolution is lost is somewhat subjective. Several researchers[2,13,14,15] follow this procedure for both homogeneous and heterogeneous reservoirs with a variety of results. Warren and Price,[15] and Stalkup[14] investigate the sensitivity to block size by plotting the response versus block length raised to a power. The power being an estimate of the global order of numerical approximation. Often this plot results in a linear relation which may be extrapolated to determine the response at zero block size. In all cases, the response continues to change as block size is reduced, giving no clear indication of a best block size. At best, one can choose a block size according to some acceptable error. Warren and Price, and Stalkup's studies were concerned with analyzing numerical errors. In their studies, all reservoir properties, including the GRS, were held constant as the computation scale was varied. Normally, no distinction is made between the computation and representation scales.

A different approach was used by Hewett and Behrens.[2] Starting with a very fine cross sectional representation of a fractal permeability field, they studied changes in reservoir response due to a varying number of model layers. This was done by performing waterflood simulations with fewer and fewer model layers, using appropriately scaled block permeabilities at each level. The computational scale and the representation scale were the same. The results were summarized by plotting the response, oil recovery at 1 pore volume injected and breakthrough time, versus the logarithm of the number of layers. As the number of layers increased from one, the response steadily changed up to about 30 layers. Increasing the number of layers past 30 had little effect, and the response seemed to reach a constant value. The number of layers at which the response stabilizes appears to occur rather abruptly. Hewett and Behrens deem this the critical resolution, beyond which macroscopic media flow properties can no longer be used.

Another study, with different results was performed by Davies and Haldorsen.[16] The fine scale was a cross section containing 150 stochastically-generated shale barriers of varying lengths and zero thickness. A grid size study was performed by holding the number of layers constant, while varying the number of columns. At each discretization level, pseudo functions where calculated from the fine scale water injection run. They found that the water breakthrough time fluctuated and was lower than that of the fine scale run for small block widths, eventually stabilizing and becoming more accurate as the block size increased.

They concluded that the horizontal block dimension of a coarse model should be greater than the largest shale expected within a block.

A number of studies are based on a layered permeability model. An early study by Testerman,[17] used a downsizing procedure which grouped individual layers into zones. The zones were defined to minimize the permeability variation within zones and maximize the variation between zones. The downsizing procedure was stopped, thus setting the number of zones, when further division produced no significant improvement in an objective function. Craig[18] performed a layer sensitivity study based on the effluent response to steady water injection in a five spot-pattern. At each level, layer permeabilities where defined by drawing from a log-normal distribution at equal percentile increments. Craig found that the accuracy of the cumulative production prediction increased with the number of layers and time and decreased with the mobility ratio and permeability variance. Based on a given level of accuracy, Craig recommended the number of layers to be used in a study. Lake and Hirasaki[19] developed a procedure for grouping layers based on the degree of crossflow between layers due to transverse dispersion. They found that for sufficiently high transverse dispersion numbers, the longitudinal spreading averaged over two or more layers could be represented by a single layer with a greater longitudinal dispersion coefficient. Similar arguments based on capillary crossflow and/or gravity equilibrium have been used in multiphase studies to select the number of layers, or to justify 2D areal models.[7,20]

III. EFFECTS OF GRS

In this section the effects of the GRS on block permeabilities and reservoir response are explored through an example permeability field and transport problem. Throughout this section, it is assumed that only permeability changes with the GRS; that is, all other model parameters are held constant at their macroscopic levels. In addition to illustrating the effects of the GRS, this example serves to determine the existence of the optimal resolution observed by Hewett and Behrens when the computation and representation scales are decoupled.

A fine scale multi-normal log-permeability field was generated on a 128x128 grid using gaussian sequential simulation.[21] The *a priori* log-permeability covariance model used in the simulation was exponential with an isotropic integral correlation range of 0.5 and a variance of 1. The

resulting realization has a log-permeability variance of 0.729. The experimental variogram was anisotropic. At a lag of 0.5, the semi-variogram reached a value of 1.12 in the x direction and 0.36 in the y direction.

A. Effects of GRS on Permeability

Several permeability fields with coarse representation scales were defined from the "point" (128x128) permeabilities. For simplicity, only representation grids of 64x64, 32x32, 16x16, 8x8, 4x4, 2x2 were investigated. Thus, the number of representation blocks is the same in each direction, $N_{repx} = N_{repy}$, and each coarse representation block contains the same integral number of point blocks. The permeability of each coarse block was taken to be the geometric average of the point permeabilities within the coarse block. Geometric averaging is chosen because it is reasonably accurate and simple.[15,22]

Grayscale images of the permeability at three GRS's are shown in Figure 1. These images qualitatively summarize the combined effects of averaging and discretization. As the GRS increases, small correlated regions of the point permeability loose distinction within the large homogeneous regions of the representation blocks.

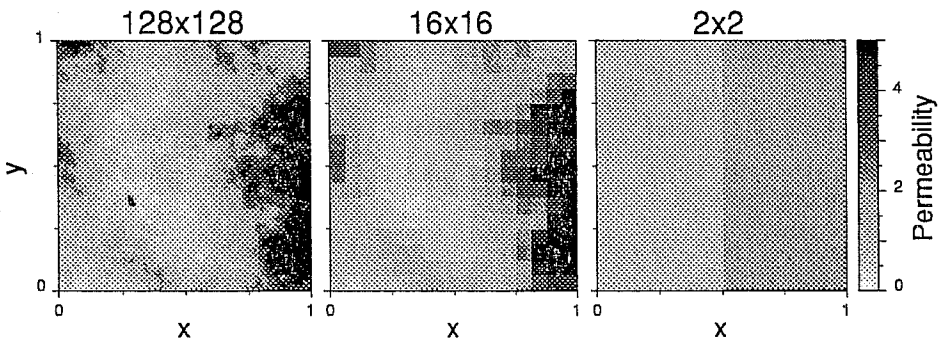

Figure 1: Permeability maps for GRS of (a) 128x128 (b) 16x16 and (c) 2x2.

Statistics of the log-permeability for each GRS are shown in Figure 2. Plots of the cumulative distribution function, Figure 2a, show the spread of the distribution about the mean decrease as the GRS increases. Furthermore, as the GRS increases the mean remains constant at 0.258, the minimum monotonically increases from a point value of -1.85, and the maximum monotonically decreases from a point value of 3.11. As shown

in Figure 2b, the variance of the log-permeability decreases approximately linearly with an increase in the representation length, $L_{rep} = 1/N_{repx}$.

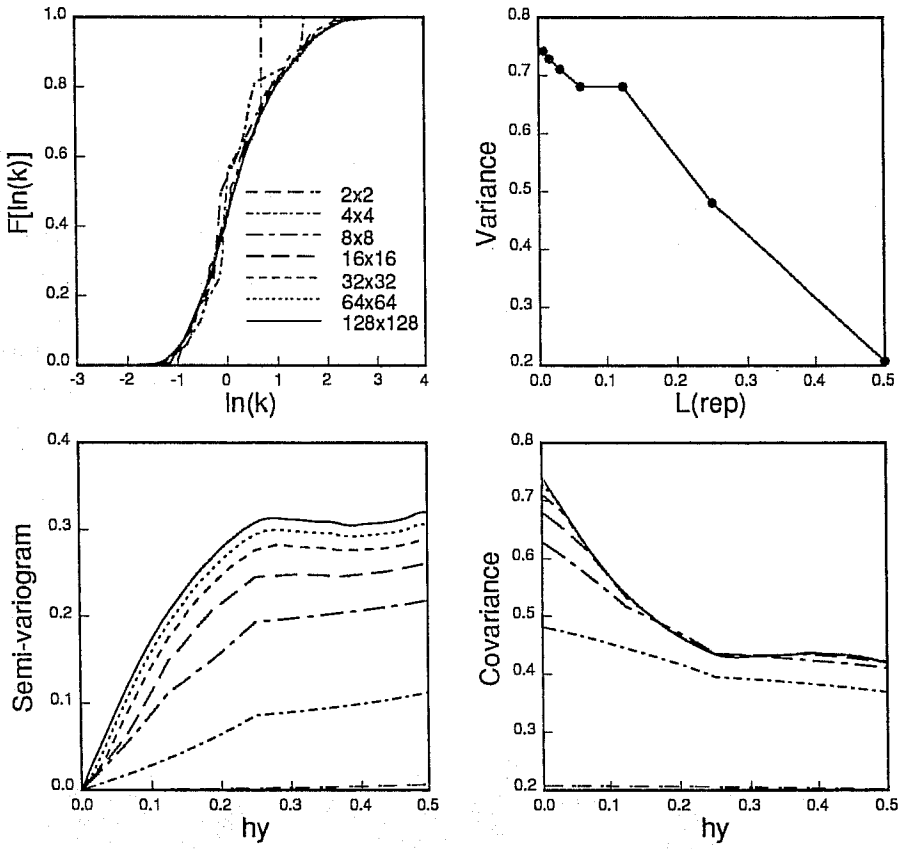

Figure 2: Effect of GRS on log-permeability statistics (a) cumulative distribution function (b) variance versus representation length (c) semi-variogram with separation vector parallel to y axis (d) covariance with separation vector parallel to y axis.

The experimental semi-variogram and covariance of the log-permeability for separation vectors parallel to the y-axis are shown in Figures 2b and c. The GRS has a strong impact on the experimental semi-variogram. The value of the semi-variogram, and hence permeability variability, is reduced at all separation distances as the GRS is increased. When L_{rep} is less than the range of the point semi-variogram, approximately 1/4, the range of the coarse semi-variogram is approximately that of the point semi-variogram. Otherwise, the range of the coarse semi-variogram is approximately equal to the L_{rep}.

When L_{rep} is less than the range of the point covariance, the coarse

GRS covariance is primarily affected at small separation distances. In this case, the coarse GRS covariance is approximately equal to the point covariance for separation distances greater than the representation scale. For separation distances less than the representation scale, the coarse GRS covariance interpolates, approximately linearly, the point covariance from a separation distance of zero to L_{rep}. Indeed, the coarse GRS covariance and semi-variograms are approximately piecewise linear for all separation distances. This linearity is a result of discretization and is expected whenever the separation vector is aligned with one of the axes of the representation grid.[23] When L_{rep} is greater than the point range, the entire coarse GRS covariance falls below the point covariance.

The effects of the GRS on the statistical properties of spatially averaged random fields is dealt with extensively in the geostatistics literature.[24,25,26] In particular, the effects of of sample size (representation scale) and sampling region (reservoir size) on univariate statistics are referred to as the *support effect*, while the effect of spatial averaging on semi-variogram and spatial covariance is referred to as *regularization.* Rubin and Gómez-Hernández[27,6] investigated the effects of block size on the covariance of effective log-transmissivities both through analytic stochastic analysis and numerical simulation. The qualitative features of their results are similar to those given here.

The primary effects of spatial averaging and discretization are to reduce univariate and spatial variability. While interesting, the effects of GRS on permeability are important only inasmuch as they impact reservoir response. The effect of GRS on reservoir response and its relation to changes in permeability are discussed in the following sections.

B. Effect of GRS on Reservoir Response

To investigate the effects of the GRS on species transport, a model transport problem was solved for each GRS. The process is that of a non-reactive tracer flowing in a single, constant density, constant viscosity phase and incompressible system. Under these assumptions, the governing equations are:[28]

$$\phi \frac{\partial C}{\partial t} + \vec{\nabla} \cdot (C\vec{u}) - \vec{\nabla} \cdot (\phi \vec{\vec{K}} \cdot \vec{\nabla} C) = 0 \tag{1}$$

$$\vec{\nabla} \cdot (k \vec{\nabla} \Phi) = 0 \tag{2}$$

$$\vec{u} = -k \vec{\nabla} \Phi \tag{3}$$

$$\vec{\vec{K}} = \left(D + \frac{\alpha_T}{\phi}|\vec{u}|\right)\vec{\vec{\delta}} + \left(\frac{\alpha_L - \alpha_T}{\phi|\vec{u}|}\right)|\vec{u}\vec{u}| \tag{4}$$

These equations are the component mass balance equation, the potential equation, Darcy's law, and an expression for the dispersion tensor. For the runs in this section the dispersion tensor was taken to be zero. In addition to the governing equations, the following initial and boundary conditions were applied:

$$\begin{aligned} C(x,y,0) &= 0 \\ C(0,y,t) &= 1 \\ \tfrac{\partial C}{\partial x}(1,y,t) &= 0 \\ \\ \Phi(1,y,t) &= 0 \\ \Phi(0,y,t) &= \Phi' \\ \frac{1}{L_y}\int_0^{L_y} u_x(0,y,t)dy &= 1 \\ u_y(x,1,t) &= u_y(x,0,t) = 0 \end{aligned} \tag{5}$$

Thus, a fluid of unit tracer concentration is injected into a constant potential inlet at $x = 0$ and displaces a similar fluid of zero tracer concentration toward a constant potential outlet at $x = 1$. The inlet boundary conditions insure that potential is constant along the inlet face and that the volumetric injection rate is unity. Thus, time is equivalent to pore volumes injected.

This problem was solved numerically using finite differences. The steady-state potential equation was discretized using central differencing (a 5-point stencil in 2D) and an iterative solution technique.[29] Convergence of the potential solution was based on the accumulated concentration error of each block.[30] The convection-dispersion equation was solved using a high-order, total variations diminishing, finite difference scheme[31] along with a high-throughput timestepping scheme.[23]

This work is concerned with improving the mathematical model through better reservoir characterization, and not with developing corrections for inadequate numerical solution techniques. To this end, the distinction between the mathematical model and solution technique is made as clear as possible. This is accomplished by decoupling the geologic representation from the computational scale — two scales which are normally paired in a common gridblock size. Unless otherwise specified, a computational scale of 256x128 is used for each simulation run, even though the GRS changes from 128x128 to 2x2. This is done to hold the

numerical errors approximately constant while the GRS is varied, thus isolating the effects of the GRS.

Grayscale images of the concentration at 0.5 pore volumes injected are shown in the top row of Figure 3, for three representation scales. These images show that the large features of the point GRS concentration front are preserved at a GRS of 16x16 but are completely lost at a GRS of 2x2. However, the 16x16 GRS front appears somewhat less smooth than the point front and has different small scale features than the point front. The bottom row of Figure 3 displays the average concentration profiles at time intervals of 0.1 pore volumes injected for the same three GRS's. The average concentration, $\bar{C}(x,t) = \frac{1}{L_y}\int_0^{L_y} C(x,y,t)dy$, is the equivalent concentration of a 1D system. These profiles further indicate the similarity between the 128x128 and 16x16 GRS runs, and their dissimilarity to the 2x2 GRS run. Furthermore, the irregular character of these profiles indicates the inappropriateness of an equivalent 1D convection-dispersion model.

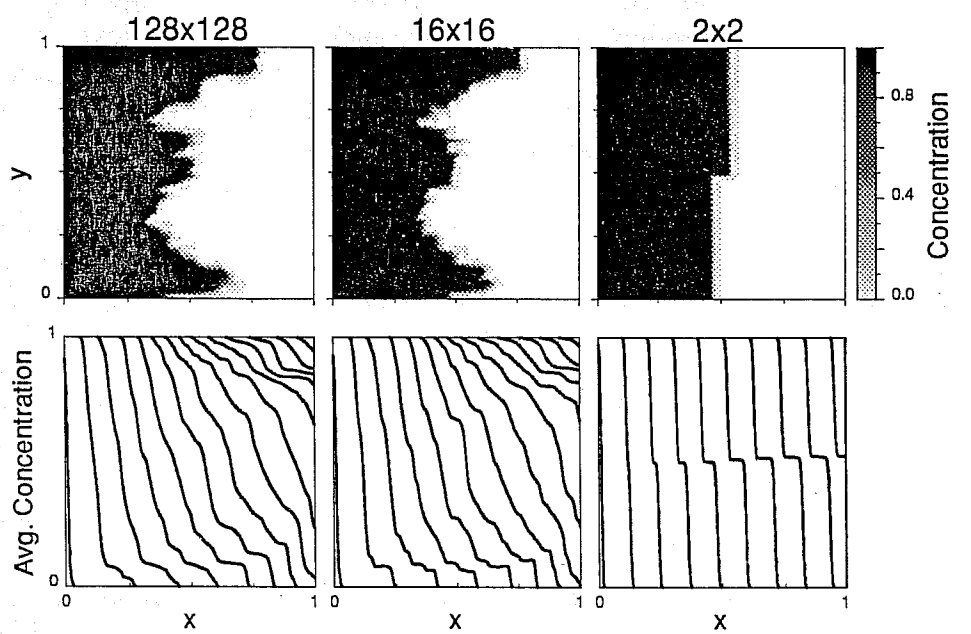

Figure 3: Effect of GRS on reservoir response using a 256x128 computational grid. (a) tracer concentration maps at 0.5 pore volumes injected (b) profiles of concentration averaged in the y-direction at 0.1 PVI time intervals.

The time evolution of the concentration profiles is summarized by a plot of the mixing zone width versus time, shown in Figure 4a. Here the

mixing zone is defined as the distance between average concentrations of 0.1 and 0.9. For early times, the mixing zone grows approximately linearly with time, indicating flux-induced mixing[1] (anomalous diffusion)[32]. The length of the mixing zone, and hence the amount of convective mixing, is smallest for the 2x2 GRS and exhibits a maximum for the point GRS. There are, however, times when the coarse GRS mixing zones are larger than that of the point mixing zone.

Figure 4c shows the effluent concentration profiles for each GRS. The effluent profile of a purely homogeneous reservoir with no dispersion would jump from zero to one at one pore volume injected, with more heterogeneous reservoirs displaying greater spread and earlier breakthrough times. The effluent profiles for the coarser GRS's have less spread than the point GRS, indicating a less heterogeneous system. However, as with the mixing zone, the results are somewhat ambiguous. For example, the 2x2 GRS reaches a concentration of 0.82 before the point GRS, while the 8x8 GRS reaches that concentration after the point GRS. The cumulative tracer production plots shown in Figure 4b are less ambiguous. The cumulative tracer production at any time increases monotonically with the GRS, with the coarser GRS's having more homogeneous character.

Figures 4d-f best illustrate the effects of GRS on the reservoir response. In these plots, a singe value which characterizes the response in some way is plotted versus the representation scale. Figures 4e and f plot the same responses as Hewett and Behrens: cumulative production at one pore volume injected and breakthrough time. Hewett and Behrens observed a critical resolution where the response did not change as the number of representation/computation layers increased (about 30). The cumulative production at 1 PVI does not show such a critical resolution. Indeed the cumulative production at 1 PVI varies approximately linearly with L_{rep}, continuing to vary at all representation lengths. For the 256x128 computational grid the breakthrough time also varies monotonically with L_{rep}. However, the rate at which the breakthrough time changes with the GRS decreases significantly below the 32x32 GRS. Furthermore, when a 128x128 computational grid is used the breakthrough time is greater for the point GRS than for the 64x64 GRS. Finally, Figure 4d shows the error in the effluent curves of the coarse GRS runs. The effluent error was calculated as the overall area between the coarse GRS effluent curve and the point effluent curve: $\int_0^{1.5} |\bar{C}_{128x128}(1,t) - \bar{C}(1,t)|\, dt$. Like the cumulative production at 1 PVI, the effluent error also varies approximately linearly with L_{rep}.

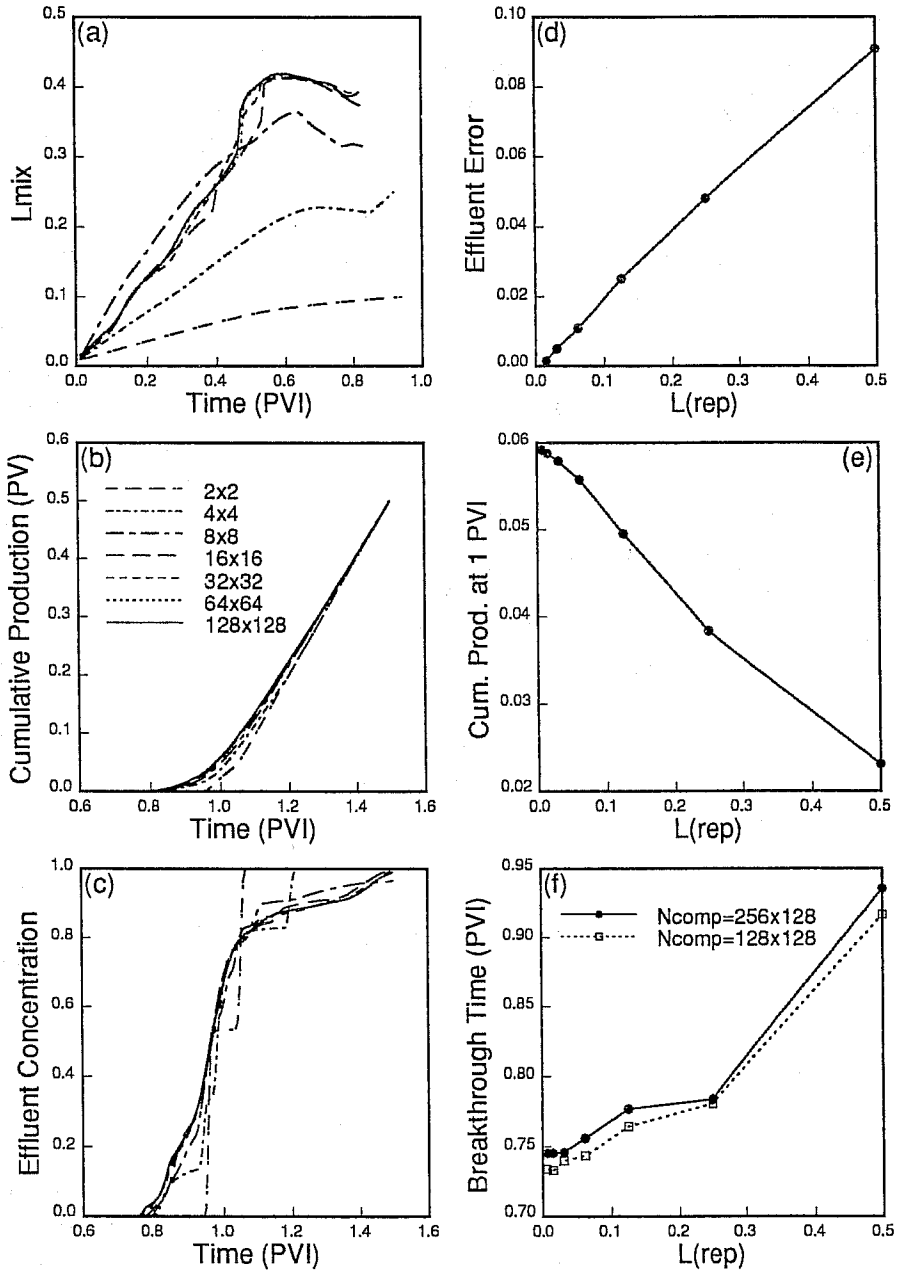

Figure 4: Effect of GRS on reservoir response using a 256x128 computational grid (a) mixing zone width (b) cumulative tracer production (c) effluent tracer concentration (d) effluent concentration error (e) cumulative tracer production at 1 pore volume injected (f) tracer breakthrough time using 256x128 computational grid and 128x128 computational grid.

C. *Discussion*

The results of this experiment are not too surprising. As the GRS decreases, the log-permeability variance and measures of convective mixing continue to increase, while the correlation range remains relatively constant. The decrease in variance is a consequence of the spatial averaging of a spatially correlated variable and the discretization of a spatial variable in a finite region. The increase in convective mixing can be attributed to increased permeability heterogeneity. The impact of permeability heterogeneity on reservoir response can be quantitatively summarized by the heterogeneity index, $\mathrm{HI} = \sigma_\kappa^2 L_\kappa$, where σ_κ^2 is the variance of the log-permeability and L_κ is the range of the log-permeability in the mean flow direction.[33,34] Unlike, some traditional measures of permeability heterogeneity which do not consider spatial correlation,[35,36] the heterogeneity index reflects both the size and variability of high and low permeability regions. As the GRS decreases the log-permeability variance increases, thus increasing the permeability heterogeneity and the amount of convective mixing. This view of the relationship between the permeability heterogeneity and the reservoir response is supported by similar character of the plots of log-permeability variance, effluent error, and cumulative production at 1 PVI versus the representation length.

The continuing change in reservoir response with GRS is particularly true for a layered geologic model. Under the same governing equations and boundary conditions used in this section, the breakthrough times of each layer are directly related to the univariate permeability distribution.[36] In general, as the number of layers increases, the discrete/layer permeability distribution should approach but never equal that of the continuous/point permeability distribution. However, there are exceptions. If the point permeability was spatially uncorrelated, spatially averaged layer permeabilities would, in theory, always yield the expected value of the point permeability. Thus, there would be no change in the model response as the number of layers changes.

The character Figures 4d and e is very similar to the plots of response versus computational block length for homogeneous systems, except that mixing is increasing rather than decreasing. Indeed, modeling the point GRS by a coarse GRS can be viewed as neglecting a low order term in the governing equations. Just as the manner in which the numerical error changes with block size depends on the numerical technique, the manner in which the representation error changes depends on the method for calculating block permeabilities.

The critical resolution observed by Hewett and Behrens was not

observed in this study. Possible explanations for their observation of a critical resolution is their coupling of the numerical and computational scales, the significant anisotropy of their permeability field, and their varying only the number of layers while the number of blocks parallel to flow was held constant. Indeed, the number of layers at the critical resolution (30) was on the order of the number of blocks parallel to flow (20). In this study, the representation length at which the rate of decrease in the breakthrough time with GRS changes significantly (0.4) is approximately the equal to the separation distance at which the x and y directional semi-variograms no longer coincide (0.5).

IV. MODELING SUB-REPRESENTATION SCALE HETEROGENEITY

The possibility that a finite GRS model may be in error, regardless of the representation scale, suggests the use of effective properties to improve model accuracy. As demonstrated in the preceding section, the error existing at a finite GRS is due to inadequate representation of permeability heterogeneity and consequently, inadequate representation of convective mixing. For miscible transport, small scale convective mixing traditionally modeled through dispersivity. In this section, a numerical experiment is performed to determine if mixing due to small *and* large scale heterogeneities can be modeled by a combination of explicit representation through a discrete geologic model and implicit representation using dispersivity. This experiment also serves as an introduction to the use of non-represented permeability to determine mixing parameter robustness.

A. Uncorrelated, Layered Permeability Experiment

To investigate the separation of permeability representation into explicit and implicit components, a stylized geologic model was constructed. The point log-permeability of this model is the sum of a spatially uncorrelated field and a layered field:

$$\kappa = \kappa_l + \kappa_w \tag{6}$$

where κ is the combined/point log-permeability, κ_l is the layered log-permeability, and κ_w is the spatially uncorrelated/white-noise log-

permeability. The layered field was constructed by randomly drawing 8 log-permeabilities from a normal distribution with a variance of 1 and a mean of 0. The white-noise field was constructed by randomly drawing log-permeabilities from a normal distribution with a variance of 0.5 and mean of 0 on a 128x128 representation grid. The realization statistics are summarized in Table 1.

Table 1: Summary of layer,white-noise and point realization log-permeability statistics.

	Layer	White-Noise	Layer+White-Noise
Mean	0.00	-0.02	-0.03
Variance	0.50	0.57	1.09
Minimum	-2.39	-1.21	-3.59
Median	0.00	0.05	-0.06
Maximum	2.59	1.44	3.77

Grayscale images of the point permeability field and its component fields are shown in the top row of Figure 5. Because the model permeabilities are constant over large regions, the permeabilities are spatially correlated for separation distances up to the representation length. Indeed, the white-noise model permeabilities are actually spatially correlated up for separation distances up to 1/128 in the x and y directions. Similarly, the layer permeability is perfectly correlated in the x-direction and correlated for separation distances up to 1/8 in the y-direction.

Simulations of flow through the point permeability field and each of its components were performed using the same governing equations, boundary conditions, and numerical techniques as in section III.. A 128x128 computational grid was used for all simulations in this section. Grayscale images of the concentration at a time of 0.5 PVI are shown in the middle row of Figure 5. These images illustrate the character of the mixing induced by each permeability field. The concentration front of the layered permeability is dominated by 8 large fingers of various sizes corresponding to each permeability layer. The concentration front of the white-noise permeability, however, is composed of a large number of fingers of similar transverse and longitudinal dimensions. The front of the point permeability is dominated by the same large fingers as the layered model, but is also affected by the white-noise permeabilities—particularly by the crossflow they induce. The relative impact of the component permeability fields on the response of the point permeability field is further demonstrated by effluent concentration and cumulative tracer production plots, top row of Figure 6.

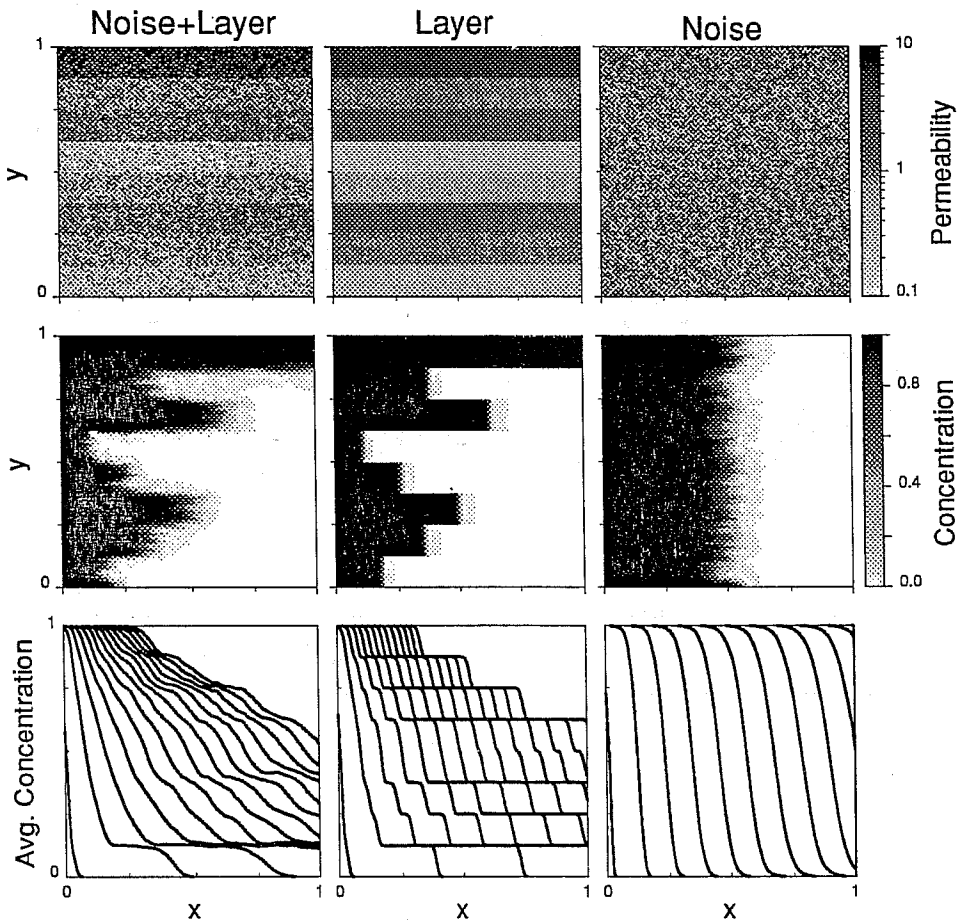

Figure 5: Point, layer, and white-noise maps and profiles (a) permeability maps (b) tracer concentration maps at 0.5 pore volumes injected (c) profiles of concentration averaged in the y-direction at 0.1 PVI time intervals.

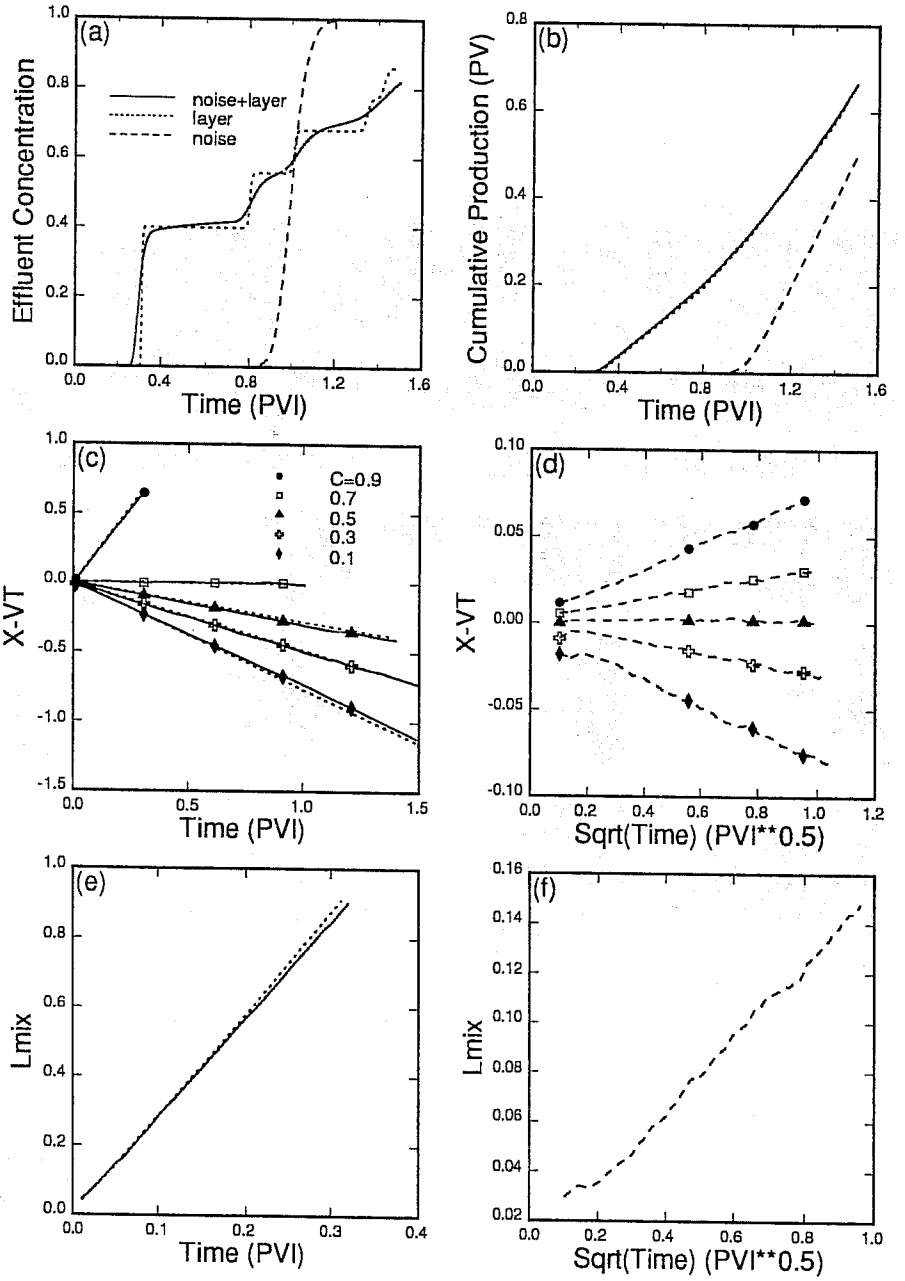

Figure 6: Point, layer, and white-noise response plots (a) effluent concentration (b) cumulative production (c) $(x_c - vt)$ for point and layer runs (d) $(x_c - vt)$ for white-noise run (e) mixing zone width for point and layer runs (f) mixing zone width for white-noise run.

Analysis of the transverse average concentration indicates the general character of the mixing induced by each of the permeability fields. The bottom row of Figure 5 shows the average concentration profiles at 0.1 PVI time intervals for each permeability field. The point and layered permeability field have complex profiles which could not be represented by a 1D convection-dispersion model. However, the profiles of the white-noise permeability field have the distinct complementary error function shape which can be represented by a 1D model with a dispersion term.

The $(x - vt)$ versus t plots in the middle row of Figure 6 describe the movement of a particular average concentration with time. The form of these plots derives from the analytic solution of the 1D convection-dispersion equation and the analytic solution of the purely convective layered reservoir problem. An approximate solution of the convection-dispersion equation under these boundary conditions is:[28]

$$C = \frac{1}{2}\mathrm{erfc}\left(\frac{x - vt}{2\sqrt{Kt}}\right) \tag{7}$$

from which,

$$x_c - vt = \left[2\mathrm{erfc}^{-1}(2C)\sqrt{K}\right]\sqrt{t} \tag{8}$$

where x_c is the location of a concentration C at a given time t and v is the fluid velocity (u/ϕ). Thus, $(x - vt)$ varies linearly with the square root of time. For a layered system under boundary conditions describe by Equations 5, an average concentration moves at a constant velocity, thus:

$$x_c = v_c t \tag{9}$$

from which

$$x_c - vt = (v_c - v)t \tag{10}$$

where v_c is the concentration velocity. In this case, $(x - vt)$ varies linearly with time. As expected, Figure 6c shows $(x - vt)$ varying linearly with time for the layered system and approximately so for the point permeability field. Such is not the case for the white-noise permeability field, where $(x–vt)$ plots linearly versus the square root of time, Figure 6d. The mixing zone width is the distance between $(x - vt)$ for 0.9 and 0.1 concentrations; that is, $L_{mix} = (x_{0.9} - vt) - (x_{0.1} - vt)$. Figure 6e shows the

It may be possible to represent the layered system behavior with a homogeneous model and a relative-permeability like function, but only for flow under the same boundary conditions.[37]

mixing zone width for the point permeability field falling slightly below the layered system. Thus, the addition of small scale heterogeneity to the layered system causes transverse mixing between layers which decreases the impact of longitudinal mixing.

1. Matching White-Noise Results

As indicated by the plots for the white-noise run, the behavior of the average concentration can be modeled by an equivalent homogeneous system and dispersion tensor. The longitudinal dispersivity for this system was estimated to be 0.0020 through analysis of the effluent concentration of the white-noise run.[38] Using this dispersivity, both the concentration profiles and the effluent concentration profiles are closely reproduced by a 1D convection-dispersion model. The transverse dispersivity for the homogeneous system was estimated to be 0.00015. The transverse dispersivity was found by simulating a flow problem through the white-noise permeability field which differed from the first run only in the inlet concentration boundary condition. In this case, the inlet concentration was specified to be 1 for $y \in (0, 0.5)$ and 0 for $y \in (0.5, 1)$. After injecting approximately 1 pore volume, the concentration in the system remains constant. The transverse dispersivity was found by analyzing the concentration profile at the outlet in a manner similar to that used for effluent concentration.

2. Matching Point Results

Because the white-noise response can be modeled using lumped parameters, it seems likely that the point response can be modeled using lumped parameters in conjunction with a layered permeability model. To determine if this is so, an attempt was made to build such a model. Initial attempts at matching the point response by adjusting the dispersivities of the original layer model indicated that some adjustment of the layer permeabilities was necessary. Hence, new layer permeabilities were calculated using the velocity field of the point model. Each new layer permeability was found such that the effluent volumetric flow rate of each layer matched that of the point model. The maximum percentage change in a layer's permeability was 6 percent. Using these permeabilities, nonlinear regression was used to to determine the optimal longitudinal and transverse dispersivities. The regression minimized the effluent error, as defined in section III., between the point and layered models. The regression gave a value of 0.002168 for the longitudinal dispersivity and

0.000152 for the transverse dispersivity.

Figure 7 shows a comparison of the point model response and the layer/dispersivity model response. The match is close, but not perfect. An improved match could probably be obtained by determining the layer permeabilities through regression.

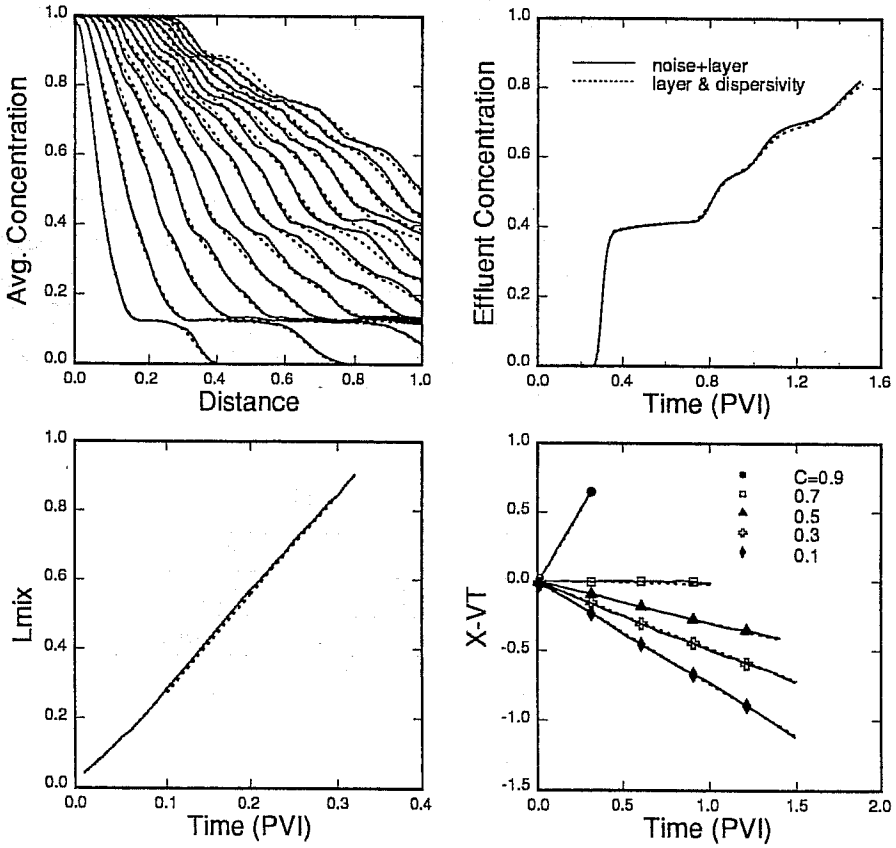

Figure 7: Comparison of original layer+white-noise model response to the layer&dispersivity model response (a) average concentration profiles (b) effluent concentration (c) mixing zone width (d) $(x_c - vt)$.

B. Discussion

The results of this experiment indicate a successful, though not perfect, attempt at representing large and small scale heterogeneity using a combination of explicit (layer permeabilities) and implicit (dispersivities) representation. Moreover, the longitudinal and transverse dispersivities

calculated from simulations through the white-noise permeability field are approximately equal to the dispersivities needed in conjunction with the layered permeabilities to match the simulation through the point permeability field. The longitudinal dispersivity needed to model flow through the white-noise field can also be estimated from the covariance of the white-noise log-permeability.[22,39,40] Under various assumptions, the asymptotic longitudinal dispersivity for steady flow through a stationary permeability field is given by:

$$\alpha_L = \int_0^\infty C_\kappa(\vec{u}\alpha)\, d\alpha \tag{11}$$

where $\vec{u}$ is the mean velocity. The covariance of the white-noise log-permeability in the x-direction is σ_κ^2 at $h = 0$ and decreases linearly to 0 at $h = L_{rep}$, remaining 0 for $h > L_{rep}$. In this case, the integral in equation 11 is the area of a triangle and $\alpha_L = \frac{1}{2}\sigma_\kappa^2 L_{rep} = 0.0019$. This value is close to that determined from the simulations. The values of the various dispersivities are summarized in Table 2.

Table 2: Summary of Calculated Dispersivities

	α_L	α_T
Point Response Regression	0.002168	0.000152
White-Noise Response	0.0020	0.00015
White-Noise Covariance	0.0019	

1. Non-Represented Permeability

The relationship between the white-noise permeability and the dispersivities used in conjunction with the layered permeability indicate the usefulness of separating the point permeability into its represented (layer) and non-represented (white-noise) components. A general model for separating the permeability into its components is:

$$\begin{aligned} k(x) &= k_r(x)k_{nr}(x) \\ \kappa(x) &= \kappa_r(x) + \kappa_{nr}(x) \end{aligned} \tag{12}$$

where $k(x)$ is the point permeability, $k_r(x)$ is the represented permeability, and $k_{nr}(x)$ is the non-represented permeability. This model is similar to ones used in geostatistics and stochastic analysis of effective properties which separate a random field into its estimated or expected value and a fluctuation.[24,22] It also related to the series representation of

a random variable as the series of component random variables.[41,24,32] If the non-represented and represented permeabilities are uncorrelated, the covariance of the non-represented can be determined from the point and represented log-permeability covariances.

$$\begin{aligned} C_\kappa(h) &= Cov[\kappa_r(x) + \kappa_{nr}(x), \kappa_r(x+h) + \kappa_{nr}(x+h)] \\ &= C_{\kappa_r}(h) + C_{\kappa_{nr}}(h) \quad \text{if } Cov[\kappa_r(x), \kappa_{nr}(x+h)] = 0 \end{aligned} \tag{13}$$

When appropriate, this relation may be used with Equation 11, to estimate the asymptotic longitudinal dispersivity associated with non-represented permeability:

$$\alpha_{L_{nr}} = \int_0^\infty (C_\kappa(h) - C_{\kappa_r}(h))\, dh \tag{14}$$

The explicit separation of the point permeability into represented and non-represented components is appealing because it gives a concrete meaning to what is being represented by the effective mixing parameters. The experiment of this section suggests that the non-represented permeability can be useful in analyzing the robustness of effective mixing parameters and perhaps in estimating value of the parameters. Indeed, it is unlikely that a coarse model, consisting of effective mixing parameters and represented permeability, could robustly represent the point permeabilities if flows through the non-represented permeabilities could not be represented by effective mixing parameters. Thus, the difficult problem of determining whether a point permeability field can be represented by a given coarse permeability field and effective mixing parameters is transformed into a simpler, more restrictive problem.

2. Robustness of Non-Represented Permeability

The simpler problem is that of determining whether a point permeability field can be represented by a homogeneous permeability and effective mixing parameters. This problem is a common one and is the subject of on going research. In particular, much work has been conducted on determining whether the spreading characteristics of tracer flows through heterogeneous permeability fields can be represented by dispersivities.[22,42,39,1,2,32,40] This research and field studies indicate that the longitudinal dispersivity necessary to characterize the spread of a front or a plume, may continue to change with distance traveled (time). If, however, the spatial correlation of the permeability field is finite the longitudinal dispersivity should reach a constant value after traveling several correlation lengths, perhaps asymptotically. In this case, the spread of a front could be correctly modeled by a finite dispersivity for all travel

distances greater than some multiple of the correlation length. For all travel distances less than this multiple of the correlation length, the front spread would be incorrectly modeled by a finite value.

Within a finite system, the dispersivity may or may not reach a constant value by the time a front has traveled the length of the system. If the dispersivity has not reached a constant value, the effluent concentration may be approximately modeled by a constant dispersivity. However, this dispersivity would only be valid for a particular system size and boundary condition. At early times, before the front has traveled across the system, the amount of spreading predicted by a constant dispersivity could be severly in error. If the flow direction were to change at a time when the front spread is in error, the error would persist. Thus, the sooner the dispersivity reaches its asymptotic value, the less sensitive the model is to changes in boundary conditions. A model of a finite system, should become more robust as the correlation length of the permeability represented by dispersivity becomes smaller.

The ability to represent the mixing induced by a particular permeability field using dispersivities depends on the character of the permeability field. For permeability fields whose statistical character is known, it may be possible to determine the robustness of a dispersivity model *a priori* by comparing the correlation length to the system length. If statistical analysis alone is not adequate, the spreading character induced by the permeability field can be determined by flow simulations. As discussed above and elsewhere, examining the effluent concentration alone is not a good indication of model robustness.[42,2,1] Instead, it is important to examine the rate at which a front or plume changes with time. As always, such flow simulations will contain errors due to numerical and geologic discretization.

V. OPTIMAL REPRESENTATION SCALE

The first experiment showed that an optimum GRS cannot generally be defined by a straightforward analysis of model response versus representation scale. The second experiment supports the common belief that a fine scale permeability field can be represented by a combination of explicit representation and representation through effective mixing parameters. However, if the spatial correlation of the non-represented permeability is large with respect to the system size, this scheme probably will not work. Fortunately, the results of the first experiment show

that the correlation length of the non-represented permeabilities can be reduced by decreasing the representation scale. At a sufficiently small GRS, mixing induced by non-represented permeabilities can be represented robustly by effective mixing parameters. Hence, this work defines the optimal representation scale as the largest scale at which the effective mixing parameters are robust.

The success of this method for choosing a GRS and constructing a robust permeability model depends on a number of things. Primarily, the spatial correlation of the non-represented permeability must decrease with the GRS. In addition, it is important to have a good scheme for determining the explicit permeability representation. Not so much for improving model robustness at the optimal GRS, but because it allows for a larger optimal GRS. Other issues and possible complications are discussed below.

A. Averaging Volume for Effective Mixing Parameters

In section IV., a single longitudinal dispersivity was used to model the mixing behavior through the non-represented permeability field. The robustness of the dispersivity was determined by analyzing a concentration averaged across the entire system, $\bar{C}(x)$. Consider a concentration which is averaged over a smaller distance, $\bar{C}_{L_{avg}}(x,y,t) = \frac{1}{L_{avg}} \int_{y-L_{avg}/2}^{y+L_{avg}/2} C(x,\alpha,t)\, d\alpha$. As L_{avg} decreases from L_y to $L_{rep} = \frac{1}{8}$ the size of the fingers in the white-noise field, Figure 5b, become large with respect to L_y. As a consequence, the behavior of $\bar{C}_{L_{avg}}(x,y,t)$ can no longer be modeled with a dispersivity. The reason for this is that the permeability correlation scale has become large compared to the averaging scale. As such, an individual permeability flow path or barrier is more likely to significantly affect the average concentration. Consequently, the average concentration is less predictable, more variable, and more difficult to model. Similar discussions on the relation to averaging volumes and variability can be found elsewhere.[42,43]

Consider, then, the commonly used procedure whereby a different effective parameter is defined for each representation block.[9,44,45] Most often, block effective parameters are defined to match flow behavior through a representation block from a fine scale simulation. The idea is to develop model robustness by matching as closely as possible the mixing occurring in each block. Unfortunately, if the correlation scale of the permeability is on the order of the representation scale or larger, the mixing behavior occurring within an individual block is not robustly

modeled by a dispersivity. Hence, the coarse model has a different dispersivity for each block, none of which is accurate (able to match a single response) or robust (able to model under various flow conditions with the same accuracy). The only hope is that the errors occurring within each block are not systematic; thus, canceling one another through the coarse of a simulation. Because heterogeneity is likely to exists at all scales, the situation is likely to get worse as the representation scale decreases. That is, the number of individual dispersivities will increase, without necessarily increasing their robustness or the robustness of the model as a whole. This partially explains the behavior observed by Davies and Haldorsen,[16] where the model only became accurate when the representation scale increased beyond that of the largest shale.

The use of a single dispersivity for the entire model has several advantages. First, it results in a simpler model. Next, the accuracy and robustness of the dispersivity increases as the representation scale decreases. This, is of coarse, crucial to applying the definition of the optimal GRS. Finally, the robustness of the dispersivity is an indication of the robustness of the model as a whole. The disadvantage of using a single dispersivity is that its determination may require regression. However, the non-represented permeability may be useful in that regard. Spatially, varying effective mixing parameters should only be necessary if the non-represented permeability is not statistically homogeneous.

B. Multi-Phase Flow, Diffusion

The term effective mixing parameter is used in this paper to emphasize that much of the discussion about the representation of permeability heterogeneity should be applicable to processes other than tracer flow. The primary feature of multi-phase flow is that functions, rather than scalar parameters may be employed in matching fine scale results. Thus, a single fine scale simulation can often be matched. The, danger then is to confuse the ability to match a single scenario with model robustness. Ideally, the robustness of a relative permeability could be determined by examining x,t diagrams of flow through the non-represented permeability.[2] Whether such a test of robustness is valid is not known.

Diffusion was assumed to be zero in both of the studies performed herein. Large amounts of diffusion lessen the growth of convective fingers due to heterogeneity by causing mass transfer between convective fingers and adjacent zones.[1,19] For a finite diffusion coefficient, the importance of the diffusion term depends on the flow rate. The higher the flow rate, the less important the diffusion term, and the greater the size of convective

fingers due to heterogeneity. Thus, a large amount diffusion should ease the representation of permeability heterogeneity. However, because this effect depends on the flow rate, the highest flow rate expected in the reservoir should be used when determining the GRS.

VI. CONCLUSIONS

- When holding all reservoir parameters but permeability at their point values, reservoir response may continue to vary as the GRS decreases.

- The optimal GRS is defined as the maximum scale at which effective mixing parameters robustly represent sub-representation scale heterogeneities.

- The non-represented permeability is useful in determining the robustness of effective mixing parameters and perhaps in determining their value.

- The optimal GRS is primarily a function of system size.

- The use of a single effective mixing parameter, averaged over the entire system, helps to simplify the model. It also insures that the effective mixing parameter will become more robust as the GRS decreases.

The second to the last conclusion depends on the spatial correlation scale of the non-represented permeability being approximately the same as the GRS. The final conclusion depends on the non-represented permeability being statistically homogenous for small representation scales. If this is not the case, it may be necessary to use different methods to calculate block permeabilities and/or allowing for spatially varying effective mixing parameters.

NOMENCLATURE

C	=	concentration
$C(h)$	=	spatial autocovariance at separation distance h
$\bar{C}$	=	spatial average concentration
$Cov(X,Y)$	=	covariance of X and Y
D	=	porous media diffusion coefficient
$E(X)$	=	expected value of X
$\mathrm{erfc}(x)$	=	complementary error function
GRS	=	geologic representation scale
h	=	separation distance (lag)
k	=	permeability
$\vec{\vec{K}}$	=	dispersion tensor
L_{rep}	=	representation length
L_x, L_y, L_z	=	system length in x,y and z directions
L_κ	=	correlation length of log-permeability
N_{rep}	=	number of representation blocks
t	=	time
$\vec{u}$	=	Darcy velocity, volumetric flux
$\vec{v}$	=	interstitial velocity
$\vec{v}_c$	=	velocity of a concentration
x	=	Cartesian direction
x_c	=	x location of a concentration
y	=	Cartesian direction
α_L,α_T	=	longitudinal and transverse dispersivity
$\vec{\vec{\delta}}$	=	identity tensor
κ	=	log-permeability
$\gamma(h)$	=	semi-variogram for separation distance h
ϕ	=	porosity
Φ	=	flow potential
σ^2	=	variance

Subscripts

l	=	layer property
w	=	white-noise property
r	=	represented
nr	=	non-represented

ACKNOWLEDGEMENTS

Thanks to André Journel and Tom Hewett for their criticisms and suggestions.

REFERENCES

1. Arya, A., Hewett, T. A., Larson, R. G., and Lake, L. W.: "Dispersion and Reservoir Heterogeneity," *SPERE* (February 1988) 139–48.

2. Hewett, T. A. and Behrens, R. A.: "Conditional Simulation of Reservoir Heterogeneity with Fractals," paper SPE 18326 presented at the 1988 SPE Annual Technical Conference and Exhibition, Houston.

3. Desbarats, A. J.: *Stochastic Modeling of Flow in Sand-Shale Sequences*, PhD dissertation, Stanford University, Stanford, CA (February 1987).

4. White, C. D.: *Representation of Heterogeneity for Numerical Reservoir simulation*, PhD dissertation, Stanford University, Stanford, CA (June 1987).

5. Haldorsen, H. H. and Lake, L. W.: "A New Approach to Shale Management in Field-Scale Models," *SPEJ* (August 1984) 447–457.

6. Rubin, Y., Gómez-Hernández, J. J., and Journel, A. G.: "Analysis of Upscaling and Effective Properties in Disordered Media," *Reservoir Characterization, II*, L. W. Lake and H. B. Carroll Jr. (eds.), Academic Press, Inc., London (1991).

7. Coats, K. H., Nielson, R. L., Terhune, M. H., and Weber, A. G.: "Simulation of Three Dimensional, Two-Phase Flow in Oil and Gas Reservoirs," *SPEJ* (1967) 377–388.

8. Hearn, C. L.: "Simulation of Stratified Waterflooding by Pseudo Relative Permeability Curves," *JPT* (July 1971) 805–813.

9. Kyte, J. R. and Berry, D. W.: "New Pseudo Functions to Control Numerical Dispersion," *SPEJ* (August 1975) 269–276.

10. Jacks, H. H., Smith, O. J. E., and Mattax, C. C.: "The Modeling of a Three-Dimensional Reservoir with a Two-Dimensional Reservoir Simulator-The Use of Dynamic Pseudo Functions," *SPEJ* (June 1974) 175–185.

11. Tollas, J. M. and McKinney, A.: "Brent Field 3-D Reservoir Simulation," paper SPE 18306 presented at the 1988 SPE Annual Technical Conference and Exhibition, Houston.

12. Coats, K. H.: "Use and Misuse of Reservoir Simulation Models," *JPT* (November 1969) 1391–1398.

13. Smith, P. J. and Brown, C. E.: "The Interpretation of Tracer Test Response from Heterogeneous Reservoirs," paper SPE 13262 presented at the 1984 SPE Annual Technical Conference and Exhibition, Houston.

14. Stalkup, F. I., Lo, L. L., and Dean, R. H.: "Sensitivity to Gridding of Miscible Flood Predictions Made With Upstream Differenced Simulators," paper SPE 20178 presented at the 1990 SPE/DOE Symposium on Enhanced Oil Recovery, Tulsa.

15. Warren, J. E. and Price, H. S.: "Flow in Heterogeneous Porous Media," *SPEJ* (September 1961) 153–56.

16. Davies, B. J. and Haldorsen, H. H.: "Pseudofunctions in Formations Containing Discontinuous Shales: A Numerical Study," paper SPE 16012 presented at the 1987 SPE Reservoir Simulation Symposium, San Antonio.

17. Testerman, J. D.: "A Statistical Reservoir-Zonation Technique," *JPT* (August 1962) 889–893.

18. Craig, Jr., F. F.: "Effect of Reservoir Description on Performance Predictions," *JPT* (October 1970) 1239–1245.

19. Lake, L. W. and Hirasaki, G. J.: "Taylor's Dispersion in Stratified Porous Media," *SPEJ* (August 1981) 459–468.

20. Silva, R. J., Niko, H., van den Bergh, J. N., and Sancevic, Z. A.: "Numerical Modeling of Gas and Water Injection in a Geologically Complex Volative Oil Reservoir in the Lake Maracaibo Area, Venezuela," paper SPE 18322 presented at the 1988 SPE Annual Technical Conference and Exhibition, Houston.

21. Gómez-Hernández, J. J.: *A Stochastic Approach to the Simulation of Block Conductivity Fields Conditioned Upon Data Measured at a Smaller Scale*, PhD dissertation, Stanford University, Stanford, CA (March 1991).

22. Gelhar, L. W. and Axness, C. L.: "Three-Dimensional Stochastic Analysis of Macrodispersion in Aquifers," *Water Resour. Res.* (February 1983) **19**, No. 1, 161–180.

23. Wattenbarger, R. C.: *Robust Representation of Permeability Heterogeneity*, PhD dissertation, Stanford University, Stanford, CA (*to be completed* 1992).

24. Journel, A. G. and Huijbregts, C. J.: *Mining Geostatistics*, Academic Press Inc., London (1978).

25. Clark, I.: *Practical Geostatistics*, Applied Science Publishers Ltd., Essex (1979).

26. Isaaks, E. H. and Srivastava, R. M.: *Applied Geostatistics*, Oxford University Press, New York (1989).

27. Rubin, Y. and Gómez-Hernández, J. J.: "A Stochastic Approach to the Problem of Upscaling of Transmissivity in Disordered Media. 1. Theory and Unconditional Simulations," *Water Resour. Res.* (April 1990) **26**, No. 4, 691–701.

28. Lake, L. W.: *Enhanced Oil Recovery*, Prentice Hall Inc., New Jersey (1989).

29. Saad, Y. and Schultz, M. H.: "GMRES: A Generalized Minimal Residual Algorithm for Solving Non-Symmetric Linear Systems," *SIAM J. Sci. Comput.* (1986) No. 7, 856–869.

30. Wattenbarger, R. A.: "Convergence of the Implicit Pressure-Explicit Saturation Method," *JPT* (November 1968) 1220.

31. Roe, P. L.: "Some Contributions to the Modelling of Discontinuous Flows," Lectures in Applied Mathematics (1985) **22**, 163–193.

32. Furtado, F., Glimm, J., Lindquist, B., and Pereira, F.: "Multi-Length Scale Computations of the Mixing Length Growth in Tracer Flows," Emerging Technologies Conference, F. Kovarik (ed.), Houston, TX (June 1990).

33. Mishra, S.: *On the Use of Pressure and Tracer Test Data for Reservoir Description*, PhD dissertation, Stanford University, Stanford, CA (September 1987).

34. Araktingi, U. G.: *Viscous Fingering in Heterogeneous Porous Media*, PhD dissertation, Stanford University, Stanford, CA (June 1988).

35. Jensen, J. L. and Lake, L. W.: "The Influence of Sample Size and Permeability Distribution on Heterogeneity Measures," *SPERE* (May 1988) 629–37.

36. Dykstra, H. and Parsons, R. L.: "The Prediction of Oil Recovery by Waterflooding," *Secondary Recovery of Oil in the United States*, API (1950).

37. Pande, K. K., Ramey, Jr., H. J., Brigham, W. E., and Orr, Jr., F. M.: "Frontal Advance Theory for Flow in Heterogeneous Porous Media," paper SPE 16344 presented at the 1987 SPE California Regional Meeting, Ventura.

38. Correa, A. C., Pande, K. K., Ramey, Jr., H. J., and Brigham, W. E.: "Prediction and Interpretation of Miscible Displacement Performance Using a Transverse Matrix Dispersion Model," paper SPE 16704 presented at the 1987 SPE Annual Technical Conference and Exhibition, Dallas.

39. Dagan, G.: "Time-Dependent Macrodispersion for Solute Transport in Anisotropic Heterogeneous Aquifers," *Water Resour. Res.* (September 1988) **24**, No. 9, 1491–1500.

40. Neuman, S. P.: "Universal Scaling of Hydraulic Conductivities and Dispersivities in Geologic Media," *Water Resour. Res.* (August 1990) **26**, No. 8, 1749–1758.

41. Serra, J.: "Les Structures Gigognes: Morphologie Mathematique et Interpretation Metallogenique," *Mineralium Deposita* (1968) **3**, 135–154.

42. Dagan, G.: "Solute Transport in Heterogeneous Porous Formations," *J. Fluid Mech.* (1984) **145**, 151–177.

43. Haldorsen, H. H.: "Simulator Parameter Assignment and the Problem of Scale in Reservoir Engineering," *Reservoir Characterization*, L. W. Lake and H. B. Carroll Jr. (eds.), Academic Press, Inc., London (1986) 293–340.

44. Lasseter, T. J., Waggoner, J. R., and Lake, L. W.: "Reservoir Heterogeneities and their their influence on ultimate recovery," *Reservoir Characterization*, L. W. Lake and H. B. Carroll, Jr. (eds.), Academic Press, Inc. (1986) 545–559.

45. Kossack, C. A.: "Scaling-Up Laboratory Relative Permeabilities and Rock Heterogeneities With Pseudo Functions for Field Simulations," paper SPE 18436 presented at the 1989 SPE Annual Technical Conference and Exhibition, Houston.

DETERMINING ORIENTATION AND CONDUCTIVITY OF HIGH PERMEABILITY CHANNELS IN NATURALLY FRACTURED RESERVOIRS

H. Kazemi
Marathon Oil Company
Littleton, Colorado

A. A. Shinta
Colorado School of Mines
Golden, Colorado

SUMMARY

All reservoirs are likely to contain natural fractures. These fractures, in general, do not form an interconnected network, but they do affect primary production and the displacement of oil by water, gas, or other displacing agents. To improve the displacement efficiency of the secondary and tertiary oil recovery processes, we do need to know fracture orientation and conductivity in a reservoir, both locally and globally. Once these information become available, remedial measures to improve oil recovery can be accomplished more prudently.

In this paper, two techniques to determine the effective orientation and conductivity of fractures in the drainage area of a cluster of wells will be presented. One technique is the classical pressure interference testing and the second technique is the use of chemical tracers. Tracer techniques should provide more resolution than the interference testing. Mathematical models will be presented for both applications.

The mathematical model for the tracer response analysis is new and uses a simple and flexible matrix-fracture transfer function. The computer code for the model executes one to two orders of magnitude faster than the conventional dual-porosity/dual-permeability formulations. Furthermore, two different nine-point finite difference schemes are used to appropriately account for the flow channeling and the permeability tensor.

I. INTRODUCTION

Folding, faulting, and subsidence of sediments over geologic time cause fracturing. The more brittle the rock, the more intensely it

fractures. Carbonate reservoirs are typically more fractured than sandstone reservoirs for this reason. Solution enlargement of the pores near fractures is possible, as is also partial or full sealing of fractures by mineral precipitation.

Natural fractures affect all phases of petroleum reservoir life from the accumulation of oil to the techniques used to manage oil production. Although fractures were known since the 1860's to exist in many oil reservoirs, it has only been in the last thirty or forty years that a significant interest in the effect of fractures on oil production has emerged.

Naturally fractured reservoirs are generally classified as "dual-porosity" where one porosity is associated with the matrix (reservoir host rock) and another porosity represents the fractures and vugs. In dual-porosity oil reservoirs, fractures provide the main path for fluid flow from the reservoir, then oil from the matrix blocks flows into the fracture space and the fractures carry the oil to the wellbore. For water-wet reservoirs, when water comes in contact with the oil zone, water imbibes into the matrix blocks to displace oil. Combinations of large flow rates, low matrix permeability, and weak imbibition result in water fingering through the fractures into the wellbore. Once fingering of water occurs, the water-oil ratio increases to large values. In oil reservoirs containing free gas, gas fingering and high gas-oil ratio could also be expected.

Fractured reservoirs come in a wide variety of rock mineralogy (carbonate, diatomite, granite, schist, sandstone, shale and coal), porosity, and permeability. Carbonates include limestone, dolomite, and chalk. Fractured limestones are prevalent in the giant and prolific fields of the Middle East. Fractured dolomites are exemplified by the San Andres formation in many West Texas fields and fractured chalks are found in Texas (Austin Chalk), North Sea (Ekofisk), and other parts of the world. Fractured sandstone/siltstone is typified by Spraberry Field in Texas and diatomite is the rock mineralogy of a producing formation in the Belridge Field in California. Fractured Monterey formation in coastal California is composed of chert, dolostone, porcellanite and organic-rich marl.

The presence of open fractures, the degree of fracture interconnectedness, and permeability anisotropy significantly affect the mechanisms responsible for oil recovery from the matrix. Viscous displacement of oil by water or gas in the matrix is often not very significant because only very small pressure gradients are generated across the individual matrix blocks that are surrounded by fractures. Solution gas drive, gravity drainage, and water imbibition are the most prevalent recovery mechanisms, but depending on the effective

size of matrix blocks much of the oil can remain in the matrix. And, this remaining oil is the target for improved oil recovery.

Many old and new ideas are being applied or considered for producing the unrecovered mobile oil from fractured reservoirs. These include the use of horizontal wells, infill wells, pattern realignment, conformance improving gels and foams, surface active agents for wettability alteration, dilute surfactant, steam, and CO_2. Infill drilling can provide a means of accessing the poorly drained segments (or compartments) of a reservoir.

To improve oil recovery from naturally fractured reservoirs one needs to quantify the channelling of injected fluids and develop a map of the flow channel distribution for remedial measures. This paper is intended to provide a viable technique to accomplish this when tracers are used.

II. DIRECTIONAL FLOW

A. Pressure Interference Testing

Directional flow results from either permeability anisotropy in an otherwise homogeneous reservoir or the presence of high permeability channels in a heterogeneous reservoir. The latter, under favorable conditions however, could effectively produce flow characteristics of an isotropic homogeneous reservoir. In fact, pressure interference testing conducted in many domestic reservoirs has produced results that support this claim. One example of such a test was reported by Gogarty as shown by Fig. 1.[1] It can be seen that the permeability magnitude varies from one part of the field to another, but the permeability major axis is southwest-northeast direction.

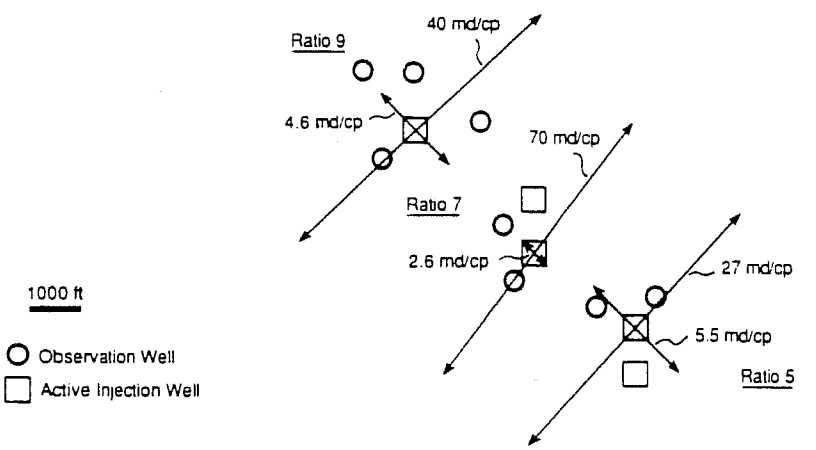

FIGURE 1. INTERFERENCE TESTING
(From Gogarty, W.B., JPT, 1983, Courtesey SPE)

Earlougher presents a technique to determine the direction and magnitude of the permeability tensor from pressure interference testing data.[2] The technique requires measurement of pressure response in at least three observation wells. The analysis of these pressures by type-curve matching (or least-squares regression technique) yields k_{xx}, k_{yy} and k_{xy} which are used to calculate k_{max}, k_{min} and θ. Equations are summarized in Appendix A.

B. Tracer Response Analysis

In this section we develop the equations for the water soluble tracers (e.g., B_r^-, I^-, and SCN^-) in waterflooding operations. Similar equations can be developed for gas tracers in gas injection operations.

In an earlier paper Kazemi, et al.,[3] presented a numerical scheme for solving an analog of the Buckley-Leverett waterflooding problem for fractured reservoirs. The waterflood equations plus tracer transport equations are presented below.

The waterflood equation is:

$$-u\frac{\partial f_{wf}}{\partial x}=\frac{\partial S_{wf}}{\partial t}+\frac{\lambda R_\infty}{\phi_f}\int_0^t e^{-\lambda(t-\tau)}\frac{\partial S_{wf}}{\partial \tau}d\tau \qquad (1)$$

Equation (1) was solved numerically as shown:

$$-u\left(f^n_{wf,i}-f^n_{wf,i-1}\right)/\Delta x_i=\left(S^{n+1}_{wf,i}-S^n_{wf,i}\right)/\Delta t$$

$$+\frac{R_\infty\lambda}{\phi_f}\sum_{j=0}^{n}\left[\left(S^{j+1}_{wf,i}-S^i_{wf,i}\right)\prod_{k=j}^{n}e^{-\lambda\Delta t_k}\right];$$

$$i=1,2,\ldots,IMAX \qquad (2)$$

$$S^{n+1}_{wf,i}-S^n_{wf,i}=\left(\frac{1}{\Delta t_n}+\frac{R_\infty\lambda}{\phi_f}e^{-\lambda\Delta t_n}\right)^{-1}$$

$$x\left\{-u\frac{f^n_{wf,i}-f^n_{wf,i-1}}{\Delta x_i}-\frac{R_\infty\lambda}{\phi_f}SUM^{n-1}\,e^{-\lambda\Delta t_n}\right\} \qquad (3)$$

$$SUM^{n-1} = \left[SUM^{n-2} + \left(S^{n}_{wf,i} - S^{n-1}_{wf,i-1}\right)\right] e^{-\lambda \Delta t_{n-1}} \; ; \; n \geq 1 \qquad (4)$$

$$SUM^{-1} = 0$$

Equation (1) uses a matrix-fracture transfer function of the form

$$R = R_{\infty}\left(1 - e^{-\lambda t}\right) \qquad (5)$$

For more flexibility in matching reservoir performance, one can easily use the following form

$$R = R_{\infty} - R_1 e^{-\lambda_1 t} - R_2 e^{-\lambda_1 t} - \ldots \qquad (6)$$

where

$$R_1 + R_2 + \ldots = R_{\infty}. \qquad (7)$$

To use Eq. (6) in Eq. (1), one should replace the transfer function

$$\tau_w = \frac{\lambda R_{\infty}}{\phi_f} \int_0^t e^{-\lambda (t-\tau)} \frac{\partial S_{wf}}{\partial \tau} d\tau$$

with

$$\tau_w = \frac{\lambda_1 R_1}{\phi_f} \int_0^t e^{-\lambda_1 (t-\tau)} \frac{\partial S_{wf}}{\partial \tau} d\tau + \frac{\lambda_2 R_2}{\phi_f} \int_0^t e^{-\lambda_2 (t-\tau)} \frac{\partial S_{wf}}{\partial \tau} d\tau + \ldots \qquad (8)$$

In the one-dimensional setting, the tracer transport equation for a given non-adsorbing tracer will be

$$-u \frac{\partial S_{wf} C}{\partial x} = \frac{\partial S_{wf} C}{\partial t} + \left[\frac{\lambda R_{\infty}}{\phi_f} \int_0^t e^{-\lambda (t-\tau)} \frac{\partial S_{wf}}{\partial \tau} d\tau\right] C \qquad (9)$$

To solve Eq. (9) numerically, we follow the format of Eq. (2) as follows:

$$-u\left(f^n_{wf,i}\,C^n_i - f^n_{wf,i-1}\;C^n_{i-1}\right)/\Delta x_i = \left(S^{n+1}_{wf,i}\,C^{n+1}_i - S^n_{wf,i}\;C^n_i\right)/\Delta t$$

$$+\left\{\frac{R_\infty\,\lambda}{\phi_f}\sum_{j=0}^{n}\left[\left(S^{j+1}_{wf,i} - S^j_{wf,i}\right)\prod_{k=i}^{n} e^{-\lambda\Delta t_k}\right]\right\} C^{n+1}_i\;;$$

$$i = 1, 2, \ldots, IMAX \qquad (10)$$

Equation (2) is first solved for $S^{n+1}_{wf,i}$; then it is substituted in Eq. (10) to solve for C^{n+1}_i

For three-dimensional field simulations, the following equations are solved simultaneously by standard fully implicit reservoir simulation techniques:

Water:

$$\Delta\left[T_{wf}\left(\Delta p_{wf} - \gamma_{wf}\,\Delta D_f\right)\right] - \tau_w + q_{wf} = \frac{V_R}{5.6146\Delta t}\,\Delta_t\left(\frac{\phi_f\,S_{wf}}{B_{wf}}\right) \qquad (11)$$

Oil:

$$\Delta\left[T_{of}\left(\Delta p_{of} - \gamma_{of}\,\Delta D_f\right)\right] - \tau_o + q_{of} = \frac{V_R}{5.6146\Delta t}\,\Delta_t\left(\frac{\phi_f\,S_{of}}{B_{of}}\right) \qquad (12)$$

where the x-components of the transmissibilities T_{wf} and T_{of} are shown below:

$$T_{wfx} = 0.001127\,\frac{\Delta y\Delta z}{\Delta x}\,k_{fxx}\left(\frac{k_r}{\mu B}\right)_{wf} \qquad (13)$$

$$T_{ofx} = 0.001127\,\frac{\Delta y\Delta z}{\Delta x}\,k_{fxx}\left(\frac{k_r}{\mu B}\right)_{of} \qquad (14)$$

The water and oil transfer functions are:

$$\tau_w = \frac{R_\infty \lambda V_R}{5.6146} \sum_{j=0}^{n} \left\{ \Delta_t \left(\frac{S_{wf}}{B_{wf}} \right) \prod_{k=j}^{n} e^{-\lambda \Delta t_k} \right\} \tag{15}$$

$$\tau_o = \frac{R_\infty \lambda V_R}{5.6146} \sum_{j=0}^{n} \left\{ \Delta_t \left(\frac{S_{of}}{B_{of}} \right) \prod_{k=j}^{n} e^{-\lambda \Delta t_k} \right\} \tag{16}$$

Tracer in water:

$$\Delta\left[T_{wf}\left(\Delta p_{wf} - \gamma_{wf} \Delta D_f\right) C + \hat{K}_{wf} \Delta C\right] - \tau_w C + q_{wf} C$$

$$= \frac{V_R}{5.6146\ \Delta t} \Delta_t \left[\left(\frac{\phi_f S_{wf} C}{B_{wf}} \right) + \left(1 - \phi_f\right) (SG)_s\, a \right] \tag{17}$$

where $\hat{K}_{wf}$ is the dispersivity coefficient multiplier, and its x-component is given by Eq. (18):

$$\hat{K}_{wfxx} = \frac{\Delta y\, \Delta z}{\Delta x} K_{wfxx} \tag{18}$$

K_{xx}, K_{xy}, and K_{yy} are the components of the dispersivity coefficient tensor as shown below:

$$K_{wfxx} = \frac{D_{wf}}{\tau_f} + \frac{1}{\phi_f S_{wf} |\vec{v}_{wf}|} \left[\alpha_{Lwf} v_{wfx}^2 + \alpha_{Twf} v_{wfy}^2 \right] \tag{19}$$

$$K_{wfxy} = K_{wfyx} = \frac{1}{\phi_f S_{wf} |\vec{v}_{wf}|} \left[\left(\alpha_{Lwf} - \alpha_{Twf} \right) v_{wfx} v_{wfy} \right] \tag{20}$$

$$K_{wfyy} = \frac{D_{wf}}{\tau_f} + \frac{1}{\phi_f S_{wf} |\vec{v}_{wf}|} \left[\alpha_{Lwf} v_{wfy}^2 + \alpha_{Twf} v_{wfx}^2 \right] \tag{21}$$

$$\vec{v}_{wf} = -\bar{\bar{k}}_f \frac{k_{rwf}}{\mu_w} \left(\nabla p_{wf} - \gamma_w \nabla D \right) \tag{22}$$

$$|\vec{v}_{wf}| = \left(v_{wfx}^2 + v_{wfy}^2\right)^{1/2} \tag{23}$$

The mathematical details and program code will appear in Ref. 4.

C. Nine-Point Difference

To properly account for either reservoir channelling or permeability anisotropy, and to reduce grid orientation we used two different nine-point schemes in the xy-plane that will be described below.

If flow channelling in a fractured reservoir is the result of reservoir heterogeneity (and not a result of permeability anisotropy) then a five-point connection grid as shown by Fig. 2 is inadequate. This problem can be greatly alleviated by using a nine-point connection grid as shown by Fig. 3. Then we superimpose a nine-point finite-difference on this grid with a weight of 1/2 for each of the eight connections to a given node; the center node will have, therefore, a weight of 4. This contrasts the 2/3 weight for the x and y directions and 1/6 weight for the diagonal direction in a standard 9-point formulation.[7] Our 1/2 weights are based on the assumption that each of the eight channels emanating from a node acts independent of each other and each channel's permeability, viscosity, and pressure gradient control the amount of flow in that channel according to Darcy's equation. It can be shown by a physical argument that the 1/2 weight is actually $\sqrt{2}/(2+\sqrt{2})$ or 0.4142. But, the use of 1/2 does not make much difference in the outcome of the calculations.

If flow channelling in a fractured reservoir is the result of permeability anisotropy, then the nine-point connection of Fig. 3 plus the use of Shiralker's nine-point coefficients[5] should produce accurate results. Shiralker's coefficients also greatly reduce grid orientation sensitivity for high mobility displacements. More information on this subject is reported by Wolcott.[6] As in Wolcott's work, we use a modified set of Shiralker coefficients (please see Appendix B) that we developed for harmonic-averaged permeability in a block-centered grid in contrast to arithmetic-averaged permeability used by Shiralkar in a point-distributed grid.

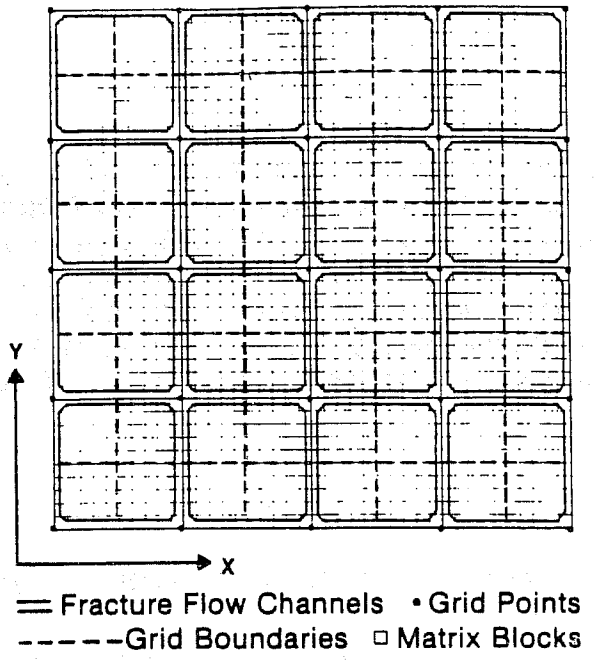

FIGURE 2. FIVE-POINT CONNECTION GRID.
(from Gilman and Kazemi, 1983, courtesy SPE)

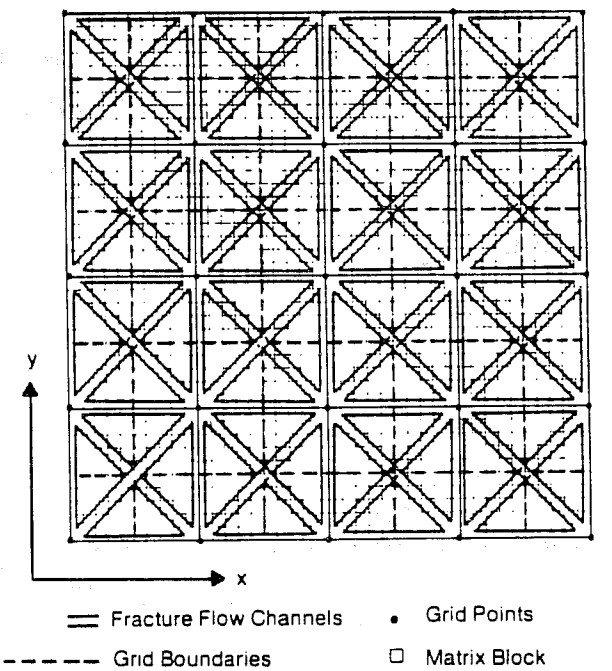

FIGURE 3. NINE-POINT CONNECTION GRID
(from Gilman and Kazemi, 1983, courtesy SPE)

III. RESULTS

We first present numerical results for a tracer injection in an inverted five-spot using two grid orientations—the diagonal and the parallel—as described elsewhere.[7] In these experiments, we use both the Shiralkar and the 1/2-weight coefficients both for a homogeneous isotropic example and an anisotropic example. The data used to evaluate the simulator is shown in Table 1. Figures 4-7 are for the homogeneous isotropic example and Fig. 8 and 9 are for the anisotropic example.

TABLE I

DATA USED TO EVALUATE SIMULATOR

B_o	=	1 RB/STB
B_w	=	1 RB/STB
p_i	=	100 psia
S_{wi}	=	0.275
μ_o	=	1.67 cp
μ_w	=	0.5 cp
$c_w = c_o$	=	10^{-5} psi^{-1}
p_{cf}	=	0
$\Delta x = \Delta y$	=	187 ft
Δz	=	20 ft
k_{rwf}	=	$k^{\cdot}_{rwf}\left(\frac{S_{wf} - S_{wrf}}{1 - S_{wf} - S_{orf}}\right)^{nw}$
k_{rof}	=	$k^{\cdot}_{rof}\left(\frac{S_{wf} - S_{orf}}{1 - S_{wf} - S_{orf}}\right)^{no}$
k^{*}_{rwf}	=	0.3
k^{*}_{rof}	=	1.0
S_{wrf}	=	S_{wrm} = 0.275
S_{orf}	=	S_{orm} = 0.375
nw	=	3.4
no	=	2.0
M	=	1 (using end-point relative permeabilities)
R_∞	=	0.07
λ_1	=	0.005 day^{-1} (0-2 MOPV)
λ_2	=	0.25 day^{-1} (2- ∞ MOPV)
ϕ_f	=	0.01
ϕ_m	=	0.20
t_{inj}	=	10 days

Onset of tracer injection at WOR = 10-15
Grid Network:
- Diagonal 6x6
- Parallel 8x8

Permeability:
- Homogeneous: $k_{xxf} = k_{yyf} = k_{45°}$ = 39,528 md
- Anisotropic: Parallel, k_{xxf} = 125,000 md, k_{yyf} = 12,500 md, k_{xyf} = 0
  Diagonal, k_{xxf} = 68,750 md, k_{yyf} = 68,750 md, k_{xyf} = 56,250 md

Injection Rate:
- Diagonal 600 B/D
- Parallel 553 B/D

Injected Tracer Concentration 20,000 ppm
Dispersion Coefficient = 0

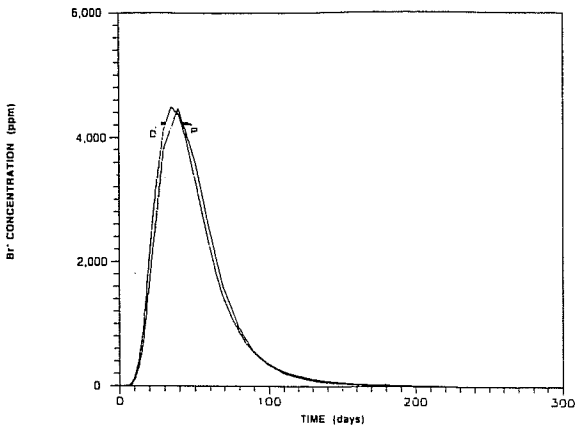

FIGURE 4. TRACER RESPONSE FOR HOMOGENOUS RESERVOIR USING SHIRALKAR NINE-POINT COEFFICIENTS.
(R_{mo}=0.07, M=1, P=parallel 8x8 grid, D=diagonal 6x6 grid)

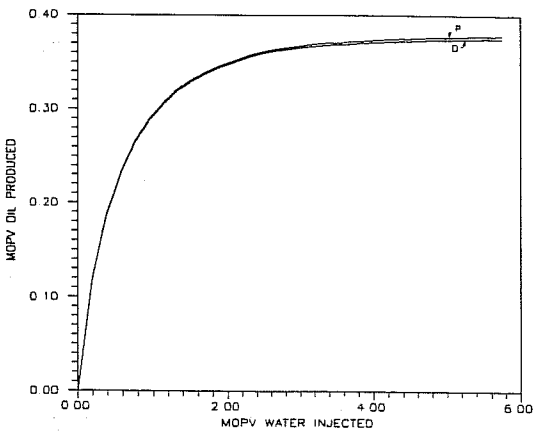

FIGURE 5. OIL RECOVERY FOR HOMOGENOUS RESERVOIR USING SHIRALKAR NINE-POINT COEFFICIENTS.
(R_{mo}=0.07, M=1, P=parallel 8x8 grid, D=diagonal 6x6 grid)

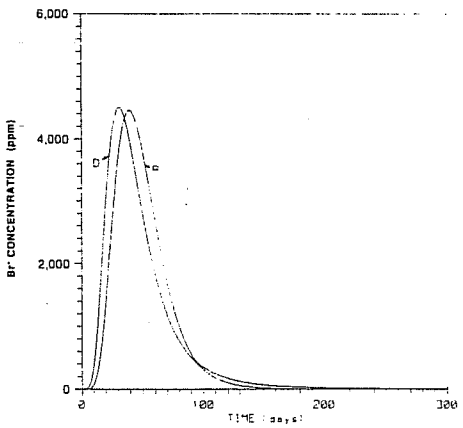

FIGURE 6. TRACER RESPONSE FOR HOMOGENOUS RESERVOIR USING 1/2 WEIGHTING NINE-POINT COEFFICIENTS.
(R_{mo}=0.07, M=1, P=parallel 8x8 grid, D=diagonal 6x6 grid)

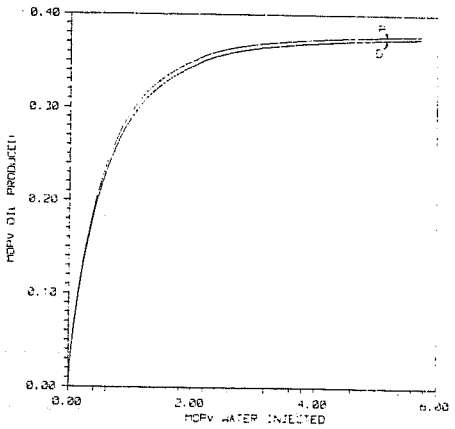

FIGURE 7. OIL RECOVERY FOR HOMOGENOUS RESERVOIR USING 1/2 WEIGHTING NINE-POINT COEFFICIENTS.
(R_{mo}=0.07, M=1, P=parallel 8x8 grid, D=diagonal 5x6 grid)

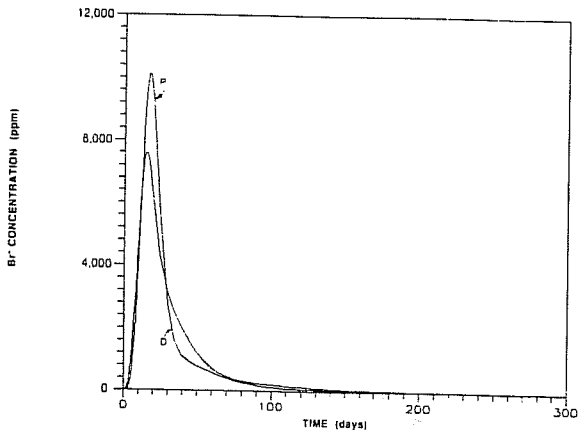

FIGURE 8. TRACER RESPONSE FOR ANISOTROPIC RESERVOIR USING SHIRALKAR NINE-POINT COEFFICIENTS.
R_{mo}=0.07, M=1, P=parallel 8x8 grid, D=diagonal 5x6 grid)

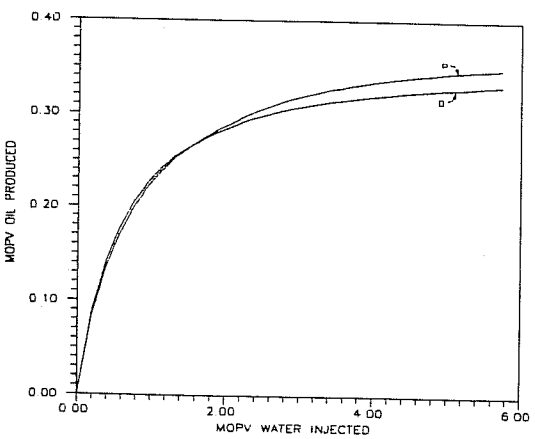

FIGURE 9. OIL RECOVER FOR ANISOTROPIC RESERVOIR USING SHIRALKAR NINE-POINT COEFFICIENTS.
(R_{mo}=0.07, M=1, P=parallel 8x8 grid, D=diagonal 5x6 grid)

Next we present a field example for an inverted five-spot waterflood pattern with data shown in Table 2. The data were modified for the purpose of this paper. The original field waterflood pattern resembles Fig. 10. Tracer was injected in the center well for 30 days. The tracer response measured in Wells A, B, C and D are the results of tracer coming from the center injector diluted by water containing no tracer from other water injectors outside the center pattern and water entering the wells from the underlying aquifer. The tracer response shown for Wells A, B, C, and D were, therefore, adjusted by material balance for the dilutions (please see Appendix C); and the simulation was performed on the shaded area as a confined five-spot pattern.

TABLE II

FIELD DATA

B_o	=	1.044 RB/STB	k_{rwf}	=	$S_{wf}^{1.2}$
B_w	=	0.998 RB/STB	k_{rof}	=	$(1 - S_{wf})^{1.2}$
p_i	=	1000 psia	$\Delta x = \Delta y$	=	54.4 ft
S_{wfi}	=	0.0	Δz	=	40 ft
μ_o	=	8 cp	ϕ_f	=	0.01 (initial estimate)
μ_w	=	0.9 cp	ϕ_m	=	0.18
p_{cf}	=	0	S_{wrm}	=	0.2
$c_w = c_\phi$	=	3.5×10^{-6} psi^{-1}	S_{orm}	=	0.3
c_o	=	1×10^{-5} psi^{-1}	k_m	=	30 md

Grid Network:
15x15x1

Injection Data:
q_{inj} = 1600 B/D
c_{inj} = 900 ppm for 30 days; tracer injection started after 10 years of production

Production Data:
Well A: q_t = 64 B/D
Well B: q_t = 700 B/D
Well C: q_t = 214 B/D
Well D: q_t = 622 B/D

Dispersion Coefficient = 0

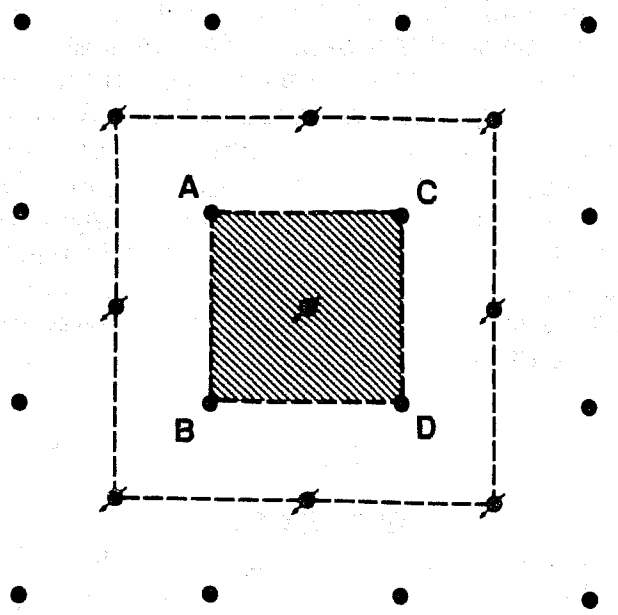

FIGURE 10. A CONCEPTUAL CONFINED FIVE SPOT PATTERN.

Input data for history matching are shown in Table 3 and the history match results are presented in Table 4. Figure 11 illustrates the concept underlying the history matching—which is based on the fact that (1) water cut is large at the time of traced injection, and, (2) saturation change in the reservoir during the tracer test is negligible.

The history match of the tracer response is shown on Fig. 12. The match is excellent and it took 10 runs to obtain the match. Table 4 shows that permeability and porosity, obtained as a consequence of the history match, vary significantly in the vicinity of each production well (i.e., in each quadrant of the pattern).

TABLE III

INPUT DATA TO START HISTORY MATCH

R_∞	=	0.09
λ	=	0.00576 day^{-1}
$k_{xxf} = k_{yyf}$	=	30,000 md
ϕ_f	=	0.01
q_t	=	400 B/D for Wells A, B, C and D

TABLE IV

HISTORY MATCH RESULTS

	Well A	Well B	Well C	Well D
q_t, B/D	64	700	214	622
WOR at injection time	10	56	11	39
ϕ_f	0.012	0.023	0.008	0.024
k_{xxf}, md	500	34,000	3,500	17,000
k_{yyf}, md	2500	28,000	500	10,000

R_∞ = 0.12

λ = 0.0005 day^{-1}

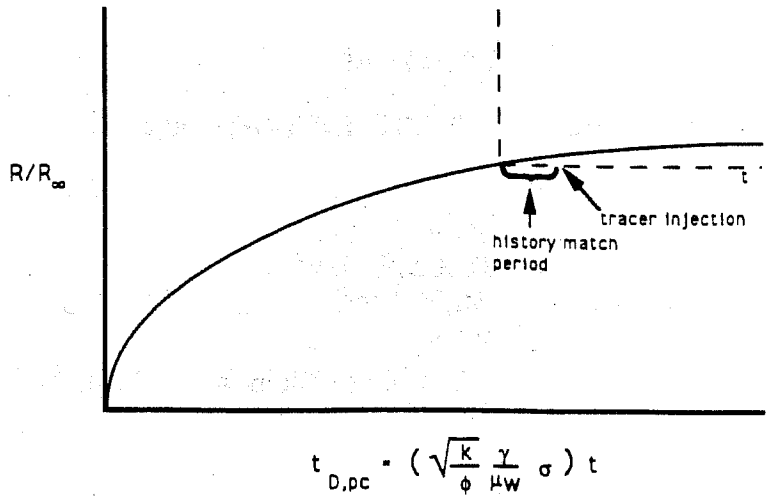

FIGURE 11. CONCEPTUAL OIL RECOVERY CURVE FROM MATRIX

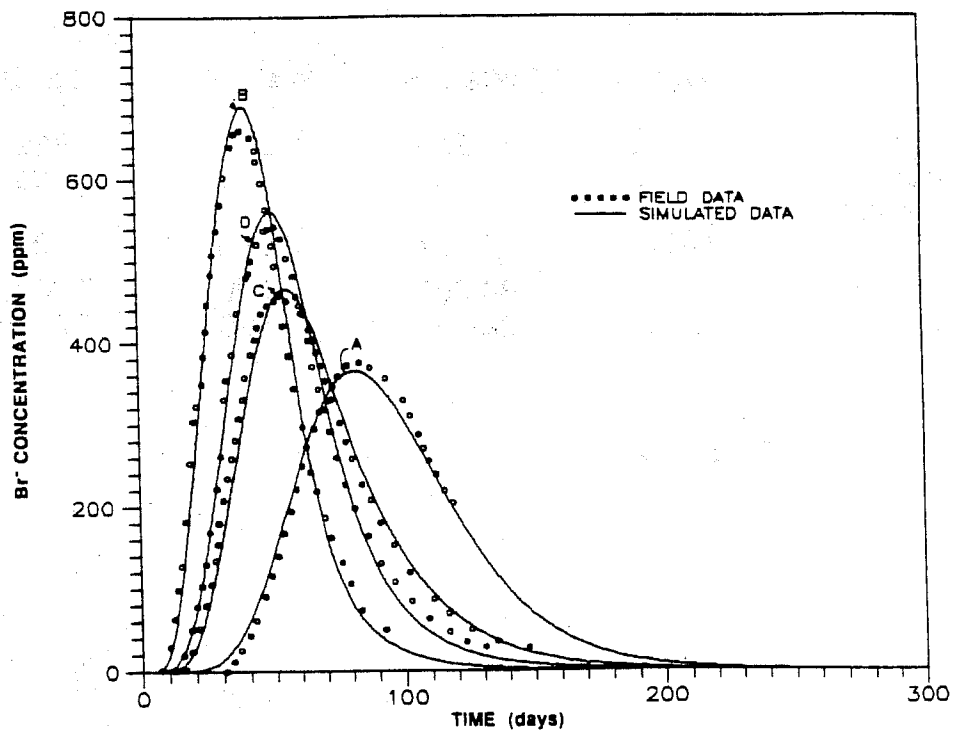

FIGURE 12. INVERTED FIVE SPOT CONFINED PATTERN TRACER PERFORMANCE HISTORY MATCH FOR WELLS A, B, C, AND D.

IV. CONCLUSIONS

From the results of this study, we conclude that:

1. The tracer transport model presented in this paper provides a practical and viable tool for determining orientation and conductivity of high permeability channels in naturally structured reservoirs. The information should be quite useful in planning remedial measures for conformance improvement, and ascertaining reservoir data useful for use in dual-porosity simulators in conjunction with improved or enhanced oil recovery modeling. The tracer transport equations for gas injection operations can be formulated similar to the equations used for waterflooding operations presented in this paper.
2. The numerical algorithm is considerably less complex and executes one to two orders of magnitude faster than the code for standard dual-porosity simulators. This permits more nodes and smaller grid spacing that should lead to more accurate numerical results. Furthermore, single-porosity simulators can be readily modified to include the matrix-fracture transfer function and the tracer transport equations.
3. History matching with this model is much simpler than the standard dual-porosity simulation since it requires considerably less complex input data.
4. While the technique of this paper can be used with non-uniform grid, a grid as close to uniform square grid as possible should be used with the nine-point finite-difference formulations presented here. For non-uniform grid, we recommend the use of controlled-volume finite-element technique. This technique is reported in Ref. 8.

V. NOMENCLATURE

B	=	formation volume factor, RB/STB
c	=	compressibility, psi^{-1}
C	=	chemical concentration, ppm
D	=	depth, positive down, ft
D	=	molecular diffusion coefficient, ft^2/D
f	=	fractional flow
h	=	height, ft
IMAX	=	maximum number of nodes
k	=	permeability, md

k_{max} = principal maximum permeability, md
k_{min} = principal minimum permeability, md
k_r = relative permeability, dimensionless
k_{xx} = xx-component of permeability tensor, md
k_{xy} = xy-component of permeability tensor, md
k_{yy} = yy-component of permeability tensor, md
$\bar{k}$ = geometric average permeability, md
$\bar{\bar{k}}$ = permeability tensor, md
K = dispersivity coefficient, ft^2/D
$K_{x\,x}$ = xx-component of dispersivity coefficient tensor, ft^2/D
$K_{x\,y}$ = yy-component of dispersivity coefficient tensor, ft^2/D
$K_{y\,y}$ = yy-component of dispersivity coefficient tensort, ft^2/D
K = dispersivity coefficient multiplier, ft^3/D
L = matrix block size, ft
M = mobility ratio
MOPV = moveable oil pore volume
p = pressure, psi
p_D = dimensionless pressure
q = flow rate, STB/D
R = recovery, fraction
R_∞ = ultimate recovery, fraction
S = saturation, fraction
SG = specific gravity
t = time, days
t_D = dimensionless time for pressure transient analysis calculations
$t_{D,pc}$ = dimensionless time for waterflood imbibition calculations
T = transmissibility, STB/psi-D
u = interstitial velocity, ft/D
v = Darcy velocity, ft/D
V_R = node volume ($\Delta x \Delta y \Delta z$), ft^3
w = fractional amount

α = dispersivity, ft
α_L = longitudinal dispersivity, ft
α_T = transverse dispersivity, ft
γ = static pressure gradient, psi/ft
γ = interfacial tension, dyne/cm
Δp = pressure change, psi
Δt = time-step size, days
Δt^* = intersection time in pressure buildup, hr
Δx = gridblock length, ft
Δy = gridblock width, ft
Δz = gridblock thickness, ft
Δ = finite difference operator
Δ_t = value at time n + 1 minus value at time n
λ = exponential recovery constant, day^{-1}
μ = viscosity, cp
ρ = density, lbm/ft^3
σ = shape factor, ft^{-2}
τ = fracture/matrix transfer term, STB/D
τ = integration variable in the convolution integral, day
θ = contact angle
ϕ = porosity, fraction

Subscripts

c = capillary
c = connate
D = dimensionless
f = fracture
i = initial
m = matrix
o = oil
r = relative
r = residual
s = solid

w = water
x = x direction
y = y direction
z = z direction
β = phase (water, oil, gas)
ϕ = rock
∞ = infinite time

Superscripts

n = time level
0 = zero time

VI. APPENDIX A

Equations for Pressure Interference Testing in Anisotropic Reservoirs

From Reference 2 and a knowledge of tensor transformation rules the following working equations were compiled for use in pressure interference test analysis:

$$\Delta p = p_i - p(t,x,y) = \frac{141.2\ qB\mu}{\sqrt{k_{max}k_{min}}h} P_D\left(\left[t_D/r_D^2\right]_{dir}\right) \tag{A-1}$$

$$\left(\frac{t_D}{r_D^2}\right)_{dir} = \frac{0.0002637t}{\phi\mu c_t}\left[\frac{k_{max}k_{min}}{\left(y^2k_{xx} + x^2k_{yy} - 2xyk_{xy}\right)}\right] \tag{A-2}$$

$$\bar{k} = \sqrt{k_{max}k_{min}} = \frac{141.2\ qB\mu(P_D)_M}{h\Delta P_M} \tag{A-3}$$

$$y^2k_{xx} + x^2k_{yy} - 2xy\ k_{xy} =$$

$$\frac{(0.0002637)\ k_{max}k_{min}}{\phi\mu c_t}\ \frac{t_M}{(t_D/r_D^2)_M} \tag{A-4}$$

$$k_{xx}k_{yy} - k_{xy}^2 = k_{max}k_{min} = \bar{k}^2 \tag{A-5}$$

$$k_{xx} = k_{min} + (k_{max} - k_{min}) \cos^2\theta \tag{A-6}$$

$$k_{yy} = k_{min} + (k_{max} - k_{min}) \sin^2\theta \tag{A-7}$$

$$k_{xy} = k_{yx} = (k_{max} - k_{min}) \sin\theta \cos\theta \tag{A-8}$$

$$k_{max} = 0.5 \left\{(k_{xx} + k_{yy}) + \left[(k_{xx} - k_{yy})^2 + 4k_{xy}^2\right]^{1/2}\right\} \tag{A-9}$$

$$k_{min} = 0.5 \left\{(k_{xx} + k_{yy}) - \left[(k_{xx} - k_{yy})^2 + 4k_{xy}^2\right]^{1/2}\right\} \tag{A-10}$$

$$\theta = \arctan\left(\frac{k_{max} - k_{xx}}{k_{xy}}\right) \tag{A-11}$$

$$\frac{k_\theta \cos^2\theta}{k_{max}} + \frac{k_\theta \sin^2\theta}{k_{mim}} = 1 \tag{A-12}$$

$$v_\theta = -0.001127 \frac{1}{\mu}\left[(k_\theta \cos_\theta)\frac{\partial p}{\partial x} + (k_\theta \sin\theta)\frac{\partial p}{\partial y}\right] \tag{A-13}$$

$|\Delta p(t,x,y)|$ is plotted vs. t on log-log paper for all the observation wells. The resulting plots are matched against a P_D vs. (t_D/r_D^2)dir log-log type curve. Once a satisfactory match is obtained, $\bar{k}$ is calculated using Eq. (A-3) at any match point M.

Next, for a fixed pressure match, Δp_M, the corresponding three time matches t_M and $(t_D/r_D^2)_M$ are read and substituted in Eq. (A-4) to form three equations in these unknowns k_{xx}, k_{xy} and k_{yy}. These are calculated and the values are substituted in Eqs. (A-9) through (A-11) to calculate k_{max}, k_{min} and θ.

VII. APPENDIX B

Modification of Shiralkar's Nine-Point Coefficients for use with Block-Centered Finite-Difference Formulation.

Shiralkar developed a robust nine-point scheme for anisotropic heterogeneous reservoirs where the transmissibilities yield positive values and reduce grid orientation effects for adverse mobility ratios. Shiralkar formulation was for point-distributed grid. We have extended his formulation for use with block-centered grid; the results yield non-negative transmissibilities.

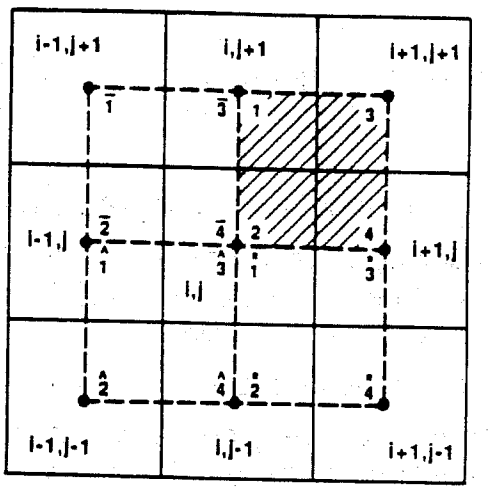

FIGURE B-1. NINE-POINT BLOCK-CENTERED GRID AND ITS RELATION TO SHIRALKAR'S POINT-DISTRIBUTED NUMBERING SCHEME.

The four-node computational element used by Shiralkar is shown by the shaded square with corner points labeled 1, 2, 3, and 4 on Fig. B-1. The conventional block-centered transmissibilities ($T_{xi+1/2,j}$, $T_{yi,\, j+1/2}$, etc.) and Shiralkar point-distributed transmissibilities (T_{24}, T_{12}, T_{23}, and T_{14}) were used to generate the modified transmissibilities ($\hat{T}_{i+1/2\, j}$, $\hat{T}_{i,\, j+1/2}$, etc.). These modified transmissibilities were used for our work as shown below:

$$\hat{T}_{i+1/2,\, j} = T_{24} + T_{1^{\bullet}3^{\bullet}} \tag{B-1}$$

$$\hat{T}_{i,\, j+1/2} = T_{12} + T_{\bar{3}\,\bar{4}} \tag{B-2}$$

$$\hat{T}^{23}_{i+1/2,\, j+1/2} = T_{23} \tag{B-3}$$

$$\hat{T}^{14}_{i+1/2,\, j+1/2} = T_{14} \tag{B-4}$$

where

$$T_{24} = \left\{ \frac{T^{24}_{xi+1/2,\, j}}{T^{24}_{xi+1/2,\, j} + T^{13}_{xi+1/2,\, j+1}} (q_x - T_{14} - T_{23}) \right\} \tag{B-5}$$

$$T_{1^{\bullet}3^{\bullet}} = \left\{ \frac{T^{1^{\bullet}3^{\bullet}}_{xi+1/2,\, j}}{T^{1^{\bullet}3^{\bullet}}_{xi+1/2,\, j} + T^{2^{\bullet}4^{\bullet}}_{xi+1/2,\, j-1}} (q^{*}_x - T_{1^{\bullet}4^{\bullet}} - T_{2^{\bullet}3^{\bullet}}) \right\} \tag{B-6}$$

$$T_{12} = \left\{ \frac{T^{12}_{yi,\, j+1/2}}{T^{12}_{yi,\, j+1/2} + T^{34}_{yi+1,\, j+1/2}} (q_y - T_{14} - T_{23}) \right\} \tag{B-7}$$

$$T_{\bar{3}\,\bar{4}} = \left\{ \frac{T^{\bar{3}\,\bar{4}}_{yi,\, j+1/2}}{T^{\bar{3}\,\bar{4}}_{yi,\, j+1/2} + T^{\bar{1}\,\bar{2}}_{yi-1,\, j+1/2}} (\bar{q}_y - T_{\bar{1}\,\bar{4}} - T_{\bar{2}\,\bar{3}}) \right\} \tag{B-8}$$

$$T_{23} = \left\{ \frac{1}{3} \frac{(q_x - q_{xy})(q_y - q_{xy})}{(q_x + q_y - 2q_{xy})} + q_{xy} \right\} \text{ for } q_{xy} \geq 0 \tag{B-9}$$

$$T_{23} = \left\{ \frac{1}{3} \frac{(q_x - q_{xy})(q_y - q_{xy})}{(q_x + q_y - 2q\delta_{xy})} \right\} \text{ for } q_{xy} < 0 \tag{B-10}$$

$$T_{14} = \left\{ \frac{1}{3} \frac{(q_x - q_{xy})(q_y - q_{xy})}{(q_x + q_y - 2q_{xy})} \right\} \text{ for } q_{xy} \geq 0 \qquad \text{(B-11)}$$

$$T_{14} = \{T_{23} - q_{xy}\} \text{ for } q_{xy} < 0 \qquad \text{(B-12)}$$

$$q_x = \frac{1}{2}\left(T^{24}_{xi+1/2,\,j} + T^{13}_{xi+1/2,\,j+1}\right) \qquad \text{(B-13)}$$

$$q_y = \frac{1}{2}\left(T^{12}_{yi,\,j+1/2} + T^{34}_{yi+1,\,j+1/2}\right) \qquad \text{(B-14)}$$

$$q_{xy} = \frac{1}{2}\left(T^{23}_{xyi+1/2,\,j+1/2} + T^{14}_{xyi+2,\,j+1/2}\right) \qquad \text{(B-15)}$$

$T^{24}_{xi+1/2,\,j}$, $T^{13}_{xi+1/2,\,j+1}$, $T^{12}_{yi,\,j+1/2}$, $T^{34}_{yi+1,\,j+1/2}$, $T^{1^*3^*}_{xi+1/2,\,j}$, $T^{2^*4^*}_{xi+1/2,\,j-1}$, $T^{\bar{3}\,\bar{4}}_{yi,\,j+1/2}$, $T^{\bar{1}\,\bar{2}}_{yi-1,\,j+1/2}$, $T^{23}_{xyi+1/2,\,j+1/2}$, $T^{14}_{xyi+2,\,j+1/2}$ are harmonic-averaged five-point functions. To calculate T^{24}_{x}, T^{13}_{x}, etc. use grid size Δx and Δy as in standard five-point formulations. To calculate T^{23}_{xy} and T^{14}_{xy} use appropriate diagonal distances between points 2 and 3 and 1 and 4, respectively.

VIII. APPENDIX C

Equations to Convert Tracer Response Concentrations in a Non-Confined Five-Spot Pattern to Concentrations For Use in a Five-Spot Window Model

As can be seen from Fig. 10, when tracer is injected in the center well of the gray-shaded area, the tracer response in wells A, B, C, and D will be diluted by water from the water injectors outside the center pattern. If we wish to isolate the gray-shaded area as a confined window for modeling purposes, the tracer dilutions have to be subtracted out. The following equations provide a procedure to accomplish this. This method should be used with caution because reservoir heterogeneities can cause fluid channeling to the outside of the "perceived" confined window area.

The cumulative amount of tracer produced in Wells A, B, . . ., are given below:

$$AMT_A = \sum_{n=1}^{N} q_{wA}^n \, C_A^n \, \Delta t_n \qquad \text{(C-1)}$$

$$AMT_B = \sum_{n=1}^{N} q_{wB}^n \, C_B^n \, \Delta t_n \qquad \text{(C-2)}$$

The fractions of tracer produced by Wells A, B, . . ., are:

$$w_A = AMT_A / (AMT_A + AMT_B + \ldots) \qquad \text{(C-3)}$$

$$w_B = AMT_B / (AMT_A + AMT_B + \ldots) \qquad \text{(C-4)}$$

The flow rates of water and oil produced by Wells A, B, . . . , in the confined window model are $\hat{q}_{wA}$, $\hat{q}_{oA}$, etc., and are given below:

$$\hat{q}_{wA} = w_A \, q_{inj} \, WOR_A \qquad \text{(C-5)}$$

$$\hat{q}_{oA} = \hat{q}_{wA} / WOR_A \qquad \text{(C-6)}$$

The concentration of tracer produced by Wells A, B, . . ., in the confined window model $\hat{C}_A$, $\hat{C}_B$, . . ., are as shown:

$$\hat{C}_A = C_A \, (q_{wA} / \hat{q}_{wA}) \qquad \text{(C-7)}$$

$$\hat{C}_B = C_B \, (q_{wB} / \hat{q}_{wB}) \qquad \text{(C-8)}$$

IX. ACKNOWLEDGEMENT

The authors thank Marathon Oil Company for permission to participate in preparation and publication of this paper. In addition, the authors are grateful to Mrs. L. L. Fitzpatrick for her creativity in formatting the equations and for typing the manuscript.

X. REFERENCES

1. Gogarty, W. B.: "Enhanced Oil Recovery Through the Use of Chemicals - Part 2," ***JPT,*** Oct. 1983, 1767-1775.

2. Earlougher, R. C., Jr.: **Advances in Well Test Analysis**, Monograph Series, SPE, Dallas, 1967, Vol. 5.

3. Kazemi, H., Gilman, J. R. and El-Sharkawy, A. M.: SPE 19849, "Analytical and Numerical Solution of Oil Recovery from Fractured Reservoirs Using Empirical Transfer Functions," 64th SPE Annual Technical Conference and Exhibition, San Antonio, TX, Oct. 8-11, 1989.

4. Shinta, A. A.: PhD Dissertation, Petroleum Engineering Department, Colorado School of Mines (to appear).

5. Shiralkar, G. S.: SPE 18442, "Reservoir Simulation of Generally Anisotropic Systems" 10th SPE Symposium on Reservoir Simulation, Houston, TX, Feb. 6-8, 1989.

6. Wolcott, K. D.: "Mixed Five-Point/Nine-Point Formulation of Multiphase Flow in Petroleum Reservoirs Using the Fully Implicit Solution Technique," M.S. Thesis, Petroleum Engineering Department, Colorado School of Mines (April 1991).

7. Ostebo, B. and Kazemi, H.: SPE 21227, "Mixed Five-Point Nine-Point Finite-Difference Formulation of Multiphase Flow in Petroleum Reservoirs," 11th SPE Symposium on Reservoir Simulation, Anaheim, CA, Feb. 17-20, 1991.

8. Fung, L. S., Hiebert, A. D. and Nghiem, L. X.: SPE 21224, "Reservoir Simulation with a Controlled-Volume, Finite-Element Method," 11th SPE Symposium on Reservoir Simulation, Anaheim, CA, Feb. 17-20, 1991.

XI. METRIC CONVERSION FACTORS

bbl x 1.589 873	E−01	=	m^3
cp x 1.0	E−03	=	Pa•s
ft x 3.048	E−01	=	m
md x 9.869 233	E−04	=	μm^2
psi x 6.894 757	E+00	=	kPa
psi^{-1} x 1.450 377	E−01	=	kPa^{-1}

SESSION 2

Field Studies and Data Needs

Co-Chairmen

Neil Humphreys, Mobil E&P Services

Charles Kerans, Bureau of Economic Geology, University of Texas

QUALITY CONTROL OF SPECIAL CORE ANALYSIS MEASUREMENTS

Eve S. Sprunt

Mobil Research and Development Corporation
Dallas Research Laboratory
Dallas, Texas

I. ABSTRACT

One of the problems in field studies utilizing laboratory data is determining whether or not the laboratory core measurements are accurate. This is particularly true of expensive special core analysis measurements. The high cost of such measurements means that usually only a few measurements are available for a given field and few or no repeat measurements are available. Our experience has shown that some of the simple and inexpensive components of special core analysis measurements may be responsible for significant errors. Separate quality control on these inexpensive measurements can improve the reliability of the costly, special core analysis measurements.

In basic core analysis measurements, porosity measurements are usually considered sufficiently accurate if they are good to half a porosity unit. However, in special core analysis tests in which the porosity is used to compute saturation, an error of half a porosity unit can translate into a large error in water saturation. Such errors are particularly troublesome for low-porosity rocks at low water saturations. Laboratory measurements whose interpretation depends on accurate determination of the water saturation include electrical resistivity, capillary pressure, and relative permeability. Inaccurate determination of the saturation can introduce curvature of the resistivity index versus water saturation crossplot and could lead to erroneous identification of a sample as having a conductive rock matrix or bound water. This is true regardless of how accurately the resistivity itself is measured. While it is prohibitively expensive to run repeat full resistivity measurements for a sample showing curvature in the resistivity index plot, the porosity should be run by several different methods to determine whether an error in porosity could be causing the

curvature. Careful evaluation of the porosity measurements can bracket the correct porosity and determine whether a significant error in porosity could be affecting the special core analysis results.

II. INTRODUCTION

In school most of us are taught to assign error estimates to laboratory measurements. However, in practice in the oil industry most laboratory measurements are reported without any confidence limits. Commercial laboratories are loathe to report error bars because their competitors will assert that they can do better. Also, few published papers contain error analysis of the reported experimental test results. Thus, many in the oil industry do not have a sense of the magnitude of errors in laboratory data.

Although error analysis is seldom presented in experimental papers, there are many papers on errors analysis of core analysis measurements. Amaefule and Keelan (1989) present uncertainty equations for many basic and special core analysis measurements. However, my experience (e.g. Sprunt et al., 1990) indicates that the magnitude of the errors they suggest is relatively optimistic.

Quite a few papers focus on error analysis of electrical measurements (Chen and Fang, 1986; Freedman and Ausburn, 1985; Hook, 1983; Hoyer and Spann, 1975; Worthington, 1975). Of these papers, Worthington (1975) and Hoyer and Spann (1975) approach the problem from an experimentalist's viewpoint examining some of the individual components of the laboratory procedures and why they cause problems.

This paper approaches the error analysis from an experimentalist's viewpoint. In particular, it will be shown how the ability to accurately determine pore volume affects special core analysis measurements that depend on porosity and saturation measurement. Particular attention is given to electrical resistivity measurements. Measurements whose interpretation depends on saturation determination are much more sensitive to errors in the pore volume than measurements that rely on the porosity. Interpretation of laboratory measurements that require saturation determination include the electrical resistivity measurements to obtain the saturation exponent, relative permeability, and capillary pressure.

III. PORE VOLUME

In understanding how the accuracy of pore volume measurements affects special core analysis measurements, it is important to understand how porosity and pore volume are determined. Measurement or calculation of pore volume is necessary for measurement of porosity. While most

people do not know how accurate pore volume measurements are, they assume porosity measurements are good to within 0.5 porosity units (pu).

Porosity ϕ is determined by measuring two of the following three quantities: pore volume (V_p), grain volume (V_g), and bulk volume (V_b).

$$\phi = \frac{V_p}{V_b} = \frac{(V_b - V_g)}{V_b} = \frac{V_p}{(V_p + V_g)} \qquad (1)$$

In an inter-laboratory comparison, Dotson et al. (1951) showed that the average deviation in porosity was 0.5 pu, but the range was from 0.3 to 1.0 pu. Thomas and Pugh (1988) use ± 0.5 pu as their "experience-based" maximum acceptable deviation in standard core plug analysis and found 65% of labs in 1987 met their quality assurance criteria, which included that standard.

If porosity measurements are used to characterize a reservoir, for example to determine average porosity of a zone or to calibrate well logs, ± 0.5 pu accuracy is usually adequate. Additional uncertainty is introduced in scaling and averaging the laboratory data. However, if the porosity measurement is used in characterization of a core plug for special core analysis measurements, a 0.5 pu error in porosity can introduce significant errors.

There are many methods of obtaining the quantities in Equation (1) (API, 1960). If the pore volume rather than the porosity is the true quantity of interest, it is best to measure the pore volume directly rather than to calculate it from the grain volume and bulk volume. Ideally, when pore volume is required for a special core analysis measurement, the pore volume should be measured directly under the same conditions as the special core analysis test. This is important because pore volume changes with pressure and because sleeve material may progressively intrude into surface porosity with increasing pressure. In practice, however, this is not always done; and ambient pore volume measurements or calculated ambient pore volumes may be corrected to overburden pressure conditions by a variety of techniques including correlations based on measurements on other samples.

Porosity errors are important when compressibility is a significant factor or when pore volume is difficult to accurately quantify. In low-porosity rocks, it is especially important to properly account for pore compressibility. Cases in which accurate determination of the pore volume is difficult include vuggy carbonates (Sprunt, 1989), low-permeability samples with high-porosity, low-porosity samples, and samples containing gypsum.

IV. SATURATION

The most common methods of determining water saturation during special core analysis are based on volumetric and gravimetric measurements (Maerefat et al., 1990), and both these methods depend directly on accurate measurement of the pore volume. Imaging techniques such as x-ray absorption, microwave absorption, and nuclear magnetic resonance do not require measurement of the pore volume.

The equation for determining water saturation (S_w) volumetrically is:

$$S_w = \frac{(V_p - V_o)}{V_p} \tag{2}$$

where V_o is the volume of water expelled from the sample.

If the sample is small and has low porosity, it is very difficult to accurately measure changes in saturation because very small amounts of fluid are expelled. For example, a sample of a 10-percent porosity rock, 1 inch in diameter and 1 inch long expels only 0.13 cc for a 10-percent change in water saturation. If a 1.5-inch diameter, 1-inch long sample is used, 0.29 cc corresponds to the same 10-percent change in water saturation. It is possible to measure the water saturation of the larger sample more accurately.

When samples are selected for special core analysis measurements, it is a good idea to check the pore volume of the sample. If preserved samples are to be used for the test, the pore volume can be estimated using the porosity of an adjacent sample. Using the accuracy to which fluid changes can be determined, you can then determine whether or not the saturation changes during the special core analysis test can be determined sufficiently accurately. In most cases a pore volume of 5 cc or more is desirable.

Figures 1 and 2 illustrate how the error in water saturation increases with decreasing porosity and decreasing water saturation. These figures were generated, assuming that the entire porosity error is attributable to an error in the pore volume. Frequently, bulk volume determination is a source of errors (Thomas and Pugh, 1988); but if pore volume is not directly determined, the error in bulk volume translates into an error in pore volume. The main warning of these figures is that accurate measurements are required on low-porosity samples, especially at low-water saturations if special core analysis measurements that depend on water saturation are to be meaningful.

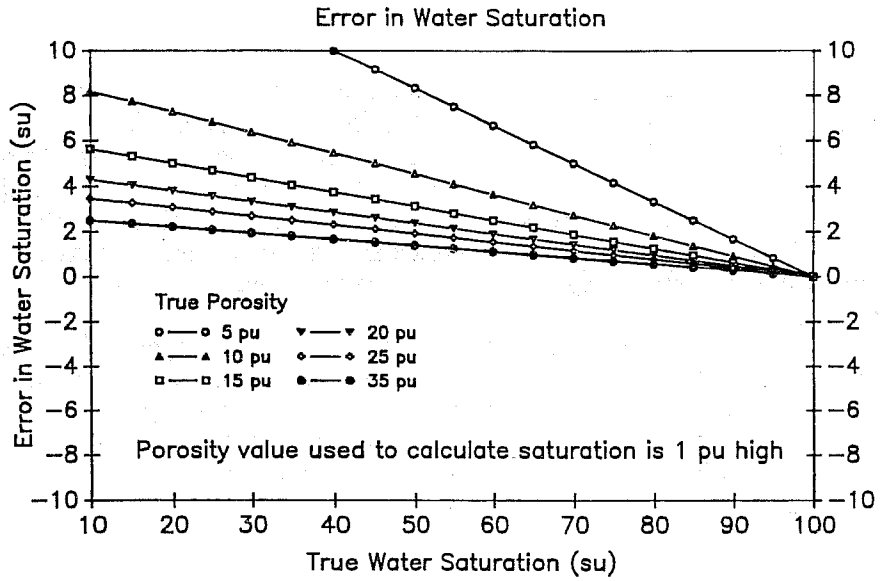

Figure 1: The error in water saturation was calculated as a function of water saturation assuming that all the error in the porosity measurement is in the pore volume.

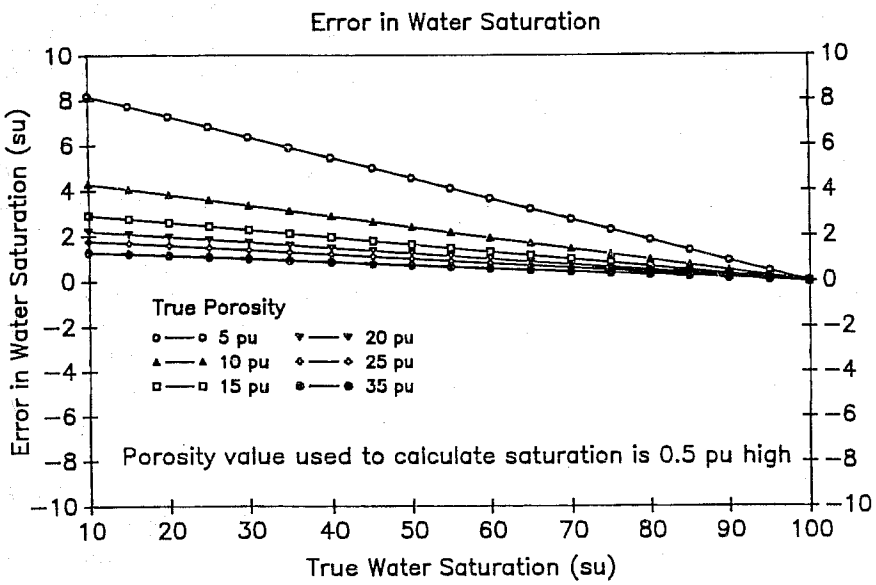

Figure 2: The error in water saturation was calculated as a function of water saturation assuming that all the error in the porosity measurement is in the pore volume. Porosity is commonly assumed to be good to within 0.5 pu.

V. CEMENTATION EXPONENT

Cementation exponent, m, was defined by Archie (1942) in the equation $F = \phi^{-m} = R_o/R_w$, where F is the formation factor, R_o is the resistivity of the fully brine saturated rock, R_w is the resistivity of the brine, and ϕ is porosity. Assuming the correct cementation exponent was 2.0, the formation factors were calculated for a range of porosities from 5 to 35 percent. These values of the formation factor were then used to calculate cementation exponents using porosities that were in error by $\pm$ 0.5 and $\pm$ 1.0 pu (Figure 3).

The error in cementation exponent from a 1 pu error in porosity is less than 5 percent if the porosity is 10 pu or greater. For a 0.5 pu error, the error in cementation exponent is less than 2.5 percent for samples with porosity of 10 pu or more. Except for low porosity rocks, normally acceptable errors in porosity do not introduce serious errors into the determination of the cementation exponent.

VI. SATURATION EXPONENT

The saturation exponent is defined by Archie(1942) in the equation $R = R_o/S_w^{-n}$ where R is the resistivity of the rock at some partial saturation and S_w is the water saturation. If the correct value of the saturation exponent is assumed to be 2.0, the value of the resistivity index, R/R_o, can be calculated for different values of water saturation. Assuming a perfect Archie rock, the resistivity index was calculated for values of saturation between 10 and 100 percent.

In an Archie (1942) rock, the saturation exponent is the slope of the straight line fitted to the bi-logarithmic crossplot of resistivity index versus water saturation. On the bi-logarithmic crossplot of true resistivity index versus apparent water saturation (Figure 4), only the saturations corresponding to the correct porosity are perfectly fitted by a straight line. If the measured porosity is too low, connecting the data points gives a line which curves downward, because the apparent water saturation for any resistivity reading is too low. If the measured porosity is too high, the line connecting the data points curves upward, because the apparent water saturation for any resistivity reading is too high.

While volumetric determination of the saturation is commonly used to monitor saturation during resistivity or other special core analysis measurements which depend on saturation, a crosscheck of the final volumetric saturation with a Dean-Stark extraction saturation is recommended. If the extraction saturation is greater than the final volumetric saturation, the pore volume may be erroneously low.

Determination of the saturation exponent is complicated because the errors in porosity cause curvature in the bi-logarithmic crossplot of

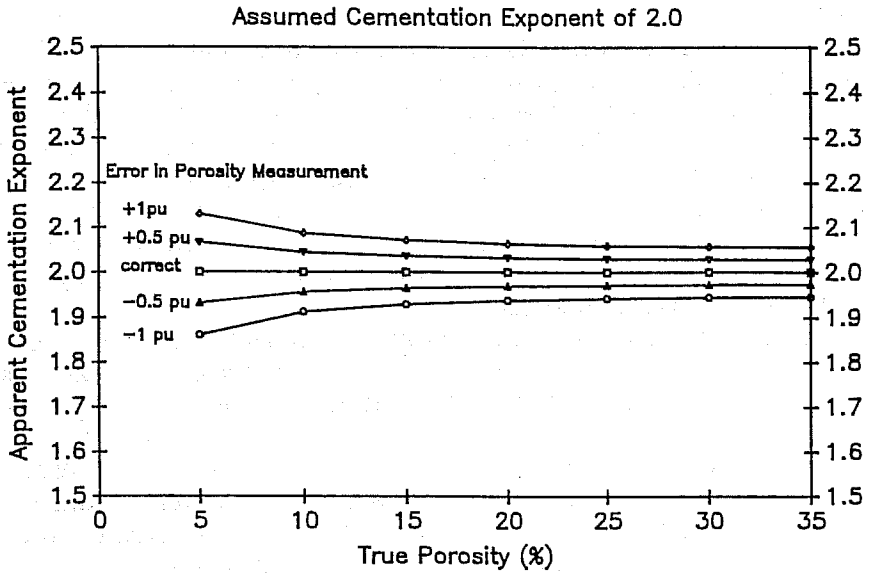

Figure 3: The cementation exponent was calculated for different errors in the porosity assuming that the true cementation exponent was 2.0.

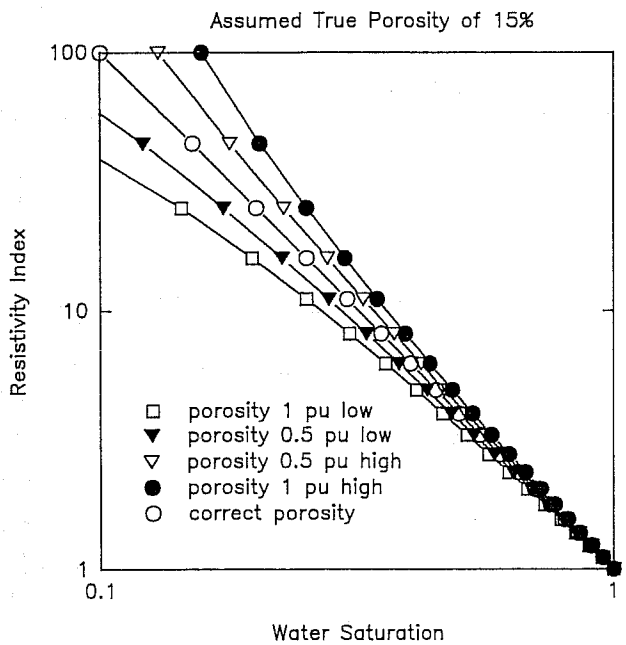

Figure 4: In this crossplot, only the assumed true porosity of 15% gives a straight line relationship. If the porosity used to calculate water saturation is too low, the data curve downward. If the porosity used to calculate the water saturation is too high, the data curve upward.

resistivity index versus water saturation. If the saturation exponent is determined by fitting a least-squares line to the data and forcing the line through the 100 percent water saturation and resistivity index equal to 1.0 point, the slope of that least-squares line and, hence, the saturation exponent depend on the minimum water saturation used. The error in saturation exponent decreases as the data analysis is limited to higher water saturations (Figures 5, 6, and 7). When only the data above an apparent water saturation of 50 percent are used, an error in porosity of 1 pu causes an error of almost 10 percent in the saturation exponent of a sample with 15 pu. The error in saturation exponent increases rapidly with decreasing porosity for porosities less than 15 pu.

The objective of measuring the saturation exponent in the laboratory is to use that exponent in the Archie equation to calculate water saturation from log data. However, the error in the water saturation of the plug sample due to the erroneous pore volume may not be the same as the error in the water saturation calculated using the laboratory-determined saturation exponent. The error is altered because the saturation exponent is determined from a linear fit to nonlinear data (Figure 4). Depending on how the straight line is fitted to the nonlinear data (Figures 5, 6, and 7), the error in water saturation calculated using the apparent saturation exponent may be larger or smaller than the error in the laboratory measurement of saturation.

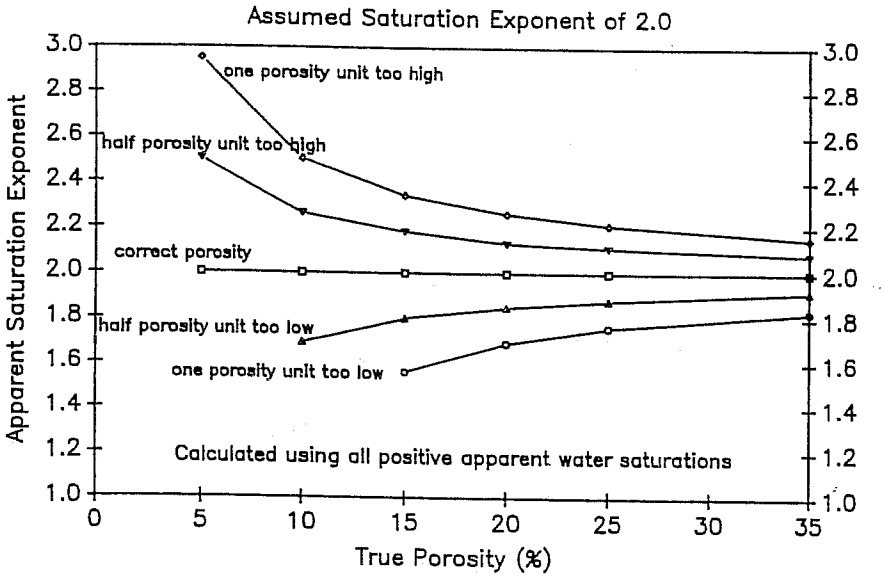

Figure 5: The saturation exponent was obtained from a least squares fit to the resistivity index/water saturation plot with the line forced through the point of 100 percent water saturation and resistivity index of 1.0.

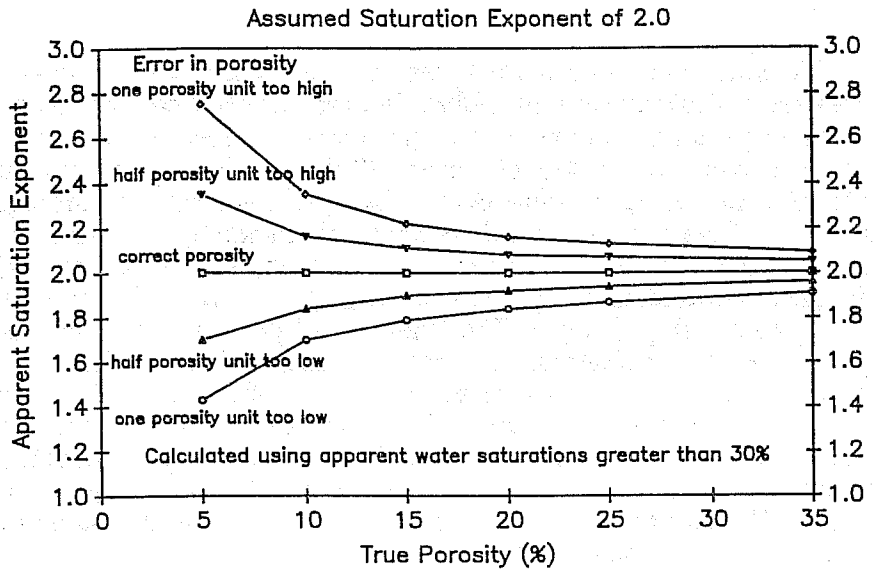

Figure 6: The same plot as in Figure 5, but this time only apparent water saturations greater than 30 percent were used to determine the saturation exponent.

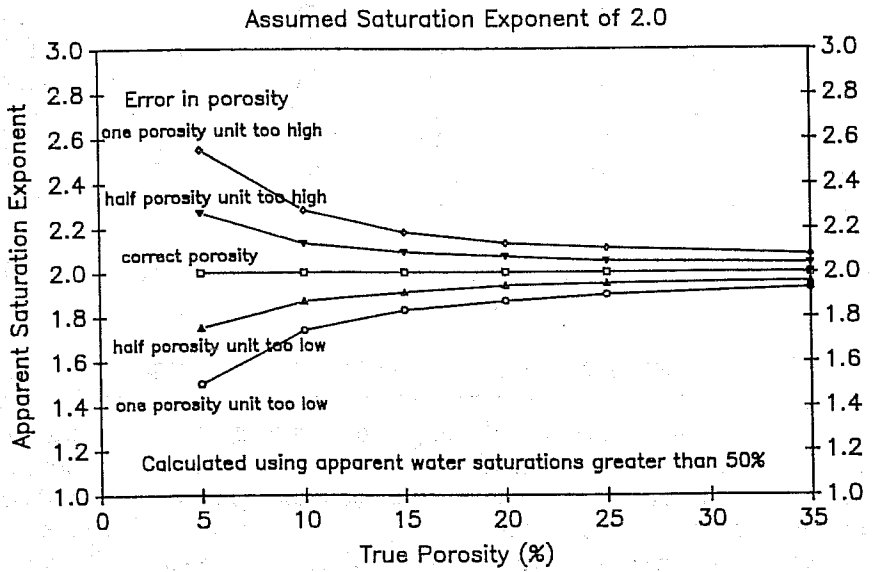

Figure 7: The same plot as in Figure 5, but this time only apparent water saturations greater than 50 percent were used to determine the saturation exponent.

VII. SAMPLE DATA

Determination of the correct pore volume to use in tests on vuggy carbonates is difficult (Sprunt, 1989). For each of eight samples with varying vug sizes and amounts of vuggy porosity, a service company reported two different values of porosity (Table 1). Both porosity values were calculated using the same Boyle's Law grain volume measurement. The "caliper" porosity used a bulk volume determined by measuring the length and diameter of the plug samples with calipers. The caliper porosity is frequently erroneously high because the plugs are not perfect cylinders and may have chipped edges. The "summation" porosity was calculated using a pore volume determined from the volume of fluid required to saturate the samples. The summation porosity is often too low because surface vugs will not retain water. This "summation" porosity is not the same as the "summation of fluids" porosity in which the gas, oil, and water contents are determined independently and summed to determine the pore volume. The true porosity of these samples probably falls between the caliper and summation porosity values.

Table I: Vuggy Carbonate Samples

	Porosity (%)		Saturation Exponent		Cementation Exponent	
Sample	Caliper	Summation	Caliper	Summation	Caliper	Summation
3	17.1	15.7	1.22	1.74	1.93	2.03
5	12.6	11.5	1.24	1.70	1.80	1.88
8	11.6	11.3	1.14	1.26	1.77	1.80
10	12.4	11.4	1.14	1.78	1.83	1.90
12	8.4	7.7	1.21	1.54	1.73	1.79
19	14.2	13.7	1.30	1.59	1.83	1.86
22	19.7	19.1	1.53	1.71	1.97	2.01
29	24.4	24.1	1.54	1.63	2.06	2.08
Average	15.1	14.3	1.29	1.62	1.86	1.92

For these samples we do not know the correct porosity, the correct cementation exponent, or the correct saturation exponent. The electrical resistivity data were interpreted using both sets of porosity measurements. As predicted by the hypothetical calculations, the differences in porosity make little difference in the cementation exponent (Table 1), even though the porosity differences are as high as 1.4 pu. The porosity differences corresponded to large differences in the saturation exponents (Table 1).

Some pore geometries, such as those associated with clay coatings or microporosity, can cause curvature in the resistivity index/water saturation relationship (de Waal et al., 1989; Dicker and Bemelmans, 1984; Diederix, 1982; Givens, 1987; and Swanson, 1985). The analysis here has shown

that curvature may also be due to errors in the porosity and, hence, in the water saturation determination. In some cases it may be difficult to differentiate between curvature due to errors in porosity measurement and curvature due to rock properties or other effects. However, for these clean, carbonate samples, curvature in the resistivity crossplot is probably due to errors in porosity measurement.

In the data for these clean carbonates, the curvature appears to be due to porosity measurement errors because the direction of curvature depends on the type of porosity measurement used to calculate saturation. The direction of curvature due to porosity errors indicates whether the porosity is erroneously high or low. The data generated using the caliper porosity form either a linear or an upward curving trend on the bi-logarithmic resistivity index/water saturation plot because that porosity, when in error, is too large (Figures 8 and 9). The corresponding data based on summation porosity form either a linear or a downward curving trend because that porosity, when in error, is too low (Figures 8 and 9). Since this formation is not clay bearing and we know that porosity measurement is a problem for this formation, analysis of these crossplots on a sample-by-sample basis can aid in determining which value of porosity is probably more reliable for each sample.

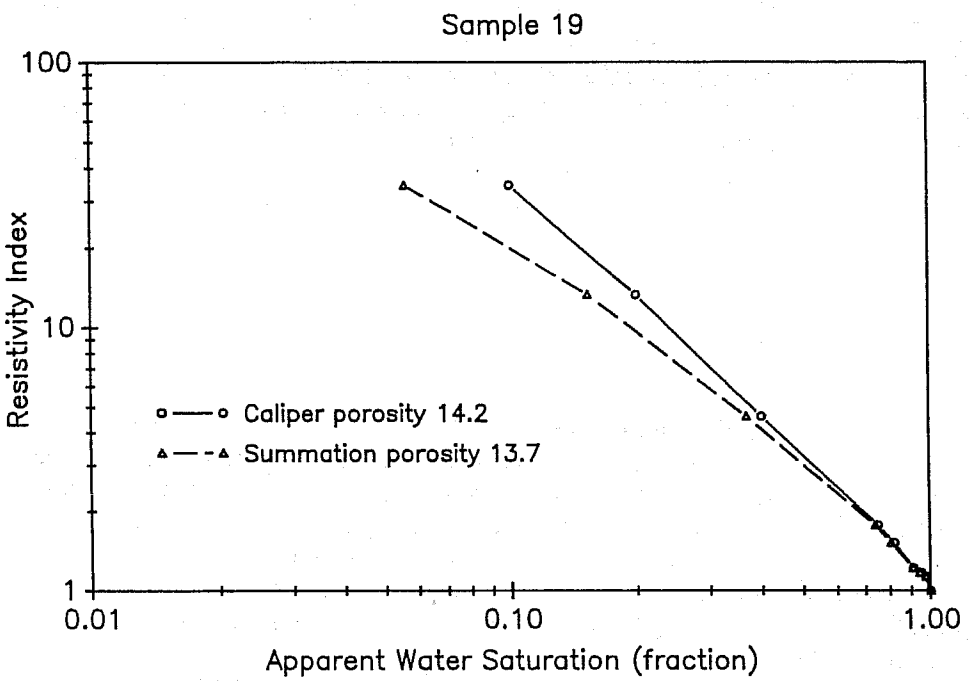

Figure 8: Each laboratory measurement of the fluid content of sample 19 was used to calculate apparent water saturation using the pore volumes obtained from the caliper porosity and the summation porosity. These apparent water saturations were then used in the resistivity index versus apparent water saturation crossplots. Table 1 gives the saturation exponents.

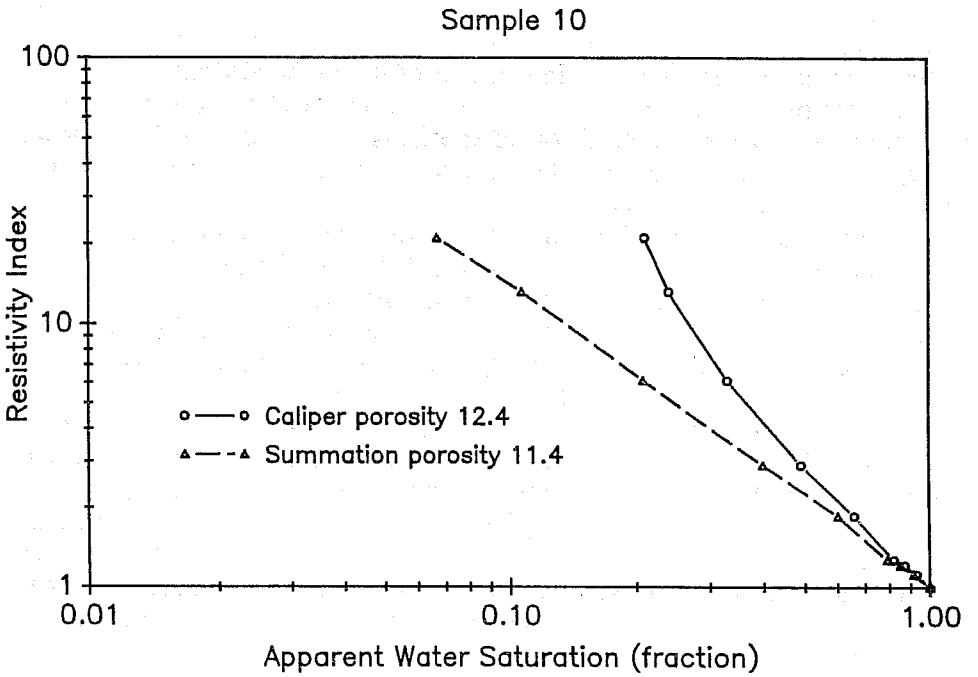

Figure 9: Each laboratory measurement of the fluid content of sample 10 was used to calculate two values of apparent water saturation using the pore volumes obtained from the caliper porosity and the summation porosity. These apparent water saturations were then used in the resistivity index versus apparent water saturation crossplots. Table 1 lists the saturation exponents, which were determined by fitting a least-squares line through the data points and forcing the line through the point 1,1.

VIII. CONCLUSIONS

Quality control programs are generally restricted to routine core analysis. Even in routine measurements, which include porosity and single phase permeability, the importance of accurate measurements is sometimes not recognized because a 0.5 pu error in routine porosity may not be significant when the core values are averaged to evaluate reserves. This paper shows that errors in porosity that are acceptable for routine core analysis, can introduce significant errors in special core analysis measurements.

The cementation exponent is less sensitive to errors in porosity measurement than the saturation exponent (Figure 10). The differences between the values of the cementation exponents increase as the difference in porosities increase (Figure 11), but porosity measurement will probably not be the major source of error in measurement of the cementation exponent. Errors, such as mis-measurement of the brine salinity or

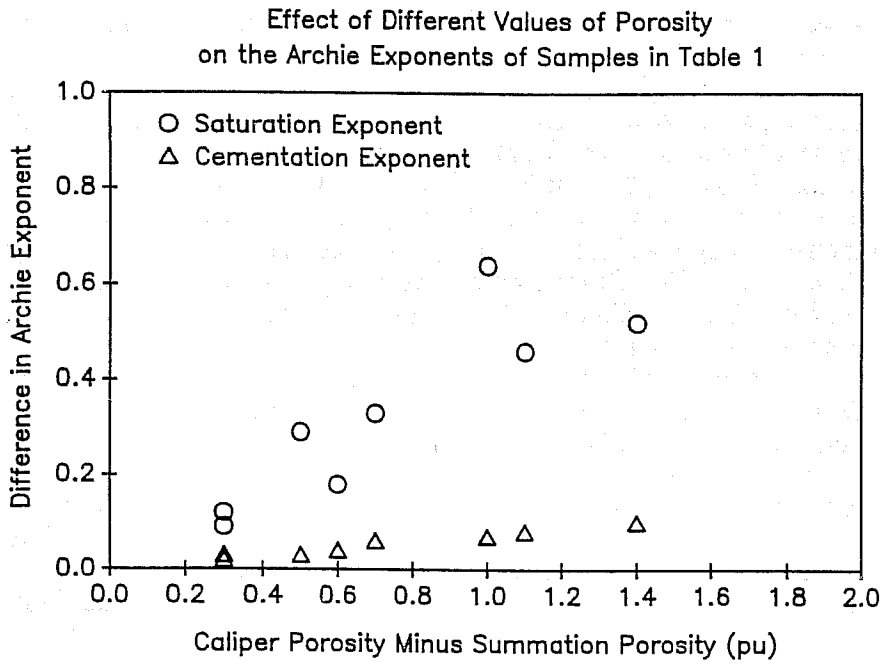

Figure 10: The effect of differences in porosity is much smaller on the cementation exponent than on the saturation exponent.

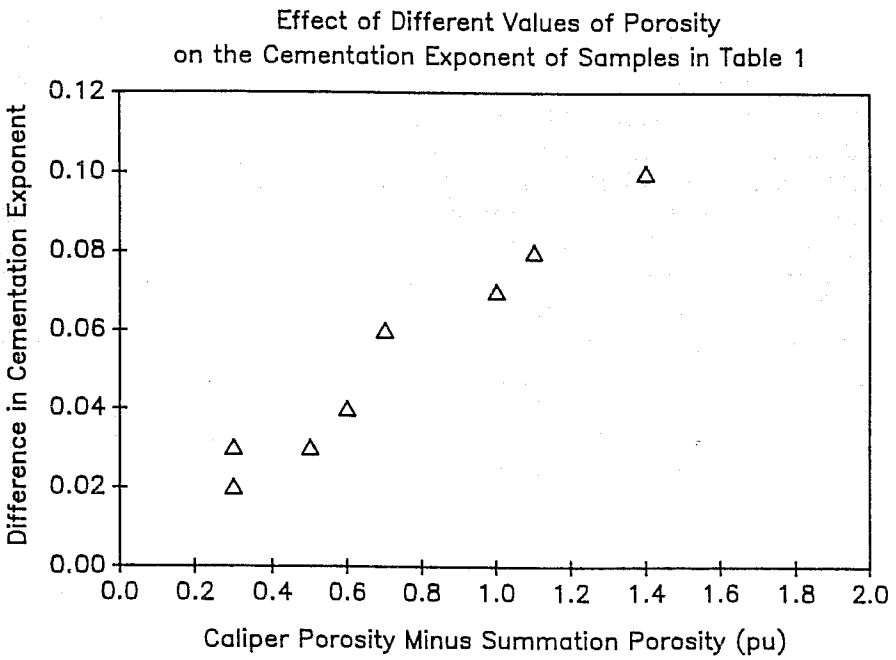

Figure 11: This figure shows on an expanded vertical scale that the difference in cementation exponent increases with the difference in porosity.

mis-measurement of the electrode spacing as discussed in Sprunt, Maute, and Rackers (1990), will probably be more significant than porosity errors.

Errors in porosity can introduce large errors into the determination of the saturation exponent. Inaccurate pore volume measurements can cause curvature of data on the bi-logarithmic resistivity index water saturation crossplot. However, this curvature is not necessarily due to errors in porosity measurement. Curvature has been attributed to various pore geometries (Dicker and Bemelmans, 1984; Diederix, 1982; Givens, 1987; and Swanson, 1985). Other nonlinearities may be introduced by nonuniform fluid distributions (Sprunt et al., 1991). It is important to try to differentiate between laboratory errors and physical phenomena.

If curvature is observed in laboratory measurements, it would be prudent, if possible, to measure the porosity/pore volume by more than one technique and to carefully quality control those techniques. Measuring porosity is far less expensive than measuring electrical resistivity as a function of water saturation. A single set of electrical measurements can be evaluated using porosity/pore volume measurements obtained by different techniques. In evaluating the porosity/pore volume measurement techniques, it should be determined whether the porosities obtained will tend to be above or below the true value. If different techniques are used and the resistivity measurements curve upward or downward depending on the technique as in the sample data presented in this paper, the curvature is probably due to errors in the porosity measurement and not the underlying rock properties. If the data always curve in the same direction with only the magnitude of the curvature changing, the curvature is probably due to the rock properties.

In some reservoirs, such as tight gas sands or fractured carbonates, the average formation porosity may be around 10 pu or less. In planning special core analysis tests on such formations, it is important to consider whether the results will be sufficiently accurate (Figures 1 and 2). It may be necessary to have stringent quality control and/or revise the test procedures. In some cases, sufficiently accurate data may not be obtainable with existing techniques. The accuracy of the measurements for low-porosity samples should be kept in mind in planning laboratory testing. Errors in pore volume measurement are most serious for low porosity samples and when the pore volume is used to calculate saturation. For such samples commonly accepted accuracy tolerances for routine core analysis measurements may introduce unacceptably large errors in the parameters obtained from special core analysis.

REFERENCES

Amaefule, J. O., and D. K. Keelan, 1989, Stochastic Approach to Computation of Uncertainties in Petrophysical Properties, Transactions of the Society of Core Analysts, v. 1, paper SCA-8907.

American Petroleum Institute, 1960, API Recommended Practice 40 (RP40), Recommended Practice for Core Analysis Procedure, 55 pp.

Archie, G. E. 1942, The Electrical Resistivity Log as an Aid in Determining Some Reservoir Characteristics, Trans. AIME, v. 198, pp. 54-62.

Chen, H. C., and J. H. Fang, 1986, Sensitivity Analysis of the Parameters in Archie's Water Saturation Equation, *The Log Analyst,* v. 27, No. 5, pp. 39-44.

de Waal, J. A., R. M. M. Smits, J. D. de Graaf and B. A. Schipper, 1989, Measurement and Evaluation of Resistivity Index Curves, SPWLA 30th Annual Symposium, Paper II.

Dicker, A. I. M., and Bemelmans, W. A., 1984, Models for simulating electrical resistance of porous media, SPWLA 25th Annual Logging Symposium, June 10-13, 1984, Paper HH.

Diederix, K. M., 1982, Anomalous relationships between resistivity index and water saturations in the Rotliegend sand (The Netherlands), SPWLA 23rd Annual Logging Symposium, July 6-9, 1982, Paper X.

Dotson, B. J., R. L. Slobod, P. N. McCreery, and J. W. Spurlock, 1951, Porosity Measurement Comparisons by Five Laboratories, Petroleum Transactions, AIME, vol. 192, pp. 341-346.

Freedman, R., and B. E. Ausburn, 1985, The Waxman-Smits Equation for Shaley Sands: I. Simple Methods of Solution; II. Error Analysis, *The Log Analyst*, v. 26, No. 2, pp. 11-24.

Givens, W. W., 1987, A Conductive Rock Matrix Model (CRMM) for the Analysis of Low-Contrast Resistivity Formations, *The Log Analyst*, v. 28, n. 2, pp. 138-151.

Hook, J. R., 1983, The Precision of Core Analysis Data and Some Implications for Reservoir Evaluation, SPWLA 24th Annual Logging Symposium, Paper Y.

Hoyer, W. A., and M. M. Spann, 1975, Comments on Obtaining Accurate Electrical Properties of Cores, SPWLA 16th Annual Logging Symposium, Paper B.

Maerefat, N. L., B. A. Baldwin, A. A. Chaves, G. A. LaTorraca, B. F. Swanson, 1990, SCA Guidelines for Sample Preparation and Porosity Measurement of Electrical Resistivity Samples, Part IV - Guidelines for Saturation and Desaturating Core Plugs during Electrical Resistivity Measurements, *The Log Analyst*, v. 31, No. 2, pp. 68-75.

Sprunt, E. S., 1989, Arun Core Analysis: Special Procedures for Vuggy Carbonates, *The Log Analyst,* v.30, no 5, pp. 353-362.

Sprunt, E. S., 1990, Proposed Electrical Resistivity Form, *The Log Analyst*, v. 31, n. 2, pp. 89-93.

Sprunt, E. S., K. P. Desai, M. E. Coles, R. M. Davis, and E. L. Muegge, 1991, CT Scan-Monitored Electrical Resistivity Measurements Show Problems Achieving Homogeneous Saturation, *SPE Formation Evaluation*, v. 6, No. 2, pp. 134-140.

Sprunt, E. S., R. E. Maute, and C. L. Rackers, 1990, An Interpretation of the SCA Electrical Resistivity Study, *The Log Analyst*, v. 31, n. 2.

Swanson, B. F., 1985, Microporosity in Reservoir Rocks: Its Measurement and Influence on Electrical Resistivity, *The Log Analyst*, v. 26, n. 6, pp. 42-52.

Thomas, D. C., and V. J. Pugh, 1989, A Statistical Analysis of the Accuracy and Reproducibility of Standard Core Analysis, *The Log Analyst*, v. 30, No. 2, pp. 71-77.

Worthington, A. E., 1975, Errors in the Laboratory Measurement of Formation Resistivity Factor, SPWLA 16th Annual Logging Symposium, Paper D.

EVALUATION, RELEVANCE, AND APPLICATION OF HIGH RESOLUTION PERMEAMETER DATA IN RESERVOIR MODELING

By Torgrim Jacobsen, Trond Hoye, Jan Ole Aasen,
Alister MacDonald, and Alan Grindheim
IKU
Trandheim, Norway

ABSTRACT

Shallow marine and deltaic facies have been subjected to permeameter analysis in outcrops (Ferron Sandstone, Utah, Scarbourough Formation, Yorkshire) and cores (Tarbert Formation, Gullfaks Field). Fluvial sequences have also been studied in both outcrops (Scalby Formation, Yorkshire), and cores (Ness Formation, Oseberg Field). The total database comprises 8000 permeameter measurements. These data have been compared with the various facies interpretations, and a variety of statistical analyses have been used to characterize the mean, variability, frequency distribution and spatial structure of permeability within each facies. Permeameter data from the cored sequences have been compared with conventional core plug data, and permeability estimates based on wireline log data. The permeability data have been used as input into stochastic heterogeneity modelling routines, and the strengths and weaknesses of the different measurement techniques have been evaluated.

The mean value of core plug and permeameter measurements are very similar within any sequence, thus confirming the reliability of the permeameter measurements. The correspondence with log derived permeability estimates is poorer, reflecting greater differences in sampling volumes and weaknesses in the log calibration procedure. The results further corroborate the close dependency of permeability on depositional facies. Different facies are characterized by different means, standard deviations, frequency distribution types, and vertical correlation lengths. Permeameter derived frequency distributions are characterized by normal (Gaussian) distributions for the most homogeneous facies types and increasing left skewness with increasing degree of heterogeneity: passing from normal to square-root normal to log normal. The core plug data, in contrast, display log normal distributions for all facies, whereas log data display both square root normal and log normal distributions, but with no clearly defined facies relationship. The results indicate both sample volume and facies dependence for the distribution types. The calculated empirical variograms to not fit the conventional

spherical model. Many of the variograms are however characterized by pronounced, repetitive hole effects reflecting periodicity of the small-scale heterogeneities.

High resolution permeameter data are useful for quantifying thin, high and low permeability beds, and provide the best statistical description of permeability for stochastic modelling purposes. The most important disadvantage is that the small sampling volume complicates any scale-up procedure based on permeameter data. Permeameter data are also potentially useful for improving core/log calibrations, especially in heterogeneous sequences.

COMPARISON OF DIFFERENT HORIZONTAL FRACTAL DISTRIBUTIONS IN RESERVOIR SIMULATIONS

R. A. Beier
H. H. Hardy

Conoco Inc.
Ponca City, Oklahoma

ABSTRACT

Past studies have demonstrated that porosity logs in vertical wells have a fractal character called fractional Gaussian noise (fGn). This observation triggered the application of fractal geostatistics to describe reservoir heterogeneity. These applications require knowledge of not only the vertical statistical character but also the horizontal character. In early studies, workers assumed a different fractal character in the horizontal direction called fractional Brownian motion (fBm). More recent analyses of outcrop and core photos and porosity logs in horizontal wells have found fGn in the horizontal direction. The purpose of the present study is to compare reservoir simulations using fGn and fBm horizontal distributions. A mature waterflood in a carbonate reservoir serves as a test case. Simulated water cuts in both types of distributions match field data. Still, the fGn distributions should be more representative of reservoirs, because they are consistent with outcrop and core photographs, and horizontal well data.

I. INTRODUCTION

Fractal geostatistics is a numerical technique to generate distributions of reservoir properties, such as porosity and

permeability, for reservoir simulation. Conventional reservoir simulations often embed reservoir heterogeneity in relative permeability curves that must be determined by trial and error methods. Workers[1-6] claim fractal distributions greatly reduce the man-hours required for history matches and still accurately predict reservoir performance. Fractal geostatistics have been applied to both waterflood and CO_2 field projects.

The application of fractal geostatistics to reservoirs is based on the observation that porosity logs in vertical wells have a fractal character. Hewett[1] concluded the fractal structure found in vertical well logs is fractional Gaussian noise (fGn). Well spacing is usually much too large to determine the statistical structure in the horizontal direction. To carry his work forward, Hewett postulated that the horizontal structure is a different distribution called fractional Brownian motion (fBm).

Recently, other workers have analyzed the horizontal structure of sedimentary layers. Hardy[7] analyzed distributions of dark and light regions in photographs of cores and outcrops. Values within any vertical trace were found to have the same distribution as found in vertical well logs - fGn. These results suggest the photos capture the same statistics of reservoir properties as that seen in well logs. Horizontal traces were also found to be fGn, not fBm. In the core photos, the horizontal layering is due to different standard deviations of values in the horizontal and vertical directions rather than a difference in the fractal character.

Crane and Tubman[8] and Hardy[9] recently analyzed porosity logs from horizontal wells in both sandstone and carbonate formations. All cases show fGn structure, the same as found in the photograph study.

The purpose of the present study is to compare vertical cross sections based on either fGn or fBm in the horizontal direction. The cross sections are tested by performing flow studies and comparing the simulated water cuts with field production data. A mature waterflood in a carbonate reservoir serves as a case study. A hybrid finite difference/streamtube technique[6] provides an areal simulation of the waterflood.

II. HISTORY OF MATURE WATERFLOOD

Our case study is a carbonate reservoir in southeastern New Mexico. The majority of development drilling occurred in

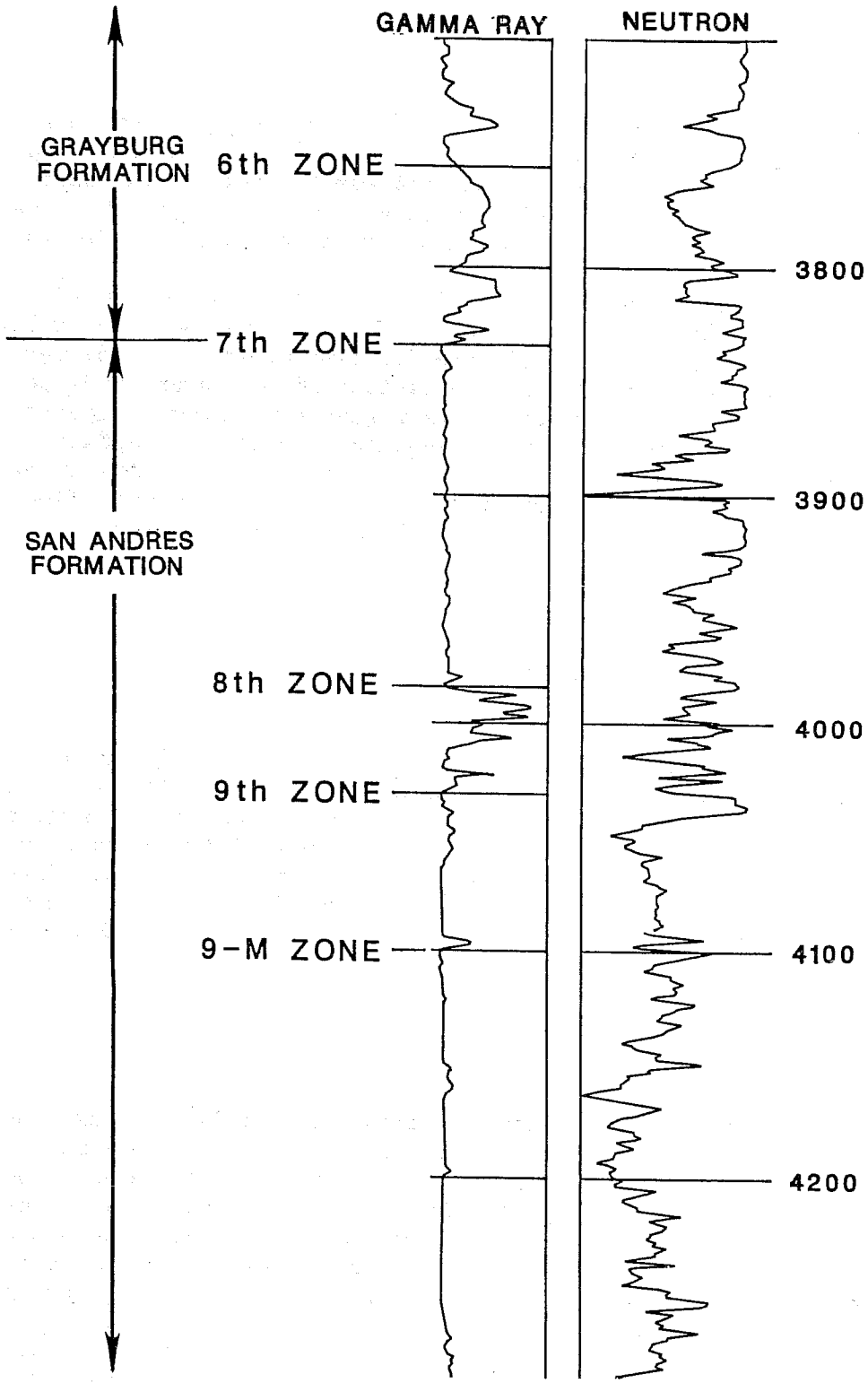

Fig. 1. Typical porosity log for Grayburg and San Andres formations.

the early 1940's. Wells produce from Grayburg dolomitic sands(mainly the Sixth zone) and three San Andres dolomite pay zones (Seventh, Upper Ninth, and Ninth Massive) at depths ranging from 3,600 to 4,300 feet as shown in Figure 1. The primary production mechanism of the reservoir was solution gas drive.

Waterflood operations on 5-spot patterns were phased in during the mid to late 1960's. The original 40-acre well spacing was infilled to 20 acres to form inverted 9-spot patterns in the early 1970's. Operations of the inverted 9-spot patterns generally remained unchanged for nearly 20 years. This long period of nearly constant operating conditions supports our use of a typical well pattern to represent an entire section (1 square mile). We focus on the waterflood performance in two adjacent sections that we call Area A and Area B.

III. FRACTAL DISTRIBUTIONS

The fractal character found in well logs describes a scaling relationship in sedimentary structures. The scaling relationship says that the small variations of reservoir properties seen at the core size are a scaled down version of the large scale variations seen at the reservoir scale. This scaling relationship can occur in several ways. Two common fractal relationships are fGn and fBm. References 1 and 9 give examples of both.

A. fGn Cross Sections

The method to generate fGn cross sections is based on previous studies[7,9] of core and outcrop photographs. The method generates good forgeries of core photos. Here we use the method to generate property distributions between wells. The resulting distributions are consistent with the core photo study and horizontal well data. The mathematical details of this process are found in the Appendix. A brief verbal description follows.

The first step is to identify reservoir units. In our field case, the production interval is divided into the Grayburg and San Andres formations. We treat each formation separately and later stack the two generated cross sections to form the final section. A representative well pair is chosen from each study area.

Digitized Sidewall Neutron Porosity (SNP) logs provide porosity measurements. The log readings are calibrated to core measured porosities with linear scaling. The corrected porosity log values are depth adjusted by stretching and compressing the depth values to align the tops and bottoms of each formation. Linear interpolation is used to fill in the array, giving a layered image. Fractal noise is then added to the image.

The amount of fractal noise added depends on how closely the depth adjusted well logs correlate. At each depth, the difference between the two log porosities is computed. Then, the total variance of these differences is calculated for the entire log section under study. If the two logs are identical, the total variance is zero and no fractal noise needs to be added. In practice, the variance is nonzero and the amount of added fractal noise increases as the total variance increases. Generation of fractal noise requires a value of the intermittency exponent, H. To evaluate H, we apply R/S analysis, spectral density analysis, and variogram analysis to the SNP logs. (See References 1 and 10.) A value of 0.87 applies to both formations. The SNP logs provide readings at one-half- foot intervals. However, the vertical spatial resolution of the SNP tool is about two feet. For this reason, only readings at two-foot intervals are used to generate a porosity cross section with square grids (2 ft by 2 ft).

It is important that the square grids in the generated cross section have sides corresponding to the vertical spatial

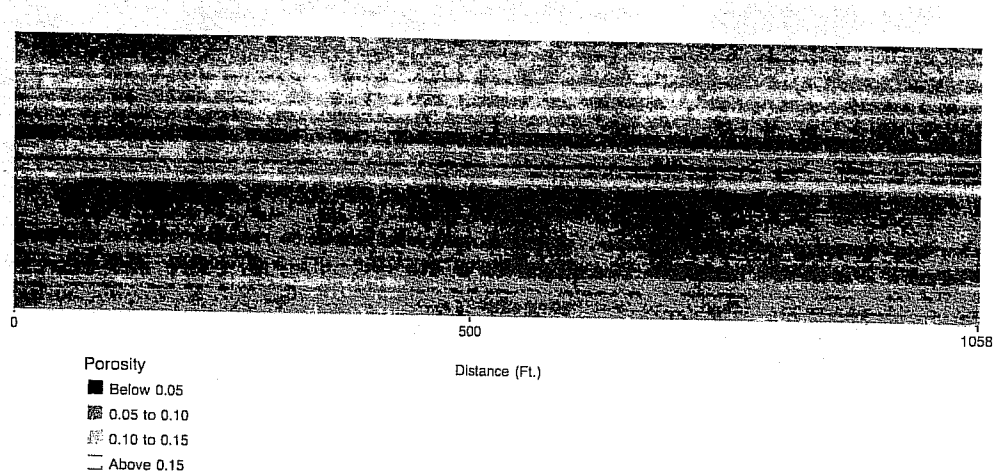

Fig. 2. Fractal distribution of porosity for Area A based on fGn in the horizontal direction (fine grid).

resolution of the logging tool. This ensures the proper amount of fractal noise is added to the layered image. If larger grid blocks are used in the generated cross section, the amount of noise measured at the porosity log scale (2 ft by 2 ft) is incorrectly added at the larger grid block scale. In geostatistical terminology, the support size of the measured values should correspond to the support size of the generated cross section.

A fine scale cross section (2 ft by 2 ft grids) for Area A is shown in Figure 2. The number of grids in this 512 by 150 array is too large for flow simulations. For this reason, a coarser grid must be obtained. This is done by reducing the number of grids in the horizontal direction. The fine scale grid values for porosity are scaled up using arithmetic averaging. The number of vertical grids remains unchanged at 150 (Figure 3).

Horizontal permeabilities are treated in the following way. Horizontal permeabilities are first assigned to the fine grid as a function of porosity by the formula

$$k = a\ 10^{b\phi} \qquad (1)$$

Values of a and b are set to 0.001 and 33.3, respectively. With these values, the permeability covers 5 log cycles as the porosity ranges from 2 to 17 porosity units. A coarser grid of horizontal permeability is obtained by applying harmonic

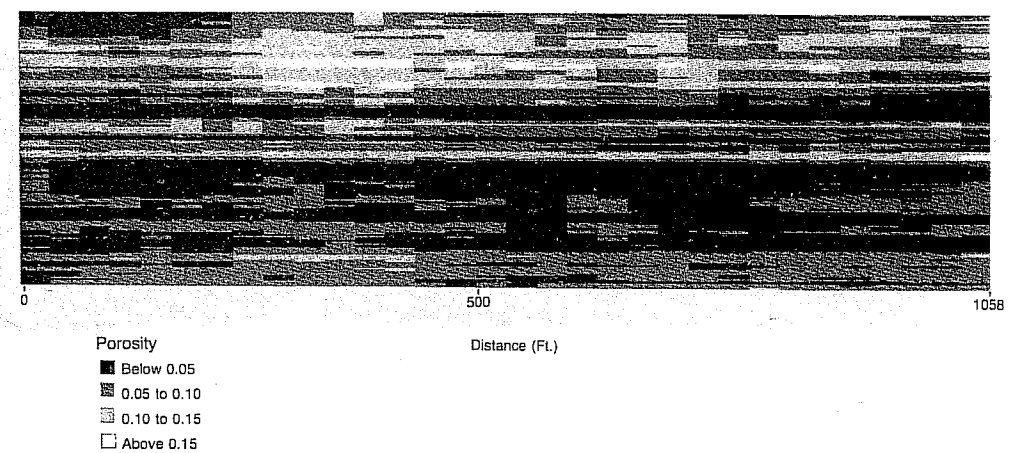

Fig. 3. Fractal distribution of porosity for Area A based on fGn in the horizontal direction (coarse grid).

averaging only in the horizontal direction. Figure 4 is the final coarse cross section for permeability. The permeability ranges in Figure 4 correspond to the porosity ranges in Figure 3 through Equation 1.

B. fBm Cross Sections

The method outlined by Hewett and Behrens[3] generates the fBm cross sections. Again, the corrected and depth adjusted log porosities are placed on the vertical edges of the cross section, followed by linear interpolation to produce a layered image. But now the added fractal noise is a different type and is added in a different manner. The result is fBm in the horizontal direction and fGn in the vertical direction. Details are provided in the Appendix. The resulting porosity

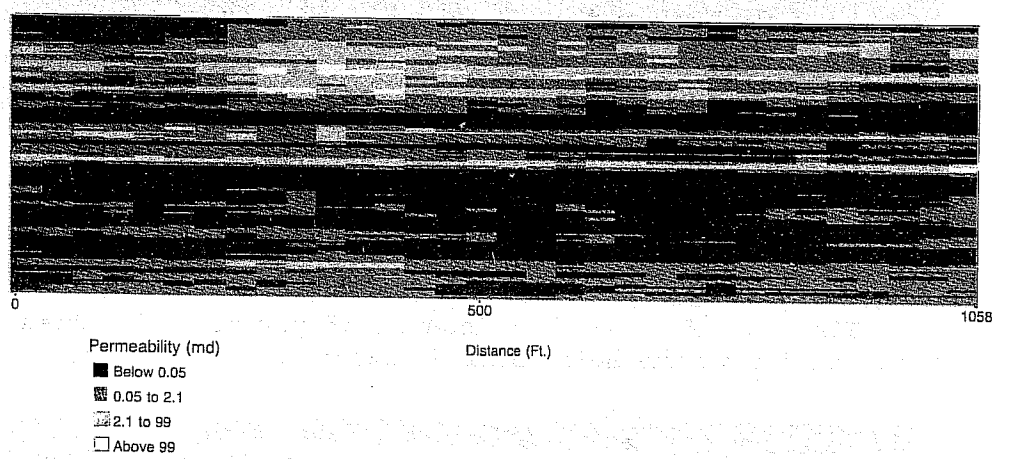

Fig. 4. Fractal distribution of permeability for Area A based on fGn in the horizontal direction (coarse grid).

cross section (Figure 5) is more layered than the fGn cross section (Figure 3). With the fBm method, a coarse porosity grid is generated directly. Equation 1 is applied directly to the coarse porosity grid to get the corresponding horizontal permeability map.

C. Other Cross Sections

For comparison in reservoir simulations, two simple porosity distributions are also considered--linear interpolation and layer cake. Figure 6 shows a cross section based

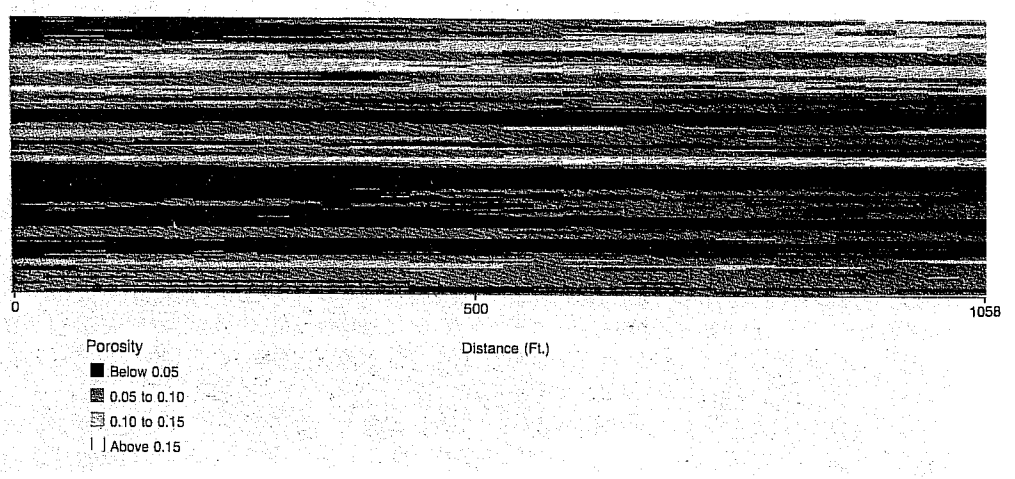

Fig. 5. Fractal distribution of porosity for Area A based on fBm in the horizontal direction (coarse grid).

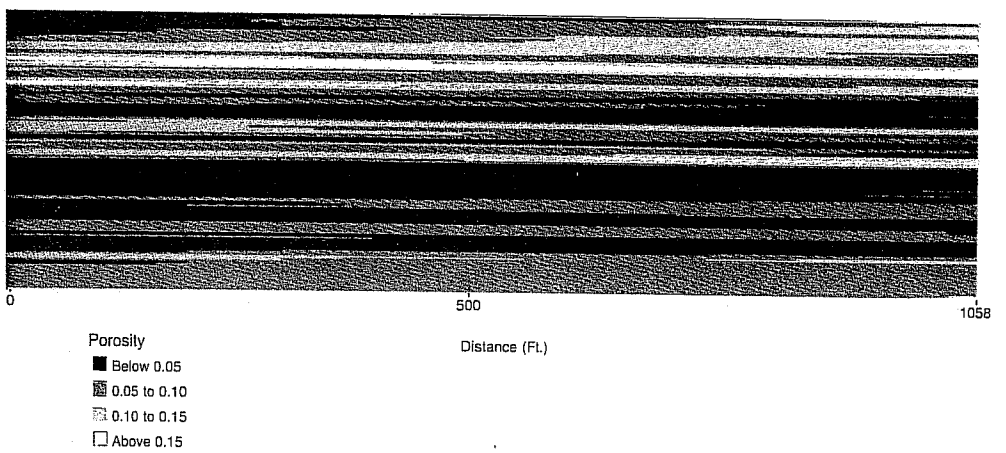

Fig. 6. Linear interpolation of porosity for Area A (coarse grid).

on linear interpolation between wells. A figure is not included for the layer cake case, but it is created by taking the porosity values from the well at the right-hand edge and extending them across the cross section. In all cross sections, the vertical permeability is set to 0.1 times the horizontal permeability at the coarse grid scale.

IV. COMPARISON WITH FIELD PRODUCTION DATA

The above cross sections are tested by performing flow studies using a hybrid finite difference/streamtube method.[6] The generated fractal distributions are input to a conventional reservoir simulator to make fractional flow curves for the cross section. Fluid displacements in the field project are calculated by incorporating the fractional flow curves in a streamtube model. The hybrid finite difference/streamtube method predicts water cuts as a function of pore volumes of water injected but not rates of injection or production. The time coordinates in the following graphs are obtained by simply honoring historical production rates.

Fluid displacement calculations are performed without adjusting any available parameters except initial water saturations. For the waterflood field case, water cuts are as large as 35 percent at the start of the waterflood. Evidently, these high initial water cuts are due to water transition zones with some possible water encroachment from edges and underlying aquifers. These high initial water cuts made it necessary to adjust the initial water saturations in the simulations to produce correspondingly high initial water cuts.

As shown below, flow simulations based on either fGn or fBm cross sections match field water cut data. Although the initial water saturations assumed for each type of cross section are not always identical, both sets are reasonable. If field water cuts are the only criteria, fGn and fBm type cross sections are equally good for this case with close well spacing (20 acres per well). Close well spacing may diminish the differences between the two types of cross sections. As the well spacing decreases, simple linear interpolation becomes more valid and the importance of fractal noise diminishes. Still, the fGn distributions should be more representative of reservoirs, because they are consistent with outcrop and core photographs, and horizontal well data.

A. Waterflood in Area A

Simulation results based on a single fBm cross section show good agreement with field water cuts (Figure 7). This result is consistent with earlier studies.[1-6] The initial water saturations are chosen to give a good match of the fBm curve to the field data. The chosen water saturations give an initial water fractional flow of 7 percent in both the Grayburg and San Andres formations. Water cuts based on the linear interpolation cross section are near the fBm cross section curve. On the other hand, a single fGn cross section gives lower water cuts throughout the waterflood.

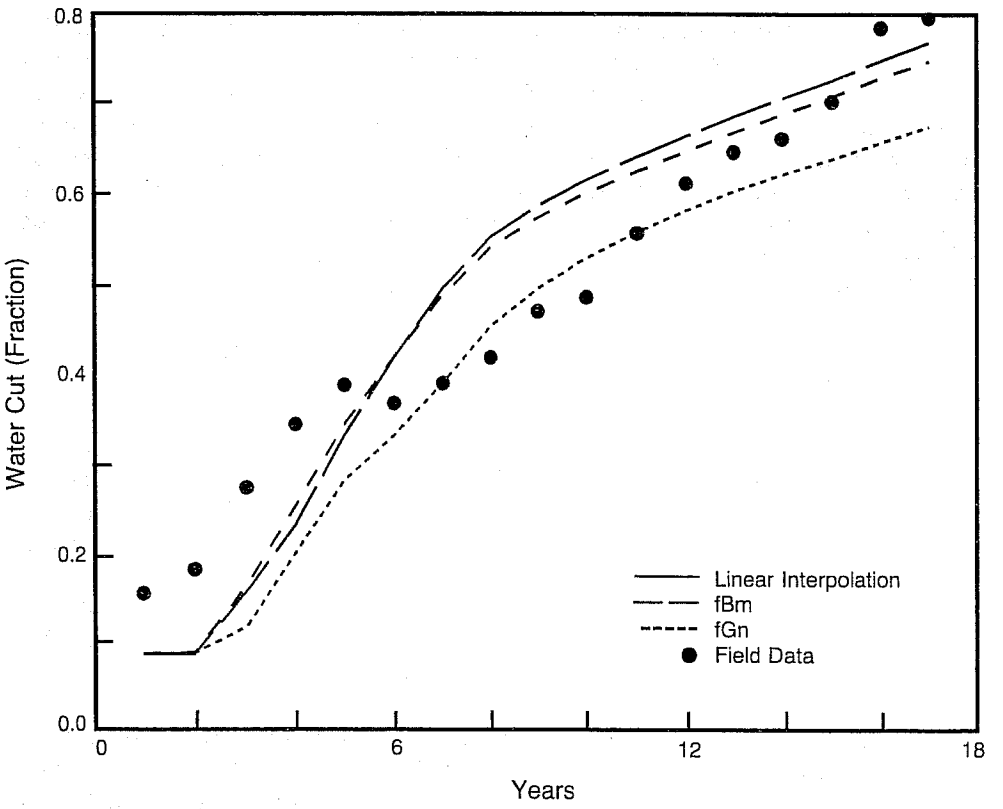

Fig. 7. Simulated water cuts in Area A compared to field data.

Increasing the initial water saturations improves the fGn curve match (Figure 8). Here the initial water saturations are set to give an initial water fractional flow of 12 percent. This value is closer to the initial water cut seen in the field than the 7 percent used in the fBm case.

The statistical model can generate an unlimited number of realizations. For Area A, flow simulations on 20 fGn realizations give a range of water cut curves represented by the shaded region in Figure 8. For reference, water cut curves are also shown for linear interpolation and layer cake cross

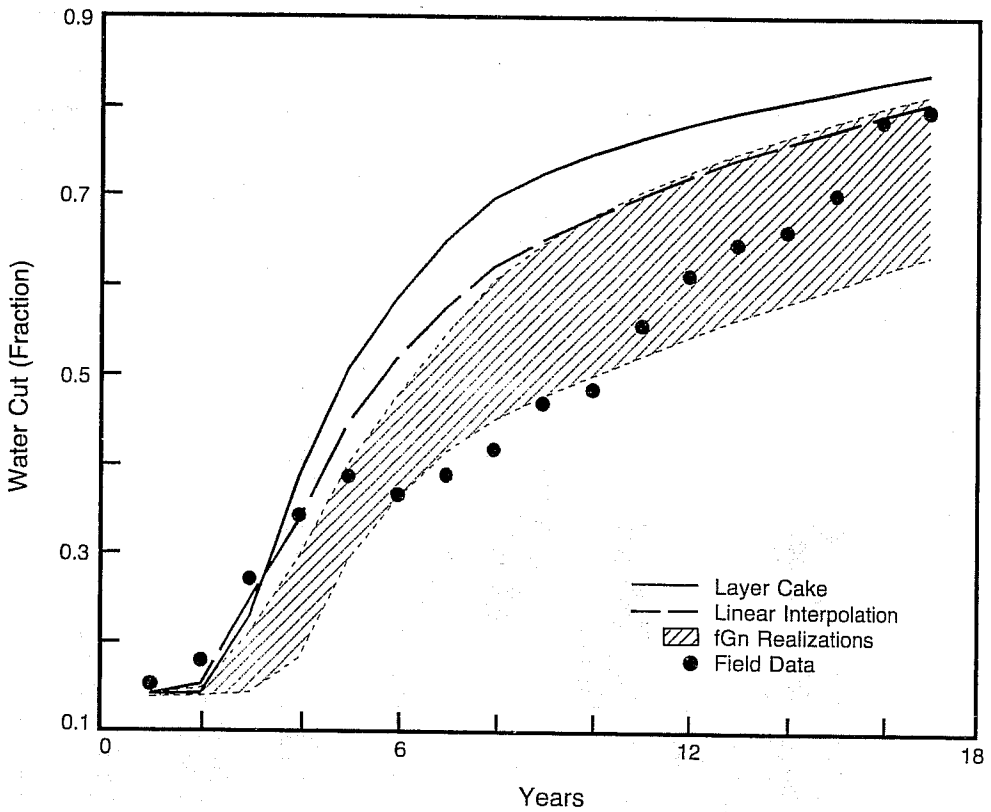

Fig. 8. Simulated water cuts for 20 fGn realizations for Area A (higher S_{wi}).

sections. The frequency distribution of cumulative oil production is displayed in Figure 9. For a 10-acre pattern element, the cumulative oil production ranges from 109 to 135 MSTB with a mean of 122 MSTB. For the layer cake case, the cumulative oil production of 81 MSTB is substantially less than all fGn cases. Correspondingly, the water cut curve is above all the fGn curves (Figure 8). The linear interpolation case has a cumulative oil production of 104 MSTB, which is slightly less than the range of all the fGn cases. Flow simulations on 20 fBm type cross sections give a broader histogram (Figure 9) where the cumulative oil production ranges between 105 to 143 MSTB with a mean of 125 MSTB. In the water cut curves shown in Figure 10, the linear interpolation case lies within the band corresponding to fBm cross

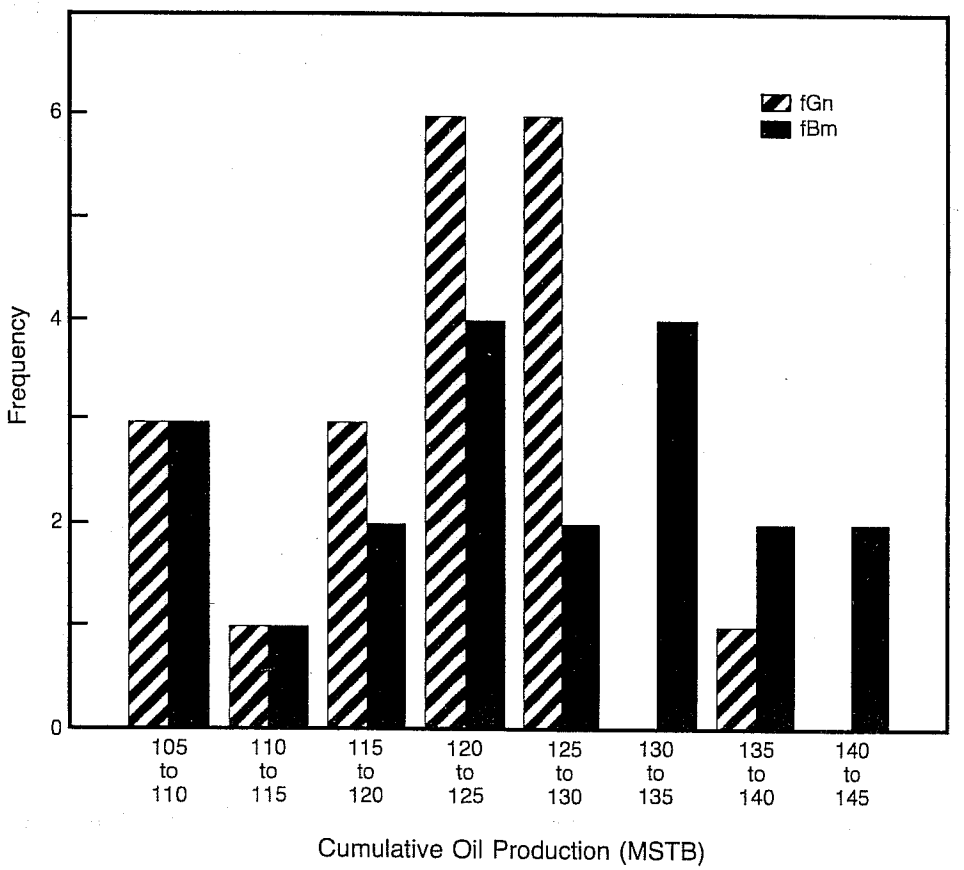

Fig. 9. Histogram of cumulative oil production for 20 fGn and 20 fBm realizations (10 acre pattern element in Area A).

sections. Recall the fBm cross sections have higher initial water saturations in order to match the field water cuts. With these higher saturations, the linear interpolation case gives a cumulative oil production of 120 MSTB. This value is slightly below the mean of the fBm type cross sections. Again, the layer cake cross section gives the lowest cumulative oil production of 95 MSTB.

As mentioned above, the initial water saturations used in the simulations are different for the fGn and fBm cross sections. Within the uncertainty of the field data, both sets are reasonable. Therefore, flow simulations based on either fGn or fBm cross sections match field water cuts.

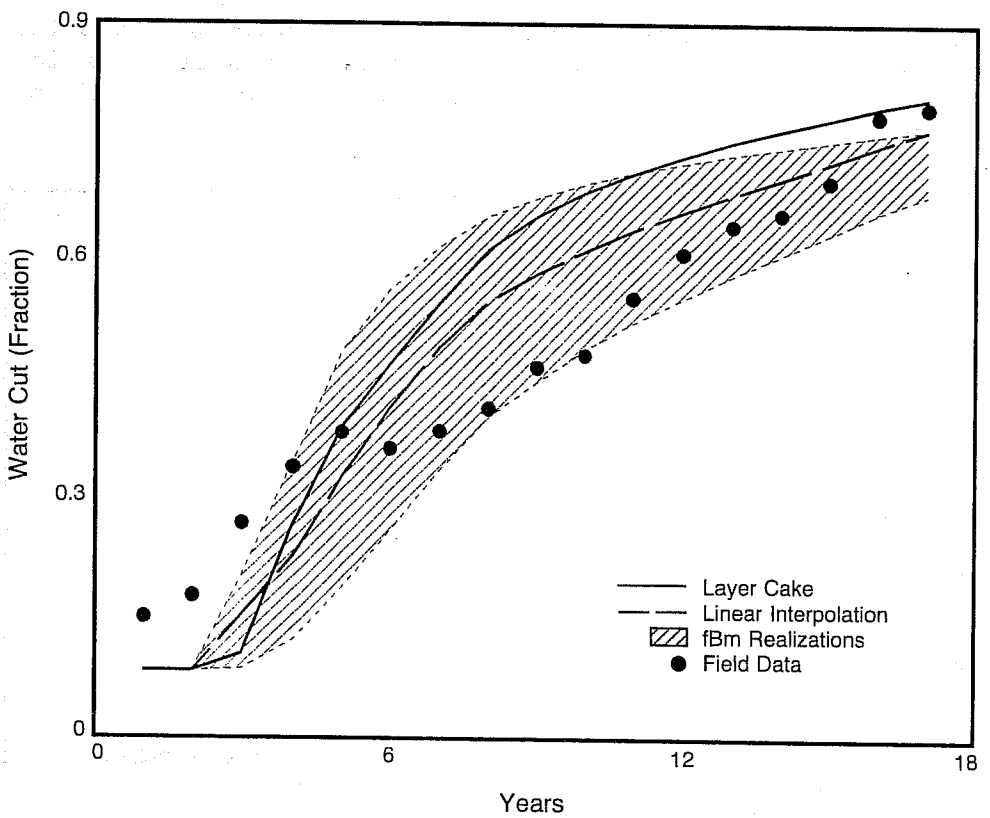

Fig. 10. Simulated water cuts for 20 fBm realizations for Area A (lower S_{wi}).

B. Waterflood in Area B

Flow simulations for Area B give similar agreement with field water cut data for both fGn and fBm cross sections (Figure 11). For both cross sections, the initial water saturations are set to give an initial water fractional flow of 17 percent in all zones at reservoir conditions.

V. SINGLE PHASE LINEAR FLOW

All the above comparisons deal with water cut predictions but do not consider flow rates. The hybrid finite difference/streamtube method does not predict injection/production rates or effective permeabilities. A simple evaluation of the sensitivity of effective permeability is made below by comparing pressure drops across different vertical cross sections for the same flow rates with a single phase. The width of the cross section is constant.

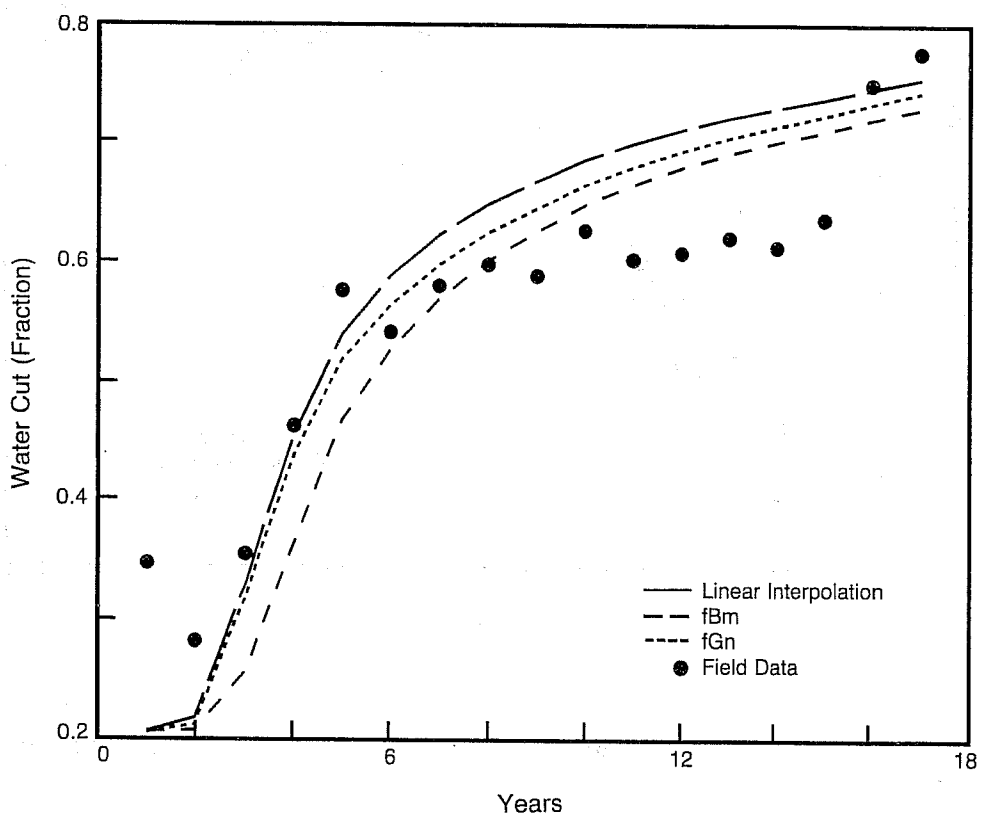

Fig. 11. Simulated water cuts in Area B compared to field data.

The permeabilities for linear flow cannot be used directly to predict injection/production rates in the field. The flow patterns in the field case are more complicated. In the present study, estimates are limited to 2-D reservoir descriptions. The connectivity may be different in a full 3-D distribution of reservoir properties. Still, variations in 2-D permeabilities should give some indication of the corresponding 3-D variations.

As shown below, the permeability can vary by a factor of 10 among the different types of vertical cross sections. At least for this waterflood case study, the permeability is much more sensitive than water cut to the type of reservoir property distribution.

A. fGn Cross Sections

The permeabilities in Figure 12 have been normalized by dividing the effective permeability of each cross section by

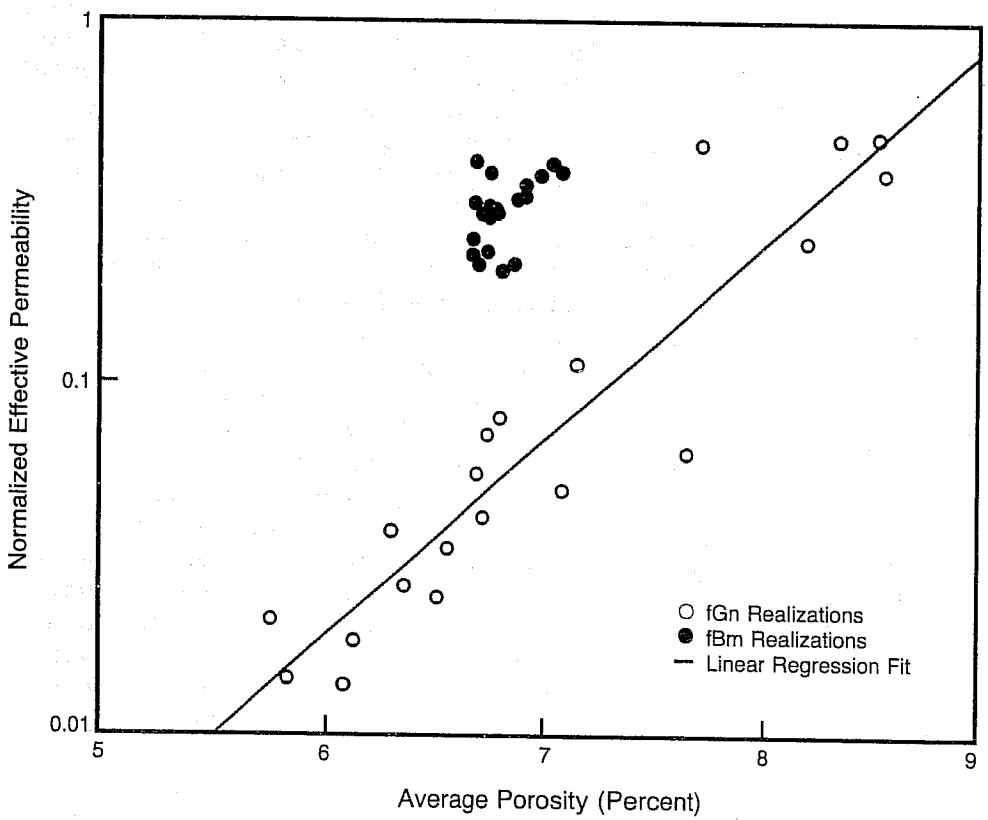

Fig. 12. Effective permeabilities for fGn and fBm realizations for Area A.

the effective permeability of the layer cake cross section. The normalized permeabilities are shown for 20 fGn realizations. The average porosity varies among the different realizations. In generating the cross sections, the average porosity is allowed to fluctuate about the average of the input porosities from the well data (see Appendix). As would be expected from the porosity/permeability relationship (Equation 1), the permeability increases with increasing average porosity. For the average well porosity (6.85 percent), the normalized permeability is 0.055. This permeability is nearly a factor of 20 less than the layer cake permeability. The normalized permeability for the linear interpolation cross section is 0.48, or about a factor of 2 less than the layer cake permeability. Effective permeabilities vary greatly among the different types of cross sections.

B. fBm Cross Sections

Although the field water cut data can be matched with either fGn or fBm cross sections, the corresponding permeabilities are different (Figure 12). The permeability for the fGn cross sections is typically a factor of 5 smaller. This difference can be partially explained by the application of the permeability/porosity transform (Equation 1) at different grid scales in the two methods. For the fGn cross section, Equation 1 is applied at the fine grid scale in Figure 2. The subsequent harmonic averaging to coarsen the grid puts the most weight on the lowest permeability. Since this harmonic averaging step is not included in the fBm procedure, the fGn procedure may give lower permeabilities. Even so, the harmonic averaging does not account for the entire permeability difference. If we apply Equation 1 at the coarser scale for both types of distributions, the fGn cross sections have permeabilities that are still about a factor of 2 to 3 lower.

The fBm methodology for producing cross sections gives much less variation in the average porosity among realizations (Figure 12). The fBm procedure constrains the mean porosity of the <u>entire</u> cross section to the mean value of the well data. On the other hand, the fGn methodology matches the mean porosity of the <u>edges</u> with the mean value of the well data. (See the Appendix for details.) For the fGn cross sections, the greater scatter in porosity carries over to effective permeabilities.

VI. CONCLUSIONS

Flow simulations based on either fGn or fBm cross sections match field water cut data from a mature carbonate reservoir. The initial water saturation is the only parameter adjusted to obtain a match. This adjustment is necessary due to initial water production from transition zones. Although the initial water saturations assumed for each type of distribution are not always identical, both are reasonable. Still, the fGn distributions should be more representative of reservoirs, because they are consistent with outcrop and core photos and horizontal well data from other reservoirs.

Flow simulations on 20 fGn realizations give cumulative oil versus cumulative injection curves that fall within a band of 11 percent about their mean curve. Similarly, the fBm cross sections give a band of 16 percent about their mean curve. Thus, the band is slightly narrower for the fGn cross sections. In addition, the fGn distributions have lower effective permeabilities (linear flow) than the fBm distributions.

The field case studied has close well spacing (20 acres per well). We suspect larger well spacing will increase the differences between the two types of cross sections. As the well spacing increases, simple linear interpolation and fBm are expected to become poorer representations for reservoir heterogeneity.

APPENDIX

A. fGn Cross Section Generation

To build fGn cross sections, the left and right edges of a cross section, $a_{j,k}$, are filled with well log data (L_k for the left edge well log data and R_k for the right edge well log data):

$$a_{1,k} = L_k \;\&\; a_{NX,k} = R_k \;,\; for\; k = 1, NY \qquad \text{(A-1)}$$

where

NX = number of grids in the x direction (horizontal)
NY = number of grids in the y direction (vertical)

A linear interpolation is made between the edges of the array:

$$a_{j,k} = a_{1,k} + \frac{(a_{NX,k} - a_{1,k})}{(NX - 1)} \times (j - 1) \qquad \text{(A-2)}$$

The amount of fGn noise to be added is calculated. It is assumed that the well logs have been put on depth, and therefore, differences between the left and right log values (other than an overall trend) are the result of noise. To calculate the amount of noise, first any overall trends are removed by subtracting the average of each log from each log value. This gives

$$\phi_k(L) = L_k - \overline{L} \qquad \text{(A-3)}$$

where

$$\overline{L} = \frac{1}{NY}\sum_{k=1}^{NY} L_k \qquad \text{(A-4)}$$

and

$$\phi_k(R) = R_k - \overline{R} \qquad \text{(A-5)}$$

where

$$\overline{R} = \frac{1}{NY}\sum_{k=1}^{NY} R_k \qquad \text{(A-6)}$$

The variance, V, of the difference in the two logs without trends is calculated,

$$V = \frac{1}{2\ NY}\sum_{k=1}^{NY} (\phi_k(L) - \phi_k(R))^2 \qquad \text{(A-7)}$$

V corresponds to the variogram at lag NX of the noise that needs to be added.

A noise array is now constructed from the appropriate spectral density, S, of fGn noise. The spectral density of the noise to be added is

$$S(\omega_x, \omega_y) = \frac{A}{[(\omega_x)^2 + (\omega_y)^2)]^{\beta}} \qquad \text{(A-8)}$$

with

$$\omega_x = 2\pi f_x \tag{A-9}$$

$$\omega_y = 2\pi f_y \tag{A-10}$$

$$\beta = H \quad where \quad 0.5 < H < 1 \tag{A-11}$$

Here f_x and f_y are the x and y frequencies in Fourier space.

The noise array, $\eta_{j,k}$, is generated with H determined from a fractal analysis of the well logs. As a discrete inverse Fourier transform, the noise array, $\eta_{j,k}$, is generated from Equation A-8 as follows:

$$\eta_{i,j} = \sum_{m=1}^{NX} \sum_{n=1}^{NY} a_{m,n} e^{2\pi i [(j-1)(m-1)/NX + (k-1)(n-1)/NY]} \tag{A-12}$$

where

LX = separation of the wells (in feet)
LY = thickness of the cross section (in feet)

Here,

$$a_{m,n} = R_{m,n} e^{i\theta_{m,n}} \tag{A-13}$$

where

$$R^2_{m,n} = \frac{1}{[(m-1)^2 + (LX/LY)^2 (n-1)^2]^\beta}$$

except

$$for \ \frac{NX}{2} \geq m-1 \geq 0 \ \ \& \ \ \frac{NY}{2} \geq n-1 \geq 0 \tag{A-14}$$

$$R_{1,1} = 0.0 \tag{A-15}$$

Because of symmetry requirements,

$$R_{m,NY+2-n} = R_{m,n} \quad for \quad \frac{NX}{2} \geq m > 1 \ \ \& \ \ \frac{NY}{2} \geq n > 1 \tag{A-16}$$

The phase angle, $\Theta_{m,n}$, is defined as a random number between $-\pi$ and $+\pi$ for the range of m and n values satisfying

$$\frac{NX}{2} \geq m-1 \geq 0 \ \ \& \ \ \frac{NY}{2} \geq n-1 \geq 0 \tag{A-17}$$

and

$$\frac{NX}{2} > m - 1 > 0 \quad \& \quad NY - 1 \geq n - 1 > \frac{NY}{2} \tag{A-18}$$

Finally, the 2-D Fourier transform requires the following:

$$a_{NX+2-m,1} = a^*_{m,1} \quad for \quad \frac{NX}{2} \geq m > 1 \tag{A-19}$$

$$a_{1,NY+2-n} = a^*_{1,n} \quad for \quad \frac{NY}{2} \geq n > 1 \tag{A-20}$$

$$a_{NX+2-m,NY+2-n} = a^*_{m,n} \quad for \quad \frac{NX}{2} \geq m > 1 \ \& \ NY \geq n > 1 \tag{A-21}$$

$$a_{\frac{NX}{2}+1,NY+2-n} = a^*_{\frac{NX}{2}+1,n} \quad for \quad \frac{NY}{2} \geq n > 1 \tag{A-22}$$

Here a^* is the complex conjugate of a. For a most accurate distribution, only one-half to one- fourth of the original distribution should be retained (Reference 11), but for this work, the entire array is used.

Note $\eta_{j,k}$ only needs to be generated to agree with Equation A-8 to within a multiplicative constant, because $\eta_{j,k}$ will be rescaled to the well data before it is used. Equation A-15 makes the average of the noise array to be equal to zero.

The desire now is to adjust the variogram of lag NX of the generated noise array to be equal to V. An indirect approach to this produces a more stable solution than a direct one. A direct approach would be to do a linear scaling which would set the variogram of lag NX equal to V. But if it is assumed that the variogram of the generated noise array has reached its sill for a lag equal to the well separation, then the variance of the noise array, v_n, is equal to the variogram of lag NX. Since there are many more values in the variance than in the variogram of lag NX, the variance produces a more stable estimate of the variogram of lag NX. The variance of the array is therefore used for scaling the noise. The variance of the noise array, v_n, is calculated as follows:

$$v_n = \frac{1}{NX\ NY} \sum_{j=1}^{NX} \sum_{k=1}^{NY} (\eta_{j,k} - \bar{\eta})^2 \tag{A-23}$$

with

$$\overline{\eta} = \frac{1}{NX\ NY}\sum_{j=1}^{NX}\sum_{k=1}^{NY}\eta_{j,k} \qquad \text{(A-24)}$$

Since the average value in the generated noise array is zero, the following linear scaling gives an array, $H_{j,k}$, with the desired amount of noise and zero mean (see the "linear scaling" section at the end of this Appendix):

$$H_{j,k} = \eta_{j,k}\sqrt{V/V_n} \qquad \text{(A-25)}$$

The scaled noise array, $H_{j,k}$, is then added to the linear interpolation array, $A_{j,k}$:

$$B_{j,k} = A_{j,k} + H_{j,k} \qquad \text{(A-26)}$$

The inclusion of the linear interpolation array introduces trends in any horizontal trace. These trends alter the statistical structure of the fGn in any horizontal trace. An alternative method is to replace the linear interpolation array in Equation A-26 with a layer cake array. Then the porosity value at a given depth would be the average of the two edge values. The sum of the layer cake array and the fGn noise array would still have fGn statistical structure. However, the resulting cross section would not honor the input well log values at the edges as well as the procedure with linear interpolation. We use linear interpolation in the present study.

With linear interpolation, $B_{j,k}$ in Equation A-26 has a total variance greater than the variance of the original log data. The average of the resulting array, $B_{j,k}$, is unchanged from the linear interpolation array, since the average of the noise array, $H_{j,k}$, is zero.

One final linear scaling is made. Its purpose is to adjust the variance and average of the edges of the array to agree with the variance and average of the log data. This is done so that the edges of the final cross section will closely match the input well log data.

The linear scaling which gives the desired variance and average is the following:

$$C_{j,k} = \left[\frac{V_L}{V_H}\right]^{1/2}(B_{j,k} - \overline{B_H}) + \overline{B_W} \qquad \text{(A-27)}$$

where

$$\overline{B_W} = (\overline{L} + \overline{R})/2 \qquad \text{(A-28)}$$

$$\overline{B_H} = [\ \overline{B_1} + \overline{B_{NX}}\ ]/2 \tag{A-29}$$

$$v_L = \left[\frac{1}{NY}\sum_{k=1}^{NY}(L_k - \overline{L})^2 + \frac{1}{NY}\sum_{k=1}^{NY}(R_k - \overline{R})^2\right]/2 \tag{A-30}$$

$$v_H = \left[\frac{1}{NY}\sum_{k=1}^{NY}(B_{1,k} - \overline{B_1})^2 + \frac{1}{NY}\sum_{k=1}^{NY}(B_{NX,k} - \overline{B_{NX}})^2\right]/2 \tag{A-31}$$

$$\overline{B_1} = \frac{1}{NY}\sum_{k=1}^{NY} B_{1,k} \tag{A-32}$$

$$\overline{B_{NX}} = \frac{1}{NY}\sum_{k=1}^{NY} B_{NX,k} \tag{A-33}$$

The variance and average value of the edges of the final array, $C_{j,k}$, are now the same as the variance, v_L, and average, B_W, of the input well log data from both wells. As a result of scaling the edges rather than the overall array average to the well log data, the overall average and variance of the final array may be greater than or less than the average and variance of the input well log data for a particular realization.

When fGn cross sections are generated for the field study, they are generated using log porosities and square grids, 2' x 2'. Horizontal permeabilities are assigned using Equation 1. The grids are then made more coarse (2' x 16'). This is done with three calculations. First, the horizontal permeability of the larger grid is set equal to a harmonic average of the small grids that make it up. Second, the vertical permeability of the larger grid is set equal to 0.1 times the large grid horizontal permeability. Third, the porosity of each large grid is set equal to the arithmetic average of the porosities of the small grids.

B. fBm Cross Section Generation

Hewett and Behrens[3] describe the method to build fBm cross sections. Following their method, the left and right edges of a cross section, $a_{j,k}$, are filled with well log data as shown in Equation A-1. A linear interpolation is made between the edges of the array as shown in Equation A-2.

fBm noise is now generated. This noise is actually fBm in the horizontal direction and fGn in the vertical direction.

fBm noise is now generated. This noise is actually fBm in the horizontal direction and fGn in the vertical direction. The noise is generated from an equation for the spectral density similar to the way fGn noise was generated. As a discrete inverse Fourier transform, the noise array, $\eta_{j,k}$, is generated in the same manner as fGn (Equations A-12 through A-22) except

$$R^2_{m,n} = \frac{1}{[(m-1)^2 + c^2(n-1)^2]^{\beta} j^2} \tag{A-34}$$

with

$$c = NX/NY \tag{A-35}$$

and

$$\beta = H + 1 \quad where \quad 0.5 < H < 1 \tag{A-36}$$

Note that this aspect ratio, c, is based on the number of grids, not the physical dimensions of the cross section. As with fGn, $\eta_{j,k}$ only needs to be generated to within a multiplicative constant, because $\eta_{j,k}$ will be rescaled to the well data before it is used.

The noise array, $\eta_{j,k}$, is now scaled so that the total variance of the noise array, v_T, matches the variance of the well logs, v_L. This is done by the following linear scaling of the noise array:

$$\psi_{j,k} = \left[\frac{v_L}{v_T}\right]^{1/2} \eta_{j,k} \tag{A-37}$$

where

$$v_T = \frac{1}{NX\ NY} \sum_{j=1}^{NX} \sum_{k=1}^{NY} (\eta_{j,k} - \bar{\eta})^2 \tag{A-38}$$

$$\bar{\eta} = \frac{1}{NX\ NY} \sum_{j=1}^{NX} \sum_{k=1}^{NY} \eta_{j,k} \tag{A-39}$$

and v_L is defined by Equation A-30.

The next step is to add the noise array, $\eta_{j,k}$, to the linear interpolation array, $a_{j,k}$, in such a way that the edges of the final array are similar to the original log data. This is done by a procedure outlined by Journel.[12] First, a linear interpolation between the edges of the noise array is made,

$$d_{j,k} = \eta_{1,k} + \frac{(\eta_{NX,k} - \eta_{1,k})}{(NX - 1)} \times (j - 1) \qquad \text{(A-40)}$$

This array, $d_{j,k}$, is subtracted from the original noise array so that the edges of the new noise array are zero:

$$e_{j,k} = \eta_{j,k} - d_{j,k} \qquad \text{(A-41)}$$

The resulting array, $e_{j,k}$, is now added to the linear interpolation array, $a_{j,k}$,

$$f_{j,k} = a_{j,k} + e_{j,k} \qquad \text{(A-42)}$$

As with fGn, one final linear scaling is made. The purpose is to adjust the variance of the final array to the variance of the well logs while preserving the average of the edges of the array to the average of the well log data. The linear scaling which gives the desired result is the following:

$$g_{j,k} = \left[\frac{v_L}{v_F}\right]^{1/2} (f_{j,k} - \overline{f_e}) + \overline{f_L} \qquad \text{(A-43)}$$

where

$$v_F = \frac{1}{NX\ NY}\sum_{j=1}^{NX}\sum_{k=1}^{NY} (f_{j,k} - \overline{f})^2 \qquad \text{(A-44)}$$

$$\overline{f} = \frac{1}{NX\ NY}\sum_{j=1}^{NX}\sum_{k=1}^{NY} f_{j,k} \qquad \text{(A-45)}$$

$$\overline{f_e} = \left[\frac{1}{NY}\sum_{k=1}^{NY} f_{1,k} + \frac{1}{NY}\sum_{k=1}^{NY} f_{NX,k}\right]/2 \qquad \text{(A-46)}$$

$$\overline{f_L} = [\ \overline{L} + \overline{R}\ ]/2 \qquad \text{(A-47)}$$

and v_L is defined by Equation A-30. $\overline{L}$ and $\overline{R}$ are defined by Equations A-4 and A-6, respectively.

When fBm cross sections are generated for the field case, they are generated from porosity log data at the scale they are to be used (here 2' x 16'). No coarsening up of the grid is performed. As with fGn, horizontal permeabilities are assigned to the grids using Equation 1. Vertical permeabilities are set to 1/10 the horizontal permeabilities.

C. Linear Scaling

Linear scaling is used several times in generating cross sections. The basis of this is described here. One Gaussian distribution can be changed into another Gaussian distribution while preserving the relationship of all of the point values if a linear transformation is made. To go from a Gaussian distribution with mean, μ_1, and standard deviation, σ_1, to another Gaussian distribution with mean, μ_2, and standard deviation, σ_2, each value in the first array, x_j, is changed into each value in the second array, y_j, as follows:

$$y_j = \left[\frac{\sigma_2}{\sigma_1}\right](x_j - \mu_1) + \mu_2 \qquad \text{(A-48)}$$

The linear scaling equations used for fGn and fBm cross section generation can be derived from Equation A-48 by noting that the variance of a distribution is equal to its standard deviation squared.

ACKNOWLEDGEMENTS

A computer program from B. H. Caudle at the University of Texas at Austin was used in part of the streamtube calculations. The authors also thank Conoco Inc. for permission to publish this paper.

REFERENCES

1. Hewett, T. A.: "Fractal Distributions of Reservoir Heterogeneity and Their Influence on Fluid Transport," paper SPE 15386 presented at the 1986 SPE Annual Technical Conference and Exhibition, New Orleans, Oct. 5-8.

2. Emanuel, A. S., Alameda, G. K., Behrens, R. A., and Hewett, T. A.: "Reservoir Performance Prediction Methods Based on Fractal Geostatistics," SPE Reservoir Engineering (August 1989) 311-318.

3. Hewett, T. A. and Behrens, R. A.: "Conditional Simulation of Reservoir Heterogeneity With Fractals," SPE Formation Evaluation (September 1990) 217-225.

4. Mathews, J. L., Emanuel, A. S., and Edwards, K. A.: "A Modeling Study of the Mitsue Stage 1 Miscible Flood Using Fractal Geostatistics," paper SPE 18327 presented at the 1988 SPE Annual Technical Conference and Exhibition, Houston, Oct. 2-5.

5. Tang, R. W., Behrens, R. A., and Emanuel, A. S.: "Reservoir Studies With Geostatistics To Forecast Performance," SPE Reservoir Engineering (May 1991) 253-258.

6. Hewett, T. A. and Behrens, R. A.: "Scaling Laws in Reservoir Simulation and Their Use in a Hybrid Finite Difference/Streamtube Approach to Simulating the Effects of Permeability Heterogeneity," Reservoir Characterization II, L. W. Lake, H. B. Carroll, Jr., and T. C. Wesson (eds.), Academic Press, San Diego, California (1991) 402-441

7. Hardy, H. H.: "The Fractal Character of Photos of Slabbed Cores," to appear in Mathematical Geology

8. Crane, S. D. and Tubman, K. M.: "Reservoir Variability and Modeling With Fractals," paper SPE 20606 presented at the 1990 SPE Annual Technical Conference and Exhibition, New Orleans, LA, September 23-26.

9. Hardy, H. H.: "Fractal Analysis of Core Photographs with Application to Reservoir Characterization," presented at the NIPER/DOE Third International Reservoir Characterization Technical Conference, Tulsa, Nov. 3-5, 1991.

10. Feder, J.: Fractals, Plenum Press, New York, 1988.

11. Saupe, D.: "Algorithms for Random Fractals," The Science of Fractal Images, Heinz-Otto Peitgen and D. Saupe (eds.), Springer-Verlag, New York (1988) 71-136.

12. Journel, A. G. and Huijbregts, Ch. J.: Mining Geostatistics, Academic Press, New York, 1978.

Investigating Infill Drilling Performance and Reservoir Continuity Using Geostatistics

D. S. Wolcott, ARCO Alaska, Inc.
A. K. Chopra, Atlantic Richfield Co.

I. INTRODUCTION

One of the objectives of a field development program is to determine the maximum well spacing that will effectively drain the reservoir. While widely spaced wells have proven to be effective, field experience is showing infill drilling produces substantial additional recovery.[1-3] In heterogeneous reservoirs, infill drilling increases reservoir continuity and enhances areal and vertical sweep efficiencies. For reservoir management and economic reasons it is important to predict the performance and additional recovery from infill drilling. Traditionally, reservoir descriptions have been generated, at interwell locations, using algorithms which result in smoothed predictions. The use of homogeneous or smoothed descriptions is not adequate because important mechanisms are not considered. Incorporation of heterogeneities in reservoir simulators is important but cannot be conducted with conventional mapping techniques. The use of geostatistics provides a framework for incorporating reservoir heterogeneities at interwell locations in the description.

For many years, the mining industry has used geostatistics to evaluate the quality, quantity and orientation of ore bodies.[4-9] The term geostatistics refers to statistical techniques that account for spatial continuity and variability. Continuity is an essential feature of natural phenomena, but not easily quantified using traditional deterministic techniques. The importance of incorporating the spatial variability in an

optimal weighting system was first recognized by Drozdov, a Russian hydrometeorologist, in the early 1940's. The first elementary kriging method of regression was done by Krige,[9] who applied his techniques to gold mines in South Africa. Matheron[4] provided a foundation for geostatistics and gave the name of "regionalized variables" to the variables typical of a phenomenon having a spatial correlation structure. More recently, Lorenz,[10] Tsonis,[11] and Tennekes[12] have applied stochastic methods for weather forecasting. Geostatistics provides methods for predicting uncertainty by creating multiple realizations of the reservoir description. The probabilistic framework is useful because it leads to a system of equations for determining the estimate and uncertainty.

In recent years, the petroleum industry has placed greater emphasis on these techniques for reservoir characterization because of their promise to integrate data and provide a framework for describing interwell heterogeneities.[13-23] The key issues in reservoir characterization are the estimation and representation of key reservoir properties at interwell locations, prediction of reservoir performance, and the understanding of reservoir heterogeneity. The precise level of detail required and suitable techniques are not well-defined in the industry. The detail that must be described in a reservoir description depends on its intended use and varies for different processes and reservoirs.[24-27]

Several approaches of estimation have relied on deterministic interpolation of key reservoir properties based on a geological model of the reservoir. The geological model is based on thin sections, core descriptions, sedimentology of the region, and the associated interpretation.[27-34] In some of these approaches, boolean methods are applied successfully to represent geology. However, in other instances, contour maps are drawn manually or by computer to honor the well data. These contour maps are then translated to a grid suitable for reservoir simulation. Currently, many traditional mapping techniques minimize the inherent geological heterogeneities or do not consider them. These descriptions may generate inaccurate results when used with flow simulators. The industry wide application of geostatistics is still limited in reservoir engineering because of lack of understanding of how reservoir heterogeneity, generated using geostatistical techniques, affects fluid flow and reservoir performance.[35] Most of the previous work on flow simulation using geostatistical realizations has focused on using two-dimensional cross sections with streamtube models.[21,22]

This paper presents an investigation of infill drilling performance and reservoir continuity using geostatistics and a reservoir simulator. The study area is the A4 Sandstone Formation, drillsite 1E (DS-1E), in the Kuparuk River Field (Fig. 1). The A4 Sandstone, particularly DS-1E, was chosen because of the higher density of wells in this area. The DS-1E has variable (40 to 160-acre) spacing compared to the remainder of

the field developed on 160-acre spacing. Also, previous geologic studies have correlated the lithofacies of subunits of A4 interval resulting in a high resolution geologic description of this drillsite.[36]

The maps generated from kriging and conditional simulations are used in a three-dimensional black oil reservoir simulator. We show that inclusion of heterogeneities using conditional simulation predicts recovery efficiencies different from those predicted by kriging, a smoother mapping technique. Also presented are reservoir performance predictions showing lower recovery efficiencies for thinner beds and additional recovery from infill drilling.

II. RESERVOIR GEOLOGY AND SUBUNIT DATA

The Kuparuk River Field, discovered in 1969, is on the North Slope of Alaska, near the western edge of the Prudhoe Bay Unit. The field produces from two distinct intervals. The lower of these is the A interval which is composed of five sand bodies (A1 through A5, Fig. 1).[37] The interval is characterized by lenticular, shingled, sheet-like sandstone bodies. A4 sand body is the major producing sand of the A interval in DS-1E. These sands were deposited in a regressive shelf setting during the Lower Cretaceous age. The best reservoir-quality rocks are amalgamated deposits of multiple episodic storms; whereas, the thinner, lower quality reservoir sands represent isolated storm events. Sandstone beds in these facies range from 0.5 to 8 feet thick.

A4 sand is divided into eight subunits which are named according to the geologic nomenclature as: A, B1, B2, B3, B4, C1, C2, and C3 (Fig. 2). The A subunit is the lower sand and C3 subunit the upper. The eight subunits are characterized as hummocky, cross stratified and flaser bedded sandstone.[38] They are discrete flow units within the A4 sandstone body and are separated by mappable shale sequences. These shale sequences restrict vertical flow during waterflood.

The geologic experience in this area indicates higher permeability typically occurs in the thicker zones.[36,39] A correlation of increasing permeability with thickness was obtained from core data. Shown in Fig. 3 is the geometric mean of permeability versus total thickness for each subunit . An example linear model is shown demonstrating the trend. The higher permeabilities are generally associated with the thicker amalgamated beds and lower permeabilities with the thin single event beds. A similar relationship has been observed by other investigators for another sandstone deposit.[40]

Ankerite, a carbonate authigenic mineral, is a common diagenetic cement in the A4 Sandstone and is present in five of the subunits. This cement fills the porosity and creates permeability barriers. The effect of ankerite zones was included in the reservoir descriptions.

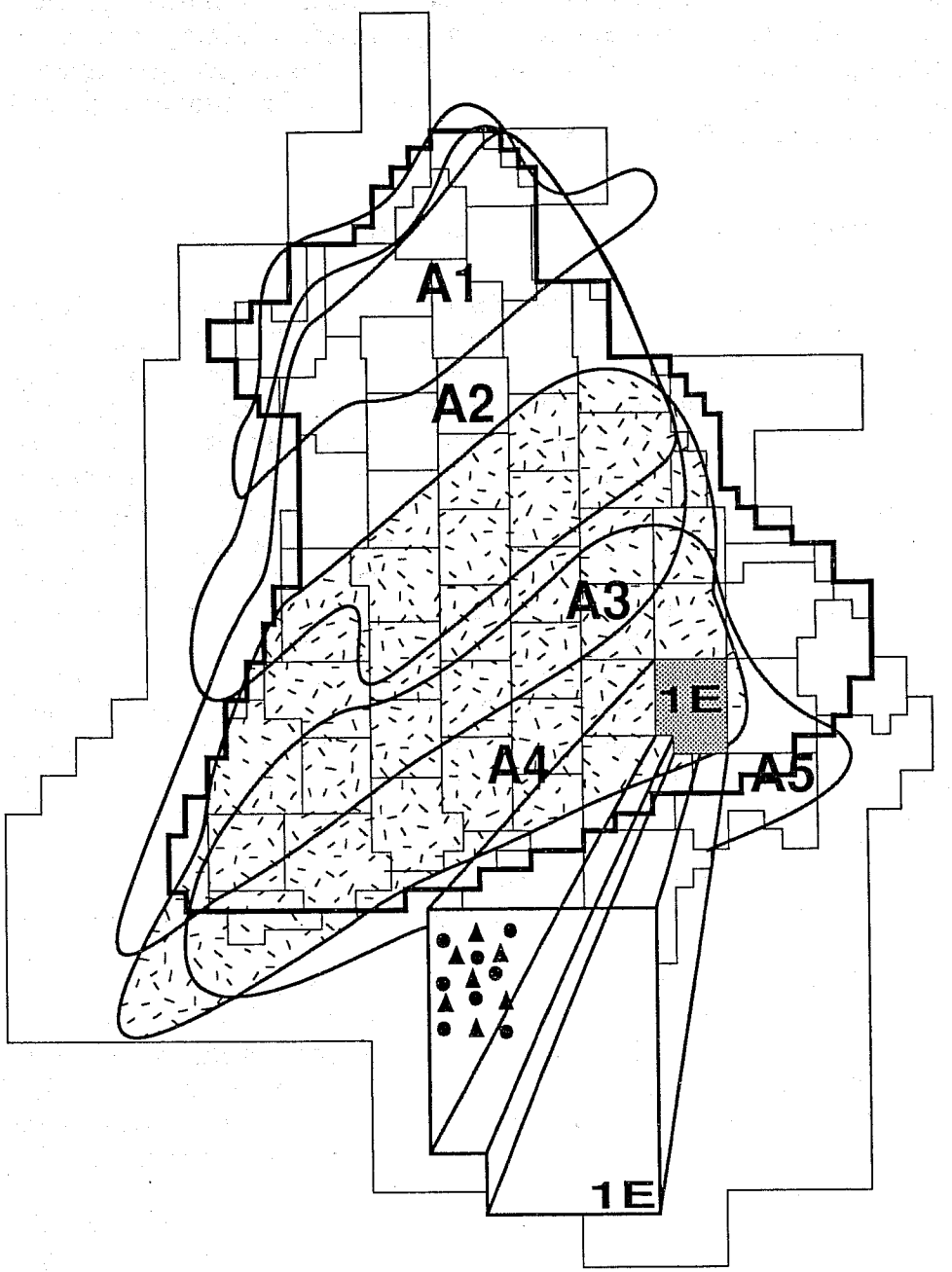

Fig 1. Locality map of the A Sands and Drillsite 1E, Kuparuk River Field.

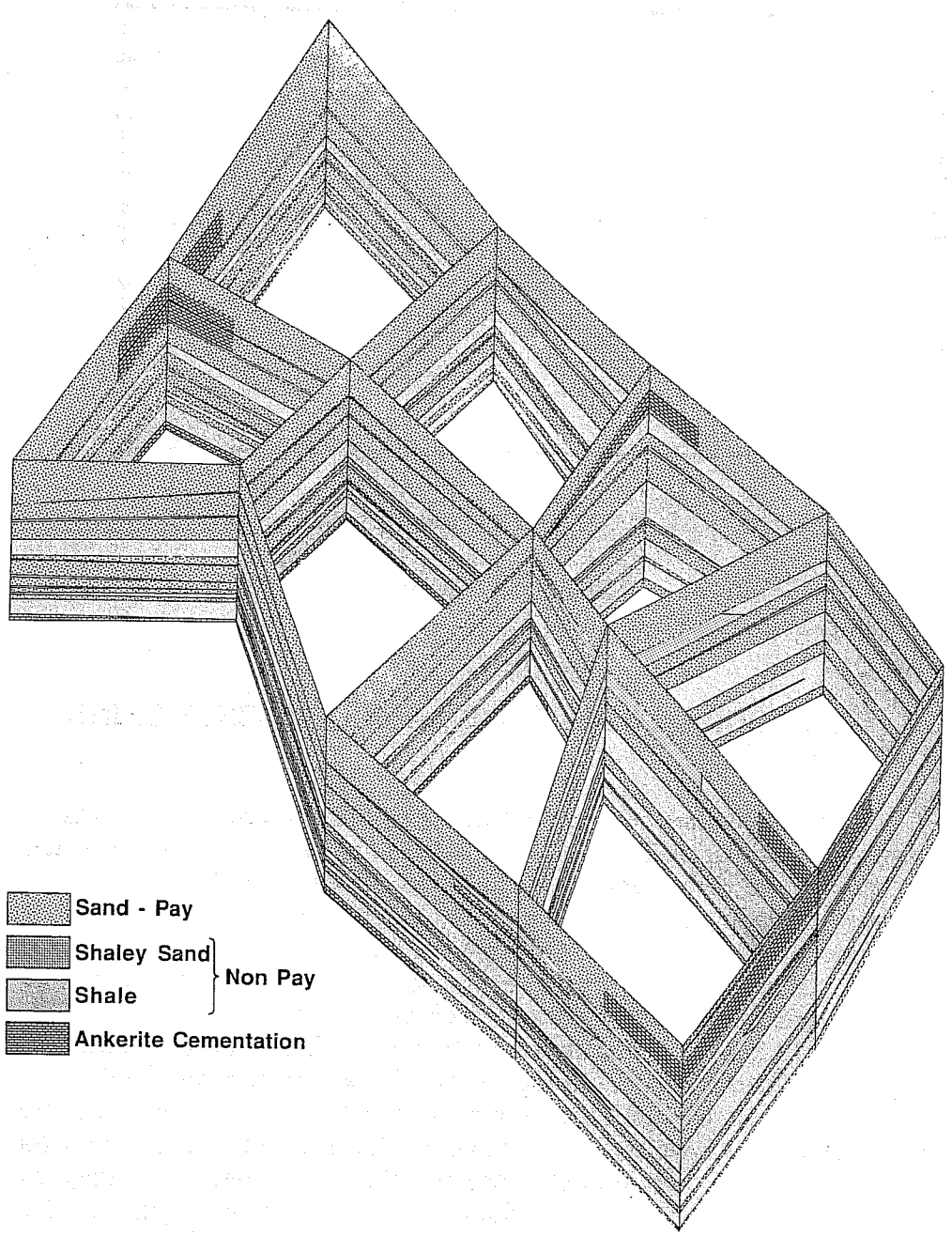

Fig. 2. Fence diagram of the Kuparuk A4 sandstone body in Drillsite 1E, Kuparuk River field (Copyright 1991 SPE, SPE 22164, International Arctic Technology Conference, May 29-31, 1991 in Anchorage AK).

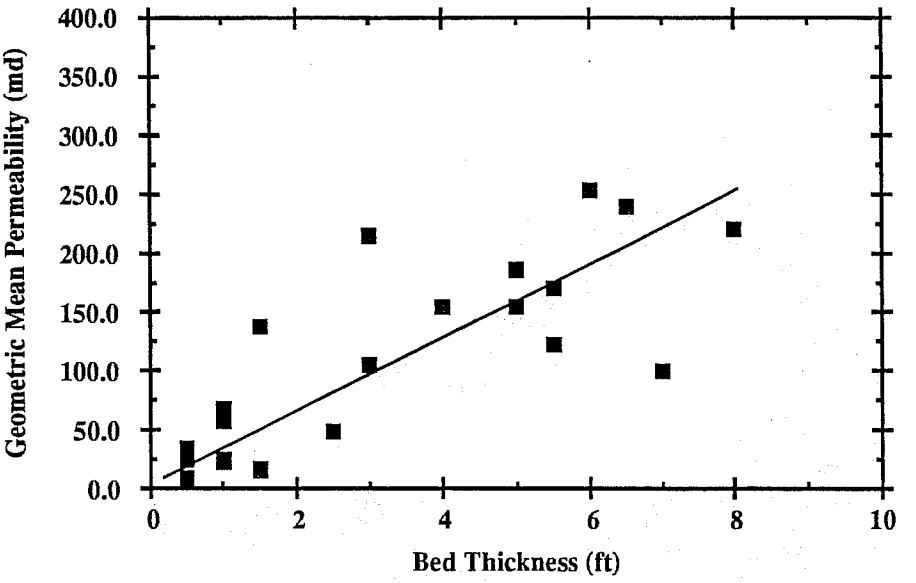

Fig. 3. Geometric mean of permeability for each subunit by thickness with an example linear model.

III. VARIOGRAM EVALUATION AND INFERENCE USING ANALOGS

The first step in evaluating reservoir heterogeneity was to construct semi-variograms for each subunit, using gross thickness data for each of the eight subunits. The gross thickness is the total subunit thickness including ankerite zones. The important values derived from an experimental variogram are its shape, nugget, sill and range. Range is the distance after which the data are not correlated, nugget generally represents the measurement error or lack of small scale correlation of the data, and sill is a measure of sample variance. The Appendix shows the method to calculate a semi-variogram and Clark[41] gives more detail.

For each of the eight subunits in DS-1E, thickness data are available from 15 wells. To confidently infer a semi-variogram with information from 15 data points alone is difficult. Therefore, information from an analog formation was included to interpret the variograms. This improved the understanding of the continuities and thickness distributions occurring in storm-generated shelf sandstones.

The analog studied was the Miri Formation[42] from the Seria Field in Brunei, Borneo. This field was chosen as an analog because it is a storm-generated shelf sandstone and considered to be depositionally similar to the Kuparuk River Field.[36] The Seria Field has wells drilled on two to seven acre spacing and contains six sand layers. An example

Miri thickness map for the B sand is in Fig. 4. Since this field was sampled on such a close spacing and the number of wells is large, the confidence in the resulting semi-variogram is greater. Therefore, the character of the semi-variograms at interwell scale is better-understood.

The most notable contributions from the Miri semi-variograms were the approximate values for nugget, range and sill. In Fig. 5, the normalized variograms of four Miri sands and a spherical model are shown. The normalized variograms were obtained by dividing each variogram by its variance. Two significant observations are: a) the nugget values are approximately zero, and b) correlations exists for the first 2000 ft. Although the variograms do show a nested structure at 2500 ft, this structure was not observed from the limited data in Kuparuk DS-1E. This lack of similarity is not significant because the scale of interval heterogeneities for DS-1E wells is less than the distance at which the nested structure is observed. Other possible methods for deducing the variogram are the use of outcrop analogs[43-44] and soft seismic derived correlations.[45-48] The data can be further conditioned by pressure transient tests.[49] These methods were not used in the present study.

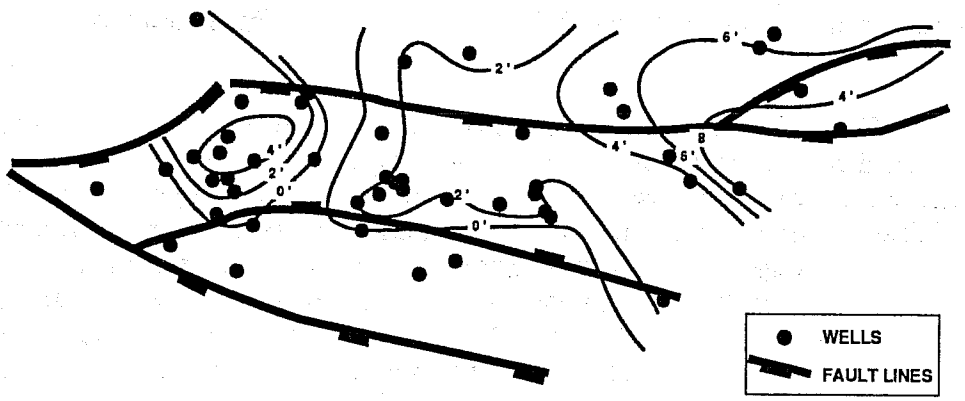

Fig. 4. Thickness map, B-Sand, Miri Formation, Seria Field, Borneo (Atkinson et al., Canadian Society of Petroleum Geologists, 1986).

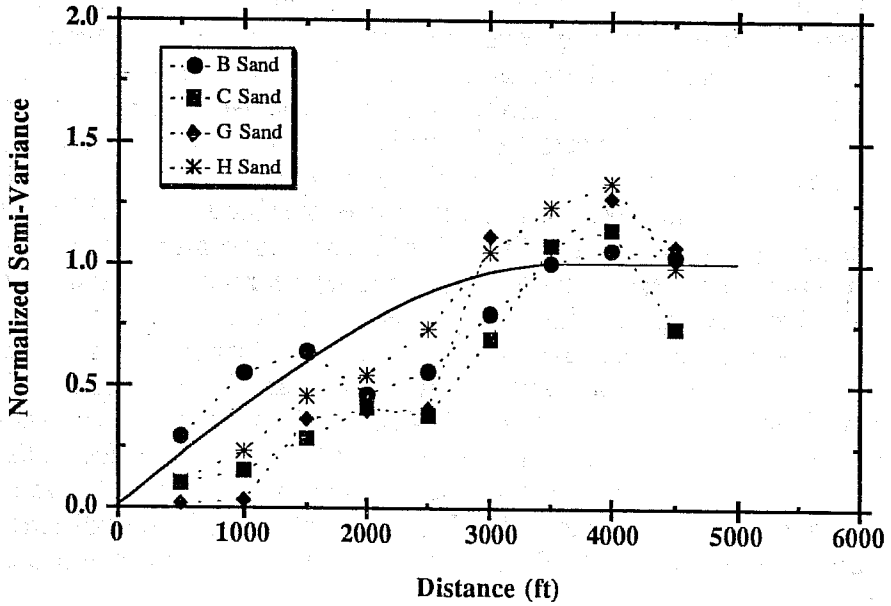

Fig. 5. Example spherical model with the normalized omni-directional semi-variograms of thickness, Miri Formation, Seria Field, Borneo.

The information from the Miri analog was used when fitting the spherical models to the Kuparuk semi-variograms. Because of the large distance between wells and less number of wells in the Kuparuk DS-1E, sufficient statistics were not always available for semi-variance values below the range of the semi-variogram. In such cases, as a first approximation to the Miri analog, the sill was set equal to the variance, the range was set at 3000 feet and nugget was set to zero. Then, the model was fine tuned by raising or lowering the sill until the best fits through the Kuparuk experimental semi-variograms were obtained. Different spherical models were fit to the experimental semi-variograms of thickness for all the subunits. Fig. 6 is a histogram of the C3 subunit. All the normalized semi-variograms and an example spherical model for the subunit C3 are shown in Fig. 7

For subunits A, B1, B3, C2 and C3, a semi-variogram of ankerite thickness was also generated. Because limited ankerite data were available for each layer, only one composite ankerite semi-variogram was generated using the data from all five layers. A spherical model was fit to the composite variogram.

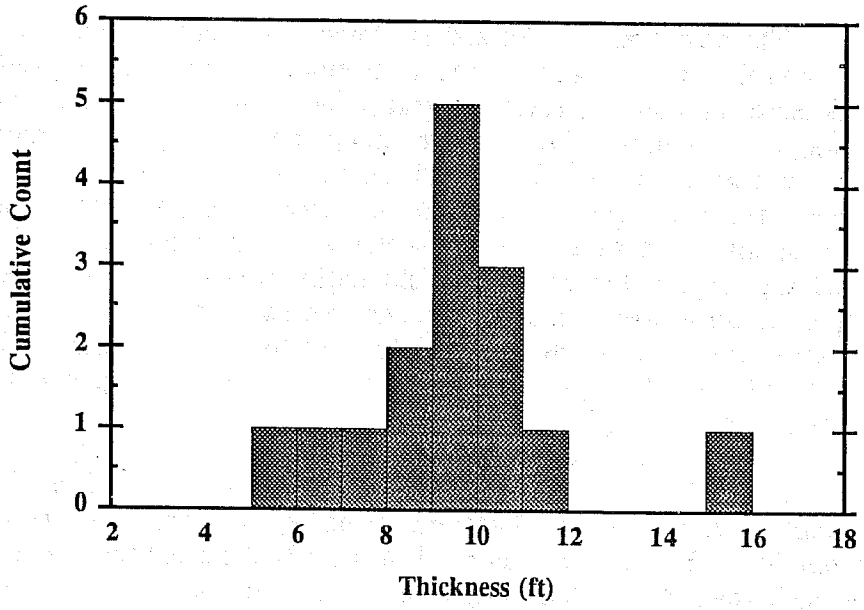

Figure 6 - Histogram of thickness for Subunit C3.

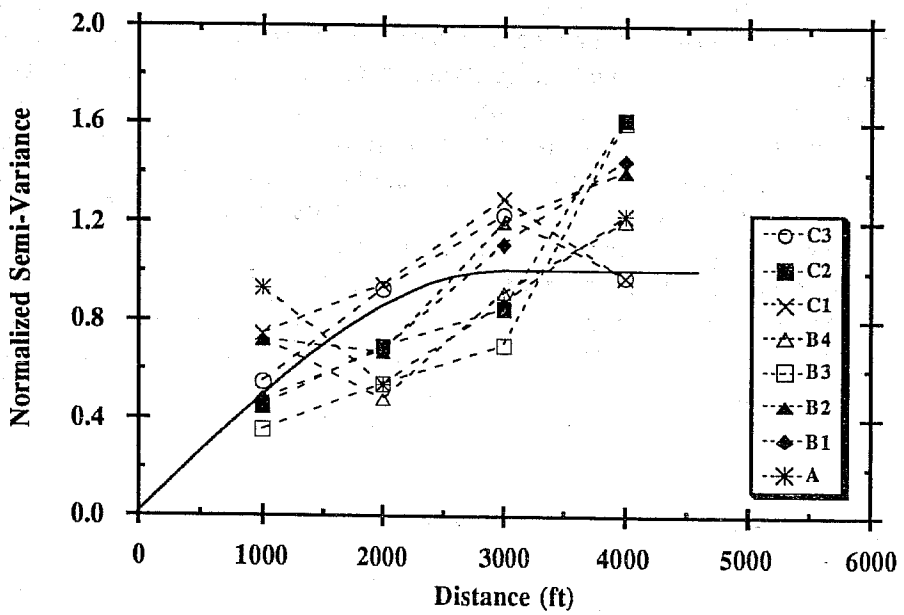

Figure 7 - Normalized omni-directional semi-variograms for different subunits and the spherical model for subunit C3.

IV. KRIGING AND CONDITIONAL SIMULATIONS

The variogram model and the thickness data at wells, for each of the subunits, were input in the conditional simulator to predict the thicknesses at interwell reservoir grid points. The conditional simulation package is a commercial program using the turning bands method to generate realizations.[50] Ten conditional simulation realizations and one kriged map were generated. The ankerite variogram model and the ankerite thickness data from the wells were input into the conditional simulator. Again, ten conditional simulation realizations and one kriged map of ankerite were generated for the five subunits containing ankerite. For these subunits, the ankerite thicknesses for maps 1 through 10 were subtracted from their gross thickness maps. The resulting maps are the net thickness maps (Fig. 8).

The permeability values for each of the descriptions were computed using a permeability-net thickness correlation (Fig. 9). Porosity values were determined using a porosity-permeability correlation. This method may result in slightly different total pore volume for each realization. The kriged pore volume was the average of all-different realizations. To account for these differences, the pore volume injected for each realization is normalized by its total pore volume.

For each of the eight subunits, ten conditional realizations and the kriged map are possible reservoir descriptions honoring the known data and spatial correlation structure. The kriging technique is similar to the more traditional mapping techniques minimizing the estimation variance. The resulting kriged maps have smooth contours and gradual transitions. However, the conditional simulations incorporate a level of heterogeneity known to exist.[38] These maps do not have smooth contours and the transitions may be more abrupt. Conditional realizations are generated by using the kriged map as the base map and using variogram information to infer the possible range of values at interwell locations. For thickness, the kriged map is compared with a conditional realization in Fig. 8. A similar comparison of the maps for permeability is shown in Fig. 9. The permeability maps are derived from their respective thickness maps. The kriged maps are smooth, whereas the conditional realizations have a more ragged appearance. Ten conditional realizations were generated to approximate the total range of geologic possibilities.

V. RESERVOIR FLOW SIMULATION

The recovery variations among different realizations and effect of infill drilling were studied using the flow simulator. For infill drilling, the well configurations and number of patterns need to be considered in addition to reservoir heterogeneities. Four producers at the corners of a pattern flood are equivalent to one producing well in a homogeneous

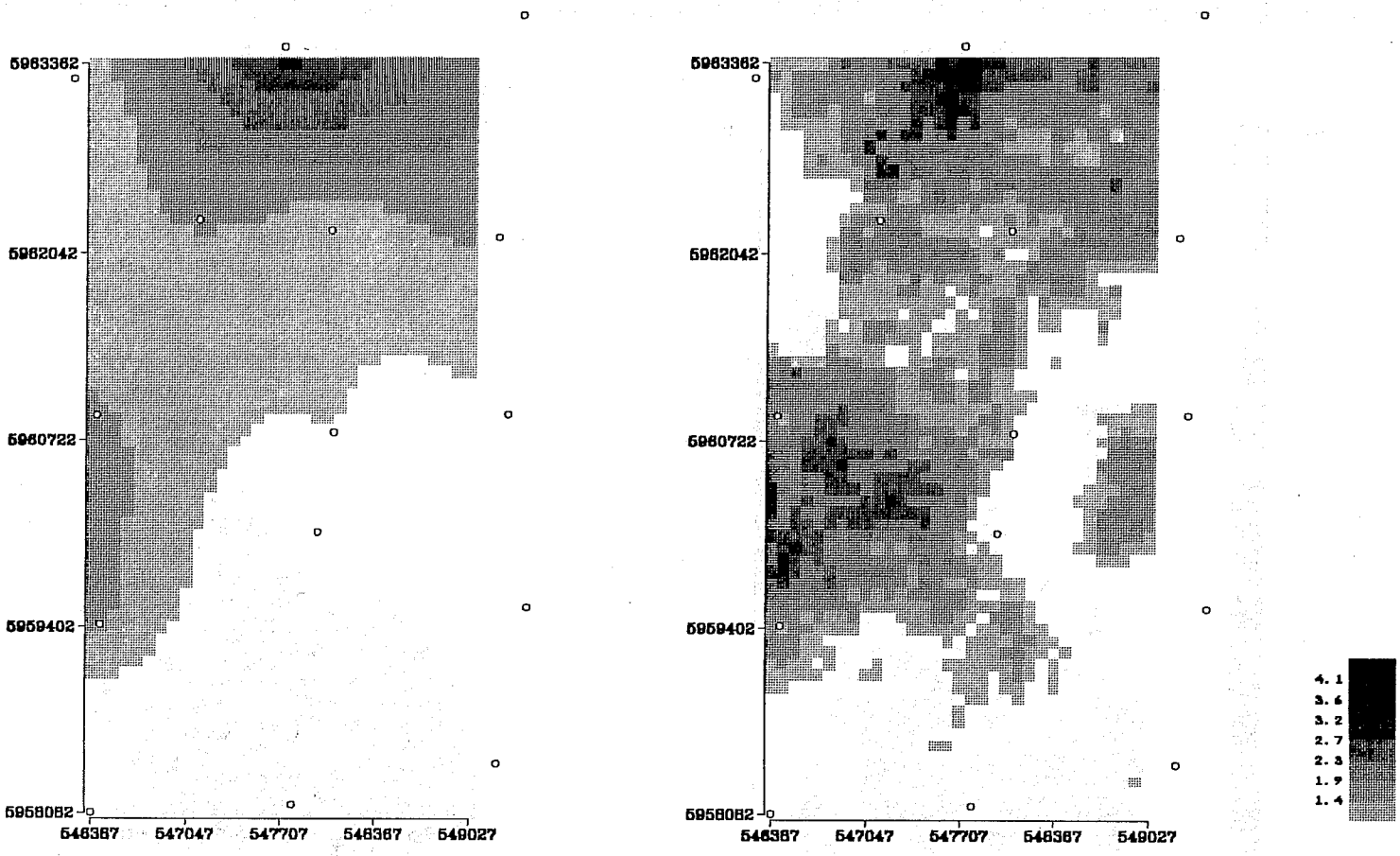

Fig. 8. Example kriged and conditionally simulated maps of Subunit B4 (Copyright 1991 SPE, SPE 22164, International Arctic Technology Conference, May 29-31, 1991 in Anchorage AK).

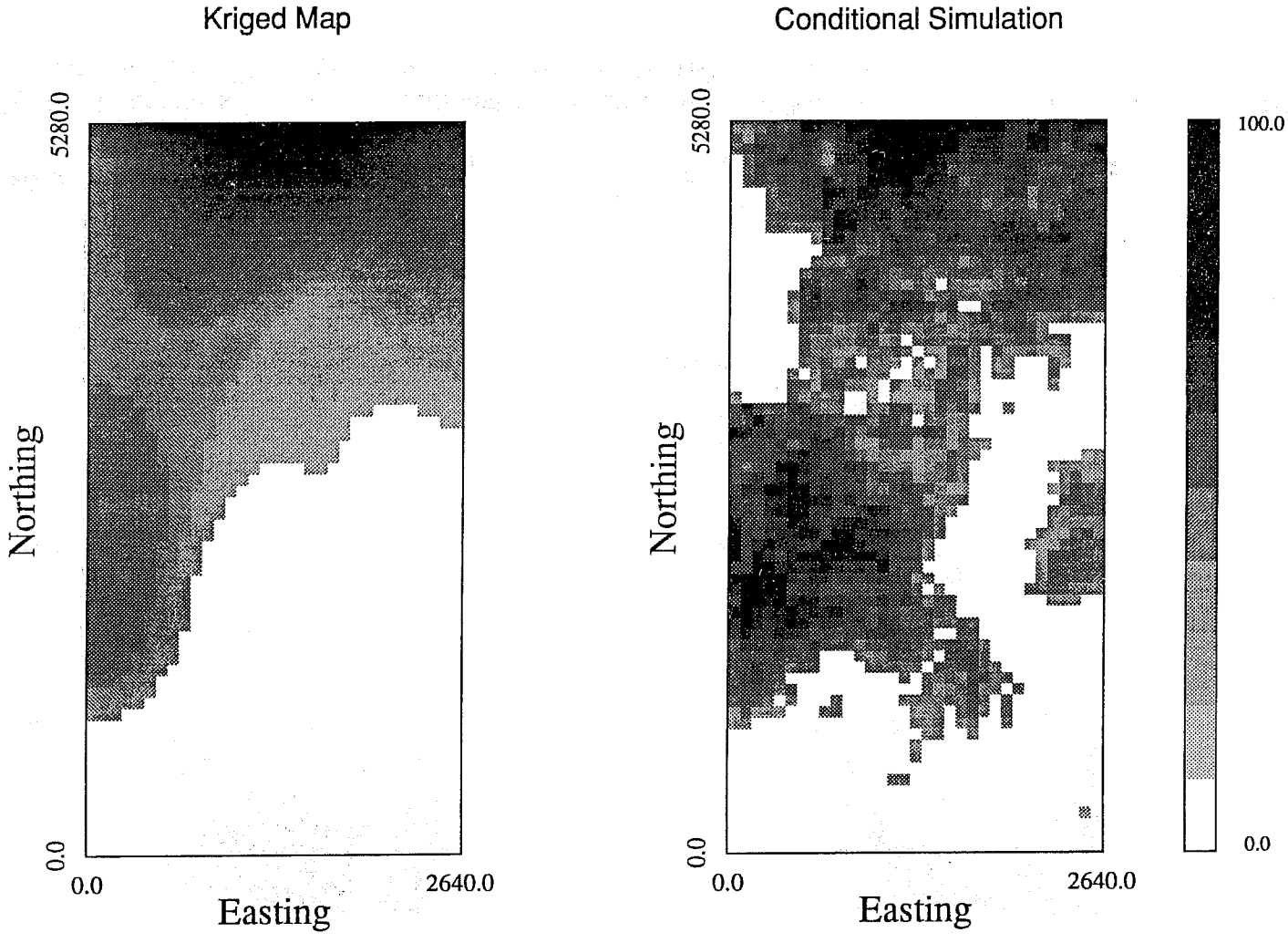

Fig. 9. Example permeability maps for the kriged and conditionally simulated maps for Subunit B4 (Copyright 1991 SPE, SPE 22164, International Arctic Technology Conference, May 29-31, 1991 in Anchorage AK).

reservoir description. Studying one specific configuration would not provide a realistic measure of the benefit of infill drilling for heterogeneous geology. Scaling up the performance of one or a few patterns with pre-defined configurations may not represent full field performance. One good alternative may be to use descriptions from unconditional simulations to evaluate the effect of infill drilling. When the reservoir description is conditioned to well data, we can study different well configurations and choose the best one for additional recovery from infill drilling on the specific drillsite.

The configurations shown in Fig. 10, for 160, 80 and 40-acre spacings, were found to be the best for additional recovery from infill drilling of DS-1E. On the 160-acre spacing, there are three water injectors and three oil producers. On the 80-acre, all 160-acre injectors were converted to producers and two injectors added. The 160 and 80 acre wells are converted to injectors for the 40-acre case, and seven producers added. The ten conditional realizations and one kriged map were incorporated in a black oil reservoir simulator for each of the configurations.

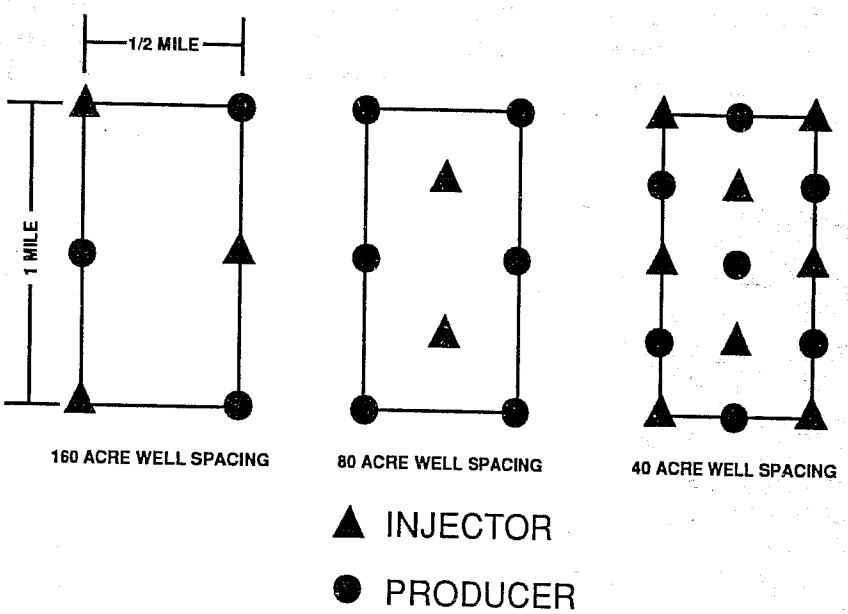

Fig. 10. Location of the simulation wells for 160, 80 and 40 acre spacing (Copyright 1991 SPE, SPE 22164, International Arctic Technology Conference, May 29-31, 1991 in Anchorage AK).

Each layer in the reservoir flow simulator represents a geological subunit. The 1 X 0.5 square mile area of each layer is divided into 2145 grid blocks of 82.5 X 82.5 square feet (Fig. 11). There are 33 grid blocks

in the easting direction and 65 grid blocks in the northing direction. The total number of grid blocks for eight layers is 17,160. Because of the continuous shales between the subunits, the vertical transmissibilities are set to zero. Hence, comparisons of the areal sweep efficiencies of individual subunits are easily conducted.

The fluid property data are based on fluid samples from the A-sand in DS-1E. The gravity of the fluid is 21.8° API. The initial reservoir pressure and the bubble point pressure are 3150 and 2535 psia, respectively. The relative permeability data are also for the A-sand. The average connate water saturation is 18% and the average residual oil saturation to water is 16.9%. The average porosity is 22% and the absolute permeability to air varies between 20 md and 300 md.

The shut-in logic in the simulator was such that when a well's producing WOR reached 19, the well was shut-in. Once all the producing wells were shut-in, the simulation was complete. A prudent field practice is to cement squeeze the high WOR layers. However, this was considered impractical for closely spaced thin subunits within the A4 sand body. Therefore, subunits were not shut-in selectively in the simulator.

Production and injection for the 160, 80 and 40-acre cases for 11 descriptions were examined by layer and well. The individual layer production was examined because thicker continuous layers masked the recovery efficiency from the thinner less continuous layers.

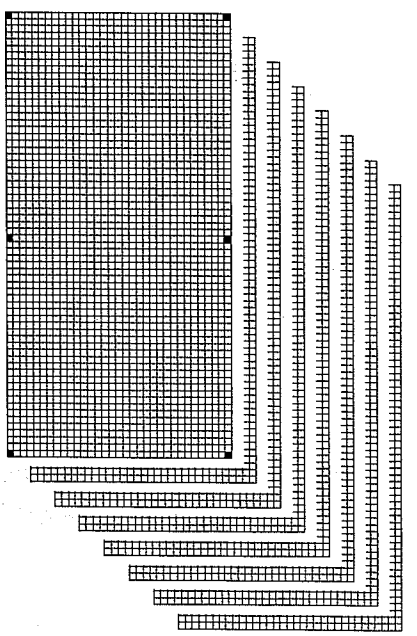

Fig. 11. High resolution description of the eight subunits in DS-1E. 33 X 65 grid blocks per layer and 8 layers, 17,160 grid blocks total.

VI. RESULTS

A. Recovery Variation

The normalized recovery efficiency is plotted versus pore volume injected for the 11 realizations for each well spacing. The normalized recovery efficiency is the recovery from a particular realization divided by the recovery obtained from the kriged reservoir description for the 160 acre spacing. For the Kuparuk DS-1E, there are significant recovery differences between kriged and conditionally simulated descriptions (Figs. 12 through 14). As seen, the kriged recoveries are always higher than the conditional recoveries through all ranges of pore volumes injected. This is true for 160, 80 and 40-acre well spacings. The conditional recoveries are lower because conditional simulations generate a more heterogeneous picture of the reservoir. Also, conditional simulations provide a technique to assess uncertainty in the performance predictions based on limited available data.

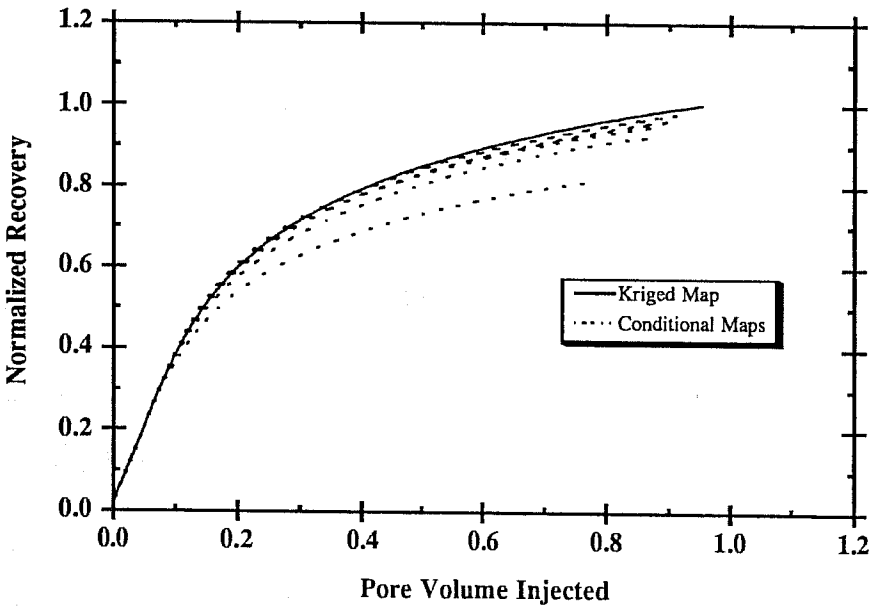

Figure 12 - Normalized recovery response for eleven realizations on 160 acre spacing.

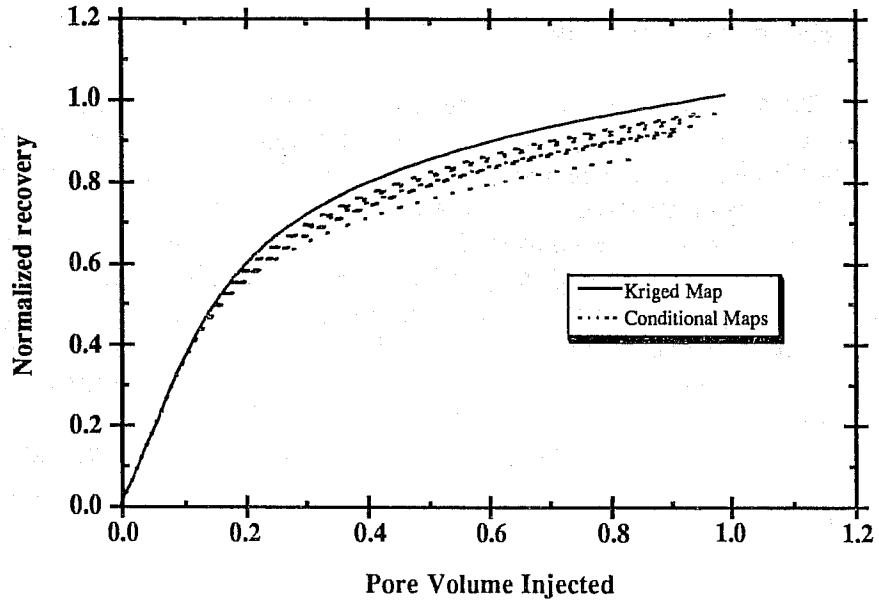

Figure 13 - Normalized recovery response for eleven realizations on 80 acre spacing.

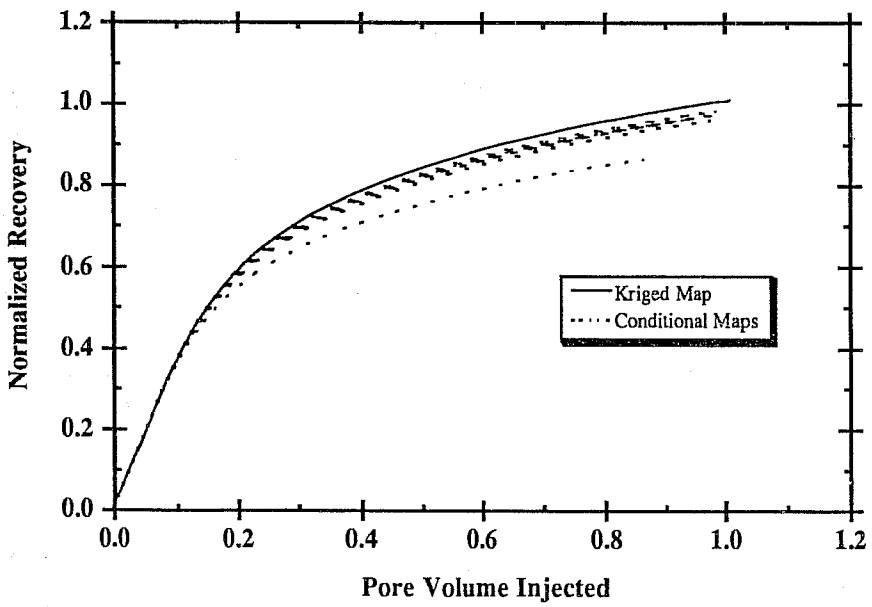

Figure 14 - Normalized recovery response for eleven realizations on 40 acre spacing.

The previous discussion is on recovery predictions for all eight layers. The normalized recovery efficiency for each layer was examined to understand the effect of conditional simulation on characterization and response of individual layers. Examples of the thickness maps for the thin (subunit B4) and thick (subunit C1) subunits are in Figs. 8 and 15. The thin subunit has more discontinuities and the thick subunit is more homogeneous.

The results show the conditional simulation has a bigger effect on recovery of thinner subunits. For example, in Fig. 16, subunit B4 has a recovery efficiency for the kriged map much larger than the conditional realization recoveries. Similarly, the other thin subunits (A, B1, B2, and B3) have recovery efficiencies more affected by the discontinuities incorporated in the mapping. The inclusion of the heterogeneities in the thin sands results in a lower predicted recovery efficiency. The conditional realizations incorporate believed heterogeneities which are smoothed by a kriged map. The normalized recovery efficiency, hence the sweep efficiency, depends on heterogeneity and mobility ratio. The recovery efficiency in the thinner subunits would be affected even more for adverse mobility ratio displacements.

The recovery efficiency predictions for the thicker subunits C1, C2, and C3, are not affected significantly by the description method. For the thick C1 subunit, the kriged recovery is approximately the average of the conditional realization recovery predictions (Fig. 17). This implies that conditional simulation for the thicker subunits does not introduce discontinuities impacting recovery adversely. The fluctuations around the kriged recovery curve reflect the uncertainty in the reservoir description based on available data.

Based on these results, a correlation is suggested between recovery efficiency and subunit thickness. The average of recovery of all realizations for each subunit was plotted against the corresponding average thickness for the 160 acre well spacing (Fig. 18). The figure shows a strong correlation between the two variables. Moreover, the recovery efficiency begins to reduce significantly for layers with average thickness less than 4 feet. The thickest subunit, C3, consistently has the highest recovery efficiency. As thinning progresses, so does the reduction in recovery efficiency. For subunit thickness less than 4 feet, the trend is very abrupt. The correlation between recovery efficiency and thickness (not shown in this paper) also occurs in the 80 and 40-acre well spacings. The results show the reduction in the overall recoveries, when conditionally simulated maps are used, is caused by low recovery efficiency in the thinner subunits.

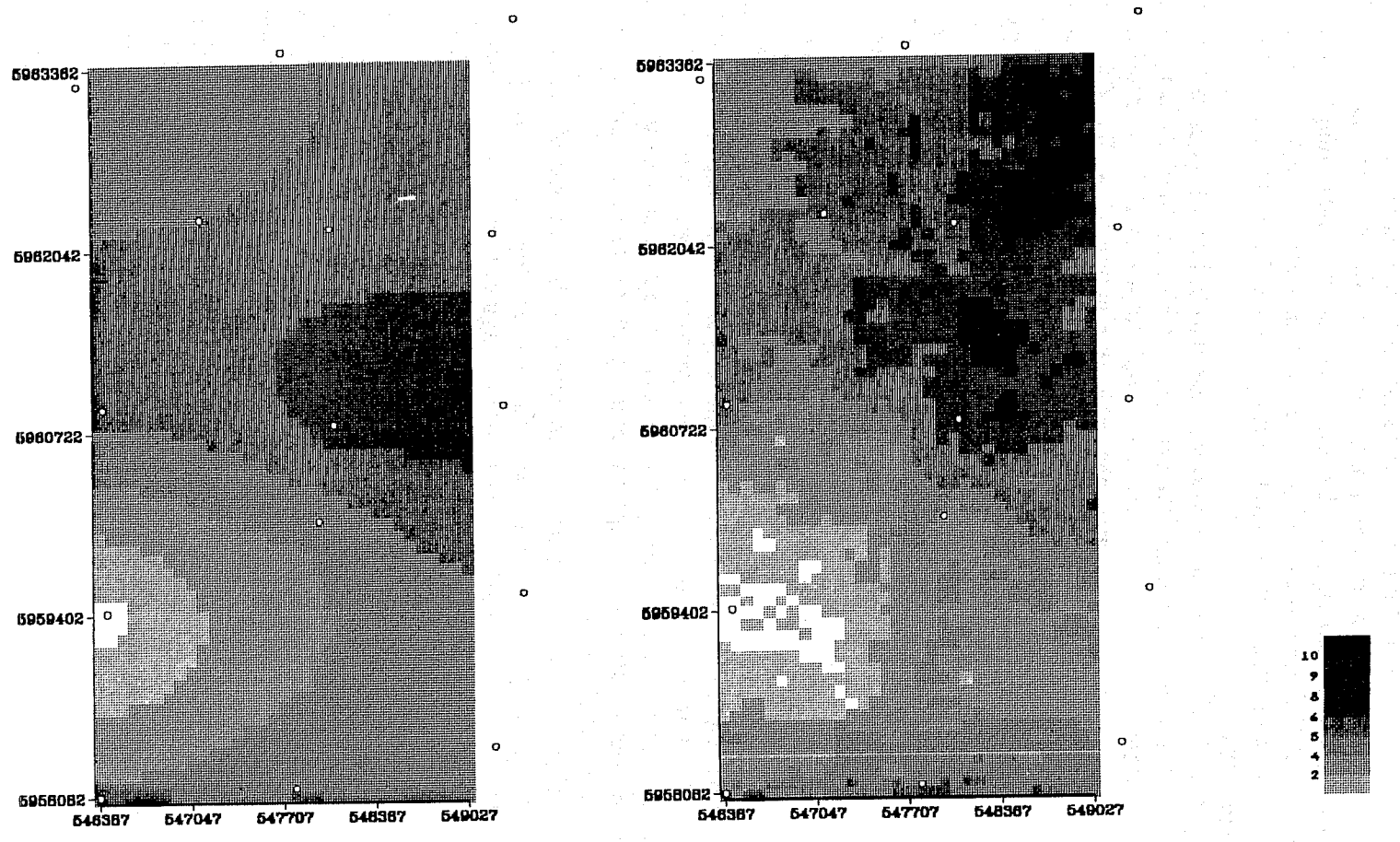

Fig. 15. Kriged and conditionally simulated map of Subunit C1 (Copyright 1991 SPE, SPE 22164, International Arctic Technology Conference, May 29-31, 1991 in Anchorage AK).

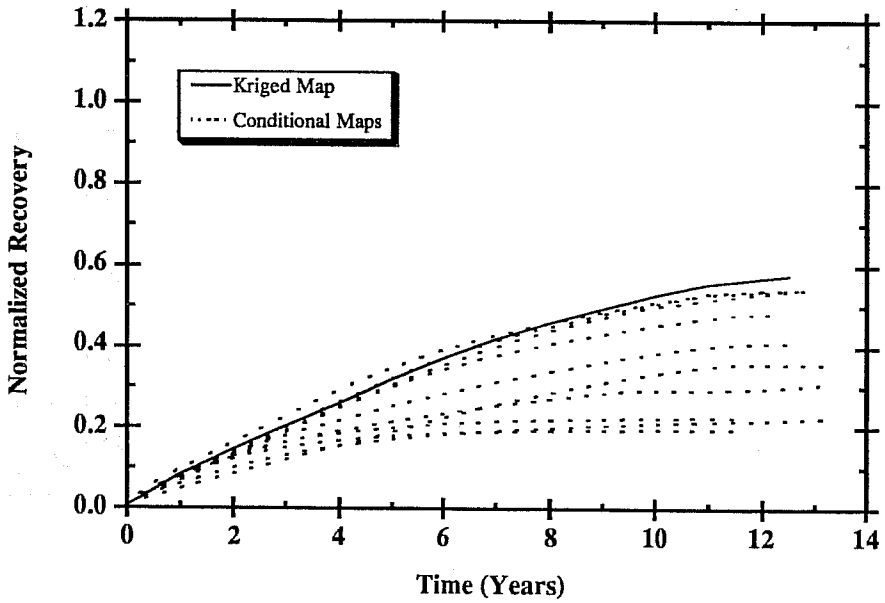

Figure 16 - Normalized recovery response of eleven realizations on 160 acre spacing for Subunit B4.

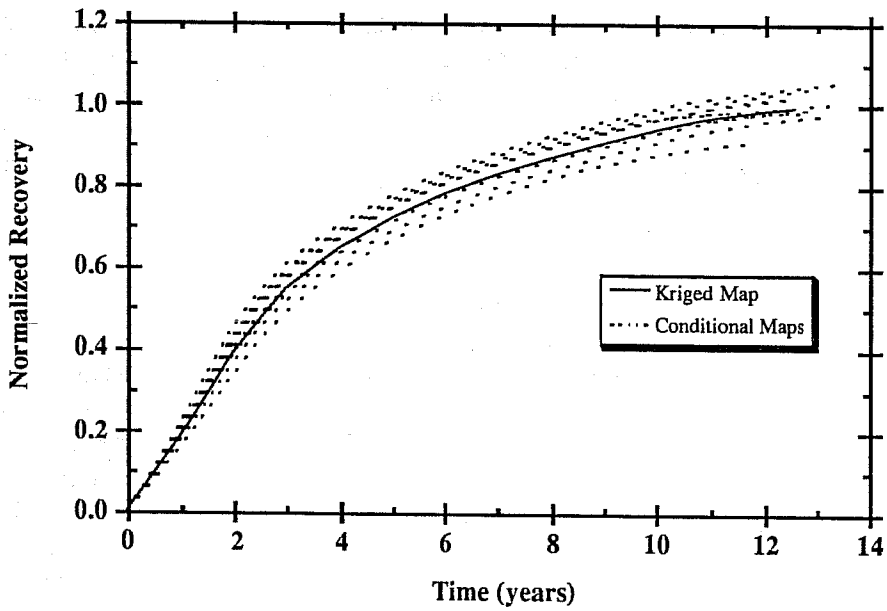

Figure 17 - Normalized recovery response of eleven realizations on 160 acre spacing, Subunit C1.

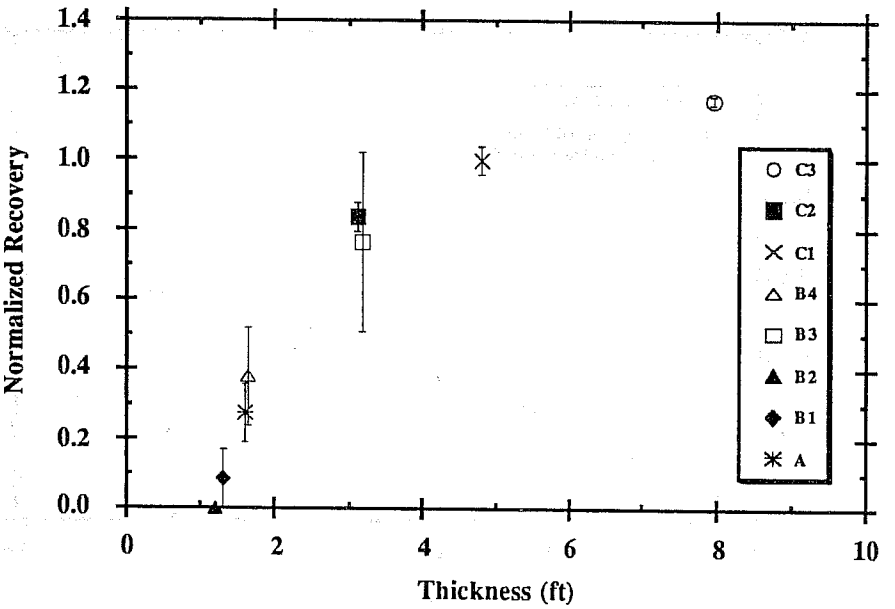

Figure 18 - Average normalized recovery with error bars from 160-acre flow simulated realizations.

Average layer thickness alone, however, is not a complete estimator of recovery efficiency. Other factors, variance and correlation structure, influence recovery. For instance, in Fig. 18, the C2 and B3 subunits have close to the same average thickness, but the recovery efficiencies for the B3 subunit are lower and distributed more widely than the C2 subunit. This is because the B3 subunit, where it exists, can be very thick but then thins out quickly. The C2 subunit is areally continuous, and does not vary greatly in thickness.

B. Additional Recovery from Infill Drilling

The recoveries from flow simulations of 40 acre well spacing were subtracted from 160-acre well spacing for each of the subunits to evaluate the additional recovery from infill drilling. Fig. 19 shows the additional recovery versus average subunit thickness and an approximate curve drawn through the results. The additional recovery from infill drilling increases as the average thickness decreases.

The additional recovery from infill drilling was also calculated for 160-acre to 80-acre case. Though not shown in this paper, the same basic trends are observed. However, the magnitude of additional recovery for subunits less than three feet is not as large as observed for

160-acre to 40-acre case. This is because the discontinuities in the thin subunits limit recovery at larger well spacing. Such trends were less pronounced and not easily discernible using kriged maps. As shown in Fig. 20, the kriged map estimates are more widely scattered and attempting to fit a correlation through the data without conditional map results (Fig. 19) would be difficult.

The average of the normalized recoveries from the 10 conditional realizations for each of the infill cases is in Fig. 21. There is a correlation between higher recovery efficiencies and closer well spacing. The average 80-acre well spacing recovery efficiency is higher than the 160-acre recovery efficiency and the 40-acre recovery efficiency is higher than the 80-acre recovery efficiency.

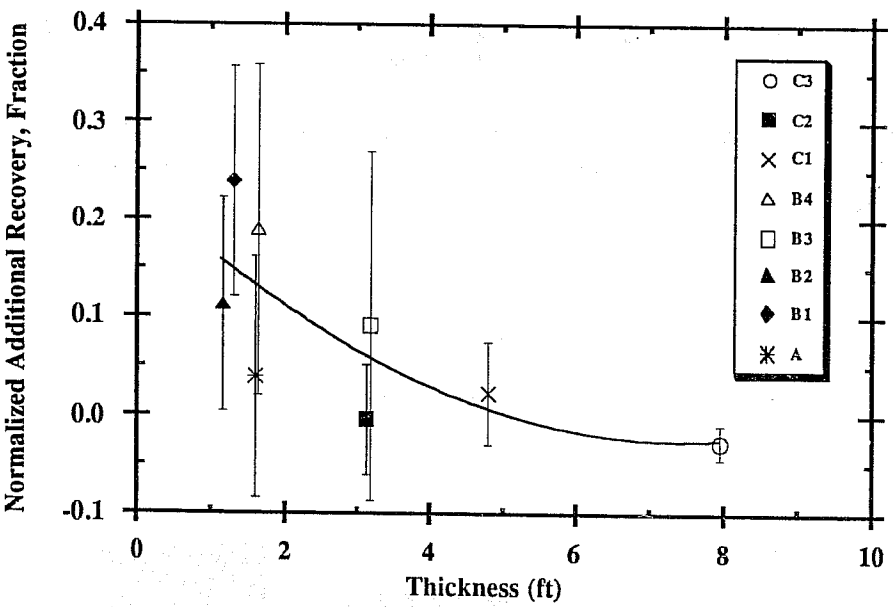

Figure 19 - Normalized conditional average additional recovery (fraction of 160 acre kriged map recovery) with error bars of 160 to 40 acre spacing.

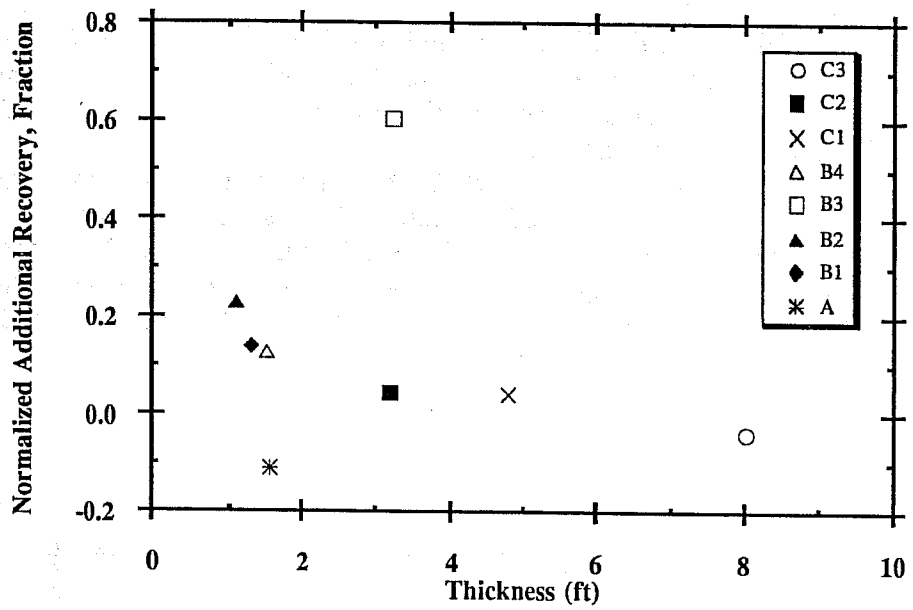

Figure 20 - Normalized kriged average additional recovery (fraction of 160 acre kriged map recovery) of 160 to 40 acre spacing.

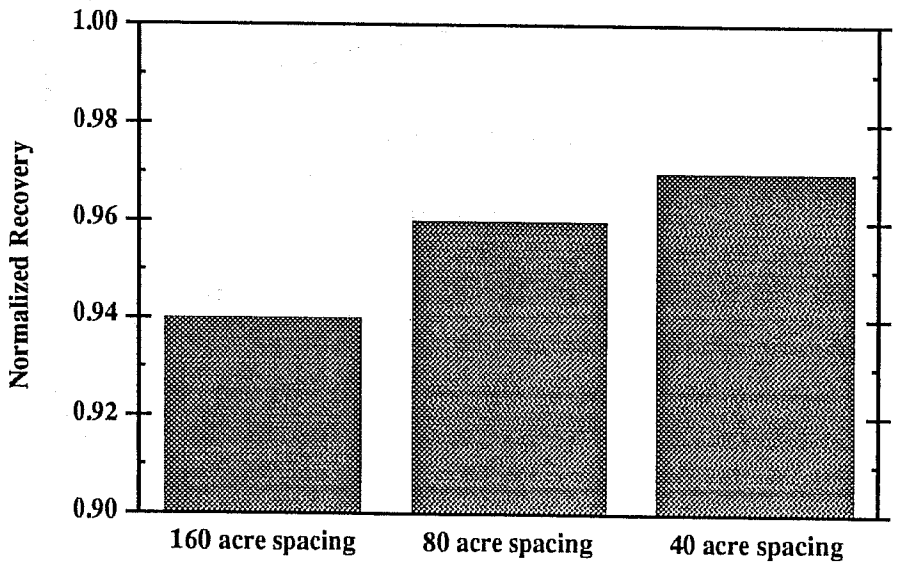

Figure 21 - Average recovery from Conditional Realizations.

VII. CONCLUSIONS

1) Recovery efficiencies from conditional simulation realizations are lower than smooth kriged map recovery efficiencies.

2) A correlation between recovery efficiency and thickness is observed. Thin beds (less than 4 ft) have lower recovery efficiency, whereas thick beds (more than 7 ft) have a higher recovery efficiency.

3) Reservoir performance predictions of the conditional simulation realizations for different well spacings show additional recovery benefits from infill drilling. Smaller well spacing gives higher recovery efficiency, agreeing with field experience. Other sand bodies and other areas of the field having thinner subunits will have even higher additional recovery from infill drilling.

4) The additional recovery predictions from infill drilling from 160-acre to 40-acre spacing is significantly higher for subunits less than five feet thick. The same trend is observed in the 160-acre to 80-acre case, except the additional recovery for subunits less than three feet is not as large. This is caused by the scale of heterogeneity generated by conditional simulations.

5) Geostatistics provides an effective framework to quantify the uncertainty in reservoir performance and allows us to develop an understanding of the additional recovery from infill drilling from different subunits.

VIII. FUTURE RESEARCH

The recovery variations and additional recoveries, predicted for the DS-1E area, are based on thickness and permeability variations. Additional recovery from infill drilling can be substantially higher in other parts of the field with higher proportions of thin discontinuous beds. Other correlations (e.g., permeability-porosity) may introduce different nature of heterogeneity. Other forms of heterogeneities, such as faulting, can also increase additional recovery estimates.

Turning bands conditional simulation was considered adequate within the scope of the present investigation because it provides insight regarding the effect of heterogeneity vis-a-vis smooth maps. From geologic experience, these predictions show a level of heterogeneity believed to be more realistic than the kriged maps. Future work will also address the modern techniques of indicator simulation[13], simulated annealing.[19,20] and scaleup techniques.[51]

IX. NOMENCLATURE

a	= range (ft)
C	= sill or variance
g(h)	= variance as a function of h
h	= distance between points (lag)
N(h)	= pairs of Z values separated by h
$Z(x_i)$	= Z value at point x_i
$Z(x_i+h)$	= Z value at distance h from point x_i

X. ACKNOWLEDGEMENTS

We thank ARCO and the Kuparuk Unit Co-owners for permission to publish this paper. Technical reviews from John Bolling, Jim Lorsong and Wesley Monroe were helpful and appreciated. We especially thank Mark Scheihing for providing his geologic interpretations. Thanks to Dave Bell, Windsong Fong and Gary Woodling for their help. Thanks are also due to SPE for granting use of the text and figures contained in SPE paper 22164, presented at the International Arctic Technology Conference, May 29-31, 1991 in Anchorage AK.[39]

XI. REFERENCES

1. Barber, A.H., George, C.J., Stiles, L.H., and Thompson, B.B.:"Infill Drilling To Increase Reserves-Actual Experience in Nine Fields in Texas, Oklahoma, and Illinois," JPT, August, 1983, 1530-38.
2. Newn, K.T.C., Slik, P., and Tan, B.C.: "Infill Development in an Old Field," OSEA 88188, February 1988.
3. Gould, T.L., and Sarem, A.M.S.: "Infill Drilling for Incremental Recovery," JPT,March, 1989, 229-37.
4. Matheron, G.:"The Theory of Regionalized Variables and its Applications", Paris School of Mines, Cah. Cent. Morphologie Math., 5 Fontainebleau.
5. Ripley, B. D.: *Spatial Statistics,* John Wiley & Sons, New York City (1981).
6. Matheron, G.: "The Intrinsic Random Functions and Their Applications," *Advances in Applied Probability* (1973) **5**, 439-68.
7. Journel, A. G. and Huijbregts, C. J.: *Mining Geostatistics,* Academic Press (1978).
8. Isaaks, E. H. and Srivastava, R. M.: *Applied Geostatistics,* Oxford university Press, New York (1989).
9. Krige, D.G.: "A Statistical Analysis of Some of the Borehole Values in the Orange Free State Goldfield", J. Chem. Metall Min. Soc., South Africa, J3, 47-70.

10. Lorenz, E.N.:"Nonlinear Statistical Weather Predictions", paper presented at the 1980 World Meteorological Organization Symposium on Probabilistic and Statistical Methods in Weather Forecasting, Nice, France, Sept. 8 - 12.
11. Tsonis, A.A.: "Chaos and Unpredictability of Weather", Weather (June, 1989) 449 No. 6, 258-63.
12. Tennekes, H.: "Outlook: Scattered Showers", Bull., American Meteorological Soc. (April, 1988) 6g, No. 4, 368-72.
13. Journel, A. G. and Alabert, F. G.: "New Method for Reservoir Mapping," *JPT* (Feb. 1990) 212-18.
14. Journel, A. G. and Gomez-Hernandez, J. J.: "Stochastic Imaging of the Wilmington Clastic Sequence," paper SPE 19857 presented at the 1989 SPE Annual Technical Conference and Exhibition, San Antonio, Oct. 8-11.
15. Da Costa e Silva, A. J.: "A New Approach to the Characterization of Reservoir Heterogeneity Based on the Geomathematical Model and Kriging Technique," paper SPE 14275 presented at the 1985 SPE Annual Technical Conference and Exhibition, Las Vegas, Sept. 22-25.
16. Dubrule, O. and Haldorsen, H. H.: "Geostatistics for Permeability Estimation," *Reservoir Characterization*, L. W. Lake and H. B. Carrol Jr. (eds.), Academic Press Inc., Orlando, FL (1986) 223-48.
17. Delfiner, P., Delhomme, J. P., and Pelissier-Combescure, J.: "Application of Geostatistical Analysis to the Evaluation of Petroleum Reservoirs with Well Logs," paper presented at the 1983 SPWLA Annual Logging Symposium, Calgary, July 27-30.
18. Dubrule, O.: "A Review of Stochastic Models for Petroleum Reservoirs," paper presented at the 1988 British Soc. Reservoir Geologists Meeting on Quantification of Sediment Body Geometries and Their Internal Heterogeneities, London, March 1-2.
19. Farmer, C. L.: "The Mathematical Generation of Reservoir Geology," paper presented at the 1989
IMA European Conference on the Mathematics of Oil Recovery, Cambridge, July 25-27.
20. Farmer, C. L.: "The Generation of Stochastic Fields of Reservoir Parameters with Specified Geostatistical Distributions," *Mathematics in Oil Production,* S. Edwards and P. King (eds.), Oxford Science Publications, Clarendon Press, Oxford (1988) 235-52.
21. Hewett, T. A.: "Fractal Distributions of Reservoir Heterogeneity and Their Influence on Fluid Transport," paper SPE 15386 presented at the 1986 SPE Annual Technical Conference and Exhibition, New Orleans, Oct. 5-8.

22. Matthews, J. L., Emanuel, A. S., and Edwards, K. A.: "Fractal Methods Improve Mitsue Miscible Predictions," *JPT* (Nov. 1989) 1126-42.
23. Goggin, D. J. *et al.*: "Permeability Transects in Eolian Sands and Their Use in Generating Random Permeability Fields," paper SPE 19586 presented at the 1989 SPE Annual Technical Conference and Exhibition, San Antonio, Oct. 8-11.
24. Chopra, A. K., Stein, M. H., and Ader, J. C.: "Development of Reservoir Descriptions to Aid in Design of EOR Projects," SPERE (May 1989) 143-150.
25. Chopra, A. K., Stein, M. H., and Dismuke, C. T.: "Prediction of Performance of Miscible Gas Pilots," paper SPE 18078 presented at the 1988 SPE Annual Technical Conference and Exhibition, Houston, Oct.2-5.
26. Chopra, A. K.: "Reservoir Descriptions Via Pulse Testing: A Technology Evaluation," paper SPE 17568 presented at the 1988 SPE International Meeting on Petroleum Engineering, Tianjin, China,Nov.1-4.
27. Weber, K. J. and van Geuns, L. C.: "Framework for Constructing Clastic Reservoir Simulation Models," Paper SPE 19582 presented at the 1989 SPE Annual Technical Conference and Exhibition, San Antonio, Oct. 8-11.
28. Allen, J. R. L.: "Studies in Fluviatile Sedimentation: An Exploratory Quantitative Model for the Architecture of Avulsion-Controlled Alluvial Suites," *Sedimentary Geology* (1978) **21**, 129-47.
29. Knutson, C. F.: "Modeling of Noncontinuous Fort Union Mesaverde Sandstone Reservoirs, Piceance Basin, Northwestern Colorado," *SPEJ* (Aug. 1976) 175-88.
30. Bridge, J. S. and Leeder, M. R.: "A Simulation Model of Alluvial Stratigraphy," *Sedimentology* (1979) **26**, 617-44.
31. Augedal, H. O., Stanley, K. O., and Omre, H.: "SISABOSA, a Program for Stochastic Modelling and Evaluation of Reservoir Geology," Report SAND 18/86 presented at the 1986 Conference on Reservoir Description and Simulation with Emphasis on EOR, Oslo, Sept. 5-7.
32. Gundesf, R. and Egeland, O.: "SESIMIRA–A New Geological Tool for 3-D Modeling of Heterogeneous Reservoirs," paper presented at the 1989 Intl. Conference on North Sea Oil and Gas Reservoirs, Trondheim, May 8-11.
33. Wadsley, A. W., Erlandsen, S., and Geomans, H. W.: "HEX, A Tool for Integrated Fluvial Architecture Modeling and Numerical Simulation of Recovery Processes," paper presented at the 1989 Intl. Conference on North Sea Oil and Gas Reservoirs, Trondheim, May 8-11.

34. King, P. R.: "The Connectivity and Conductivity of Overlapping Sandbodies," paper presented at the 1989 Intl. Conference on North Sea Oil and Gas Reservoirs, Trondheim, May 8-1.
35. Chopra, A. K.,Severson, C. D. and Carhart, S. R., "Evaluation of Geostatistical Techniques for Reservoir Characterization," SPE paper 20734 presented at the 65th Annual Technical Conference held in New Orleans, LA., September 23-26, 1990.
36. Scheihing, M.H.: "Reservoir Anatomy of the Kuparuk A4-Sandstone Body, Kuparuk Field, North Slope of Alaska," Internal ARCO Report, AOGC, 1988.
37. Masterson, W. D. and Paris, C. E.: "Depositional History and Reservoir Description of the Kuparuk River Formation, North Slope, Alaska," Alaskan North Slope Geology, Pacific Section SEPM, Guidebook 50, Tailleur, I. and Weimer, P. Eds., 1987.
38. Gaynor, Gerard C., and Scheihing, Mark H.:"Shelf Depositional Environments and Reservoir Characteristics of the Kuparuk River Formation (Lower Cretaceous), Kuparuk Field, North Slope, Alaska," Giant Oil and Gas Fields: A Core Work Shop, Lamando, A. J. and Harris, P. M., eds., SEPM Core Work Shop #12 V. 1, March, 1988, pp. 333-389.
39. Wolcott, D.S. and Chopra, A. K.; "Incorporating Reservoir Heterogeneity Using Geostatistics to Investigate Waterflood Recoveries for Drillsite 1E, A4 Sandstone Body, Kuparuk River Field, Alaska," paper SPE 22164 presented at the International Arctic Technology Conference held in Anchorage, Alaska, May 29-31, 1991.
40. Jacobsen, T. and Rendall H.: "Permeability Patterns In Some Fluvial Sandstones. An Outcrop Study From Yorkshire, North East England." Continental Shelf and Petroleum Technology research Institute A/S, IKU (1989), No. 89.055.
41. Clark, Isobel: *Practical Geostatistics*, Elsevier Publishers, Essex,(1984).
42. Atkinson, C.D., B.G. Goesten, A. Speksnijder, and W. van der Vlugt: "Storm-generated sandstone in the Miocene Miri Formation, Seria Field, Brunei (N.W. Borneo)," R. J. Knight and J. R. McLean, (eds.), Shelf Sands and Sandstones: Can. Soc. Petrol. Geol. Memoir 11 (1986), 213-240.
43. Kittridge, M. G. *et al*: "Outcrop/Subsurface Comparisons of Heterogeneity in the San Andres Formation," paper SPE 19596 presented at the 1989 SPE Annual Technical Conference and Exhibition, San Antonio, Oct. 8-11.
44. Guerrillot, D. *et al.*: "An Integrated Model for Computer Aided Reservoir Description: From Outcrop Study to Fluid Flow Simulations," paper presented at the 1989 European Symposium on Improved Oil Recovery, Budapest, April 25-27.

45. Robertson, J. D.: "Reservoir Management Using 3-D Seismic Data," *The Leading Edge* (Feb. 1989) **8**, No. 2, 25-32.
46. Nolen-Hoeksema, R. C.: "Future Role of Geophysics in Reservoir Engineering," paper presented at the 1988 Joint SEG/EAEG Research Workshop on Reservoir Geophysics, Dallas, July 31-Aug. 3.
47 Doyen, P. M., Guidish, T. M., and de Buyl, M. H.: "Monte Carlo Simulation of Lithology From Seismic Data in a Channel-Sand Reservoir," paper SPE 19588 presented at the 1989 SPE Annual Technical Conference and Exhibition, San Antonio, Oct. 8-11.
48. Martinez, R. D., Cornish, B. E., and Seymour, R. H.: "An Integrated Approach for Reservoir Description Using Seismic, Borehole, and Geologic Data," paper SPE 19581 presented at the 1989 SPE Annual Technical Conference and Exhibition, San Antonio, Oct. 8-11.
49. Alabert, F. G.: "Constraining Description of Randomly Heterogeneous Reservoirs to Pressure Test Data: A Monte Carlo Study," paper SPE 19600 presented at the 1989 SPE Annual Technical Conference and Exhibition, San Antonio, Oct. 8-11.
50. Delhomme, J. P., Chiles, J. P., "Conditional Simulation Package for BLUEPACK Geostatistics System (SIMPAC)," Centre De Geostatistique et de Morphologie Mathematique, Fontainbleu, France, 1976.
51. Gomez-Hernandez and Journel, A. G.: "Stochastic Characterization of Grid-Block Permeabilities: From Point Values to Block Tensors," paper presented at the 1990 2nd European Conference on the mathematics of Oil Recovery, Arles, France, Sept. 11-14.

APPENDIX

The semi-variograms were calculated by:

$$\gamma(h) = \frac{\Sigma[Z(x_i) - Z(x_i + h)]^2}{2 * N(h)} \qquad (1)$$

The spherical models were calculated by:

$$\gamma(h) = C * \left(\frac{3h}{2a} - \frac{h^3}{2a^3}\right), \quad h < a$$
$$= C, \quad h \geq a \qquad (2)$$

A COMPARISON OF OUTCROP AND SUBSURFACE GEOLOGIC CHARACTERISTICS AND FLUID-FLOW PROPERTIES IN THE LOWER CRETACEOUS MUDDY J SANDSTONE

David F. Mayer

Department of Petroleum Engineering
Colorado School of Mines
Golden, Colorado

Mark A. Chapin[1]

Department of Geology and Geological Engineering
Colorado School of Mines
Golden, Colorado

I. INTRODUCTION

Outcrop studies have been made to help define the external geometry of reservoirs, their internal architecture, and the distribution of fluid-flow properties between wells. In these types of studies analogous outcrops in the same formation or in similar depositional environments as producing fields are used.

This paper compares characteristics of the Muddy (J) Sandstone observed in outcrops and in cores from the Peoria Field in Colorado. These comparisons were made to determine if the outcrops were analogous to equivalent strata in the subsurface and if outcrop observations and measurements could assist in the construction of fluid-flow models.

---

[1]Present address: Shell Offshore, Inc., New Orleans, Louisiana.

II. STRATIGRAPHY OF THE J SANDSTONE IN THE DENVER BASIN

This study compares reservoir properties and geologic characteristics of outcrops and subsurface reservoir rocks from the J Sandstone which is the upper most unit of the Dakota Group in the Denver Basin in Colorado. The Lower Cretaceous Dakota Group was deposited over the Jurassic Morrison Formation and consists of both marine and nonmarine rocks (Figure 1).

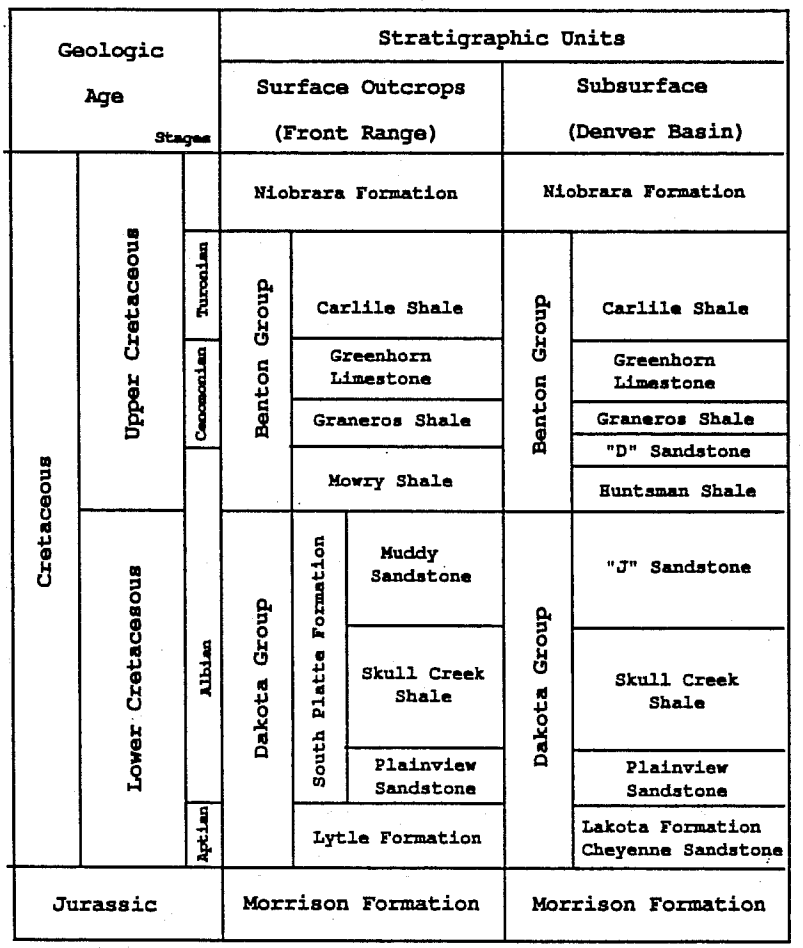

Fig. 1. Surface and subsurface stratigraphic units of the Denver Basin and Front Range outcrops.

A. Fort Collins Member

The Skull Creek Shale of the Dakota Group was deposited in the Cretaceous Western Interior Seaway in the Peoria Field area and on its margins as seen in outcrops near Morrison, Colorado (Figure 2) (1). The Skull Creek Shale contact with the overlying Muddy (J) Sandstone is transitional and indicates a rapid regression of the sea (2). This lower portion of the Muddy (J) Sandstone has been called the Fort Collins Member or the J-3 unit in the Denver Basin (3). The J-3 unit includes the Fort Collins Member and also floodplain and crevasse splay deposits above the regional unconformity but below channel sands (J-2 interval) in the Horsetooth Member discussed below.

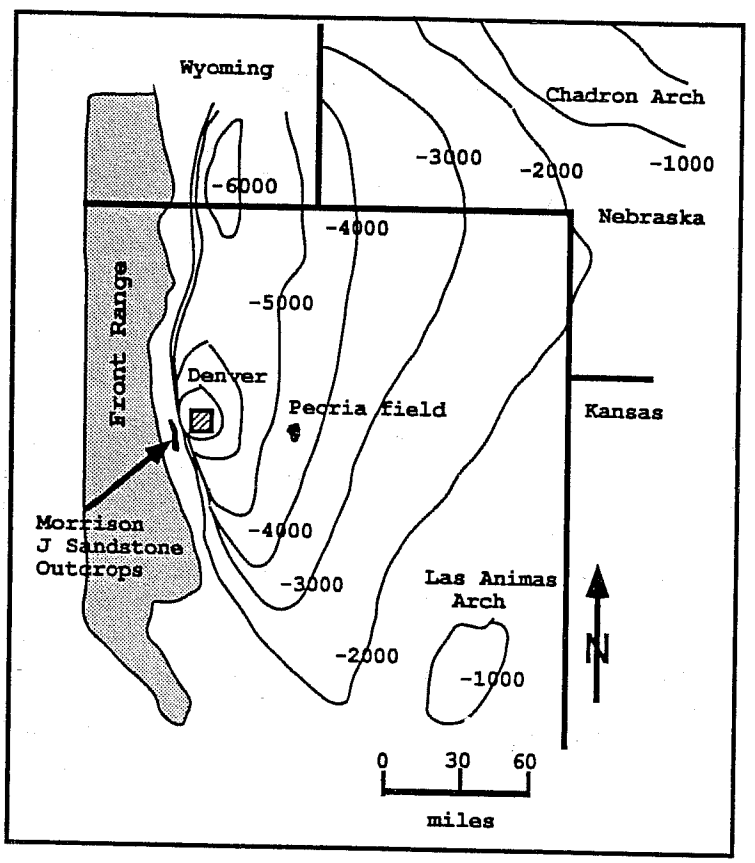

Fig. 2. Structure contours on top of the Precambrian (modified from Matuszczak (4)).

The Fort Collins Member is composed of an upward coarsening, bioturbated sandstone which has been interpreted to be a delta front facies deposited as a result of the regression of the Western Interior Sea (5). These marine sandstone deposits are truncated by a regional unconformity caused by the continued drop in sea level which allowed erosion of marine sediments (3). Basement block movement formed topographic lows that created drainage paths to the regressing sea which incised valleys into the underlying strata (3). The Fort Collins Member was partially removed from higher elevations and in some cases was totally removed from the valleys.

B. Horsetooth Member

The rise in sea level which followed caused backfilling of the incised valleys with floodplain, crevasse splay, distributary channel, fluvial, estuarine, and overbank deposits. These valley-fill deposits have been referred to as the J-2 unit in the Denver Basin (6). Strata deposited above the lowstand unconformity also have been called the Horsetooth Member of the Muddy (J) Sandstone (3).

C. Transgressive Marine Deposits

The continued rise in sea level filled valleys and deposited coastal plain sediments over the entire region. This transgression of the sea caused the shoreline to move over the coastal plain. Shoreface erosion occurred and a transgressive surface of erosion moved across the coastal plain sediments (3). A bioturbated sandstone was deposited above this erosion surface as the sea continued its transgression. This sand, which is at the top of the Muddy (J) Sandstone and the Dakota Group, is referred to as the J-1 unit in the Denver Basin. Figure 3 is a summary of the sequence of sediments which resulted from these events (7).

As the sea level continued to rise marine silt and mud (Mowry Shale and Huntsman Shale of the Benton Group) were deposited over the Muddy (J) Sandstone. Deposition and subsidence caused burial of the Muddy (J) Sandstone to continue through the late Cretaceous and into the Cenozoic when the Laramide Orogeny ended

burial and deformed the Denver Basin to its current condition. The uplift allowed erosion of overlying strata exposing sediments of the Lower Cretaceous along the western edge of the Denver Basin (3).

The Peoria Field produces from fluvial channel and splay sands in the J-2 unit of the Muddy (J) Sandstone in the Denver Basin (7). The J-1, J-2, and J-3 units have not been defined in outcrops. However, the rocks studied in outcrop are channel sands deposited on an erosion surface cut into the Skull Creek Shale (1). The characteristics of these channel sand bodies are compared below.

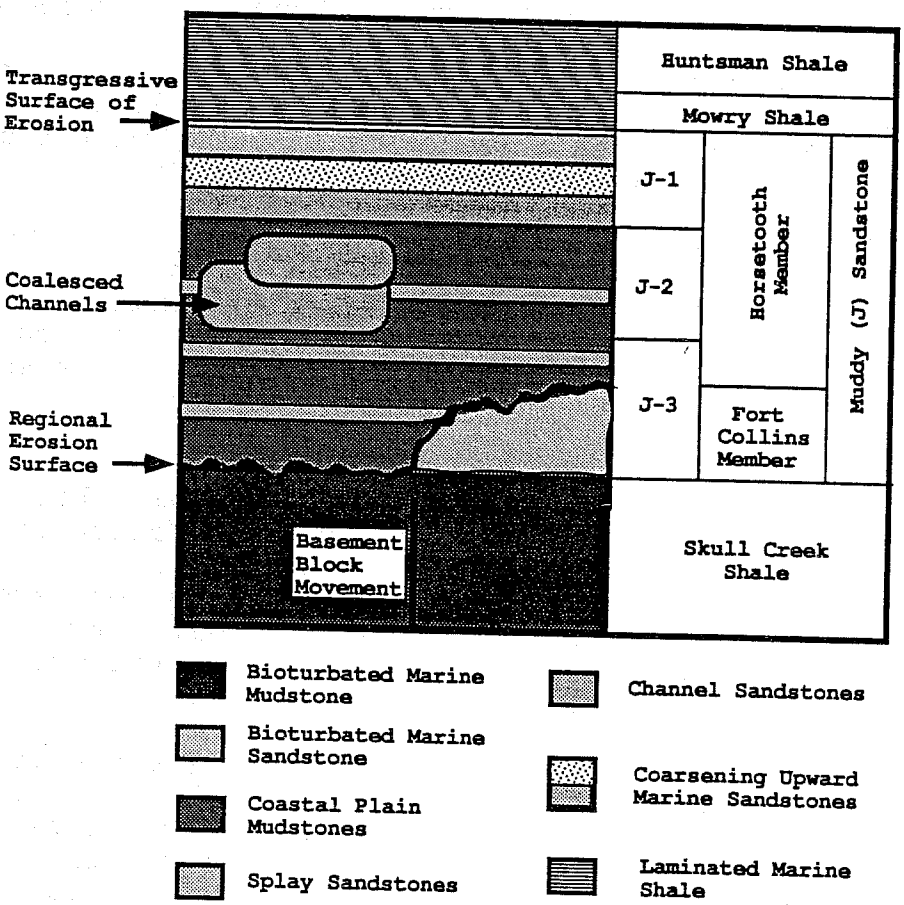

Fig. 3. Muddy (J) Sandstone stratigraphy in the Denver Basin (modified from Chapin (7)).

III. A COMPARISON OF LITHOFACIES IN THE PEORIA FIELD AND IN OUTCROPS

Cores and outcrop sections were described and small-scale lithologic units with associated grain sizes, clay content, and biological and physical sedimentary structures were grouped together into facies. Five facies were distinguished from these descriptions of which two were reservoir facies (7). Similar facies were found in outcrop sections and near-surface cores and in cores from the Peoria Field. These five facies are described below.

1. Crevasse splay and splay channels composed of coarsening-up units of planar and rippled laminae, with thin, trough cross-stratified beds at the top. This unit is productive in several wells in the Peoria Field but has not contributed a significant amount of production.
2. Fine-grained vertical accretion deposits made up of parallel-laminated and convolute-laminated overbank mudstones from marshes, lakes, and brackish bays were found in the Peoria Field area. Outcrop overbank facies are composed of tidal-flat sandstones and mudstones.

Three facies were used to describe point bar deposits in the Peoria Field. This same succession of facies was observed in channels found in outcrops. These point bar and channel facies have been designated Facies I, II, and III with the numbers indicating their succession from the base to the top of a channel.

3. Facies I consists of trough cross-stratified and massive sandstone and a minor amount of planar-laminated sandstone. Trough cross-stratified structures usually range from .5 to 1.5 feet in thickness in Peoria Field cores. Facies I represents the basal channel fill of a point bar. Deposits above basal scours commonly consist of mudclast-rich sandstones made up of clay rip-up clasts or mudstone break-up structures. Lateral accretion surfaces with mudstone drapes

trough cross-stratified sandstone units have been observed in several wells. Facies I in outcrop is comprised mainly of cross-stratified structures, both trough and planar-tabular sets. Large sand bars also can be found in outcrops and are included with cross-stratified structures in the comparisons which follow. This facies contains the best reservoir rock and the largest grain sizes.

4. Ripple-laminated sandstone is the predominant stratification type found in Facies II in the Peoria Field. Mudstone draped ripple laminations as well as thin, trough cross-stratified and massive beds also can be found in this facies. Facies II typically consists of lower energy sediments deposited over Facies I. These are deposits of the middle to upper point bar, but Facies II also can occur as the lowest facies in a channel above the scour surface in partial abandonment fills. In outcrop Facies II contains more trough cross-stratified sandstone than in the Peoria field. Facies II also is considered to contain reservoir sands but these are of poorer quality than those of Facies I.
5. Facies III consists mainly of ripple-laminated sandstone which is finer grained than that found in Facies II and contains a much greater quantity of mud drapes. Wavy or flaser bedding and convolute bedding also can be found. This facies can be present either as a thin interval at the top of point bar deposits or as a thick, abandoned channel fill (7).

Over 200 sieve analyses were performed on outcrop and Peoria Field samples. Most of the samples ranged from fine-grained to very-fine-grained sand. Several samples from Facies I were lower-medium grained and vertical accretion deposits were made up of silt-sized grains.

The average of the mean grain diameters of Facies I samples from the Peoria Field was found to be 2.63 phi units and the average Trask sorting coefficient was 1.14 (lower-fine grained, very-well-sorted sand). The average Facies II sample was well-sorted, upper-very-fine-grained sand with an average Trask sorting coefficient of 1.24 and a mean grain diameter of 3.10

phi units. Facies III samples were well sorted, lower-very-fine-grained sand.

Peoria Field samples from Facies I were finer grained and better sorted than those from outcrop core plugs. The average Facies I outcrop sample was composed of well-sorted, upper-fine-grained sand with a Trask sorting coefficient of 1.21 and an average grain diameter of 2.40 phi units. Outcrop samples from Facies II were found to have a mean grain diamater of 3.14 phi units and a Trask sorting coefficient of 1.26 making the average sample well-sorted, upper-very-fine-grained sand.

The differences in the mean grain diameters between the facies exhibits an upward-fining pattern. This upward-fining pattern within a channel was found to occur in steps between facies but within facies grain size changes were erratic with intervals of larger or smaller grain sizes dispersed through a generally upward-fining trend. Within Facies I it was common to find smaller grain sizes immediately above the basal scour surface.

Chapin determined the percentage of each facies within channelbelts in the Peoria Field and in outcrops (7). This comparison is shown in Figure 4.

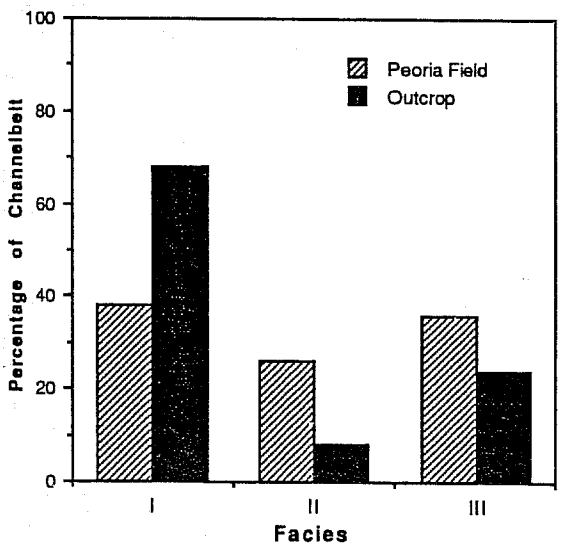

Fig. 4. Distribution of facies within channelbelts (from Chapin (7)).

IV. COMPARISON OF EXTERNAL SANDBODY GEOMETRIES

Genetic units have distinct internal arrangements of facies and characteristic dimensions and geometries. This enables the distribution of facies identified in cores or outcrops to be used to infer the geometry of a sedimentary body. Comparisons of the distribution of stratification types within similar facies, of the proportion of facies within channelbelts, and the nature of overbank deposits between outcrops and the Peoria Field indicate differences in stream geometries (7).

Sandstone bodies observed in outcrop exhibit both downstream accretion in the form of large cross-bed sets with steep foresets deposited as bars within the channels and lateral accretion identified by the existence of epsilon cross-bedding with a upward-fining sequence occurring in steps. Deposits outside the channels contain tidal flat sandstones and mudstones which indicate the channels were located in a nearshore environment. These facies relationships indicate Facies I, II, and III in outcrop were probably deposited by low-sinuousity distributary channels (7). Others have found that low-sinuousity channels can contain downstream-accreting, longitudinal and transverse bars (5) and also point bars (8).

Cores from the Peoria Field were found to have a fining-up sequence of sediments occurring in steps, a decrease in the scale of the sedimentary structures moving up through a facies, and a thicker and more developed Facies II sandstone than the outcrop sections. Outcrops contain less Facies II than the Peoria Field and include more cross-stratified sandstone in this unit. The overbank deposits in the Peoria Field do not contain evidence of a nearshore environment and mainly consist of coarsening-up vertical accretion to crevasse splay sequences. Large cross-bed sets and planar-tabular cross-stratification were not observed in the Peoria Field cores. The sandstone from Facies I, II, and III in the Peoria Field were probably deposited by moderate- to high-sinuousity meandering streams of the coastal plain (7).

Within the Peoria Field two levels of meanderbelt sandbodies were found. These two levels of coalesced meanderbelts exhibited varying degrees

of interconnectedness (7). Channels and the distribution of facies within the channels were mappable sandbodies in the Peoria Field (7).

V. DIAGENETIC CHANGES AND THE EFFECT OF CONFINING STRESS

Quartz overgrowths, authigenic kaolinite, and feldspar dissolution creating secondary porosity are the most prominent diagenetic features found in samples from the Peoria Field and from outcrops. Samples from both locations showed similar diagenetic features when observed using a scanning electron microscope.

Both surface and subsurface rocks from Facies I and II are texturally mature, quartz-rich sandstones. Quartz overgrowths are the most common cement and cause a significant reduction of the original porosity. Kaolinite which occurs as a pore-filling clay was found to be the most abundant authigenic clay making up approximately 3 to 4 percent of the rock (9). Other clays present in small amounts in Peoria Field samples include illite, smectite, and mixed-layer clays (9). Outcrop samples contain small amounts of illite and pyrite (10).

The dissolution of feldspars has caused the formation of secondary porosity. Thin sections from outcrop samples generally exhibited greater amounts of kaolinite and secondary porosity than Peoria Field samples (7). This is probably due to fresh water moving through the outcrops.

The initial burial history of both outcrop and Peoria Field rocks were similar but the Laramide Orogeny and subsequent erosion of the overburden exposed the Muddy (J) Sandstone along the western edge of the Denver Basin. Because of their similar initial burial histories, diagenetic modifications, and cementing, outcrop and subsurface reservoir rocks were believed to have similar compressibility characteristics. This was confirmed by measurements of pore volume and permeability on outcrop and Peoria Field samples at different values of confining stress. Figure 5a and b show that similar

changes occur to surface and subsurface samples with the application of confining stress.

(a)

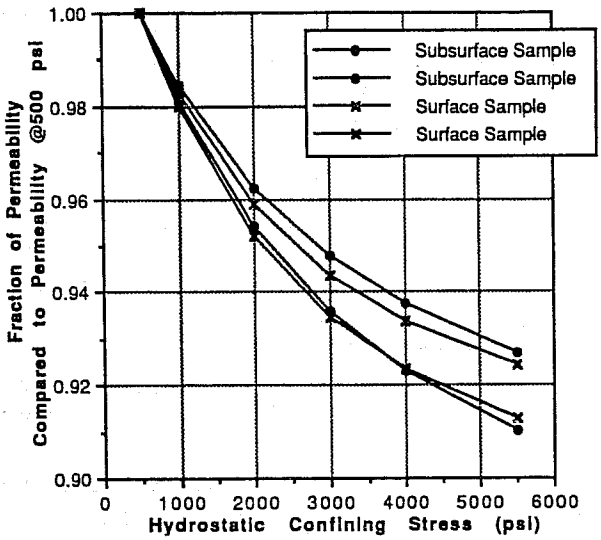

(b)

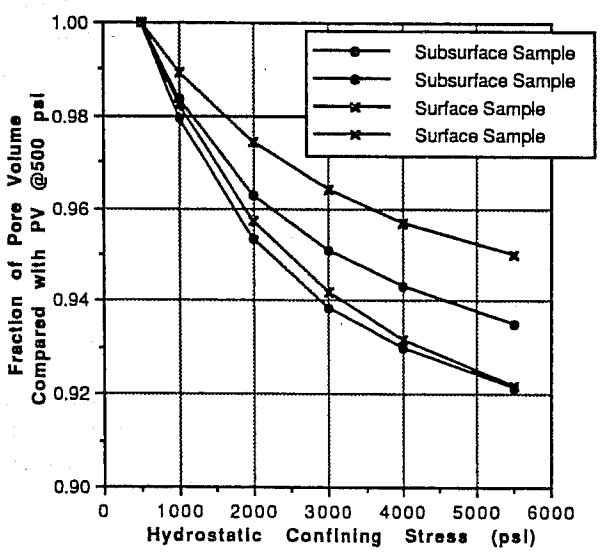

Fig. 5. (a) Permeability versus net stress. (b) Pore Volume versus net stress.

VI. PORE TYPES IN OUTCROP AND SUBSURFACE ROCKS

Based on sieve analysis, mercury injection curves, and air permeabilities it was found that the two reservoir facies contained six pore types, three within Facies I and three within Facies II. These pore types are associated with specific stratification types. The following list describes the six pore types which were found:

1) Lower-medium-grained through upper-fine-grained trough and planar-tabular cross-bedded strata and horizontal-laminated beds within Facies I with grain sizes ranging from 1.8 to 2.4 phi units.
2) Massive beds within Facies I.
3) Lower-fine-grained, cross-bedded strata within Facies I with grain sizes between 2.4 and 2.9 phi units.
4) Cross-bedded and massive beds within Facies II with grain sizes between 2.9 and 3.1 phi units.
5) Ripple-laminated beds which do not have mud drapes. This pore type from Facies II was found to have mean grain sizes between 3.0 and 3.4 phi units.
6) Ripple-laminated beds with mud drapes and mean grain sizes between 3.4 through 3.8 phi units. This pore type also includes wavy and convolute laminated beds and mud break-up beds within Facies II.

Figures 6a and b show mercury injection curves from outcrop and Peoria field samples for different stratification types. Mercury injection curves measured on outcrop samples were found to have wider pore throat distributions than Peoria Field samples from the same stratification type. In most cases the outcrop samples also had lower displacement pressures than subsurface samples. Because grain sizes and sorting factors were similar for surface and subsurface samples the wider distribution of pore throat sizes is believed to be caused by the greater amount of secondary porosity found in outcrop samples.

Channels and facies within the channels were mappable but the vertical and areal distribution of

pore types within each facies could not be mapped with any degree of certainty. For this case geostatistical techniques are required to map the distribution of pore types within each facies.

(a)

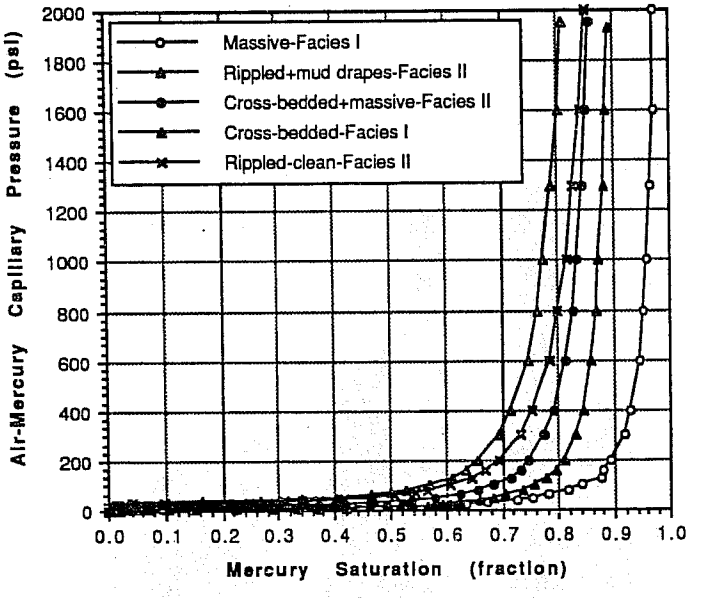

(b)

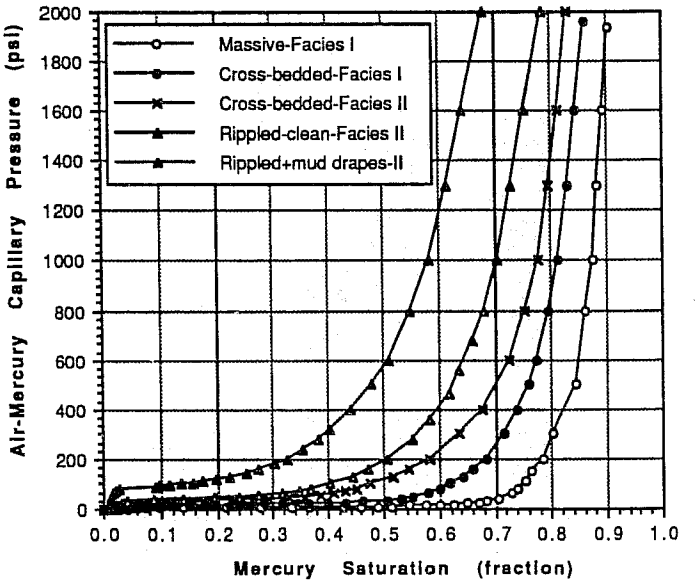

Fig. 6. (a) Mercury injection curves measured on subsurface samples. (b) Mercury injection curves measured on outcrop samples.

Figures 7a and b show the distribution of the pore types found in outcrops and in Peoria Field cores. Outcrops contained greater amounts of coarser-grained, cross-bedded sandstone in Facies I and more cross-bedded sandstone within Facies II than the Peoria Field. Peoria Field samples contained more ripple laminated sandstone in Facies II than outcrops.

(a)

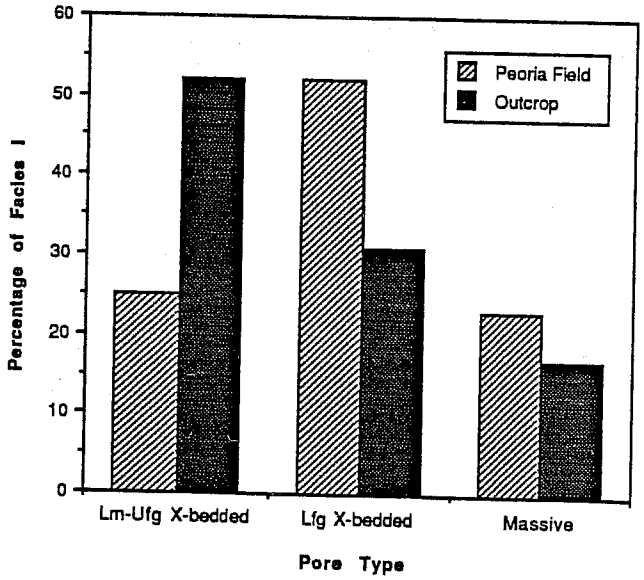

(b)

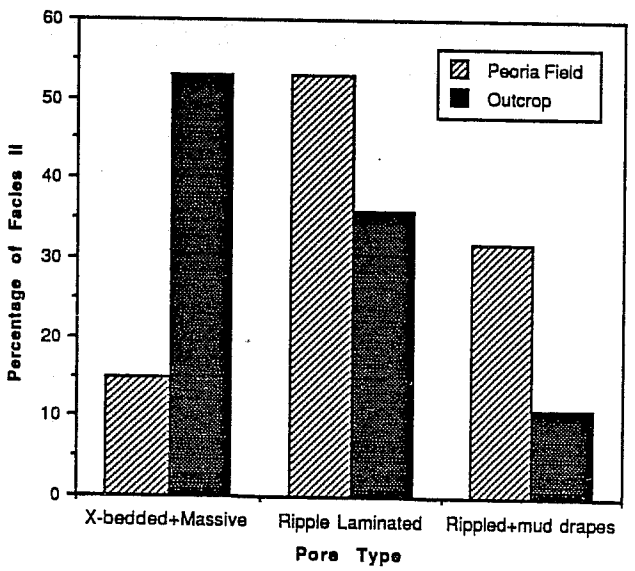

Fig. 7. (a) Distribution of pore types within Facies I. (b) Distribution of pore types Facies II.

VII. PERMEABILITY CHARACTERISTICS

Porosity and permeability values measured on outcrop samples from Facies I and II were greater than those from the Peoria Field. Permeability-porosity crossplots using core plug data from outcrop and Peoria Field samples are shown in Figure 8a and b. Data from each facies are identified on these graphs. These data indicate that each of the reservoir facies is associated with a different permeability population. Histograms of these populations show permeability values for each facies to be lognormally distributed and porosity to be normally distributed.

(a) (b)

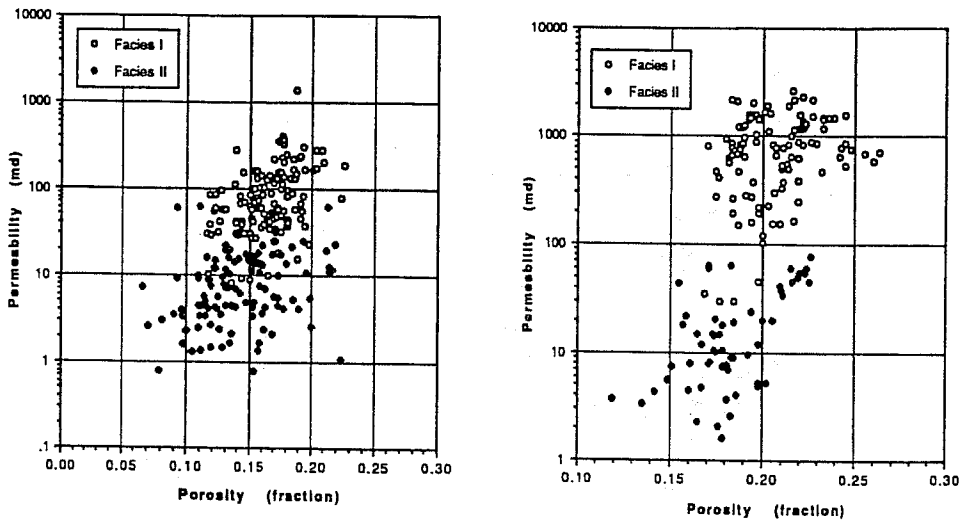

Fig. 8. (a) Permeability-porosity crossplot of Peoria Field data. (b) Crossplot of outcrop data.

Minipermeameter measurements were made on cores from nine wells and core plug data were measured on cores from twenty wells in the Peoria Field. Figure 9 shows the distribution of facies and pore types and their corresponding permeabilities in Peoria Unit #67. A Dykstra-Parsons plot of minipermeameter data from this well is shown in Figure 10. A Dykstra-Parsons coefficient computed from the best-fit straight line representing all the permeability data for this well was equal to .86 indicating a heterogeneous reservoir. However, the data shown in Figure 10 do not fall on a single line; instead, several straight-line segments can be identified.

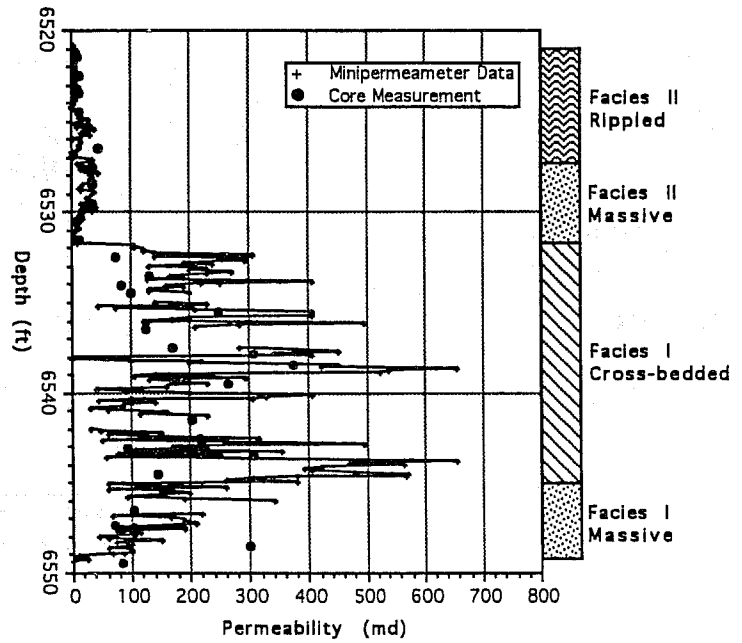

Fig. 9. Distribution of permeability, pore types, and facies in Peoria Unit #67.

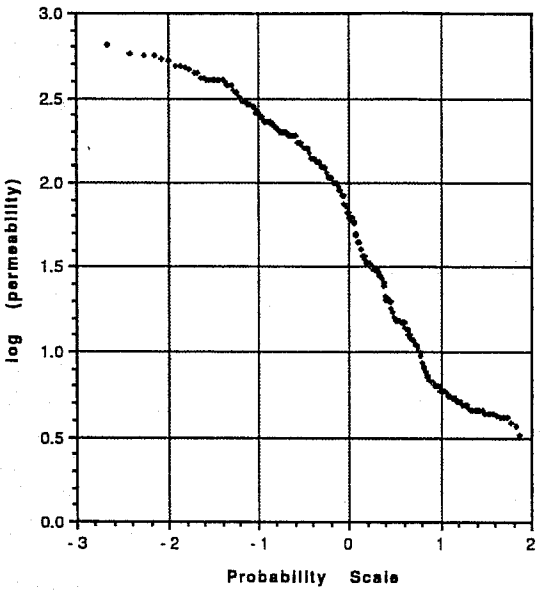

Fig. 10. Dykstra-Parsons plot of minipermeameter data from Peoria Unit #67.

In order to determine if permeability was related to smaller reservoir units the permeability data first were classified by facies and then by pore type. Each of the straight-line segments observed in Figure 10 was found to be associated with a particular facies or pore type. All of the sampled wells exhibited this behavior. Population statistics were computed and Dykstra-Parsons plots constructed for each facies and pore type present in each sampled well. Histograms of permeability data from each pore type were lognormal distributions. Core plug permeability values from Facies I and II were used to construct the Dykstra-Parsons plot

shown in Figure 11. Only 40 permeability measurements were available for this graph. From this plot it is difficult to detect the existence of different permeability populations. The greater number of permeability measurements obtained using a minipermeameter enabled more detailed features to be identified on the Dykstra-Parsons plots.

The Dykstra-Parsons coefficients and geometric mean permeabilities computed for each facies and pore type in this well are shown below:

- All core plug permeability data = .74 and 51. md.
- All minipermeameter data = .86 and 53. md.
- Minipermeameter data - Facies I = .58 and 163. md.
  - Lower-fine-grained cross-bedded - Facies I = .47 and 192. md.
  - Masssive - Facies I = .43 and 87. md.
- Minipermeameter data - Facies II = .62 and 11.4 md.
  - Massive - Facies II = .37 and 23.7 md.
  - Ripple laminated - Facies II = .51 and 8.0 md.

From these data it can be seen that Peoria Unit #67 is composed of two permeability populations each related to a reservoir facies. Each facies is more homogeneous than the total reservoir thickness. The large difference in permeabilities between Facies I and II is due to the difference in grain size between these two facies.

The permeability population of each facies contains several smaller permeability populations which are related to different pore types. Pore types are more homongeneous than the facies in which they are found. Differences in permeability between different pore types are believed to be caused by differences in packing and grain sizes in different stratification types. These observations indicate that a single Dykstra-Parsons coefficient can be a misleading indication of heterogeneity when a reservoir is composed of distinct zones with different permeability populations.

A Dykstra-Parsons plot of 165 core plug permeabilities taken from outcrop samples is shown in Figure 12. Facies and pore types in outcrops exhibited similar characteristics to those observed in the Peoria Field. The average permeability of each pore type was greater in outcrops than in the Peoria Field.

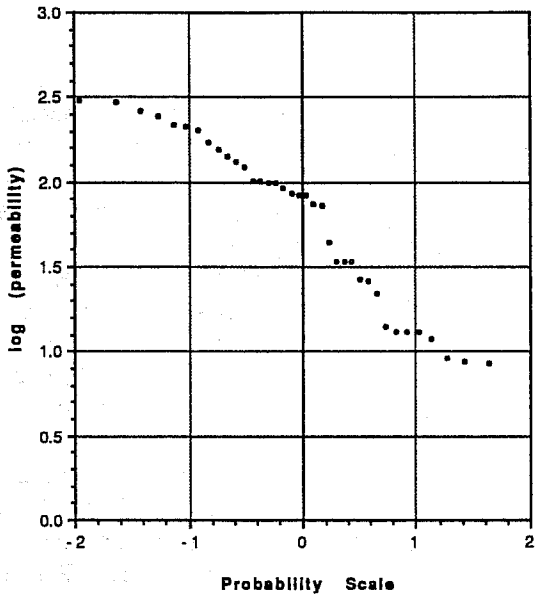

Fig. 11. Dykstra-Parsons plot of core plug permeabilities from Peoria Unit #67.

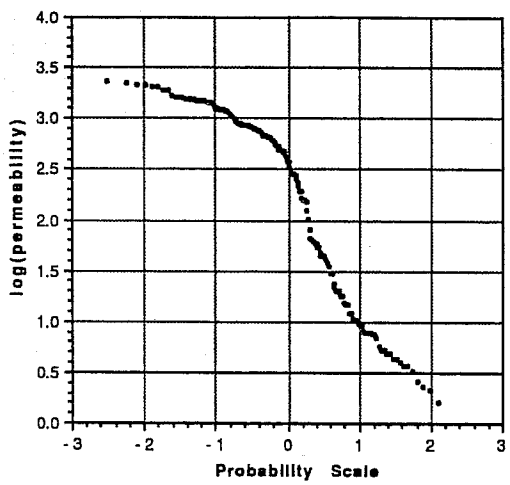

Fig. 12. Dykstra-Parsons plot of outcrop permeability data from core plug measurements.

VIII. CAPILLARY PRESSURE AND RELATIVE PERMEABILITY CHARACTERISTICS

Restored-state, oil-water relative permeability and capillary pressure measurements were made on outcrop and Peoria Field samples from each pore type. Oil-water capillary pressure curves measured during primary drainage are displayed in Figure 13a and b. These measurements were performed at reservoir temperature using a synthetic brine and Peoria Field crude oil in a centrifuge. The oil-water capillary pressure curves do not follow the same patterns observed in mercury injection measurements.

The initial water saturations from Peoria Field samples ranged from 17 to 30 percent. Capillary pressure data were not measured on a ripple-laminated sample with mud drapes from the Peoria Field. However, the other Peoria Field curves indicate this pore type probably would contain oil but at a high water saturation. Outcrop samples had a much broader range of initial water saturation values. Both of the ripple-laminated pore types from outcrops exhibited very large initial water saturations and probably would not be productive in the subsurface.

Forced imbibition and secondary drainage curves provided data to compute the USBM wettability index of each core plug (11). This index varies from +1.0 for strongly water-wet rock to -1.0 for strongly oil-wet samples. The wettability index measured for each pore type is listed below:

1. Peoria Field samples
   a. Facies I
      - Massive = .1932
      - Cross-bedded = -.0043
   b. Facies II
      - Massive = -.2151
      - Ripple laminated = -.4424
2. Outcrop samples
   a. Facies I
      - Massive 1.153
      - Cross-bedded = -.0259
   b. Facies II
      - Cross-bedded = .180
      - Ripple laminated (no mud drapes) = .127

(a)

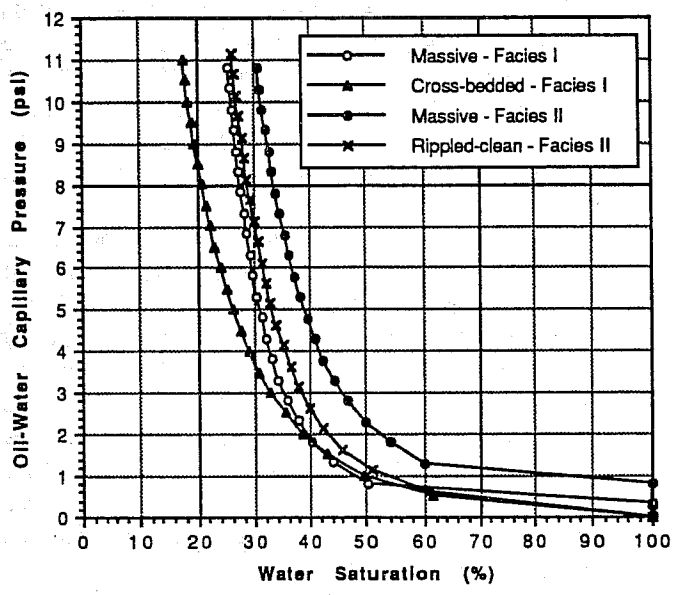

(b)

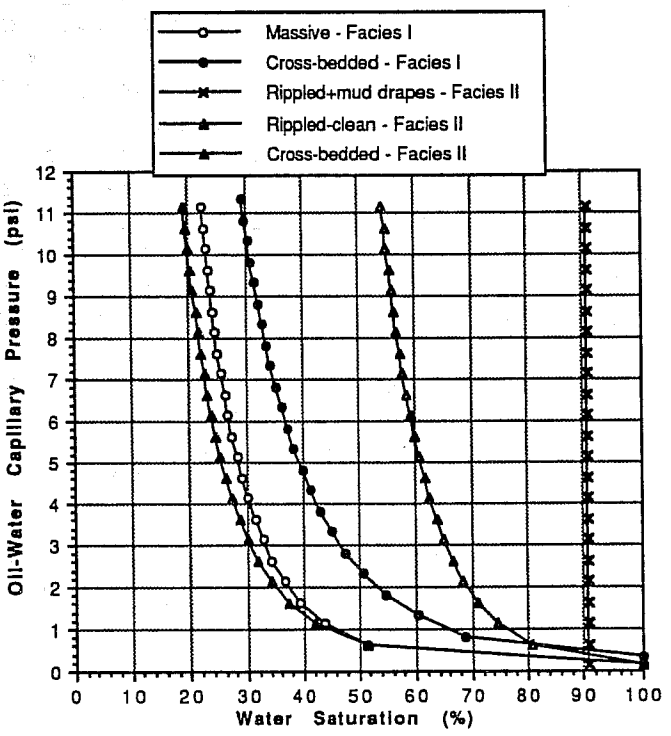

Fig. 13. (a) Oil-water capillary pressure curves from Peoria Field samples. (b) Oil-water capillary pressure curves from outcrop samples.

Oil-water relative permeability measurements were performed at reservoir conditions on outcrop and Peoria Field samples. Peoria Field data from Facies I and II are shown in Figures 14a and b and outcrop measurements are displayed in Figures 15a and b. These curves were measured during an imbibition process.

Relative permeability curves from pore types in Facies II measured on both surface and subsurface samples show a very similar character. The Peoria Field samples from Facies II were moderately oil wet and the outcrop samples were slightly water wet. These curves show oil to be mobile over a wide range of water saturations. However, small oil relative permeability values combined with low absolute permeabilities measured in Facies II indicate this facies would not provide a significant contribution to the oil production rate.

Each pore type within Facies I exhibited unique relative permeability characteristics. Peoria Field samples from Facies I had neutral to slightly water-wet wettability characteristics. Residual oil saturations of samples from Facies I in the Peoria Field were greater than those from Facies II.

Large differences in the wettability of different pore types in outcrop samples from Facies I are believed to have caused the differences in their relative permeability characteristics. Massive samples from outcrops were strongly water wet, had large values of oil relative permeability at initial water saturation, and had the largest residual oil saturation of any sample. Cross-bedded outcrop samples were found to have neutral wetting and extremely low residual oil saturations. The relative permeability characteristics of this pore type were similar to those found in Facies II samples.

The differences in relative permeability characteristics of pore types within Facies I should be accounted for in fluid flow models.

(a) (b)

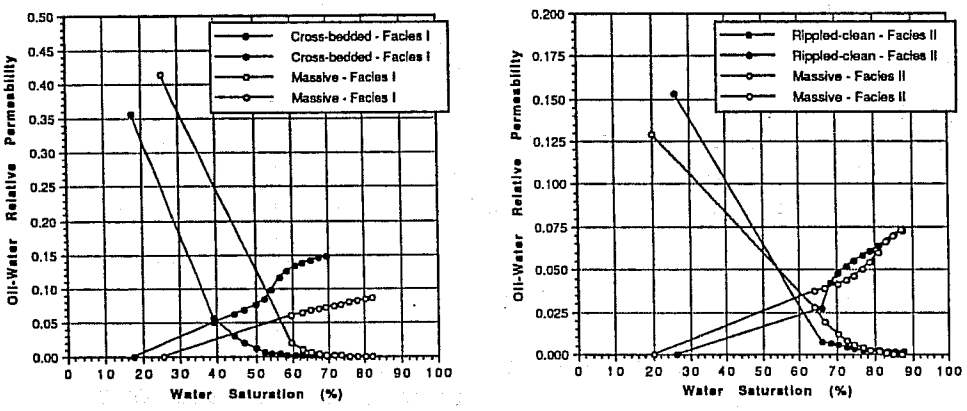

Fig. 14. (a) Peoria Field oil-water relative permeability curves from Facies I. (b) Peoria Field oil-water relative permeability curves from Facies II.

(a) (b)

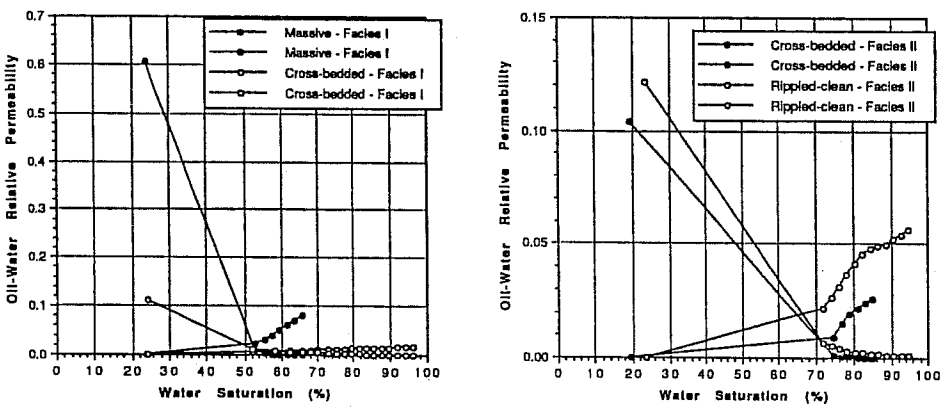

Fig. 15. (a) Outcrop oil-water relative permeability curves from Facies I. (b) Outcrop oil-water relative permeability curves from Facies II.

IX. SUMMARY AND CONCLUSIONS

Comparisons of outcrop and subsurface rocks from equivalent strata in the Muddy (J) Sandstone were made to help define the interwell character of channel sands in the Peoria Field for fluid-flow models. Outcrops were found to have grain sizes, sedimentary structures, and facies successions within channel deposits similar to those in the Peoria Field. From these observations two reservoir facies were identified in both surface and subsurface rocks. The proportion of each facies within channels and the distribution of stratification types comprising each facies were different in outcrops and in the Peoria Field.

Channels observed in outcrops were interpreted to be low-sinuousity distributary channels and Peoria Field channel facies were thought to be moderate- to high-sinuousity, fluvial, point bar sands deposited on the coastal plain.

Mercury injection characteristics, grain size analyses, and permeability populations showed that the two facies were each composed of three different pore types. Each pore type was associated with one or several stratification types. Similar pore types were found in outcrops and Peoria Field cores. However, the properties of each pore type differed between the surface and subsurface. Also, the amount of each pore type within the two reservoir facies was different in outcrops and Peoria Field cores. Oil-water relative permeability and capillary pressure curves were different for each pore type and between surface and subsurface samples from similar stratification types.

For this case an outcrop study was useful for determining how fluid-flow properties are related to rock types and for establishing the number of units (pore types) needed for reservoir description. These results indicate the need to consider the distribution of stratification types or pore types within a facies when scaling up reservoir properties for fluid-flow models in this type of reservoir.

ACKNOWLEDGMENTS

The authors would like to thank Marathon Oil Company for performing the relative permeability and capillary pressure measurements and the porosity and permeability measurements at different values of confining stress.

REFERENCES

1. Weimer, R.J. and Land, C.B., Jr.: "Field Guide to Dakota Group (Cretaceous) Stratigraphy Golden-Morrison Area, Colorado," The Mountain Geologist, v. 9, no. 2-3, p.241-267.

2. MacKenzie, D.B.: "Post-Lytle Dakota Group on West Flank of Denver Basin, Colorado," The Mountain Geologist, v. 8, no. 3, 1971, p.91-131.

3. Weimer, R.J. and Sonnenberg, S.A.: "Sequence Stratigraphic Analysis of Muddy (J) Sandstone Reservoir, Wattenberg Field, Denver Basin, Colorado," in Petrogenesis and Petrophysics of Selected Sandstone Reservoirs of the Rocky Mountain Region, E.B. Coalson, ed. RMAG, 1989, Denver, CO, p. 197-220.

4. Matuszczak, R.A.: "Wattenberg Field, Denver Basin, Colorado," The Mountain Geologist, v. 10, 1973, p. 99-105.

5. Land, C.B. and Weimer, R.J.: "Peoria Field, Denver Basin, Colorado - J Sandstone Distributary Channel Reservoir," in Depositional Modeling of Detrital Rocks, SEPM Core Workshop No. 8, August 1985, Golden, CO, p. 59-82.

6. Harms, J.C.: "Stratigraphic Traps in a Valley Fill, Western Nebraska," AAPG Bull., v. 50, no. 10, Oct. 1966, p.2119-2149.

7. Chapin, M.A.: "Quantification of Multiscale Rock-Property Variations in Fluvial Systems for Petroleum Reservoir Characterization," unpublished Ph.D. dissertation, 1989, Colorado School of Mines, Golden, Colorado.

8. Bridge, J.S., Smith, N.D., Trent, F., Gabel, S.L., and Bernstein, P.: "Sedimentology of a Low-Sinuousity River, Calmus River, Nebraska Sand Hills," Sedimentology, v. 33, p. 851-870.

9. Beckham, E.: "Diagenesis of the Muddy Sandstone (Cretaceous), Peoria Field, Denver Basin, Colorado," unpublished M.S. thesis, The University of Texas at Austin, 1974, Austin, TX.

10. MacMillen, L.T.: "Stratigraphy of the South Platte Formation (Lower Cretaceous), Morrison-Weaver Gulch Area Jefferson County, Colorado," unpublished M.S. thesis, 1974, Colorado School of Mines, Golden, CO.

11. Anderson, W.G.: "Wettability Literature Survey-Part 2: Wettability Measurement," JPT, Nov. 1986, p. 1246-1262.

INTEGRATED OUTCROP AND SUBSURFACE RESERVOIR CHARACTERIZATION: CARBONATE SEQUENCE STATIGRAPHY AND RESERVOIR BEHAVIOR OF THE GIANT ANETH OIL FIELD, SE UTAH

By F. M. Wright and L. J. Weber
Mobil Exploration and Producing U. S. Inc.
Midland, Texas

ABSTRACT

Since discovery of the Aneth field (1956), 360 MMBO (~1250 MMOOIP) have been produced from Middle Pennsylvanian (Desmoinesian) carbonates of the Ismay and Desert Creek intervals. Improved prediction and identification of by-passed, banked, and/or undeveloped oil is possible within the Aneth oil field through integration of reservoir production/performance data and a strong geologic framework. Sequence stratigraphic analysis results in high-resolution time-based facies correlations that approximate flow zones. A less reliable lithostratigraphic (rock-based) zonation scheme was used in the field for 30 years; production anomalies (e.g., rapid CO_2 breakthrough) were inexplicable without numerous reservoir bounding faults. Recently, evaluation of ~~12,000 feet (3,660 m) of core indicates that interwell and reservoir performance variations are related to temporal and spatial heterogeneity of carbonate depositional environments and associated early diagenesis.

This new sequence stratigraphic framework for the Desmoinesian section in southeastern Utah incorporates: 1) surface exposures at Honaker Trail, located 40 miles (64 km) west of the Aneth field, 2) well logs near the outcrop area, and 3) core and well logs in the Greater Aneth field and allows correlation of genetically related lithofacies. The stratified reservoirs of Aneth occur within transgressive systems tracts, highstand systems tracts, and to a lesser extent lowstand systems tracts.

Distinctive facies stacking patterns and associated diagenetic trends resulted in the formation of highly stratified Desert Creek and Ismay reservoirs. Sequence stratigraphy provides an improved framework for correlation and mapping of reservoir facies. This work focuses on integration and iteration of production/performance data with the geologic framework to better define zones of fluid flow.

COMPARISON OF GEOSTATISTICAL CHARACTERIZATION METHODS FOR THE KERN RIVER FIELD©

Joseph P. Vogt

Exploration & Production Technology Department
Texaco, Inc.
Houston, Texas

ABSTRACT

Three dimensional conditional simulation (3DCS) is a method to interpolate reservoir characteristics such as porosity, permeability, and facies between wells. 3DCS is usually thought to be the best characterization technique for flow studies. However, this method is also quite CPU intensive. Other geostatistical techniques, such as pseudo 3D conditional simulation (P3DCS), 3D kriging (3DK), and pseudo 3D kriging (P3DK) are less CPU intensive. Therefore it is important to know when P3DCS, 3DK, and P3DK can be substituted for 3DCS. In this paper, we will answer this question for the Kern River Field in California.

© A substantial portion of this paper is from SPE 22338, which will be published in the proceedings of the SPE International Meeting on Petroleum Engineering to be held in Beijing, China, March 24-27, 1992.

I. INTRODUCTION

The Kern River Field is located northeast of Bakersfield, California on the southeastern edge of the San Joaquin Valley (Figure 1). The field was discovered in 1899 and ranks as the fifth largest in the United States in original oil in place.[1,2]

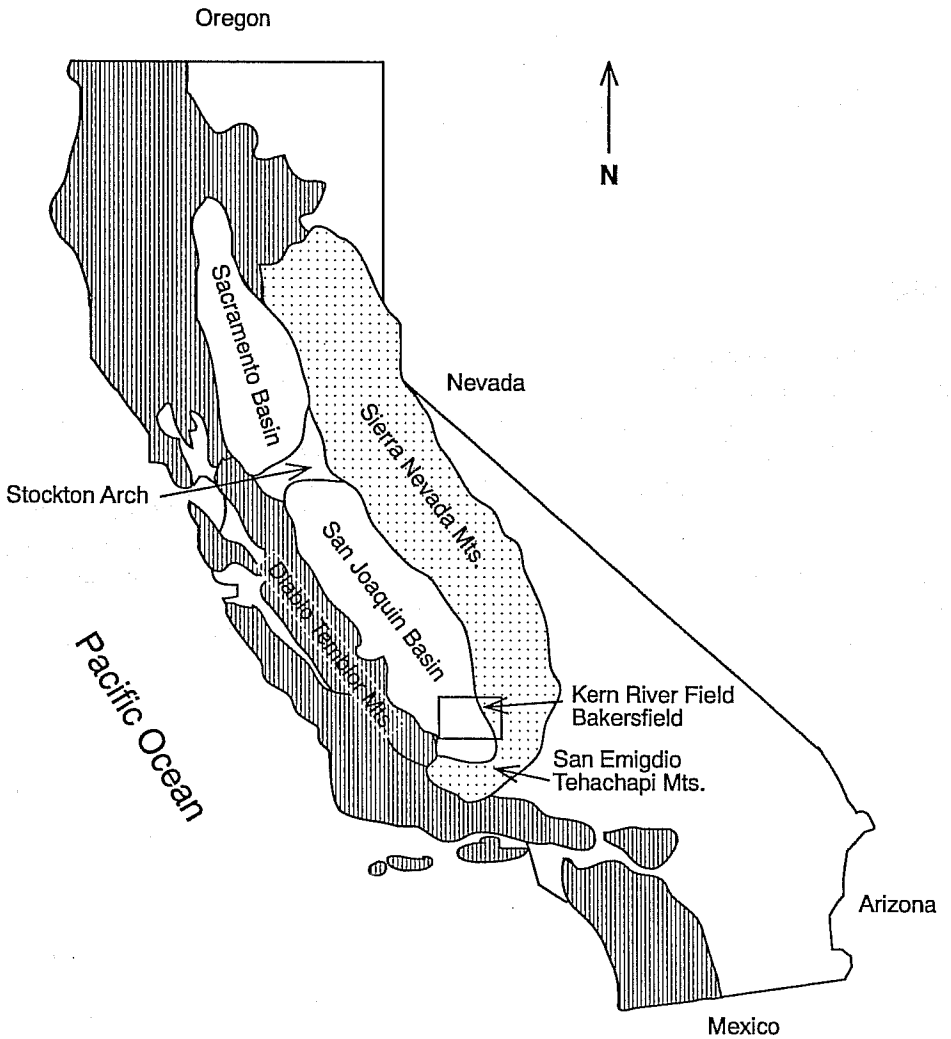

Figure 1. Kern River location.

For the first fifty years of its life, Kern production was slowed by the high viscosity of the crude (12 Pa.s (12,000 cp)) at the reservoir temperature of 20-30°C (68-86°F). Beginning in the mid-1950's, bottomhole heaters, steam stimulation, and finally steam displacement rejuvenated the field in a development program that continues to this day. Overall field production has plateaued and now appears to be slowly decreasing. Intensive geological and engineering efforts are being made to produce as much of the remaining oil as practical. These efforts include the use of geostatistics to help develop geological models at both the well-to-well and field-wide scales.

Even with today's computers, geostatistical software can be expensive to run. Therefore it's important to use the least CPU intensive modeling technique that will still accurately characterize the reservoir. Previous work[3] has shown that conditional simulation is better than kriging for characterizing the permeability of a 2 ft by 2 ft Berea sandstone slab. By comparing outcrops with geostatistical results, we've found that conditional simulation is also better than kriging for predicting the shale continuity at Kern River. In this paper, therefore, we'll regard 3DCS as reality. The other three methods will be compared to 3DCS on the basis of (1) shale continuity predictions and (2) CPU time.

In addition to comparing geostatistical techniques, this paper points out two important limitations of most commercial gridding software that claims to be 3D. First, most software works in only one plane at a time. The resulting 3D grid, then, is really made up of a series of independent 2D grids (i.e., pseudo 3D). For reservoirs that have small variability (high correlation) perpendicular to these 2D grids, the resulting 3D grid is not realistic. Second, most (all?) commercial software uses algorithms that, like kriging, do not reproduce the statistics and texture of the original data. Rather, these algorithms underpredict the extreme values of the data and smooth it out spatially. The physical results of this second shortcoming will be seen in the course of this paper.

II. SOFTWARE

The geostatistics software we used uses conventional kriging[4] and two different types of simulation: the turning bands method (tbm)[4] and the matrix decomposition method (mdm).[5] Some general comments are offered below.

For conventional kriging, Gaussian elimination is used to solve the kriging equations.

For single conditional simulation realizations, the tbm is faster than the mdm. The tbm is not used for three dimensional (3D) problems, however, because in 3D, mathematical difficulties can be encountered when using fractal variograms. These difficulties do not occur with the tbm in 2D.

For single conditional simulation realizations, the mdm is slow compared to the tbm because the decomposition of the covariance matrix in the mdm takes a long time. However, as the number of realizations increases, the mdm becomes relatively more efficient because the same matrix decomposition can be used for all the realizations.

In summary, it's best to use the tbm for a small number of 2D realizations. For a large number of realizations or for a 3D problem, mdm is best.

III. STATISTICS

The short normal resistivity data used in this paper came from two "typical" wells (5510053 and 5510076, also called Reed Crude A53 and Reed Crude A76, respectively) in the central portion of the Kern River Field. The sample probability density function (pdf) from the wells is shown in Figure 2.

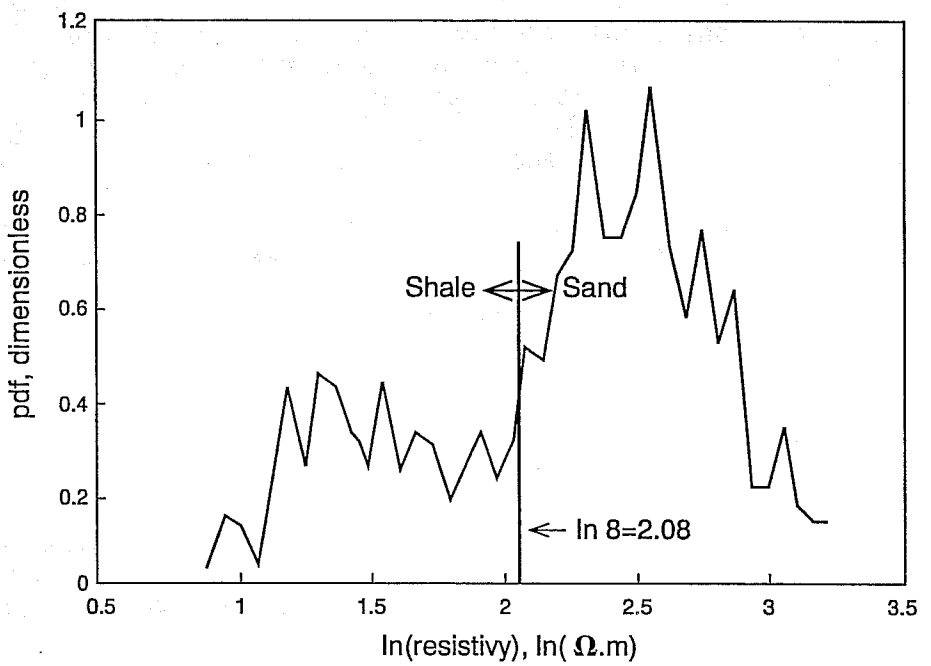

Figure 2. Sample probability density function (PDF)

Notice that the sample pdf is bimodal, that is, it has two humps. The first hump (low resistivity values) comes from shale, and the second hump (high resistivity values) comes from sand.

Normally, data from more than two wells would be used to generate resistivity statistics and variograms. The purpose of this paper, however, is to demonstrate techniques rather than create a highly accurate Kern River model. For demonstration purposes, then, data from only two wells is sufficient.

IV. VARIOGRAPHY

Kriging as well as the tbm and the mdm require a variogram as input.

The first step in making a variogram is to stratigraphically correlate the wells that are going to be used.[6] This was done for 5510053 and 5510076.

After plotting the vertical variogram, it was decided to fit it with a fractional Gaussian noise fractal model, whose equation is[7]

$$2\gamma(h,\delta) = v\delta^{2H-2}\left(2 - \left(\frac{h}{\delta}+1\right)^{2H} + 2\left(\frac{h}{\delta}\right)^{2H} - \left|\frac{h}{\delta}-1\right|^{2H}\right) \quad (1)$$

In this equation, V is a fitting constant, δ is a length which is often taken as the data interval, and H is the fractal exponent. In this study, instead of taking δ as the data interval, it is taken as 0.01 times a correlation length, which is discussed in the next paragraph.

By definition, fractal variograms do not have ranges or correlation lengths.[7] Random field generation methods such as the tbm or the mdm, however, require a correlation length as input.[4,5] So in order to use such methods to generate random fractal fields, we defined artificial correlation lengths that are equal to or greater than the ranges of the data. This will not affect the problem physically because the variogram is strictly fractal within the range of the problem. However, it does satisfy the mathematical need to have a correlation length.

For the vertical direction, only 305 m (1000 ft) of data was available, so the vertical correlation length was taken as 305 m (1000 ft). An R/S analysis[8] gave the value of the fractal exponent H as 0.85. The constant V was obtained from the condition that the variogram at 305 m (1000 ft) equal the

variance of the resistivity, which is 100. This gave V equal to 117.29 $(\Omega.m)^2$.

A picture of the vertical variogram is shown in Figure 3.

Next a plot was made of the horizontal variogram. It was also fitted with the fractional Gaussian noise fractal model of Equation (1). It was assumed that both the variance and fractal exponent H of the resistivity in the horizontal direction are equal to their values in the vertical direction. Then the three constants V, δ, and correlation length for the horizontal direction were determined from the three conditions that (1) δ for the horizontal direction is equal to 0.01 times the horizontal correlation length, that (2) the horizontal variogram curve at the well spacing (which is 122 m (400 ft)) passes through the calculated variogram data point (which is 100 $(\Omega.m)^2$), and that (3) the value of the horizontal variogram at its correlation length is equal to the variance of the resistivity in the horizontal direction. This gives values of V of 354.73 $(\Omega.m)^2$, δ of 122 m (400 ft), and correlation length of 12,192 m (40,000 ft) for the horizontal direction.

A picture of the horizontal variogram is shown in Figure 3.

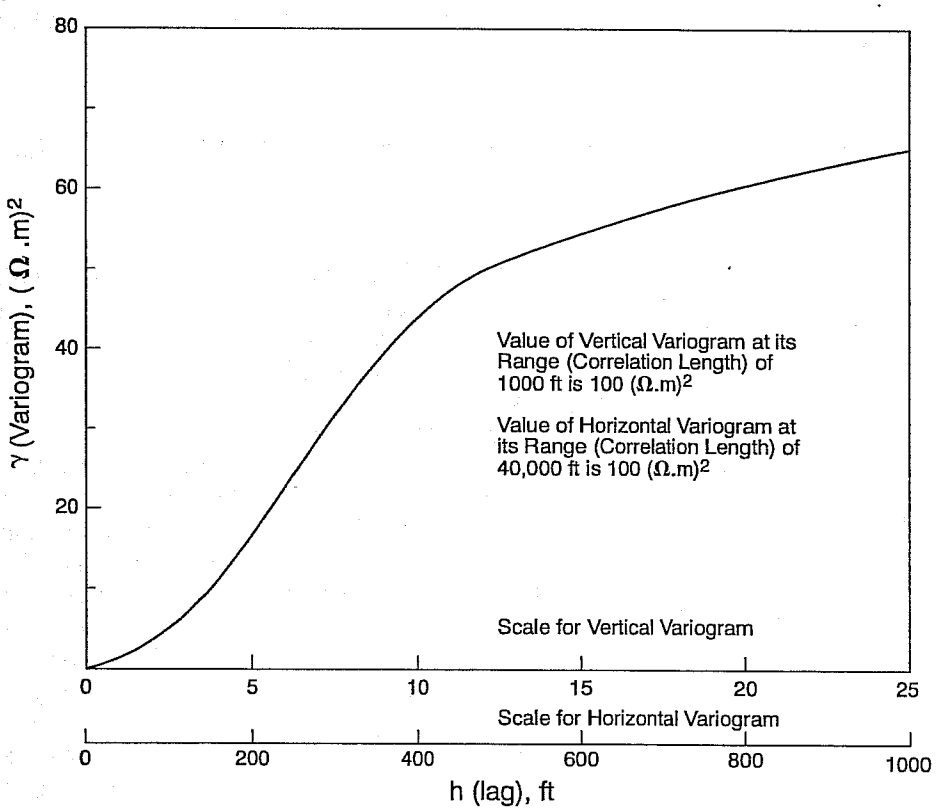

Figure 3. Vertical and horizontal resistivity variograms.

V. WELLS

Studies subsequent to this one are being conducted to arrive at geological and engineering conclusions for specific portions of the Kern River Field. Our purpose here, however, is to compare how four different geostatistical methods interpolate properties between wells.

The simplest and most conclusive way to compare geostatistical methods is to first generate artificial wells and then to use the different methods to interpolate between them. Using generated wells insures that the random variable being studied is stationary, assures that the data set contains no outliers, avoids the step of scale-up averaging of resistivity values, allows us to put the wells exactly where we desire, and generally makes the study easier to conduct and interpret.

In this study, we generated nine wells with the 61 m (200 ft) spacing shown in Figure 4. Each well has twenty equally spaced resistivity values. These values were generated by using the 3DCS method. The fractional Gaussian noise variograms in Figure 3 were used as input. Even though the wells were generated artificially, they cannot be qualitatively distinguished from actual Kern River wells.

VI. ESTIMATION AND SIMULATION

A. Introduction

Resistivity values between wells can be obtained by estimation (e.g., kriging) or simulation (e.g., the tbm or the mdm).

Kriging estimates a value at a point by taking a weighted linear combination of the values at neighboring points. The weights are chosen to make the estimate unbiased (the average error of a series of estimates is zero) and to minimize the variance of the errors. Kriging always honors the data.

Because of the assumptions on which it is based (zero average error and minimum variance of the error), kriging is a relatively accurate interpolation method. However, in general, the statistics of kriged values are different than the data used as input to the kriging procedure. In particular, the kriged results have fewer extreme values (i.e., have a smaller standard deviation) than the input data. Further, the variogram is not preserved. Kriged maps are usually smoother than reality. Thus kriging is most appropriate for such tasks as calculating an

average reservoir property. An example is average porosity values to be used in reserves calculations.

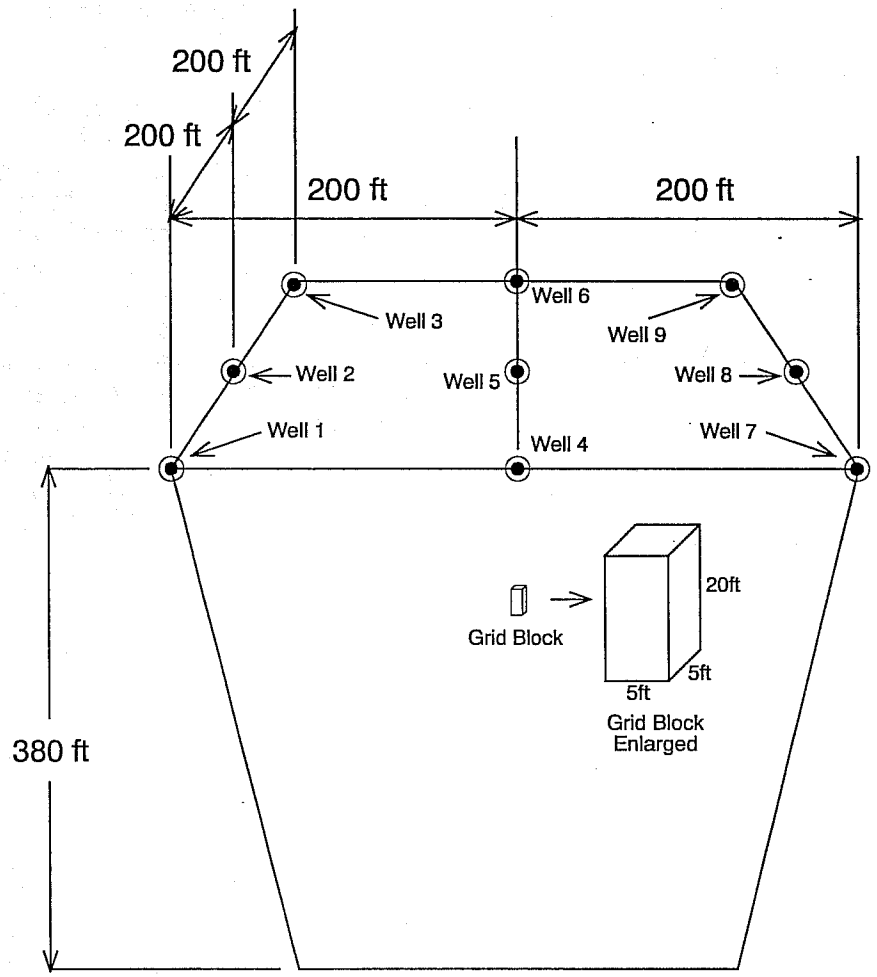

Note:
(1) The 200 and 300 ft Dimensions are Measured Between th Middle of Grid Blocks

(2) The Grid Contains 81x81x20=131,220 Blocks

Figure 4. Grid dimensions and well locations.

Simulation generates points in space that have the same histogram and variogram as the input data. In gridding applications, it duplicates the texture of the exhaustive data set. Thus simulation is most appropriate for calculating a property, such as permeability, that will be used in flow simulations. This is because flow is controlled by the extreme values of permeability rather than its average value. The disadvantage of simulation is that its average error is larger than kriging.

In this paper, the pseudo 3D techniques are mathematically the same as the true 3D methods except that the pseudo techniques are applied to one layer at a time while the true 3D methods are applied to all the layers simultaneously.

Using the resistivity values from the nine wells shown in Figure 4 as input, the P3DK, 3DK, P3DCS, and 3DCS methods were all applied. In all four cases, the value of the variogram (60.3 $(\Omega.m)^2$) at the layer thickness (20 ft) is 60.3% of the sample variance (100 $(\Omega.m)^2$). Qualitatively, this means that there is a large variability (small correlation) between layers. In such cases, pseudo 3D techniques will work almost as well as the corresponding true 3D method.

B. p3dk

The 3DK method (using a search ellipse with 1000 ft horizontal semi-axes) was applied at each of the grid nodes indicated in Figure 4. This gave a total of 81x81x20 = 131,220 resistivity values. Then, based on experience at Kern River, all nodes with resistivity values greater than 8 Ω.m were taken as sand, and all nodes with resistivity values less than 8 Ω.m were taken as shale.

C. 3dk

This method is the same as P3DK except (1) a search ellipsoid with horizontal and vertical semi-axes of 1000 ft and 40 ft, respectively, replaces the search ellipse of P3DK and (2) data in all layers within the search ellipse is used simultaneously for kriging.

D. p3dcs

Same as P3DK except a conditional simulation technique[4] is used instead of kriging.

E. 3dcs

Same as 3DK except a conditional simulation technique[4] is used instead of kriging.

VII. COMPARISON OF RESULTS

A. Physics

Current wisdom at Kern River is that permeability differences within the sands do not significantly affect fluid flow. Rather, shale continuity is what governs fluid movement.

For some layers (e.g., layers 1, 2, 3, 5, and 8), all four geostatistics results predict about the same shale continuity. To save space, these layers are not pictured. For other layers (e.g., layers 4, 6, 7, and 9), the four methods predict different results. The differences (see Figures 5 and 6) are:

(1) fourth layer: 3DCS predicts a shale in the lower right hand corner that the other methods do not predict

(2) sixth layer: P3DCS and 3DCS show more sand continuity than P3DK and 3DK

(3) seventh layer: P3DCS shows a break in the shale in the lower left hand corner, but the other three methods do not

(4) ninth layer: P3DK and 3DK predict very small holes in the shale only at the middle of the upper edge, whereas P3DCS and 3DCS predict larger holes at these locations as well as holes at the middle of the right hand edge; in addition, P3DCS predicts holes at the middle of the front edge.

The most important difference between the four geostatistical methods is illustrated by layer nine. Both kriging methods predict that this layer is a shale barrier. Both conditional simulation methods, however, predict that this shale has holes in it. This shows that the kriging methods sometimes obliterate critical features because kriging tends to give overly smooth results. For this reason, kriging methods (or any of the other commonly used gridding techniques that give overly smooth results) are not recommended for simulating the shales at Kern River.

B. Computer Time

Table 1 gives CPU time to generate an 81x81x20 grid block model using each of the four geostatistics methods. The 3DCS method, which is the best technique for predicting shale continuity, also takes the most CPU time. It is followed, in descending order of time, by 3DK, P3DCS, and P3DK.

Table 1 also gives some indication of how the number of layers affects CPU time for the various methods. As expected, for only one layer, there is little or no CPU time advantage in using the pseudo 3D methods. For twenty layers, however, there is a substantial advantage.

Table 1 shows that kriging is much faster than conditional simulation for one layer, but is not so much faster for twenty layers.

TABLE I. CPU time for four geostatistical methods.*

Interpolation Method	User CPU Time† (sec)	System CPU Time† (sec)	Total CPU Time† (sec)
P3DK	72.32/ 3.70	3.86/0.30	76.18/ 4.00
3DK	290.14/ 3.03	12.61/0.23	302.75/ 3.26
P3DCS	100.34/29.16	3.15/0.93	103.49/30.09
3DCS	330.94/35.75	19.13/8.79	350.07/44.54

* Run on a Cray XMP 216 with a UNICOS operating system

† (Time to Run a 20 Layer Model)/(Time to Run a 1 Layer Model)

Finally, notice that the time it takes to run twenty layers using the P3DCS method is much less than twenty times the time for one layer. This is because the spectral density function in the tbm only has to be calculated one time, regardless of the number of layers in the model.

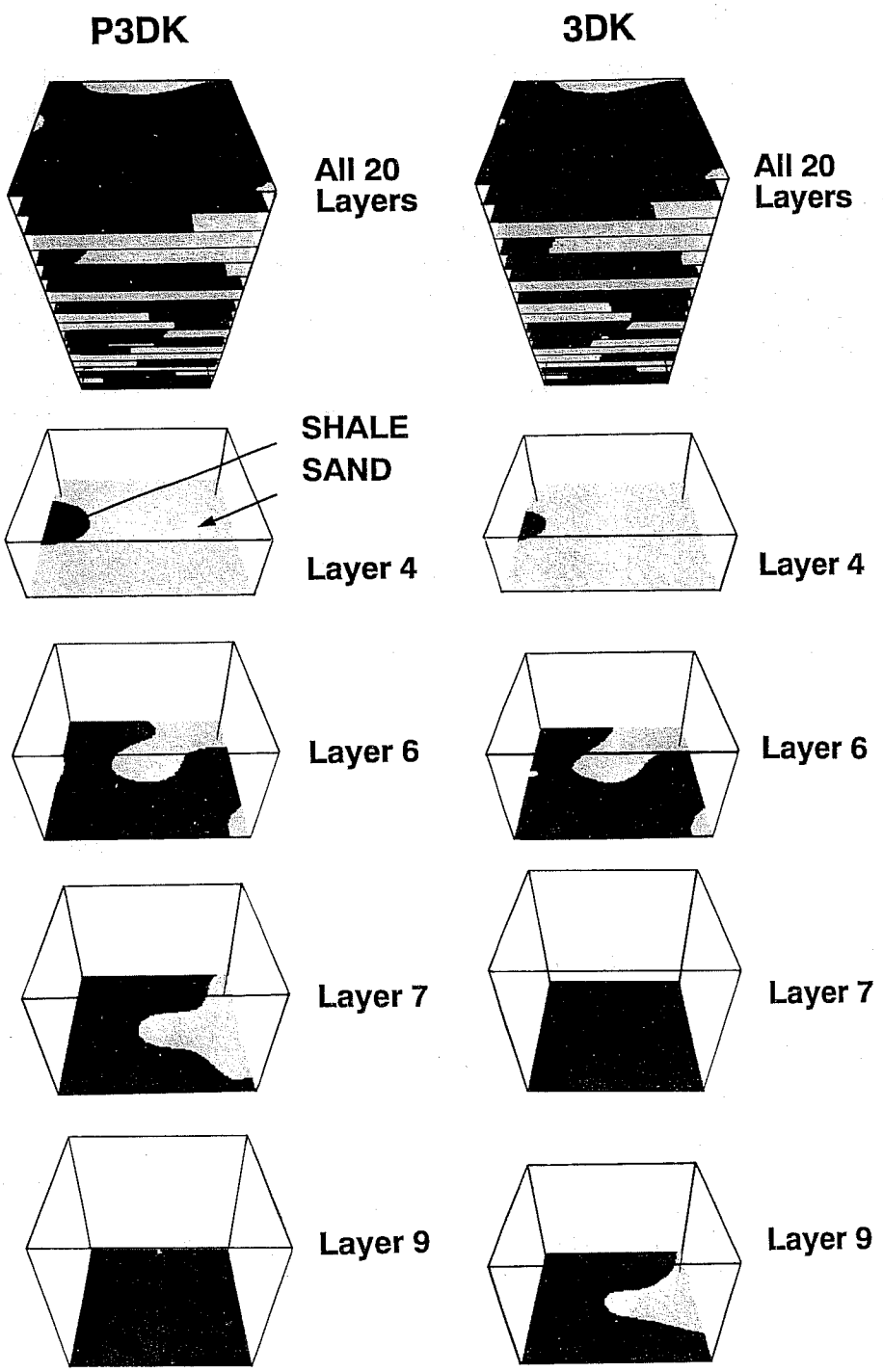

Figure 5. P3DK and 3DK results.

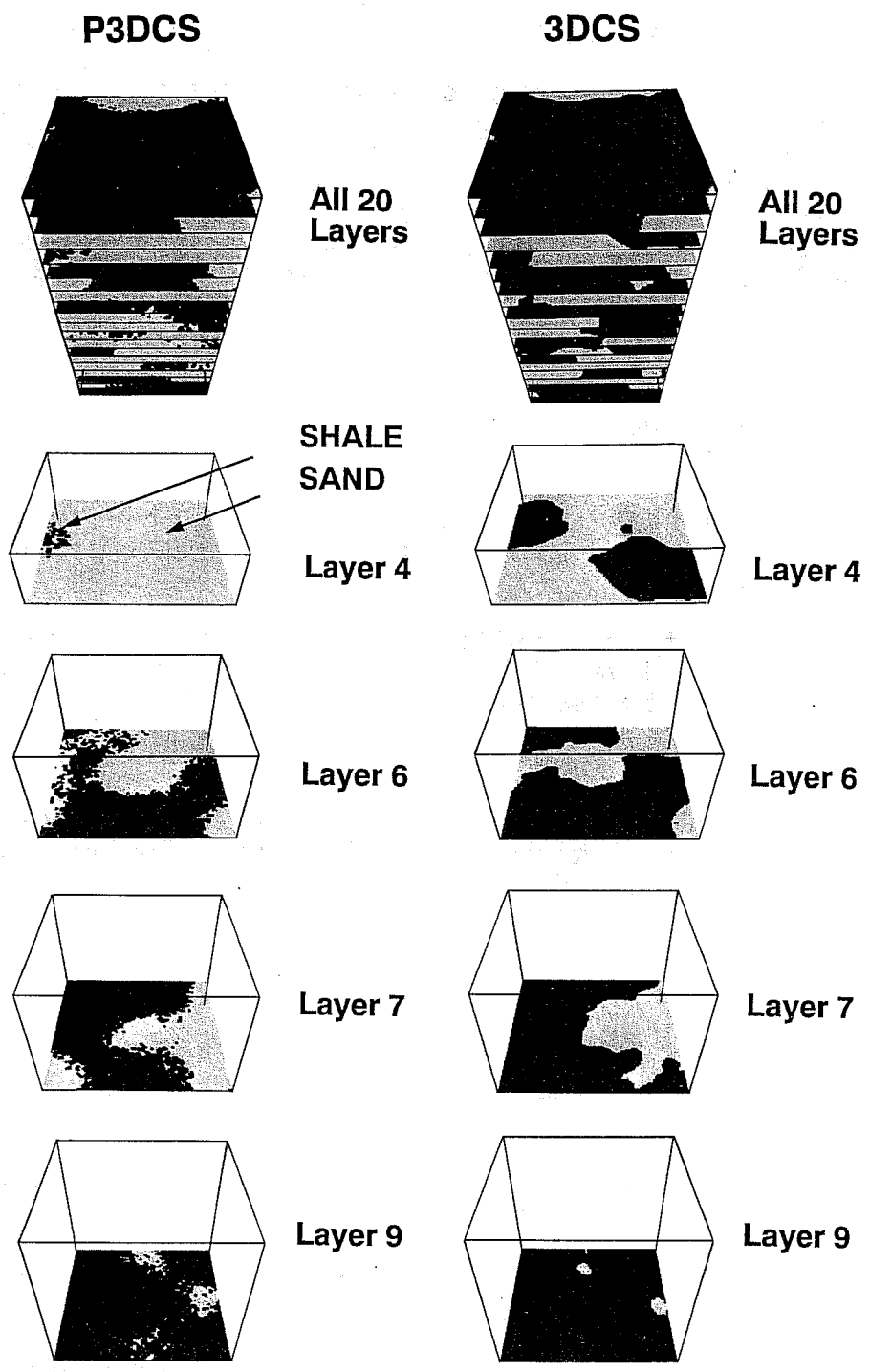

Figure 6. P3DCS and 3DCS results.

C. Cost Effectiveness

To determine the most cost effective geostatistics method to characterize the Kern River Field for flow simulation, we can eliminate the P3DK and 3DK methods because, as pointed out in the physics section, these techniques can give unrealistic results. The P3DCS results are qualitatively similar enough to 3DCS that they can usually be used for screening purposes at a considerable cost reduction (70% for twenty layers and 32% for one layer).

VIII. CONCLUSIONS

1. P3DK and 3DK (and all other algorithms used in commercial gridding packages) overpredict shale continuity at Kern River.

2. 3DCS is the best method for predicting shale continuity in the Kern River Field. P3DCS is a good screening method because it gives results similar to 3DCS but uses less CPU time (32% less for a one layer model and 70% less for twenty layers).

3. In general, P3DCS will give results similar to 3DCS whenever the vertical variability between layers is large (vertical correlation between layers is small).

IX. GLOSSARY

conditional simulation: A simulation that honors the input data.

correlation length: The maximum distance over which the value of a variable influences neighboring values.

estimation: A process that uses sample information to predict values in areas that have not been sampled.

fractal: A property is called fractal if it looks similar at all scales.

fractional Gaussian noise: A generalization of Gaussian noise (H = 1) in which the exponent H can take on fractional values from 1/2 to 1.

histogram: A curve that indicates the probability that a variable has a given value.

kriging: An estimation method that minimizes the expected value of the squared error of an estimate.

mdm (matrix decomposition method): An averaging method that generates a random field of numbers in space with a given histogram and variogram.

pseudo 3D: When a gridding process for a series of parallel planes is done independently in each plane, the collective grid is called pseudo 3D.

realization: One possible set of outcomes of a series of values in space.

probability density function: A type of histogram.

R/S analysis: An analysis which uses the range R in the values of a random variable and the standard deviation S of the variable to determine the similarity exponent H.

search ellipse or ellipsoid: An ellipse (2D) or ellipsoid (3D) within which one searches for points that are to be used for some purpose, such as kriging, etc.

simulation: A process that generates a random field of numbers in space with a given histogram and variogram.

tbm (turning bands method): A spectral method that generates a random field of numbers in space with a given histogram and variogram.

variability: High variability (low correlation) means that the value at a point is not related to the value of neighboring points.

variance: The average of the squared difference between a variable and its mean.

variogram: A curve that describes how a property can vary in space as a function of the distance between two points.

ACKNOWLEDGEMENTS

I thank Dr. A. P. Yang for using his software to generate the P3DK, 3DK, P3DCS, and 3DCS grids discussed in this paper.

REFERENCES

1. Brelih, D. A. and Kodl, E. J.: "Detailed Mapping of Fluvial Sand Bodies Improves Perforating Strategy at Kern River Field", paper SPE 20080, presented at the 1990 California Regional Meeting, Ventura, April 4-6.

2. Kodl, E. J., Eacmen, J. C., and Coburn, M. G.: "A Geologic Update of the Emplacement Mechanism within the Kern River Formation at the Kern River Field", from Structure, Stratigraphy, and Hydrocarbon Occurences of the San Joaquin Basin, California, J. G. Kuespert and S. A. Reid (eds.), Publication of SEPN Pacific Section and AAPG, June 1, 1990, pp. 59-71.

3. Journel, A. G. and Alabert, F. G.: "Focusing on Spatial Connectivity of Extreme-Valued Attributes: Stochastic Indicator Models of Reservoir Heterogeneities", paper SPE 18324, presented at the 1988 Annual Technical Conference and Exhibition, Houston, Oct. 2-5.

4. Journel, A. G. and Huibregts, Ch. J.: Mining Geostatistics, Academic Press, New York, 1978.

5. Fogg, G. E., Lucia, F. J., and Senger, R. K.: "Stochastic Simulation of Interwell-Scale Heterogeneity for Improved Prediction of Sweep Efficiency in a Carbonate Reservoir", Reservoir Characterization II, L. W. Lake, H. B. Carroll, Jr. and T. C. Wesson (eds.), Academic Press, New York, 1991: pp. 355-381.

6. Journel, A. G. and Gomez-Hernandez, J. J.: "Stochastic Imaging of the Wilmington Clastic Sequence", paper SPE 19857, presented at the 1989 Annual Technical Conference and Exhibition, San Antonio, Oct. 8-11.

7. Hewett, T. A.: "Fractal Distributions of Reservoir Heterogeneity and Their Influence on Fluid Transport", paper SPE 15386, presented at the 1986 Annual Technical Conference and Exhibition", New Orleans, Oct. 5-8.

8. Mandlebrot, B. B. and Wallis, J. R.: "Robustness of the Rescaled Range R/S in the Measurement of Noncyclic Long Run Statistical Dependence", Water Res. Res. (Oct. 1969), 5, 5, 967-988.